UNCLASSIFIED

AD 460000

DEFENSE DOCUMENTATION CENTER

FOR

SCIENTIFIC AND TECHNICAL INFORMATION
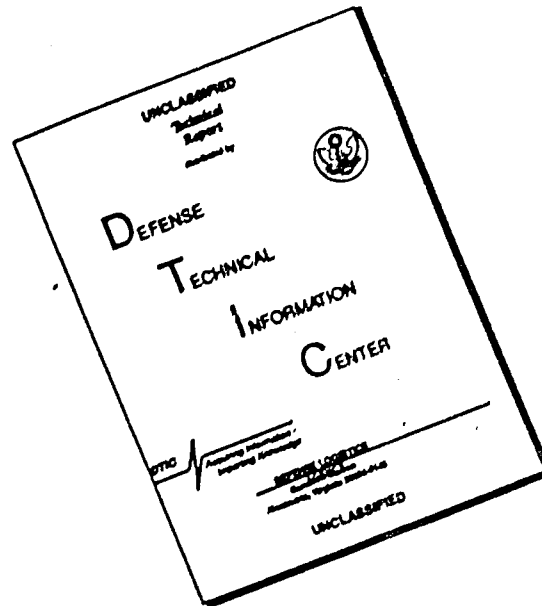
CAMERON STATION ALEXANDRIA, VIRGINIA

UNCLASSIFIED

DISCLAIMER NOTICE

THIS DOCUMENT IS BEST
QUALITY AVAILABLE. THE COPY
FURNISHED TO DTIC CONTAINED
A SIGNIFICANT NUMBER OF
PAGES WHICH DO NOT
REPRODUCE LEGIBLY.

THE
SHOCK AND VIBRATION
BULLETIN

DECEMBER 1964

A Publication of
THE SHOCK AND VIBRATION
INFORMATION CENTER
U.S. Naval Research Laboratory, Washington, D.C.

Office of
The Director of Defense
Research and Engineering

THE
SHOCK AND VIBRATION
BULLETIN

DECEMBER 1964

A Publication of
THE SHOCK AND VIBRATION
INFORMATION CENTER
U.S. Naval Research Laboratory, Washington, D.C.

The 34th Symposium on Shock, Vibration
and Associated Environments was held in
Pacific Grove, California on 13-15 ` ober
1964. The Army was host.

Office of
The Director of Defense
Research and Engineering

CONTENTS

PART 2

Mathematical Analysis

Computers in Design

Design Teehniques

PAPERS APPEARING IN PART 1
Part I - Confidential
(Titles Unclassified)

PROGRESS IN THE NAVY'S WAR ON SHOCK
    H. L. Rich, David Taylor Model Basin

FACTORS AFFECTING THE DEFINITION OF DESIGN AND TESTING CRITERIA FOR
    NAVAL SHOCK RESISTANT EQUIPMENT
    P. B. Wishart, Naval Construction Research Establishment

ANALYTICAL METHODS FOR PREDICTION OF MECHANICAL SHOCK ENVIRONMENT
    FOR SHIPBOARD EQUIPMENT OF SUBMARINES SUBJECTED TO UNDERWATER
    EXPLOSIONS
    M. Pakstys, Jr., General Dynamics/Electric Boat

GROWTH IN SHOCK AND VIBRATION ANALYSIS AND CORRESPONDING
    DESIGN IMPROVEMENTS
    E. G. Fischer, C. R. Brown, and A. A. Parr, Westinghouse Electric Corporation

PAPERS APPEARING IN PART 3

Mechanical Impedance

Shock and Vibration Isolation

Shock

PAPERS APPEARING IN PART 4

Instrumentation

Section 1
MATHEMATICAL ANALYSIS

PREDICTION OF LAUNCH VEHICLE TRANSONIC BUFFETING FROM WIND TUNNEL DATA

R. E. Bieber
Lockheed Missiles and Space Company
Huntsville, Alabama

A problem which has attracted widespread attention in recent years is prediction of the dynamic response of a vertical-rising ballistic missile or spacecraft to random pressure fields which occur during transonic flight. Because of the practical importance of this problem extensive wind tunnel measurements have been made on rigid scale models of various vehicle configurations. Time histories of the unsteady pressures have been obtained by means of closely-spaced pressure transducers located at the model surface. The present paper develops a method for applying empirical wind tunnel data of this type to the prediction of the beam bending response of a full-scale vehicle.

The wind tunnel measurements are used to formulate a model of the inflight random pressure field. This requires application of best available scaling laws to the wind tunnel data. A statistical model which synthesizes the random pressure field as a process nonstationary in space but stationary in time is employed.

From the mode shapes of the dynamic system and unsteady pressure field empirical model, the statistics of the generalized forces are solved for. The problem then reduces to one of spectral analysis of a multi-dimensional linear system. Finally, the methods developed have been applied to the calculation of the transonic buffet bending moment response for a particular launch vehicle.

INTRODUCTION

Wind tunnel and flight test measurement programs reveal that conventional launch vehicles develop boundary layer turbulence during transonic flight. This excitation and resulting vibration is generally referred to as transonic buffeting. Here "transonic" is used loosely since this buffet phenomenon can occur over a wide range of Mach numbers depending on the body shape. A comprehensive review of launch vehicle buffeting is given by Rainey [1]. The present paper develops an analytical method for predicting the vibration response of the full-scale vehicle from fluctuating pressure data collected in wind tunnel tests of rigid scale

models. Among those who have applied such methods to actual vehicles are Goldberg [2] and Bieber [3].

The turbulent aerodynamic boundary layer can excite both local panel vibrations and gross elastic body motions of the vehicle. In the present paper the vehicle will be synthesized as a beam and the bending response studied; however, similar techniques can be applied to the panel vibration problem.

The following assumptions will be used in solving for the statistics of the beam bending moment response.

1. The pressure fluctuations in the turbulent boundary layer can be represented as a normal random process, nonstationary in space, but stationary in time.

1

2. The unsteady pressures as measured at the surface of the body are unaffected by lateral motions of the body. Thus "rigid" model pressure measurements can be employed.

3. Fluctuating pressure data can be scaled from model to full-scale vehicle.

4. Linear equations of motion are valid.

In regard to the first assumption, for actual flight through the transonic region the random pressure field is nonstationary in both time and space. Therefore, the mean-square buffet response at some location on the vehicle will start at some low level of intensity, build up to some maximum intensity, and then decay to some low level again. In order to simulate this nonstationary effect the transient response to a stationary random pressure field suddenly impressed on the system will be investigated.

WIND TUNNEL DATA

Wind tunnel tests performed over the past few years on launch vehicle scale models have provided a valuable source of experimental data for flight dynamic analyses. In Refs. 4-7 a large volume of unsteady pressure data collected from wind-tunnel tests of rigid scale models is presented. The tests were conducted in the Ames Research Center's 14-foot transonic wind tunnel with a nominal Mach number range of 0.60 to 1.20. The longitudinal distribution of fluctuating pressure was measured by means of closely spaced pressure transducers mounted along the top center-line of each of the models for various positive and negative angles of attack. A large number of model configurations ranging from simple cone-cylinder shapes [7] to complicated "hammerhead" shapes [6] were tested. Also, in Ref. 8 unsteady pressure data collected on 1.6 and 8 percent scale models of a large manned space vehicle mounted in the Langley Research Laboratory 16-foot transonic tunnel are presented.

For both the Ames and Langley tests a statistical description of the random pressures in the form of ΔC_p (rms) versus model station is given. Spectral density analyses were performed on a limited number of measurements. Since the data were intended primarily for low frequency aeroelastic response studies the frequency range of the model data is limited to approximately 500 cps.

MODEL OF RANDOM PRESSURE FIELD

For the type of wind tunnel data discussed in the previous section it is desired to construct a model for the random pressure field. Consider any pair of fluctuating pressure measurements $p(x, \theta, t)$ and $p(\xi, \upsilon, t)$, where (x, θ) and (ξ, υ) are locations on the surface of the model and $0 \le t \le T$. The pressures of interest will always be measured from the static or steady pressure level so that time averages are zero:

$$E[p(x, \theta, t)] = E[p(\xi, \upsilon, t)] = 0 . \tag{1}$$

Since the pressure process is assumed normal or Gaussian, the construction of an empirical model reduces to finding a suitable correlation function, i.e.,

$$\rho_p(x, \xi, \theta, \upsilon, \tau) = \frac{E[p(x, \theta, t)\ p(\xi, \upsilon, t + \tau)]}{\sigma_p(x, \theta)\ \sigma_p(\xi, \upsilon)} . \tag{2}$$

where σ_p is the measured rms pressure and a function of the spatial coordinates (nonstationary) and ρ_p is the correlation function but assumed to be only a function of the difference in time (stationary).

Unfortunately the average products $E[p(x, \theta, t)\ p(\xi, \upsilon, t + \tau)]$ required in Eq. (2) are usually not obtained in the reduction of the wind tunnel data; consequently certain assumptions must be made about the form of the correlation function.

Perhaps the simplest model is one which is separable into spatial and temporal correlation functions,

$$\rho(x, \xi, \theta, \upsilon, \tau) = f(|x - \xi|)\ g(|\theta - \upsilon|)\ h(\tau) . \tag{3}$$

where $f(\ )$, $g(\ )$, and $h(\ )$ each have the properties

$$f(\lambda) = f(-\lambda)$$
$$|f(\lambda)| \le 1 \tag{4}$$
$$f(0) = 1 .$$

The spectral density corresponding to Eq. (3) also has a simple form,

$$\Phi_p(\omega; x, \xi, \theta, \upsilon) = \sigma_p(x, \theta)\ \sigma_p(\xi, \upsilon)$$
$$\times\ f(|x - \xi|)\ g(|\theta - \upsilon|)\Phi(\omega) . \tag{5}$$

where

$$\Phi(\omega) = \frac{2}{\pi} \int_0^\infty \cos \omega\tau\ h(\tau)\ d\tau . \tag{6}$$

The spectral density function Eq. (5) is in general complex; however, in this particular case

the imaginary part (quadspectrum) vanishes. Also the real part (cospectrum) differs from any primary spectrum only by a scale factor; the primary spectrum being defined as,

$$\Phi_p^*(\omega; x, \theta) = \sigma_p^2(x, \theta) \; f(0) \; g(0) \; \Phi(\omega)$$
$$\sigma_p^2(x, \theta) \; \Phi(\omega) . \tag{7}$$

The most commonly assumed form of the correlation function incorporates a convecting field velocity, V_c

$$\rho = f(|x - \xi| - V_c \tau) \; g(|\theta - \vartheta|) \; h(\tau) . \tag{8}$$

This model has been used successfully in describing the behavior of the turbulent boundary layer along solid walls. For the three-dimensional bodies of interest there are indications [1] that the convecting pressure field feature is present but not as predominant as in the solid wall experiments.

In the following sections, the beam vibration response due to a random pressure field with separable correlation function Eq. (3) will be derived. Whether the separable model, the convecting model, or some other model is the most realistic one, however, will require considerably more wind tunnel data reduced to the form of correlation functions or alternately spectral density functions.

SCALING LAWS

Scaling laws applicable to the model fluctuating pressure data are the object of continuing research. Wind tunnel test programs are in progress for establishing empirical scaling laws from tests of different percent scale models. In the present paper, very simple scaling laws are proposed. These have been partially substantiated by experiment.

The rms or standard deviation of the fluctuating pressure will be scaled by the dynamic pressure, i.e.,

$$\sigma_{p_2} = \frac{\tilde{q}_2}{\tilde{q}_1} \sigma_{p_1} , \tag{9}$$

where

p_1 = model fluctuating pressure,

p_2 = corresponding full-scale pressure, and

$\tilde{q}$ = dynamic pressure.

In the notation of Refs. 4-8 the full-scale ΔC_p (rms) is identical to that of the model.

The question of the nondimensional frequency to be used in scaling the spectral density function is more difficult. Most investigators propose some form of the "Strouhal number," i.e.,

$$s = \frac{\omega \ell}{V} . \tag{10}$$

where

ω = frequency,

ℓ = characteristic length, and

V = velocity.

The characteristic length will be taken as the main body diameter (the turbulent boundary layer thickness is almost universally accepted for boundary layer noise along solid walls). For velocity the free stream velocity will be used. The frequency scaling then becomes

$$\omega_2 = \frac{V_2}{V_1} \frac{D_1}{D_2} \omega_1 , \tag{11}$$

which together with Eq. (9) determines the scaling of the spectral density function.

$$\Phi_{p_2}(\omega_2) = \left(\frac{\tilde{q}_2}{\tilde{q}_1}\right)^2 \frac{V_1}{V_2} \frac{D_2}{D_1} \Phi_{p_1}(\omega_1) \tag{12}$$

In Ref. 8 the proposed scaling laws resulted in fair agreement between results obtained on the 1.6 and 8 percent models.

EQUATIONS OF MOTION

In predicting the response of a dynamic system to random excitation, except in a few special cases, one is limited to linear systems. For the beam vibration problem under consideration modal analysis techniques will be applied. Thus, second order linear differential equations in the generalized coordinates will be solved.

For a vehicle with control elements these equations are usually coupled, i.e.,

$$\sum_{j=1}^{n} \left(A_{ij}\ddot{q}_j(t) + B_{ij}\dot{q}_j + C_{ij}q_j(t)\right) = Q_i(t), \tag{13}$$
$$i = 1, 2, \ldots n,$$

where $q(t)$ is the generalized displacement and $Q(t)$ is the generalized force. In a dynamic loads analysis, however, uncoupled equations will usually suffice. In the present analysis, the following simplified equations will be used.

$$\ddot{q}_i(t) + B_i \dot{q}_i(t) + \omega_i^2 q_i(t) = \frac{Q_i(t)}{G_i} , \qquad (14)$$

$$i = 1, 2, \ldots n ,$$

where B_i is the ith mode damping coefficient, ω_i the elastic beam natural frequency, and G_i the generalized inertia. The damping coefficient B_i is assumed to be of the form

$$B_i = a_i + b_i + c_i , \qquad (15)$$

where a_i, b_i, and c_i represent structural, control system, and aerodynamic damping, respectively.

For a practical vehicle structure the natural frequencies can usually be computed with reasonable accuracy. The structural, control system, and aerodynamic damping are, however, extremely difficult to predict and conservative estimates or experimental data are often needed.

In the present study the bending moment will be considered as the significant structural response. In terms of the modal displacements,

$$M(x, t) = \sum_{i=1}^{n} M_{1i}(x) \, q_i(t) . \qquad (16)$$

The unit moment $M_{1i}(x)$ is computed by

$$M_{1i}(x) = \omega_i^2 \int_0^x d_{x_2} \int_0^{x_2} m(x_1) \, \phi_i(x_1) \, dx_1 , \qquad (17)$$

where $m(x)$ is the beam mass distribution and $\phi_i(x)$ the mode shape.

MEAN-SQUARE RESPONSE

Under the assumption of normal random pressure field and linear equations of motion the bending moment response is also normally distributed. The statistics of the bending moment at a particular station are sought. Since the time average of the unsteady pressure was taken as zero, the average bending moment is also zero. Therefore, the problem reduces to solving for the variance which is also the mean-square response in this case.

From the bending moment as given by Eq. (16), the mean-square can be written

$$E\left[M^2(x, t)\right] = \bar{M}^2(x) = \sum_i M_{1i}(x) \, \bar{q}_i^2$$
$$+ 2 \sum_{i \neq j} M_{1i}(x) \, M_{1j}(x) \, \overline{q_i q_j} . \qquad (18)$$

The variances $\bar{q}_i^2$ and cross-variances $\overline{q_i q_j}$ are, however, not easily obtainable. In fact, it is first necessary to solve for the statistics of the generalized forces. Subsequently $\bar{q}_i^2$, $\overline{q_i q_j}$, and $\bar{M}^2(x)$ will be found by introducing an "equivalent white noise" spectral density for the generalized forces and then applying multi-dimensional spectral analysis.

From the definition of generalized force,

$$Q_i(t) = N(x, t) \, \phi_i(x) \, dx \qquad (19)$$

the cross-correlation can be written,

$$E\left[Q_i(t) Q_j(t+\tau)\right] = E\left[\int_0^L N(x, t) \, \phi_i(x) \, dx \right.$$

$$\times \left. \int_0^L N(\xi, t+\tau) \, \phi_j(\xi) \, d\xi\right]$$

$$= \int_0^L \phi_i(x) \, dx \int_0^L \phi_j(\xi)$$

$$\times E\left[N(x, t) N(\xi, t+\tau)\right] d\xi . \qquad (20)$$

In terms of the random pressure field the normal force, $N(x, t)$, is
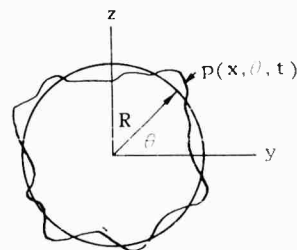
$$N(x, t) = R(x) \int_0^{2\pi} p(x, \theta, t) \sin \theta \, d\theta \qquad (21)$$

and

$$E\left[N(x, t) N(\xi, t+\tau)\right] = R(x) \, R(\xi) \int_0^{2\pi} \sin \theta \, d\theta$$

$$\times \int_0^{2\pi} \sin \upsilon \, E\left[p(x, \theta, t) \, p(\xi, \upsilon, t+\tau)\right] d\upsilon . \qquad (22)$$

By substituting for $E\left[p(x, \theta, t) \, p(\xi, \upsilon, t+\tau)\right]$ from Eq. (3),

4

$$E[N(x,t)N(\xi,t+\tau)] = R(x)R(\xi)\int_0^{2\pi} \sigma_p(x,\upsilon)\sin\theta\,d\upsilon$$

$$\times \int_0^{2\pi} \sigma_p(\xi,\upsilon)\sin\upsilon\,f(|x-\xi|)\,g(|\theta-\upsilon|)\,h(\tau)\,d\upsilon . \tag{23}$$

In order to simplify the solution of Eq. (23) the standard deviation of the pressure at a particular station will be assumed constant in the circumferential direction,

$$\sigma_p(x,\theta) = \sigma_p(x) ; \tag{24}$$

then

$$E[N(x,t)N(\xi,t+\tau)] = K^2 R(x)R(\xi)$$

$$\times \sigma_p(x)\sigma_p(\xi)\,f(|x-\xi|)\,h(\tau) \tag{25}$$

with

$$K^2 = \int_0^{2\pi}\sin\theta\,d\theta\int_0^{2\pi}\sin\upsilon\,g(|\theta-\upsilon|)\,d\upsilon . \tag{26}$$

It can be shown that K is bounded by $0 \le K \le 4$. This result is obtained by solving Eq. (25) for the two limiting cases,

(1) $\rho(|\theta-\upsilon|) = \delta(|\theta-\upsilon|)$

(2) $\rho(|\theta-\upsilon|) = 1(|\theta-\upsilon|), \quad 0 \le \theta \le \pi$

$\qquad\qquad = -1(|\theta-\upsilon|), \pi \le \theta \le 2\pi .$

By substituting Eq. (25) into Eq. (20), the cross-correlation function for the generalized forces is finally obtained,

$$E[Q_i(t)Q_j(t+\tau)] = K^2 h(\tau)\int_0^L R(x)\sigma_p(x)\phi_i(x)\,dx$$

$$\times \int_0^L R(\xi)\sigma_p(\xi)\phi_j(\xi)\,f(|x-\xi|)\,d\xi$$

$$= \overline{Q_i Q_j}\,h(\tau) , \quad i,j = 1,\dots,n. \tag{27}$$

From Eq. (27) it can be seen that the generalized forces are also stationary, with spectral density functions

$$\Phi_{Q_i Q_j}(\omega) = \overline{Q_i Q_j}\,\Phi(\omega) , \tag{28}$$

where $\Phi(\omega)$ is given by Eq. (6).

Knowing the spectral density functions Eq. (28), the variances and cross-variances $\bar{q}_i^2$ and $\overline{q_i q_j}$ can be solved for. For instance, if $Q_i(t)$ is "white noise," $0 \le \omega \le \alpha$, with spectrum intensity $\bar{Q}_i^2\Phi$, then an exact solution for the steady-state displacement variance is

$$\bar{q}_i^2 = \frac{\pi \bar{Q}_i^2 \Phi}{2B_i \omega_i^2 G_i^2} . \tag{29}$$

Furthermore, it is well known that for a lightly damped system and a relatively smooth spectrum a good approximation to the displacement variance is

$$\bar{q}_i^2 \cong \frac{\pi \bar{Q}_i^2 \Phi_i}{2B_i \omega_i^2 G_i^2} \tag{30}$$

where Φ_i is the amplitude of the actual spectrum at the natural frequency ω_i. In the present analysis the following "equivalent multidimensional white noise" spectral density model will be used:

$$\Phi_{Q_i Q_j}^{W.N.}(\omega) = \overline{Q_i Q_j}\,\sqrt{\Phi_i}\,\sqrt{\Phi_j}\,1(\omega), \quad i,j=1,\dots,n. \tag{31}$$

By following the methods of Ref. 9, the responses $\bar{q}_i^2$ and $\overline{q_i q_j}$ can be solved for. In Ref. 9 the variance matrix of the response vector of a second order linear differential system acted on by "white noise" forcing functions is determined using the algorithm of the Fokker-Planck equation. A digital computer program was written for carrying out the numerical computations.

Letting r_{ii} and r_{ij} denote the variances $\bar{q}_i^2$ and $\overline{q_i q_j}$ due to unit spectral densities

$$\Phi_{Q_i Q_j}^{W.N.}(\omega) = 1(\omega) , \quad i,j = 1,\dots,n , \tag{32}$$

the mean-square bending moment is given by

$$\bar{M}^2(x) = \sum_i M_{1i}^2(x)\,\bar{Q}_i^2\,\Phi_i\,r_{ii}$$

$$+ 2\sum_{i\neq j} M_{1i}(x)M_{1j}(x)\overline{Q_i Q_j}\sqrt{\Phi_i}\,\sqrt{\Phi_j}\,r_{ij}. \tag{33}$$

The question arises as to how this mean-square response builds up with time. This nonstationary part of the solution can also be obtained by the methods of Ref. 9. For the lightly damped system under consideration, however, a good approximation to the transient mean-square bending moment is given by

5

$$\overline{M}^2(x,t) = \sum_i M_{1i}^2(x)\,\overline{q}_i^2 \left[1 - e^{-B_i t}\right]$$

$$+ 2 \sum_{i \neq j} M_{1i}(x)\,M_{1j}(x)\,\overline{q_i q_j} \left[1 - e^{-\left(\frac{B_i + B_j}{2}\right)t}\right].$$

$$(34)$$

APPLICATION TO LAUNCH VEHICLE

The methods developed will be applied to the prediction of transonic buffet loads for a full-scale launch vehicle. The vehicle configuration is shown in Fig. 1. The results obtained are presented in greater detail in Ref. 2.

Scale model wind tunnel tests were performed in the Ames Research Laboratory's 14-foot transonic tunnel. The critical distribution of rms fluctuating pressure during these

tests occurred at a Mach number of 0.80 and angle-of-attack of 4 degrees. In Fig. 1, $\triangle C_p$ (rms) as measured along the top centerline of the model (windward side for $\alpha = -4$ degrees) is shown. Results for $\alpha = +4$ degrees could also have been used since there was little difference between the windward and leeward side rms pressures. The $\triangle C_p$ (rms) distribution provides the function, $\sigma_p(x)$, required in the mean-square response computation.

The first three bending mode shapes for the vehicle are plotted in Fig. 2 along with a listing of the first three natural frequencies and generalized inertias. The lowest natural frequency is 2.54 cps.

A very important system parameter in this type of analysis is the damping. The structural damping was conservatively estimated at 1/2 percent critical for the first mode and 1 percent for the higher modes. The control system
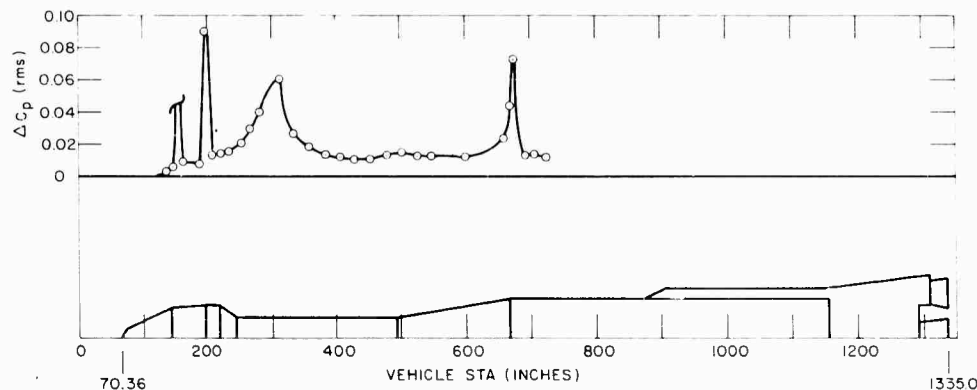
Fig. 1 - Advent 0.1 scale model rms pressure -- M = 0.80, α = -4 degrees
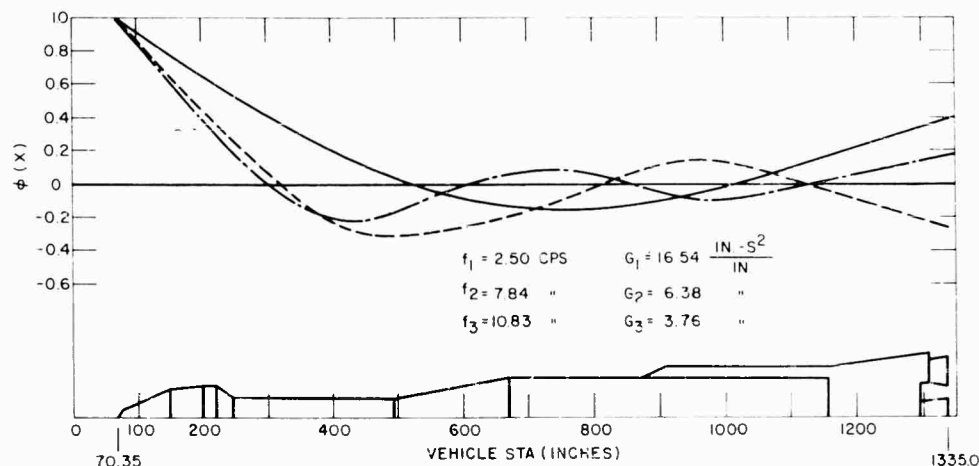
Fig. 2 - Advent elastic bending modes

6

and aerodynamic contributions were obtained by analysis. The total in percent critical for the first three modes is tabulated below.

Mode	B_i (Percent Critical)
1	1.575
2	1.255
3	1.465

Since no spectral density analyses were performed on this model data, a spectral density shape obtained for the vehicle of Ref. 2 was used in determining the values Φ_i for the "equivalent multi-dimensional white noise" spectral density, i.e.,

$$\Phi_{Q_i Q_j}^{W.N.}(\omega) = \overline{Q_i Q_j} \sqrt{\Phi_i} \sqrt{\Phi_j} \; 1(\omega) . \quad (35)$$

After applying the scaling laws Eq. (11) and Eq. (12) the following spectral density heights were obtained:

$$\Phi_1 = 0.012 ;$$

and

$$\Phi_2 = 0.007 ;$$

$$\Phi_3 = 0.007 .$$

The cross-variances $\overline{Q_i Q_j}$ were computed according to Eq. (27),

$$\overline{Q_i Q_j} = K^2 \int_0^L R(x) \, \sigma_p(x) \, \phi_i(x) \, dx$$

$$\times \int_0^L R(\xi) \sigma_p(\xi) \phi_j(\xi) f(|x-\xi|) d\xi . \quad (36)$$

Since no circumferential correlation data was available for estimating, $\rho(|\theta - \nu|)$, the value of K from Eq. (26) could not be computed. An intermediate value ($0 \leq K \leq 4$) of $K = 2$ was selected.

The longitudinal correlation, $f(|x-\xi|)$, occurring in Eq. (36) has an extremely important effect on the final results; consequently several parametric cases were considered (again in the absence of data reduced to correlation or cross-spectral density form).

1. $f(|x-\xi|) = f(\lambda) = \delta(\lambda)$,
   zero correlation,

2. $f(\lambda) = 1(\lambda)$,
   unit correlation,

3. $f(\lambda) = e^{-\lambda/52.22}$,   (37)
   2-diam correlation,   (Cont.)

4. $f(|x-\xi|) = f(\lambda) = e^{-\lambda/26.11}$,
   1-diam correlation, and

5. $f(\lambda) = e^{-\lambda/13.05}$,
   1/2-diam correlation.   (37)

Cases 1 and 2 are the limiting cases of "independent observations" and "perfect correlation." Cases 3-5 refer to $f(\lambda)$ decaying to 1 percent of its maximum value in two-main body diameters, one-main body diameter, and one-half-main body diameters, respectively.

For the zero correlation case the computation of $\overline{Q_i Q_j}$ from Eq. (36) reduces to solving

$$\overline{Q_i Q_j} = K^2 \int_0^L R^2(x) \sigma_p^2(x) \phi_i(x) \phi_j(x) \, dx , \quad (38)$$

and for unit correlation,

$$\overline{Q_i Q_j} = K^2 \left[\int_0^L R(x) \sigma_p(x) \phi_i(x) \, dx \right]$$

$$\times \left[\int_0^L R(x) \sigma_p(x) \phi_j(x) \, dx \right] . \quad (39)$$

For cases 3-5 a matrix solution was used.

$$\overline{Q_i Q_j} = \Delta x^2 K^2 [\phi] [R(x) \sigma_p(x)]$$

$$\times [f|x-\xi|] [R(x)\sigma_p(x)]^T [\phi]^T . \quad (40)$$

The ith row of the ϕ matrix is the ith mode shape evaluated at equal intervals $x_1, \ldots, x_k$. The matrix $R(x)\sigma_p(x)$ is a k×k diagonal matrix. The correlation matrix $f(|x-\xi|)$ is a k×k symmetric matrix with unit diagonal elements and equal elements equal distances away from the diagonal.

The variances r_{ii} and cross-variances r_{ij} due to unit white noise spectral density Eq. (32), were computed by the methods of Ref. 9. The mean-square bending moment (using the first three bending modes) was computed from Eq. (33). The first bending mode contributed greater than 95 percent of the total.

The 3σ extreme value bending moments versus vehicle station for each of the five cases of longitudinal correlation are plotted in Fig. 3. One can observe that the extreme values for the unit correlation case are approximately ten times those for the zero correlation case. Although final judgment must be reserved
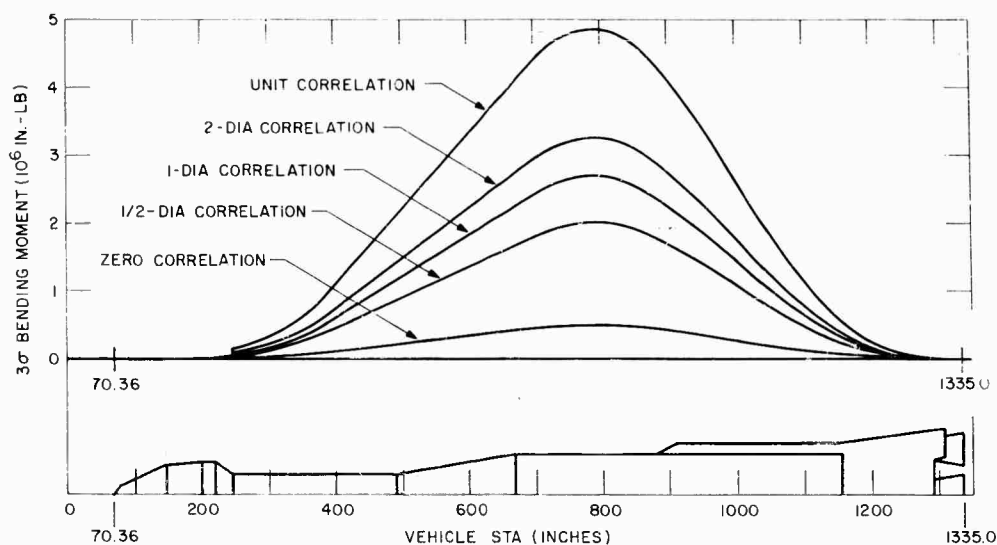
Fig. 3 - Advent 3σ bending moment distribution

until actual correlation data is available, both of the limiting cases are considered unreasonable. The one-diam correlation results were used as transonic buffeting design limit loads for this particular vehicle.

Figure 4 shows the buildup of the transient mean-square response versus time. Assuming that the transonic fluctuating pressure field exists over a Mach number range corresponding to a flight time of 10 seconds, then the transient mean-square will achieve approximately 99 percent of its steady-state value.

Finally it should be pointed out that the above results are those due to the transonic random pressure field. These must be combined in a rational way with the wind or other
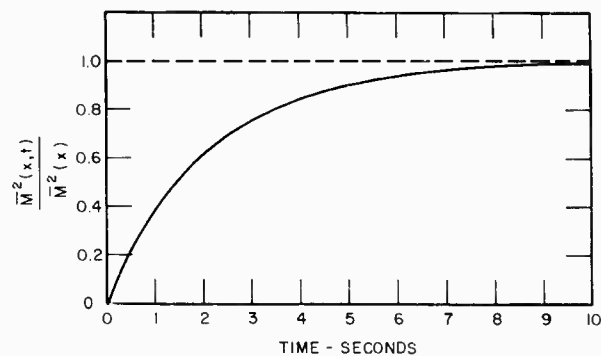
Fig. 4 - Advent mean-square bending moment versus time

steady loading occurring during transonic flight in obtaining the total flight loads for this condition.

REFERENCES

1. A. G. Rainey, "Progress on the Launch-Vehicle Buffeting Problem," AIAA Fifth Annual Structures and Materials Conference, Palm Springs, Calif. (Apr. 1964).

2. A. P. Goldberg and J. D. Wood, "Dynamic Loads in the Atlas—Able 5 During Transonic Buffeting," Space Technology Laboratories, STL TM-600-0000-19075 (1960).

3. R. E. Bieber, "Estimated Advent Load Response to Transonic Random Pressure Field," Lockheed Missiles and Space Company, LMSC 448565 (1961).

4. C. F. Coe, "Steady and Fluctuating Pressures at Transonic Speeds on Two Space Vehicle Payload Shapes," National Aeronautics and Space Administration, NASA TM X-503 (1961) (Confidential).

5. C. F. Coe, "The Effects of Some Variations in Launch Vehicle Nose Shape on Steady and Fluctuating Pressures at Transonic Speeds," National Aeronautics and Space Administration, NASA TM X-646 (1962) (Confidential).

6. J. B. Nute, "Steady and Fluctuating Pressures at Transonic Speeds on Hammerhead Launch

Vehicles," National Aeronautics and Space Administration, NASA TM X-778 (1962) (Confidential).

7. C. F. Coe and A. J. Kaskey, "The Effects of Nose Bluntness on the Pressure Fluctuations Measured on 15- and 20-Degree Cone Cylinders at Transonic Speeds," National Aeronautics and Space Administration, NASA TM X-779 (1963) (Confidential).

8. G. W. Jones, Jr. and J. T. Toughner, Jr., "Investigation of Buffet Pressures on Models of Large Manned Launch Vehicle Configurations," National Aeronautics and Space Administration, NASA TM D-1633 (1963).

9. M. C. Wang and G. E. Uhlenbeck, "On the Theory of Brownian Motion II," Reviews of Modern Physics, Vol. 17, No. 2 and 3 (April-July 1945).

*   *   *

SPACECRAFT ADAPTER RESPONSE TO FLUCTUATING PRESSURE

George A. Watts
NASA Manned Spacecraft Center
Houston, Texas

The bluffness of manned spacecraft launch configurations causes the transonic aerodynamic regime to begin at low subsonic Mach numbers. The sharp corners cause separated flow with oscillating shocks at the points of reattachment; and protrusions and bracings cause thick boundary layers of turbulence. These in turn, produce an intense, randomly-fluctuating pressure field over the surface of the spacecraft, its adapter, and the booster forebody (Fig. 1).

individual vibration modes. For shells of conventional manufacture these modes are lightly damped and consist of combinations of numbers of circumferential waves and axial half-waves (Fig. 2). The natural frequencies and detailed shapes depend on the mass and stiffness distributions of the walls. Each mode has a generalized (or effective) mass (M_n) which is found by summing up the masses of all elements of the shell after each has been weighted by the square of its modal displacement.

Fig. 1 - Typical space vehicle configuration showing transonic aerodynamics

A) TWO AXIAL HALF WAVES

B) SIX CIRCUMFERENTIAL WAVES
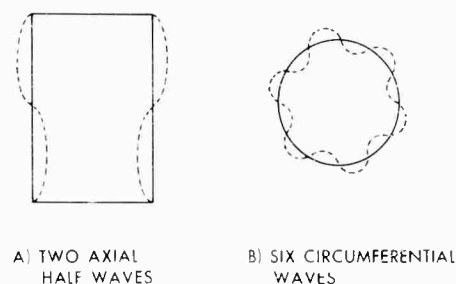
Fig. 2 - Typical shell mode shapes

Adapters generally are cylindrical shell-like structures reinforced by a few shallow rings and longitudinal stiffeners. They are not normally pressure stabilized, as are the booster tanks, nor are they attached to strong pressurized cabins, as are the spacecraft walls. This makes them uniquely vulnerable to the fluctuating pressure environment.

The response of the adapter may be assumed to be the sum of the responses of its

The response of each mode depends on its damping, natural frequency, generalized mass, and the generalized force produced by the random pressure field on that mode. The generalized force is the sum of the forces (pressure-times-area) acting on elements of area weighted by modal displacement. Since the pressure on each element of area is a function of time, the generalized force is a function of time also. In the present case this force is a stationary random function of time and may be characterized by a power spectrum $f_n(\omega)$, that is,

$$\frac{(\text{force})^2}{\text{radian per second}}$$

which is a function of frequency.

The mean squared response of the nth mode, treated as a single degree of freedom [1], is then

NOTE: References appear on page 18.

$$\bar{w}_n^2 = \frac{\pi}{4\gamma_n} \frac{f_n(\omega_n)}{M_n^2 \omega_n^3} ,$$

where

w_n = displacement of nth mode at its nondimensionalizing point,

γ_n = damping of the nth mode, C/C_{cr},

M_n = generalized mass of the nth mode,

ω_n = natural frequency of the nth mode, rad/sec, and

$f_n(\omega_n)$ = generalized force power spectral value at the natural frequency of the nth mode.

The generalized force depends on two characteristics of the pressure field; the pressure power spectrum $\Phi(\omega)$, that is

$$\frac{(psi)^2}{radian\ per\ second}$$

as a function of frequency, and its distribution over the shell surface, and the nondimensionalized pressure cross-correlation power spectrum $\varphi_{ij}(\omega)$ between pairs (ij) of areal elements which make up the shell. The power spectrum $\psi_{ij}(\omega)$ is the average value of the cosine of the phase difference of the pressures at the points i and j at the frequency ω. The generalized force power spectrum is readily calculated in the following way: [2]

$$f_n(\omega) = (W_1^n S_1)^2 \Phi_1 + 2W_1^n W_2^n S_1 S_2 \varphi_{12} \Phi_1^{1/2} \Phi_2^{1/2}$$

$$+ 2W_1^n W_3^n S_1 S_3 \varphi_{13} \Phi_1^{1/2} \Phi_3^{1/2} + \ldots$$

$$+ (W_2^n S_2)^2 \Phi_2 + 2W_2^n W_3^n S_2 S_3 \varphi_{23} \Phi_2^{1/2} \Phi_3^{1/2} + \ldots$$

$$+ (W_3^n S_3)^2 \Phi_3 + \ldots$$

where

W_1^n, W^n = normalized displacements of the nth mode at the points 1, 2, . . . on the surface of the shell

S_1, S_2 = elements of shell surface area associated with each point

φ_{12} = normalized pressure cross-correlation power spectrum between points 1 and 2

Φ_1 = pressure power spectral density at point 1.

It is, therefore, a straightforward problem to calculate the rms response of each mode and, from knowledge of the mode shape, determine the rms displacement or acceleration at any point of the shell. It is also possible to factor each element of mass of the shell by its acceleration and thus determine the structural loading in the mode. From this loading the distribution of stresses throughout the shell in this mode can be analyzed.

The stress in a single mode is a random sine function of time with the number of peaks, per unit increase in amplitude per 100, rapidly decreasing with increasing amplitude in what is known as a Rayleigh [3] distribution.

The rms stress for all modes at a point in the structure is obtained by summing the squares of the rms stress of each of the modes at that point and taking the square root. The distribution of peaks is then between a Rayleigh distribution and a normal, or Gaussian, distribution depending on the number of modes and the contributions by each mode.

To obtain the complete stress picture at the point in the shell, the static stresses due to overall body loads and static pressure differences must be added to the dynamic stresses. From this point forward, the assessment of structural adequacy becomes a matter of philosophy, none of which is very sound. One line of reasoning supposes that "nature opposes infinities" and limits dynamic stresses to an upper bound. This upper bound is often taken as three times the rms value (or 3 sigma). The 3 sigma value plus static stress is then treated as a limit stress at which the structure will not yield. If, for example, an ultimate factor of 1.5 is applied to the limit, the structure will not fail at that stress.

Another line of reasoning establishes a small allowable failure rate, and then checks to see that statistically this rate is not exceeded. Obviously, assigning any allowable failure rate to a man-carrying vehicle is an odious undertaking.

The mode shapes and frequencies may be determined either by analysis or experimentation, but the structural damping can only be found by experiment. The distribution of stresses can usually be readily calculated for each mode but it can also be found experimentally. The pressure-power spectrum distribution over the shell surface can be found

12

experimentally in wind tunnels, or by flight test. The cross-correlation spectra between pairs of points over the surface alone have defied practical determination by any means. Experimental methods do exist for measuring the cross spectra, but they demand painstaking effort and precision apparatus. This is partly the result of the wind tunnel model data being 1/scale higher than full scale in frequency. The problem is compounded by the need for a much greater amount of cross-correlation data than power spectrum data. In fact, if the shell is broken up into n elements, the number of spectral plots required are n power spectrum and

$$\frac{n}{2}(n-1)$$

cross-spectrum. For example, 100 elements become 100 power spectral plots but close to 5000 cross-correlation spectral plots. In practice, this number can usually be reduced somewhat by ignoring the small values which occur between points great distances apart, but the requirement still hobbles a practical solution.

The lack of cross-correlation data completely frustrates the ability to calculate directly the response of the modes. In searching for a way to circumvent this lack, it was noticed that the first few flights in a series leading to the eventual flights of lightweight production structures employed boilerplate structures of the same external aerodynamic configuration. It was further noticed that, although the boilerplate structure was much heavier and stiffer, it was broken up into panels of approximately the same size as those on the production structure. It appeared that the modes and frequencies of the boilerplate structure would be similar to those of the production structure and should, therefore, in flying along the same trajectory, be excited by similar forcing functions. Furthermore, the strength of the boilerplates would not be in question since the mass of the boilerplates is several times larger than that of the production structures and, therefore, would allow only small deflections.

It was, therefore, decided to determine the modes, frequencies, damping, and generalized masses of the boilerplate vehicles before flight, and then to measure the mean squared response of each of the modes by using accelerometers during the flight test. From these measurements the forcing functions could be deduced from the first equation. Then, even though the actual correlation was not known, the effects of the correlation on the modes would be known, and the forcing functions could be applied directly to a calculation of the response of the

lightweight production structure. It was, in effect, as if the entire boilerplate structure had been calibrated as a microphone and was being used to measure the fluctuating pressures.

The cylindrical boilerplate adapter shell was as shown in Fig. 3. The lowest frequency mode, Fig. 4, had two circumferential waves and a frequency of 47 cps. The mode shape is shown as contours of equal acceleration on the developed surface of the shell; the solid lines showing convex areas, and the dashed lines, the concave. Figures 5-7 show other modes and frequencies up to 267 cps. From these mode shapes and a knowledge of the surface-mass distribution, generalized masses were calculated. The damping ratio of each mode was found by two methods: first, by letting the vibrations decay freely and measuring the logarithmic decrement, and secondly, by measuring the frequency span between the half-power points of the resonant response curve. The two methods agreed well, and the damping ratios are shown by the circles in Fig. 8. For
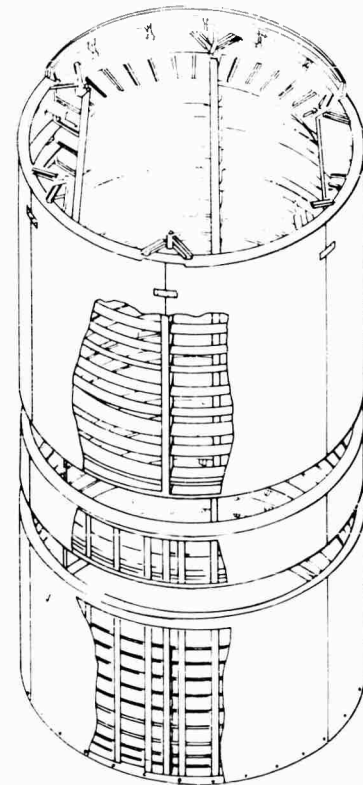
Fig. 3 - Boilerplate adapter construction. Adapter consists of an aluminum shell reinforced by thin rings and stringers attached by rivets.

13
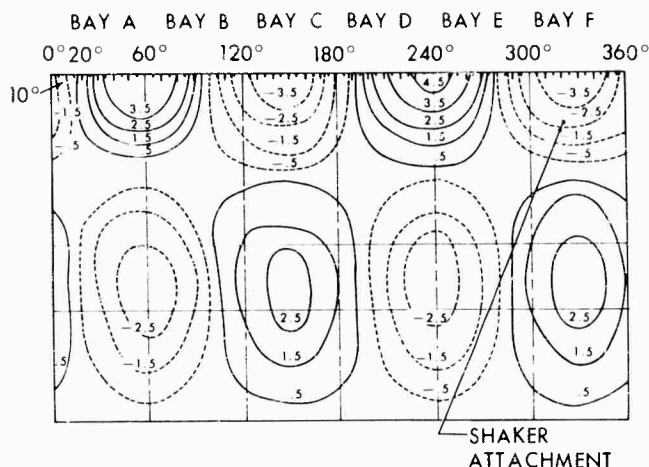
Fig. 4 - Contour map of constant acceleration
for boilerplate adapter--(g's peak) 47 cps
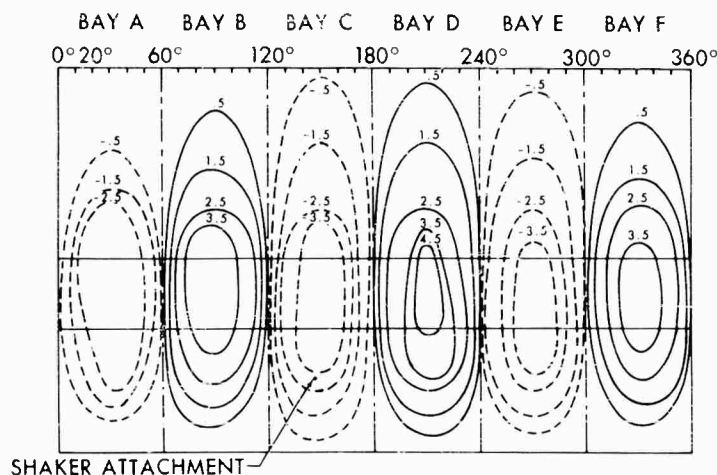
Fig. 5 - Contour map of constant acceleration
for boilerplate adapter--(g's peak) 90 cps

interest's sake, the damping values for a slightly
tapered adapter, 10 feet in diameter and 5 feet
long, made of magnesium skin spot-welded to
magnesium stringers are also sho n. Damping
values for a 16-inch diameter, 16 inches long,
electrodeposited copper shell of very thin walls
are also shown [4].

Although no consistent trend of damping
ratio with either frequency or wave number
could be found, it was generally noted that the
damping was very low, with the bulk of the data
less than 1 percent of critical.

Figure 9 shows a harmonic analysis of the
accelerations measured at a point in the adapter
at the maximum excitation level (that is, M =0.9,

q = 550 psf). Figure 9 also shows responses at
several of the modes defined in the ground tests,
for example, at 141,199, and 267 cps. Rather
large responses are seen at significantly higher
frequencies, but these result in only small de-
flections and correspondingly small stresses,
as shown in the harmonic analysis of stresses
at a point in the shell in Fig. 9.

At the present point in the program, eval-
uation of the forcing functions of the various
modes excited in flight is taking place. Soon
the modes, frequencies, and damping of the pro-
duction structure will be experimentally meas-
ured; the response will be deduced; and a year
or so hence, the verification of the answer in a
production flight test will take place.

14
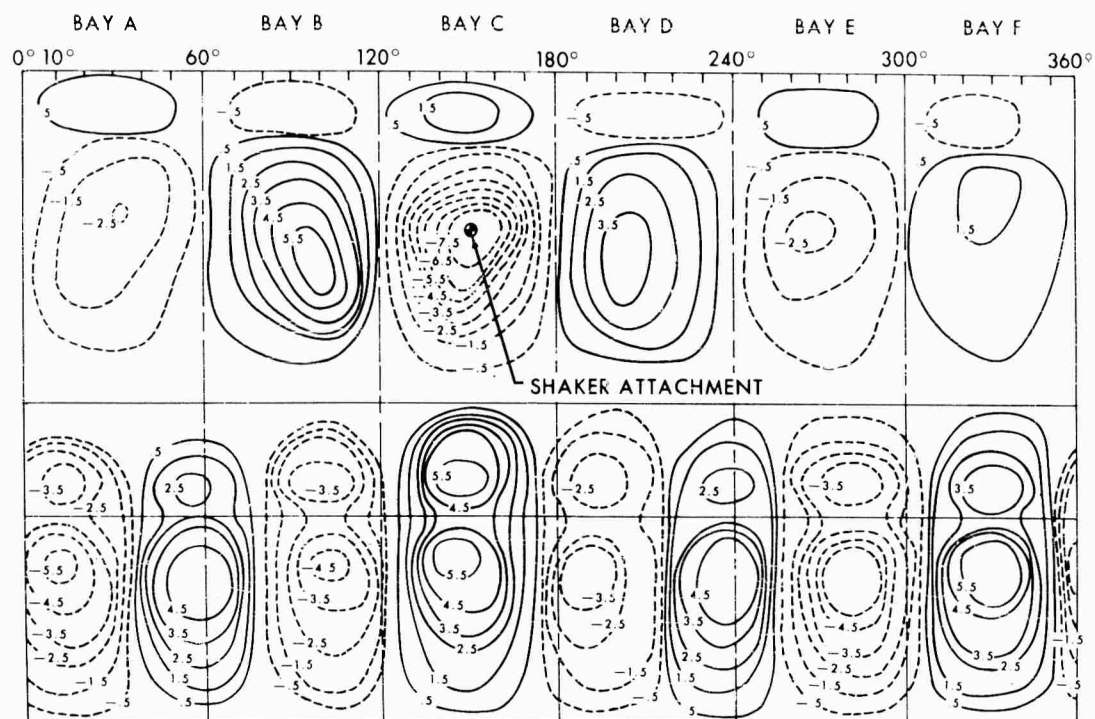
Fig. 6 - Contour map of constant acceleration
for boilerplate adapter--(g's peak) 141 cps
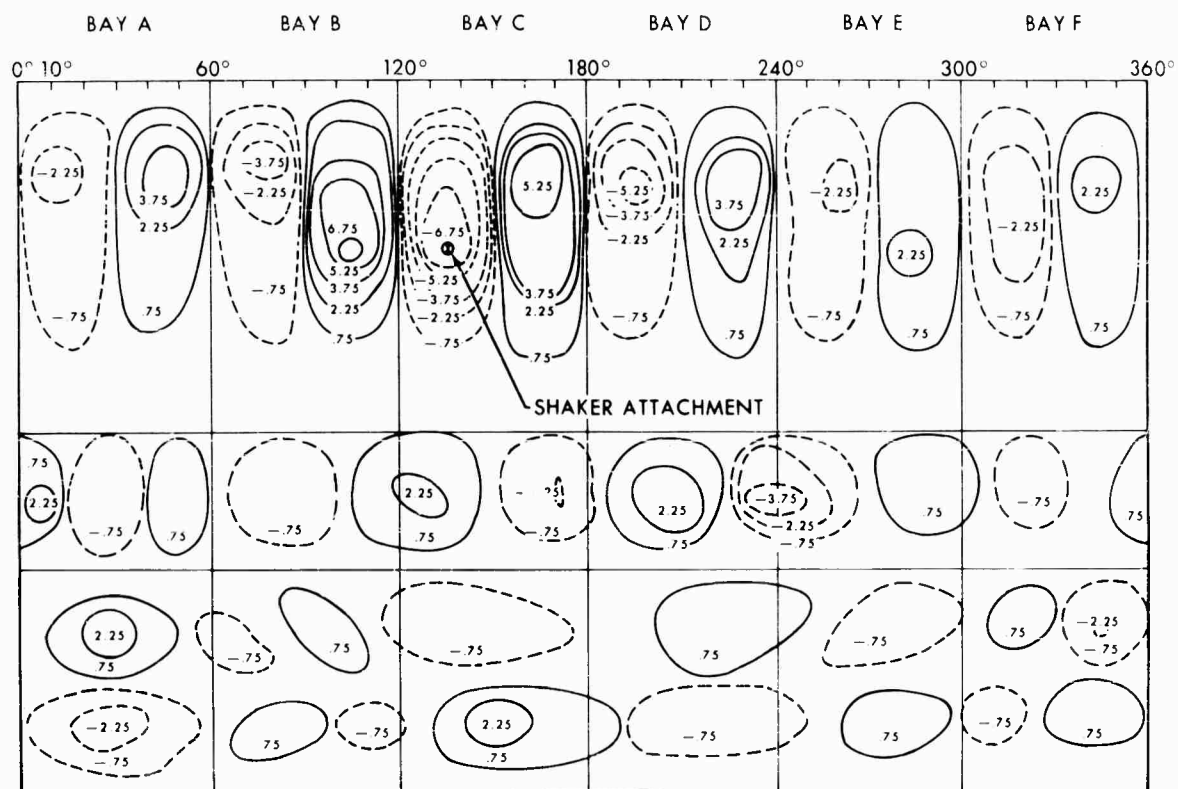
Fig. 7 - Contour map of constant acceleration
for boilerplate adapter--(g's peak) 267 cps

15
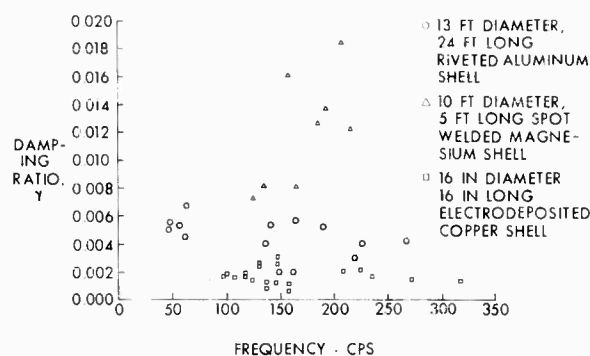
Fig. 8 - Damping ratios for several adapter configurations
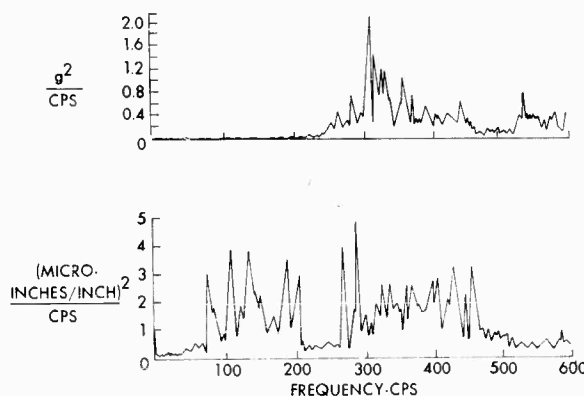
Fig. 9 - Adapter radial acceleration. Power spectrum--(M = 0.9), and adapter strain power spectrum--(m = 0.9).

Generally speaking, it would be desirable to find a way to deduce the response of light-weight production adapters without first having to fly a boilerplate version. An attempt has been made to do this by applying wind-tunnel measured-power spectra and experimental vibration data. Without correlation data on the specific configuration it would be advantageous to know if there were any physical upper and lower bounds to the response of a mode; that is, if forms of the correlation existed which would produce values of the response which could not be exceeded and undershot.

It is clear from the second equation that the maximum response occurs when φ_{ij} is always unity and has the same sign as the product $w_i^n w_j^n$. This is the same as saying that the pressure must be directed inward, wherever the mode is dished in, and directed outward, wherever the mode is dished out, or that the pressures are no longer spatially random but are distributed according to the sign of the mode shape. The magnitude of the pressure at each point would be the spectrum value determined from wind tunnel test.

The minimum response would occur when the φ_{ij} were all zero. This would still yield a response because full correlation would exist across each element of area; however, as elements of area are reduced in size (but increased in number), the response would reduce so that in the limit with zero (or random) correlation the response is zero.

Evaluation of these limits helps the solution of the problem very little because the actual response is generally much less than the maximum. Ratios of the actual rms response of spacecraft adapters to the maximum (or correlation factors C_n) have been evaluated from recent flight test data and are generally less than 0.1.

16

The values of C_n are a function only of air flow geometry, the frequency considered, and the shell mode shape. They are not a function of the intensity of fluctuating pressure, its spectral distribution, or the generalized mass or damping of the mode.

It is hoped that values of C_n can be evaluated for different spacecraft external configurations and adapter modal patterns and frequencies, and that a systematic variation can be found so that boilerplate testing in the future will not be necessary. With this set of data it will then only be necessary to determine the fluctuating pressure intensity and spectral distribution. It is, therefore, important to know if tests on small scale models in wind tunnels will supply this data.

Figure 10 shows the distribution of rms pressure over a spacecraft and its adapter at Mach number = 0.9 and zero angle of attack as observed in flight, and compares it with several values measured in a wind tunnel under the same conditions. It should be noticed that they differ in an inconsistent manner by about 50 percent. At each of the two stations, X = 138 inches and X = 270 inches, pressure power spectra were measured. They are shown in Fig. 11 and are compared with wind tunnel plots corrected to full scale frequency. The distributions are quite similar with peaks occurring at approximately the same frequencies. The squaring of the pressures tends to accentuate the differences. The ragged appearance of the flight data is caused by the narrow band filter.

Answers deduced from present day wind-tunnel data could easily be in error by a factor of two, even if the correct C_n were known.
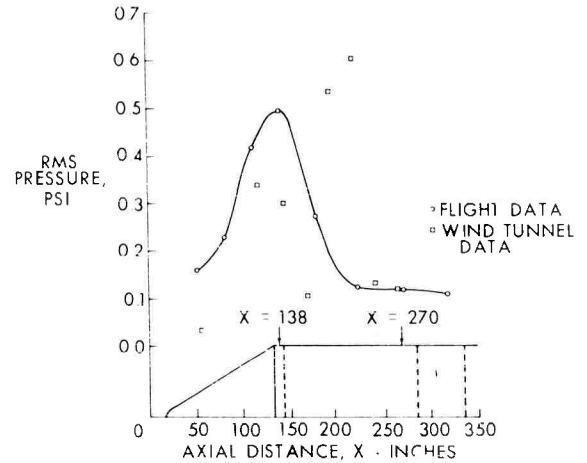
Fig. 10 - Fluctuating pressure distribution (m = 0.9)

CONCLUSIONS

1. Efficient methods to measure pressure cross-correlation power spectra at closely spaced intervals over adapters would greatly aid the prediction of shell mode response.

2. Evaluation of the values of C_n on full scale and model adapters and classifying them according to air flow geometry (vehicle configuration), frequency, and adapter-mode shape should eventually lead to a solution of the response problem without recourse to cross-correlation data.

3. Wind-tunnel techniques and electronic-measuring and data-analysis equipment should
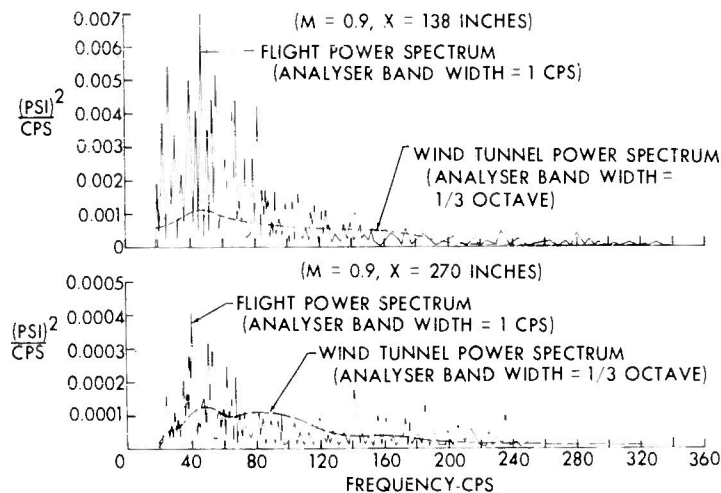
Fig. 11 - Power spectrum of fluctuating pressure

17

be improved so that better agreement with full scale data can be attained.

4. Studies of structural and aerodynamic damping should be pursued to better the understanding of damping at high frequencies.

5. Great improvement is needed in the ability both to predict analytically and to verify experimentally the high frequency mode shapes and frequencies of shell-like structures.

REFERENCES

1. W. T. Thompson and M. V. Barton, J. Appl. Mech., 24, 248-251 (June 1957).

2. Y. C. Fung, "The Analysis of Wind-Induced Oscillation of Large and Tall Cylindrical Structures," Space Technology Laboratories, Inc., STL/TR-60-0000-09134 (June 1960).

3. C. M. Harris and C. E. Crede, Shock and Vibration Handbook (McGraw-Hill Book Company, Inc., New York, N.Y. 1961), Vol. 1, chap. 11, p. 9.

4. G. A. Watts, "Vibration and Damping of Thin-Walled Cylinders," Thesis: California Institute of Technology (1962).

*   *   *

SUBHARMONIC BEHAVIOR OF THIN-WALLED ELASTIC BEAM

Wai Keung Tso
Norair Division
Northrop Corporation
Hawthorne, California

During a resonant testing of thin-walled beams of monosymmetric open section for coupled torsional and bending vibrations, certain nonlinear behavior of the beam was observed. By considering the beam as system, the shaking table excitation the input to the system, and the response of the beam the output of the system, the phenomenon can be described as being a high order subharmonic oscillation of the system under special conditions. When the shaking table frequency was at a multiple or near multiple of the fundamental frequency of the system and the system had one of its higher natural frequencies at the table frequency, the response of the system was made up of both harmonic and subharmonic oscillations, with the subharmonic oscillations having a frequency close to the fundamental frequency of the system.

Alternatively, the phenomenon can be described in terms of the vibrational modes of the beam. When a higher mode was excited externally, the fundamental mode was also excited under special conditions, resulting in a high order subharmonic oscillation of the system. This phenomenon was very critical of the exciting frequency. The range of exciting frequencies over which such subharmonic behavior was possible depended on the amplitude of the external excitation. Also, the transition from harmonic to subharmonic oscillation depended on the path of approach to the critical region. Over a narrow range of exciting frequencies, the system could be shock excited into subharmonic oscillations or could be returned to harmonic oscillations through external means. In other words, there existed two stable steady states within this narrow range of table frequency. The system displayed the "jump" phenomenon as commonly known in nonlinear mechanics.

Such behavior cannot be predicted from the linearized theory of coupled torsional and bending vibrations of thin-walled beams. It is believed that such subharmonic behavior was caused by the nonlinear couplings of the different modes of the system.

INTRODUCTION

Generally when a thin-walled beam of uniform asymmetrical section is subjected to dynamic excitation, both bending and torsional vibrations will result. Due to the low torsional rigidity of thin-walled beams of open section, the problem of coupled bending and torsional vibrations is of particular interest. The existing theories for the coupled vibrations of thin-walled beams of open section are due to Vlasov [1] and Gere [2]. A more refined theory is proposed by Tso [3] which includes the effect of

NOTE: References appear on page 25.

shear strain due to bending and warping of the beam. From the theories, it is shown that the motions of the beam can best be described by three generalized coordinates ζ, η, and θ. ζ and η are displacement coordinates of a section of the beam about the shear center in the directions of the two principal axes of the section, and θ denotes the rotation of the section about the shear center. When the section is asymmetrical, all three generalized coordinates are dynamically coupled. Therefore, even if the external excitation is along a principal direction, all three coordinates will be excited, resulting in coupled torsional and bending vibration. If the section of the beam has one axis of symmetry, say η is directed along the axis of

symmetry, the theories show that the coordinates ζ and θ are dynamically coupled, but the coordinate η is not coupled with the rest of the coordinates. Thus, if the external excitations are in the η direction, only the coordinate η is excited, resulting in uncoupled bending vibrations only. When the excitation is along the ζ direction, both ζ and θ will be excited, leading to coupled torsional and bending vibrations; however, η will not be excited in this case.

The resonant test was carried out on thin-walled sections with one axis of symmetry and the excitation was applied in the direction perpendicular to the axis of symmetry so that coupled torsional and bending vibrations would be excited.

All three theories are linearized theories; the assumption is that the rotation of the section is so small that it is justified to use the approximations $\sin \theta = \theta$, and $\cos \theta = 1$. It was shown experimentally [3] that the theories give good results under most circumstances when the beam is long. Because of the linearization process, however, the theories can predict only harmonic response of the beam under external excitation. The observed nonlinear behavior of the beam during the test necessitates a reexamination of the linearized theories under special conditions.

The phenomenon can be described in terms of the vibrational modes of the beam. Under the condition that a higher mode of the beam had a resonant frequency at a multiple or near multiple of the fundamental frequency, there was a tendency for the fundamental mode to be excited also when the external excitation was at or near the resonant frequency of the higher mode, resulting in a high order subharmonic oscillation. The following is a detail account of the experiment and observations.

EXPERIMENTAL SETUP

The sectional shape of the thin-walled beam used for the test was that of a circular split ring. Such a shape was specified by three parameters, the radius a, the thickness c, and the central angle subtended by the two radii joining the edges of the section to the center 2Φ, as shown in Fig. 1. Such specimens were realized by splitting thin-walled circular aluminum tubes along their lengths with the proper central angle. The actual aluminum tubes used had an outer diameter of 2 inches and a thickness of $1/16$ inch. Two specimens were prepared, one subtending a central angle of 180 degrees (half ring), and the other an angle of

270 degrees. The specimens were examined to insure that any pretwist resulting from the release of internal stresses during the cutting process was negligibly small. One end of the specimen was cast into a block of "Cerobase," a low melting high density alloy, to form a built-in end. The other end was left free so that the system constituted a cantilever. The specimen was cast in such a way that the axis of symmetry of the section would be perpendicular to the direction of the excitation. With the specimen mounted in this way, there would be little or no excitation in the direction parallel to the axis of symmetry and hence the uncoupled bending vibration in that direction would not be excited. The block was mounted rigidly onto the shaking table as shown in Fig. 2.

A Ling shaker was used with a B&K oscillator control to supply the input to the beam.
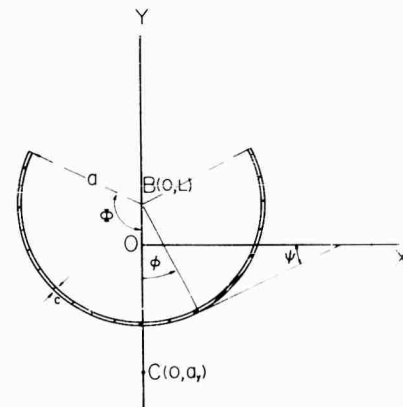
Fig. 1 - Split ring section of semi-central angle Φ

Fig. 2 - Mounting of test specimen on shaker

20

The frequency of the shaker was measured by a counter. By using a 1-second gate time, the frequency of the shaker could be determined to within ±1 cps. The response of the beam was measured by optical means. The Optron Displacement Follower was used. By attaching a special target on the beam, the displacement at that particular point of the beam could be measured by the Optron. A signal proportional to the displacement of the target was sent out from the Optron and was fed into an oscilloscope. The experiment was performed with the shaking table acceleration being kept constant.

OBSERVATION AND RESULTS

The nonlinear behavior was first observed on the response of the specimen with the section shape of a half-ring (i.e., Φ = 90 degrees) at a beam length of 35 inches. For a small range of the exciting frequency near the resonant frequency of the sixth mode* (a bending predominant mode with one node), the response of the beam was not harmonic but consisted of a superposition of two sinusoidal waves. The frequencies of the two waves were identified by means of a wave analyzer in connection with a Berkeley Counter. In this case, one component of the signal had the shaker's frequency of 490 cps and the other component had a frequency of 35 cps. Visual inspection of the mode shape of the beam indicated that the beam was essentially vibrating at the first mode, and 35 cps was very close to the fundamental frequency of the system. The frequency ratio showed that the system was executing a 14th subharmonic oscillation.

The range of table frequencies over which such subharmonic behavior was possible depended on the amplitude of excitation of the table. The larger the excitation, the wider was the critical range. In the case cited, the range was from 489-493 cps for an excitation of 2g constant acceleration of the shaking table. The corresponding ranges for 4g and 6g constant acceleration were 486-493 cps and 484-493 cps, respectively.

The transition from harmonic to subharmonic oscillation also depended on the path of approach to the critical region. When the critical region was approached from above by decreasing the table frequencies slowly, the transition was comparatively insensitive to external disturbance. When the critical region was approached from below, the transition was sudden

---

*The modes are numbered in an ascending order of the magnitude of their respective frequencies.

and highly sensitive to external disturbance. Over a narrow range of exciting frequencies, the system could be shock excited into subharmonic oscillations or could return to harmonic oscillations through external means. In other words, there existed two stable steady-states within this narrow range of table frequency. In the case cited, this multi-stage range was 489-490 cps for the 2-g constant acceleration excitation. The corresponding figures for the 4-g and 6-g constant acceleration were 486-488 and 484-486 cps, respectively. Plots of the response against table frequency are shown in Fig. 3, corresponding to an excitation of 2-g and 4-g constant acceleration. The response plotted was the rms value of the displacement at the midpoint of the beam normalized to the value of the displacement at a frequency of 480 cps. It should be pointed out that the frequency plotted is the table frequency and not the frequency of the specimen. The plot shows at least qualitatively the response of the beam as the critical region was approached from both directions. It also illustrates the existence of the "jump" region. At 493-cps frequency, it was at the borderline stage of entering the critical region and the amplitude of the response became very critical to slight variations of the table frequency.

An effort was made to detect the existence of any other subharmonics, using the wave analyzer to scan the whole frequency range. Also, the table frequency was changed to integral multiples of the resonant frequency of the first mode. Both efforts failed to detect any further subharmonics.

As the beam was shortened, this phenomenon was observed again at beam lengths of 32, 29, 26, and 23 inches. In every instance the driving mode (the mode which was performing harmonic oscillation) was bending predominant with one node, and the companion mode (the mode which executed subharmonic oscillation) was the fundamental mode which was torsional predominant with no nodes. For the second test specimen with a section of semi-central angle Φ = 135 degrees, similar behavior occurred at beam lengths of 39 and 34 inches. The resonant frequencies of the driving mode and the companion mode in various cases are shown in Table 1. It can be seen in each case that the higher mode resonant frequency was a multiple or near multiple of the first mode resonant frequency.

In order to eliminate the possibility that such behavior could be caused by the shaker due to unbalanced moments from the specimen, a double cantilever system was cast. The

21

RESPONSE (Amplitude)

$\Phi = 90°$ LENGTH = 35"

x   FOR   INCREASING   FREQUENCY
o   FOR   DECREASING   FREQUENCY

ACCELERATION   AT   4g

TABLE
FREQUENCY
(cps)

RESPONSE (Amplitude)

ACCELERATION   AT   2g

TABLE
FREQUENCY
(cps)
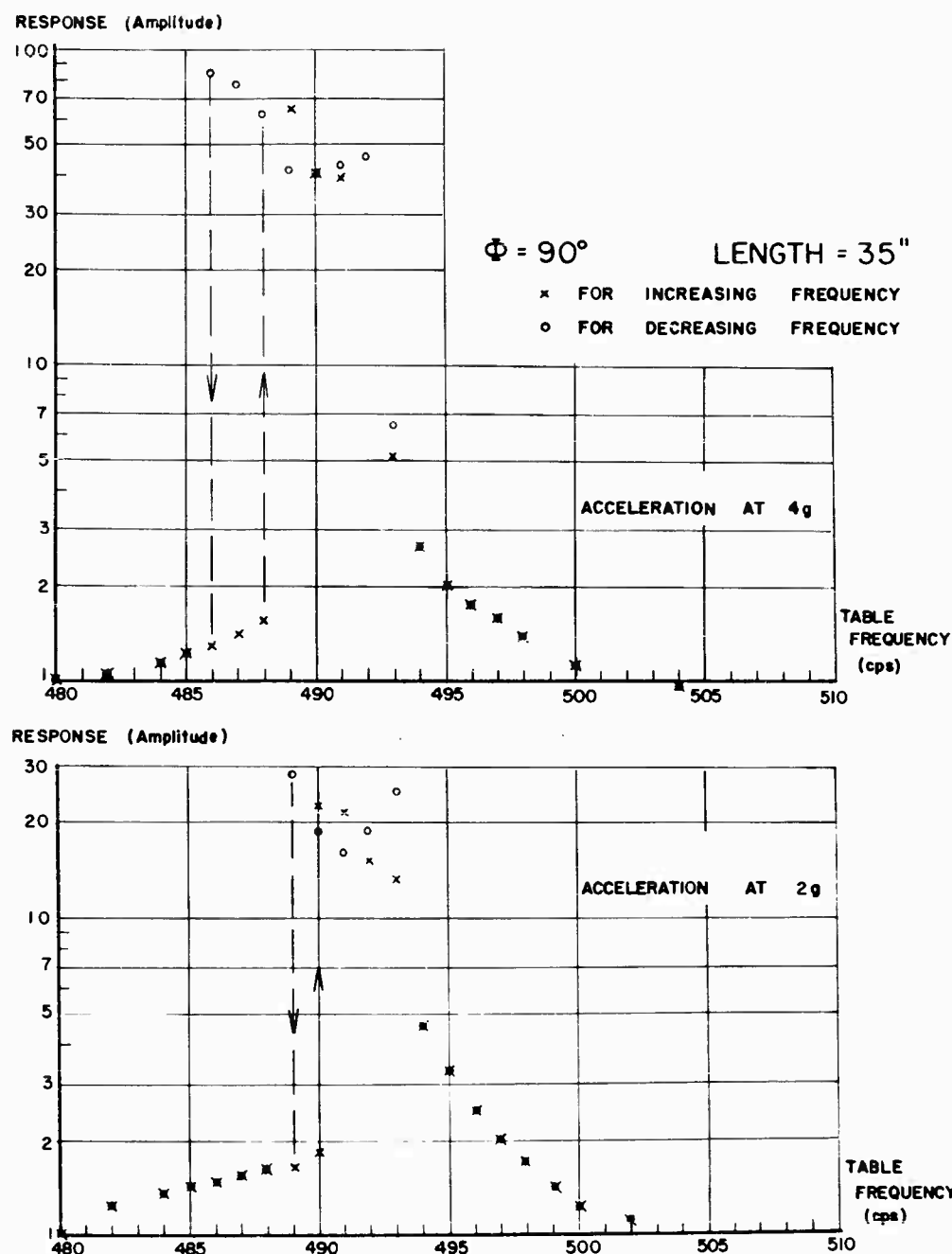
Fig. 3 - Mid-beam response at critical range

section used was Φ = 90 degrees and it was arranged in such a way that the system was symmetric in bending and antisymmetric in torsion relative to the shaking table. Such a system could not exert moments on the shaker. Similar subharmonic vibrations were observed for this specimen at a beam length of 38-1/8 inches. The responses at the midpoint of one cantilever in this system as seen on the oscilloscope are shown by a series of photographs as the table frequency varies. The shaker was set at a constant acceleration of 4g. At each frequency in Figs. 4 and 5, the upper trace represents the response of the beam measured by the Optron. The lower trace is the acceleration of the shaker measured by an accelerometer on the table top. The acceleration trace essentially gives a frequency scale to the response trace.

22

TABLE 1
Resonant Frequencies of Driving Mode and Companion Mode
under Subharmonic Vibration Conditions

Cross Section (degrees)	Beam Length (inch)	Frequency of Driving Mode f_D (cps)	Frequency of Companion Mode f_C (cps)	f_D/f_C
$\Phi = 90$	35	490	35	14.0
$\Phi = 90$	32	576	38-39	15.0
$\Phi = 90$	29	694	43	16.1
$\Phi = 90$	26	853	50	17.0
$\Phi = 90$	23	1050	62	17.0
$\Phi = 135$	39	572	26	22.0
$\Phi = 135$	34	736	31	23.8
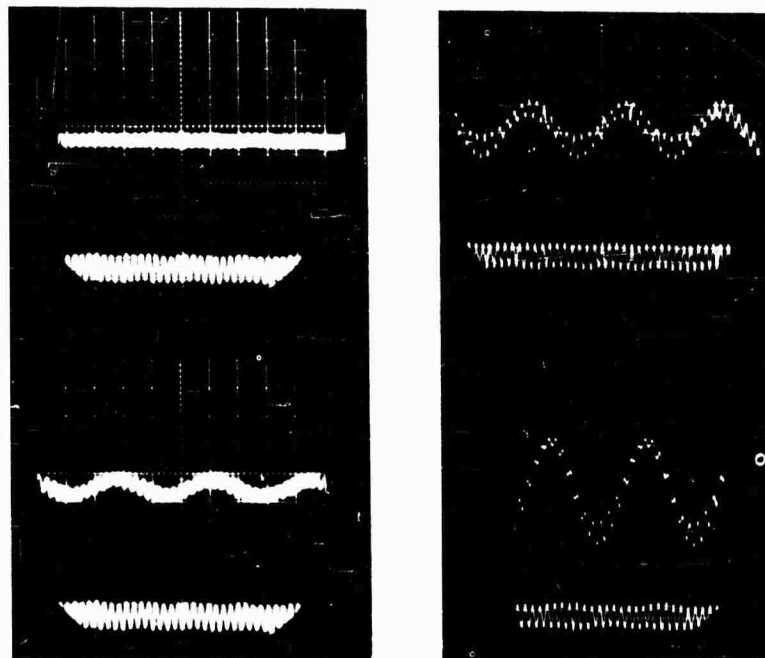
Fig. 4 - Subharmonic responses at
405, 406, 407, and 409 cps

At a table frequency of 405 cps, the response shows the beam is vibrating at the same frequency as the shaker and there is no subharmonic oscillations. At 406 cps, subharmonic oscillations begin to set in. The responses at 407 cps and 409 cps show the superposition of the harmonic and subharmonic vibrations. Also, they show the rapid increase in amplitude of the subharmonic oscillations. At 410 cps, it is seen that the amplitude of the harmonic oscillations begins to grow; because the table frequency is near the resonant frequency of the driving mode.

The response at 412 cps shows the increase in amplitudes of both the harmonic and subharmonic oscillations. At 413 cps, the maximum response of the beam is shown. The subharmonic response at 414 cps shows the disappearance of the subharmonic oscillations resulting in a pure harmonic vibration of large amplitude, corresponding to the resonant condition of the driving mode. Further increase in the table frequency results in a decrease in amplitude of the harmonic response, since the resonance of the driving mode has passed.

23
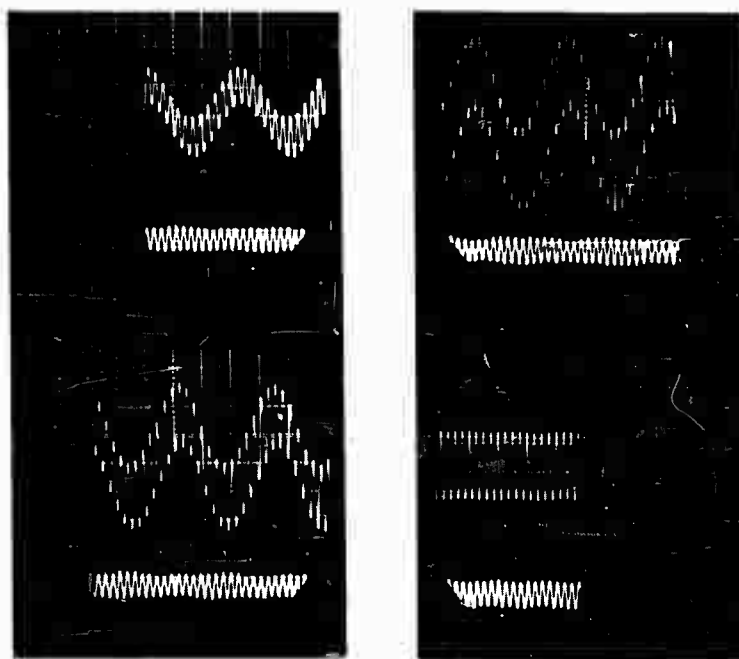
Fig. 5 - Subharmonic responses at
410, 412, 413, and 414 cps

The subharmonic frequency in this case was close to 32 cps, the frequency of the first mode. Again, visual inspection of the mode shape indicated that the companion mode was the first mode. The frequencies 414 cps and 32 cps give a ratio of 12.9, or 13. Thus, the system was executing a 13th order subharmonic oscillation. This ratio can also be obtained by counting the number of cycles of the high frequency oscillations in one cycle of subharmonic oscillations in the pictures shown.

It should be noted that the response shown on the photographs is the displacement of a point at the middle of the beam. If the displacement at the tip of the beam were taken for illustration, the difference in amplitudes due to subharmonic oscillations would even be greater. The subharmonic behavior of the system is much more violent than the resonant motion of the driving mode.

Another point to be noted is the narrow range of external exciting frequencies over which such subharmonic vibration is possible. In all cases observed, the width of such range is no more than 1 or 2 percent of the frequency of the external excitation. It is perhaps due to this fact that, as far as the author knows, such behavior has not been reported before.

DISCUSSION

In order to analyze such behavior, the linearizing assumption of $\sin\theta = \theta$, $\cos\theta = 1$ in the theories cannot be used. This leads the governing equations for ζ, η, and θ to a set of coupled nonlinear partial differential equations of extreme complexity [3]. Simplification of the equations leads to the consideration of a simplified model to represent the system. In the simplified model, two modes, the driving mode and the companion mode, of the system are considered. The two modes are coupled together nonlinearly. The response of the driving mode subjected to external excitation is taken to be harmonic. The analysis then reduces to the parametric excitation of the companion mode through its coupling with the driving mode. A detail analysis by Tso and Caughey [4] shows that provided the amplitude and the frequency of the parametric excitation satisfied certain relationships, the companion mode can be excited to perform periodic motion with a period which is a multiple integral values of the period of the driving mode.

CONCLUSION

The purpose of this paper is to report the existence of certain dynamic behavior of

24

thin-walled elastic beams of monosymmetric open section which is not predictable from the existing linearized theories. It is believed that such behavior can be attributed to the nonlinear coupling of modes of the coupled torsional and bending vibrations under special circumstances.

Experimental observations suggest that a necessary condition for the subharmonic behavior is that the resonant frequency of the driving mode be a multiple or near multiple of the frequency of the companion mode.

The subharmonic oscillation causes the beam to vibrate with a much larger amplitude than the ordinary harmonic response. Such violent motion can lead to failure if it is not

foreseen and allowed for in design. Such behavior has been generated in the laboratory, and it is conceivable that it can happen in structures where such beams are used and coupled torsional and bending vibration of such member is possible. Therefore, it is believed that the reported phenomenon is interesting both from the theoretical and practical point of view.

ACKNOWLEDGMENT

The testing was done in the Vibration Laboratory in the Thomas Engineering Laboratory, California Institute of Technology, Pasadena, California.

REFERENCES

1. V. Z. Vlasov, Thin Walled Elastic Beams (Translated from Russian; published by Israel Program for Scientific Translations, Jerusalem, 1961), 2d ed.

2. J. M. Gere, and Y. K. Lin, J. App. Mech., 25, 373-378 (1958).

3. W. K. Tso, "Dynamics of Thin-Walled Beams of Open Section," Dynamics Laboratory Report, California Institute of Technology (June 1964).

4. W. K. Tso, and T. K. Caughey, "Parametric Excitation on a Nonlinear System," submitted to J. App. Mech. for publication.

DISCUSSION

Dr. Morrow (Aerospace Corp.): I wonder if you would venture an opinion as to whether these subharmonics could be induced by a random excitation at the higher frequencies?

Mr. Tso: The excitation from our shaker is sinusoidal. I am not sure whether the subharmonics would be excited by the random. I do hesitate to say that it is the main cause although there is bound to be sufficient random noise in the system to excite the fundamental mode to some extent. Due to the nonlinear coupling mechanism this excitation will be amplified somewhat, particularly since the material damping is small.

Dr. Morrow: My question really had to do with whether it might be excited by random vibration out in flight as opposed to having been excited in the test.

Mr. O'Hearne (Martin Co.): At the point at which you had two stable solutions, were they both subharmonics?

Mr. Tso: No. The lower branch is harmonic.

Mr. O'Hearne: Pure harmonic?

Mr. Tso: It is pure harmonic. Any jumps, then, is a superposition of harmonic motion and subharmonic motion due to the action of two modes, the driving mode and the companion mode. The photographs show one spot which is the superposition of two modes.

Mr. O'Hearne: Do superharmonics appear in your experiment at all?

Mr. Tso: They are not observed at all.

*   *   *

PREDICTION AND MEASUREMENT OF VIBRATION RESPONSE
OF THE PEGASUS MICROMETEOROID MEASURING SATELLITE

C. E. Lifer and R. G. Mills
Propulsion and Vehicle Engineering Laboratory
Marshall Space Flight Center
Huntsville, Alabama

All too often in structural design programs, dynamic loads are not considered at all or at best are given only courtesy consideration. The Vibration and Acoustics Branch at Marshall Space Flight Center contends that, from conception through final design, a knowledge of the structural response characteristics is necessary information. This paper presents a case example in support of this philosophy.

The National Aeronautics and Space Administration, in late 1962, initiated a competitive RFQ to design, fabricate, and deliver a spacecraft with evaluation of the hazards presented by meteoroids in the 200- to 700-mile altitude range as its primary mission. The satellite was to be the payload for two vehicles already scheduled as a part of the Saturn I development program. Therefore, the spacecraft development program was not governed alone by its own unique mission requirements, but in addition by the restrictions placed on it by the Saturn I vehicle configuration and environments.

The Pegasus satellite consists of two wings deployed about a rectangular center section. Each wing is composed of seven hinged sections initially stacked within the boilerplate Apollo service module. The overall undeployed package is 197 inches long, 85 inches wide, and 19 inches deep.

The schedule was almost prohibitively short, thus greatly accentuating all of the development problems encountered. This paper deals with only one of many, specifically, the dynamic environment response loads.

The dynamic environment generated by mechanical, acoustic, and aerodynamic excitation is described in a set of specifications for each MSFC vehicle. The vehicle is divided into zones of similar structure, with each zone defined by a statistical compilation of vibration data obtained from both static and flight tests. This information has been developed through both analytical techniques and statistical studies developed for this purpose, and proven adequate for design and test purposes.

A vibration analysis was performed to determine the longitudinal response loads for use in a stress analysis of the Pegasus support structure. The analysis was based on a simple rigid body model because details of the capsule design were not available. This analysis indicated failure loads.

With this development, a concentrated effort on dynamic analysis with more refined models was begun by MSFC and the Fairchild Stratos Corporation. The loads obtained from these analyses dictated structural modifications to the basic design. Successive analyses which incorporated these changes were performed.

Because of the short schedule and the high dynamic response indicated by analysis, a structural dynamic test model was built and tested to the predicted vibration environment. Its purpose was the verification of

INTRODUCTION

In February 1963, the National Aeronautics and Space Administration (NASA) awarded to the Fairchild Stratos Corporation (FSC) a contract to develop and manufacture a satellite for the primary purpose of evaluating the hazards presented by meteoroids in the 200- to 700-mile altitude range. The vehicle selected for this satellite was the eighth Saturn I, and flight schedules at that time required that the first flight assembly be delivered in June 1964; this allowed only little more than a year for development, testing, and manufacture.

The configuration proposed by FSC and chosen by NASA is shown in Fig. 1. The spacecraft consists of two wings, each wing composed of seven hinged sections. During boost into orbit the wings are folded into a package 197 inches long, 85 inches wide, and 19 inches deep,

and placed inside the boilerplate Apollo service module as shown in Fig. 1.

The deployed wings will provide a detection surface area of 2000 square feet, with a wing span of 96 feet. A total system weight of under 4000 pounds was permissible, with approximately 3400 pounds allocated to the satellite.

The function of the satellite is to record impacts of meteoroids and to transmit to earth by means of radio telemetry information on the frequency of occurrence and size of the impacting meteoroids. The detector panels are capacitors whose electrical properties will be altered by penetrations upon impact. Use of several different capacitor plate thicknesses and laboratory calibration of the electrical discharge pulse will permit meteoroid size determination.
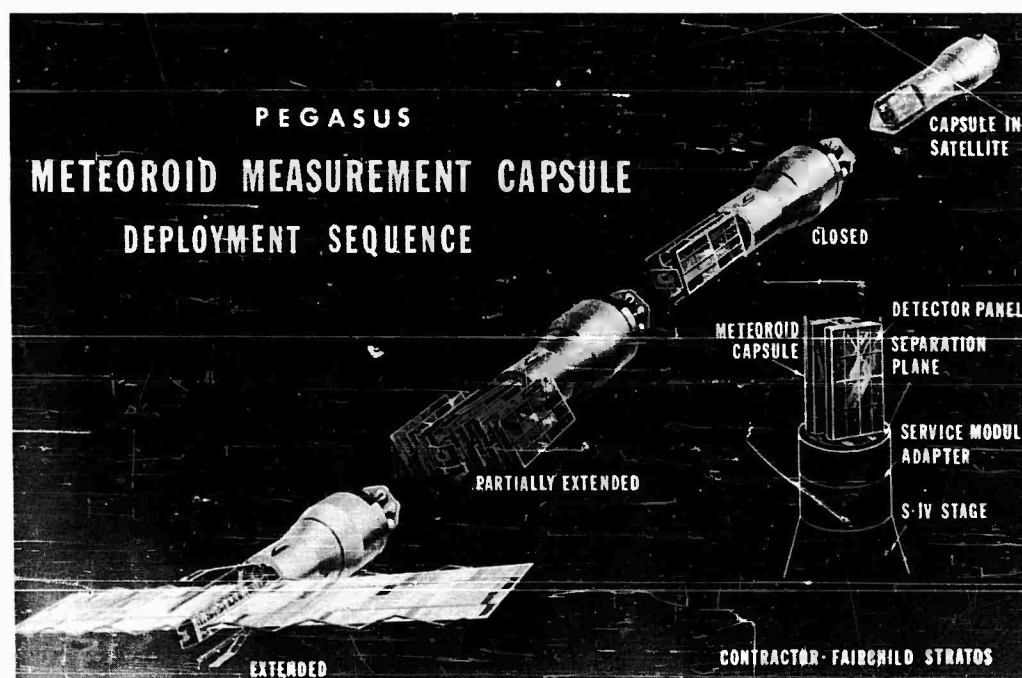
Fig. 1 - Pegasus configuration

The strict weight limitations and the unique structural configuration imposed severe design and test problems. These problems were compounded by the dynamic environments imposed by the Saturn I booster, and because of the short schedule they required unusually extensive and thorough design analyses.

The intent of this paper is to illustrate the manner in which dynamic analysis was used to improve the system design, and how laboratory test results correlated with analytical assumptions and calculations.

ENVIRONMENT SOURCES

The vibration, acoustic, and shock environment specifications which were used in the design analysis and testing of the Pegasus equipment and structure were derived from measurements made on Saturn I, Block I, vehicles and from theoretical studies of the Apollo adapter structure and the spacecraft configuration. Figure 2 shows the Saturn I vehicle with a Jupiter nosecone from which flight data

were used in establishing environments. Significant portions of the launch which provided data were the ignition and lift-off phase, in which the payload is subjected to mechanical excitation and acoustical energy reflected from the launch pad, and the transonic and maximum aerodynamic pressure periods of flight during which the adapter shroud is buffeted by aerodynamic pressure fluctuations. The adapter and its relation to the Pegasus assembly is shown in Fig. 3. Theoretical techniques of predicting adapter structure environments from acoustic pressures were used in conjunction with the measurements to derive the environment specifications. The mass and elastic properties of the Pegasus were considered in this study, since the impedance of the payload greatly affects the shell vibration amplitudes. These techniques are described [1].

The vibration environments predicted for the interface between the Pegasus and the adapter at the six support points are shown in

NOTE: Reference appears on page 35.
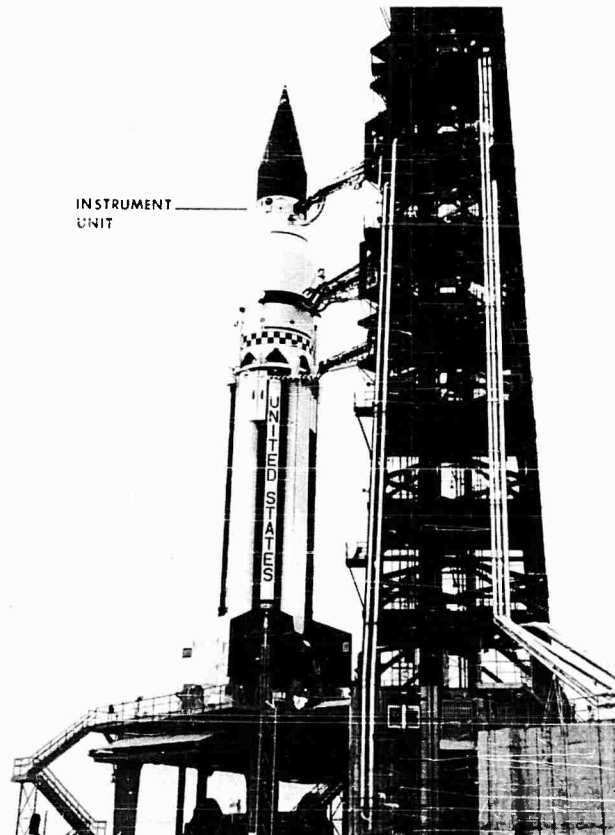
INSTRUMENT UNIT

Fig. 2 - Saturn I vehicle with Jupiter nosecone
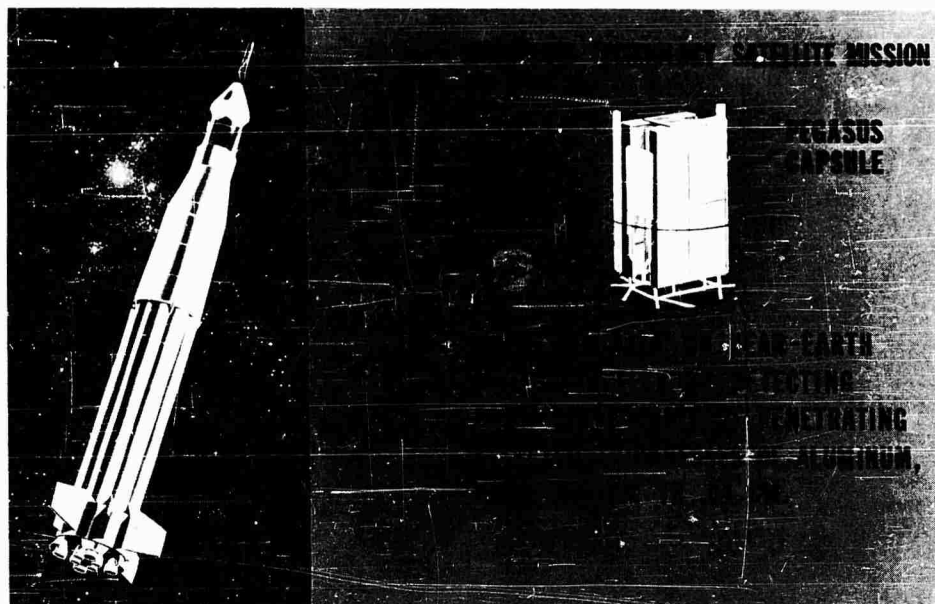
Fig. 3 - Saturn I vehicle showing Pegasus location

Fig. 4. A comparison of the predicted environments and environmental measurements on the sixth Saturn instrument unit structure is shown in Fig. 5.

ANALYSIS

The first vibration analysis work was performed by the Analysis Section at MSFC in support of preliminary design of the satellite supporting structure. At this time no stiffness information or design details were available, and the satellite was represented as a rigid body. The analysis model is shown in Fig. 6.

The satellite is represented by M_2 and a portion of the adapter section structure is represented by M_1. The spring elements (K) represent the stiffnesses of the shell structure and the spacecraft support structure. The purpose of this analysis was to provide designers with approximate loads on the supports resulting from vibration response in flight.

The response motions of the system described above were studied with an analog computer. Since the motion of M_1 represents the predicted environments, the relative motion of M_2 to M_1 was used directly to calculate response loads. The support structure loads were found
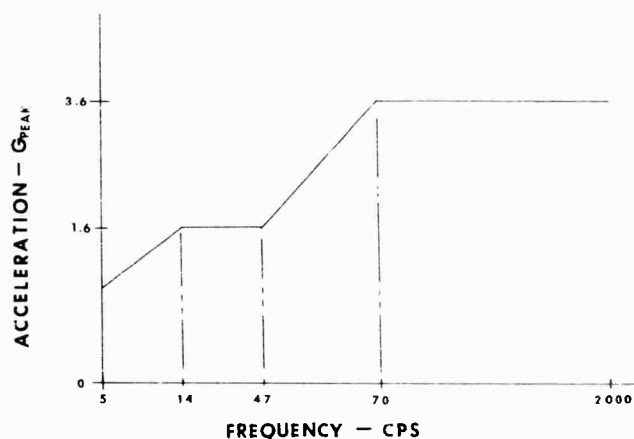
Fig. 4 - Pegasus predicted vibration environments

30
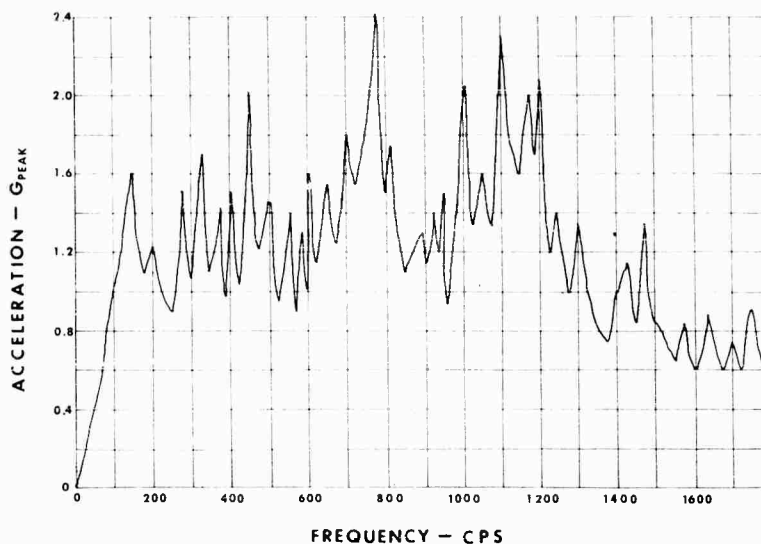
Fig. 5 - Saturn I instrument unit flight measurements
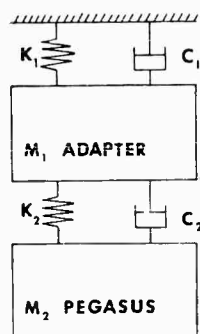
Fig. 6 - First analysis model

to be excessive due to response in the lateral direction. This was primarily the result of having the supports placed far below the center of gravity of the satellite so that large moments had to be reacted by the supports.

The increased weight of the support structure required to withstand the response loads was not practical, and the loads were not considered accurate enough for design criteria. A more detailed analysis was required and dynamics personnel of FSC were requested to provide vibration analysis of the satellite, and to provide MSFC with an accurate spring-mass model of the system. The models derived from the FSC study are shown in Fig. 7, and include mass and stiffness representations of the detector panels, panel mounts, wing frames, center section, and support structure.

Analyses of these models were performed with numerical techniques of matrix iteration

on digital computers. Response loads in each spring element and response displacements of some mass elements were calculated from the mode shapes, frequencies, and predicted environment levels, and with analog computer solution of differential equations of motion.

In the longitudinal analysis, the equation

$$\left[Y_M \right] = W_M^2 \left[K \right]^{-1} \left[M \right] \left[Y_M \right]$$

was solved for the eigenroots and eigenvectors of the system using the Stodola matrix iteration method. An analog computer solution of the Lagrangian equations of motion was used to calculate the system response to an excitation of M_1. Since the motion of M_1 was defined as the environment, the relative motion of M_1 to M_2 was used to calculate the force in K_2. This force was distributed equally to the six spacecraft support points.

The matrix iteration method described above was employed to find the coupled natural frequencies and mode shapes of the lateral model. The system response to an input at the adapter section was determined using a normal mode approach in which only the first four modes were considered.

After the equations of motion were decoupled and the first four modes were isolated, an analog computer solution was used to determine the generalized coordinate accelerations. The response loads were calculated in terms of a moment and lateral force at the lower support

31

WING RESTRAINTS

OUTRIGGERS

CANISTER ISOLATION

TONGUE AND GROOVE
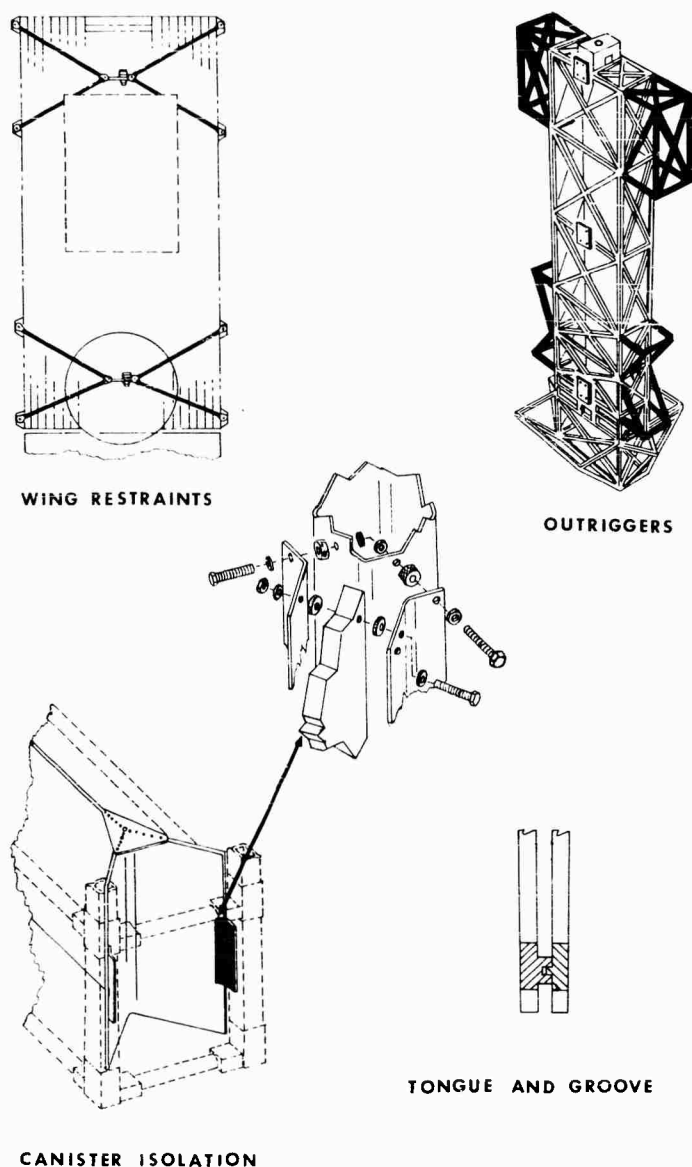
Fig. 7 - Design modifications

and a lateral force at the top support from the equation:

$$\begin{bmatrix} M_L \\ S_L \\ S_T \end{bmatrix} = \begin{bmatrix} A \end{bmatrix} \begin{bmatrix} J \end{bmatrix} \begin{bmatrix} \phi \end{bmatrix} \begin{bmatrix} \ddot{q} \end{bmatrix},$$

where

M_L = moment at lower support,

S_L = lateral force at lower support,

S_T = lateral force at top support,

J = generalized mass,

ϕ = eigenvector of frequency,

$\ddot{q}$ = generalized coordinate accelerations, and

A = matrix defining the moments and shears at each support due to a unit load at each lumped mass of the system.

Parallel analyses were conducted by FSC in which the structure was idealized into a lumped parameter system. The matrices which

define the structural characteristics were derived in two ways: (1) by equivalent springs based on assumed load paths with simplified bending and axial members; and (2) by deflection influence coefficients based on an energy solution for unit loads applied to the actual redundant structure.

The inertia matrices consisted of concentrated masses acting at a point assumed to be the center of gravity of locally distributed weight. The differential equations of motion for forced vibration were solved to obtain a transmissibility equation in matrix notation:

$$\left[T_m\right] = \left\{1 - W^2 \left[S_{mn}\right]\left[M_m\right] + i\left[g_m\right]\right\}^{-1} \left\{1 - i\left[g_m\right]\right\},$$

where

$i = (-1)^{1/2}$

T = transmissibility,

W = frequency,

S = flexibility influence coefficients, deflection at m due to load at n,

M = mass, and

g = nondimensional damping coefficient.

The transmissibility equation was solved on an IBM 7090 computer for a range of W's,

including all structural resonances, to obtain a plot of response versus frequency for each station of the model. The internal loads were then obtained directly from the response calculations by using the unit solution matrix which defines the flexibility matrix.

A subsequent strength analysis indicated that these loads would cause failure. The primary contributor to the high response loads was the cantilevered condition of the spacecraft basic structure. Since the forward lateral restraint proposed by dynamics engineers of MSFC and FSC had been rejected, it was necessary to demonstrate the necessity of having it incorporated into the design.

The vibration analysis was extended to include design modifications in an attempt to reduce the response loads as much as possible, and to provide a structure which would withstand the loads. This approach produced the modifications shown in Fig. 8 and described below.

1. The wing frame member sizes were made proportional to the expected loads and the detector panels were "detuned" from coupling. The detector panel "detuning" was accomplished by providing an arbitrary difference in the support mount spring rate, and reducing the dynamic magnification across the support through use of a high damping elastomer. Since the

LONGITUDINAL   **LATERAL**
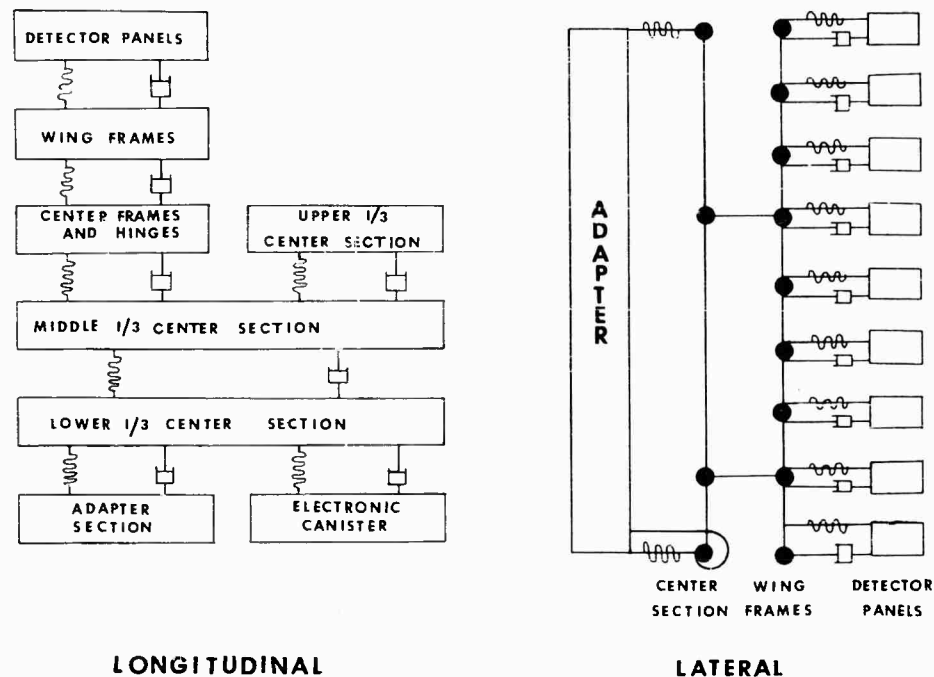
Fig. 8 - Refined analysis models

panels make up about 1/3 of the total spacecraft mass this reduced the loads significantly.

2. A tongue-and-groove connection was added between each wing frame to transfer the shear from frame to frame directly to the center section in order to reduce amplitude of vibration during longitudinal excitation.

3. The single strap binding the wing frames together was replaced by a double strap, and by adding outriggers between each stack to transfer lateral loads directly to the center section. This modification reduces the lateral bending response of the wing frames.

Although these modifications showed significant reductions, the response loads were still excessive and the lateral natural frequency of the spacecraft was within the range of the Saturn bending mode frequencies. When the results of the analysis program was presented, the decision was made to provide a forward lateral restraint. This raised the frequencies and lowered the response loads to acceptable values.

TESTING

The original Pegasus test program did not provide for vibration development testing of the spacecraft assembly prior to final qualification testing of a prototype model. This qualification test was scheduled just before delivery of the first flight model. It was apparent from the vibration analyses that early development testing would be extremely beneficial to the program. A dynamic test model (DTM) was built and tested to qualification levels.

The DTM was a full scale model, structurally, mechanically, and dynamically similar to the prototype. It was intended as a tool for evaluating the structural response characteristics and defining any necessary modifications to reduce excessive responses.

The lateral axis test arrangement is shown in Fig. 9. The lower support structure flexibility was simulated in the specimen-to-fixture adapters, and the forward support flexibility was provided by the tower structure. The longitudinal axis test was accomplished by rotating the shakers to the vertical position as shown in Fig. 10.

Two MB Electronics C-210 shakers were used to subject the specimen to the predicted Saturn vibration environment. The test procedure consisted of a 10-minute sinusoidal sweep
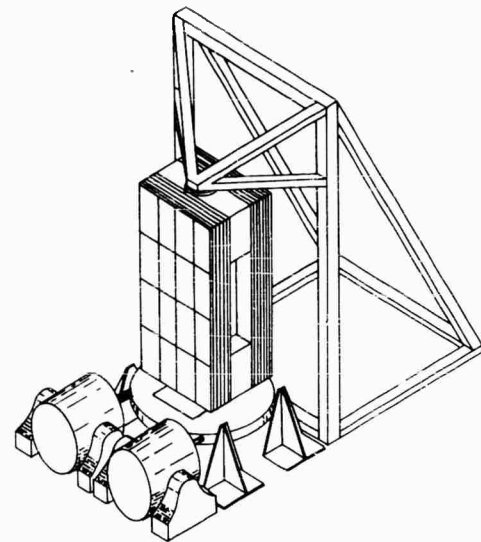
Fig. 9 - Lateral DTM test setup
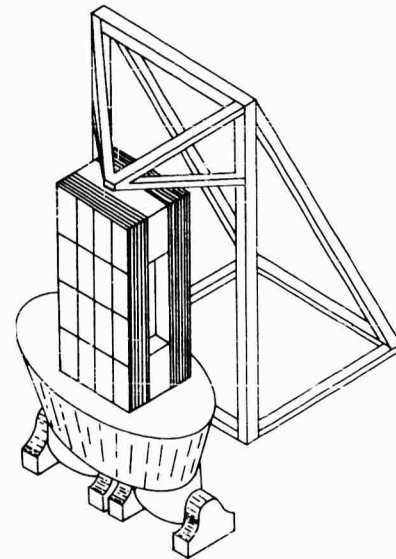
Fig. 10 - Longitudinal DTM test setup

from 5 to 2000 cps and a 5-minute resonant dwell at the major resonant frequencies. This test procedure applied to the three orthogonal axes. Low level survey sweeps were conducted in each axis prior to the high level sweeps. The maximum input level was 3.6 g_{peak} as shown in Fig. 4.

Instrumentation consisted of 22 channels of continuous accelerometer recordings, 12 channels of continuous strain gage bridge

circuit recordings, and 24 channels of single (dynamic) strain gage recordings.

Three low level sweeps were conducted in each axis prior to the high level test. Twenty-two different accelerometers and 36 different strain gages were monitored during each sweep. From this data the locations of highest response were selected for continuous recording during the high level test. The strain gages were recorded on oscillograph and the accelerometers were recorded on magnetic tape, played back through an X-Y plotter and presented as plots of acceleration vs frequency.

The strain measurements were used to calculate the stress (and thus the load) in structural members throughout the spacecraft. The accelerometer data was used in determining frequency, mode shapes, and distribution of dynamic magnification throughout the spacecraft.

The test demonstrated the overall structural integrity of the spacecraft in that no failures occurred. The frequencies and modes of vibration and the dynamic load distributions obtained during testing agreed with those predicted by analysis.

The dynamic loads measured by the strain gages were lower than those predicted by analysis. Peak longitudinal load measured in the lower support structure was 13,940 pounds and the predicted load was 16,250 pounds. The loads measured in the lateral direction was 4550 pounds compared with a 6550 pound predicted load. The error was approximately 15 percent in the longitudinal direction and 30 percent in the lateral direction. The difference is probably due to the conservative estimate of damping used in the analysis. An investigation is planned in an effort to simulate the DTM test results by adjusting the analysis parameters, thereby defining a more accurate analytical model.

CONTRIBUTIONS TO DESIGN BY VIBRATION ANALYSIS

The results of vibration analysis had significant effects on the final design of the Pegasus satellite. The most outstanding of these effects was the incorporation of a forward lateral support.

The forward support had been considered in the conceptual design phase, but had not been justified by static considerations. It was left then for the dynamics analyst to develop the supporting evidence and to demonstrate the need for the support. This need was adequately demonstrated by both MSFC and FSC analyses.

In addition to demonstrating the necessity for a lateral forward restraint the analysis program uncovered design modifications that greatly increased the overall structural integrity of the system.

The initial design of the wing frame structure called for similar structural member sizes throughout for simplicity in design and fabrication, and for identical detector panel installation hardware for each panel. Vibration analyses performed by FSC showed these design approaches would result in high dynamic response loads. As a result, more efficient designs were developed in which the frame members were made proportional to the load and detector panel responses were "detuned" by using isolators as mounts.

Excessive response amplitudes of the wing stack as a result of longitudinal excitation was reduced by a tongue-and-groove arrangement which transferred shear directly to the center section and thus reduced the load on the hinges. The lateral bending response of the wing stack was reduced by changing the method of binding it together and adding outriggers to transfer load directly to the center section.

The high response amplitudes of the electronic canister predicted by analysis were confirmed during DTM tests. A more detailed analysis of the canister was performed in which a stiffener system and an isolation mounting system were developed that would reduce the high frequency response amplitudes.

The purpose of this paper has been to point out that structural vibration response should be a design consideration in todays space vehicles where engine noise and aerodynamically generated sound pressure levels exceed 160 db. Vibration analysis techniques should be employed during the design phase so that problems are uncovered prior to testing and design modifications are easily incorporated.

REFERENCE

1. Barrett, Robert E., "Statistical Techniques for Describing Localized Vibratory Environ- ments of Rocket Vehicles," NASA Technical Note D-2158, July 1964.

*   *   *

SPECTRA OF NONSTATIONARY RANDOM PROCESSES

G. P. Thrall
Measurement Analysis Corporation
Los Angeles, California

INTRODUCTION

The concept of a power spectrum associated with a stationary random process has been developed and applied to the analysis of physical problems for many years. It is a fact, however, that many random phenomena have nonstationary characteristics which cannot be neglected. For example, the vibration which a missile undergoes during the boost phase has a mean square value which fluctuates quite rapidly and thus causes the spectrum to vary with time.

The purpose of this paper is to develop several approaches to defining a useful spectral density function for nonstationary random processes. A spectral decomposition which is the double Fourier transform of the nonstationary covariance function is derived in a later section entitled "Double Frequency Spectra." The result is a spectral density function involving two frequency variables. A second approach, which is based upon narrow band filtering and ensemble averaging gives a time dependent power spectrum and this is developed in the section entitled "Time Varying Power Spectra." Finally, a third spectral decomposition is arrived at by taking a time average of the time dependent spectrum. It is pointed out that the averaged spectrum has the advantage of being a directly measurable quantity. Finally a detailed comparison is made of the three spectral decompositions and recommendations for further research is presented in the section entitled "Spectrum of a Periodic Nonstationary Process."

SPECTRAL REPRESENTATION

Let $x(t)$ be a zero mean, nonstationary random process. Since $x(t)$ has zero mean for all t, its covariance function is given simply by

$$R_x(t_1, t_2) = E[x(t_1) x(t_2)] , \quad (1)$$

NOTE: References appear on page 45.

and depends explicitly on the times t_1 and t_2, rather than on the time difference $(t_2 - t_1)$ as is the case for stationary random processes. Because of the two dimensional nature of the covariance function, it will be seen that the various spectral decompositions are also two dimensional.

Double Frequency Spectra

A spectral decomposition involving two frequency variables may be obtained by introducing a new random process $X(t)$ which is defined as the Fourier transform of the original nonstationary process $x(t)$. Thus,

$$X(t) = \int_{-\infty}^{\infty} x(t) e^{-i\omega t} dt , \quad (2)$$

where

$$\omega = 2\pi f . \quad (3)$$

The right side of Eq. (2) may not exist in terms of ordinary integration theory and $X(f)$ must be interpreted as a symbolic function [1], in the same way that the Dirac delta function, $\delta(\cdot)$, is a symbolic function. In fact, if $x(t)$ is set equal to one for all t, it follows from the properties of the Dirac delta function that

$$X(f) = \int_{-\infty}^{\infty} e^{-i\omega t} dt = \delta(f) .$$

Certain properties of $X(f)$ are immediately apparent from the definition. Since $x(t)$ has zero mean, the expected value of $X(t)$ is zero:

$$E[X(f)] = \int_{-\infty}^{\infty} E[x(t)] e^{-i\omega t} dt = 0 . \quad (4)$$

$X(f)$ will in general be a complex random process and can be written as

37

$$X(f) = X_1(f) + iX_2(f) , \qquad (5)$$

where $X_1(f)$ and $X_2(f)$ are real random processes.

The covariance function of $X(f)$ will be denoted by $S_x(f_1, f_2)$ for reasons which will be explained shortly, and is defined by

$$S_x(f_1, f_2) = E\big[X(f_1) X^*(f_2)\big] , \qquad (6)$$

where $(*)$ denotes the complex conjugate operation. Equation (6) is the standard definition of the covariance function of a (possibly complex) random process [2]. It should be noted that $S_x(f_1, f_2)$ must be interpreted as a symbolic function since it is the expected value of two random symbolic functions. By expanding Eq. (6) in terms of $X_1(f)$ and $X_2(f)$

$$S_x(f_1, f_2) = E\Big\{ \big[X_1(f_1) + iX_2(f_1)\big] \big[X_1(f_2) - iX_2(f_2)\big] \Big\}$$

$$= E\big[X_1(f_1) X_1(f_2)\big] + E\big[X_2(f_1) X_2(f_2)\big]$$

$$- i\Big\{ E\big[X_1(f_1) X_2(f_2)\big] - E\big[X_1(f_2) X_2(f_1)\big] \Big\}$$

$$= S_{11}(f_1, f_2) + S_{22}(f_1, f_2)$$

$$- i\big[S_{12}(f_1, f_2) - S_{21}(f_1, f_2)\big] , \qquad (7)$$

where

$$S_{jk}(f_1, f_2) = E\big[X_j(f_1) X_k(f_2)\big] , \quad j,k = 1,2 .$$

The real part of $S_x(f_1, f_2)$ is the sum of the individual covariances of $X_1(f)$ and $X_2(f)$, while the imaginary part is the difference of the covariance between $X_1(f)$ and $X_2(f)$. Along the line $f_1 = f_2 = f$, $S_x(f,f)$ is real and gives the mean square content of $X(f)$ at the frequency f.

Returning to Eq. (6), another expression for $S_x(f_1, f_2)$ may be obtained by using Eq. (2):

$$S_x(f_1, f_2)$$

$$= E\left[\int_{-\infty}^{\infty} x(t_1) e^{-i\omega_1 t_1} dt_1 \int_{-\infty}^{\infty} x(t_2) e^{i\omega_2 t_2} dt_2 \right]$$

$$= \iint_{-\infty}^{\infty} E\big[x(t_1) x(t_2)\big] e^{-i(\omega_1 t_1 - \omega_2 t_2)} dt_1 dt_2$$

$$= \iint_{-\infty}^{\infty} R_x(t_1, t_2) e^{-i(\omega_1 t_1 - \omega_2 t_2)} dt_1 dt_2 . \qquad (8)$$

This result shows that $S_x(f_1, f_2)$ is the double Fourier transform of the covariance function of $x(t)$ and is called the generalized power spectral density function.

In the stationary case, Eq. (8) reduces to the standard Wiener-Khintchine relation. This will now be shown. If the change of variable

$$t = \frac{t_1 + t_2}{2}$$

$$\tau = t_2 - t_1$$

$$\qquad\qquad (9)$$

$$f = \frac{f_1 + f_2}{2}$$

$$g = f_2 - f_1$$

is made, then Eq. (8) becomes, in the stationary case,

$$S_x(f, g) = \iint_{-\infty}^{\infty} R_x(\tau) e^{-i 2\pi (f\tau + gt)} dt \, d\tau$$

$$= \delta(g) \int_{-\infty}^{\infty} R_x(\tau) e^{-i 2\pi f\tau} d\tau . \qquad (10)$$

In terms of the original frequency variables, the above relationship is

$$S_x(f_1, f_2) = \delta(f_2 - f_1) \int_{-\infty}^{\infty} R_x(\tau) e^{-i 2\pi \frac{f_1 + f_2}{2} \tau} d\tau \qquad (11)$$

which means that $S_x(f_1, f_2)$ is zero everywhere except along the line $f_1 = f_2 = f$ where the two dimensional density is infinite. Clearly, this indicates that the spectral density has been reduced to a one dimensional density. By integrating out the delta function, Eq. (10) becomes

$$S_x(f) = \int_{-\infty}^{\infty} S_x(f, g) \, dg = \int_{-\infty}^{\infty} R_x(\tau) e^{-i\omega\tau} d\tau , \qquad (12)$$

which is the Wiener-Khintchine relation.

The one-dimensional nature of $S_x(f_1, f_2)$ in the stationary case implies that, if $f_1 \neq f_2$, the $X(f_1)$ and $X(f_2)$ are always uncorrelated and, in particular, are independent if $x(t)$ is Gaussian. For a nonstationary process, the fact that $S_s(f_1, f_2)$ has a two-dimensional structure means that there is correlation between the content of the process at f_1 and that at f_2.

Through the transformation in variables of Eq. (9), the parameters may be expressed as

$$t_1 = t - \frac{\tau}{2},$$

$$t_2 = t + \frac{\tau}{2},$$

$$\quad (13)$$

$$f_1 = f - \frac{g}{2},$$

and

$$f_2 = f + \frac{g}{2}.$$

In terms of t and τ, the nonstationary autocorrelation function $R_x(t_1, t_2)$ becomes $R_x(t, \tau)$ where

$$R_x(t_1, t_2) = E\left[x(t_1) x(t_2)\right]$$

$$= E\left[x\left(t - \frac{\tau}{2}\right) x\left(t + \frac{\tau}{2}\right)\right]$$

$$= R_x(t, \tau). \quad (14)$$

Note that $R_x(t, \tau)$ is an even function of τ, that is,

$$R_x(t, -\tau) = R_x(t, \tau). \quad (15)$$

In terms of f and g, the generalized nonstationary power spectral density function $S_x(f_1, f_2)$ becomes $\mathcal{S}_x(f, g)$ where

$$S_x(f_1, f_2) = E\left[X(f_1) X^*(f_2)\right]$$

$$= E\left[X\left(f - \frac{g}{2}\right) X^*\left(f + \frac{g}{2}\right)\right]$$

$$= \mathcal{S}_x(f, g). \quad (16)$$

Note that $\mathcal{S}_x(f, g)$ is an even function of g, namely

$$\mathcal{S}_x(f, -g) = \mathcal{S}_x(f, g). \quad (17)$$

In place of Eq. (8), there results

$$\mathcal{S}_x(f, g) = \iint_{-\infty}^{\infty} R_x(t, \tau) e^{-i 2\pi(f\tau + gt)} dt\, d\tau. \quad (18)$$

The inverse double Fourier transform gives

$$R_x(t, \tau) = \iint_{-\infty}^{\infty} \mathcal{S}_x(f, g) e^{i 2\pi(f\tau + gt)} dg\, df. \quad (19)$$

These relations are discussed further in a report by Bendat, et al. [3].

A major limitation to the usefulness of $S_x(f_1, f_2)$ or $\mathcal{S}_x(f, g)$ in engineering applications where data is a nonstationary random process [4] is that it is not subject to direct measurement. Rather, $S_x(f_1, f_2)$ must be found by performing the double Fourier transformation on the covariance function $R_x(t_1, t_2)$. The problem lies in the fact that there is no way to observe $X(f)$ experimentally. A different nonstationary spectral decomposition which does not have this measurement problem will be presented in the next section.

Time Varying Power Spectra

Let $x_i(t)$ be a single record of a zero mean, nonstationary process $x(t)$ which is operated upon as shown below.
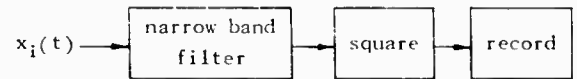
We will assume that the filter is an ideal rectangular filter with a transfer function given by

$$H(\nu) = 1, \qquad f - \frac{B}{2} < |\nu| < f + \frac{B}{2}$$

$$= 0, \qquad \text{elsewhere} \quad (20)$$

where B is the filter bandwidth and f is the center frequency. Although the filter is not physically realizable, it is a good approximation to many narrow band filters.

The corresponding weighting function is simply the Fourier transform of $H(\nu)$ so that

$$h(t) = \int_{-\infty}^{\infty} H(\nu) e^{i 2\pi \nu t} d\nu$$

$$= \frac{\sin (\pi B t)}{\pi t} \cos (2\pi f t)$$

$$= \frac{\sin (\alpha t)}{\pi t} \cos (\omega t), \quad (21)$$

where the last equality of Eq. (21) is obtained by letting

$$\alpha = \pi B$$

and $\quad (22)$

$$\omega = 2\pi f.$$

39

The filter output is given by

$$x_i(t,f,B) = \int_{-\infty}^{\infty} h(p)\, x_i(t-p)\, dp \qquad (23)$$

and is the instantaneous value of that part of $x_i(t)$ which lies within the bandwidth B centered at the frequency f. The output of the squaring device is obtained by squaring both sides of Eq. (23) so that

$$x_i^2(t,f,B) = \left(\int_{-\infty}^{\infty} h(p)\, x_i(t-p)\, dp\right)^2$$

$$= \iint_{-\infty}^{\infty} h(p)\, h(q)\, x_i(t-p)\, x_i(t-q)\, dp\, dq \,. \qquad (24)$$

It should be noted that the right side of Eq. (24) is always positive since it represents the square of a real function of time.

By recording $x_i^2(t,f,B)$ as a function of time, repeating the filter-square-record operation N times, and ensemble averaging, an estimate of the average value of $x^2(t,f,B)$ is obtained. Letting N become arbitrarily large will cause the estimate to converge to the true average value. Thus,

$$E\big[x^2(t,f,B)\big] = \lim_{N\to\infty} \frac{1}{N} \sum_{i=1}^{N} x_i^2(t,f,B) \qquad (25)$$

To compute $E\, x^2(t,f,B)$ mathematically, one must take the expected value of Eq. (24). This yields

$$E\big[x^2(t,f,B)\big] = \iint_{-\infty}^{\infty} h(p)\, h(q)\, R(t-p,\, t-q)\, dp\, dq \,, \qquad (26)$$

where $R(t_1,t_2)$ is the covariance function of $x(t)$. Equation (26) may be expressed in terms of the double frequency spectrum by using the relation

$$R(t_1,t_2) = \iint_{-\infty}^{\infty} S(f_1,f_2)\, e^{i[\omega_1 t_1 - \omega_2 t_2]}\, df_1\, df_2. \qquad (27)$$

Substitution of Eq. (27) into Eq. (26) gives

$$E\big[x^2(t,f,B)\big] = \iint_{-\infty}^{\infty} h(p)\, h(q) \iint_{-\infty}^{\infty} S(f_1,f_2) \qquad (28)$$
(Cont.)

$$\times\, e^{i[\omega_1(t-p)-\omega_2(t-q)]}\, df_1\, df_2\, dp\, dq$$

$$= \iint_{-\infty}^{\infty} \left(\int_{-\infty}^{\infty} h(p)\, e^{-i\omega_1 p}\, dp\right)\left(\int_{-\infty}^{\infty} h(q)\, e^{i\omega_2 q}\, dq\right)$$

$$\times\, S(f_1,f_2)\, e^{i(\omega_1-\omega_2)t}\, df_1\, df_2$$

$$= \iint_{-\infty}^{\infty} H(f_1)\, H^*(f_2)\, S(f_1,f_2)$$

$$\times\, e^{i(\omega_1-\omega_2)t}\, df_1\, df_2\,. \qquad (28)$$

This result states that $E\, x^2(t,f,B)$ is the Fourier transform of a weighted version of the double frequency spectrum of $x(t)$. The form of Eq. (28) is similar to the relationship between the input and output spectra of a linear filter when the input is stationary, namely,

$$S_{out}(f) = H(f)\, H^*(f)\, S_{in}(f)\,. \qquad (29)$$

One may now define the time varying spectral density as follows:

$$s(t,f) = \lim_{B\to\infty} \frac{1}{B}\, E\big[x^2(t,f,B)\big]\,. \qquad (30)$$

From Eq. (28), $s(t,f)$ may be written as

$$s(t,f) = \lim_{B\to 0} \frac{1}{B} \iint_{-\infty}^{\infty} H(f_1)\, H^*(f_2)\, S(f_1,f_2)$$

$$\times\, e^{i(\omega_1-\omega_2)t}\, df_1\, df_2\,. \qquad (31)$$

Unfortunately, the limiting operation and the integration may not be interchanged because $1/B$ does not approach a finite limit as B approaches zero. Thus, it is not possible to simplify Eq. (31) by performing the limiting operation first.

Using Eq. (26), the time varying spectrum may be expressed as

$$s(t,f) = \lim_{B\to 0} \frac{1}{B} \iint_{-\infty}^{\infty} h(p)\, h(q)\, R(t-p,\, t-q)\, dp\, dq \qquad (32)$$

It should be noted that the filter bandwidth is contained implicitly in the product $[h(p)\, h(q)]$. As before, the limiting operation and integration cannot be interchanged so that the integration must be performed first.

40

To measure $s(t, f)$ experimentally, one would need a large collection of records so that an ensemble averaging could be performed. An alternative approach, when only one or a few records are available, is to use some form of curve fitting on $x^2(t, f, B)/B$ to estimate the functional form of $s(t, f)$. A major limitation to the usefulness of $s(t, f)$ is that it must be determined for each frequency of interest. Thus, the entire sequence of filtering, squaring, recording, and averaging must be performed at some initial frequency f_1, and then repeated at all other frequencies of interest. The result of this processing is to generate a family of one-dimensional functions, $s(t, f_i)$, $i = 1, \ldots, N$, which approximates the two-dimensional function $s(t, f)$.

Time Averaged Spectrum

A function related to the time varying spectrum, and which may have important applications in the characterization of nonstationary processes, is the time average of $s(t, f)$. This average spectrum is defined by

$$\overline{S}(f) = \frac{1}{T} \int_T s(t, f) \, dt , \tag{33}$$

where T is the time interval of interest. The value of T could be the entire duration of the nonstationary process, in which case a limiting operation may be involved, or some smaller interval, such as a tape loop length, in which the spectral structure of the process is of particular interest.

Problems which are of concern here deal with questions of the length of T required to give an accurate estimate of $S(f)$, and the sampling variability of these estimates for different nonstationary processes. These matters are not easy to solve analytically, and may require considerable experimental testing for various cases of interest. The time averaged spectrum $\overline{S}(f)$ for a nonstationary process, however, is easy to measure and can result in significant savings in processing requirements over other means of describing the process. Finding an appropriate short averaging time to use for different nonstationary processes can lead to a meaningful interpretation of how nonstationary power spectra change with time.

From Eq. (32), it follows that

$$\overline{S}(f) = \frac{1}{T} \int_T \lim_{B \to 0} \iint_{-\infty}^{\infty} h(p) \, h(q) \, R(t - p, t - q) \, dp \, dq \, dt$$

$$= \lim_{B \to 0} \iint_{-\infty}^{\infty} h(p) \, h(q) \left[\frac{1}{T} \int_T R(t - p, t - q) \, dt \right] dp \, dq . \tag{34}$$

In the second equality, the order of integration has been interchanged. This operation is justified by the fact that the "t" integration is independent of the limiting operation and assuming all integrals exist. Let $\overline{R}(p - q)$ be defined by

$$\overline{R}(p - q) = \frac{1}{T} \int_T R(t - p, t - q) \, dt . \tag{35}$$

Then,

$$\overline{S}(f) = \lim_{B \to 0} \iint_{-\infty}^{\infty} h(p) \, h(q) \, \overline{R}(p - q) \, dp \, dq . \tag{36}$$

The function $\overline{R}(p - q)$ is seen to be the average covariance function of the random process when time trends have been smoothed over. It is easily shown that $\overline{R}$ is strictly a function of the difference $(p - q)$ and is thus the covariance function of a stationary process. We are justified, therefore, in employing all the results available for stationary processes in studying the time averaged spectrum.

The meaning of Eq. (36) is that $\overline{S}(f)$ is the mean square value of the frequency f of a stationary process with covariance function, $\overline{R}(p - q)$. Another expression for $\overline{S}(f)$ may be obtained by noting that, in the stationary case, the spectrum and covariance function are Fourier transform pairs; thus,

$$\overline{S}(f) = \int_{-\infty}^{\infty} \overline{R}(\tau) \, e^{-2\pi i \tau} \, d\tau . \tag{37}$$

SPECTRUM OF A PERIODIC NONSTATIONARY PROCESS

In this section the double frequency and time averaged spectra will be calculated for a particular type of nonstationary process to illustrate the results of the preceding section. The time dependent spectrum will not be calculated because of analytical difficulties.

Let $x(t)$ be a random process composed of the product of a zero mean, stationary process, $y(t)$, and the periodic function, $\cos(\omega_0 t)$:

$$x(t) = \cos(\omega_0 t) \, y(t) . \tag{38}$$

The covariance function of $x(t)$ may be computed as follows:

$$R_x(t_1, t_2) = E\left[x(t_1) \, x(t_2) \right]$$

$$= \cos(\omega_0 t_1) \cos(\omega_0 t_2) \, E\left[y(t_1) \, y(t_2) \right]$$

$$= \cos(\omega_0 t_1) \cos(\omega_0 t_2) \, R_y(t_2 - t_1) . \tag{39}$$

If the change of variable,

41

$$t = \frac{t_1 + t_2}{2}$$

$$\dot{\tau} = t_2 - t_1 \tag{40}$$

is made in Eq. (30), it is seen that

$$R_x(t,\tau) = \frac{1}{2} \left[\cos(\omega_0 \tau) + \cos(2\omega_0 t) \right] R_y(\tau) . \tag{41}$$

Note that

$$R_x(t,0) = \frac{1}{2} \left[1 + \cos 2\omega_0 t\, R_y(0) \right] \geqq 0 \quad \text{for all } t. \tag{42}$$

In general, however, $R_y(t,\tau)$ may be positive or negative.

Substitution of Eq. (35) into Eq. (18) shows that

$$\mathscr{S}_x(f,g) = \frac{1}{4}\,\delta(g) \left[S_y(f - f_0) + S_y(f + f_0) \right]$$

$$+ \frac{1}{4} \left[\delta(g - 2f_0) + \delta(g + 2f_0) \right] S_y(f). \tag{43}$$

where $\delta(g)$ is the Dirac delta function defined by

$$\delta(g) = \int_{-\infty}^{\infty} e^{-i 2\pi g t}\, dt . \tag{44}$$

Equation (44) shows that the function $\mathscr{S}_y(f,g)$ exists only along the lines $g = 0$ and $g = \pm 2f_0$ in the (g,f) plane.

The time averaged power spectrum may be obtained by integrating Eq. (39) with respect to t after making the substitutions $t_1 = t - p$, $t_2 = t - q$. Upon performing these operations, it is found that

$$\overline{R}_x(p - q) = \frac{1}{2} \cos\left[\omega_0(p - q) \right] R_y(p - q) . \tag{45}$$

From Eq. (37), the time averaged spectrum is

$$\overline{S}_x(f) = \frac{1}{2} \int_{-\infty}^{\infty} \cos(\omega\tau) \cos(\omega_0\tau) R_y(\tau)\, d\tau$$

$$= \frac{1}{4} \left[S_y(f - f_0) + S_y(f + f_0) \right] . \tag{46}$$

Thus, for a periodic nonstationary process, the effect is to shift the spectrum by $\pm f_0$ and to divide the peak spectrum amplitude by four. In particular, a single peaked spectrum for $S_y(f)$

centered at $f = 0$ is changed into a double peaked spectrum for $\overline{S}_x(f)$ centered at $f = \pm f_0$. One must be careful to interpret such a result correctly when dealing with nonstationary data.

To illustrate Eq. (46), consider the case where a stationary random process $y(t)$ has a Gaussian spectrum given by

$$S_y(f) = e^{-af^2}. \tag{47}$$

Substitution into Eq. (46) yields

$$\overline{S}_x(f) = \frac{1}{4} \left[e^{-a(f - f_0)^2} + e^{-a(f + f_0)^2} \right]$$

$$= \frac{1}{2} e^{-a(f^2 + f_0^2)} \cosh(2af_0 f) . \tag{48}$$

Note that $\overline{S}_x(f)$ is nonnegative for all values of f, in agreement with physical requirements.

EXPERIMENTAL RESULTS

In order to verify some of the analytical results derived previously, a brief experimental program was carried out. Because of the fact that analog equipment was used, only the time averaged power spectrum was studied since the other two spectral decompositions require ensemble averaging.

The nonstationary random signal used for the experiments was of the form

$$x(t) = \cos(\omega_0 t)\, y(t) ,$$

where $y(t)$ was a band-limited stationary random signal. The signal $y(t)$ was created by feeding the output of a random noise generator through a narrow bandpass filter. The narrow band noise signal $y(t)$ was then fed into one channel of a multiplier while a sine wave signal from an oscillator was fed into the other channel. The resulting nonstationary signal out of the multiplier was analyzed using a single filter continuous scan type power spectral density analyzer.

Two specific nonstationary signals were analyzed as follows:

1. the product of a 25-cps sine wave and a 20-cps bandwidth noise signal with a 100-cps center frequency (Fig. 1), and

2. the product of a 35 cps sine wave and a 50-cps bandwidth noise signal with a 100-cps center frequency (Fig. 2).

42
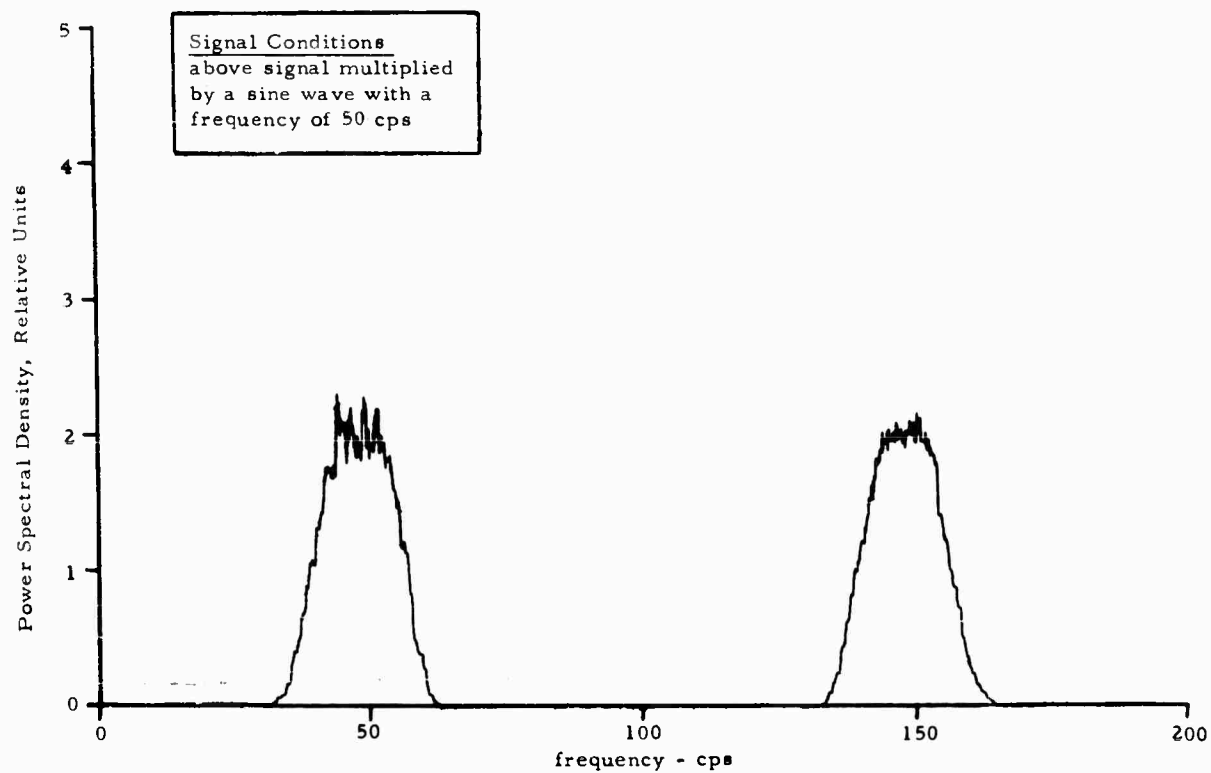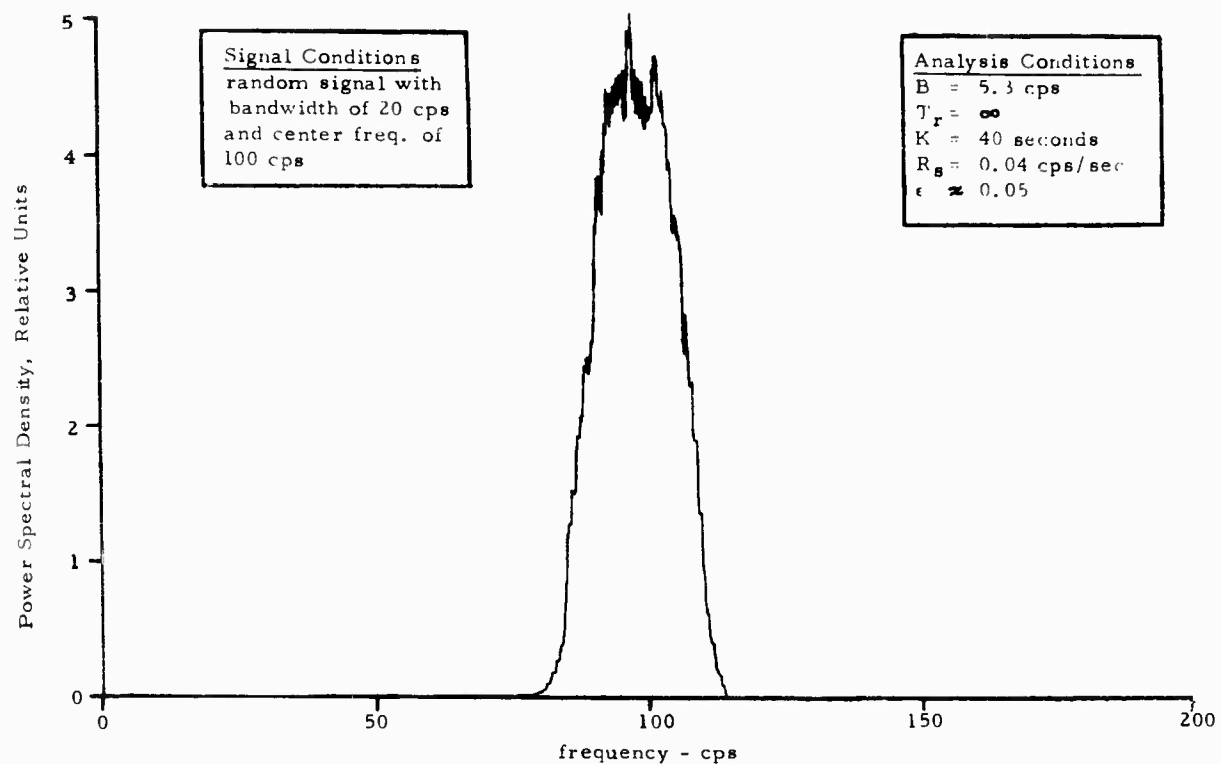
Fig. 1 - Spectrum of sine wave modulated noise: random signal with bandwidth of 20 cps and center frequency of 100 cps
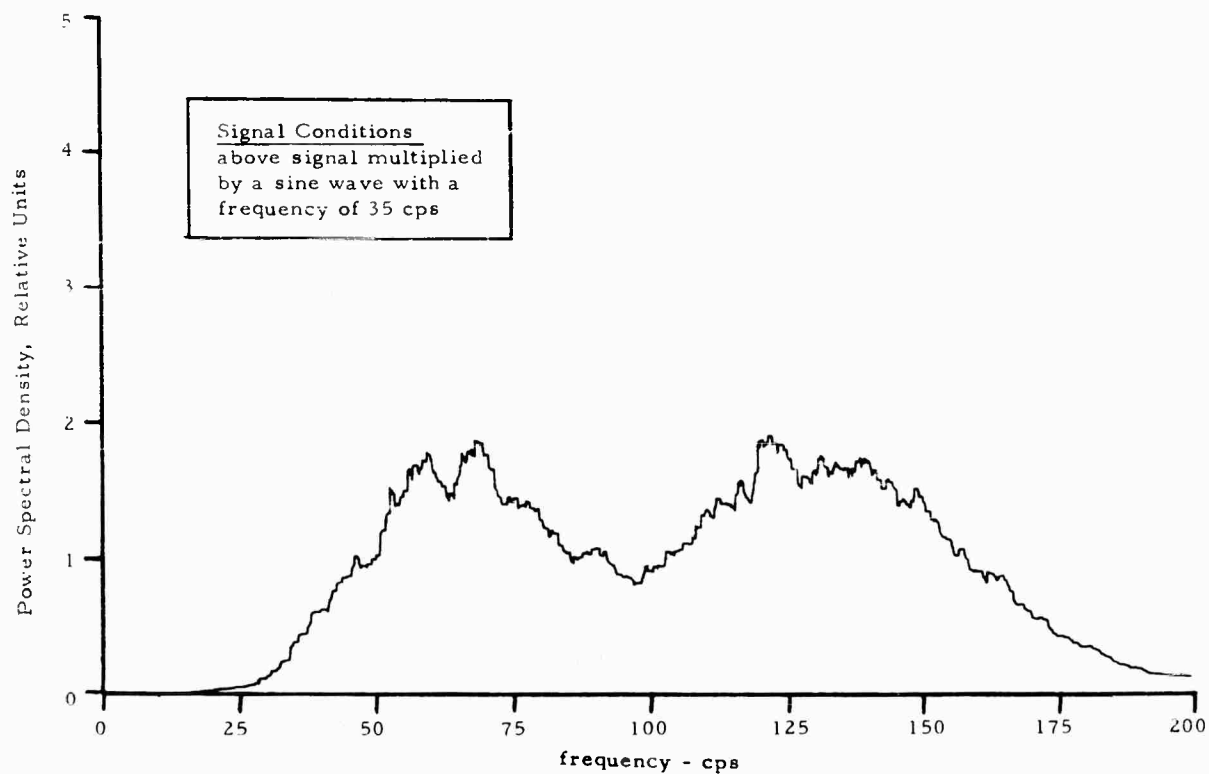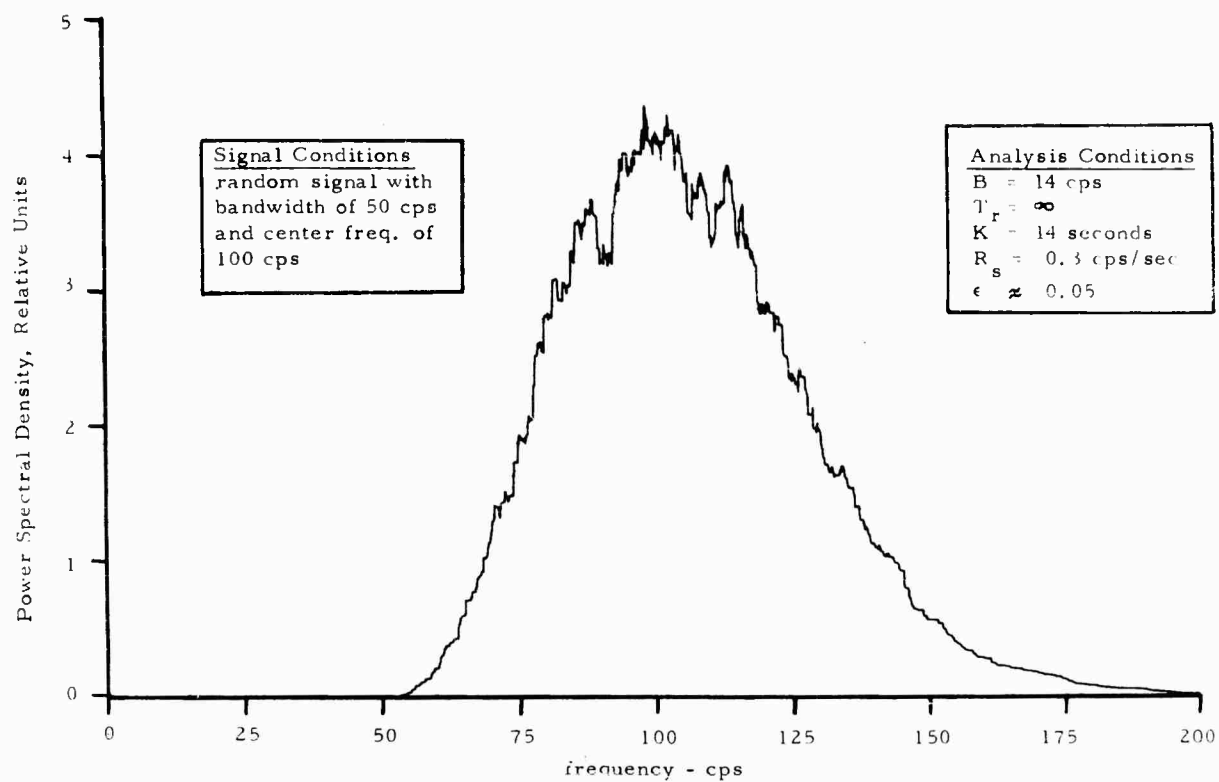
Fig. 2 - Spectrum of sine wave modulated noise: random signal with
bandwidth of 50 cps and center frequency of 100 cps

44

The power spectral density analysis was performed using an analyzer filter bandwidth that was about 1/4 the spectral width of the noise signal. Specifically, for case (a), $B = 5.3$ cps and for case (b), $B = 14$ cps. The RC averaging time constant K for the output was sufficient to produce a BT product of 400 and hence, a normalized standard deviation for the resulting power spectral density measurement of $\epsilon = 0.05$. Specifically, for case (a), $K = 40$ seconds, and for case (b), $K = 14$ seconds. The scan rate R_s was selected to allow about 3 RC time constants per analyzer filter bandwidth. Specifically, for case (a), $R_s = 0.05$ cps/second, and for case (b), $R_s = 0.3$ cps/second. Since the signal being analyzed was continuous without limit (there was no recirculation of signal data), the sample record length T_r was effectively unlimited.

The plots shown in Figs. 1 and 2 clearly indicate the sum and difference shifting of the stationary spectrum caused by the sine wave modulation.

CONCLUSIONS AND RECOMMENDATIONS

In the previous sections three approaches to the spectral decomposition of nonstationary random processes have been derived and illustrated. As was stated in the introduction, the purpose of this study is to develop a useful spectral density function for these types of processes. This goal, however, can be taken in two contexts: first, to provide an adequate analytical description of the frequency structure of the process, and secondly, to provide a quantity which can be easily measured experimentally.

It was shown in the second section that the double frequency spectrum and time varying spectrum both give an analytical description of the frequency structure. Each approach contains essentially the same information, but in different formats. In the case of the double frequency spectrum, the correlation between frequencies is given, while the time varying spectrum indicates relations between frequency and time. The choice of which one to apply to a particular nonstationary process would depend upon the nature of the overall problem and the type of information desired about the process.

The one major drawback to these two spectral decompositions is the two-dimensional nature of the functions. In one case, the spectrum is specified in terms of two frequency variables, and in the other case as a function of time and frequency. This leads to a significant measurement problem since many records must be collected, processed, and averaged in order that a good estimate be obtained. For many practical situations, it is not feasible to obtain the requisite number of records because of the high cost of experimentation. This would be the case in estimating the spectrum of missile launch vibration, for example. Finally, it should be noted that the amount of data processing required to generate an estimate of a two-dimensional spectrum will be quite large compared to the estimation of the spectrum of a stationary process.

Essentially the reverse of the statements presented above apply to the time averaged spectrum. While it is relatively easy to estimate from one or a few records, the time structure of the spectrum is lost due to the averaging operation. In situations where the power density changes appreciably with time, this information could be quite important but would not be available. It is true, however, that the time average spectrum may be used to estimate the time varying spectrum at selected time points. This could be accomplished by taking a short time average about the point of interest.

This paper has covered some of the mathematical aspects of spectral decompositions of nonstationary processes; however, much still remains to be done. In particular, practical methods to estimate the time varying, time average, and short time average spectrum need to be developed and an error analysis performed to determine the relationships between record length, sample size, averaging time, and bandwidth.

REFERENCES

1. B. Friedman, Principles and Techniques of Applied Mathematics (John Wiley and Sons, Inc., New York, N.Y., 1946), p. 136.

2. M. Loeve, Probability Theory (D. Van Nostrand Company, New York, N.Y., 1960), p. 465.

3. J. S. Bendat, L. D. Enochson, G. H. Klein, and A. G. Piersol, "Advanced Concepts of Stochastic Processes and Statistics for Flight Vehicle Vibration Estimation and Measurement," ASD-TDR-62-973, Aeronautical Systems Division, AFSC, USAF, WPAFB, Ohio. December 1962. (AD 297 031).

4. J. S. Bendat, Principles and Applications of Random Noise Theory (John Wiley and Sons, New York, N.Y., 1958).

Dr. Morrow (Aerospace Corp.): I'd like to add a couple of comments to this. The second of the two methods, the time dependent spectrum, is essentially a rigorous definition of the concept in terms of an operation that is difficult to carry out in practice because one must acquire an ensemble of records to work with. What we do in practice is to make a compromise. Instead of averaging over an ensemble we average over a brief interval of time which, hopefully, is not longer than the interval in which the vibration can be considered stationary. That, of course, brings up a couple of problems one has to look at. The first concerns just how stationary it is in the interval. At least one has to make an intuitive peace with this problem. Secondly, there are some uncertainties that arise out of the length of the sample used. In any event if one compares this approach of a time dependent spectrum with one which is averaged over the entire record I think there is something additional that should be pointed out. When you consider one of these intervals by itself you can make a good case for considering the vibration to be Gaussian. At least you can make a good case for saying that if there were some deviations from the Gaussian it would make very little change in what happens at the failure point. So now if you choose to average over the entire record of a nonstationary process then the associated distribution is not necessarily Gaussian. In other words if you mix two signals of unequal strength the distribution can remain Gaussian. If, however, you apply two signals of unequal strength in sequence the overall distribution is undoubtedly not Gaussian.

*   *   *

RESPONSE OF MULTI-DEGREE-OF-FREEDOM SYSTEM

TO RANDOM EXCITATION

R. C. Binder
University of Southern California
Los Angeles, California

A method of analysis is presented which is convenient and direct for systems up to seven degrees of freedom. Considering lightly damped systems, the roots of the frequency or characteristic equation are obtained by an approximation procedure; this procedure provides a good approximation which can be improved if necessary. The mean-square response is found using available integrals. The method is illustrated by a numerical example.

INTRODUCTION

In many applications it would help considerably to have available a convenient, relatively simple method of analyzing a multi-degree-of-freedom system for random excitation. Various proposals have been presented [1,2]. A particular method may have certain advantages and certain limitations. For example, the use of a particular method may depend on the type of computer available. This paper presents a method which is convenient in certain cases and might be regarded as an alternate or extension of the method presented by McCalley [3].

OUTLINE OF GENERAL METHOD OF APPROACH

Considering lightly damped systems, the roots of the frequency or characteristic equation are obtained by an approximation method explained by Myklestad [4]. This provides a good first approximation which can be improved, if necessary, by various established numerical methods. The mean-square-response is found by using integrals presented by Crandall and Yildiz [5] and Solodovnikov [6]. The procedure will be illustrated by a numerical example.

EXAMPLE—FREQUENCY EQUATION STUDY

Consider the lightly damped system shown in Fig. 1, with two masses M_1 and M_2, two

NOTE: References appear on page 50.

springs with spring rates K_1 and K_2, and two dampers with viscous coefficients C_1 and C_2. The displacement of mass M_1 is x_1, the displacement of mass M_2 is x_2, and the externally applied shaker forces are F_1 and F_2. Let t represent time. Application of the dynamic equation to each mass gives the relations

$$M_1 \frac{d^2 x_1}{dt^2} + \left[C_1 + C_2\right] \frac{dx_1}{dt} - C_2 \frac{dx_2}{dt}$$

$$+ \left[K_1 + K_2\right]x_1 - K_2 x_2 = F_1, \qquad (1)$$

and

$$M_2 \frac{d^2 x_2}{dt^2} - C_2 \frac{dx_1}{dt} + C_1 \frac{dx_2}{dt} - K_2 x_1 + K_2 x_2 = F_2. \qquad (2)$$

For the transient solution, with no external excitation, a start is made with a relation of the form
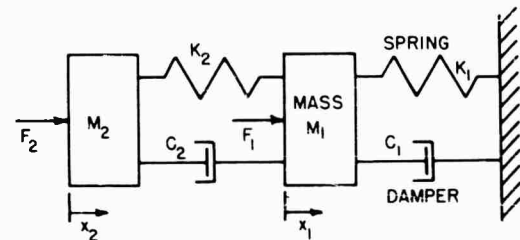
Fig. 1 - Example of lightly damped system with two degrees of freedom, Mass: M_1 = 5.0 lb, M_2 = 2.0 lb; Spring: K_1 = 818 lb/in, K_2 = 1000 lb/in; Damper: C_1 = 0.78 ft-lb/sec

$$x = Ae^{rt} , \qquad (3)$$

where A is displacement amplitude, and r is a coefficient. Let A_1 represent the displacement amplitude for mass M_1, and A_2 is the displacement amplitude for mass M_2. Then Eqs. (1) and (2) become

$$\left[M_1 r^2 + (C_1 + C_2)r + K_1 + K_2\right]A_1 - \left[C_2 r + K_2\right]A_2 = 0 \quad (4)$$

$$- \left[C_2 r + K_2\right]A_1 + \left[M_2 r^2 + C_2 r + K_2\right]A_2 = 0. \quad (5)$$

Solving Eqs. (4) and (5) simultaneously yields the frequency or characteristic equation

$$r^4 + r^3 \left[\frac{C_2}{M_2} + \frac{C_1 + C_2}{M_1}\right] + r^2 \left[\frac{K_2}{M_2} + \frac{K_1 + K_2}{M_1} + \frac{C_1 C_2}{M_1 M_2}\right]$$

$$+ r \left[\frac{K_2 C_1 + K_1 C_2}{M_1 M_2}\right] + \frac{K_1 K_2}{M_1 M_2} = 0 . \qquad (6)$$

Equation (6) can be written in the simpler form

$$r^4 + B_1 r^3 + B_2 r^2 + B_3 r + B_4 = 0 , \qquad (7)$$

where B_1, B_2, B_3, and B_4 each is a constant.

One of various possible procedures will be used for determining the complex roots of the frequency equation. By way of background explanation, Myklestad [4] has indicated that the frequency equation for a single-degree-of-freedom system can be written in the form

$$r^2 + r2\delta p + p^2 = 0 , \qquad (8)$$

with the roots

$$r_1 = -\delta p + ip\sqrt{1 - \delta^2} , \qquad (9)$$

and

$$r_2 = -\delta p - ip\sqrt{1 - \delta^2} , \qquad (10)$$

where p is the natural undamped frequency, δ is the damping factor (ratio of damping coefficient to the critical damping coefficient), and $i = \sqrt{-1}$. Let

$$a = \delta p . \qquad (11)$$

Then Eq. (8) can be written as

$$r^2 + r2a + p^2 = 0 . \qquad (12)$$

With this background explanation, refer to the system shown in Fig. 1. It is convenient to consider the whole system as having as many damped modes as there are degrees of freedom. The procedure involves the determination of the natural undamped frequencies; for $C_1 = 0$ and $C_2 = 0$, Eq. (7) becomes

$$r^4 + B_2 r^2 + B_4 = 0 . \qquad (13)$$

Let $r = ip$. Then Eq. (13) becomes

$$p^4 - B_2 p^2 + B_4 = 0 . \qquad (14)$$

with the four values of p as

$$\pm p_1 \pm p_2 . \qquad (15)$$

For a lightly damped system, these root values provide a very close approximation for the damped frequency values; this is illustrated by Eqs. (9) and (10). Then it is assumed that each damped mode can be represented by a second-degree frequency equation of the form

$$\left[r^2 + 2a_1 r + p_1^2\right]\left[r^2 + 2a_2 r + p_2^2\right] = 0 , \quad (16)$$

where

$$a_1 = \delta_1 p_1 , \qquad a_2 = \delta_2 p_2 .$$

Expanding gives

$$r^4 + 2(a_1 + a_2)r^3 + (p_1^2 + 4a_1 a_2 + p_2^2)r^2$$

$$+ 2(a_1 p_2^2 + a_2 p_1^2)r + p_1^2 p_2^2 = 0 . \quad (17)$$

The next step is a comparison of Eqs. (17) and (7). By comparing the coefficients of the r^3 and r terms, the following two linear equations are obtained:

$$2a_1 + 2a_2 = B_1 \qquad (18)$$

and

$$2a_1 p_2^2 + 2a_2 p_1^2 = B_3 . \qquad (19)$$

Solving Eqs. (18) and (19) simultaneously gives numerical values for a_1 and a_2. From known values of a_1 and a_2, the damping factors δ_1 and δ_2 can be computed, and thus the complex roots can be expressed in the form given by Eqs. (9) and (10)

$$r_1 = -\delta_1 p_1 \pm ip_1 \sqrt{1 - \delta_1^2} \qquad (20)$$

and

$$r_2 = -\delta_2 p_2 \pm ip_2 \sqrt{1 - \delta_2^2} . \qquad (21)$$

48

If it is desired to check or refine this calculation, one of various established numerical methods can be used.

Use of the foregoing method gives frequency values of 32.4 and 86 cps and damping factors of $\delta_1 = 0.0081$ and $\delta_2 = 0.013$.

RESPONSE DUE TO RANDOM EXCITATION

The impedance ratio $z(\omega)$, a function of angular frequency ω, is defined by the relation

$$z(\omega) = \frac{\text{Force}}{\text{Displacement}} . \tag{22}$$

The magnitude of impedance is $|z(\omega)|$. Let $P_F(\omega)$ represent power spectral density of the exciting force, and $P_x(\omega)$ the power spectral density of the displacement x. Then the following relations hold:

$$|z(\omega)|^2 = \frac{P_F(\omega)}{P_x(\omega)} \tag{23}$$

$$\overline{X^2} = \int_0^\infty P_x(\omega)\, d\omega \tag{24}$$

$$\overline{X^2} = \int_0^\infty \frac{P_F(\omega)\, d\omega}{|z(\omega)|^2} . \tag{25}$$

By assuming white-noise input, Eq. (25) can be written in the form

$$\frac{\overline{X^2}}{P_F} = \int_0^\infty \frac{d\omega}{|z(\omega)|^2} = \int_0^\infty |H(\omega)|^2\, d\omega . \tag{26}$$

where $|H(\omega)|$ is the reciprocal of the magnitude of impedance. There is a question about the integration of Eq. (26) for particular cases. Following are the integrals adapted from Crandall and Yildiz [5] which provide integrals for cases up to two degrees of freedom and from Solodovnikov [6] which provide integrals for cases up to seven degrees of freedom.

Examples of Integrals Adapted from Refs. [5] and [6]

$$H(\omega) = \frac{i\omega E_1 + E_0}{-\omega^2 D_2 + i\omega D_1 + D_0} \tag{I}$$

Integral for (I) is

$$\int_0^\infty |H(\omega)|^2\, d\omega = \frac{\pi}{2}\left[\frac{E_1^2 + \frac{E_0^2}{D_0}D_2}{D_1 D_2}\right] .$$

$$H(\omega) = \frac{-i\omega^3 E_3 - \omega^2 E_2 + i\omega E_1 + E_0}{\omega^4 - i\omega^3 D_3 - \omega^2 D_2 + i\omega D_1 + D_0} . \tag{II}$$

Integral for (II) is

$$\int_0^\infty |H(\omega)|^2\, d\omega =$$

$$\frac{\pi}{2}\left[\frac{\frac{E_0^2}{D_0}(D_2 D_3 - D_1) + D_1(E_2^2 - 2E_1 E_3) \longrightarrow \atop + D_3(E_1^2 - 2E_0 E_2) + E_3^2(D_1 D_2 - D_0 D_3)}{D_1(D_2 D_3 - D_1) - D_0 D_3^2}\right] .$$

EXAMPLE—STEADY-STATE SOLUTION STUDY

Next consider the steady-state solution for the system shown in Fig. 1. A start is made with solutions of the form

$$x_1 = x_{10} e^{i\omega t} \tag{27}$$

and

$$x_2 = x_{20} e^{i\omega t} , \tag{28}$$

where x_{10} is the displacement amplitude for x_1, and x_{20} is the displacement amplitude for x_2. Substitution in Eqs. (1) and (2) gives the result

$$\left[(K_1 + K_2) - \omega^2 M_1 + i(C_1 + C_2)\omega\right]x_{10}$$
$$- \left[K_2 + iC_2\omega\right]x_{20} = F_1 \tag{29}$$

$$-\left[K_2 + iC_2\omega\right]x_{10} + \left[K_2 - \omega^2 M_2 + iC_3\omega\right]x_{20} = F_2 . \tag{30}$$

Consider the case in which $F_1 = 0$. The transfer function x_{20}/F_2 can be determined, as by means of the Cramer rule. Use of the numerical values listed in Fig. 1 gives the relation

$$H(\omega) = x_{20}/F_2$$
$$= \frac{21.5 \times 10^5 - 16.1\omega^2 + i138\omega}{\omega^4 - i17.34\omega^3 - 33.3 \times 10^4 \omega^2 + i15.21 \times 10^5 \omega + 12.2 \times 10^9} . \tag{31}$$

49

Equation (31) is type (II) (see previous section); the use of the integral from the previous section gives the final result

$$\overline{x^2} \, P_F = 5.13 \times 10^{-4},\qquad (32)$$

in units of the foot-pound-second system. For a given input excitation, the displacement response can be determined.

CONCLUDING REMARKS

The foregoing method involves two major steps, the solution of the frequency equation and the integration of the response equation. Using presently available integrals, the method is convenient and direct for systems up to seven degrees of freedom.

REFERENCES

1. R. M. Mains, "The Probable Response of Multi-Degree-Of-Freedom Systems To Random Shock and Vibration," Supplement to Shock and Vibration Bulletin No. 23 (June 1956).

2. C. T. Morrow, "Resonant RMS Acceleration," Appendix 5, Section A, Fundamentals of Guided Missile Packaging, RD 219/3 (July 1955).

3. R. B. McCalley, Jr., "The Evaluation of Random-Noise Integrals," Shock and Vibration Bulletin No. 25, Part II (Dec. 1957).

4. N. O. Myklestad, Fundamentals of Vibration Analysis (McGraw-Hill Book Co., Inc., New York, N.Y., 1956) page 215.

5. S. H. Crandall and A. Yildiz, J. Appl. Mech., 29, 267-275 (June 1962).

6. V. V. Solodovnikov, Introduction to the Statistical Dynamics of Automatic Control Systems (Dover Publications, New York, N.Y., 1960) pages 299-301.

*   *   *

STRUCTURAL RESPONSE TO A VELOCITY-DEPENDENT
STOCHASTIC EXCITATION*

W. J. Stronge and G. K. Fisher
Supersonic Track Division
U.S. Naval Ordnance Test Station

A theoretical analysis of the forced vibrations of a single-degree-of-freedom, linear system having viscous damping is presented. The vibrations are excited by the system traveling over a specific random surface — the Supersonic Naval Ordnance Research Track (SNORT). Thus, the time-history of the forcing function and the statistical measures of the response reported here depend on the velocity of the system along that track. The response of this model has been related to a dynamic loading factor for track vehicles that corresponds, within a factor of 2, to experimental measurements.

INTRODUCTION

Several informative applications of statistical methods for determining the response of a mechanical system to a random excitation have been presented recently [1-4]. Because of the generality of the treatment in most of these current works, however, their usefulness to the engineer in the field who does not have a good background in statistical methods is limited. The information presented in this paper is intended to provide a relatively simple method of determining system response characteristics by using hand calculations and a simple mechanical model.

The model consists of a discrete parameter single-degree-of-freedom linear system having viscous damping. This system is excited by traveling at a constant velocity over an uneven surface such as a roadway, rail, or ground surface, where the random surface can be represented by a stationary stochastic process. The system is assumed to maintain contact with the rigid surface without friction. The absolute acceleration and relative displacements of the system in response to a particular stochastic process are determined as a function of the vehicle velocity, damping ratio, and natural frequency. These functions are then related to a design dynamic loading factor which

depends upon the probability of exceeding some maximum amplitude.

The particular random process considered is based on the measured contour of the rail of a high-velocity test track (SNORT).† The method of measurement of this rail roughness gives rise to a spectral density with distance along the track as its argument. A smoothed analytical representation of this excitation is transformed into the time-dependent frequency domain by introducing the variable velocity. This quasi-stationary analysis has agreed within a factor of two with experimental results obtained thus far for the response of a system even when the system is accelerating at rates of up to 200 ft/sec^2.

THEORY OF LINEAR SINGLE-
DEGREE-OF-FREEDOM
VIBRATING SYSTEMS

The forcing function of the simple, discrete-parameter mechanical system used in this study is caused by a velocity-dependent displacement excitation applied at the foundation. The motions of the system in response to this excitation [5]

---

†SNORT, located at the U.S. Naval Ordnance Test Station, China Lake, California, offers 4.1 miles of precision aligned track for the research testing of missile systems, warheads, aircraft, and aircraft components traveling at supersonic velocities.

are analyzed below. Consider the system shown in the following sketch:
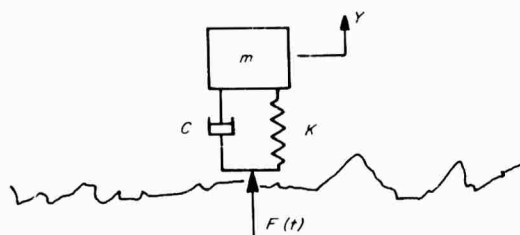
Mechanical system vibration model

The differential equation of motion for this system is

$$m\ddot{y} + c\dot{y} + ky = F(t) , \qquad (1)$$

or

$$\ddot{y} + 2\zeta\omega_n\dot{y} + \omega_n^2 y = R(t) , \qquad (2)$$

where

$$\omega_n = \sqrt{k/m} ,$$

$$\zeta = c/c_{cr} ,$$

$$c_{cr} = 2\sqrt{km} ,$$

and

$$R(t) = F(t)/m .$$

When the absolute motions of the system are sought and the motions of the base, rather than the excitation forces, are known, Eq. (2) becomes

$$\ddot{y} = 2\zeta\omega_n(\dot{y}_t - \dot{y}) + \omega_n^2 (y_t - y) . \qquad (3)$$

The motions of the base (track) are denoted by the subscript t. The relative motions between the body and the track are obtained by referring the coordinate system to the body. With $Z = y - y_t$ the equation of motion is

$$\ddot{Z} + 2\zeta\omega_n\dot{Z} + \omega_n^2 Z = -\ddot{y}_t . \qquad (4)$$

Periodic Excitation

When $R(t)$ is a periodic function, the response, $y(t)$, can be found by several different methods. The Fourier series method described here is applicable when the disturbing force can be described by a trigonometric series.

$$F(t) = a_0/2 + \sum_{n=1}^{\infty} (a_n \cos n\omega t + b_n \sin n\omega t), \qquad (5)$$

where ω is some fundamental frequency of the excitation.

The coefficients, a_n and b_n, of the Fourier series are a measure of the amplitude of that part of the forcing function, $F(t)$, having a frequency $n\omega$. The frequency spectrum of a periodic forcing function, $F(t)$, will be discrete. Each frequency composing the spectrum will have two 90-degree out-of-phase components with coefficients a and b:
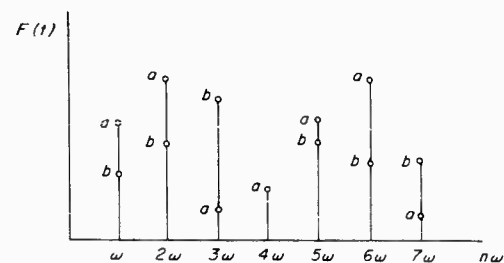
Periodic frequency spectrum

In considering the forced vibration of a linear system, the response is obtained by superimposing the vibrations produced by each term in the Fourier series, Eq. (5), applied individually to the system. Thus, the problem of analyzing the response to a periodic excitation that can be described by a trigonometric series becomes one of finding the generalized response to a sinusoidal excitation [6]. The model used with a sinusoidal track waveform is shown below:
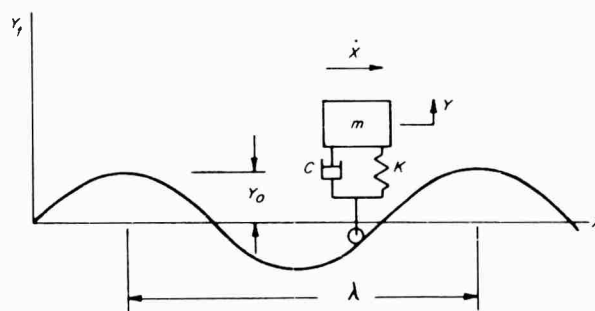
Vibration model traveling over sinusoidal wave

The diameter of a wheel, rolling on the track without friction, is infinitely small. The sinusoidal wave of amplitude y_o has a wavelength λ. The track function can be written

$$y_t = y_o \sin \frac{2\pi x}{\lambda} . \tag{6}$$

Take $k = 2\pi/\lambda$, where k is the wave vector. Note that, when the mechanical system is traveling over the waveform, x becomes a function of time:

$$y_t = y_o \sin kx(t) . \tag{7}$$

This function is then differentiated to obtain the time-dependent excitation due to a sinusoidal waveform.

Random Excitation

Random forcing functions are those excitations composed of variables whose instantaneous values are not predictable. A random variable is a real valued function defined on some sample space consisting of all possible outcomes, where the statistical probability distribution of the variable on the sample space is described by an n-dimensional probability density function. A stochastic process is an ensemble of random variables depending on some argument such as time or distance. The stochastic process is said to be stationary if the probability distribution remains invariant with translation of the argument.

The expectation of a random variable, x, defined over some discrete sample space of numerically distinct events with x_i values — each with probability p_i — is

$$E(x) = \sum_n x_i p_i . \tag{8}$$

When the sample space is continuous,

$$E(x) = \int_{-\infty}^{\infty} x p(x)\, dx , \tag{9}$$

where $p(x)$ is the probability density function. The expected value, $E(x)$, of the random variable is equal to the mean, μ, or statistical average of x.

The moments of the probability density function are pertinent in describing the distribution of the random variable. The nth moment is

$$E(x^n) = \int_{-\infty}^{\infty} x^n p(x)\, dx , \tag{10}$$

from which it can be seen that the mean is just the first moment. The second moment about the mean, called the variance, δ^2, is particularly important in the practical analysis of stochastic processes. Thus,

$$\delta_x^2 = E\left[x - \mu_x\right]^2 = E\left[x^2\right] - \mu_x^2 . \tag{11}$$

The variance is the first moment describing the dispersion of the random variable [7].

With these statistical terms defined, one can now look for the input-output relationships of a system excited by some particular stochastic process. Either the Fokker-Planck or the Fourier series method can be used to determine statistical measurements of the random vibrations excited in a system by a particular stochastic process. The Fokker-Planck method solves a partial differential equation of the diffusion type for the probability distribution of the response. This equation is generally solvable only for excitations with a white spectrum* in which the response will always have a normal or Gaussian distribution. The Fokker-Planck method is amenable to non-Gaussian excitations, and is generally applied to nonstationary problems.

The Fourier series method which does not need a white spectral density, requires a Gaussianly distributed excitation process to determine the response distribution function uniquely. The Weiner-Khintchine theorem relating the autocorrelation and the spectral density is most important to this method. The Fourier series method, usually applied to stationary processes, is used in this study because of the interest in other than white excitation spectrums [1].

The relationship in the time domain between the input, $e(t)$, and the output of a linear system is

$$y(t) = \int_{-\infty}^{t} h(t - \tau)\, e(\tau)\, d\tau . \tag{12}$$

Here, $h(t)$ is the unit impulse response of the system and τ is the lag. If $e(t)$ can be expressed as a Fourier transform, the Fourier

*A white spectrum has a constant amplitude from a frequency of $-\infty$ to $+\infty$.

53

transform of y, $y(j\omega)$, can be found. Hence, in the frequency domain

$$y(j\omega) = H(j\omega) E(j\omega) . \qquad (13)$$

When $e(t)$ is a stationary stochastic process it is described by the Fourier transform pairs, $S_e(\omega)$, the spectral density, and $R(\tau)$, the auto-correlation function.

Using the Weiner-Khintchine theorem, the output spectrum $S_x(\omega)$ is

$$S_x(\omega) = H(j\omega) H(-j\omega) S_e(\omega) = |H(j\omega)|^2 S_e(\omega) . \qquad (14)$$

where $H(-j\omega)$ is the complex conjugate of $H(j\omega)$.

The variance of the response is found by integrating the response spectrum $S_x(\omega)$. Thus,

$$E[y^2] = \int_{-\infty}^{\infty} |H(j\omega)|^2 S_e(\omega) d\omega . \qquad (15)$$

This relationship is fundamental to the development of the response characteristics to stochastic excitations [2].

VEHICLES HAVING CONSTANT VELOCITY

When the mechanical system is traveling with a constant velocity over the stationary waveform, the steady-state vibration solutions can be found by applying the excitation function to the system transfer function. The transmissibility of the system is found by analyzing the response to a sinusoidal excitation. The transfer function, derived from this transmissibility, applies to the random excitation as well as to the periodic excitation, since the Fourier series method of solution is being used.

Calculation of Transfer Functions

For a constant velocity, the time dependent function is determined by $x(t) = \dot{x}t$. Differentiating the track displacement function (Eq. (7)) with respect to time, the following track description is obtained

$$y_t = y_o \sin \omega t ,$$

$$\dot{y}_t = y_o \omega \cos \omega t , \qquad (16)$$

$$\ddot{y}_t = y_o \omega^2 \sin \omega t ,$$

where the forcing function frequency, ω, is equal to $k\dot{x}$.

Transmissibility of Absolute Motions. Absolute motions of the mass have an excitation function,

$$R(t) = \omega_n^2 y_t + 2\zeta\omega_n \dot{y}_t .$$

Substituting Eq. (16) into this function, the explicit sinusoidal track excitation function is obtained; i.e.,

$$R(t) = y_o 2\zeta\omega\omega_n \cos \omega t + y_o\omega_n^2 \sin \omega t . \qquad (17)$$

Because the terms in this expression are two vectors, oriented 90 degrees apart and having the same angular velocity,

$$R(t) = y_o\omega_n \left(1 + \frac{4\zeta^2\omega^2}{\omega_n^2} \right)^{1/2} \sin(\omega t - \psi) , \qquad (18)$$

where

$$\psi = \tan^{-1} \frac{2\zeta\omega}{\omega_n} .$$

This excitation function is applied to the differential equation of motion for the system, Eq. (2). By assuming a sinusoidal response solution, Eq. (2) becomes

$$C(\omega_n^2 - \omega^2) \sin \omega t + 2C\zeta\omega\omega_n \cos \omega t = R(t) \qquad (19)$$

or

$$C\omega_n^2 \left[\left(1 - \frac{\omega^2}{\omega_n^2} \right)^2 + \frac{4\zeta^2\omega^2}{\omega_n^2} \right]^{1/2} \sin(\omega t - \alpha)$$

$$= y_o\omega_n^2 \left(1 + \frac{4\zeta^2\omega^2}{\omega_n^2} \right)^{1/2} \sin(\omega t - \psi) , \qquad (20)$$

where

$$\alpha = \tan^{-1} \frac{2\zeta\omega\omega_n}{\omega_n^2 - \omega^2} .$$

Defining the transmissibility as the relative amplitude of the response to the amplitude of the excitation,

$$H_A = \frac{C}{y_o} , \qquad (21)$$

54

the transmissibility for absolute motions has been found to be

$$H_A = \left[\frac{1 + \dfrac{4\zeta^2\omega^2}{\omega_n^2}}{\left(1 - \dfrac{\omega^2}{\omega_n^2}\right)^2 + \dfrac{4\zeta^2\omega^2}{\omega_n^2}} \right]^{1/2} \quad . \quad (22)$$

If a harmonic excitation of the form $e^{i\omega t}$ were used as the forcing function, and if a response of the same form were assumed, the transfer function in complex notation [3] would be

$$H_A(i\omega) = \frac{\omega_n^2 + 2i\zeta\omega\omega_n}{\omega_n^2 - \omega^2 + 2i\zeta\omega\omega_n} \quad . \quad (23)$$

The transmissibility for absolute motion is shown in Fig. 1.

Transmissibility of Relative Motions. The transmissibility of relative motions can be found in the same manner as is used for absolute motions. In this case, the excitation function, $R(t)$, is equal to $-\ddot{y}_t$. Hence, from Eq. (16) the relative motion excitation from a sinusoidal track is

$$R(t) = y_o\omega^2 \sin \omega t \quad . \quad (24)$$

This excitation function is substituted into the equation of motion for the system Eq. (4). Then the differential equation for relative motion can be written

$$C_r(\omega_n^2 - \omega^2)\sin\omega t + 2C_r\zeta\omega\omega_n\cos\omega t = y_o\omega^2\sin\omega t \quad . \quad (25)$$

The transmissibility of relative motions in response to this sinusoidal track excitation, with the transmissibility defined as before, is then
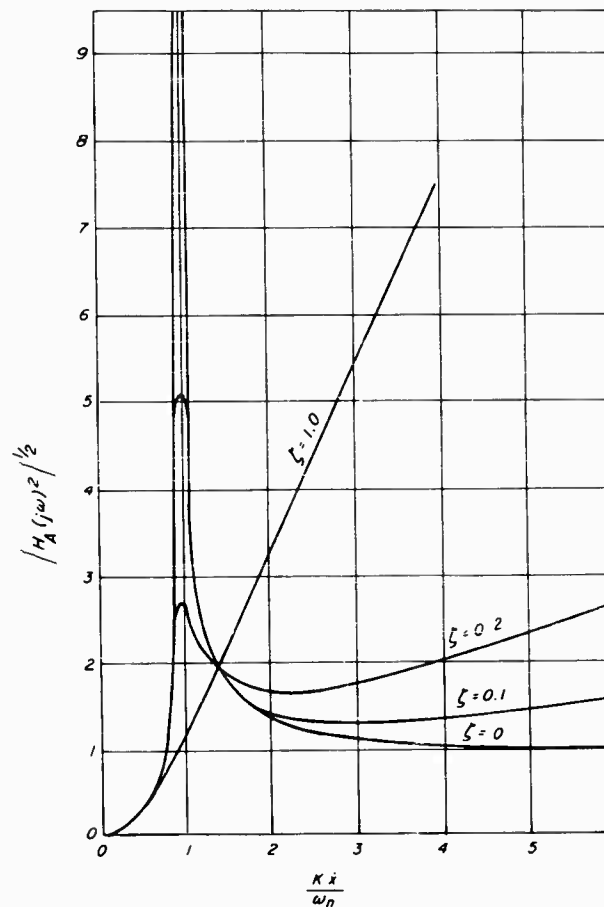
Fig. 1 - Transmissibility of absolute motions

$$H_B \quad \frac{C_r}{y_o} \; . \qquad (26)$$

$$H_B = \frac{\dfrac{\omega^2}{\omega_n^2}}{\left[\left(1 - \dfrac{\omega^2}{\omega_n^2}\right)^2 + \dfrac{4\zeta^2\omega^2}{\omega_n^2}\right]^{1/2}} \; . \qquad (27)$$

This transfer function could also have been found in complex notation [3] by starting with an excitation of the form $e^{i\omega t}$. In that case,

$$H_B(i\omega) = \frac{\omega^2}{\omega_n^2 - \omega^2 + 2i\zeta\omega\omega_n} \; . \qquad (28)$$

The transmissibility of relative motions, as a function of the damping ratio ζ, is shown in Fig. 2.

Response to a Periodic Excitation

The periodic excitation can be thought of as composed of a number of sinusoids. With the appropriate transfer functions, the response is merely the product of the forcing function and the transfer function.

Absolute Response. The absolute motions of the mass in response to the sinusoidal track excitation will be

$$y = y_t H_A = y_o H_A \sin(\omega t - a) , \qquad (29)$$

$$\dot{y} = \dot{y}_t H_A = y_o \omega H_A \cos(\omega t - a) , \qquad (30)$$

and

$$\ddot{y} = \ddot{y}_t H_A = y_o \omega^2 H_A \sin(\omega t - a + \pi) . \qquad (31)$$
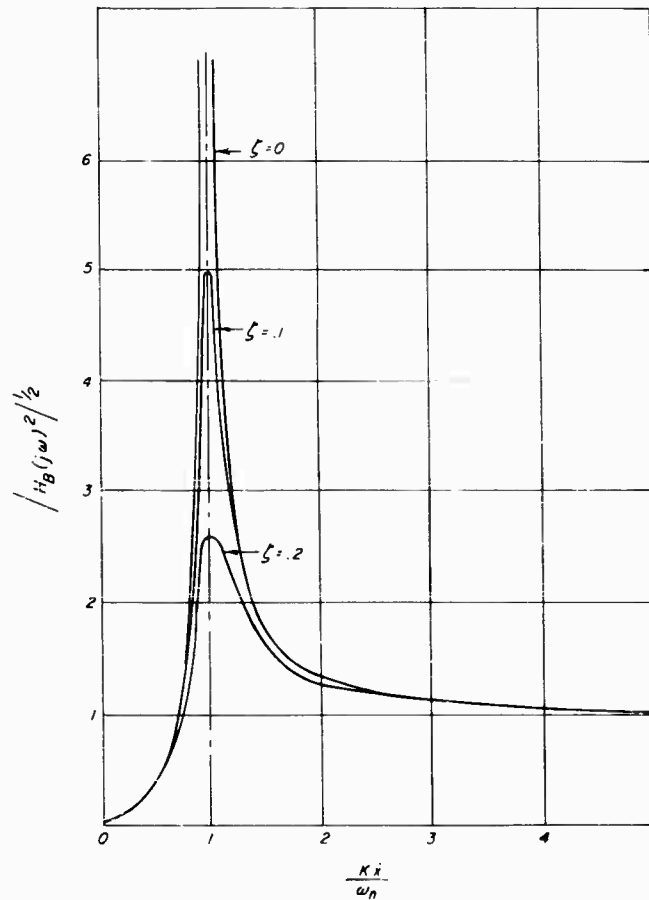
Fig. 2 - Transmissibility of relative motions

56
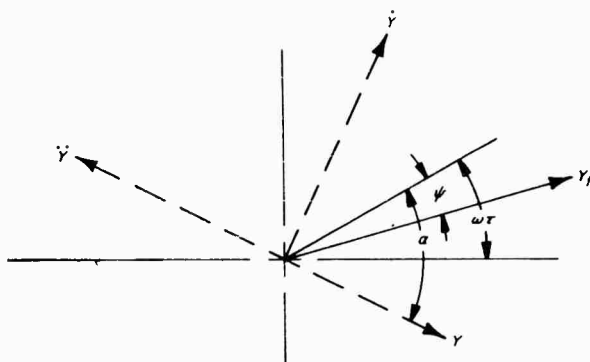
Phase relationships between the forcing function and the response

For the case of oscillatory motion (damping less than unity) the absolute acceleration response is highly spiked near the resonant frequency. Higher frequency excitations result in a response which asymptotically approaches a value $2\zeta\omega/\omega_n$ due to the velocity-dependent nature of the damping. (The displacement response is relatively independent of damping ratio and excitation frequency in this range.)

Relative Response. The relative displacement response is of prime importance because it is directly related to the stress in the spring of the system. The relative displacements between the mass and the track are

$$Z = Z_t H_B = y_o H_B \sin (\omega t - \alpha). \qquad (32)$$

The maximum relative displacement response occurs when the excitation frequency equals the natural frequency of the system. At this point, the stress in the isolator is a maximum, and varies inversely with the damping ratio. For forcing functions higher than the natural frequency, the relative-displacement transmissibility asymptotically approaches unity.

Response to Random Excitations

The random roughness of the track forms a stationary stochastic process and can be used as a velocity-dependent forcing function of the system. To use the Fourier series method of solution, the description of the stochastic process should be in the frequency domain — a spectral density distribution. The excitation function can then be written in terms of the excitation spectral density, $S_e(\omega)$, at a differential frequency element, $\Delta\omega$. A displacement excitation with $S_e(\omega)$ in units of ft^2/rad/sec is

$$y_t^2 = S_e(\omega)\,\Delta\omega. \qquad (33)$$

A velocity excitation spectrum, $S_{e'}(\omega)$, in units of ft^2/rad/sec becomes

$$\dot{v}_t^2 = \omega^2 y_t^2 = S_{e'}(\omega)\Delta\omega. \qquad (34)$$

Acceleration excitation spectrums, $S_{e''}(\omega)$, are commonly given in terms of g^2/rad/sec.

$$\ddot{y}_t^2 = \omega^4 y_t^2 = S_{e''}(\omega)\Delta\omega. \qquad (35)$$

In this form of the spectral density, which is the mean square value of the excitation function in the frequency domain, the relationship with the Fourier-series expansion of the excitation function is emphasized.

The expected value of the mean squared response is just the variance of the response for an unbiased distribution function. The well-known result for the response, given in Eq. (15), is

$$E[y^2] = \int_{-\infty}^{\infty} S_e(\omega)\,|H_A(i\omega)|^2\,d\omega.$$

The same result will be obtained for the absolute velocity and acceleration response when excited by their respective excitations. Thus,

$$E|\dot{y}^2| = \int_{-\infty}^{\infty} S_{e'}(\omega)\,|H_A(i\omega)|^2\,d\omega, \qquad (36)$$

and

$$E[\ddot{y}^2] = \int_{-\infty}^{\infty} S_{e''}(\omega)\,|H_A(i\omega)|^2\,d\omega. \qquad (37)$$

Other forms of the response can be found from any specific excitation by using Eqs. (34) and (35).

It can be seen that

$$\frac{S_{e''}(\omega)}{\omega^4} = S_e(\omega). \qquad (38)$$

Therefore, the acceleration response, in units of g^2, to a displacement excitation spectrum, in units of ft^2/rad/sec, will be

$$E[\ddot{y}^2] = \int_{-\infty}^{\infty} \frac{\omega^4 S_e(\omega)}{g^2}\,|H_A(i\omega)|^2\,d\omega, \qquad (39)$$

and the displacement response in ft^2 to an acceleration excitation spectrum, $g^2/rad/sec$, will be

$$`E[y^2] = \int_{-\infty}^{\infty} \frac{g^2 S_{e''}(\omega)}{\omega^4} |H_A(i\omega)|^2 \, d\omega . \quad (40)$$

The relative response can be obtained by using the same manipulations. The relative displacement response, in ft^2, to a displacement excitation spectrum, $ft^2/rad/sec$, is

$$E[Z^2] = \int_{-\infty}^{\infty} S_e(\omega) |H_B(i\omega)|^2 \, d\omega , \quad (41)$$

while the response to an acceleration excitation spectrum in $g^2/rad/sec$ will be

$$E[Z^2] = \int_{-\infty}^{\infty} \frac{g^2 S_{e''}(\omega)}{\omega^4} |H_B(i\omega)|^2 \, d\omega . \quad (42)$$

For solutions of integrals of this form, the expression must be convergent in the limit as $\omega \to \infty$. The integral can then be solved by contour integration [8]. If, however, $S_e(\omega)$ can be expressed as an even valued polynomial, analytic in the interval $-\infty$ to ∞, and if it has a root with all poles in the upper half plane and none on the real axis, then tabulated values of the integral can be found in several sources [4,9,10].
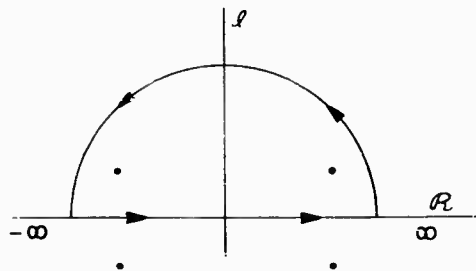
Integration of complex function

Response to SNORT Excitation

The SNORT rail-roughness excitation has a nonwhite spectral representation. (The analysis of this spectrum from discrete measurements is reported in Ref. 11.) The assumption is made that the track contour is a stationary stochastic process; i.e., this sample of track is representative of the entire length of track.

An approximation made to the spectrum grossly smoothed the spectrum but resulted in an analytical expression that could be used in the tabulated integrals. This function, which is a polynomial with complex roots, has been superimposed on the spectrum in Fig. 3. In general, some polynomial that will allow integration if the function remains bounded can be found for any spectrum. This particular expression for the SNORT spectral density as a function of the wave vector, k, is:

$$S_e(k) = \frac{2 \times 10^{-4}}{(1/3 + k^2)^2} . \quad (43)$$

This amplitude is for a spectrum taken from 0 to ∞. The expression is analytical, symmetrical, decays rapidly, and meets the restrictions discussed previously in all respects.

Because this spectrum was analyzed from measurements made along the track where the argument of the random variable is distance, it is wavelength-dependent. To transform the spectrum into the usual frequency domain, the spectrum must be weighted over the waveform by the velocity of the mechanical system. The product of a wave vector and velocity will be the frequency of that wave vector. To maintain the proper density, the ordinate of Fig. 3 must be divided by velocity, since

$$S_e(\omega) = \frac{2 \times 10^{-4}}{\dot{x} \left[1/3 + (\omega/\dot{x})^2 \right]^2} \quad (44)$$

or

$$S_e(\omega) = \frac{2 \times 10^{-4} \dot{x}^3}{\left[a^2 + \beta^2 \right]^2 \omega_n^4} . \quad (45)$$

where

$$a = \frac{\dot{x}}{\omega_n \sqrt{3}}$$

and

$$\beta = \frac{\omega}{\omega_n} .$$

The relative displacement response to this displacement excitation spectrum is determined by using Eq. (41). After identifying the complex roots, Eq. (45) can be written

$$S_e(\omega) = \frac{2 \times 10^{-4} \dot{x}^3}{\omega_n^4 (\beta - ia)^2 (\beta + ia)^2} , \quad (46)$$

and the transfer function will be

58
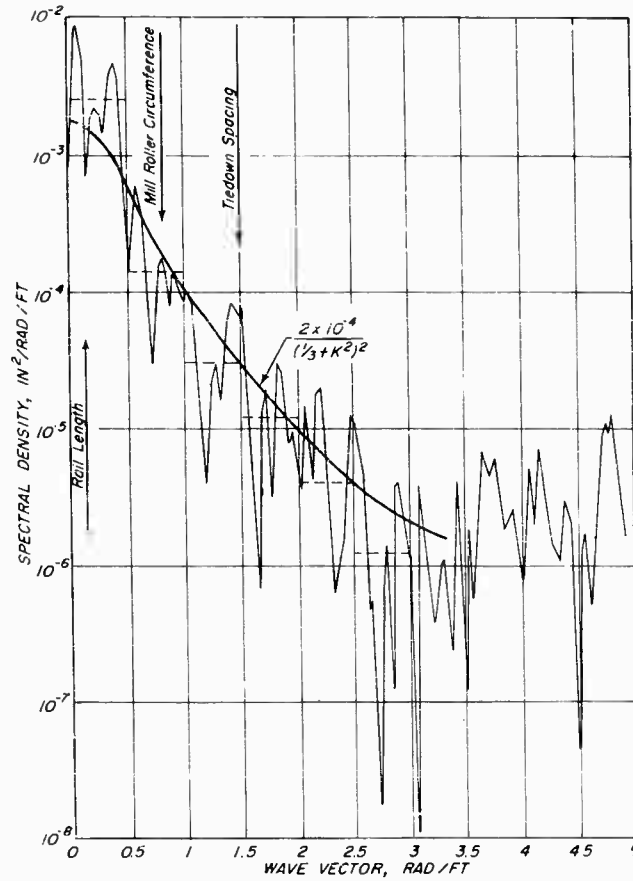
Fig. 3 - Periodogram analysis of SNORT
west rail profile over 100-ft interval

$$|H_B(i\omega)|^2 = \frac{\beta^4}{(1 + 2i\zeta\beta - \beta^2)(1 - 2i\zeta\beta - \beta^2)} , \quad (47)$$

Then, by evaluating Eq. (41) using the tables of
Ref. 10, we obtain

$$E[z^2], \text{ in.}^2 = \frac{10^{-4} \pi 3\sqrt{3} \, a^3 (1 + \zeta a)}{2\zeta \left[(1 + a^2)^2 + 4\zeta a(1 + a^2 + \zeta a)\right]} \quad (48)$$

The square root of this variance of the relative
displacement response has been plotted as
Fig. 4.

The absolute acceleration response to the
track displacement excitation can be found from
Eq. (39).

By applying $S_e(\omega)$ from Eq. (46), and for
$|H_A(i\omega)|^2$,

$$|H_A(i\omega)|^2 = \frac{1 + 4\zeta^2 \beta^2}{(1 + 2i\zeta\beta - \beta^2)(1 - 2i\zeta\beta - \beta^2)} \quad (49)$$

and

$$E[\ddot{y}^2], \, g^2 =$$

$$\frac{10^{-4}\pi 3\sqrt{3} \, \omega_n^4 \, a^3 (1 + \zeta a + 4\zeta^2 + 16\zeta^3 a + 16\zeta^4 a^2 + 4\zeta^3 a^3)}{2(386)^2 \zeta \left[(1 + a^2)^2 + 4\zeta a(1 + \zeta a + a^2)\right]} .$$

$$(50)$$

This absolute acceleration response of the
mass to the track excitation has been plotted as
Fig. 5.

The response characteristics of this sys-
tem have been strongly influenced by the shape
of the spectral approximation, Fig. 3, and in
particular, by the shoulder at approximately
$k = 0.4$. In the frequency domain, the excita-
tion from this wavelength will occur at the
natural frequency of the system when $a = 1.5$.
It is near this point that the relative displace-
ment is a maximum and the character of the
absolute acceleration changes from vibrations

59
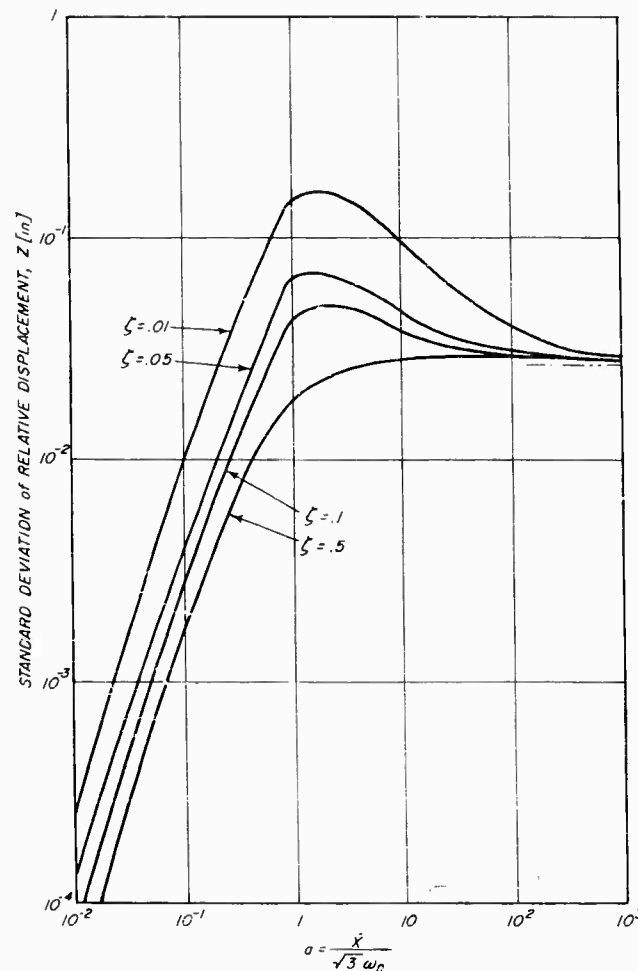
Fig. 4 - Relative displacement response
to the SNORT excitation

at the natural frequency to a response consist-
ing primarily of higher frequency components.

The effect of velocity on the response can
be investigated by considering the quasi-steady-
state, or slowly accelerating, system. Increas-
ing velocities tend to sweep the natural fre-
quency of the system from right to left on the
abscissa of Fig. 3. The relative displacement
response increases in amplitude until it ac-
quires a velocity where $a \cong 1.5$. Here, the
lightly damped system passes through a maxi-
mum relative displacement whose magnitude
depends on damping ratio but is independent of
natural frequency. Higher velocities result in
the response asymptotically approaching a
value

$$E[z^2] = 8 \times 10^{-4} \quad \text{as} \quad a \to \infty,$$

which is independent of the damping ratio.
The absolute acceleration rms response

increases at the 1.8 power of velocity up to ap-
proximately $a = 1$. Here a transition of the
principal excitation frequencies occurs because
of the particular shape of the excitation spec-
trum. The amplitude of the rms response at
any particular velocity then depends directly on
the natural frequency of the system, while the
influence of damping ratio depends upon the
particular value of "a" at which the system is
operating. Knowledge of these response char-
acteristics is of primary importance in under-
standing the various system parameter influ-
ences on the response behavior.

DESIGN APPLICATIONS

Since the preceding sections have described
the general response characteristics of a single-
degree-of-freedom oscillator excited by the
particular excitation spectrum of Fig. 3, design

60
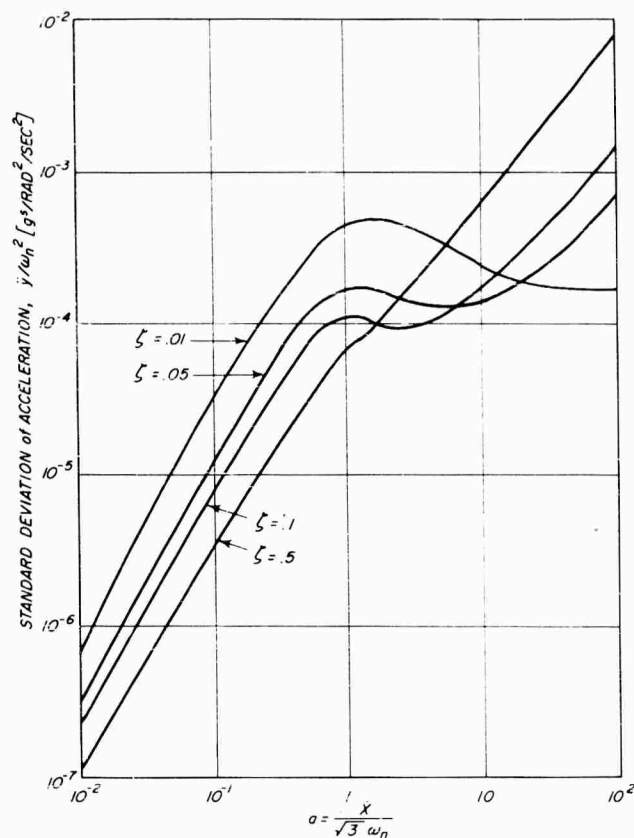
Fig. 5 - Acceleration response to the
SNORT excitation

applications will be confined to those applicable to supersonic tracks. It now remains to examine the characteristics of the response spectra and draw some conclusions which will be useful to the design and isolation of rocket sleds.

One characteristic is the relationship between the peak values of the vibration response and the statistical response measurements that have been calculated. Since the input to this particular single degree-of-freedom oscillator is a stochastic process, so is the output. However, due to the highly spiked nature of the transmissibility of the oscillator (Figs. 1 and 2), and since the excitation can be considered as a complex waveform of randomly varying amplitude, the oscillator will transmit most of the excitation energy near its natural frequency, and thus will act as a narrow bandpass filter. Although the oscillator will vibrate primarily at its natural frequency, it is also receiving energy at every frequency in its bandwidth and will, therefore, exhibit a random beat

phenomenon.* Since only the spectral density of the input is known, this random envelope cannot be determined; however, it is assumed that the output is a Gaussian process by arguing the central limit theorem. The distribution of the peak values of the response will then be Rayleigh. If the Rayleigh distribution of peaks is assumed, the probability that the ratio of a given response, y, to the expected response, $\bar{y}$, exceeds some specified value during any one cycle is given by Ref. 12 and plotted in Fig. 6,

$$P\left[\frac{|y_1|}{\bar{y}}\right] = \exp\left(-y_1^2/2\bar{y}^2\right) . \qquad (51)$$

The probability that the amplitude will never exceed some maximum value y_1,

*If a simple oscillator is excited by two frequencies in its bandwidth, it will exhibit the phenomenon of "beats"; i.e., the envelope of the amplitude of its oscillations will vary in a periodic manner depending on the difference in the two exciting frequencies.

61
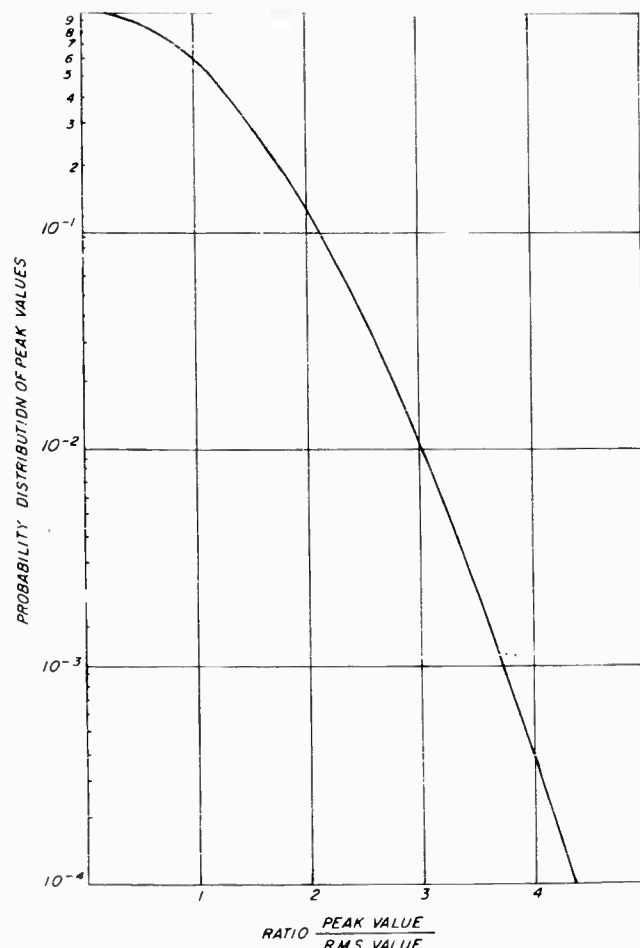
Fig. 6 - Rayleigh distribution of peak values
for narrow band random output

compared to the maximum expected value $\bar{y}_{max}$, during some number of say ωt cycles, can be determined by finding the product of the probabilities of each of the cycles. (The probability that the ratio $y_1/\bar{y}$ will not exceed some value during any one of a set of cycles is mutually exclusive.) Because the variance $\bar{y}$ of all the cycles is not equal if the velocity is not constant, the individual probabilities must be weighted with respect to the maximum expected value $\bar{y}_{max}$. Therefore, the probability of not exceeding some ratio $y_1/\bar{y}_{max}$ in ωt cycles is:

$$P\left[\frac{y_1}{\bar{y}_{max}}\right] = \Pi_{(\omega t)}\left[1 - \exp\left(-\frac{y_1^2}{2\bar{y}_{max}^2}\right)\left(\frac{y_{max}^2}{y^2}\right)\right]. \quad (52)$$

In order to evaluate Eq. (52) for a constant velocity where $\bar{y} = \bar{y}_{max}$, 57 cycles are required before there is a 50-50 chance of finding a y_1

greater than $3 \bar{y}_{max}$, while for $\bar{y} = (3/4) \bar{y}_{max}$, 288 cycles are required.

From the experimental evidence available to date, the assumption of $y_1/\bar{y}_{max} = 3$ is realistic for typical track tests and is used to estimate the maximum amplitudes from the rms values derived in the analysis.

Of immediate concern is the transfer of results obtained for the simple oscillator having a single point of contact with the rail, to a sled having two or more points of contact. It is possible to obtain at least qualitative results if the sled can be considered as a rigid body mounted on relatively soft springs at its points of contact, with spring constants so chosen that the vertical mode is decoupled. Using the decoupled model and considering only vertical oscillations, the range of interest in the parameter "a" used in Figs. 4 and 5 can be determined

62

for use in operational sled designs. Thus, for a sled with a 15-cps natural frequency,

$$a = \frac{\dot{x}}{\sqrt{3}\ 2\pi 15} = \begin{cases} 0.61 & \text{for } \dot{x} = 100 \text{ fps} \\ 6.1 & \text{for } \dot{x} = 1000 \text{ fps}. \\ 12.2 & \text{for } \dot{x} = 2000 \text{ fps} \end{cases}$$

Therefore, for most sleds (and certainly for all those with an isolation system) the maximum response range of interest will be in the domain

$$1 < a_{max} < 10 .$$

It is seen from Fig. 4 that the preceding values of "a" will always pass through the maximum values of the expected relative dis-placement response. Since in a linear spring the relative displacement is directly proportional to the loading factor, the force exerted by the spring on the rigid mass can be determined. This result can be generalized to determine the dynamic loading factor (DLF), thus

$$DLF = \frac{\delta_{dynamic} + \delta_{static}}{\delta_{static}} .$$

$$\delta_{static} = \frac{Mg}{k} = \frac{g}{\omega_n^2} ,$$

where

M = mass of body,

g = acceleration due to gravity 386 in/sec^2,

k = spring constant, lb/in., and

ω_n = natural frequency, rad/sec.

Therefore,

$$DLF = \frac{\delta_{dyn}\ \omega_n^2}{g} + 1 . \quad (53)$$

Now, assuming a damping coefficient of $\zeta = 0.05$ and reading the maximum expected displacement of Fig. 4, the dynamic load factor becomes:

$$DLF_{(\zeta = 05)} = \left(\frac{7\omega_n^2 \times 10^{-2}\ (3)}{g}\right) + 1 , \quad (54)$$

where the factor $y_1/\bar{y} = 3$ has been chosen arbitrarily since less than 1 percent of the peaks occurring at the maximum response have an amplitude exceeding 3 times the rms. Equation (53) is plotted on Fig. 7. It will be noted that,

in general, Eq. (53) yields dynamic loading factors much lower than those currently in use for sled design. Since the equation includes no consideration of aerodynamic loading, loading due to aerodynamic forces must be superimposed on the loading due to the track excitation. A recent study by Sonnenburg [13] rather conclusively confirms that the loading on a sled can be resolved into a more-or-less constant, rail-induced force superimposed on the varying aerodynamic loads.

To better understand the characteristics of vibration isolation and attenuation, reference is again made to Fig. 5. As stated previously, the oscillator vibrates primarily at its natural frequency; from Fig. 5, this appears to be a valid assumption for values of "a" less than 1. In the region of "a" between 1 and approximately 7, the acceleration response flattens out and then begins to diverge for values of "a" greater than 10. This divergence is caused by the magnification of accelerations associated with frequencies higher than the natural frequency. The divergence is due primarily to the particular shape of the SNORT spectrum (Fig. 3). Since the acceleration response for any given value of "a" is directly proportional to its natural frequency, it is advisable to choose a lightly damped, low-frequency system to keep acceleration response as low as possible. For any structure chosen, however, the response spectrum will be distorted by contributions of frequencies higher than the natural frequency at values of "a" greater than 10.

EXPERIMENTAL RESULTS

Experimental evidence of the influence of natural frequency upon the structural response of sleds has been acquired from reed gages (steel cantilever springs with mass attached to the tips) [14]. Each one scratches a target indicating the maximum excursion of the mass. This measurement can be equated to a static force that gives the same structural response. This is equivalent to an experimentally measured dynamic loading factor that any component, located at the same position and having the same natural frequency and damping, would experience. The measurements shown in Fig. 8 were made on a sled that attained a maximum speed of 710 fps after 2 seconds. The solid lines depict the range of maximum amplitudes measured directly over the shoe during three instrumented runs, and the dashed lines depict measurements taken at the inboard end of the tubular steel axles. Although very few sled structures have natural frequencies as high as those shown in Fig. 8, the plot indicates the
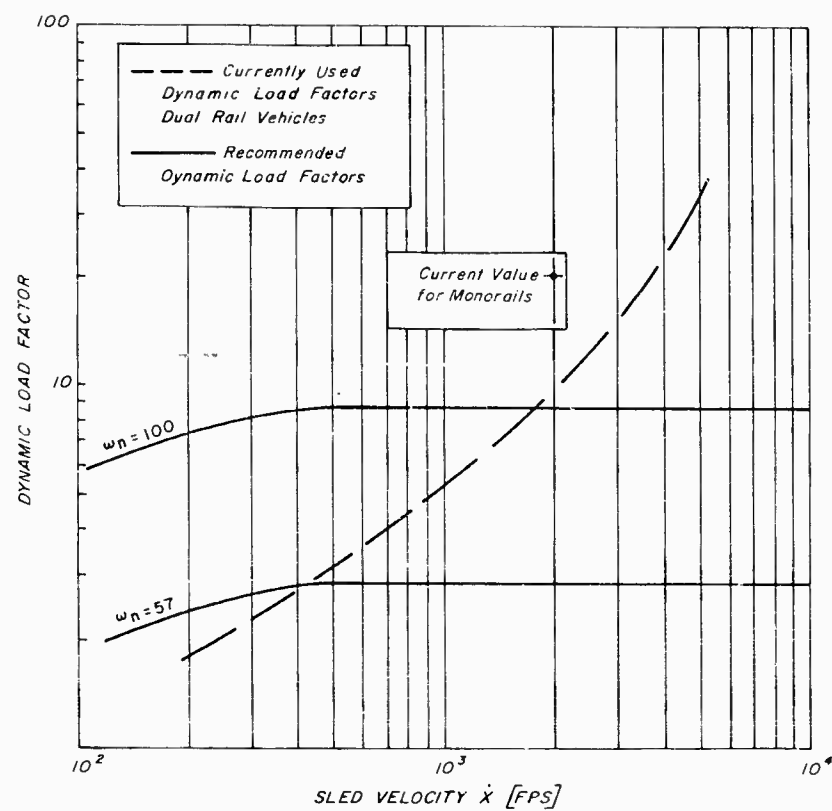
Fig. 7 - Dynamic load factor with $\zeta = 0.05$
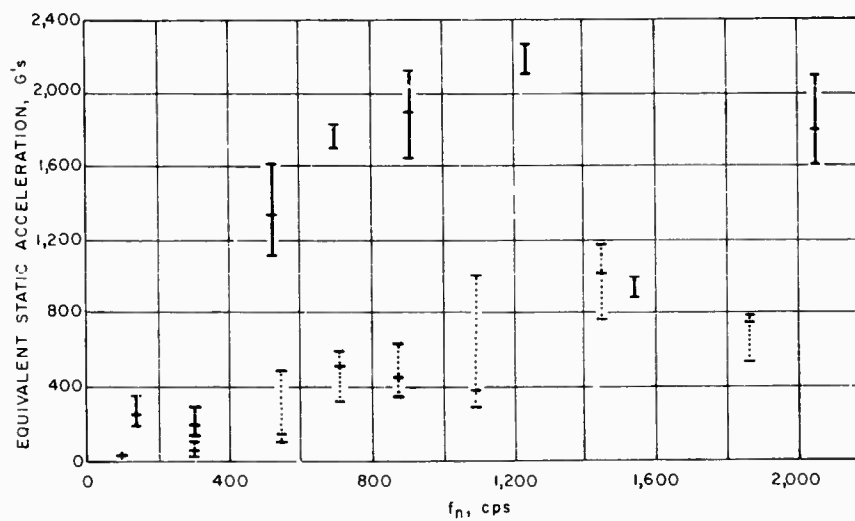
Fig. 8 - Reed gage measurements of dynamic loading

64
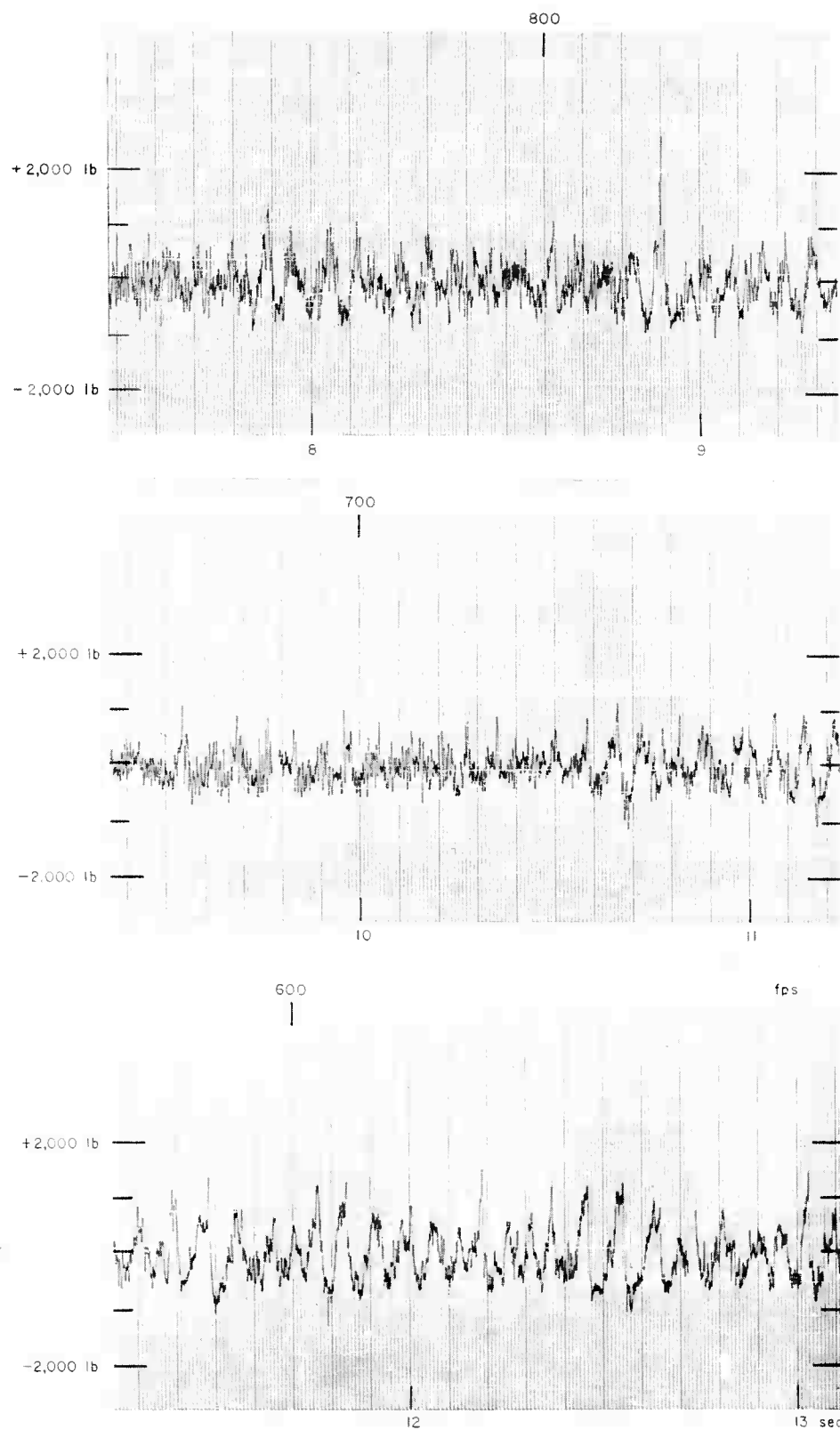
Fig. 9 - Sample frequency response record

increasing dynamic loading factor required for higher frequency components, and the attenuation of vibration amplitude that a suspension component, such as the axle, can yield.

To date, experimental results that include the time history of the response have been obtained only for the relative displacement of a decoupled sled with six points of support, and only qualitative confirmation of the theoretical model has been obtained. These experimental data, which consist of readings taken during several runs, were obtained from strain gages affixed to the center axle of the sled (Fig. 9). This sample record clearly shows the response to be primarily at a frequency $f = 14$ cps with an rms amplitude value of approximately 500 lb. A maximum amplitude of approximately $3 \bar{y}$ has been observed on the average of once a run. From data obtained by shaking the sled, it has an observed natural frequency of $f_n = 13$ cps with burned out motors. The damping ratio of its rubber isolator mounts is between $0.05 < \zeta < 0.10$, while the spring constant $k = 7530$ lb/in.

By applying the above sled parameters to Fig. 4, it is found that $\bar{y}_{max} = 5.6 \times 10^{-2}$ in.; the expected force exerted by the isolator then becomes $(k)(\bar{y}_{max}) = 422$ lb.

Although the experimental evidence appears to be in quite good agreement with the information obtained from the theoretical model, the record was obtained as the sled was constantly accelerating, making it extremely difficult to do a statistical analysis. To achieve a reasonable statistical confidence, final comparison of the theoretical and operational models must await the evaluation of sample data taken from several runs of a sled traveling at constant velocity, or from a large ensemble of records.

CONCLUSIONS

This analysis has demonstrated a concise method for calculating the response of a mechanical system to a broad general class of random excitations. The spectral density of the process need not be "white" nor need the excitation be a displacement process. We would like to emphasize that it was by going to the source of the vibrations and then transforming this excitation into the time domain that the velocity-dependent structural response arose. This is contrary to the approach currently popular in missile component design in which the response in one vehicle is analyzed and extrapolated to later designs.

One unfortunate aspect of the simple approach advocated here is that the calculations involve an integration across the product of the excitation and transmissibility spectrums. Hence, undamped systems (which involve an unbounded function) cannot be solved, and only statistical measures of the composite response are obtained. A qualitative impression of the spectral density distribution of the response can be obtained by examining the transmissibility of various wavelengths at a particular velocity.

Vibration and strain gage records obtained during approximately 10 runs of three vehicles have qualitatively confirmed the hypotheses. The amplitudes were within a factor of 2 of those predicted. Such agreement is perhaps fortuitous, but it certainly is encouraging in light of the relatively crude mathematical model. This excellent agreement is believed to result from the inclusion of an isolation system which limits and controls the vibrations of the complex sled structures. Therefore, it seems evident that a properly designed isolation system not only reduces the stresses in the structure, it also makes the problem of their prediction tractable.

REFERENCES

1. H. J. Stumpf, "The Response of Mechanical Systems to Random Exciting Forces," U.S. Naval Ordnance Test Station, China Lake, Calif. NAVORD Report 7010, NOTS TP 2365 (Dec. 1, 1959).

2. J. W. Miles and W. T. Thomson, "Statistical Concepts in Vibration," in Shock and Vibration Handbook (McGraw-Hill Book Co. Inc., New York, N. Y., 1961) Chap. 11.

3. D. C. Karnopp, "Basic Theory of Random Vibrations," in Random Vibrations (The MIT Press, Cambridge, Mass., 1963) Vol. 2.

4. S. H. Crandall and W. D. Mark, Random Vibration in Mechanical Systems (The Academic Press, New York, N. Y., 1963).

5. S. P. Timoshenko, Vibration Problems in Engineering (Van Nostrand, Princeton, N. J., 1955) 3rd Edition.

6. E. A. Guillemin, The Mathematics of Circuit Analysis (The Technology Press, Cambridge, Mass., 1949).

7. Niels Arley and K. Rander Buch, Probability and Statistics (John Wiley and Sons, Inc., New York, N. Y., 1950).

8. C. R. Wylie, Advanced Engineering Mathematics (McGraw-Hill Book Co., Inc., N. Y. 1960) 2d Edition.

9. H. J. James, N. B. Nichols, and R. S. Phillips, Theory of Servomechanisms (McGraw-Hill Book Co., Inc., New York, N. Y. 1947).

10. G. C. Newton, L. A. Gould, and J. F. Kaiser, Analytic Design of Linear Feedback Controls (John Wiley and Sons, Inc., New York, N. Y., 1957).

11. W. J. Stronge, "An Analysis of Sampled Data Taken From A Continuous Record Containing Periodic Components," Department of Engineering, University of California, Los Angeles, California, Research in Engineering Report #299 (May 1963).

12. C. E. Crede, "Failure Resulting From Vibration," Random Vibration (The MIT Press, Cambridge, Mass., 1963) Vol. 2.

13. P. N. Sonnenburg, "Recent Developments in Sled Structural Dynamics," paper presented at the ISTRACON Structures Working Group, Holloman Air Force Base (Jan. 28, 1964).

14. R. W. Flygare and S. Rubin, "Evaluation of a Reed Gage for Shock Studies," Soc. Exp. Stress Analysis Proceedings, Vol. XVI, No. 2, pp. 97-108 (1958).

*   *   *

VIBRATIONS OF A CANTILEVER BEAM CONSIDERING A
NON-RIGID WALL SUPPORT*

H. F. Cooper, Jr.
Bell Telephone Laboratories, Inc.
Whippany, New Jersey

The effects of a non-rigid wall support on the natural frequencies, mode shapes, and forced response of a cantilever beam are studied, and graphs of the first several natural frequencies and mode shapes as functions of the wall stiffness are presented. The wall support is represented by linear and torsional springs so that the effect of the wall's stiffness in translation and rotation are considered in terms of the two spring constants.

The response solution is given formally for the cantilever loaded with any of the usual forcing functions, and is particularly evaluated for a triangular (in time) uniform pressure pulse. Numerical results are given for a particular triangular pulse and several wall stiffnesses; and it is found that the wall stiffness can have an appreciable effect on the response characteristics.

INTRODUCTION

W. J. O'Donnel considers the static deflection of a cantilever beam due to the elasticity of the support wall [1], and of built-in beams in general [2]. He shows that the error incurred by treating beams as being rigidly built-in is significant for typical cases encountered in design work. It is shown herein that the support stiffness may significantly affect the dynamic characteristics of the cantilever.

The natural frequencies and mode shapes as functions of the rotational and translatory spring stiffness at the wall, α' and β' (see Fig. 1) are determined, and the displacement response of the cantilever due to an arbitrary forcing function ($f(x,t)$) is determined formally in terms of an eigenfunction expansion. Numerical results are given for the case where $f(x,t)$ is a uniform (in x) triangular (in t) pulse.

Since the characteristic equation and the expression for the eigenfunctions involve the hyperbolic functions, difficulties are experienced with a direct application of numerical techniques (such as subtracting one large
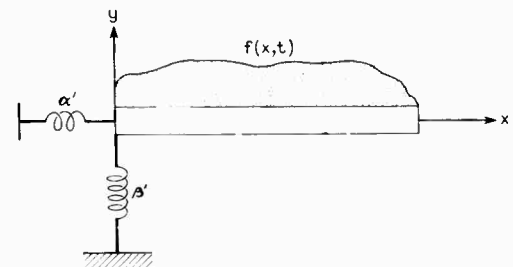
Fig. 1 - Mathematical model

number from another which is very close to the first number). A procedure for avoiding these difficulties is described.

FORMULATION OF THE PROBLEM

The differential equation for a beam of constant cross section and density, neglecting shear and rotatory inertia, is given by the Bernoulli-Euler Theory as Eq. (1) where subscripts denote partial differentiation. The boundary conditions are given by Eq. (2), and it is assumed that the cantilever is initially relaxed so that $y(x,o) = y_t(x,o) = 0$. Upon introduction of the non-dimensional variables in Eq. (3), Eqs. (1) and (2) are transformed into Eqs. (4) and (5).

$$EI\ y_{xxxx} + \rho A\ y_{tt}\ =\ f(x,t) \qquad (1)$$

$$\alpha'y_x(o,t) - EI\ y_{xx}(o,t) = 0 \qquad y_{xx}(\ell,t) = 0$$
$$\beta'y(o,t) + EI\ y_{xxx}(o,t) = 0 \qquad y_{xxx}(\ell,t) = 0 \qquad (2)$$

$$\xi = \frac{x}{\ell}\ ; \qquad \tau = t\ \sqrt{\frac{EI}{\rho A \ell^4}}\ = \frac{t}{\nu} \qquad (3)$$

$$\alpha = \frac{\alpha'\ell}{EI}\ ; \qquad \beta = \frac{\beta'\ell^3}{EI}$$

$$y_{\xi\xi\xi\xi} + y_{\tau\tau}\ =\ \frac{\ell^4}{EI}\ f(\ell\xi,\nu\tau)\ =\ g(\xi,\tau) \qquad (4)$$

$$y_\xi(o,\tau) - \frac{1}{\alpha}\ y_{\xi\xi}(o,\tau) = 0 \qquad y_{\xi\xi}(1,\tau) = 0 \qquad (5)$$

$$y(o,\tau) + \frac{1}{\beta}\ y_{\xi\xi\xi}(o,\tau) = 0 \qquad y_{\xi\xi\xi}(1,\tau) = 0\ .$$

The dimensionless stiffness parameters, α and β, Eq. (3), may be given a physical interpretation in terms of the two single degree of freedom models in Fig. 2. The tip deflection of the cantilever due to a uniformly distributed unit load is given from strength of materials as $\ell^4/8EI$. The total moment at the wall is given by $\ell^2/2$ and the angular deflection of a line drawn from the wall support to the deflected tip position is $\ell^3/8EI$. Thus, the angular spring constant at the wall simulating cantilever elasticity is $\alpha_o = 4EI/\ell$. For the second single degree of freedom model (simple spring mass) the equivalent spring constant is $\beta_o = 8EI/\ell^3$. Thus, the parameters α and β are proportional to the ratios of the wall stiffness (to rotation as translation) to the cantilever stiffness (based on the corresponding single degree of freedom model).

$$\alpha = \frac{4\alpha'}{\alpha_o}\ ; \quad \beta = \frac{8\beta'}{\beta_o}\ ; \quad \frac{\alpha'}{\alpha_o} = \frac{\alpha}{4}\ ; \quad \frac{\beta'}{\beta_o} = \frac{\beta}{8}\ . \qquad (6)$$
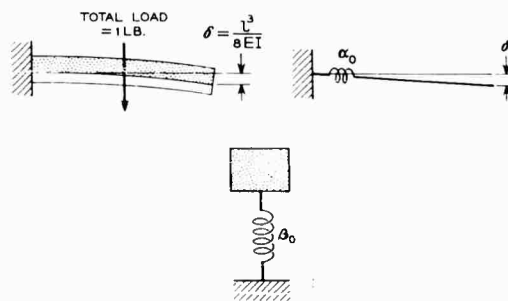
Fig. 2 - Lumped parameter models

SOLUTION

The method of solution was to determine the eigenfunctions and eigenvalues of the homogeneous form of Eq. (4) and to expand the forced deflection in terms of the eigenfunctions. It may be shown that the homogeneous boundary value problem is self-adjoint; therefore, its eigenvalues constitute a countably infinite set, and its eigenfunctions constitute a complete orthogonal set [3].

Assuming an oscillatory solution for the homogeneous form of Eq. (4) in the form of $y_n(\xi,\tau) = \psi_n(\xi)\epsilon^{i\omega_n\tau}$ and following standard procedure, one arrives at the characteristic equation (7) and an expression (to within an arbitrary constant) for the eigenfunctions Eq. (8). To facilitate later analysis, an orthonormal set of eigenfunctions φ_n are defined in Eq. (11).

$$a_n + b_n \cos k_n \cosh k_n + \frac{1}{2}(c_n - d_n)\sin k_n \cosh k_n$$
$$- \frac{1}{2}(c_n + d_n)\cos k_n \sinh k_n = 0 \qquad (7)$$

$$\psi_n\ =\ \zeta_n \cos k_n\xi + \mu_n \sin k_n\xi + \eta_n \cosh k_n\xi + \sinh k_n\xi \qquad (8)$$

$$k_n\ =\ \sqrt{\omega_n}$$

$$a_n\ =\ 1 + k_n^4/\alpha\beta \qquad c_n\ =\ -2k_n/\alpha \qquad (9)$$
$$b_n\ =\ 1 - k_n^4/\alpha\beta \qquad d_n\ =\ 2k_n^3/\beta$$

$$\zeta_n\ =\ \frac{1}{D_n}\left[a_n \sin k_n - d_n \cosh k_n + b_n \sinh k_n\right]$$

$$\mu_n\ =\ \frac{1}{D_n}\left[-a_n \cos k_n - b_n \cosh k_n + c_n \sinh k_n\right] \qquad (10)$$

$$\eta_n\ =\ -\frac{1}{D_n}\left[a_n \sinh k_n + b_n \sin k_n + d_n \cos k_n\right]$$

$$D_n\ =\ a_n \cosh k_n + b_n \cos k_n + c_n \sin k_n$$

$$\varphi_n\ =\ \frac{\psi_n}{\lambda_n}\ ; \qquad \lambda_n\ =\ \int_0^1 \psi_n^2\,d\xi \qquad (11)$$

$$\int_0^1 \varphi_m \varphi_n\,d\xi\ =\ \delta_{mn} = 1 \qquad m = n$$
$$= 0 \qquad m \neq n$$

The inhomogeneous differential equation and associated boundary conditions are satisfied

by Eq. (12) provided q_n is a solution of Eq. (13) [4]. For the case of relaxed initial conditions, q_n is given by Eq. (14) so that the solution is given formally by Eq. (15).

$$y(\xi, t) = \sum_{n=1}^{\infty} q_n(\tau) \, \varphi_n(\xi) \tag{12}$$

$$\ddot{q}_n + \omega_n^2 q_n = \int_0^1 g(\xi, \tau) \varphi_n(\xi) \, d\xi = C_n(\tau) \tag{13}$$

$$q_n(\tau) = \frac{1}{\omega_n} \int_0^\tau C_n(t) \sin \omega_n(\tau - t) \, dt \tag{14}$$

$$y(\xi, \tau) = \sum_{n=1}^{\infty} \frac{\varphi_n(\xi)}{\omega_n} \int_0^\tau C_n(t) \sin \omega_n(\tau - t) \, dt . \tag{15}$$

For the particular case of a uniform, triangular pressure pulse (Fig. 3), $f(x, t)$ is given by the product of the width of the cantilever and the pressure time history. For this case $C_n(\tau)$ is given by Eq. (16) and $q_n(\tau)$ is given by Eq. (19).
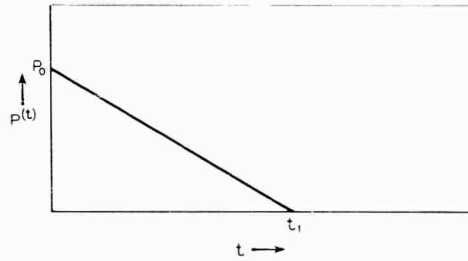
Fig. 3 - Pressure time history

$$C_n(\tau) = \kappa \gamma_n p(\nu t) \tag{16}$$

$$\kappa = \frac{w \ell^4}{EI} \tag{17}$$

$$\gamma_n = \frac{1}{k_n \lambda_n} \Big[\zeta_n \sin k_n + \mu_n (1 - \cos k_n)$$
$$+ \eta_n \sinh k_n + \cosh k_n - 1 \Big] \tag{18}$$

$$q_n = \frac{\kappa P_o \gamma_n}{\omega_n^3 \tau_1} \Big[\omega_n (\tau_1 - \tau) + \sin \omega_n \tau - \omega_n \tau_1 \cos \omega_n \tau \Big]$$
$$0 < \tau \leq \tau_1 \tag{19}$$
(Cont.)

$$q_n = \frac{\kappa P_o \gamma_n}{\omega_n^3 \tau_1} \Big[(1 - \cos \omega_n \tau_1) \sin \omega_n \tau$$
$$+ (\sin \omega_n \tau_1 - \omega_n \tau_1) \cos \omega_n \tau \Big] \quad \tau > \tau_1. \tag{19}$$

COMPUTER STUDY

The I.B.M. 7090 Computer was used to determine the roots of Eq. (7) (eigenvalues), the mode shapes Eq. (8) (eigenfunctions), and the forced response of the cantilever Eq. (12) as functions of α and β. A direct application to the characteristic equation and the equations defining φ_n, λ_n, and γ_n as they are given in the preceding sections leads to erroneous results due to difficulties inherent in the digital computer (taking the difference of two large numbers which differ in higher significant places only, for example). Thus, the equations developed in previous sections were altered so that meaningful results could be obtained.

Since the eigenvalues, k_n, make up an unbounded countable set, it is natural to observe the behavior of the relevant expressions as k_n increases without bound. The expressions from Eqs. (7) and (10) may be written as in Eqs. (20) and (21) by dividing numerator and denominator by $\epsilon^{k_n}/2$. Also, Eq. (8) may be written as in Eq. (22).

$$\left(b_n - \frac{c_n + d_n}{2} \right) \cos k_n + \frac{c_n - d_n}{2} \sin k_n + 2a_n \epsilon^{-k_n}$$
$$+ \left[\left(b_n + \frac{c_n + d_n}{2} \right) \cos k_n + \frac{c_n - d_n}{2} \sin k_n \right] \epsilon^{-2k_n} = 0 \tag{20}$$

$$\zeta_n = \frac{1}{L_n} \left[b_n - d_n - (b_n + d_n) \epsilon^{-2k_n} + 2a_n \epsilon^{-k_n} \cos k_n \right]$$

$$\mu_n = \frac{1}{L_n} \left[-b_n + c_n - (b_n + c_n) \epsilon^{-2k_n} + 2a_n \epsilon^{-k_n} \cos k_n \right] \tag{21}$$

$$\eta_n = \frac{1}{L_n} \left[-a_n \left(1 - \epsilon^{-2k_n} \right) - 2\epsilon^{-k_n} (d_n \cos k_n + b_n \sin k_n) \right]$$

$$L_n = a_n \left(1 + \epsilon^{-2k_n} \right) + 2\epsilon^{-k_n} (b_n \cos k_n + c_n \sin k_n)$$

$$\psi_n = \zeta_n \cos k_n \xi + \mu_n \sin k_n \xi$$
$$+ (\eta_n + 1) \frac{\epsilon^{k_n \xi}}{2} + (\eta_n - 1) \frac{\epsilon^{-k_n \xi}}{2} . \tag{22}$$

71

As $k_n \to \infty$;

$$\zeta_n \to \frac{b_n - d_n}{a_n} \to -1 , \qquad \mu_n \to \frac{-b_n + c_n}{a_n} \to 1 ,$$

and $\eta_n \to -1$. By a simple algebraic manipulation, $(\eta_n + 1)$ and $(\eta_n - 1)$ is given by Eq. (23). As $k_n \to \infty$; $Y_n \to -1$ and $Z_n \to \cos k_n - \sin k_n$. From Eq. (20) as $k_n \to \infty$, $\tan k_n \to -\infty$ so that $\cos k_n \to 0$ and $\sin k_n \to -1$; thus $Z_n \to 1$.

$$(\eta_n + 1) = \frac{2}{L_n} \left[(b_n - d_n) \cos k_n + (c_n - b_n) \sin k_n + a_n \epsilon^{-k_n} \right]$$

$$= 2 Z_n \epsilon^{-k_n}$$

(23)

$$(\eta_n - 1) = \frac{2}{L_n} \left[-a_n - \epsilon^{-k_n} \left[(d_n + b_n) \cos k_n + (b_n + c_n) \sin k_n \right] \right]$$

$$= 2 Y_n .$$

The normalized form of Eq. (22) may then be written as in Eq. (24) in which the magnitude of each term is bounded above by 1 for large k_n. λ_n is given in the appendix in terms of Y_n and Z_n. The only other alteration involves re-writing Eq. (18) for γ_n in terms of Y_n and Z_n as in Eq. (25). The equations which were used in the program were (12), (19), (20), (24), and (25); with ζ_n, μ_n, η_n, Y_n, and Z_n as defined by Eqs. (21) and (23), and λ_n as defined in the appendix.

$$\varphi_n = \frac{1}{\lambda_n} \left[\zeta_n \cos k_n \xi + \mu_n \sin k_n \xi + Z_n \epsilon^{-k_n (1 - \xi)} + Y_n \epsilon^{-k_n \xi} \right]$$

(24)

$$\gamma_n = \frac{1}{\lambda_n k_n} \left[\zeta_n \sin k_n + \mu_n (1 - \cos k_n) + Z_n - 1 - Y_n \epsilon^{-k_n} \right] .$$

(25)

RESULTS

Variation of Natural Frequencies

Figures 4-7 are semi-logarithmic plots of the first four eigenvalues ω_n. The natural frequencies for a given beam in cps may be determined from the plots by use of Eq. (26).

$$f_{no} = \frac{\omega_{nn}}{2\pi} = \frac{\omega_n}{2\pi\nu} \ (\text{cps}) .$$

(26)

As seen in Fig. 4, ω_1 depends predominantly upon β for

$$\alpha > 10^2 \left(\frac{\alpha'}{\alpha_o} > 25 \right) ;$$

predominantly upon α for

$$\beta > 10^2 \left(\frac{\beta'}{\beta_o} > 12.5 \right) ;$$

and for $\alpha > 10^2$, $\beta > 10^2$, ω_1 is approximately what it would be for a rigid wall support ($\alpha = \beta = \infty$). The major variation in ω_1 occurs for $10^{-2} < \alpha < 10^2$; $10^{-2} < \beta < 10^2$. Figures 5-7 may be interpreted in a similar manner. For $\alpha > 10^2$.

$$\beta > 10^3 \left(\frac{\alpha'}{\alpha_o} > 25, \quad \frac{\beta'}{\beta_o} > 125 \right) ,$$

the rigid wall model is adequate for determining ω_2 (and ω_1). For $\alpha > 10^2$,

$$\beta > 10^4 \left(\frac{\alpha'}{\alpha_o} > 25, \quad \frac{\beta'}{\beta_o} > 1250 \right) ,$$

the rigid wall model is adequate for determining ω_4 and ω_3 (as well as ω_2 and ω_1).

It will be noted that as n increases (higher frequencies), the major variation of ω_n for a given α occurs for a region of larger and larger β. For example, for $\alpha = \infty$, the major change in ω_4 is for $10^2 < \beta < 10^4$ while the major change in ω_1 occurs for $10^{-2} < \beta < 10^2$. This trend was noticed for the higher frequencies as well as those presented here.

Variation of the Mode Shapes

The first three mode shapes (φ_n; $n = 1, 2, 3$) for various values of α and β are given in Figs. 8-12. In Fig. 8 ($\alpha = \infty$) the model is rotationally rigid at the wall ($\varphi_n^I(0) = 0$) but may have translatory motion depending on the value of β. In Fig. 9 ($\beta = \infty$) the model is rigid to translation ($\varphi_n(0) = 0$) at the wall but may have rotational motion depending on the value of α. In Figs. 10-12 the model may both rotate and translate at the wall. The dotted lines in these figures indicate the model shape for the cantilever with rigid wall supports.

From these figures it is clear that the translatory stiffness (β) of the wall support appreciably affects the mode shapes, especially the higher modes. For example, in Fig. 8 the second mode shape with $\beta < 100$ is very much like the first mode shape for the cantilever with a rigid wall support.

72

Fig. 5 - Second natural frequency

Fig. 4 - First natural frequency

73
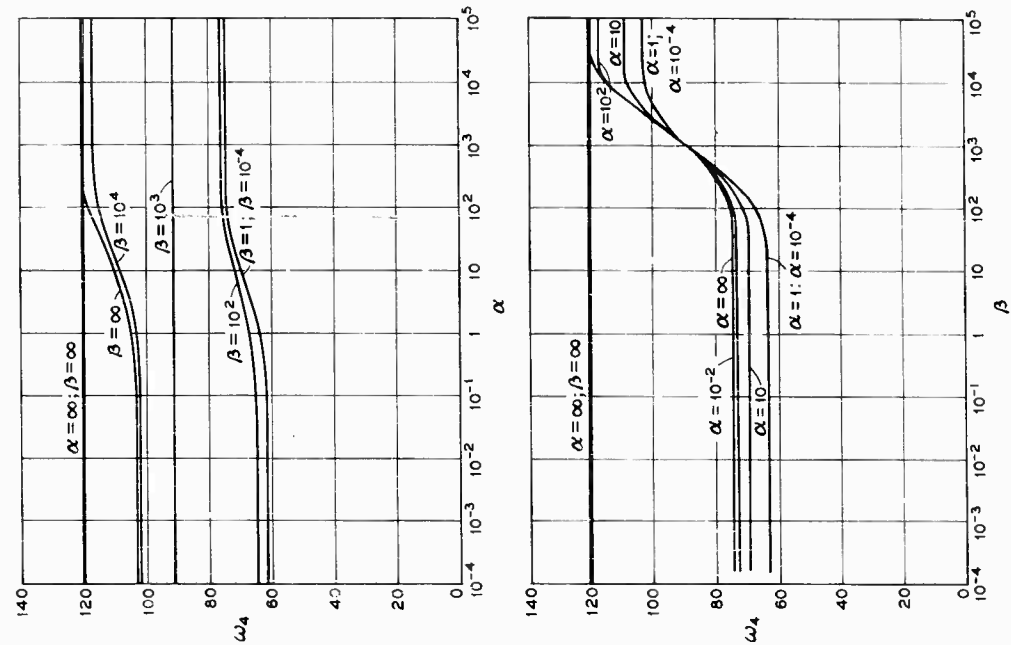
Fig. 7 - Fourth natural frequency
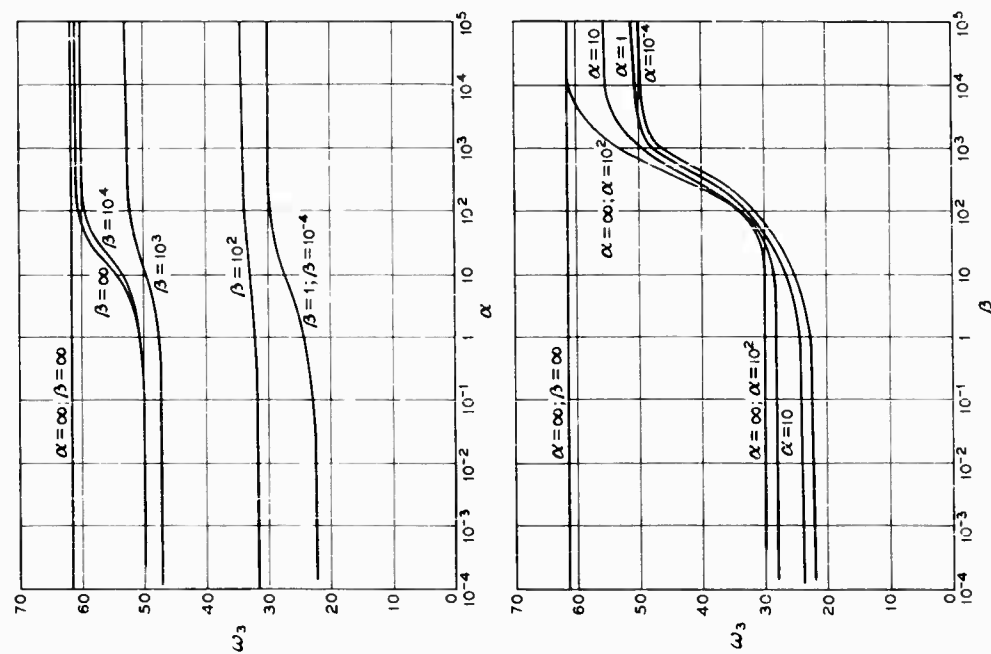
Fig. 6 - Third natural frequency

74
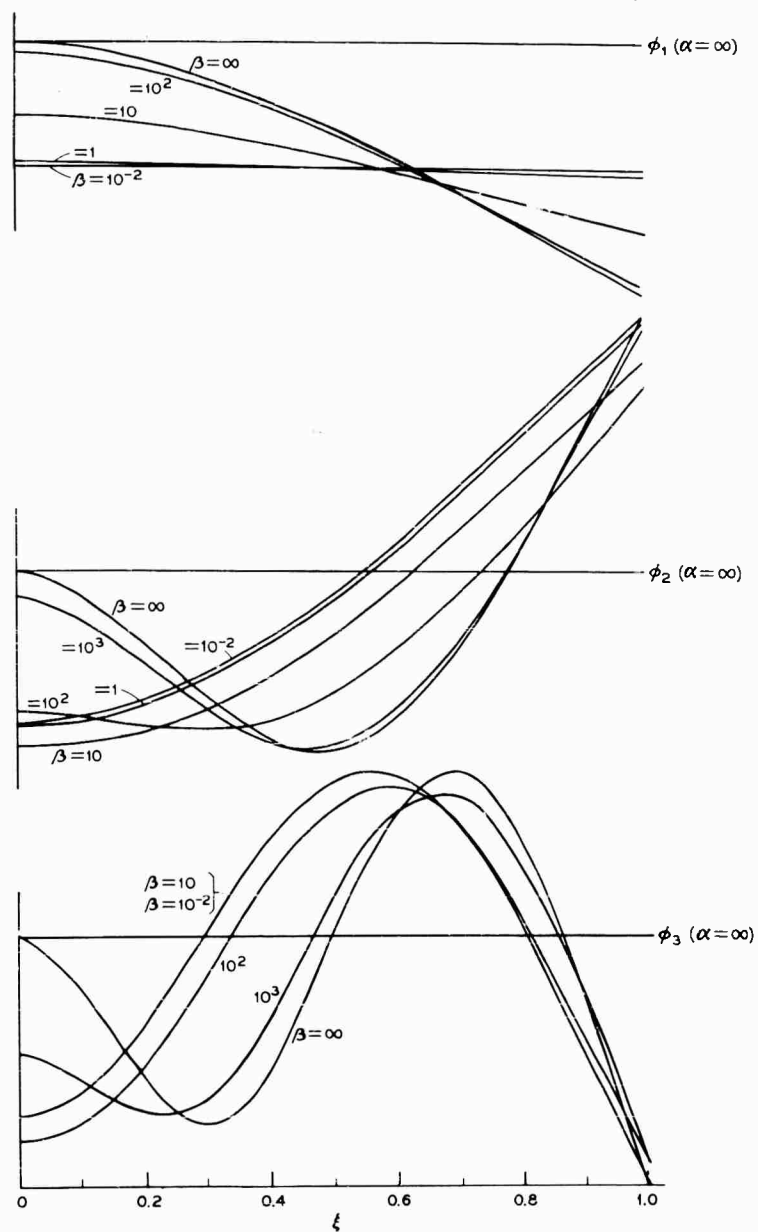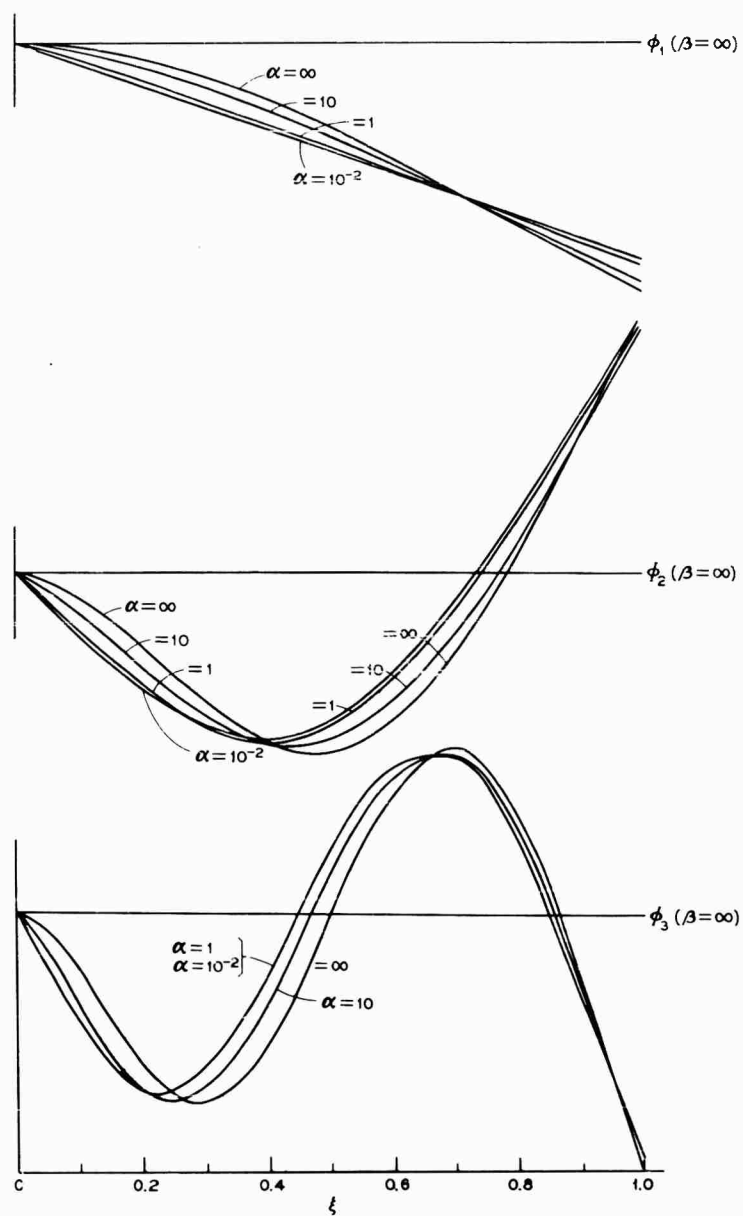
Fig. 8 - Mode shapes: $\alpha = \infty$

Fig. 9 - Mode shapes $\beta = \infty$
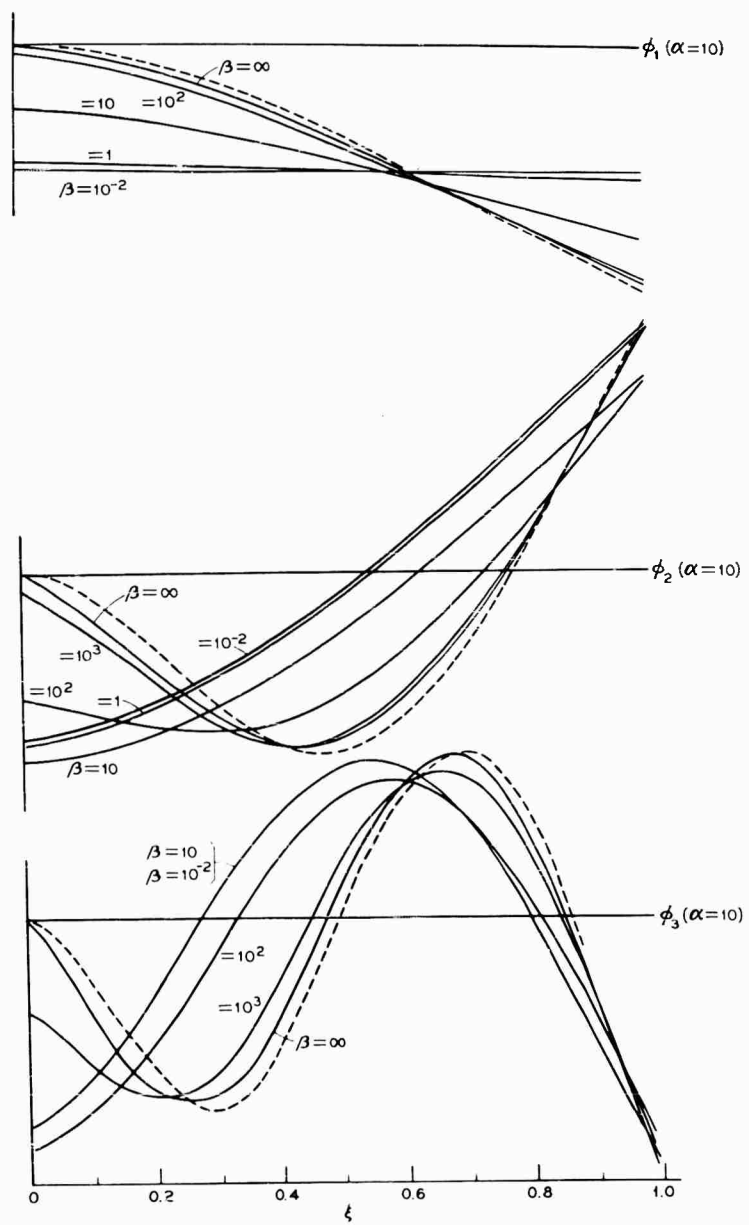
Fig. 10 - Mode shapes: $\alpha = 10$
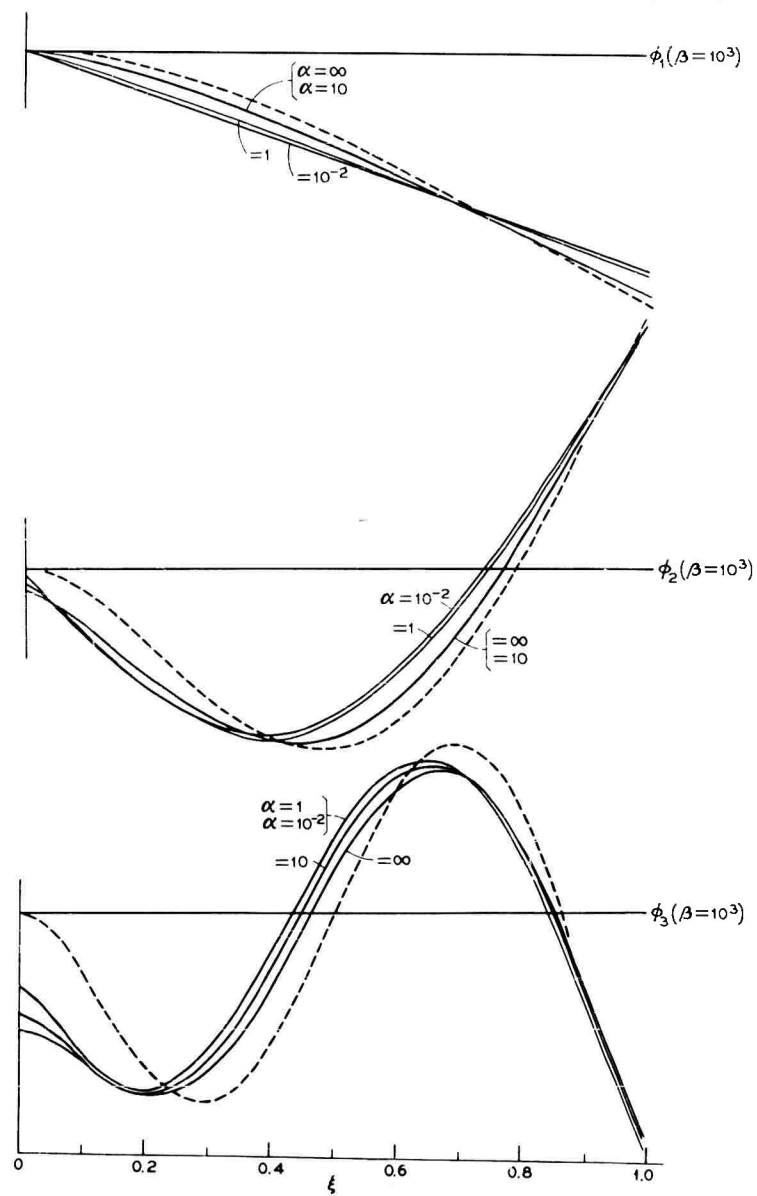
Fig. 11 - Mode shapes: $\beta = 10^3$

78
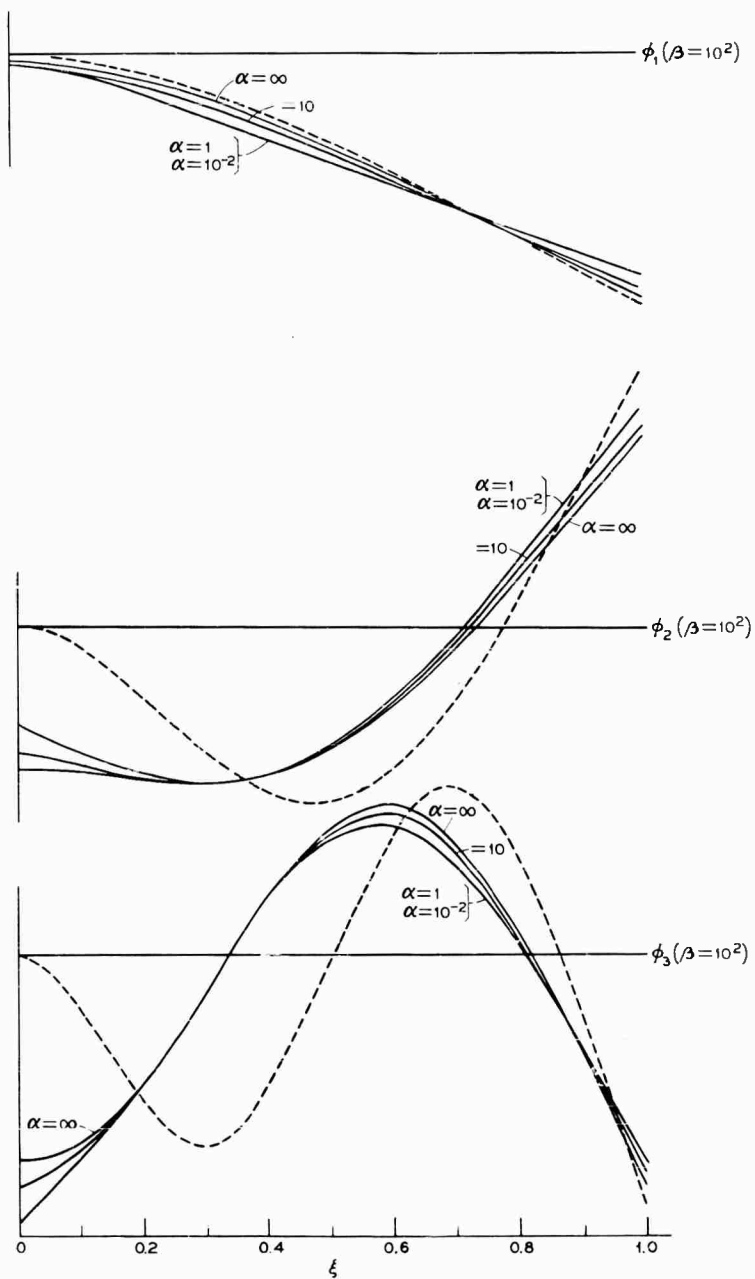
Fig. 12 - Mode shapes: $\beta = 10^2$

From Figs. 9, 11 and 12 it appears that the general mode shape is not affected as much by the rotational stiffness (α) as by the translatory stiffness (β). It will be noted in all of the figures that as the stiffness is decreased, the point at which the mode shape intersects the equilibrium line moves toward the wall (to the left).

Forced Deflection for $\tau_1 = 0.5$
and Three Values of α and β

If Eq. (19) is rewritten in the symbolic form Eq. (26), then a non-dimensional forced solution may be written as in Eq. (27). Note that the static solution from strength of materials for a cantilever loaded uniformly by a pressure P_o is given by $y_s = P_o \kappa/8$, so that Eq. (27) may be as $y/8y_s$.

$$q_n = \kappa P_o Q_n(\tau_1, \tau) \qquad (26)$$

$$\frac{y}{\kappa P_o} = \sum_{n=1}^{\infty} \varphi_n(\xi)\, Q_n(\tau_1, \tau) . \qquad (27)$$

Figure 13 gives a time history of the beam deflection for three cases: $\alpha = \beta = \infty$ (rigid wall); $\alpha = 10^3$, $\beta = 10^2$; and

$$\alpha = 10^3, \quad \beta = 8 \left(\frac{\beta'}{\beta_o} = 1 \right) .$$

In these cases the positive phase duration of the pressure pulse (τ_1) was taken as 0.5. From Fig. 4, for $\alpha = \beta = \infty$, $\omega_1 \approx 3.5$ so that the fundamental non-dimensional period is given by $2\pi/\omega_1 \approx 1.8$. Thus, τ_1 is slightly greater than a quarter period of the fundamental mode of vibration for a rigid wall.

It is clear that there are many combinations of parameters (α, β, τ_1) which might be of interest; however, only these three were chosen to demonstrate the results that are possible. There is little difference between the rigid wall case and the second case ($\alpha = 10^3$, $\beta = 10^2$) as might have been expected from the results in the previous sections. In both cases the "dynamic factor" [5] is approximately given by $y/y_s \approx 8\,(0.11) = 0.88$. The dynamic factor for a single degree of freedom model with an equivalent stiffness of the cantilever under a corresponding forcing function is 0.9 [5]. This close comparison was expected since Eq. (27) after 10 terms was given by the first term ±15 percent for early terms and ±5 percent for later terms. The series apparently converged to three places after five terms.

From the third case considered (wall translational stiffness equal to the cantilever static stiffness), it is seen that the peak displacement is approximately 3/2 of the rigid cantilever
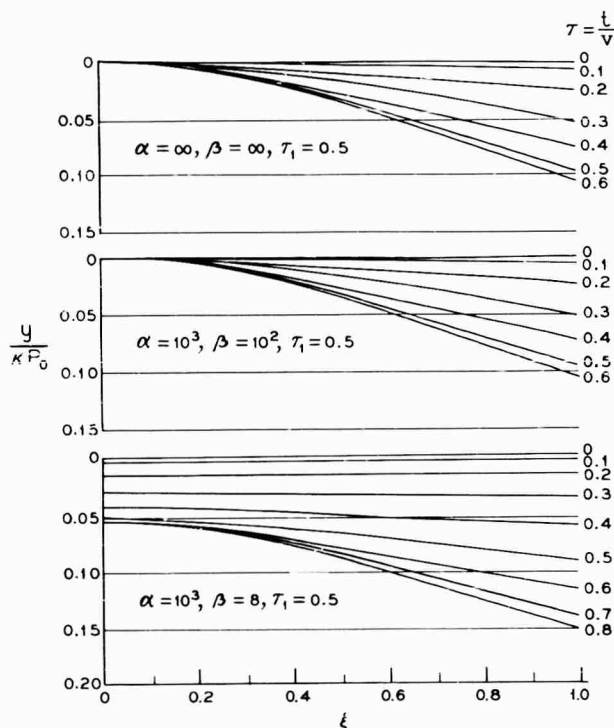
Fig. 13 - Forced response

80

peak displacement (for $\tau_1 = 0.5$). Note that $\tau \approx 0.2$ before the cantilever begins to respond flexurally.

DISCUSSION AND CONCLUSIONS

The first several flexural mode shapes and natural frequencies are given very closely by the Bernoulli-Euler Theory [6]; hence, the results of the sections entitled "Variation of Natural Frequencies" and "Variation of Mode Shapes" are adequate for the usual design considerations of natural frequencies and mode shapes. Similarly, if one is concerned with the steady state response of the cantilever with a non-rigid wall support the procedure leading to the results of the previous section should be adequate for determining the displacements. If one is concerned, however, with the transient response, a more elegant theory must be applied (for example the Timoshenko beam theory) to account for the shear effects which may predominate during very early times [7].

LIST OF SYMBOLS

A   cross-sectional area (in.^{2})

$C_n(\tau)$ parameter (in.)

D_n, L_n dimensionless parameters

E   Young's modulus (psi)

I   area moment of inertia (in.^{4})

P_o peak reflected pressure (psi)

W   beamwidth (in.)

$\cdot_n, z_n$ dimensionless parameters

a_n, b_n, c_n, d_n dimensionless parameters

$f(x,t)$ forcing functions (lb/in.)

f_{no} frequency (cps)

$g(\xi, \tau)$ reduced forcing function =
$$\frac{\ell^4}{EI} f(\ell\xi, \nu\tau) \ (in.)$$

k_n dimensionless parameter $(\sqrt{\omega_n})$

ℓ beam length (in.)

$p(t)$ reflected pressure time history (psi)

$q_n(\tau)$ generalized coordinate (in.)

t   time (sec)

t_1 positive phase duration (sec)

x   length along the beam (in.)

y   deflection (in.)

y_s static deflection of a cantilever under a uniform pressure P_o (in.)

α' torsional spring constant (# in./rad)

α reduced torsional spring constant (rad)$^{-1}$

α_o equivalent beam torsional stiffness (# in./rad)

β' translatory spring constant (lb/in.)

β reduced translatory spring constant (dimensionless)

β_o equivalent beam translatory stiffness (lb/in.)

γ_n parameter (in.^{3})

ζ_n, μ_n, η_n dimensionless parameters

κ loading parameter = $W\ell^4/EI$ (cu. in./lb)

λ_n normalizing parameter

ξ normalized position coordinate = x/ℓ

τ nondimensional time coordinate = t/ν

τ_1 nondimensional positive phase duration = t_1/ν

ν time parameter = $\sqrt{\rho A\ell^4/EI}$ (sec)

ψ_n eigenfunction

φ_n orthonormal eigenfunction

ω_n dimensionless circular frequency (rad)

ω_{no} circular frequency = ω_n/ν (rad/sec)

ρ beam density

REFERENCES

1. W. J. O'Donnell, J. Appl. Mech., 27, 461 (1960).

2. W. J. O'Donnell, Paper No. 62-WA-16, ASME Convention (1962).

3. E. A. Coddington and N. Levinson, Theory of Ordinary Differential Equations (McGraw-Hill Book Co., New York, N.Y., 1955).

4. R. Courant and D. Hilbert, Methods of Mathematical Physics (McGraw-Hill Book Co., New York, N.Y., 1953), Vol. 1, p. 309.

5. L. S. Jacobsen and R. S. Ayre, Engineering Vibrations; With Applications To Structures and Machinery (McGraw-Hill Book Co., New York, N.Y., 1958), p. 170.

6. R. A. Anderson, J. Appl. Mech. 20, 504 (1953).

7. H. H. Bleich and R. Shaw, J. Appl. Mech. 27, 132 (1960).

Appendix

EVALUATION OF THE NORMALIZING FUNCTION

$$\psi_n^2 = \zeta_n^2 \cos^2 k_n \xi + \mu_n^2 \sin^2 k_n \xi + \eta_n^2 \cosh^2 \xi + \sinh^2 \xi$$

$$+ 2\zeta_n \mu_n \sin k_n \xi \cos k_n \xi + 2\zeta_n \eta_n \cos k_n \xi \cosh k_n \xi$$

$$+ 2\zeta_n \cos k_n \xi \sinh k_n \xi + 2\mu_n \eta_n \sin k_n \xi \cosh k_n \xi$$

$$+ 2\mu_n \sin k_n \xi \sinh k_n \xi + 2\eta_n \sinh k_n \xi \cosh k_n \xi \quad . \tag{28}$$

Since

$$\lambda_n^2 = \int_0^1 \psi_n^2 \, dx \; ;$$

it may be shown that

$$\lambda_n^2 = \frac{1}{2k_n} \Big\{ k_n \left(\zeta_n^2 + \mu_n^2 + \eta_n^2 - 1 \right) + \left(\zeta_n^2 - \mu_n^2 \right) \sin k_n \cos k_n$$

$$+ 2\zeta_n \mu_n \sin^2 k_n + 2(\mu_n \eta_n - \zeta_n) + 2\eta_n \sinh^2 k_n + \left(\eta_n^2 + 1 \right) \sinh k_n \cosh k_n$$

$$+ 2 \Big[(\zeta_n \eta_n - \mu_n) \cos k_n + (\zeta_n + \mu_n \eta_n) \sin k_n \Big] \sinh k_n$$

$$+ 2 \Big[(\zeta_n \eta_n + \mu_n) \sin k_n + (\zeta_n - \mu_n \eta_n) \cos k_n \Big] \cosh k_n \; . \tag{29}$$

Note:

$$\sinh k_n = \frac{\epsilon^{k_n} - \epsilon^{-k_n}}{2}$$

$$\cosh k_n = \frac{\epsilon^{k_n} + \epsilon^{-k_n}}{2}$$

$$\sinh^2 k_n = \frac{\epsilon^{2k_n} + \epsilon^{-2k_n}}{4} - \frac{1}{2} \tag{30}$$
(Cont.)

$$\sinh k_n \cosh k_n = \frac{\epsilon^{2k_n} - \epsilon^{-2k_n}}{4} \ . \tag{30}$$

Thus, Eq. (29) can be replaced by

$$\lambda_n^2 - \frac{1}{2k_n} \left\{ k_n \left(\zeta_n^2 + \mu_n^2 + \eta_n^2 - 1 \right) + \left(\zeta_n^2 - \mu_n^2 \right) \sin k_n \cos k_n \right.$$

$$+ 2\zeta_n \mu_n \sin^2 k_n + 2(\mu_n \eta_n - \zeta_n) - \eta_n + (\eta_n + 1)^2 \frac{\epsilon^{2k_n}}{4} - (\eta_n - 1)^2 \frac{\epsilon^{-2k_n}}{4}$$

$$+ \epsilon^{k_n} \left[(\zeta_n \eta_n - \mu_n + \zeta_n - \mu_n \eta_n) \cos k_n + (\zeta_n + \mu_n \eta_n + \zeta_n \eta_n + \mu_n) \sin k_n \right]$$

$$\left. + \epsilon^{-k_n} \left[(-\zeta_n \eta_n + \mu_n + \zeta_n - \mu_n \eta_n) \cos k_n + (-\zeta_n - \mu_n \eta_n + \zeta_n \eta_n + \mu_n) \sin k_n \right] \right\} \ . \tag{31}$$

Note:

$$\zeta_n \eta_n - \mu_n + \zeta_n - \mu_n \eta_n = (1 + \eta_n)(\zeta_n - \mu_n)$$

$$\zeta_n + \mu_n \eta_n + \zeta_n \eta_n + \mu_n = (1 + \eta_n)(\zeta_n + \mu_n)$$

$$-\zeta_n \eta_n + \mu_n + \zeta_n - \mu_n \eta_n = -(\eta_n - 1)(\zeta_n + \mu_n) \tag{32}$$

$$-\zeta_n - \mu_n \eta_n + \zeta_n \eta_n + \mu_n = (\eta_n - 1)(\zeta_n - \mu_n) \ .$$

And from Eqs. (22) and (23) of the body of this paper — $\eta_n + 1 = 2Z_n \epsilon^{-k_n}$; and $\eta_n - 1 = 2Y_n$. So that Eq. (51) becomes

$$\lambda_n^2 = \frac{1}{2k_n} \left\{ k_n \left(\zeta_n^2 + \mu_n^2 + \eta_n^2 - 1 \right) + \left(\zeta_n^2 - \mu_n^2 \right) \sin k_n \cos k_n \right.$$

$$+ 2\zeta_n \mu_n \sin^2 k_n + 2(\mu_n \eta_n - \zeta_n) - \eta_n + Z_n^2 - Y_n^2 \epsilon^{-2k_n}$$

$$+ \left[(\zeta_n - \mu_n) \cos k_n + (\zeta_n + \mu_n) \sin k_n \right] \left[2Z_n \right]$$

$$\left. + \left[-(\zeta_n + \mu_n) \cos k_n + (\zeta_n - \mu_n) \sin k_n \right] \left[2Y_n \epsilon^{-k_n} \right] \right\} \ . \tag{33}$$

* * *

83

Section 2
COMPUTERS IN DESIGN

DIGITAL COMPUTER APPLICATION
TO NONLINEAR VIBRATIONS

F. H. Collopy and R. Serbagi
AVCO CORPORATION
Wilmington, Massachusetts

INTRODUCTION

There are numerous dynamic problems
being encountered continually in structural
systems which do not exhibit an ideal linear
behavior. The engineer can solve these prob-
lems by: (1) linearizing and solving for the
idealized linear system; (2) utilizing the analog
computer to solve the more realistic nonlinear
system; and (3) utilizing a digital computer to
solve the nonlinear problem by numerical
schemes. There are times when it is prudent
from an engineering viewpoint to use approach
(1) and reduce the complexities of the problem.
One must rely on experience, however, to pro-
vide the degree of caution required when making
such engineering assumptions. Oftentimes non-
linearities may be the controlling factor in a
design or analysis and should be accounted for.
The analog computer has been widely used to
solve the nonlinear differential equations which
describe a nonlinear system. With the improve-
ment within the last decade of the high-speed
digital computer and the development of many
numerical routines, there exist certain distinct
advantages in using the digital computer to
solve nonlinear vibration problems for a wide
range of applications.

It is the purpose of this paper to indicate
the significance of the digital computer in solv-
ing nonlinear problems. This is accomplished
by (1) knowledge of the digital computer and its
uses, (2) ability to communicate with the digital
computer through a general purpose program,
(3) ability to recognize and solve special dynam-
ics problems utilizing this general purpose
program, and (4) addition of certain flexibilities
by the programmer which will enable the

dynamicist to write in his own language the
peculiarity of the particular problem.

An illustrative problem is contained in the
appendix to better emphasize the thesis of this
paper.

DIGITAL COMPUTER PROBLEM
   SOLUTION

Techniques for Handling Input

The disadvantages of most digital computer
programs for solving nonlinear dynamics prob-
lems arise when the engineer encounters diffi-
culties in matching a physical system to the
mathematical constraints of the digital program.
Generally, it is impossible to make minor
changes to the program if it doesn't fit the
problem exactly. The types of changes the en-
gineer usually desires to make are: (1) changes
in the forcing functions; (2) changes in the non-
linear terms; (3) the selection of more output
variables; (4) additional operations, such as
saving maximum values of some variables; (5)
calculating stresses, bending moments, and the
like; and (6) the plotting of any or all of these
values as a function of time.

It is advantageous for the engineer to have
a program with the input in a language not too
different from his own. In this way, the engi-
neer can communicate directly with the com-
puter and ask the program to perform a wide
range of calculations, and at the same time not
be frustrated by the procedures of asking a
programmer to make continuous changes to
existing programs (which entails the rigorous

checkout period causing frustrating time delay in solving a problem). One example of a language to accomplish this is FORTRAN, the most widely used computer language. FORTRAN is an acronym for FORmula TRANslation. Similar problem-oriented languages in other digital computing systems are ALGO, COBOL, BALGOL, JOVIAL, and so on. The two procedures involved in utilizing these languages are: (1) presenting the problem to the computer in a language it can understand (FORTRAN, and so forth); and (2) compiling, which is a procedure that transforms the FORTRAN instructions into the proper elementary machine instructions to solve the problem. The use of FORTRAN is governed by a strictly regimented set of rules that must be followed in formulating equations and instructions to the computer. It is advisable for any engineer intending to use this language to familiarize himself with it, preferably by formal instruction. Special 1-week courses, which are offered in various educational institutions, serve as an excellent introduction.

Instead of requiring the engineer to utilize the strict formulation of instructions needed in the use of FORTRAN, it would be highly desirable for the program to accept statements less strict than FORTRAN. For example, if the engineer wants the forcing function to be

$$F(t) = 10 + 100t^2 \quad \text{for} \quad t < 5.0$$

and

$$F(t) = 0 \quad \quad \text{for} \quad t \geq 5.0$$

then, he would write

$$F = 10.0 + 100.0*T**2. \quad T - LT - 5.0$$

$$F = 0.0 \quad \quad , \quad T - GT - E - 5.0,$$

where T - LT - 5.0 means time less than 5.0.

T - GT - E - 5.0 means time greater than or equal to 5. Writing the above instructions completely in FORTRAN would require slightly more effort.

If the engineer wants to plot $(x_1 - x_2) \cdot 10^6$, then he would write

$$PLOT \ [x(1) - x(2)] * 1.0E6 ,$$

or, if upon completion of the problem he wants to output the maximum value of $x_1 \cdot x_2$, he writes

$$Max \ [x(1) * x(2)] .$$

If the engineer wanted to formulate these instructions by means of compiling a subroutine

written in a strict FORTRAN-like language, the effort required would be greater.

Either of the two preceding techniques for utilizing a digital computer will reduce the work of the engineer required to solve a particular problem. Also, it will allow him to solve a large variety of problems without the constant aid of the programmer. The important role that the programmer plays is in the construction of the digital computer so that the engineer can solve the various problems encountered in nonlinear systems by merely specifying the nonlinearities as input to the program.

Linear Vibration Problems

The differential equations of motion for a mechanical system under vibration which has viscous damping are most commonly presented as

$$[M]\ddot{X} + [C]\dot{X} + [K]X = F(t) , \quad (1)$$

where $[M]$, $[C]$, and $[K]$ are, respectively, the mass, damping, and stiffness coefficient matrices of the system; F is the forcing function as a function of time, and X is the generalized displacement coordinate. Equation (1) represents the general form of a set of linear, ordinary differential equations. There are many useful numerical methods for solving these equations on a digital computer. Methods which utilize a Runge-Kutta integration routine are the most common because the procedure involved is remarkably simple for digital programming.

Nonlinear Vibration Problems

The most common form of a nonlinear vibration problem is the multi-degree-of-freedom system with a nonlinear forcing function:

$$[M]\ddot{X} + [C]\dot{X} + [K]X = F(\dot{X}, X, t) . \quad (2)$$

It is easily recognized that the left side of Eq. (2) is identical to the left side of Eq. (1). This indicates that (2) (the nonlinear equations) might be solved much the same way as (1) (the linear equations). In the solution of Eq. (1) by a numerical integration scheme, a set of constant values are obtained at each incremental time step by evaluating the forcing function $F(t)$ external to the main program. These values are then presented to the main program at each time step. Since the calculation of the forcing function, F, is performed external to the main program, the process involved in the

86

method of solution of Eq. (2) can be identical to that of Eq. (1). This can be accomplished if the ability to describe the nonlinear forcing function, $F(\dot{X}, X, t)$, as part of the input to the computer is made flexible enough for practical applications. It is maintained that the programmer easily can provide this flexibility to the dynamicist.

A more general set of nonlinear equations of motion which contain nonlinear stiffness or damping functions could be written as:

$$[M]\ddot{X} + [C(\dot{X}, X, t)]X + [K(\dot{X}, X, t)]X = F(\dot{X}, X, t) , \quad (3)$$

where certain terms within the damping matrix, $[C]$, or the stiffness matrix, $[K]$, are functions of velocity, displacement, and time. An approach whereby the nonlinear equations of (3) can be solved by utilizing the same computer program as used to solve the nonlinear equations of (2) is described as follows:

1. Expand Eq. (3) in a nonmatrix form.

2. In each equation transpose all nonlinear terms which are on the left side of the equation to the right side and the transposed terms can now be considered as part of the nonlinear forcing function.

3. Since Eq. (3) is now basically the same as Eq. (2), all previous comments on the solution of Eq. (2) are applicable.

The following illustrations are presented to demonstrate the above discussion:

1. Equation (4) is nonlinear due to the $\dot{y}y^2$ term,

$$\ddot{y} + \dot{y}y^2 + ky = F_1 . \quad (4)$$

By rewriting Eq. (4), so that all nonlinear terms are on the righthand side of the equation, we obtain Eq. (5) which is solvable by the previous discussion,

$$\ddot{y} + ky = F_1 - \dot{y}y^2 . \quad (5)$$

2. Equation (6) is the equation of a pendulum with damping proportional to the square of the angular velocity; and the equation is nonlinear if large deflections are assumed. This equation is transformed into Eq. (7) and is solvable by means of the aforementioned technique:

$$\ddot{X} + C\dot{X}|\dot{X}| + k \sin X = 0 ; \quad (6)$$

$$\ddot{X} = -[C\dot{X}|\dot{X}| + k \sin X] . \quad (7)$$

Once the engineer has formulated his problem in the above form, he need only to specify the linear portion which is the three constant

matrices, $[M]$, $[C]$, $[K]$, and the nonlinear portion which is the general forcing function. The forcing function is then specified in a FORTRAN-like language.

For example, using Eqs. (5) and (7), the engineer would write, as input, the following forcing function statements:

for Eq. (5),

$$F = D(1) - XD*X**2 ,$$

and

for Eq. (7),

$$F = -[D(4)*XD*ABS(XD) + D(2)*\sin(X)] ,$$

where $D(1)$, $D(2)$, ... etc., represent constant whose values can be included in the input data.

This method of inputting allows for complete flexibility in defining the forcing function. Other options which can be implemented easily by the programmer is to allow the engineer to call for additional calculations and printouts based on the results of the integration routine.

TYPES OF DYNAMIC NONLINEARITIES

Illustrations of nonlinearities which can exist in dynamic systems which would require particular formulation and which would be solvable by a digital computer program as described in this paper are given below.

Nonlinear Stiffness

Cushioning material exhibits nonlinear load-deflection characteristics as shown in Figs. 1-3.
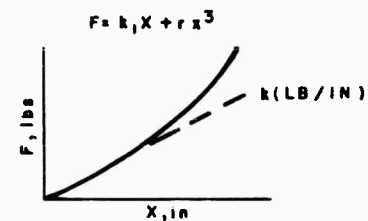
Fig. 1 - Cubic elasticity

Nonlinearities occur in systems where springs act over only part of the displacement range. Such a physical system and its piecewise linear force deflection curve is shown in Fig. 4.
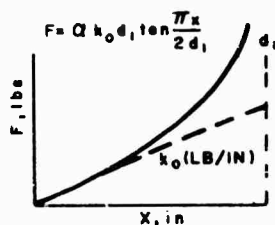
Fig. 2 - Tangent elasticity
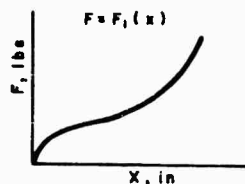
Fig. 3 - Anomalous elasticity
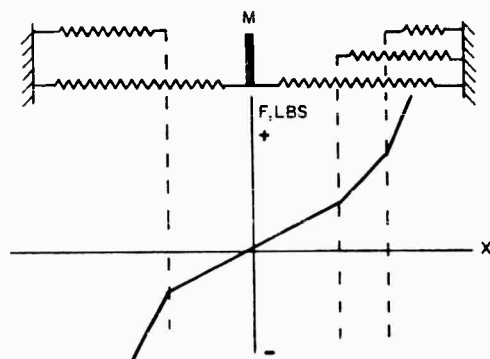
Fig. 4 - Discontinuous springs

An elastoplastic structure, one which has an initial elastic stress-strain curve but which has a subsequent inelastic part with uniform resistance after yielding, as is characteristic of honeycombed materials, has an idealized load-deflection curve as shown in Fig. 5.

Nonlinear Damping

One type of nonlinear damping is evidenced in a form of Rayleigh's equation:

$$\ddot{x} - (a_1 - a_2 \dot{x}^2) \dot{x} + w^2 x = 0 . \tag{8}$$

Also, Eq. (6) contains a nonlinear damping expression, $c \dot{x} |\dot{x}|$.
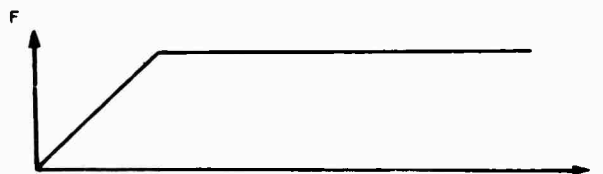
Separation Problem

In order to investigate the dynamic characteristics of staging effects and separation loading on missile systems and re-entry vehicles, the dynamicist has to describe accurately when the subsystems separate or when they rejoin each other. Figure 6 shows a separation problem which could be encountered. An impulse, I, imparted to system A and B (initially one system) in the directions shown could cause A and B to separate from each other and after separation would cause each system to vibrate as a separate system. If, however, T was a steady thrust load it could, depending on the ratio of T and I, cause A and B to rejoin after separating or prevent them for ever separating. The equations describing this problem would be piecewise linear. This problem could be readily solved by the type of digital computer utilization technique presented in this paper.

WIDE-RANGE APPLICATIONS

The generality of such a solution provides a technique for investigating many classical forms of nonlinear differential equations which can eventually be reduced to a form of Eq. (2). There are many branches of science other than vibrations whose behavior is described by nonlinear differential equations. To name a few, there are acoustics, astronomy, electronics, aerodynamics, hydraulics, and cable telegraphy. The general introduction to the book by N. W. McLachlan, Ordinary Nonlinear Differential Equations in Engineering and Physical Sciences, serves as an excellent reference for historical background on the field of nonlinear differential equations, their application, and solutions.

To illustrate the wide range of applicability of a digital computer program as described herein, some examples of classical nonlinear differential equations widely studied by scientists and engineers are listed.

Fig. 5 - Elastoplastic resistance
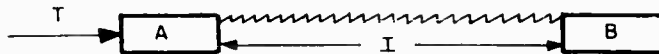
Fig. 6 - Separation system

van Der Pol's Equation

In the area of self-sustained oscillations are such systems as electrical systems containing vacuum tubes, self-sustained vibration in mechanical systems resulting from the action of solid friction, the "chattering" of the brake shoes against the wheels of a railroad car when the brakes are applied, aerodynamic effects on suspension bridges, and the like.

The general form of differential equation used in the field of electronics to represent the behavior of the triode-oscillator was studied quite extensively by B. van Der Pol, namely,

$$\ddot{y} + F(y)\dot{y} + ky = 0 .$$

Hill's Equation for Mechanical-Electrical Systems

A form of Hill's equation is

$$L\ddot{X} + \frac{1}{C(t)} X = 0 ;$$

this equation represents a mechanical-electrical system containing a circuit having an inductance and condenser in series. The most common application of this type of equation is in stability work.

Surge Tank Applications in Hydroelectric Power Plants

The differential equations of motion to describe the motion of the water level in a surge tank installation are

$$\ddot{X} + a_1 |X|\dot{X} + a_2 = Q/r .$$

Large Deflection Theory of a Pendulum

The nonlinear differential equations of motion of a pendulum with quadratic damping, such as would be encountered if a pendulum were immersed in a fluid, are

$$\ddot{X} + C\dot{X}|\dot{X}| + k \sin X = 0 .$$

Lane-Emden Equation

This equation, used to describe the gravitational equilibrium of a gaseous configuration in stellar structure, is

$$\ddot{\theta} + \frac{2}{t} \dot{\theta} + \theta^u = 0 .$$

Mathieu's Equation

Mathieu's equation, which represents a string being driven by an attached vibrating reed, is of the form

$$\ddot{X} + \left[(a + bx^2) - 2c \cos \theta\right]x = 0 .$$

There are many more examples that can be cited from the vast amount of literature dealing with nonlinear differential equations [1-4].

CONCLUSIONS

For a wide cross section of disciplines, it has been demonstrated that the solution of nonlinear differential equations easily can be accomplished by means of a general purpose digital computer program. For the programmer, it has indicated what type of flexibilities should be included in the formulation of dynamic response programs, and has illustrated a unique but simple approach to digital computer solutions of nonlinear vibrations. For the dynamicist, this paper illustrates the capabilities provided by the programmer so that the dynamicist can readily solve a wide range of dynamic problems containing various nonlinearities. For engineers and scientists working in fields unrelated to vibrations who, however, become involved with nonlinear differential equations, this paper indicates an approach which may be taken to solve these equations with a digital computer.

NOTE: References appear on page 92.

ILLUSTRATIVE PROBLEM

The physical problem considered is shown in Fig. A-1 and it is desired to describe the response of the system to a forcing function $f(t)$. A digital computer was used for solving this problem and the output appears as displacement, velocity, and acceleration of each mass at every 0.025 millisecond for 0.5 millisecond. In addition to the digital output, plots of the same coordinates will be made, including a plot of the relative displacement between masses 1 and 2. The nonlinear portion of this example is in the spring force $K_2 X_2$ which is represented as $\alpha X_2 + \beta X_2^2$.
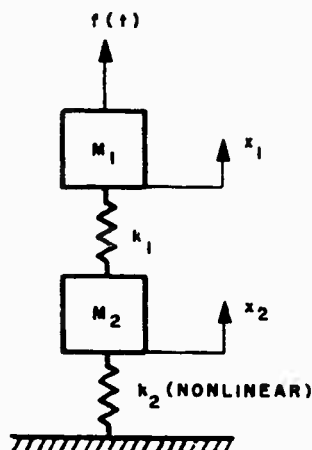
Fig. A-1 - Sample problem

The equations of motion of the system are:

$$M_1 \ddot{X}_1 + K_1(X_1 - X_2) = f$$

$$M_2 \ddot{X}_2 + K_1(X_2 - X_1) + \alpha X_2 + \beta X_2^2 = 0$$

or

$$[M]\ddot{X} + [K]X = F,$$

where

$$X = \begin{bmatrix} X_1 \\ X_2 \end{bmatrix} \quad [M] = \begin{bmatrix} M_1 & 0 \\ 0 & M_2 \end{bmatrix} \quad [K] = \begin{bmatrix} K_1 & -K_1 \\ -K_1 & K_1 + \alpha \end{bmatrix}$$

and

$$F = \begin{bmatrix} f \\ -\beta X_2^2 \end{bmatrix},$$

where

$$f = \begin{cases} (t+1)10^6 & t < 0.00025 \\ 0 & t \geq 0.00025 \end{cases}.$$

The constants used in the sample problem are

$$M_1 = 10., \quad M_2 = 100., \quad K_1 = 10^{10},$$
$$\alpha = 10^{10}, \text{ and } \beta = 10^{14}.$$

By using the input language described in the main body of this paper, the input can easily be written:

```
M(1,1)10.          M(2,2)100.
K(1,1)1.E10        K(1,2) - 1.E10
K(2,1) - 1.E10     K(2,2)2.E10
```

Initial Time 0, Final Time 0.0005

Print Time 0.000025, Plot Time 0.000025

PLØT X(1), XD(1), XDD(1), X(2), XD(2), XDD(2)

PLØT X(1) - X(2)

F_1 = 1E6* (T + 1.0), if T - LT - 0.00025

F_1 = 0, if T - GT - E - 0.00025

F_2 = - 1E14*X(2)**2

END OF DATA.

It is apparent from this problem that the engineer need only specify the peculiarities of his problem in a language similar to his own. The results appear on the following pages. Only the plots are contained in this paper since it would be space-consuming to show actual numerical output.

91

TRANSIENT RESPONSE
CASE   I   MEMO
COORDINATE   2

TIME - MILLISECONDS

TRANSIENT RESPONSE
CASE   I   MEMO
COORDINATE   2

TIME - MILLISECONDS

TRANSIENT RESPONSE
CASE   I   MEMO
COORDINATE   2

TIME - MILLISECONDS
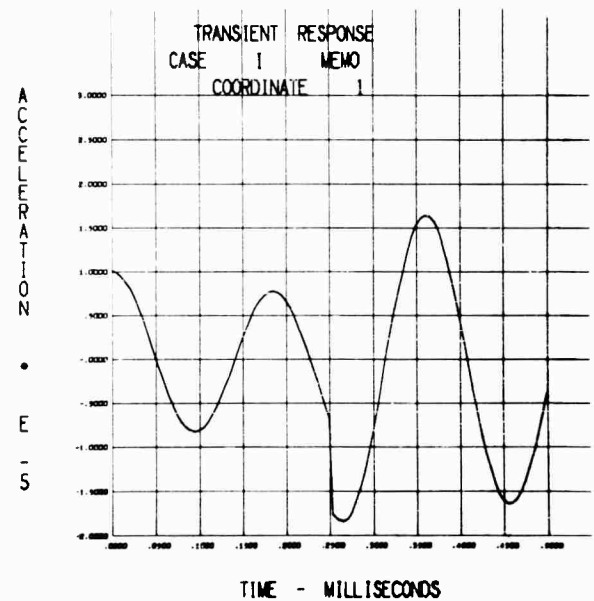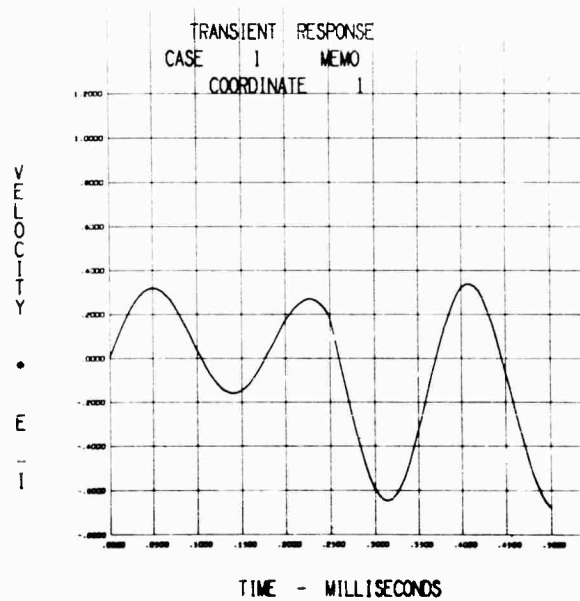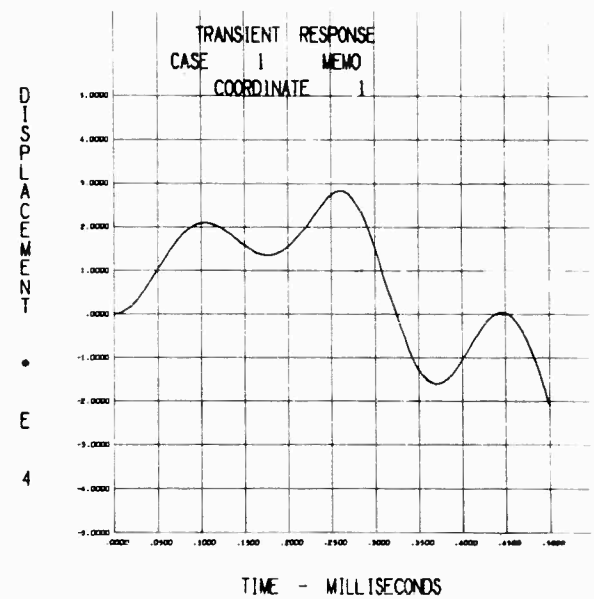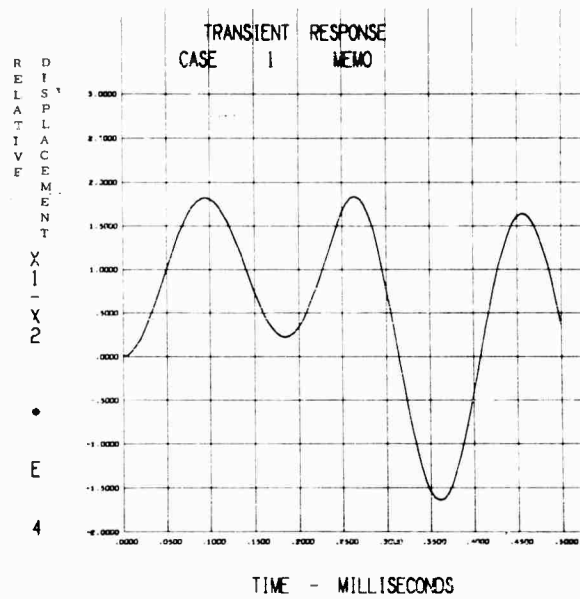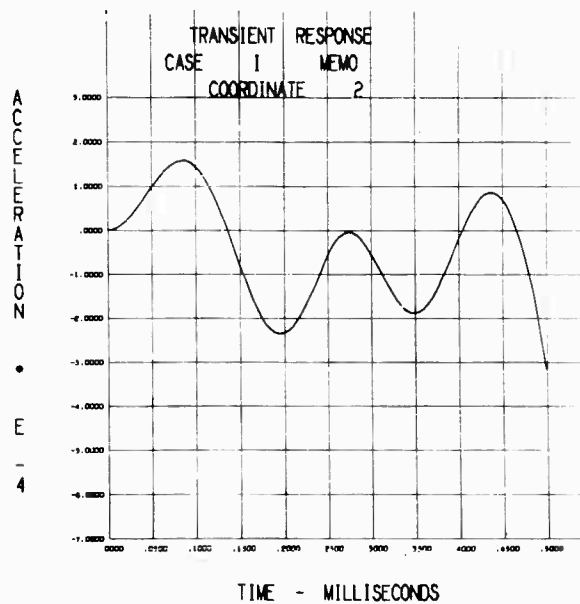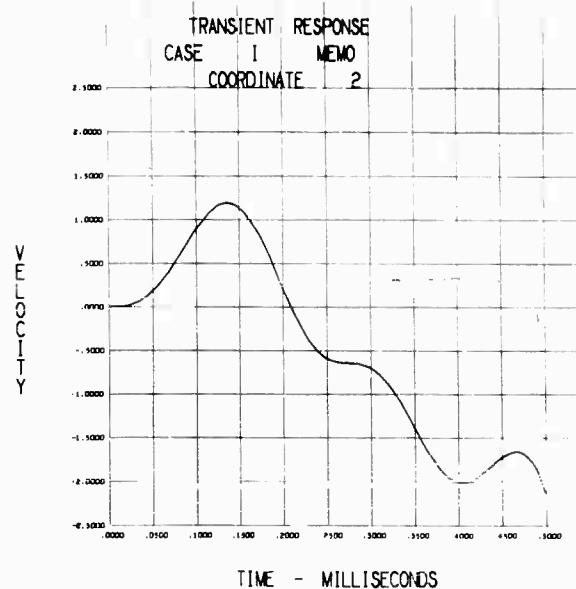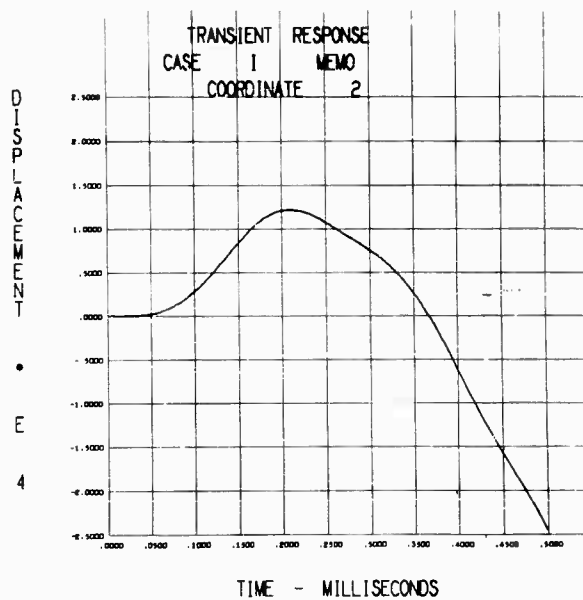
REFERENCES

1. J. J. Stoker, Nonlinear Vibrations (Interscience Publishers, Inc., New York, N. Y., 1950).

2. J. P. Den Hartog and R. M. Heiles, J. Appl. Mech., 3, A127-A130 (1936).

3. T. von Karman, Bull. Amer. Math. Soc., Vol. 46, No. 8 (Aug. 1940), pp. 615-683.

4. J. G. Baker, "Forced Vibrations With Nonlinear Spring Constants," Trans. Am. Soc. Mech. Eng., Vol. 54, 1932.

*   *   *

INTEGRATION OF A COMPUTER INTO THE DESIGN PROCESS

A. L. Head, Jr. and G. Harris
LTV Vought Aeronautics Division
Dallas, Texas

Integration of a computer into the design process is an essential ingre-
dient in the successful design of modern flight vehicles. The broad
requirements of a design-integrated computer system are defined as
flexibility, speed, and economy. The various characteristics which
provide these features are discussed in detail. A system meeting these
requirements is discussed with emphasis on its operational aspects.

Integration of a computer into the design process is an essential ingredient in the successful design of modern flight vehicles. As a particular design evolves, potential problem areas must be recognized and acceptable solutions determined. The modern high speed computer is a powerful tool for use in obtaining effective and timely solutions to these problems. To adapt such a complex tool to the design process, an automated system of computer operation is invaluable. Such a system provides the function of adapting the computer to the job at hand in order to provide answers on an overnight basis by using simplified instructions as input.

The broad requirements of a design-integrated computer system may be simply stated as flexibility, speed, and economy. The system must be flexible regarding problem size, type, and complexity to solve efficiently the vast range of problems which are encountered during the design process. In addition, such a system must be readily adaptable to new types of problems as they arise.

The real key to a design-integrated computer system is the speed of operation. From the viewpoint of the engineer this means speed in "turnaround time" — the time required, after submittal of problem, to obtain answers. In particular this should mean overnight service to avoid delays. Flexibility and speed are closely related, since it is the flexibility of the system which circumvents the necessity for special programming and checkout of new problems with associated time delay and potential errors.

Similarly, speed and economy are closely related. The actual machine efficiency or speed in computing time is of extreme importance, but it is only a part of the total picture. The actual measure of speed and economy is a balance between computing time, turnaround time, probability of errors, extent of reruns, and required manhours.

To examine in more detail some of the characteristics of a computer system which provides the features of flexibility, speed, and economy, consider the following requirements:

1. modular system

2. problem formulation and submission by engineer

3. automatic data filing and recall

4. high degree of automation

5. economical machine operation with growth potential.

A modular computer system may be described as one in which an engineering problem is solved by using a sequence of relatively simple computing routines with the sequencing performed automatically by a master system routine, according to a set of instructions in a simple language. This may be contrasted with a non-modular system wherein a single specialized routine is used to solve a particular type of problem. Basically, the ingredients of a modular system consist of the system or governing routine, a library of individual computing

routines, and a system of communication between the engineer and the machine. The main advantage of a modular system is the inherent flexibility and adaptability to new types of problems. The main disadvantage of such a system is a reduction in machine computing time efficiency when compared with the specialized routine approach. This is partially offset by the fact that protective and recovery devices are possible with a modular system that enables mistakes to be corrected with minimum cost. For example, if incorrect answers are obtained due to an error, the problem needs only to be repeated from the point of the error. The level of modulation or degree to which the library of routines is subdivided is a tradeoff between flexibility and machine economy. Indeed, a typical system will have varying degrees of modulation; that is, the library will contain many routines which are specialized combinations of other library routines.

Problem formulation and submittal by the engineer at the working level is mandatory for rapid service. The engineer develops a familiarity with the capabilities and limitations of the computer and its governing system. As a result, problems are formulated from the beginning for efficient computer operations. Direct communication between the engineer and the machine, except for keypunch and operating personnel, eliminates the technical middleman together with the associated time delays and potential misunderstandings. Consequently, the speed and accuracy with which results are obtained are greatly increased. Since the average engineer is not familiar with programming language or the internal working of the machine, the system language or means of communication must be extremely simple and as foolproof as possible. This enables the working engineer to use the computer on a routine, everyday basis. As a result, the computer becomes truly integrated into his day-to-day work.

Automatic data filing and recall provides a means whereby data may be stored on tape and recalled for use in subsequent problems. This feature eliminates the time required to prepare and keypunch frequently used data; hence, it contributes significantly towards the minimization of turnaround time.

A high degree of automation is required to eliminate time and error caused by the human factor. Once data for a particular problem are prepared, the computer itself must perform the functions of collecting additional data and necessary library routines, executing the computing phase, filing data, and printing the results.

Machine economy is extremely important, because it is a major part of the overall economy of the computer operation. Growth potential is required both from the viewpoint of ability to add additional modules to the system and also from the viewpoint of adaptability of the system to new generations of computing machines.

A system having many of the above characteristics has been in operation at Ling-Temco-Vought for several years. This system, called PAS (Production Assembly System), has effectively made the modern high speed computer an integral part of the design process. PAS was conceived in the mid-1950's and has been continuously improved and expanded since that time. The flexibility and growth potential in the basic system has allowed PAS to survive three generations of computing machines.

PAS may be defined as a modular programming and operating computing system oriented toward matrix arithmetic. The problem originator, by making use of the various computing routines which make up the PAS library, can solve any particular problem by using extremely simple instructions as input. PAS also contains a data filing and retrieving system. Supplied or calculated data may be stored on magnetic tape for future use. The system, when so instructed, will retrieve any stored data for use in a particular problem.

PAS provides the working engineer with a method of communication with the computer without requiring him to understand the programming language or the internal working of the machine. The basic means of communication is the Problem Plan Form. By use of this form, the engineer specifies the operations to be performed, their sequence, the data to be used and the data's source, and the disposition of the problem results. The plan form may be described as a series of boxes with each box containing the information necessary for the computer to perform a particular operation or portion of the problem. A routine number and box number describe the operation to be performed and its order within the problem. The data to be used are indicated by a type number, data code (title), and data size. The source of the data and the disposition of the results are also indicated. Space is provided for the engineer to add remarks or notes to the plan form for future reference. The plan form is illustrated and described in detail in Fig. 1. It is emphasized that the key to the plan form is its simplicity and adaptability to simple mechanical checks to insure that it is properly filled out for a particular problem.

94

Fig. 1 - Sample problem plan form

Although the main purpose of the plan form is one of communication, it also provides a valuable documentary record of work performed. The plan form listing is extremely neat and easily filed, and it provides a detailed record of how each problem was actually solved together with the data used. An example of such a listing is shown in Fig. 2.

Although the governing routine portion of the system is the heart of PAS, the working engineer is more concerned with the library of individual computing routines. The PAS library of routines is quite large at the present time, numbering approximately 125. Following is a partial list of the type of routines that form this library:

Matrix Routines

    Addition
    Multiplication
    Inverse

Matrix Logic Routines

    Assembly
    Group
    Matrix Operations

Unsteady Aerodynamics Routines

    Uncompressible Airforces
    Compressible Airforces
    Supersonic Airforces

Mode Shape Routines

    Inertia
    Influence
    Mode Shape

Flutter and Response Routines

    Flutter
    Frequency Response
    Transient Response

The operational use of PAS may be described as follows. To run a particular problem, the engineer formulates the problem in a series of steps to fit available computing routines. He then prepares a problem plan form consisting of a sequence of boxes, one for each particular routine used. Each engineer has access to a PAS handbook which contains for each routine a description of what the routine does, how the plan form is

```
BY J A MALLICK              TITLE A7A WING PANEL           PROBLEM NO 5353     0101
UNIT 2-53061                POINT C MATRICES M.95          PAGE 01  OF  02     0102
DATE 07/16/64                   CORRECTIONS                CH NO      /8822    0103

010 016420 A X 8    2 MUA   0   3   3    7              S                      0104
                    3 UNITY 0   3   3   16                                     0105
                    9 MU7   0   3   3  112                                     0106

020 016420 A X B    2 MUB   0   3   3    9              S                      010B
                    3 UNITY 0   3   3   16                                     0109
                    9 MU9   0   3   3  144                                     0110

030 016460 MAT OPER 0 KA    1   3   3  112 5290 030                            0112
                    4 MU7   0   3   3  112       010                           0113
                    9 KM7   1   3   3  112                                     0114

040 016460 MAT OPER 0 KB    1   3   3  144 5290 040                            0116
                    4 MU9   0   3   3  144       020                           0117
                    9 KM9   1   3   3  144                                     0118

050 016480 SUM 8A8  0 SUMA  0   1   7    1 5290 030                            0120
                    1 KM7   1   3   3  112       030                           0121
                    2 HTCS  0   3  16    7 5290 010   M.95 CORRECTEO           0122
                    9 CA95  1  16  16   16            X PP C MAT CENTER SECT   0123

060 016480 SUM BA8  0 SUMB  0   1   9    1 5290 040                            0125
                    1 KM9   1   3   3  144       040                           0126
                    2 HTOP  0   3  28    9 5290 020   M.95 CORRECTEO           0127
                    9 CB95  1  28  28   16            X PP C MAT OUTER PANEL   012B

070 016410 8AB      1 CA95  1  16  16   16       050                          0130
                    2 TPRAL 0  16   4    1 5290 003                           0131
                    9 CA95T 1   4   4   16            L                       0132

0B0 016410 BA8      1 C895  1  2B  2B   16       060                          0204
                    2 T.RB  0  28   4    1 5290 002                           0205
                    9 C895T 1   4   4   16            L                       0206

090 016490 A PLUS B 2 CA95T 1   4   4   16       070                          0208
                    4 C895T 1   4   4   16       080   M.95 CORRECTEO COMP-   0209
                    9 CT95T 1   4   4   16            L LETELY TR ROLL PIT AR 0210

100 016700 END PROBLEM                                                       0212
```

Fig. 2 - Plan form of a typical problem

filled out, size restrictions, and other pertinent information. Having completed the plan form, the engineer then prepares any necessary supplied data on standard 80 column keypunch paper. Both plan form and data are then keypunched, verified, and returned to the engineer for checking. After any changes or corrections are made, the engineer gives approval to run the problem. The computer operating personnel load the plan form and data for the problem (normally together with several others), and the machine automatically performs the rest of the operation. The operational use of PAS is summarized in flow diagram form in Fig. 3. Appendix A contains an example of the use of PAS to obtain the cantilevered mode shapes and frequencies of a uniform beam. Included are the formulations of the problem, the PAS plan form, the supplied data, and the results.

Additional features of PAS worthy of note are the protective and recovery devices built into the system. The machine will not accept a problem unless the plan form, the PAS handbook specifications, and the required data are compatible. The individual computing routines used also have built in safeguards causing a machine stop if certain types of errors occur. A very beneficial feature is the ability to rerun only part of a problem; that is, a problem may be corrected and restarted in any box.

Three generations of computers have stretched the growth potential of PAS to the limit. To utilize more fully the increased speed and storage capability of the newer computers, an improved version of PAS called MOSS (Matrix Oriented SyStem) is being developed. Although the basic concept is the same, an automated modular system with simple communication, significant changes are being made. These include a change in communication to a Fortran-like language wherein the arithmetic statements refer to matrix operations rather than numbers as in Fortran. In addition, a means of problem segmentation is included to fully utilize available core storage, and a multiple tape data scatter system is included to reduce data retrieval time. The goal of MOSS is to retain all the advantages of PAS

ENGINEERING GROUP

FORMULATION OF PROBLEM
IN MATHEMATICAL TERMS

FORMULATION OF PROBLEM IN
TERMS OF COMPUTING ROUTINES
ON PROBLEM PLAN FORM

PREPARATION OF SUPPLIED
DATA ON STANDARD KEYPUNCH
FORMS

PLAN FORM AND SUPPLIED DATA TO COMPUTING

LISTINGS RETURNED TO ENGINEER

PLAN FORM AND DATA
CHECKED

FINAL APPROVAL TO
RUN PROBLEM

—CHANGES, CORRECTIONS, AND RERUNS

SOLUTION REVIEWED

FINAL RESULTS TO ENGINEER

COMPUTING FACILITY

PERSONNEL   MACHINE

PLAN FORM AND DATA
KEYPUNCHED AND
VERIFIED

CORRECTIONS MADE
AS NECESSARY

TAPES MOUNTED,
PLAN FORM AND
DATA LOADED

RESULT TAPE MOUNTED
AND PRINTED ON
PERIPHERAL EQUIPMENT

PAS
PROTECTIVE
SYSTEM
(COMPATIBILITY
AND ERROR STOPS)

NECESSARY ROUTINES
COLLECTED

FILED DATA COLLECTED
AS SPECIFIED ON
PLAN FORM

COMPUTING PHASE
EXECUTED

DATA FILED AND
RESULTS WRITTEN ON
TAPE

Fig. 3 – Flow diagram showing PAS operation

while increasing the system flexibility and gaining a significant increase in machine efficiency. Thus, the operational use of MOSS should further integrate the modern high speed computer into the design process.

Appendix A

AN EXAMPLE OF THE USE OF PAS TO OBTAIN THE CANTILEVERED MODE SHAPES AND FREQUENCIES OF A UNIFORM BEAM

FORMULATION OF EQUATIONS
OF MOTION

The mode shapes and frequencies of a cantilevered uniform beam are determined in this appendix to illustrate the use of PAS. Before proceeding with the PAS problem, the equations of motion will be developed. For a conservative system under the action of an external loading condition the equations of motion can be written as follows:

$$\left(\frac{1}{g}\right) [A] \{\ddot{p}\} + [F] \{p\} = \{Q\}, \qquad (A-1)$$

where

$\{p\}$ = column of independent displacements about an equilibrium position of a set of collocation points, in:

$\{\ddot{p}\} = \dfrac{d^2}{dt^2} \{p\}$ = column of accelerations, in./sec^2

$[F]$ = matrix of stiffness coefficients for set of collocation points, lb/in.

97

$[A]$ = matrix of inertial coefficients for set of collocation points, lb

$\{Q\}$ = column of external forcing functions acting at collocation points, lb

g = gravitational constant, 386 in./sec^2

$$\frac{1}{g}\,[A]\,\{\ddot{p}\} + [F]\,\{p\} = \{0\}. \qquad (A-2)$$

The solution to the homogeneous equations yields the mode shapes and frequencies of the system and is of the following form:

$$\{p\} = \{\phi\}\,\cos\,(\omega t - \alpha), \qquad (A-3)$$

where

$\{\phi\}$ = column matrix of amplitude constants, mode shape

ω = angular frequencing of oscillation, rad/sec

α = arbitrary phase angle, rad.

By substituting Eq. (A-3) into Eq. (A-2) and simplifying,

$$\left(-\frac{\omega^2}{g}\,[A] + [F]\right)\{\phi\} = \{0\}. \qquad (A-4)$$

By premultiplying Eq. (A-4) by $[E] = [F]^{-1}$ and rearranging,

$$\left([E]\,[A] - \lambda[I]\right)\{\phi\} = \{0\}, \qquad (A-5)$$

where

$[E] = [F]^{-1}$ = matrix of influence coefficients for set of collocation points, in./lb,

$\lambda = g/\omega^2$, in. = eigenvalue,

$[I]$ = unity matrix.

For a solution other than the trivial one of $\{\phi\} = \{0\}$ to exist the determinant of Eq. (A-5) must equal zero,

$$\left|\,[E]\,[A] - \lambda[I]\,\right| = 0. \qquad (A-6)$$

Expansion of Eq. (A-6) yields an n-order polynomial in λ. It can be proved that all the roots are real and positive. For each root, λ_i, there corresponds a frequency

$$\omega_i = \sqrt{g}\,\sqrt{\frac{1}{\lambda_i}} \quad \text{or} \quad f_i = \frac{\omega_i}{2\pi} = \frac{\sqrt{g}}{2\pi}\sqrt{\frac{1}{\lambda_i}}\,\text{cps}. \qquad (A-7)$$

For each root there also exists

$$\{p\}_i = \{\phi\}_i\,\cos\,(\omega_i t - \alpha_i). \qquad (A-8)$$

The most general solution to Eq. (A-2) is a linear combination of solutions given by Eq. (A-8).

$$\{p\} = \sum_{i=1}^{n}\{\phi\}_i\,\cos\,(\omega_i t - \alpha_i) - \sum_{i=1}^{n}\{\phi\}_i\,q_i$$

$$= [\phi]\,\{q\}, \qquad (A-9)$$

where

$[\phi]$ = modal matrix,

$\{q\}$ = column matrix of principal coordinates.

Instead of formally expanding Eq. (A-5) to obtain the modal columns and frequencies as indicated above, Eq. (A-5) can be placed in a convenient iteration form as follows:

$$\left([E]\,[A]\right)\{\phi\} = \lambda\,\{\phi\}. \qquad (A-10)$$

There exists in the PAS library a mode shape iteration routine based upon Eq. (A-10) that can be used for solving mode shape problems. Consequently, to obtain the modes and frequencies for any conservative system, it is only necessary to determine the influence coefficient matrix, $[E]$, and the inertial matrix $[A]$.

CANTILEVERED UNIFORM BEAM

The influence coefficient matrix for a cantilevered uniform beam is of the following form:

$$[E] = \frac{\ell^3}{EI}\,[\bar{E}], \qquad (A-11)$$

where

ℓ = length of beam, in.

EI = modulus of flexural rigidity, lb-in.

$[\bar{E}]$ = matrix of dimensionless influence coefficients.

The inertial matrix is of the form

$$[A] = w\ell\,[\bar{A}], \qquad (A-12)$$

98

where

   w = running weight distribution, lb/in.

   $[\overline{A}]$ = matrix of dimensionless inertial coefficients.

   By substituting Eqs. (A-11) and (A-12) into Eq. (A-10)

$$[E][A]\{\phi\} = \overline{\lambda}\{\phi\} , \qquad (A-13)$$

where

$$\overline{\lambda} = \frac{EI}{w\ell^4}\frac{g}{\omega^2} .$$

Thus,

$$\omega = \frac{\sqrt{g}}{\ell^2}\sqrt{\frac{EI}{w}}\sqrt{\frac{1}{\overline{\lambda}}} \text{ or } f = \frac{\sqrt{g}}{2\pi\ell^2}\sqrt{\frac{EI}{w}}\sqrt{\frac{1}{\overline{\lambda}}}\text{cps.} (A\text{-}14)$$

PAS PROBLEM AND RESULTS

   To illustrate the use of PAS, a problem to obtain the mode shapes and frequencies of a
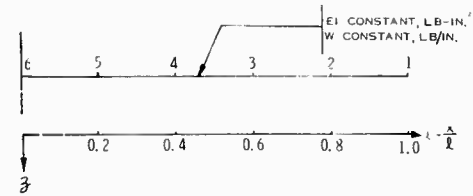
Fig. A-1 - Schematic of cantilevered uniform beam

cantilevered uniform beam is included hereinafter. Figure A-1 is a schematic diagram of the beam showing six collocation points. The PAS plan form and supplied data are shown in Fig. A-2 for a uniform beam of EI = 1 lb-in.^{2}, w = 1.0 lb/in., and ℓ = 1.0 in. The results are presented in Fig. A-3. These results show the computer listing of $[\overline{E}]$, $[\overline{A}]$, $[\phi]$, f's, and $\overline{\lambda}$'s. The mode shapes are shown as plots in Fig. A-4.

```
BY J D CHANEY              TITLE UNIT BEAM MODES        PROBLEM NO 5515       0101
UNIT 2-53061                                            PAGE 01  OF  01       0102
DATE 09/22/64                        .                  CH NOAG222C/1220      0103

010 015011 BEAM INERTIA 1 XPP   0   1   6   1          S                      0104
                        2 SW    0   2   4   1          S                      0105
                        9 W     0   6   6   1      L  UNIFORM BEAM MASS       0106
                        9 C     0   1   3   1      L  MATRIX - UNIT LENGTH    0107
                        9 A     0   6   6   1      L  AND RUNNING MASS        0108

020 021180 STR INF COEF 1 XPP   0   1   6   1   010  .                        0110
                        2 EI    0   2   4   1          S                      0111
                        9 K     0   6   3   1      L  INFLUENCE CCEFFICIENT   0112
                        9 TVMP  0  12   6   1      L  MATRIX - UNIT LENGTH    0113
                        9 E     0   6   6   1      L  AND BENDING STIFFNESS   0114

030 015030 MODE SHAPE   0 E     0   6   6   1   020   UNIT BEAM MODES AND     0116
                        1 A     0   6   6   1   010   FREQUENCIES             0117
                        9 P     0   6   4   1      L                          0118
                        9 LA    0   1   4   1      L                          0119
                        9 CN    0   1   4   1      L                          0120
                        9 CHE   0   4   4   1      L                          0121

040 016700 END PROBLEM                                                        0123

    XPP        5515 010   001 006 001 0 FLOATING

    1 01             50 20000000 50 40000000 50 60000000 50 80000000 51 10000000

    SW         5515 010   002 004 001 0 FLOATING

    1 01             50 50000000 51 10000000 51 10000000
    2 01 50 50000000 51 10000000 51 10000000 51 10000000

    EI         5515 020   002 004 001 0 FLOATING

    1 01             50 50000000 51 10000000 51 10000000
    2 01 50 50000000 51 10000000 51 10000000 51 10000000
```

Fig. A-2 - Plan form and supplied data for cantilevered uniform beam problem

Fig. A-4 - Mode shapes and frequencies for cantilevered uniform beam

$f_1 = 10.96\sqrt{\dfrac{EI}{w\ell^4}}$

$f_2 = 71.69\sqrt{\dfrac{EI}{w\ell^4}}$

$f_3 = 218.38\sqrt{\dfrac{EI}{w\ell^2}}$

$f_4 = 469.03\sqrt{\dfrac{EI}{w\ell^2}}$

$\xi = \dfrac{x}{\ell}$

RELATIVE AMPLITUDE

$\bar{A}$

5515	010	006	006	001	0
	010	006	006	001	0

```
101 49+66666665 49+33333333 00+00000000 00+00000000 00+00000000 00+00000000
201 49+33333333 50+13333333 49+33333333 00+00000000 00+00000000 00+00000000
301 00+00000000 49+33333333 50+13333333 49+33333330 00+00000000 00+00000000
401 00+00000000 00+00000000 49+33333330 50+13333334 49+33333333 00+00000000
501 00+00000000 00+00000000 00+00000000 49+33333333 50+13333334 49+33333333
601 00+00000000 00+00000000 00+00000000 00+00000000 49+33333333 49+66666660
```

$\bar{E}$

5515	020	006	006	001	0

```
101 50+33333333 50+23466666 50+14400000 49+69333334 49+18666667 00+00000000
201 50+23466666 50+17066666 50+10800000 49+53333333 49+14666667 00+00000000
301 50+14400000 50+10800000 49+71999998 49+37333333 49+10666667 00+00000000
401 49+69333334 49+53333333 49+37333333 49+21333334 48+66666669 00+00000000
501 49+18666667 49+14666667 49+10666667 48+66666667 48+26666667 00+00000000
```

$\emptyset$

5515	030	006	004	001	0

```
101 51+19966286 51+20300324 51+20467469 51-18786672
201 51+14461436 49+82269865 51-11028185 51+18786875
301 50+91823154 51-12591620 51-11172779 50-93932646
401 50+45751292 51-14343982 51+11637847 50-93933450
501 50+12711033 50-63313785 51+13924443 51+18786693
```

f

5515	030	001	004	001	0

```
101 52+10960613 52+71689917 53+21837978 53+46903496
```

$\bar{\lambda}$

5515	030	001	004	001	0

```
101 49+81387533 48+19024419 47+20502306 46+44444410
```

Fig. A-3 - Results of cantilevered uniform beam problem

DYNAMIC RESPONSE ANALYSIS OF
COMPLEX MECHANICAL SYSTEMS

S. F. Mercurio and F. E. Niechniedowicz
Sperry Gyroscope Company
Division of Sperry Rand Corporation
Great Neck, New York

A digital computer program has been developed by the Sperry Gyro-
scope Company that will calculate the influence coefficients of a com-
plex mechanical system, its resonant frequencies, and the mode shapes
of the system. It uses three simply-obtained inputs: (1) Geometry of
the mechanical system; (2) Mass lumping of the system; and (3) Flexi-
bility of the system in sections between coordinates, assuming one co-
ordinate end fixed.

INTRODUCTION

By using simply-obtained inputs that accu-
rately yield, as verified by actual tests, the dy-
namic response, mode shape, and influence co-
efficients of a mechanical system, we have
developed a digital computer program that has
reduced the dynamic response analysis of a
complex mechanical system to a systematic
procedure. The program, which consists of
writing the equations of motion and solving
these equations by a numerical iteration tech-
nique, requires three simply-obtained inputs:

1. Geometry of the mechanical system,

2. Mass lumping of the system, and

3. Flexibility of the system (in sections
between coordinates).

The flexibilities are expressed as cantilever
beam flexibilities.

Based on these simply-obtained inputs, the
digital computer will calculate the influence
coefficients of the system, the resonant fre-
quencies of the system (including the fundamen-
tal and higher modes), and the mode shapes of
the system.

The principle advantage of the computer
program for the dynamic response of complex
mechanical systems is that parameter varia-
tions of a given system are easily performed.
Once the geometry of the mechanical system is
defined, the mass and flexibility of the mechan-
ical components may be varied such that the
optimum system may be designed. The results
are obtained quite speedily. For example, the
first three modes and corresponding mode
shapes may be obtained for a system with up to
26 degrees of freedom in less than 45 seconds
of computer time on a machine such as a
UNIVAC 1107.

The capability of the program is 60 coor-
dinates with cross-coupling effects existing
among all 60 coordinates. The largest ship-
borne tracking radar (the ARIS 40-foot antenna
and mount assembly) while undergoing opera-
tional modification, was analyzed using this pro-
gram. The results of this method of analysis
were compared to the actual test results and
were found to be in close agreement.

In the test the ARIS shipborne antenna and
mount assembly were dynamically tested in two
steps: first the 40-foot antenna was investigated
and underwent extensive vibration tests to de-
termine its natural frequencies and the corre-
sponding mode shapes; second, the antenna and
mount combination underwent similar tests.

THEORY

The basic theory of analysis, which is em-
ployed in the computer program, is outlined by
the following relationships.

A conservative system vibrating about the
equilibrium position, with small angular and

linear motions, can be expressed in matrix form by Eq. (1):

$$|M_{ij}||\ddot{X}_j| + |K_{ij}||X_j| = 0, \qquad 1 \leq i \leq n \qquad (1)$$
$$1 \leq j \leq n .$$

The solution to Eq. (1) for free vibration is expressed by Eq. (2):

$$|X_j| = |X_{oj} \cos wt|, \quad 1 \leq j \leq n. \quad (2)$$

Differentiating Eq. (2) with respect to time results in Eq. (2a):

$$|\ddot{X}_j| = - w^2 \cos wt |X_{oj}|, \quad 1 \leq j \leq n . \qquad (2a)$$

If Eqs. (2) and (2a) are then substituted into Eq. (1) the following result is obtained:

$$- w^2 |M_{ij}||X_{oj}| + |K_{ij}||X_{oj}| = 0, \quad 1 \leq i \leq n \qquad (3)$$
$$1 \leq j \leq n .$$

Equation (3) may be rewritten by premultiplying the $|K_{ij}|$ matrix and premultiplying the $|M_{ij}|$ matrix by the inverse of the stiffness matrix. The result of the preceding operations with the collection of terms yield Eq. (4):

$$|K_{ij}|^{-1}|M_{ij}||X_{oj}| = 1/w^2 |X_{oj}|, \quad 1 \leq i \leq n \qquad (4)$$
$$1 \leq j \leq n .$$

Since $|K_{ij}|^{-1} = |F_{ij}|$, then

$$|F_{ij}||M_{ij}||X_{oj}| = 1/w^2 |X_{oj}|, \quad 1 \leq i \leq n \qquad (4a)$$
$$1 \leq j < n .$$

The flexibility matrix may be expressed as shown in Eq. (5):

$$|B_{ji}|^T |f_{ij}||B_{ij}| = |F_{ij}|, \quad 1 \leq i \leq n \qquad (5)$$
$$1 \leq j \leq n .$$

Where $|f_{ij}|$ is the component flexibility matrix, the component flexibility is defined as the fix end cantilever rotations and translations between the coordinates and includes cross coupling effects.

If Eq. (5) is substituted into Eq. (4a) the resulting expression is given by Eq. (6):

$$|B_{ji}|^T |f_{ij}||B_{ij}||M_{ij}||X_{oj}| = 1/w^2 |X_{oj}|, \qquad (6)$$
$$1 \leq i \leq n$$
$$1 \leq j \leq n .$$

Equation (6) demands for its solution a series of matrix multiplications and iterations which is extremely applicable to the computational procedures of a high speed digital computer. The digital computer is supplied with the static equilibrium matrix $|B_{ij}|$, the mass matrix $|M_{ij}|$, and the component flexibility matrix $|f_{ij}|$. The programmed computer then calculates the influence coefficients of the system,

$$|f_{ij}| = |B_{ji}|^T |f_{ij}||B_{ij}| ; \qquad (6a)$$

the dynamic matrix of the system,

$$|U_{ij}| = |F_{ij}||M_{ij}| ; \qquad (6b)$$

and the lowest natural frequency and mode shape of the system by means of an iterative procedure.

The next operation of the program is then to employ an orthogonal transformation on Eq. (6) such that the next higher modes of vibration and the next high mode shape may be obtained. This procedure is then repeated until a predetermined mode is reached.

The elevation vibrations model of the ARIS ships antenna and mount assembly is shown in Fig. 1. Coordinates 1 to 8 indicate displacement, while coordinates 9 to 24 indicate rotations. The set at static equilibrium matrix values, or the B_{ij} matrix, is given in Table 1. All values of B_{ij} which do not appear in Table 1 are zero.

As a typical example, the value of B_{1-2} is 1 and B_{1-10} is 142 because a unit load applied at coordinate one would cause a unit shear at coordinate two. This same unit load at coordinate one would cause a moment at coordinate 10 of 142. Therefore B_{1-10} is 142 (the reader should consult Ref. [1] for the applicable theory). The corresponding component flexibility matrix values are given in Table 2 and their corresponding mass matrix values are given in Table 3. Values of flexibilities and mass that do not appear in Tables 2 and 3 are zero. The flexibilities used are component flexibilities namely the fixed end cantilever rotations and translations between coordinates. With all the parameters in Tables 1, 2, and 3 as inputs to the computer program, the computer calculated the natural frequencies of this ARIS 40-foot antenna and mount as shown in Table 4.

The actual results obtained during testing showed a first mode natural frequency of approximately 7.5 cps.

Similar computations and tests have been run for the train axis model. Computer results were 8.14 cps and actual measurements gave approximately 8 cps.

NOTE: References appear on pages 105 and 106.
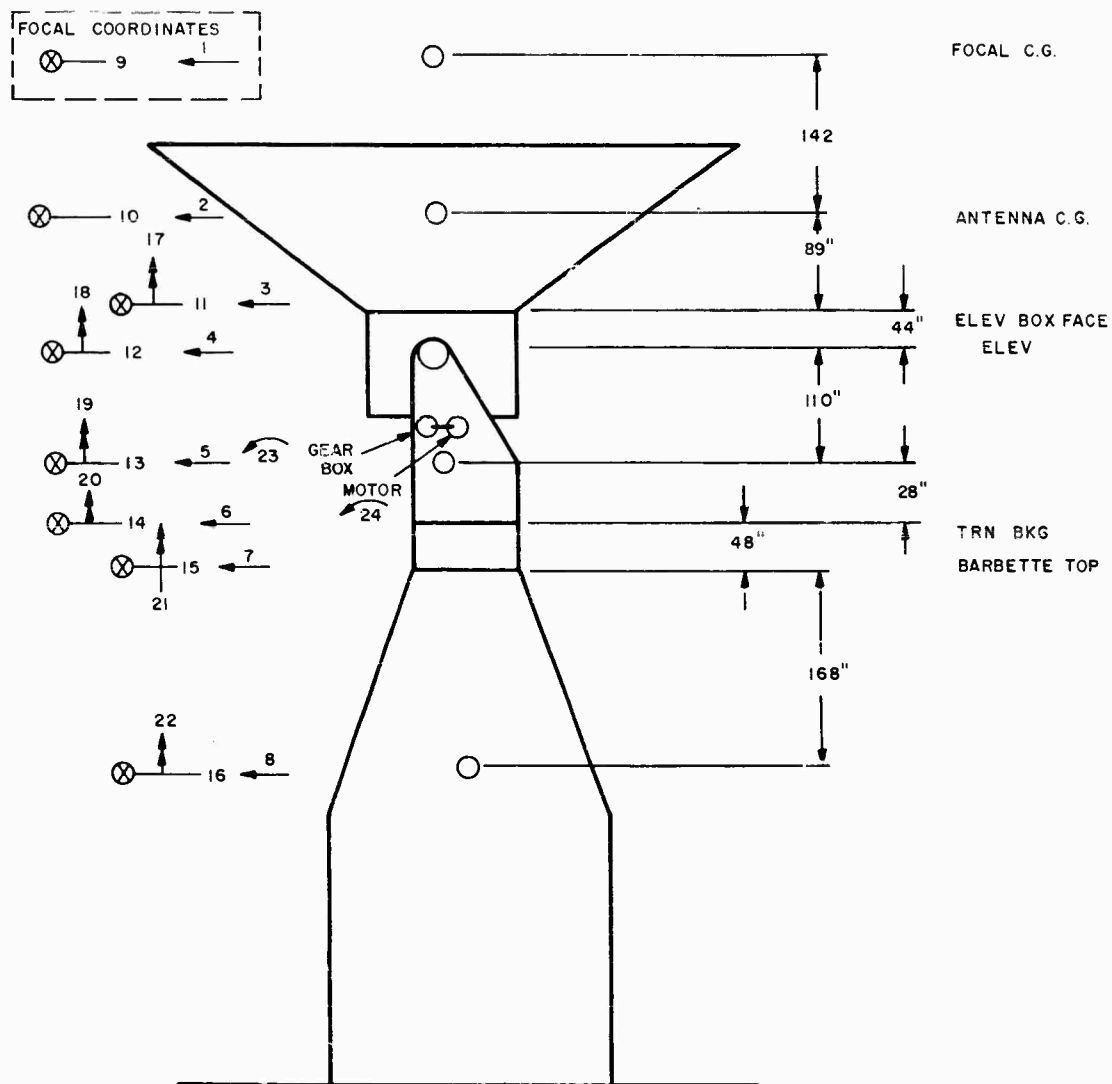
Fig. 1 - Elevation vibration model

TABLE 1
Matrix Inputs, Elevation Model

$B_{1-1} = 1$

$B_{2-1} = B_{2-2} = 1$

$B_{3-1} = B_{3-2} = B_{3-3} = 1$

$B_{4-1} = B_{4-2} = B_{4-3} = B_{4-4} = 1$

$B_{5-1} = B_{5-2} = B_{5-3} = B_{5-4} = B_{5-5} = 1$

$B_{6-1} = B_{6-2} = B_{6-3} = B_{6-4} = B_{6-5} = B_{6-6} = 1$

$B_{7-1} = B_{7-2} = B_{7-3} = B_{7-4} = B_{7-5} = B_{7-6} = B_{7-7} = 1$

$B_{8-1} = B_{8-2} = B_{8-3} = B_{8-4} = B_{8-5} = B_{8-6} = B_{8-7} = B_{8-8} = 1$

$B_{9-9} = 1$

$B_{10-1} = 142$

$B_{10-9} = B_{10-10} = 1$

$B_{11-1} = 231 \quad B_{11-2} = 89$

$B_{11-9} = B_{11-10} = B_{11-11} = 1$

$B_{12-1} = 0 \quad B_{12-2} = 0$

$B_{12-12} = 1 \quad B_{13-3} = 154$

$B_{13-1} = 385 \quad B_{13-2} = 243$

$B_{13-9} = B_{13-10} = B_{13-11} = B_{13-12} = 1$

$B_{13-13} = 1$

$B_{13-23} = B_{13-24} = 1$

$B_{14-1} = 413$

$B_{14-2} = 271$

$B_{14-3} = 182$

$B_{14-4} = 138$

$B_{14-5} = 280$

$B_{14-9} = B_{14-10} = B_{14-11} = B_{14-12} = 1$

$B_{14-13} = B_{14-14} = 1$

$B_{14-23} = B_{14-24} = 1$

$B_{15,1} = 461$

$B_{15,2} = 319$

$B_{15,3} = 230$

$B_{15,4} = 186$

$B_{15,5} = 76$

$B_{15,6} = 48$

$B_{15-9} = B_{15-10} = B_{15-11} = B_{15-12} = 1$

$B_{15,13} = B_{15,14} = B_{15-15} = 1$

$B_{15-23} = B_{15-24} = 1$

$B_{16,1} = 629$

$B_{16,2} = 487$

$B_{16,3} = 398$

$B_{16,4} = 354$

$B_{16,5} = 244$

$B_{16,6} = 216$

$B_{16-9} = B_{16,10} = B_{16,11} = B_{16,12} = 1$

$B_{16,13} = B_{16,14} = B_{16,15} = B_{16,16} = 1$

$B_{16,23} = B_{16-24} = 1$

$B_{17,17} = 1$

$B_{18,17} = B_{18,18} = 1$

$B_{19,17} = B_{19,18} = B_{19,19} = 1$

$B_{20,17} = B_{20,18} = B_{20-19} = B_{20-20} = 1$

$B_{21,17} = B_{21,18} = B_{21-19} = B_{21-20} = 1$

$B_{21-21} = 1$

$B_{22-17} = B_{22-18} = B_{22-19} = B_{22-20} = 1$

$B_{22-21} = B_{22-22} = 1$

$B_{23-1} = 375$

$B_{23-2} = 133$

$B_{23-3} = 44$

$B_{23-9} = B_{23-10} = B_{23-11} = 1$

$B_{23-23} = 1$

$B_{24-1} = 275$

$B_{24-2} = 133$

$B_{24-3} = 44$

$B_{24-9} = B_{24-10} = B_{24-11} = 1$

$B_{24-23} = B_{24-24} = 1$

TABLE 2
Flexibility Input, Elevation Model
(rad/in.-lb or in./lb)

$f_{1-1} = .327 \times 10^{-5}$	$f_{11-11} = .107 \times 10^{-9}$
$f_{2-2} = .198 \times 10^{-5}$	$f_{12-4} = .1435 \times 10^{-8}$
$f_{2-10} = .222 \times 10^{-7}$	$f_{12-12} = .222 \times 10^{-10}$
$f_{3-3} = .307 \times 10^{-6}$	$f_{13,13} = .700 \times 10^{-11}$
$f_{3-11} = .225 \times 10^{-8}$	$f_{14,6} = .874 \times 10^{-10}$
$f_{4-4} = .940 \times 10^{-7}$	$f_{14-14} = .917 \times 10^{-11}$
$f_{4-12} = .1435 \times 10^{-8}$	$f_{15,7} = .174 \times 10^{-9}$
$f_{6-6} = .272 \times 10^{-10}$	$f_{15,15} = .229 \times 10^{-11}$
$f_{6-14} = .874 \times 10^{-10}$	$f_{16,8} = .156 \times 10^{-9}$
$f_{7-7} = .1396 \times 10^{-6}$	$f_{16,16} = .111 \times 10^{-11}$
$f_{7-15} = .174 \times 10^{-9}$	$f_{17-17} = .310 \times 10^{-6}$
$f_{8-8} = .1164 \times 10^{-6}$	$f_{18-18} = .408 \times 10^{-7}$
$f_{8-16} = .156 \times 10^{-9}$	$f_{20-20} = .442 \times 10^{-8}$
$f_{9-9} = .169 \times 10^{-7}$	$f_{21-21} = .117 \times 10^{-11}$
$f_{10-2} = .222 \times 10^{-7}$	$f_{22-22} = .995 \times 10^{-11}$
$f_{10-10} = .250 \times 10^{-9}$	$f_{23-23} = .210 \times 10^{-10}$
$f_{11-3} = .225 \times 10^{-8}$	

TABLE 3
Mass Matrix Input, Elevation Model
(in.-lb/sec^2 or lb-sec^2/in.)

$M_{1-1} = .238 \times 10^{+1}$	$M_{13-13} = .455 \times 10^{6}$
$M_{2-2} = .227 \times 10^{2}$	$M_{14-14} = .4219 \times 10^{6}$
$M_{3-3} = .168 \times 10^{2}$	$M_{15-15} = .3845 \times 10^{6}$
$M_{4-4} = .12116 \times 10^{3}$	$M_{16-16} = .1284 \times 10^{7}$
$M_{5-5} = .1292 \times 10^{3}$	$M_{17-17} = .168 \times 10^{2}$
$M_{6-6} = .1247 \times 10^{3}$	$M_{18-18} = .14036 \times 10^{3}$
$M_{7-7} = .1155 \times 10^{3}$	$M_{19-19} = .110 \times 10^{3}$
$M_{8-8} = .1906 \times 10^{3}$	$M_{20-20} = .1247 \times 10^{3}$
$M_{9-9} = .147 \times 10^{5}$	$M_{21-21} = .3052 \times 10^{3}$
$M_{10-10} = .30314 \times 10^{6}$	$M_{22-22} = .1906 \times 10^{3}$
$M_{11-11} = .321 \times 10^{5}$	$M_{23-23} = .354 \times 10^{6}$
$M_{12-12} = .156 \times 10^{6}$	$M_{24-24} = .184 \times 10^{6}$

TABLE 4

Resonant Frequencies (cps)		
1st Mode	2nd Mode	3rd Mode
7.74	9.95	10.6

CONCLUSION

In conclusion, it can be seen that the program is straightforward and uses simply-obtained inputs and will yield, as the title of this paper implies, "The dynamic response of a complex mechanical system."

NOMENCLATURE

The following nomenclature is used in this paper:

$|M_{ij}|$ = mass matrix,

$|K_{ij}|$ = stiffness matrix,

$|F_{ij}|$ = flexibility matrix,

$|f_{ij}|$ = component flexibility matrix,

$|B_{ij}|$ = static equilibrium matrix,

$|X_j|$ = coordinate matrix,

$|U_{ij}|$ = dynamic matrix,

i, j = indices,

w = frequency rad/sec,

t = time,

$|\ |^{-1}$ = inverse of a matrix,

$|\ |^{T}$ = transpose of a matrix.

REFERENCE

1. R. W. Clough, "Matrix Analysis of Beams," Journal of the Engineering Mechanics Division, Proceedings of the American Society of Civil Engineers, Proc. Paper 1494.

ADDITIONAL REFERENCES

Frank R. Berman, "Some Basic Concepts in Matrix Structural Analysis," Journal of the Structural Division, Proceedings of the American Society of Civil Engineers, Vol. 86, No. ST8 (Aug. 1960).

R. A. Frazer, W. J. Duncan, and A. R. Collar, Elementary Matrices and Some Applications to Dynamics and Differential Equations (Cambridge University Press, London, 1938).

Louis A. Pipes, Applied Mathematics for Engineers and Physicists (McGraw-Hill Book Company, Inc., New York and London, 1946).

Norris, Hasen, Biggs, Namyet, and Minami, Structural Design for Dynamic Loads McGraw-Hill Book Company, Inc., New York, Toronto, London, 1959).

*   *   *

CONSIDERATIONS OF CAPTIVE FIRING VIBRATION ON NONOPERATING PROPULSION SYSTEM COMPONENTS

Gerald Sardella
Martin Marietta Corporation
Martin Company, Baltimore Division
Baltimore, Maryland 21203

An analysis was performed on the individual spring-mass systems of components in a launch vehicle propulsion system to determine their response to vibration during static firing. These components were selected because they are not subjected to pressurization and propellant mass loadings during captive firing, but nevertheless must be unaffected by the additional period of vibration environment.

The individual spring-mass systems were parts of three types of valves and one regulator. Analog simulation of a typical spring-mass system enabled the evaluation of the presence or absence of system loadings by a variation of damping, spring, and force parameters. The system excitation was provided by a random spectrum shaped to the predicted vibration environment level.

The results emphasized pressure preloading as a means of eliminating or significantly reducing valve and regulator system responses. Consideration of these results, similarity of valve dynamic systems, and the unpredictable aspects of the detrimental effects of vibration exposure clearly warranted a conservative approach to operational recommendations. The requirement that all valve poppets remain closed (or seated) for unpressurized engine captive firing was established and pressure loadings to ensure operational success were recommended according to the statistical analysis of the analog study.

INTRODUCTION

Under normal launch vehicle operational conditions, propellants are loaded and systems are pressurized prior to engine firing. Forces resulting from the presence of these fluids and pressures form an integral part of each valve and regulator dynamic system in the form of spring, damping, and force parameters. Complete absence of such forces would, therefore, create a dynamic system whose response to the vibration environment could be affected.

This consideration of propulsion components arises during lower stage static captive firing with unloaded upper stages. In this configuration, the propulsion components will be subjected to additional time periods of vibration under zero propellant loadings for which they were not originally designed. There is much concern over the effect of such operations on

particular components regarding performance or life, or both. The objective of this analysis was to study the individual spring mass systems of each component, evaluate the system loading effects in view of possible component degradation and to establish requirements of propellant and pressurization levels to assure component protection in this mode.

BASIC CONSIDERATIONS

Classifications of Components

The following components were considered for study (three are shown schematically in Fig. 1): valve A, solenoid valve; valve B, relief valve; valve C, check valve; valve D, relief valve; and gas regulator. The valve and regulator assemblies are considered in this analysis as similar dynamic systems since they each

contain one or more single-degree-of-freedom spring-mass systems which act independently while providing the required pressure and flow performance. These spring-mass systems, which are primarily the main and pilot poppets differing only in dynamic parameter magnitudes, are operationally comparable whether normally seated or unseated. The check valve contains two flappers restrained by torsion springs which are identical single-degree-of-freedom systems. The analysis treated these valve systems as spring supported concentrated mass particles in determining the response to and the effects of vibration environments.
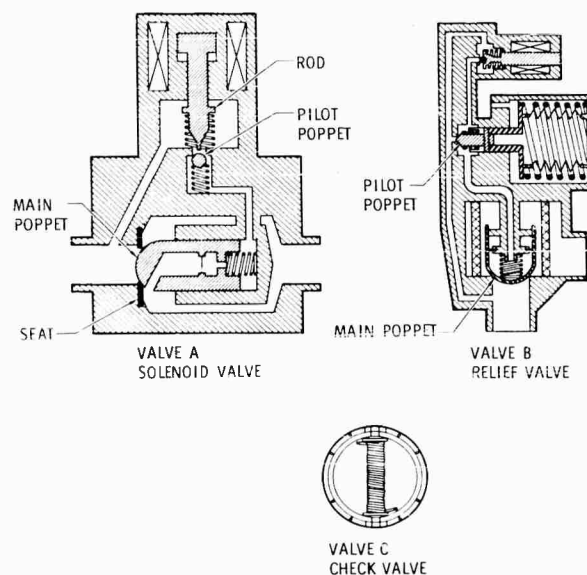
Fig. 1 – Components studied

Detrimental Effects

Consideration of the detrimental effects of excessive inertia forces for the valve type components resolved into the following areas: (1) valve seat permanent deformation, (2) spring fatigue, and (3) poppet bottoming. Generally, although spring fatigue is a possibility, low stresses during spring extension and compression due to the limited travel make this aspect unlikely even for extended periods of operation. Damage to the poppet due to bottoming would be possible if the inertia forces were sufficiently high and the impact surface (the poppet seat or the poppet "back-stop") sufficiently stiff or of peculiar design to generate poppet surface irregularities. The extent of such damage would require experimental determination. The most probable mode of failure or performance

degradation for valves would be leakage or poor valve seating due to permanent valve seat deformation under vibratory inertia loads.

Analysis Approach

Similarity of the valve and regulator dynamic systems suggested formation of a generalized type approach for the various aspects of vibration response. The solenoid main poppet was selected as a typical poppet configuration for detailed response analysis and dynamic parameter studies. Since the poppet spring is preloaded and the plastic valve seat spring rate is orders of magnitude greater, nonlinearities are introduced in the force-deflection relationship which are not readily treated analytically. This consideration is characteristic of the other valve type systems. Due to these nonlinearities, determination of the response to the random vibration environment and the magnitude of poppet seat forces required a solution which an analog computer could provide. With a judicious parameter study, the effects of spring, damping, and pressure preloads could be sufficiently generalized such that the results would not only be utilized for the solenoid valve but applied to the other systems without a similar analog study.

Since the solenoid valve assembly is mounted on the primary structure with no intermediate bracketry between the primary structure and the valve assembly, the vibration environment is, therefore, transmitted directly to the valve case. The vibration spectrum utilized for the valve analysis was that considered to be a conservative estimate of the environment at the valve interface. The response of the main poppet to this environment was evaluated and applied to the other valves and regulator. The analysis was confined to the unpressurized static captive fire mode, and acceptable operational recommendations in this configuration was the objective.

ANALOG STUDY

Problem Description

Due to the nonlinearities in the force-deflection relationships, the equations of motion for the solenoid valve main poppet describe the system separately for positive and negative relative motion of the poppet mass and the case. Since there is no attachment to the seat, the system can be represented schematically for the unseated region (positive relative motion: $x_r > 0$) as follows.

108
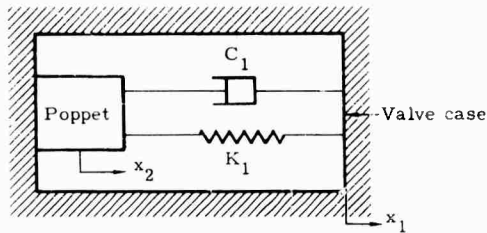
The equation of motion to describe this system can be written as

$$M \ddot{x}_r + C_1 \dot{x}_r + K_1 x_r + F_s + M \ddot{x}_1 = 0$$

or

$$M \ddot{x}_r + C_1 \dot{x}_r + K_1 (x_r + x_o) = F(t), \quad (1)$$

where

$$F(t) = - M \ddot{x}_1,$$

$$x_r = x_2 - x_1, \text{ and}$$

$$K_1 x_o = F_s = \text{spring preload.}$$

Negative relative motion $(x_r < 0)$ introduces the spring and damping properties of the valve seat for consideration. This "seated region" is represented schematically as shown below.
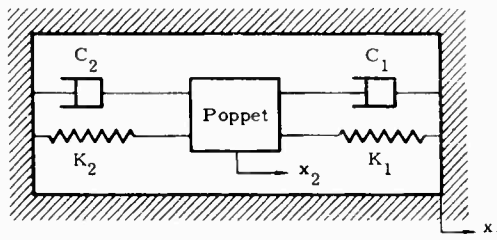
The equation of motion describing this system can be written

$$M \ddot{x}_r + (C_1 + C_2) \dot{x}_r + (K_1 + K_2) x_r + F_s + F_p = F(t). \quad (2)$$

where

$$C_2 = \text{valve seat damping,}$$

$$K_2 = \text{valve seat spring,}$$

$$F_s = \text{preload, poppet spring, and}$$

$$F_p = \text{preload, pressure force.}$$

An analog solution was programmed for the response of the main poppet to the forcing function $F(t)$ utilizing Eq. (1) for positive x_r and Eq. (2) for negative x_r. The function $F(t)$, representing the vibration excitation, was derived by shaping white noise to the required power spectral density. Figure 2 shows a comparison of the random shaped forcing function used for the analog study with that defined as the component design environment.

Analog representation of the following parameters were programmed for the solution: (1) x_r positive, (2) x_r negative, (3) $\ddot{x}_r$, (4) $\dot{x}_r$, (5) $F(t)$, and (6) seat forces, defined as $C_2 \dot{x}_r + K_2 x_r$ for negative x_r. In addition, a statistical distribution of seat force and a measure of percent of time x_r is positive was also programmed. The total time under static captive fire vibration was considered to be 60 seconds.
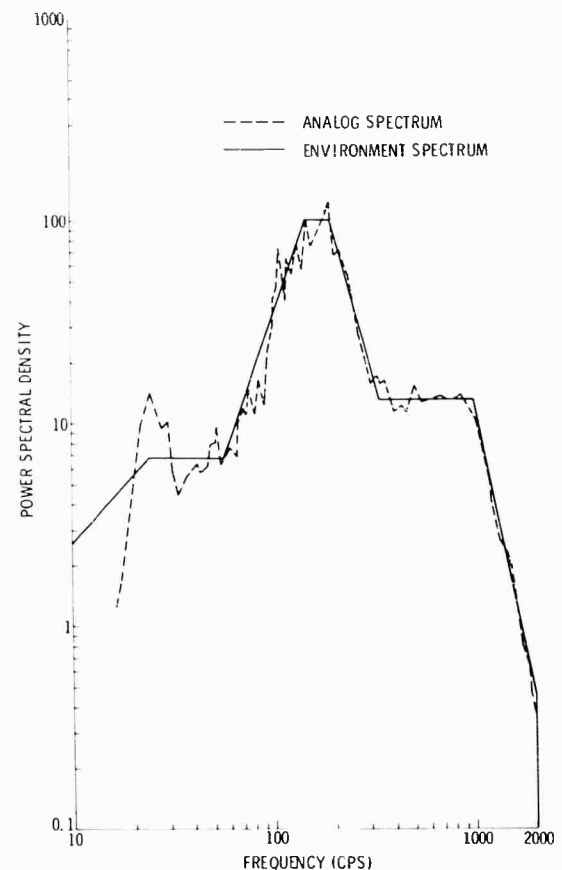
Fig. 2 - Random forcing function spectrum

109

Results of Analog Study

A range of damping and spring constants (C_2 and K_2) was selected to establish the effects on response due to the variation of these parameters for the plastic seat or other types of seats in other valve poppet systems. These effects, evaluated in terms of the percent of the total time the poppet is off the seat, are plotted in Figs. 3(a) and 3(b). Damping effects were found to be negligible for systems with damping greater than 2 percent critical. Spring variation effects were found to be negligible for systems whose resonances were above the 10- to 2000-cps band of excitation. During these variations (with zero pressure preload), the main poppet was off the seat up to 32-percent of the total time, the largest amount of time for the system resonance within the range of excitation. Poppet dynamic seat forces were found to exceed the 3σ (σ = standard deviation) value of the rms vibration environment for up to 10 percent of the total time.
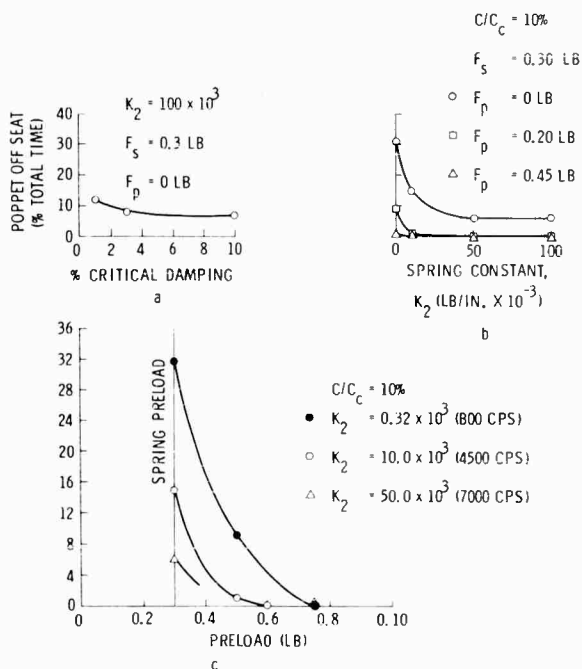
Fig. 3 - Parameter variation effects on poppet response

Pressure preloads, F_p, were introduced for comparison with the zero pressure preload runs. Increments of pressure force equivalent to inertia loads based on 3, 4, and 5σ on the rms environment were applied to the main poppet mass. Figures 3(c), 4(a), and 4(b) show
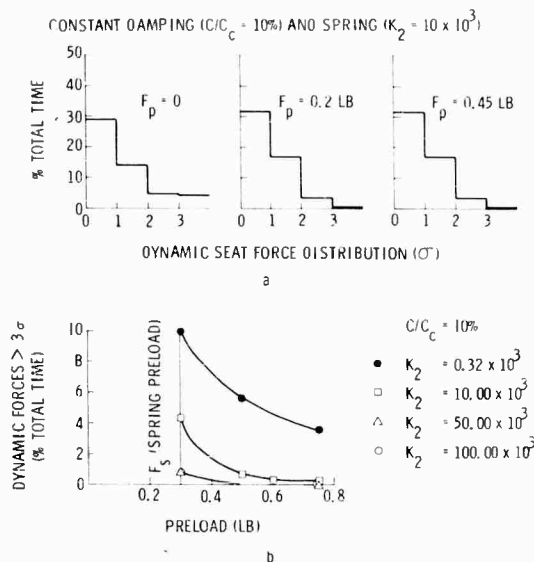
Fig. 4 - Dynamic seat force distribution and transients

the effect of these pressure loads on the poppet response in terms of percent of total time off the seat and in terms of seat force distribution. For the nonresonant system (frequencies above 2000 cps), the percent of time for the poppet off the seat was reduced to less than 1 percent for the lowest increment of pressure force and to a negligible amount (estimated less than 0.1 percent) for the largest increment of pressure force. Dynamic seat forces were reduced to 1 percent of the time in excess of 3σ for the lowest increment of pressure force and to a negligible amount (less than 0.1 percent of the time) for the largest increment of pressure force. The resonant system (approximately 800 cps) also experienced reductions in these areas due to the addition of pressure preloads. The time off the seat was reduced to 9 percent for the lowest pressure level (3σ) and to 0.8 percent for the largest trial value of the pressure forces (5σ). Seat forces were also substantially less. For the lowest force increment, dynamic forces over 3σ occurred only 5.5 percent of the total time and was reduced to 3.5 percent of the time for the largest increment of force.

APPLICATION OF ANALOG RESULTS

The results of the parameter study indicated that the elimination of poppet travel and reduction of seat forces and force transients can be accomplished through the addition of pressure preloads. Pressure forces equivalent to inertia loads based on 3σ should be considered a minimum for elimination of poppet seat

forces and force transients resulting from poppet travel for stiff valve systems. This will apply to systems where the poppet seat spring is sufficiently stiff (resonant frequency greater than 2000 cps) that a 1:1 transmissibility of vibration to the poppet can be assumed, and inertia forces for 99.7-percent probability can be computed by applying 3σ to the rms vibration environment. For resonant systems, pressure forces equivalent to inertia loads based on 5σ should be considered a minimum requirement.

Inertia forces for the spring-mass systems were computed using this approach. All system resonances were considered greater than 2000 cps with the exception of the relief valve main poppet and solenoid. Inertia forces for these two systems were computed on a 5σ basis. Comparison of these forces with the preloads for the static captive fire mode were made to evaluate the requirement for poppet seating. Inertia forces in excess of the preloads occurred in the case of the solenoid valve main poppet, the solenoid rod and the check valve. In order that the requirement for poppet seating be maintained, pressure forces are required for these components.

CONCLUSIONS

Degradation in valve type components during the captive fire configuration is most probable in the form of valve seat deformation, which can give rise to subsequent leakage problems. This leakage can be caused by minute deformation in the valve seat induced by poppet chatter. Valve chatter will occur where inertia forces due to vibration excitation exceed the spring and pressure preloads. To avoid exposure to the detrimental effects and thereby circumvent the unpredictable regions of the problem, the requirement for valve poppets to remain closed (or seated) for the static captive fire configuration was established.

The poppet seating requirement was established by the results of the analog simulation of a typical valve dynamic system. Elimination of poppet response was accomplished by the addition of pressure preloads. All systems studied had sufficient preload forces with the exception of the solenoid main poppet and rod and the check valve. Minimum pressure preloads of three times the standard deviation (3σ) were required for these components.

The approach presented is an expedient, effective, and reliable way to eliminate the most probable mode of degradation. It was demonstrated that the use of the analog computer could be an important tool in evaluating the performance of components with specific application during the component design phase.

*   *   *

A PRACTICAL APPLICATION OF A DIGITAL COMPUTER PROGRAM DURING THE DESIGN PHASE OF AN AEROSPACE STRUCTURE

Bohus T. Bata
Martin Marietta Corporation
Martin Company, Baltimore Division
Baltimore, Maryland 21203

A procedure is described which uses a digital computer program in the design of a truss structure for a missile installation of electrical and electronic components. This computer program performs a three-dimensional analysis of a complex structure with sufficient speed and ease of submittal to make possible its use during the initial-design phase. The importance of detailed analysis in the early design stages is demonstrated by describing the major changes in the evolution of the final configuration.

The structural requirements specified for the truss were that the fundamental frequency in any translational or rotational elastic mode exceed 30 cps, and that the static load design factor be as high as 16.8 g (ultimate). Due to space limitations, the truss was required to have a span of over 100 inches, with varying depth from a maximum of 21-1/2 inches to a minimum of 11-1/2 inches at midspan. The supported equipment weight of 400 pounds was distributed over the entire truss, with some larger components located at midspan.

Submittal and data interpreting technique is described. By promptly interpreting the modal data into useful information, it was possible to achieve a configuration where the entire truss, including bracketry for over 30 components, weighed less than 80 pounds with a fundamental frequency of over 40 cps. Further weight reduction was not possible due to stress and manufacturing limitations.

Up to three configurations or modifications were programmed per day, each yielding complete three-dimensional load, stress, and dynamic analyses, including modal data.

The validity of the computer program has been established by its application to classical problems of known solutions and by measured test data of complex structures.

The generalized approach of this program to static-dynamic analysis enables any structure, whether trusses, beams, shells, or combination, to be analyzed both statically and dynamically in a single submittal, thus providing the designer with a powerful tool to use during both the initial stages and detail design.

INTRODUCTION

Described in this paper is a procedure which uses an IBM 7094 digital computer in the design of a truss structure. Compared with manual methods, the procedure is a highly effective way to reduce structural weight since the computer is programmed for three-dimensional analysis, both static and dynamic, of complex structures. Moreover, its speed and ease of submittal make it useful during both the initial design phase and final detail analysis.

DESIGN REQUIREMENTS AND CONSIDERATIONS

The subject truss was to support 33 electrical and electronic components of varied sizes and shapes, with individual component weights ranging from the largest of 60 pounds to the smallest of only 2 pounds. The total weight of all components was estimated in the preliminary design to be 300 pounds, with an additional weight of 300 pounds of wiring. (These values were reduced before the final analysis to 270 pounds of components and 130 pounds of wiring.)

The truss was to be located between two dome-ended fuel tanks, accessible from three doors in the missile skin. This location called for a maximum truss span of 110 inches, with a maximum depth at midspan of only 11-1/2 inches.

The dynamic response specified for the truss was that its fundamental frequency in any translational or rotational elastic mode exceed 30 cps. The static strength requirement was based on the more severe of two conditions: (1) a vibration induced limit load factor of 7 g along any orthogonal axis plus a static limit longitudinal load factor of 2 g, or (2) a static limit longitudinal load factor of 12 g. The ultimate strength required was defined as 1.4 times the above limit load factors.

To establish the preliminary configuration, the truss was assumed to consist of tension-compression members, with structural and component masses statically distributed to adjacent tube intersections. The truss was to be supported by elastic reactions. The reaction compliances of the truss supporting structure were computed using the method of MacNeal and Bailie [1]. These compliances accounted for the bulkhead influences of the domes and smear thickness of the frames and stringers of the local cylindrical structure.

ANALYTICAL TECHNIQUE

The program performs both the static and dynamic analyses by an element-matrix force technique. The structural model consists wholly of elements, the internal loading of which can be represented by force and moment resultants at grid points. Any structural system can be synthesized by multi-mesh network of simple structural elements (tension, bending, torque,

shear, force, and moment reactions) connected together at the grid points.

The elements are classified as primary and redundant. The primary elements comprise a statically determinate basic structure, their number being equal to the number of equilibrium equations at the grid points. These equations are solved for the primary elements in terms of the redundant elements and external forces and moments. Elastic properties are assigned to the elements; redundant elements are calculated to make internal deflections compatible, and the deflections and rotations of the structure at selected grid points are then determined, leading to a deflection influence matrix on which the vibrational and dynamic analyses are based.

This program, in general, requires the following types of input information:

Geometry of structure

Selection of structural elements

Sectional and material properties

Selection of degrees of freedom

Loading conditions (static and/or time-dependent loads).

The output of the program is of three types:

1. Internal loads and stresses in all structural elements for the prescribed loading conditions (static or time-dependent), due to unit loads and normalized modal loads.

2. Deflections and rotations at selected grid points for specified loading conditions (static or time-dependent), for unit loads, or normalized modal loads.

3. Resonant frequencies and mode shapes.

A more detailed description of the analytical technique and submittal procedure is presented by Kaufman and Hall [2] and Clark [3].

CONFIGURATION SELECTION

The initial configuration (Fig. 1) was based on the premise of providing the maximum component accessibility within space limitations, while minimizing the interconnecting wire lengths. No attempt was made to analyze the truss structure; the member sizes were estimated by the designer. This truss (1A, 88

114

TRUSS CONFIGURATION NO.	TRUSS WEIGHT (LB)	RESONANT FREQUENCIES (CPS)		
		1ST	2ND	3RD
1A	88	14	25	35
1B	259	23	30	37
2A	92	24	25	31
3A	139	29	31	52
4A	142	34	41	54
4B	127	31	39	52
5A	130	47	55	63
5B	90	37	43	58
5C	82	35	41	57
5D	70	32	36	53
5E	78	34	39	55
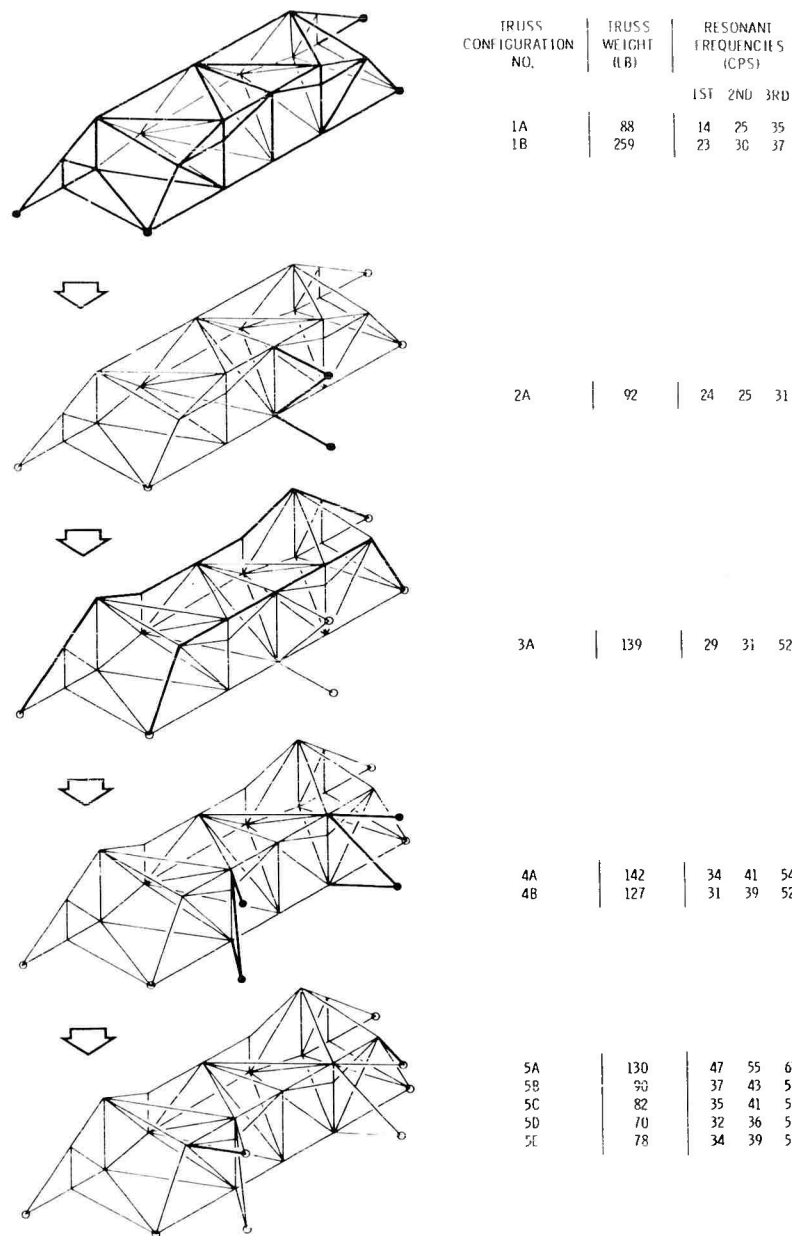
Fig. 1 - Configuration evolution, equipment truss
(preliminary design)

pounds) was programmed with the component and wiring masses statically distributed from assigned locations to adjacent grid points   The 88-pound truss weight included 10 percent (30 pounds) of component weight estimated for component brackets. The resulting resonant frequency of 14 cps was considerably below the minimum of 30 cps, and from the modal data it was concluded that increasing member sizes would not sufficiently increase the frequency of this configuration to offset increased truss

weight. To demonstrate this, the member sizes were increased to a prohibitive total weight of 260 pounds; the resulting truss frequency was only 23 cps.

The more efficient approach indicated was to restrain the midspan deflection by providing additional truss supports. Using truss 1A compliances and adding three members, truss 2A (97 pounds) had the resonant frequency raised to 24 cps. By optimizing member sizes

and further increasing the depth of truss near both ends to maximum permitted by available space, the resulting truss 3A (139 pounds) had a resonant frequency of 29 cps.

Unfortunately, the added members were in the middle of an access door. Inspection of modal data (Fig. 2) resulted in the conclusion that replacement of the above 3 members by like supports at two locations, approximately 1/3 of the span length from the ends would result in suppression of the lowest mode, yielding a further increase in resonant frequency. This addition to truss 4A (142 pounds) resulted in a 34-cps truss. Optimization of truss member sizes reduced the weight (truss 4B) to 127 pounds, with fundamental resonant frequency of 31 cps.

At this time it was noted that the upper ends of truss 4B had a larger modal deflection than midspan (Fig. 3). Two small members were added to the truss in configuration 5A (130 pounds), thereby yielding a significant increase to 47 cps. Successive reductions in member sizes reduced the truss weight to 70 pounds (truss 5D). Though this truss satisfied the minimum requirement of 30 cps, the static loading conditions resulted in excessive stresses in many members.

Truss 5E (34 cps), weighing 78 pounds and made entirely of 1.375-inch square aluminum tubing of 0.062-inch wall thickness, was selected for the final design.

FINAL ANALYSIS

During the detail design several tube members were added to the 5E truss to permit efficient component weight distribution, which resulted in some added stiffness. Four of the members were also strengthened to withstand local bending imposed by component mounts. This, combined with eventual weight reduction of supported components to 270 pounds and wiring to 130 pounds, yielded a fundamental resonant frequency of the truss of 48 cps (considerably above the minimum of 30 cps specified). As further weight reduction by decreasing member sizes was not possible because of stress and manufacturing limitations, and only the minimum value of the fundamental resonant frequency was specified, this design was released for production.

Figures 4 and 5 present the analytical model and mode shape of the fabricated truss (actual weight 76.5 pounds), which is shown in Fig. 6.

CONCLUDING REMARKS

The truss presented in this paper consisted exclusively of tension-compression elements, without considering the bending capabilities of the truss members. This was done to simplify the submittal procedure and save time, as the bending stiffness of truss members does not contribute significantly to overall truss stiffness.

The initial preliminary results were available within a week of go-ahead. Most of this time was devoted to the analytical model synthesis, with less than 10 minutes needed for obtaining the solution for a problem of this size (98 elements and 72 degrees of freedom). The required computer time for subsequent variations of the truss was less since the initial solution is retained on magnetic tape, and modifications are re-entered from the point of change in calculations. The ability to modify the problem while retaining large portions of submittal data enabled as many as three configurations to be investigated in a day.

Diversified types of structural problems have been investigated on this program, ranging from entire payload-booster structures to small but complex support structures. Problems with 1400 elements and 400 degrees of freedom have been analyzed successfully and even larger problems completed utilizing the partitioning technique.

The validity of the computer program has been established (1) by its application to classical problems of known solutions, and (2) by measured test data of complex structures analyzed.

The generalized approach of this program to structural analysis enables any structure, whether trusses, beams, shells, or a combination, to be analyzed both statically and dynamically in a single submittal, thus providing the designer with a powerful tool to use during both the initial stages and detail design of a structure.

Though the analytical solution of even the most complex structure has been reduced to a mechanical submittal routine, sound engineering knowledge is still required to synthesize correctly the analytical model that will yield the desired information, and to interpret correctly the subsequent data.

MODE FREQUENCY, 29 CPS
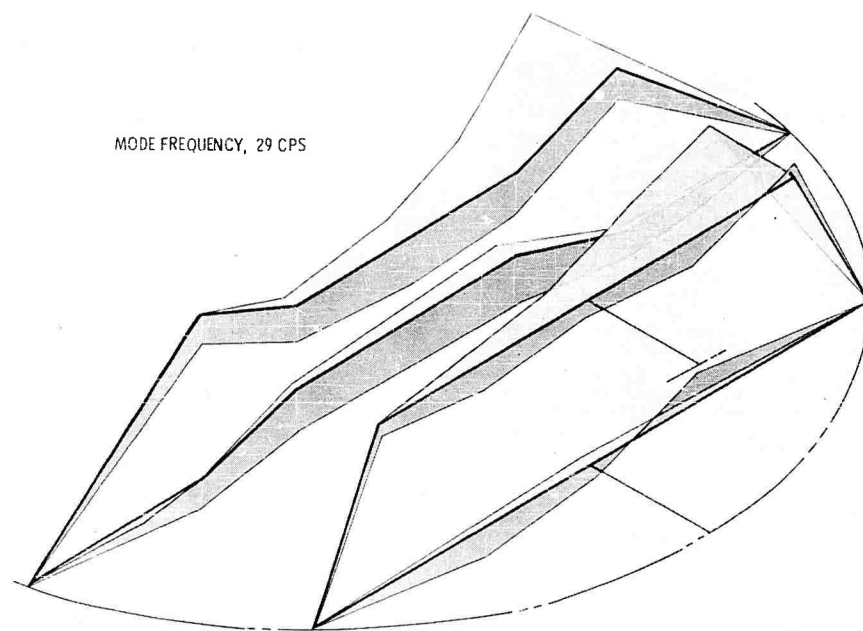
Fig. 2 - First mode, truss 3A

MODE FREQUENCY, 31 CPS
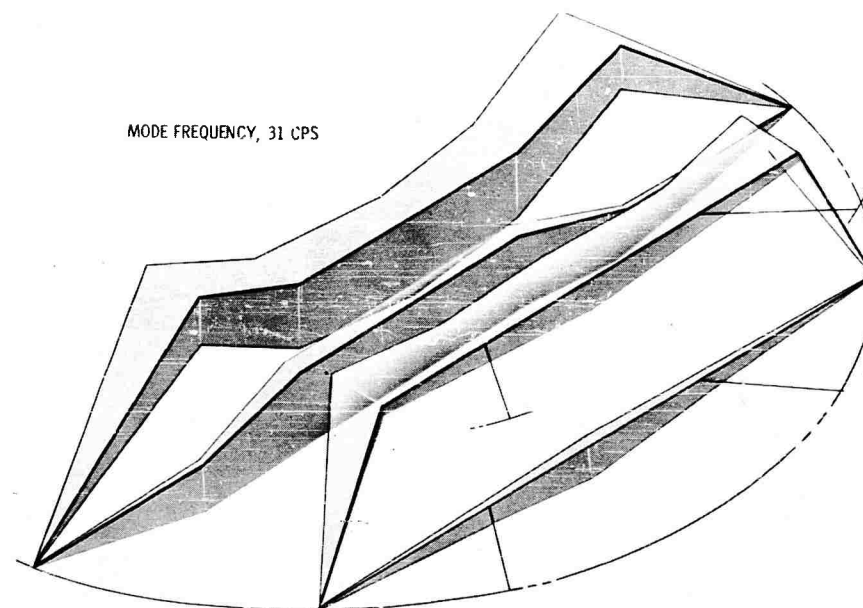
Fig. 3 - First mode, truss 4B

117
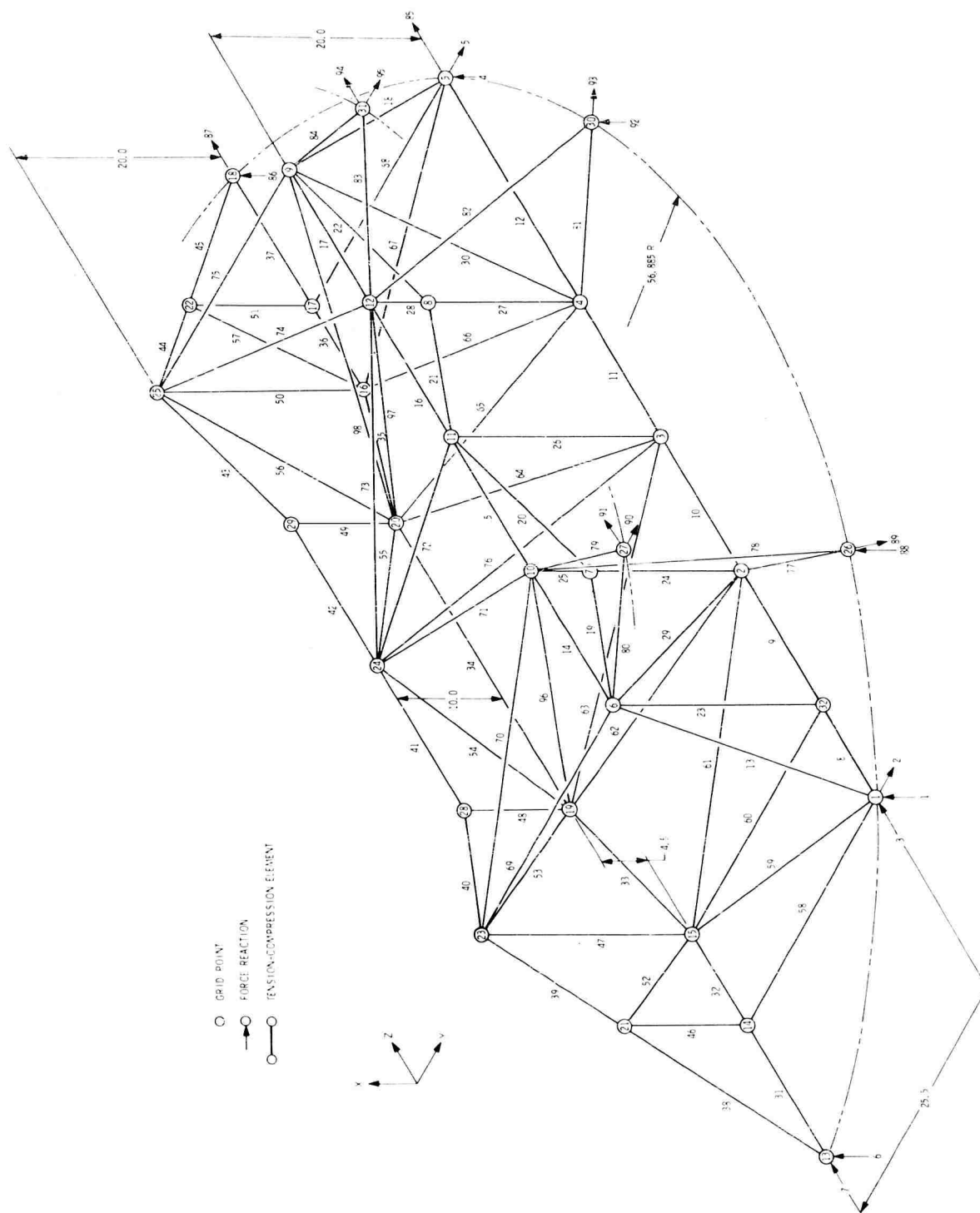
Fig. 4 – Analytical model, equipment truss

GRID POINT

FORCE REACTION

TENSION-COMPRESSION ELEMENT

118

MODE FREQUENCY, 48 CPS

Fig. 5 - First mode,
final configuration
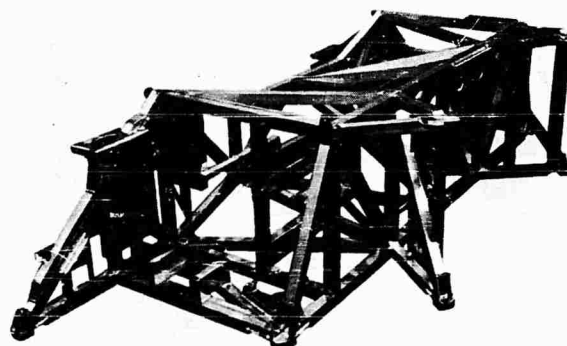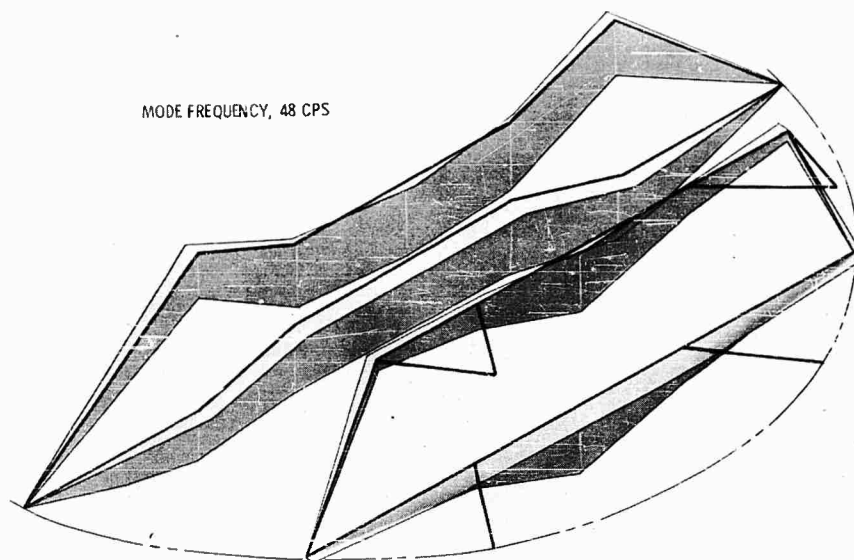
Fig. 6 - Fabricated equipment truss

REFERENCES

1. R. H. MacNeal and J. A. Bailie, "Analysis of Frame-Reinforced Cylindrical Shells, Part III — Applications," NASA TN D-402, National Aeronautics and Space Administration, Washington, D. C.

2. S. Kaufman and D. B. Hall, "A Digital Program for Static and Dynamic Analysis of Complex Structures," RM-136, Martin Marietta Corporation, Baltimore Division.

3. T. L. Clark, "SB 028 Customer Utilization Report," Martin Marietta Corporation, Baltimore Division.

*   *   *

119

STATIC AND DYNAMIC ANALYSIS BY
A MATRIX FORCE METHOD*

S. Kaufman and D. B. Hall
Martin Marietta Corporation
Martin Company, Baltimore Division
Baltimore, Maryland 21203

This paper presents a matrix-force method for static and dynamic analysis of aerospace structures by an element-matrix technique. Any structural system, such as a stiffened shell, three-dimensional truss, or a system of connected beams, can be simulated by a number of simple structural elements connected together at grid points. The technique of model synthesis and selection of elements and the matrix method of solving for stresses and deflections are developed. Attention is given to the influence of thermal inputs on the structural loads, stresses and deflections. The deflection influence matrix forms the basis of vibrational and dynamic analyses.

A somewhat unusual method of partitioning composite structures is described. Partitioning is systematized by supporting all segments independently, with fictitious elastic supports where necessary, considering all connections between segments redundant and finally eliminating the fictitious supports.

The overall method has been used successfully in handling both the statics and dynamics of swept wings, to compute thermal stresses in a thick cylinder and to reproduce accurately the natural frequencies and mode shapes of a thin cylindrical shell and the molecule ethylene.

INTRODUCTION

This paper presents a brief outline of a matrix-force method [1] for static and dynamic analysis of aerospace structures by an element-matrix technique. This method is part of an IBM 7094 digital computer program for static and dynamic analysis of structures [2]. The techniques outlined here are particularly well suited to analyzing three-dimensional-truss, plate and shell structures up to thousands of structural elements, where stresses, deflections and dynamic response are required. Shells of noncircular cross section with cutouts, stiffeners and internal compartments are also well suited to these methods, particularly when one uses partitioning to permit large numbers of elements, thereby allowing a more accurate representation of the structure.

*This paper was not presented at the Symposium.
NOTE: References appear on page 128.

The overall method is quite versatile. It has been used successfully in handling both the statics and dynamics of swept wings, thermal stresses in a thick cylinder and normal modes of cylindrical shells and molecules.

METHOD OF ANALYSIS

In the matrix force method a model of the structure consisting of a network of grid points and load carrying elements (including reactions) is constructed. The elements are divided into primary and redundant elements, the primary ones forming a base set which is just statically stable. The excess elements are designated redundants, S. The choice of the primary elements is, of course, not unique; various determinate sets can be chosen. The best sets are the ones that minimize the coupling among the remaining redundant elements, thereby yielding the best conditioned compatibility equations. Among these, the best are those utilizing the

strongest elements and shortest load paths. Therefore, this selection is important for the sake of accuracy.

The elements have the common property that their internal loads γ can be represented as force resultants at the grid points. Equations of equilibrium are established between internal forces of the elements and external forces P. The solution to these equations in matrix notation can be stated as follows:

$$\{\gamma\} = M_1\{S\} + M_2\{P\}. \qquad (1)$$

In addition to an internal load, each element has a characteristic deformation. The deformations of the elements must be selected so they are conjugate with the element loads in the virtual work sense (i.e., elongation of tension elements, end rotation of beams, displacement of supports, and the like). These deformations in matrix notation are

$$\{\delta\} = E_0\{\gamma\} + \{H\} = E_0 M_1\{S\} + E_0 M_2\{P\} + \{H\} . \qquad (2)$$

$\{H\}$ is a column matrix comprising free thermal elongations, settlement of supports, and so on. For example, the thermal elongation of a simple tension element is the product of its length, coefficient of expansion, and temperature change. The matrix E_0 is a symmetrical compliance matrix which relates the elastic portion of the deformation in each element to its own load and those of other elements.

The elastic deformation in an element relative to its own load is the product of the corresponding diagonal terms of the compliance matrix and the load; the nondiagonal terms of the matrix relates the elastic deformation of the elements to the load of other elements. For example, the diagonal compliance of a simple tension element is its length divided by the product of its modulus of elasticity and cross-sectional area. A typical example of diagonal and off diagonal (coupled) compliances is the rotation (θ) at the ends of a beam produced by moments (B) at the ends, or

$$\left\{ \begin{array}{c} \theta_1 \\ \theta_2 \end{array} \right\} = E_0 \left\{ \begin{array}{c} B_1 \\ B_2 \end{array} \right\} - \frac{\ell}{EI} \begin{bmatrix} \dfrac{1}{3} & \dfrac{1}{6} \\ \dfrac{1}{6} & \dfrac{1}{3} \end{bmatrix} \left\{ \begin{array}{c} B_1 \\ B_2 \end{array} \right\},$$

where ℓ is the length and EI the cross-section bending stiffness of the beam. Proper representation of compliances is the most important factor in analyses which replace a structure by a network of elements. The compliances for skew and triangular networks for plate and shell structures are developed by the authors [1].

Loads in the elements must be distributed so as to make their deformations compatible. In matrix notation, compatibility conditions are

$$M_1^T\{\delta\} = \{0\} . \qquad (3)$$

By means of the relationship Eq. (3) one can now relate the internal loads and deformations in terms of the external loading $\{P\}$ and $\{H\}$ as follows:

$$\{\gamma\} = \lambda\{P\} + \lambda_h\{H\} , \qquad (4)$$

and

$$\{\delta\} = E_0\lambda\{P\} + (I + E_0\lambda_h)\{H\} , \qquad (5)$$

where

$$\lambda = (I - M_1 g^{-1} M_1^T E_0) M_2 ,$$

$$\lambda_h = -M_1 g^{-1} M_1^T ,$$

$$g = M_1^T F_0 M_1, \text{ and}$$

I = the identity matrix; and superscripts T and -1 denote transposition and inversion, respectively.

Just as deformations had to be conjugate with the element loads, deflections $\{\eta\}$ must be defined to make them conjugate with the external loads $\{P\}$ so that they may be calculated by virtual work. The virtual work is made up of the product of real deformations Eq. (5), from whatever source, and the internal loads from virtual (unit) external loading $\{P\}$, identifiable as λ in Eq. (4). Whence,

$$\{\eta\} = A\{P\} + A_h\{H\} , \qquad (6)$$

where

$$A = \lambda^T E_0 \lambda$$

and

$$A_h = \lambda^T(I + E_0\lambda_h) .$$

In this method, it should be emphasized that enough reactions must be supplied as structural elements to completely restrain the structure from rigid body motion. The symmetric matrix A is sometimes called the "deflection influence matrix" for the supported structure. For the case of a free-free or partially constrained structure it can readily be modified by calculating

122

inertia forces to balance applied forces, thus eliminating the fictitious constraints.

As the size and complexity of structural analysis problems increase, we must resort to partitioning. Here, the engineer can use physical intuition to assist the mathematician in hard-to-manage matrix operations which result from large order matrices. This has been programmed and extensively illustrated [1]. Briefly, the method goes as follows. The structure is broken down into manageable segments. Each segment is restrained against rigid body motion by fictitious elastic reactions γ^s as needed. Fictitious external forces P_s are supplied at the location and in the direction of the fictitious reactions. Also provided are equal and opposite forces P_d acting at the common boundaries of the segments. These forces are treated as redundants. Deflections at the boundaries η_d and those of the segments η are computed as well as internal loads γ and fictitious reactions. These are computed in terms of the fictitious external forces, forces on the boundaries, P forces (conjugate to η deflections), and free thermal expansions, H. In abbreviated matrix notation these relationships can be stated as follows:

$$\left\{ \begin{array}{c} \eta_d \\ \eta \\ \gamma \\ \gamma^s \end{array} \right\} = \left[\begin{array}{cccc} A_b & A_c & A_d & A_e \\ A_d^T & A_g & A_i & A_m \\ \lambda_b & \lambda_c & \lambda_d & \lambda_e \\ \lambda_g & \lambda_k & \lambda_m & \lambda_o \end{array} \right] \left\{ \begin{array}{c} P_d \\ P_a \\ P \\ H \end{array} \right\} . \quad (7)$$

To satisfy compatibility, the relative deflections on the boundaries between adjacent segments defined by the virtual unit P_d loads (redundant forces) must be set equal to zero or

$$\{\eta_d\} = \{0\} . \quad (8)$$

To satisfy equilibrium at the location of the fictitious reactions, the fictitious reactions and associated fictitious loads must be made to cancel each other. That is

$$\{\gamma^s\} + \{P_s\} = \{0\} . \quad (9)$$

Equations (8) and (9) are next solved for $\{P_d\}$ and $\{P_s\}$ in terms of $\{P\}$ and $\{H\}$. This solution is substituted into Eq. (7) obtaining

internal loads and deflections for the composite structure analogous to Eqs. (4) and (6), respectively.

The deflection influence matrix obtained with or without partitioning forms the basis of the vibratory and dynamic analyses. In matrix notation the equations of motion are:

$$\{\eta\} = A[P(t) - K\ddot{\eta}(t) - G\dot{\eta}(t)] , \quad (10)$$

where $P(t)$, K and G are, respectively, the forcing function matrix, the mass matrix and the damping matrix. The computation of frequencies, mode shapes and transient response is based on the modal method [1].

EXAMPLES

Figure 1 shows the plan view for a thick-skinned, 45-degree swept wing model along with one comparison of measured deflections [3] and calculated deflections [4]. Figure 2 shows the symmetrical normal modes of a delta wing tested by the NASA [5] along with a comparison of the computed results [6].

Of particular interest for shell-type applications is the analysis [7] of a thin cylindrical shell whose gridwork for the analytical model is shown in Fig. 3. Agreement with known analytical results [8] between the first 18 axial symmetric frequencies (Table 1) is good.

As another example, a comparison of thermal stresses in an infinitely long hollow cylinder (inside radius 0.5 unit, outside radius 1.0 unit) was computed [9] by the method of this paper. The loading consisted of a logarithmic radial temperature gradient and the stresses are compared in Table 2 against a Timoshenko closed form solution [10].

Another example of particular interest in the field of molecular vibrations [11] is that of the normal modes of the molecule ethylene (C_2H_4) composed of four terminal hydrogen atoms and two interior carbon atoms. The normal modes of ethylene as computed by the method of this paper are compared in Fig. 4 against those computed by Herzberg [12]. A comparison with experimentally measured frequencies [13] is shown in Table 3.

The program has been used as an aid in solving numerous problems involving actual hardware. Some of these applications have been discussed by Mr. Bata (see page 113).

123

SPAR-RIB INTER-SECTION	COMPUTED DEFLEC-TIONS	MEASURED DEFLEC-TIONS
1	0.4544	0.4288
2	0.5283	0.5109
3	0.6093	0.6015
4	0.6955	0.6946
5	0.7828	0.7970
6	0.2263	0.2090
7	0.2840	0.2774
8	0.3436	0.3382
9	0.4110	0.4069
10	0.4877	0.4972
11	0.0638	0.0709
12	0.0949	0.1003
13	0.1234	0.1307
14	0.1563	0.1626
15	0.2029	0.2093
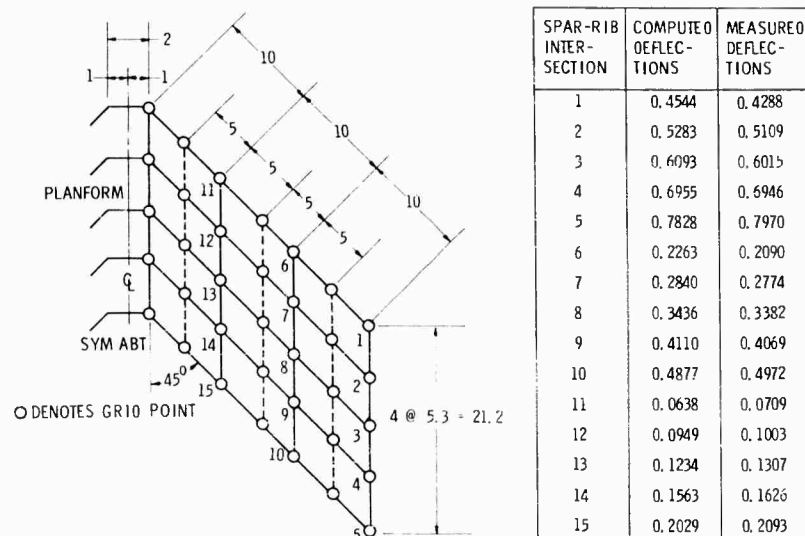
Fig. 1 - Comparison of analytical with test deflections--
45-degree swept wing model
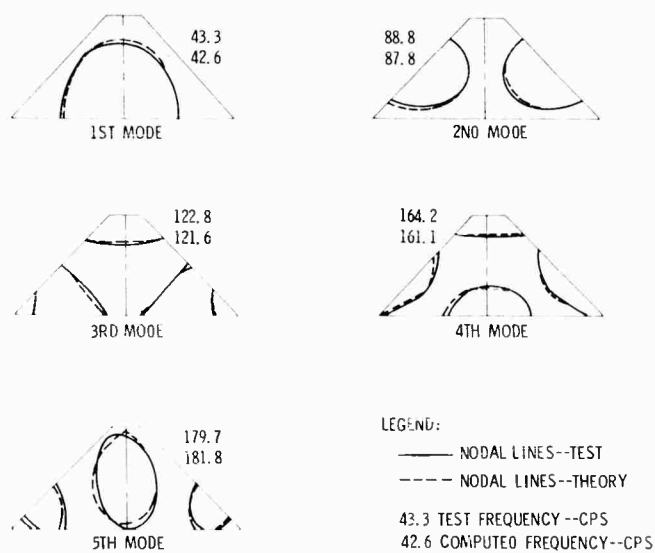
Fig. 2 - Comparison of test with theory symmetrical
modes--45-degree delta wing model

124
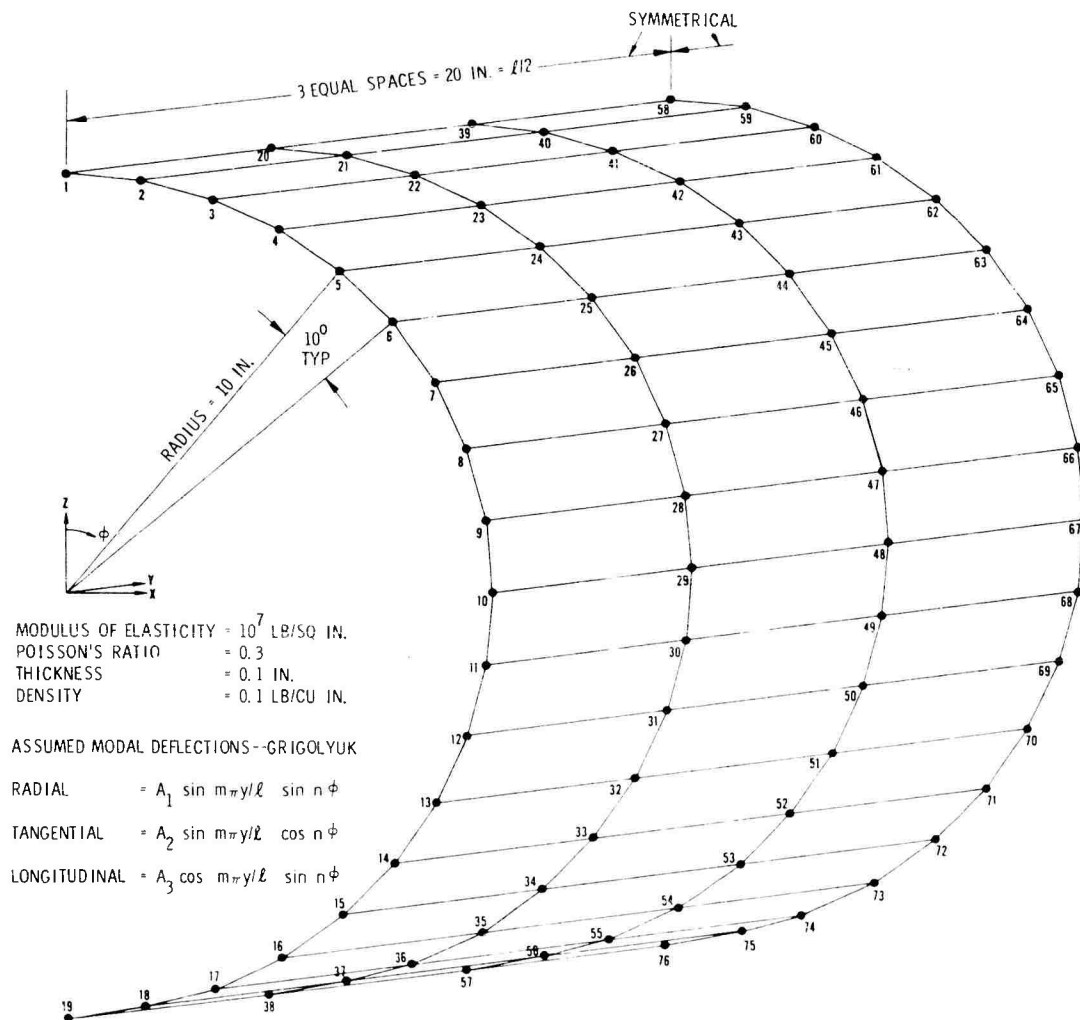
Fig. 3 - Thin cylindrical shell

TABLE 2
Thermal Stress Comparison for a Hollow Cylinder

Stresses	Radius (r)	Timoshenko Stress ($\times 10^{-4}$) Ref. [10]	Computed Stress ($\times 10^{-4}$) Ref. [9]
Circumferential	1.0	5.17	5.24
	0.9	3.64	3.70
	0.8	1.77	1.85
	0.7	Stress reversal	
	0.6	-3.69	-3.50
	0.5	-8.16	-8.41
Longitudinal	1.0	5.17	5.17
	0.9	3.15	3.19
	0.8	0.88	0.92
	0.7	-1.60	-1.65
	0.6	-4.65	-4.58
	0.5	-8.16	-8.41
Radial	0.85	-0.71	-0.74
	0.75	-1.04	-1.09
	0.65	-1.11	-1.19

αE = 1000 units (coefficient of thermal expansion times modulus of elasticity),

μ = 0.25 (Poisson's ratio),

$T = \frac{100}{\ell n2} \ell n \frac{1}{r}$ (radial temperature distribution).

TABLE 1
Thin Cylindrical Shell, Symmetric Modes

Wave Number		Frequency (cps)	
Axial m	Circumf. n	Grigolyuk Ref. [8]	Kaufman-Hall Ref. [7]
1	4	189	185
1	3	209	209
1	5	249	242
1	6	345	339
1	2	376	373
1	7	466	460
3	6	566	596
3	7	600	627
1	8	607	602
3	5	626	650
3	8	699	723
1	9	768	762
3	4	806	809
3	9	838	865
1	10	947	937
5	7	955	991
5	8	959	1038
3	10	1006	1040
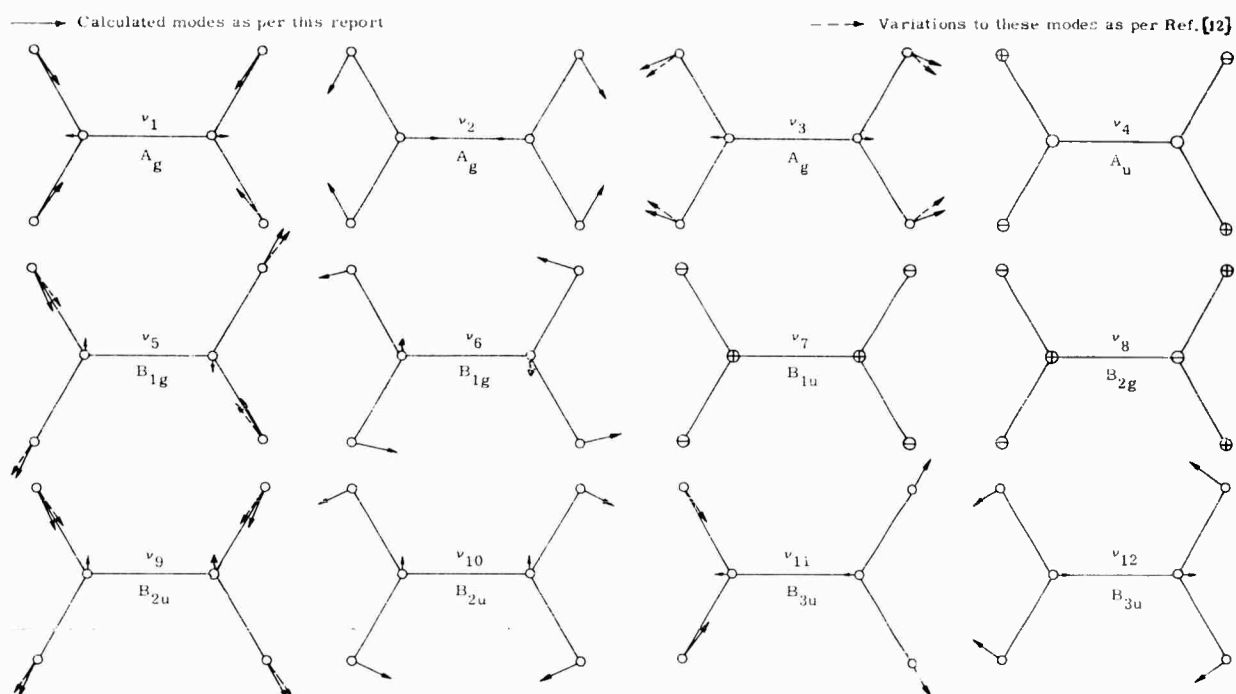
Fig. 4 - Normal modes of C_2H_4

TABLE 3
Frequency Comparison for the Molecule Ethylene

Vibration	Symmetry Specie	Frequency (cm^{-1}) Experimental (Arnett & Crawford, Ref. [13])	Computed (Ref. [11])
ν_1	A_g	3019	3015
ν_2		1623	1758
ν_3		1342	1238
ν_4	A_u	1027	1027
ν_5	B_{1g}	3075	3119
ν_6		1236	1248
ν_7	B_{1u}	949	951
ν_8	B_{2g}	943	942
ν_9	B_{2u}	3106	3104
ν_{10}		810 or 995[12]	995
ν_{11}	B_{3u}	2990	2988
ν_{12}		1444	1443

REFERENCES

1. S. Kaufman and D. B. Hall, "A Digital Program for Static and Dynamic Analysis of Complex Structures," Martin Research Memorandum RM-136, Space Systems Division, Baltimore (Sept. 1963).

2. T. L. Clark, "Customer Utilization Report SB-028 for IBM 7094 Digital Computer" (1964).

3. I. Rattinger and R. H. Gallagher, "Comparison with Test of Analytically Derived Influence Coefficients for a Thin and Thick Skinned 45° Swept Low Aspect Ratio Model Wing," Bell Aircraft Corp., Preliminary Report 9001-3252-001 (Apr. 1959).

4. H. R. Gongloff, "Comparison with Test of Analytically Derived Bending Deflections and Slopes for a Thick Skinned 45°, Swept Low Aspect Ratio Model Wing," Martin Report ER 12483, Space Systems Division (Aug. 1962).

5. E. E. Kordes, E. T. Kruszewski, and D. J. Weidman, "Experimental Influence Coefficients and Vibration Modes of a Built-up 45° Delta Wing Specimen," NACA TN-3999.

6. S. Kaufman and D. B. Hall, "Theoretical and Experimental Comparison of Influence Coefficients and Vibration Modes of a Built-up 45° Delta Wing," Martin Research Memorandum RM-131, Space Systems Division, Baltimore (1963).

7. H. R. Gongloff, "Comparison of Small Oscillations of a Thin Cylindrical Shell," Martin Research Memorandum RM-135, Space Systems Division, Baltimore (1963).

8. E. I. Grigolyuk, "Small Oscillations of Thin Resilient Conical Shells," NASA TT-F25 (May 1960), translated from Izvestia Akademi Nauk SSSR, OTD, No. 6 (1956).

9. D. Hunt and S. Kaufman, "Comparison of Thermal Stresses in an Infinitely Long Hollow Cylinder," Martin Report ER 13527, Space Systems Division, Baltimore (1964).

10. S. Timoshenko and J. N. Goodier, Theory of Elasticity (McGraw-Hill, Book Co., Inc., New York, N.Y., 1951) p. 413.

11. S. Kaufman and J. J. Kaufman, "Molecular Vibrations by a Matrix Force Method," Martin Report ER 13536, Space Systems Division, Baltimore (1964).

12. G. Herzberg, Molecular Spectra and Molecular Structure, II, Infrared and Raman Spectra of Polyatomic Molecules (D. Van Nostrand Company, Inc., New York, N.Y., 1945).

13. R. L. Arnett and B. L. Crawford, Jr., J. Chem. Physics, 18:118 (1950).

*　　*　　*

Section 3
DESIGN TECHNIQUES

SONIC AND ULTRASONIC VIBRATION SENSITIVITY
OF X-BAND MICROWAVE COMPONENTS

R. Strike and G. G. Sundberg
General Dynamics/Pomona
Pomona, California

Experience has proved that the electrical performance of microwave circuitry can be degraded through the effects of acoustic or mechanical excitations. This electrical degradation can be a critical problem in the development of high-performance, radar-homing missiles, where high-resolution microwave circuits must operate under high-amplitude vibratory excitations.

Data collected during the acoustic and vibration evaluation testing of numerous microwave components have shown that ultrasonic as well as sonic stimuli can produce unwanted changes in component electrical properties. These changes, which may be due to resonant or nonresonant mechanical responses, are of concern when the component's dynamic or steady-state electrical properties no longer fall within tolerances dictated by the intended application. Parts which have proved most prone to acoustically produced degradation include waveguide sections and both vacuum-tube and solid-state frequency control oscillators.

Dynamic changes in electrical properties in simulated missile environments, and the mechanisms of such changes, are presented for typical examples of these components. Data presented for the parts show the correlation between the acoustic excitations, the mechanical responses, and the dynamic electrical responses. In each case, the excitation frequencies above 10,000 cps are shown to be of primary importance.

INTRODUCTION

There exists a variety of phenomena wherein an acoustic or mechanical stimulus is able to perturb the steady-state functioning of an electrical circuit. Appropriately controlled, as in microphones, strain gages, or motion sensors, these phenomena lend themselves to useful applications. Yet similar phenomena can constitute a significant problem in the design of low-noise or high-stability electronics, particularly where exposure to high-level acoustic and mechanical excitations must be considered. This paper describes specific examples of undesirable perturbations in the functioning of X-band microwave components.

The reader should recognize that the significance of any perturbation depends on the intended application and that our judgement of desirability is based on missile system applications where electrical gains in excess of 10^7 are not uncommon.

ACOUSTICALLY FORCED CHANGES IN THE PROPAGATION VELOCITY CHARACTERISTIC OF A RECTANGULAR WAVEGUIDE

Techniques for computing the microwave signal distortions which are caused by certain resonant vibration responses of a rectangular

waveguide have been demonstrated.[1] These demonstrations suggested that relatively low levels of vibratory response could cause serious distortions in a signal that has been transmitted through a long section of acoustically excited waveguide. Recently we had the opportunity to check these techniques against experimental data for a section of thick-walled aluminum waveguide.

Our test specimen was a 3-foot length of the aluminum guide, which we connected as a transmission line between a microwave signal source and a matching terminal impedance. Six semiconductor strain gages were bonded to the narrow and broad walls of the guide in an orientation to indicate cross-sectional strains. The specimen was routed through the sound chamber so that only the central portion (a 2-foot length) of the guide was exposed to a broadband, random, acoustic excitation of 158.5-db overall level.[2] Figure 1 shows rms spectral analyses of the excitation, the strain in the narrow waveguide wall, and the frequency-modulation (FM) noise components which were produced in a sinusoidal microwave signal.

The correlation between mechanical responses and phase modulations as indicated by FM noise responses seems consistent with theory, even to the extent that second-harmonic vibrations produced no FM noise. Assuming first and second harmonic mode shapes as shown in Fig. 2, we also found excellent correlation between measured FM noise levels and levels which were computed from the wall-strain data.

Our technique of estimating the change in waveguide depth from strain data is as follows:

Construct the angle, α, such that the product of α and the waveguide wall half-thickness, $h/2$, equals the half change in the guide's narrow wall dimension, $\epsilon b/2$, where ϵ is the measured wall strain and b is the narrow-wall outer dimension.

For small values of α, and on the condition that the guide corners remain stationary, equivalence can be shown between α and the angle, β, which, being small, can be equated to $\tan \beta$.

This establishes the desired relationship:

$$\alpha = \frac{\epsilon b}{h} = \beta = \tan \beta = \frac{\Delta d}{b - \frac{h}{2}}$$

[1]F. J. O'Hara and G. M. Moore, The Microwave Journal 6:70-71 (1963).

[2]All sound pressure levels indicated in this report are in decibels (db) referenced to 0.0002 dynes/cm².
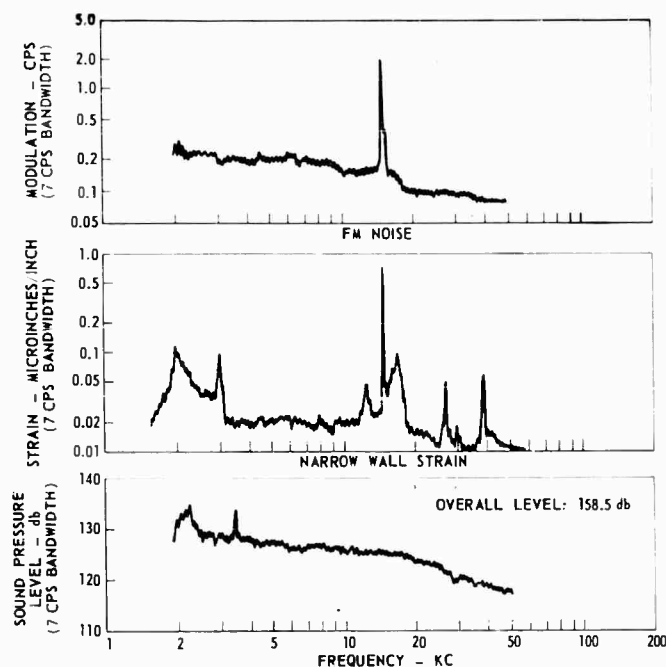
Fig. 1 - Response data for waveguide
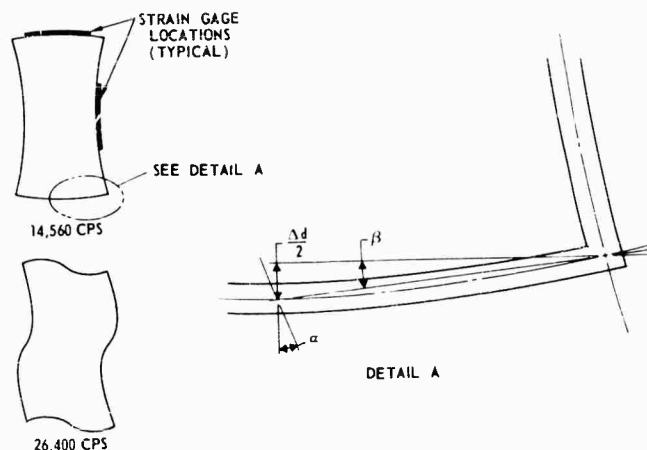
Fig. 2 - Vibration modes for waveguide

or

$$\Delta d = \frac{\epsilon b}{h} \left[b - \frac{h}{2} \right],$$

where Δd is the change in waveguide depth.

The mechanism of phase modulation can be appreciated by recognizing that any change in the internal depth of the waveguide causes a change in the velocity of electromagnetic signal propagation, which can be determined from the following equation:

$$C_g(t) = \frac{f\lambda_o}{\sqrt{1 - \left[\frac{\lambda_o}{2d(t)} \right]^2}}.$$

where f is the microwave signal frequency, λ_o is the free space wavelength, and $d(t)$ is the time dependent function which indicates instantaneous waveguide depth. These propagation velocity changes occur at the vibration frequency and cause phase modulations in proportion to the depth variations. Note that the phase modulations will increase in proportion to waveguide length, or number of microwave signal wavelengths, as long as the waveguide walls vibrate coherently along that length. The absence of phase modulation at the second vibration mode may be attributed to the zero changes in waveguide depth or, in other words, the in-phase motions of the opposite narrow walls.

A portion of the waveguide evaluation tests was devoted to determining the responses to mechanical excitations at the waveguide supports, and these additional investigations allowed us to compare the effects of acoustic and mechanical excitations. The comparison was interesting, but not surprising, as we found that localized oscillatory forces (as produced by electrically driven piezoelectric crystals) excited only localized vibrations which produced no measurable FM noise. The mass loading at the waveguide support, or piezoelectric crystal, accounts for this failure to excite the waveguide natural vibrations by essentially detuning the sections of mass-loaded guide (fundamental frequency of 12,500 cps) and the sections of unloaded guide (fundamental frequency of 14,560 cps). Even discrete frequency mechanical excitations varied through the 10,000- to 20,000-cps range failed to produce measurable FM noise or significant nonlocal vibrations of the waveguide walls.

This phenomenon of waveguide microphonics provides a vivid demonstration of the need for extended frequency range environmental testing since any test limited to the customary 10,000-cps upper frequency would have failed to excite even the fundamental vibrations. The phenomenon also illustrates how extremely small displacements (10^{-7} inches) can cause measurable changes in the electrical properties of a component. In this instance the acoustic excitation used for testing was a good approximation to the measured service environment of the waveguide, and the laboratory measurements of wall strains and FM noise were in excellent agreement with later field measurements.

MICROPHONIC RESPONSES IN A
VACUUM-TUBE MICROWAVE
SIGNAL SOURCE

Operation of the radars in radar-homing missile systems is such that signals which are transmitted or reflected between the control

131

station,[3] the interceptor missile, and the target contain information regarding the relative motions of control station, missile, and target. Parts of this information are conveyed in the form of doppler variations in the radar signal frequencies, so we find that an instrument for the evaluation of microwave signal spectral content is necessary to the radar-homing system. This instrument may be installed in the control station or in the missile. In any case, it is likely that it will be required to operate under significant vibratory excitations, and it is possible that these excitations will degrade instrument performance.

The problem may be resolved by shielding the entire instrument from excessive excitations. This approach requires unnecessarily large weight and space penalties, however, and it is usually more practical to shield at component level. In a klystron oscillator-equipped instrument the latter seems invariably true as the klystron makes significant, if not always predominant, contributions to the microwave noise threshold of the instrument. The extent of these contributions is illustrated in Fig. 3 by the amounts of FM and amplitude modulation (AM) noise which are produced by a klystron

_____

[3]The control station may be a fixed or moving land, sea, or air position. In certain instances the missile may contain all radars.

oscillator operating under a broadband, random, acoustic excitation of 135-db overall level.

The generation of video noise (composite AM and FM noise) in a klystron results from the relative motions of the tube elements, which include the heater, cathode, anode, grids, and reflector. Significant correlations have been noted between calculated, and in one instance measured, fundamental vibration frequencies for the klystron elements and the microwave signal modulation frequencies of 10,000 cps and below. The response data obtained for the klystron further emphasize the need and usefulness of extended frequency environmental testing.

MICROPHONIC RESPONSES IN A
    SOLID-STATE MICROWAVE
    SIGNAL SOURCE

The relatively high sensitivities of klystrons to acoustic or mechanical excitations make them unsuitable for many low-electrical-noise or high-level-environment applications. This deficiency can be corrected by providing the klystron with the aforementioned environment shielding or, more elegantly, by substituting an alternate signal source which is less responsive to acoustic or mechanical excitations. The most successful of these alternate sources are solid-state devices which consist

Fig. 3 - Response data for klystron

132

of a crystal controlled radio frequency (rf) oscillator and a series of frequency multipliers, filters, and amplifiers. Comparisons between ruggedized vacuum-tube and typical solid-state sources have proved that the latter are two to four orders of magnitude less responsive to vibratory excitations. This is an impressive advantage, but even these responses could prove detrimental in high-performance missile systems.

Additional investigations of this potential microphonics problem were initiated after examinations of typical microwave noise spectra indicated that all primary signal distortions were occurring at a relatively few frequencies. This finding suggested that one or a few components might be introducing these distortions, which in turn suggested that it might be feasible to reduce the responses by improving or shielding these few components. Component response level tests seemed the most straightforward way of isolating the responsive parts, particularly after estimates of mechanical resonances for the circuit mounting structure and the components revealed that only a few parts were likely to have resonances near the signal distortion frequencies. These parts included the frequency control crystal, several parallel plate capacitors, a tunable capacitor (the oscillator trim capacitor), and a relatively large diode (used with reverse bias as a trim capacitor). Preliminary testing showed that the

capacitance of each part could be affected through acoustically excited responses of the part and that three parts responded at or near the lowest frequency where microwave noise had been observed. Figure 4 shows the responses of two of these parts.

We were most interested, however, in the frequency control crystal, which proved to be responsive at each of the frequencies where major microwave signal modulations has been observed. Subsequent testing substantiated that mechanically forced resonant vibrations of the crystal blank were a predominant cause of microwave signal distortions. Figure 5 shows typical acoustic test data obtained by exposing a missile mounted signal source to a simulated missile acoustic environment and by exposing a compliantly mounted frequency control crystal to the same environment. Note the coincidences between frequencies for maximum modulations of the signal, as monitored at the output of the microwave signal analyzer, and maximum vibrations of the crystal blank. Note also that the vibration response data are measured values obtained by monitoring the piezoelectric outputs of the crystal blank, which conveniently serves as a built-in vibration sensor.

The correlation between piezoelectric response voltage and microwave signal modulations was unexpectedly good since sound pressure or mechanical force at a given frequency
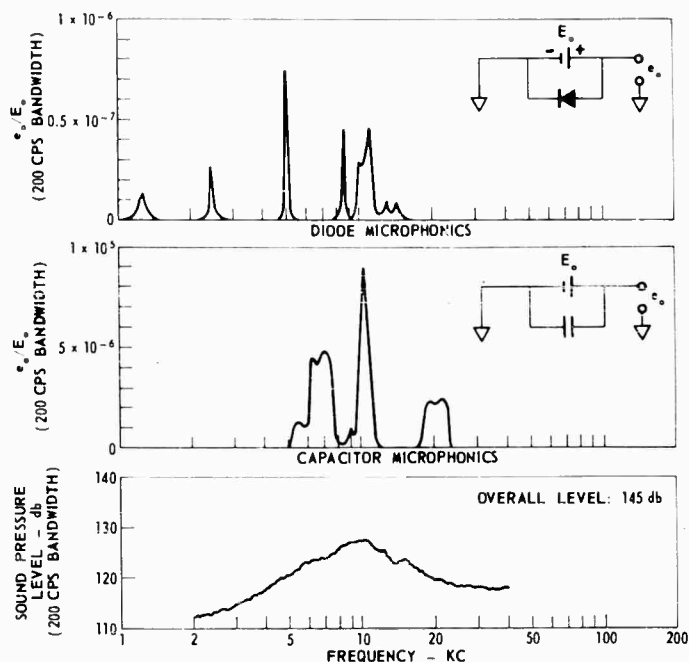
Fig. 4 - Microphonics of diode and capacitor

133
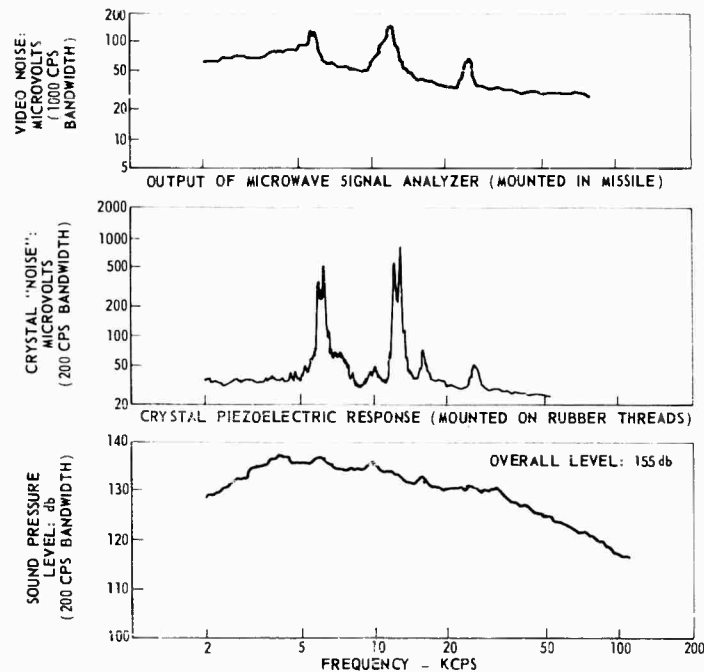
Fig. 5 - Response data for
frequency control crystal

and piezoelectric response voltage and modulation amplitude at the same frequency proved to be linearly related. This last relationship seemed to apply from unit to unit, at least where crystals had comparable mechanical and electromechanical resonances, and a signal source which employed a crystal with relatively low piezoelectric responses performed better than sources with other crystals.

The tests also provided data on the transmission of energy from crystal case to crystal blank. Figure 6 shows the construction of a typical frequency control crystal which consists simply of a quartz disc or blank, electrical leads which wholly or partially support the blank, and a gas-filled metallic or glass can which encases the blank. Crystals suspended in an acoustic field on nylon or rubber threads generated rather large piezoelectric signals, as shown in Fig. 5 but the same crystals generated virtually no piezoelectric output when one face was bonded to a massive steel block. This evaluation, the same as we used for establishing the acoustic sensitivity of mounted accelerometers, showed that restraint of acoustically
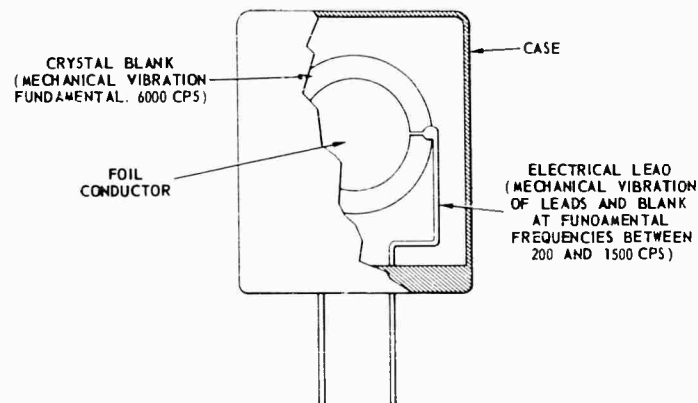
Fig. 6 - Typical frequency control crystal

excited gross motions eliminated the objection-
able responses, even though five faces of the
crystal were still exposed to acoustic excita-
tion. From this finding we can conclude that
structural couplings between the case and blank
are more important than acoustic coupling
through the gas medium.

This third example of environmentally pro-
duced microwave signal distortions illustrates
that even very small motions[4] or strains of a
critical electrical part can significantly alter
the electrical functioning of an entire micro-
wave circuit. In this instance the phenomenon
might have been detected in a conventional
acoustic test, but the extended frequency tests
made it possible to evaluate microwave signal
modulations at fundamental and higher-order
harmonic frequencies. It seems unlikely that
this problem could have been detected in an ex-
tended frequency missile vibration test since
the solid-state signal source is vibration iso-
lated from primary missile structure.

ACOUSTIC ENVIRONMENT
SIMULATION

The acoustic laboratory at General Dynam-
ics/Pomona is equipped with unique facilities
for the simulation of missile environments.
The newest of our facilities, shown in Fig. 7,
can be used either as a 2-foot-diameter
progressive-wave chamber or as a 13-cubic-
foot reverberation chamber. Low-frequency
excitations (20- to 1500-cps discrete frequency,

Fig. 7 - Acoustic facility at
General Dynamics/Pomona

narrowband, or broadband excitations) are at-
tained only under progressive-wave conditions,
so the problems of standing-wave resonances,
which seem characteristic of most small rever-
beration chambers, are avoided. Fortunately
the physical dimensions of our test specimens
are generally small enough to insure uniform
specimen excitation through sound diffraction,
thus eliminating the need for multiple specimen
orientations during low-frequency testing.
High-frequency tests (1500- to 140,000-cps
broadband excitations) are performed under
reverberant or progressive-wave conditions
(the latter if simultaneous high- and low-
frequency excitations are desired). In either
case, excellent sound field diffusivity, and spec-
tral uniformity (within tolerances of plus 4-db
and minus 0-db) have been attained, provided
that the specimen's volume did not exceed 30
percent of the test chamber volume.

The performance limitations of this newest
facility are summarized in Fig. 8, which shows

---

[4]Estimates on the basis of piezoelectric re-
sponses under 155-db acoustic excitation indi-
cate that peak-to-peak displacements of the
crystal blank center point were on the order
of 10^{-7} inches.
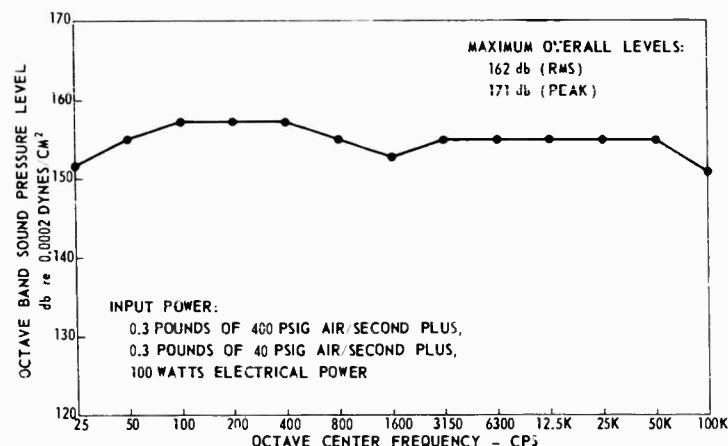
Fig. 8 - Performance limitations of acoustic facility

the envelope of true rms sound pressure levels. Both the low-frequency source, a Ling Model EPT-24 electropneumatic transducer, and the high-frequency source, impinging sonic and supersonic air jets, are capable of providing excitations which have Gaussian or near-Gaussian amplitude distributions. Sound pressure levels, spectra, and time histories can be controlled by adjusting the electrical and pneumatic inputs to the low-frequency source and the pneumatic inputs to the high-frequency source.

SUMMARY AND CONCLUSIONS

Examples have shown that high-frequency acoustic excitations can cause unique

degradations in the electrical performance of microwave components. Certain of the indicated degradations have been of sufficient consequence to require special excitation control measures (in excess of protection afforded by usual packaging) or electrical compensations in current missiles. Others are expected to become important as missile environments increase in severity or as microwave performance requirements become more stringent. Whether the problem is current or potential, the data make it apparent that limited frequency range environmental tests cannot provide a positive measure of an electrical component's responses to the broadband excitations of missile flight.

*   *   *

136

DESIGNING ELECTRONIC EQUIPMENT FOR THE COMBINED RANDOM AND SINUSOIDAL VIBRATION ENVIRONMENT

A. W. Sinkinson
RCA
Burlington, Mass.

Damage to electronic equipment during combined random and sinusoidal vibration testing is of a mechanical nature. The design engineer needs a method for mathematically determining an equivalent constant amplitude sinusoidal response for fatigue stress analysis and for empirically confirming adequate strength by a simple sinusoidal vibration test. Such a method is mathematically developed in this paper. Plots for determining the probability of peak values also are presented.

When a sinusoidal stress has various amplitudes, the fatigue damage is cumulative and is proportional to the sum of the ratios of the number of actual cycles at a particular stress to the number of cycles to failure at the same stress. A mechanical system with only one significant prime resonance as a practical approximation acts as a narrowband filter which responds to a combined wideband random plus sinusoidal input with a random amplitude single frequency sinusoid and thus lends itself to fatigue analysis by Miner's hypothesis if the character of the stress variation can be determined.

The expression for the relationship between fatigue stress and number of cycles to failure based upon the linearity of the log-S log-N curve is substituted in Miner's expression for the damage coefficient. A similar expression is set up for the damage coefficient of an equivalent constant amplitude sinusoidal stress, and the two damage coefficients are equated. The resulting equation is solved for the equivalent stress, and acceleration is substituted for stress since they are proportional within the elastic limit.

When the ratio of the sinusoidal component to the random component in combined sinusoidal and random alternating waves is greater than 3, the distribution of the envelope of the combined waves behaves like a normal law, and the probability density is defined by the usual expression. To date, the magnitudes associated with the response functions of electronic equipment for aerospace application have usually established this ratio greater than 3, and, therefore, the expression with the correct parameters can be substituted for the number of acceleration peaks at each acceleration level in the equation for the equivalent sinusoidal acceleration.

Mathematical manipulation, including approximations, allows the differential equation to be solved for the equivalent sinusoidal acceleration response. The derived expression is

$$\ddot{y}_e = \left[\left(\sqrt{\frac{2k-1}{\frac{e}{a}}} \right)^{2k} + 1 \right] \ddot{y}_s ,$$

where

$\ddot{y}_e$ = equivalent sinusoidal acceleration response

$\ddot{y}_s$ = sinusoidal component of response

The analytical design of electronic equipment to withstand a vibration environment can be divided into two parts: strength of the supporting mechanical structure and fragility of the electronic piece parts. In each case, meaningful conclusions can be made only after the response to the vibration input at critical locations has been defined. Failure in the vibration environment exhibits a mechanical nature; therefore the important response parameters are instantaneous peak values and fatigue effects. Emphasis is intended here to establish the point that determination of rms power or energy levels without further definition does not adequately evaluate mechanical damage.

For a pure sine wave input or a random Gaussian input, the literature is explicit in teaching the response function [1]. For the combined sinusoidal and random vibration input, however, there is a scarcity of teaching of a nature easily handled by the engineer who is packaging electronic equipment. Most discourses on such a response function are of such a general nature as to entail laborious mathematical analyses.

Insufficient empirical data are available to establish rigorously the adequacy of substituting a constant-amplitude, single-frequency, sine wave swept over a range of frequencies for variable-amplitude and continuous-frequency-spectrum excitation in vibration testing [2]. Inexactness of our present ability to predict mechanical fatigue contributes greatly to this inadequacy. Therefore, all vibration testing performed for satisfying contractual requirements should adhere rigorously to the specifications and not include substitutions.

During the mechanical design of electronic equipment, however, the magnitude of the mechanical loading must be determined to safeguard against failure from instantaneous peak loads or from fatigue effects. This is especially true in those instances where combined sinusoidal and random vibration is prevalent, e.g., in missiles and spacecraft, because of the need for high material efficiency to minimize weight. The two pertinent mechanical properties of materials and electronic parts are listed in the following forms: (1) peak values, such as ultimate strength for materials and shock level for parts and (2) fatigue stress versus number of sinusoidal stress reversals for materials and acceleration level in gravity units (g) over a period of sinusoidal vibration for parts. Therefore, the design can proceed if the actual expected peak loading and a sinusoidal cyclic loading equivalent to the combined sinusoidal and random loading can be estimated. Furthermore, relatively inexpensive sinusoidal vibration testing and shock testing can be performed on a mechanical model as a check on design prior to the commitment of complex electronic models.

For these reasons, as a part of the design function of RCA Aerospace Systems Division, Burlington, Mass., on the rendezvous radar and transponder for LEM, an expression was derived after Crede and Lunney [3] and Miles and Thomson [1] for computing a cyclic stress of constant amplitude which produces fatigue damage equivalent to that produced by combined sinusoidal and random vibration loading. Reference was made to the work of Rice [4] in establishing the statistical distribution of stress values and thus the probability density function of their amplitude (Fig. 1) for insertion into the expression for equivalent stress amplitude derived from considering Miner's linear theory of cumulative damage [5]. Expected peak loading was estimated by referring to Rice's plots of the distribution function of the envelope of combined sinusoidal and random functions (Fig. 2).

A mechanical system with only one significant prime resonance as a practical approximation

---

Fig. 1 - Probability density of envelope R of
$\ddot{y}(t) = \ddot{Y}_s \cos pt + \ddot{Y}_r$ -- Rice [4]

Fig. 2 - Distribution function of envelope R of
$\ddot{y}(t) = \ddot{Y}_s \cos pt + \ddot{Y}_r$ -- Rice [4]
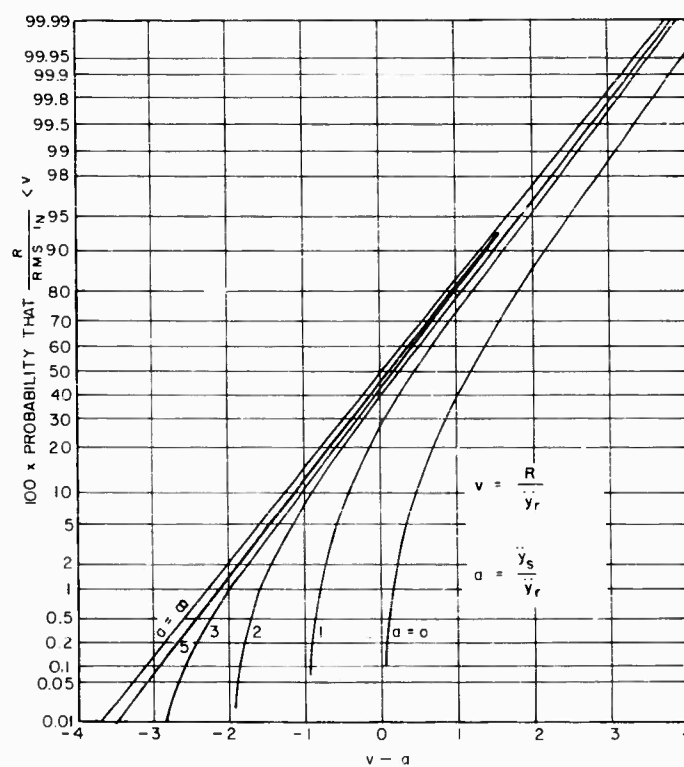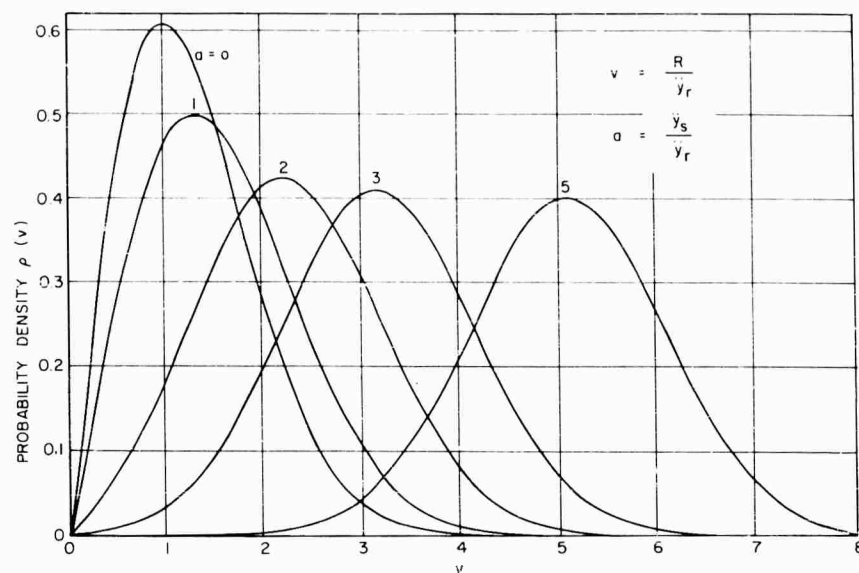
acts as a narrowband filter, which responds to a combined sinusoidal plus wideband random input with a random amplitude single-frequency sinusoid, and thus lends itself to fatigue analysis by Miner's hypothesis if the character of the stress variation is determined. For purposes of this discussion, the conventional curves showing stress versus cycles to failure, as commonly plotted for structural materials, may be idealized, as shown in Fig. 3. This is a hypothetical curve; it applies for all stress greater than the endurance limit and for all cycles greater than one. For fatigue analysis, stresses are assumed to be within the elastic limit and therefore proportional to loading (acceleration). Failure due to stresses outside the elastic range are classed as shock-induced, and therefore are referred to the distribution function of the acceleration in Fig. 2. Endurance limits are not recognized since the existence of an endurance limit depends on changes in the material produced by alternating stress at a low level $(S < S_{en})$, and intermediate excursions to higher stress levels may counteract these changes; moreover, only a few materials (notably steel) seem to possess well-defined endurance limits. Thus it is reasonable to ignore the possibility of an endurance limit when, as in the problem at hand, stress amplitudes are distributed over a wide range. The equation of the curve in Fig. 3 may be written as follows:

$$S = \frac{S_1}{N^{\frac{1}{k}}} \quad \text{or} \quad N = \left(\frac{S_1}{S}\right)^{k}, \qquad (1)$$

where N is the number of cycles to failure at the stress S, S_1 is a hypothetical stress required to cause failure at one cycle of stress reversal, and k is a constant determined by properties of the material or parts. In a
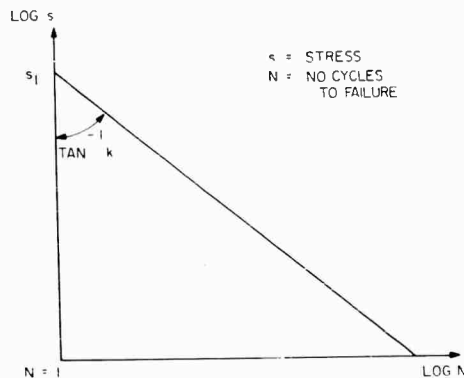
conventional endurance test, the stress experiences a cyclic variation and reaches the same amplitude at each cycle. This stress amplitude is then plotted as a function of the number of cycles to failure, and a curve such as shown in Fig. 3 results from repeated tests at different stress amplitudes. A somewhat similar endurance test in which the stress amplitude is not constant at each cycle of vibration has received some attention in recent years, and a linear theory of damage accumulation proposed by M. A. Miner may be expressed mathematically as follows:

$$D = \sum \frac{n_i}{N_i}, \qquad (2)$$

where N_i is the number of cycles of stress reversal required to produce failure at any stress S_i, and n_i is the number of cycles of stress reversal actually experienced at the stress S_i. The damage coefficient D is less than unity before failure occurs and is assumed to approach unity as damage accumulates toward the failure point.

An alternative form [1] to Eq. (1), which gives closer correlation empirically for cumulative damage, is:

$$N = \left(\frac{S_1}{S}\right)^{\lambda k},$$

where λ is another constant determined by properties of the material or parts. Recent investigations, leading to the suggestion that the damage coefficient D is not equal to unity under some circumstances, do not materially alter the conclusion reached by the following analysis.

With substitution for N from Eq. (1), the preceding Eq. (2) is written as follows:

$$D = \frac{n_i}{\left(\frac{S_1}{S_i}\right)^{\lambda k}}. \qquad (3)$$

It is convenient now to introduce an equivalent stress, S_e. This equivalent stress is based upon the conventional endurance test, wherein the stress amplitude is constant at each cycle of stress reversal, and N_e is the number of cycles to failure at the equivalent stress S_e.

$$N_e = \left(\frac{S_1}{S_e}\right)^{\lambda k}. \qquad (4)$$

It is also defined as producing the same damage after the same number of cycles as the cumulative effect of the S_i stresses.

Fig. 3 - Idealized curve for endurance properties

$$D_e = \frac{\sum n_i}{N_e} = \frac{\sum n_i}{\left(\dfrac{S_1}{S_e}\right)^{\lambda k}} . \tag{5}$$

The expression for the equivalent stress amplitude S_e required to cause the same damage as a fluctuating stress amplitude may be obtained by equating D from Eq. (3) to D_e from Eq. (5) and solving for the equivalent stress S_e.

$$\sum \frac{n_i}{\left(\dfrac{S_1}{S_i}\right)^{\lambda k}} = \frac{\sum n_i}{\left(\dfrac{S_1}{S_e}\right)^{\lambda k}} , \tag{6}$$

$$S_e = \left(\frac{\sum n_i S_i^{\lambda k}}{\sum n_i}\right)^{1/\lambda k} . \tag{7}$$

Let

S_0 indicate the stress amplitude at any cycle,

S_r indicate the rms stress due to the random component of vibration only,

v indicate the ratio S_0/S_r.

$p(v)$ indicates the probability density of stress amplitude when normalized. The integral of the expression for probability density of stress amplitude is the total number of cycles of stress reversal occurring between the stress values defined by the limits of integration; and the integral of $S_0^{\lambda k}$ times the expression for probability density of stress amplitude is the total value of the sum of the products of the number of cycles of stress reversal at a particular stress amplitude and the values of the stress amplitude occurring between the stress values defined by the limits of integration. By integration from zero to infinity, the integrals become equal to the summations in Eq. (7).

$$\sum n_i = \int_0^\infty p(v)\,dv , \tag{8}$$

$$\sum n_i S_i^{\lambda k} = \int_0^\infty S_0^{\lambda k}\, p(v)\,dv . \tag{9}$$

Equation (7) then becomes:

$$S_e = \left(\frac{\displaystyle\int_0^\infty S_0^{\lambda k}\, p(v)\,dv}{\displaystyle\int_0^\infty p(v)\,dv}\right)^{1/\lambda k} \tag{10}$$

By multiplication and division of the numerator by $S_r^{\lambda k}$, a constant,

$$S_e = \left(\frac{S_r^{\lambda k}\displaystyle\int_0^\infty \left(\dfrac{S_0}{S_r}\right)^{\lambda k} p(v)\,dv}{\displaystyle\int_0^\infty p(v)\,dv}\right)^{1/\lambda k} \tag{11}$$

$$S_e = S_r\left(\frac{\displaystyle\int_0^\infty v^{\lambda k}\, p(v)\,dv}{\displaystyle\int_0^\infty p(v)\,dv}\right)^{1/\lambda k} . \tag{12}$$

From Rice, the probability density of the envelope of the peaks of the combined sinusoidal and random stress (S_0) is:

$$p(v) = v \exp\left(-\frac{v^2 + a^2}{2}\right) I_0(av) , \tag{13}$$

where

$$v = \frac{S_0}{S_r} = \frac{R}{\ddot{y}_r} .$$

$$a = \frac{S_s}{S_r} = \frac{\ddot{Y}_s}{\ddot{y}_r} ,$$

S_s = peak stress due to the sinusoidal component of vibration only,

$I_0(av)$ is the Bessel function of order zero with imaginary argument.

The response functions for sinusoidal and random vibration are:

$$\ddot{Y}_s = Q\ddot{X}_s , \tag{14}$$

$$\ddot{y}_r = \sqrt{\frac{\pi f_n W Q}{2}} . \tag{15}$$

Therefore, with common values of $\ddot{X}_s$, W, f_n, and Q,

$$a = \frac{S_s}{S_r} = \frac{\ddot{Y}_s}{\ddot{y}_r} > 3 . \tag{16}$$

Rice has pointed out that "when av becomes large, we may replace $I_0(av)$ by its asymptotic expression. The expression for $p(v)$ is then:

141

$$p(v) \sim \left(1 + \frac{1}{8av}\right)\left(\frac{v}{2\pi a}\right)^{1/2} \exp\left(-\frac{(v-a)^2}{2}\right) . \quad (17)$$

Thus, when either a becomes large or v is far out on the tail of the probability density curve, the distribution behaves like a normal law." Because of the high value of the λk exponent on v, only large values of v are significant. Therefore,

$$p(v) \sim \frac{1}{\sqrt{2\pi}} \exp\left[-\frac{1}{2}(v-a)^2\right]. \quad (18)$$

Substituting for $p(v)$ in Eq. (12) gives

$$S_e = S_r \left(\frac{\int_0^\infty v^{\lambda k} \frac{1}{\sqrt{2\pi}} \exp\left[-\frac{1}{2}(v-a)^2\right] dv}{\int_0^\infty \frac{1}{\sqrt{2\pi}} \exp\left[-\frac{1}{2}(v-a)^2\right] dv}\right)^{1/\lambda k} . \quad (19)$$

The denominator equals unity.

To evaluate the numerator, it is convenient to change the variable by substituting $(v-a) = \sqrt{u}$.

$$\frac{1}{\sqrt{2\pi}}\int_0^\infty v^{\lambda k} \exp\left[-\frac{1}{2}(v-a)^2\right] dv$$

$$- \frac{1}{2\sqrt{2\pi}}\int_{-a}^\infty \left(\sqrt{u}+a\right)^{\lambda k} e^{-\frac{1}{2}u} u^{-\frac{1}{2}} du. \quad (20)$$

By use of gamma functions,

$$\int_0^\infty x^n e^{-ax} dx = \frac{\Gamma(n+1)}{a^{n+1}} = \frac{n!}{a^{n+1}} ,$$

$$\frac{1}{2\sqrt{2\pi}}\int_a^\infty u^{\frac{\lambda k-1}{2}} e^{-\frac{1}{2}u} du = \frac{\left(\frac{\lambda k-1}{2}\right)!}{2\sqrt{2\pi}\left(\frac{1}{2}\right)^{\frac{\lambda k+1}{2}}} ; \quad (21)$$

and by application of Stirling's formula,

$$\frac{\left(\frac{\lambda k-1}{2}\right)!}{2\sqrt{2\pi}\left(\frac{1}{2}\right)^{\frac{\lambda k+1}{2}}} = \frac{\sqrt{2\pi}\left(\frac{\lambda k-1}{2}\right)^{\frac{\lambda k}{2}} \exp\left(-\frac{\lambda k-1}{2}\right)}{2\sqrt{2\pi}\left(\frac{1}{2}\right)^{\frac{\lambda k+1}{2}}} . \quad (22)$$

Also,

$$\frac{a^{\lambda k}}{2\sqrt{2\pi}}\int_0^\infty u^{-\frac{1}{2}} e^{-\frac{1}{2}u} du = \frac{a^{\lambda k}\Gamma\left(\frac{1}{2}\right)}{2\sqrt{2\pi}\left(\frac{1}{2}\right)^{1/2}} = \frac{a^{\lambda k}\sqrt{\pi}}{2\sqrt{\pi}} = \frac{a^{\lambda k}}{2} . \quad (23)$$

Therefore,

$$S_e = S_r \left(\frac{\frac{1}{2}\left(\frac{\lambda k-1}{2}\right)^{\frac{\lambda k}{2}} e^{-\frac{\lambda k}{2}+\frac{1}{2}}}{\left(\frac{1}{2}\right)^{\frac{\lambda k+1}{2}}} + \frac{a^{\lambda k}}{2}\right)^{1/\lambda k} . \quad (24)$$

From the physical aspect of this problem, it is known that λ is usually taken as 2, the product λk is great relative to unity, and the reciprocal $1/\lambda k$ consequently is small. With these approximations introduced, Eq. (24) reduces to the following expression for the equivalent stress:

$$S_e = S_r \left[\left(\sqrt{\frac{2k-1}{e}}\right)^{2k} + a^{2k}\right]^{1/2k}$$

$$= S_s \left[\left(\frac{\sqrt{\frac{2k-1}{e}}}{a}\right)^{2k} + 1\right]^{1/2k} \quad (25)$$

$$S_e = C S_s ,$$

where

$$C = \left[\left(\frac{\sqrt{\frac{2k-1}{e}}}{a}\right)^{2k} + 1\right]^{1/2k} .$$

For values of $3 < a < 6$, and $1 < k < 50$,

$$1 < C < 2 .$$

Since stress is proportional to load, the expression for the equivalent sinusoidal response is

$$\ddot{Y}_e = \left[\left(\frac{\sqrt{\frac{2k-1}{e}}}{a}\right)^{2k} + 1\right]^{1/2k} \ddot{Y}_s , \quad (26)$$

and the equivalent sinusoidal input is:

$$\ddot{X}_e = \left[\left(\frac{\sqrt{\frac{2k-1}{e}}}{a}\right)^{2k} + 1\right]^{1/2k} \ddot{X}_s . \quad (27)$$

The mathematics leading to the expression above were checked numerically by assuming an example where

$$a = 3 ,$$

$$k = 14 .$$

Therefore,

$$C = 1.06 ,$$

$$S_e = 1.06 S_s .$$

From Eq. (19),

$$S_e = S_1 \left[\int_0^\infty v^{2k} \frac{1}{\sqrt{2\pi}} \exp\left(-\frac{1}{2}(v-a)^2\right) dv \right]^{1/2k}$$

This expression can be approximated by numerical summation as shown in Table 1. Values for

$$\frac{1}{\sqrt{2\pi}} \exp\left(-\frac{1}{2}(v-a)^2\right)$$

were taken as the ordinates in tables of the normal (Gaussian) curve, and Δv was chosen as 1; then

$$S_e \sim 5.24 S_r \sim 1.75 S_s .$$

The accuracy of the summation is limited by the coarseness of the increments and the limitations of the tables, but sufficient correlation is established for the purpose intended. The large effect of high values of v shown in Table 1 points up the importance of the occasional high acceleration levels in fatigue life.

By use of the above relationships, mechanical structure can be designed for adequate strength in fatigue, and electronic parts can be chosen on the basis of being able to withstand the equivalent vibration level for the required period of time. Also, adequate strength and electronic parts can be checked for ability to withstand peak values of vibration by choosing the probability level in Fig. 2, which provides the proper level of confidence, and then reading the normalized vibration level.

TABLE 1
Numerical Solution for Equivalent Sinusoid

$$S_e = S_r \left[\sum_{n=0}^{n=\infty} v_n^{28} \, r(v_n) \right]^{1/28} \qquad \Delta v = 1$$

$$S_e \sim (110.5 \times 10^{18})^{1/28}$$

$$p(v_n) = \frac{1}{\sqrt{2\pi}} \exp\left[-\frac{1}{2}(v_n-a)^2\right] \qquad S_r \sim 5.24 S_r$$

$$\Sigma = 110.5 \times 10^{18}$$

(1) v	(2) $v - a$	(3) $p(v)$	(4) $\log v$	(5) $28 \log v$	(6) $\log^{-1}(5)$	(7) $(3) \times (6)$
0	-3	.004400				
1	-2	.054000				
2	-1	.341300				
3	0	.398900	.477	13.3	2.0×10^{13}	
4	1	.341300	.600	16.8	6.3×10^{16}	$.02 \times 10^{18}$
5	2	.054000	.700	19.6	4.0×10^{19}	2.1×10^{18}
6	3	.004400	.778	21.7	5.0×10^{21}	22.0×10^{18}
7	4	.000134	.845	23.6	4.0×10^{23}	53.6×10^{18}
8	5	.00000149	.903	25.3	2.0×10^{25}	29.8×10^{18}
9	6	.0000000061	.954	26.7	5.0×10^{26}	3.0×10^{18}

REFERENCES

1. C. M. Harris and C. E. Crede (Eds.), <u>Shock and Vibration Handbook</u> (McGraw-Hill Book Company, Inc., New York, 1961).

2. W. D. Trotter, "An Experimental Evaluation of Sinusoidal Substitution for Random Vibrations," Bulletin No. 29 on Shock, Vibration, and Associated Environments, Part IV, page 1, June 1961.

3. C. E. Crede and E. J. Lunney, "Establishment of Vibration and Shock Tests for Missile Electronics as Derived from the Measured Environment," WADC-TR56-503, ASTIA No. AD118133.

4. S. O. Rice, "Mathematical Analysis of Random Noise," Bell Sys. Tech. J., Vol. 23, July 1944, and Vol. 24, January 1945.

5. M. A. Miner, "Cumulative Damage in Fatigue," Trans. A.S.M.E. (J. Apl. Mech., Vol. 13, No. 3, September 1945).

*   *   *

DESIGNING MECHANISMS FOR NONLINEAR DYNAMIC EFFECTS

H. F. Hunter
Lockheed-Georgia Company
Marietta, Georgia

The significance of nonlinear dynamic effects is discussed, and five design case histories analyzed in which nonlinearities proved important. These include a screwjack actuator, friction damper, empennage bearing, control surface damper, and buckled shear web. The utility of simplified analysis is emphasized, to assess predominant effects with minimum expenditure of engineering time and effort. Typical design charts are presented.

INTRODUCTION

During the past decade the tempo of structural design has been accelerated by routine usage of high-speed computers, by program management through critical path techniques, and by increased procurement through fixed-price rather than CPFF contracts. Each of these factors has complicated the process of designing for the dynamic environment: schedules are now compressed and delivery dates foreshortened, dynamic loadings customarily provide critical design conditions, and engineering deficiencies prove more expensive. The consideration of nonlinearities in the design problem confronts the dynamicist with additional complexity. This may threaten to delay an analysis, further complicate an already over-complicated mathematical representation, introduce uncertainty into the results, or otherwise harass the analysist to the point of ignoring these effects altogether. Nonlinearities may, however, exert such profound and far-reaching effects upon dynamic behavior that they cannot be intelligently ignored. It is also true in many instances that these effects may be evaluated quite satisfactorily by simplified single-degree-of-freedom analyses and the results expressed in uncomplicated design charts. Extensive documentation now exists on nonlinear single-degree-of-freedom systems, and, while by no means complete, these available results can be of surprising utility in design. It is the purpose of this paper to point out typical situations in which simplified analyses are applicable and to underline the usefulness of these results by several examples taken from recent design studies.

The following is not intended as a complete review of nonlinear structural effects or of methodology available for solving nonlinear equations. Significant nonlinearities in fairly commonplace mechanical systems are pointed out, however, and emphasis is placed upon simplified means of evaluating the associated dynamic effects.

EXAMPLE 1. DOOR WITH SCREWJACK ACTUATOR

Large aircraft cargo doors which are opened in flight by screwjack actuators are shown in Fig. 1. The stiffness requirements for the actuator and attaching structure were established by wind tunnel tests on the scaled elastic model illustrated in Fig. 2. The results showed that self-excited door oscillations of a flutter nature could exist at actuator stiffness levels below a certain critical value. The actuator used on the model was a simple variable-stiffness spring whose force-deflection relationship was always linear, but previous experience indicated that pronounced nonlinearities could be expected on the full-size actuator. For preliminary design purposes, this nonlinearity was approximated, as shown by the dotted lines of Fig. 3. Analysis revealed that the frequency of the fundamental elastic vibration mode of the door was approximately four times higher than its predicted rotation frequency: this indicated that there was weak coupling between rigid rotation and elastic modes and that, insofar as rotational oscillation of the door was concerned, a single-degree-of-freedom vibration analysis would provide
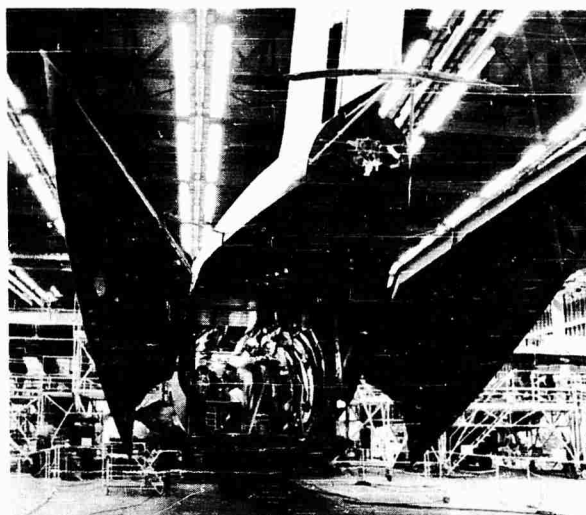
Fig. 1 - Cargo doors with
screwjack actuators

reasonable results. The equations of motion were solved by the method of piecewise linear characteristics [1]. The results are shown in Fig. 4. These curves are somewhat similar to those for a simple linear oscillator: the differences are due to nonlinear free-play effects. The deteriorating effect of backlash on natural frequency is illustrated in Fig. 5, which is taken from the free vibration case, $T/k = 0$, of Fig. 4. Experimental points, included for comparison, were taken from a laboratory model of a simple oscillator in which frictional effects were not minimized. Based upon this analysis, the required specification screwjack stiffness and free-play were established.

Following fabrication of the production actuator, tests revealed a more complicated deflection relationship than had been anticipated, as shown by the solid lines in Fig. 3. This mathematically non-odd characteristic is quite difficult to analyze exactly, and it resulted in some differences of opinion as to specification backlash compliance. This question of admissible backlash was resolved by vibration tests on the first production airplane, which showed that the requisite rotation frequency of the door was attained, even at low forced vibration amplitudes.

In summary, experience with this conventional type of screwjack actuator showed that measured actuator backlash had an appreciable degrading effect on the rotation frequency of the

designed door, which could not be ignored, and that the system was amenable to single-degree-of-freedom analysis which permitted the use of simplified design charts. Accounting for these nonlinear effects required virtually no engineering time or effort, but provided much clearer insight into the mechanical behavior of the system.

EXAMPLE 2. DOOR WITH
FRICTION DAMPER

Experimental friction dampers were installed on the same large cargo doors to evaluate the effect of additional constraint under flight loadings. The dampers consisted of hydraulically operated friction discs which rubbed along a metal quadrant as the door rotated about its hinges. Damper friction force was regulated by hydraulic pressure and could be varied in flight. The simplified mechanical system is illustrated in Fig. 6, with a solution obtained by Den Hartog [2] by the method of equivalent viscous damping. Comparison of Figs. 6 and 4 provides a first-order indication of the benefits to be expected from the damper installation. In each figure amplitude is plotted against frequency: the amplitude-limiting ability of the friction damper at F/T ratios of 0.8 and 0.9 is noteworthy. The simple Coulomb friction characteristic of Fig. 6 is never realized in practice, since the presence of backlash, reduced sliding coefficients, and flexibility in the attaching and supporting structure all combine to compromise damper effectiveness. Mathematical motion in the presence of Coulomb friction

146
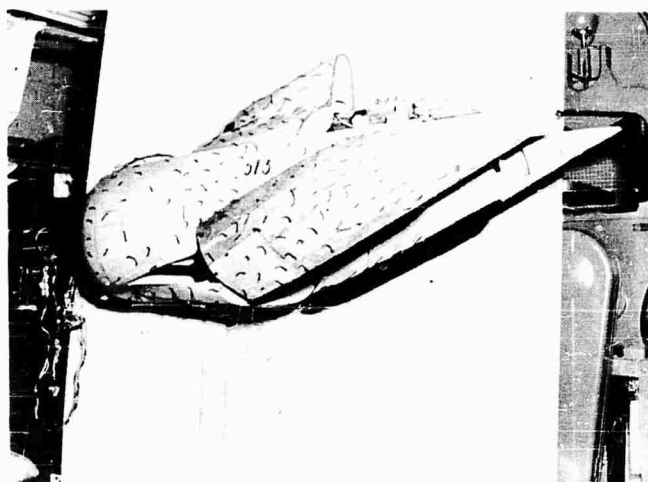
(a) Detail of construction
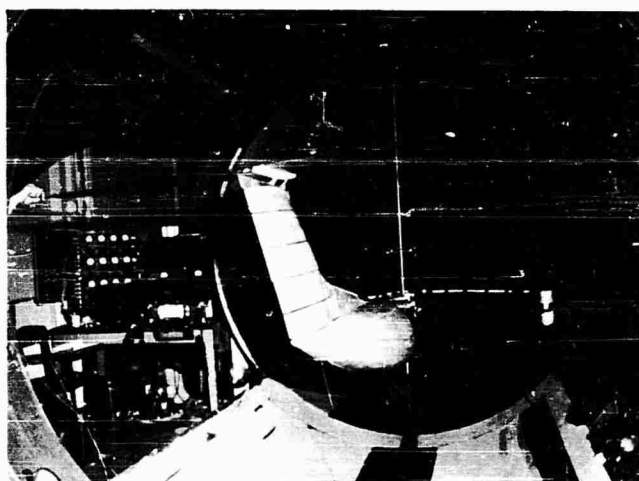
(b) Mounted in wind tunnel

Fig. 2 - Scaled elastic model
of aircraft shown in Fig. 1

is smooth and continuous: motion of the physical system is usually erratic and jerky, with considerable induced vibration from the slip-stick effect.

EXAMPLE 3. EMPENNAGE BEARING

Figure 7 illustrates a self-aligning spherical bearing which supports a large variable-pitch stabilizer. Dynamic model tests showed that the stabilizer attachment flexibility provided by this bearing had a deteriorating effect on the empennage symmetric flutter speed, so that essentially zero bearing backlash and a high stiffness level were required. The hydrocarbon composition insert, which was required for self-lubrication, initially contributed a soft, series, spring element, which resulted in the dotted load-deflection curve of Fig. 8. For moderate and large amplitudes, this relationship is approximated by $F = k_1 X^6$, where F = force, X = deflection, and k_1 = a constant of proportionality. By progressively increasing the manufactured precompression on this insert, the spring characteristic was altered to

147
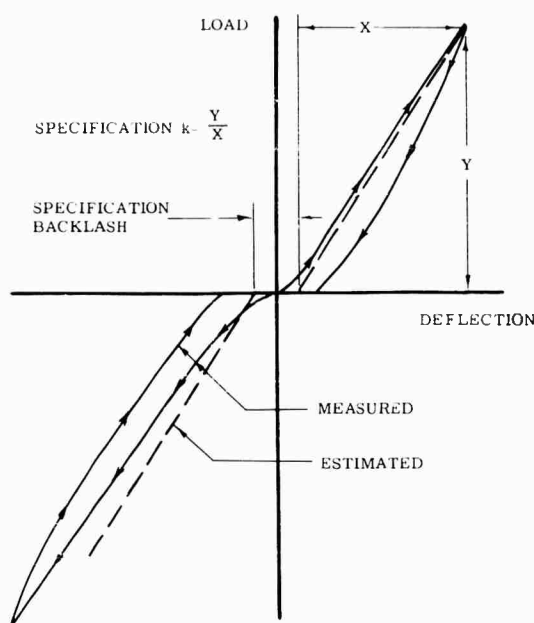
Fig. 3 - Screwjack deflection
characteristics
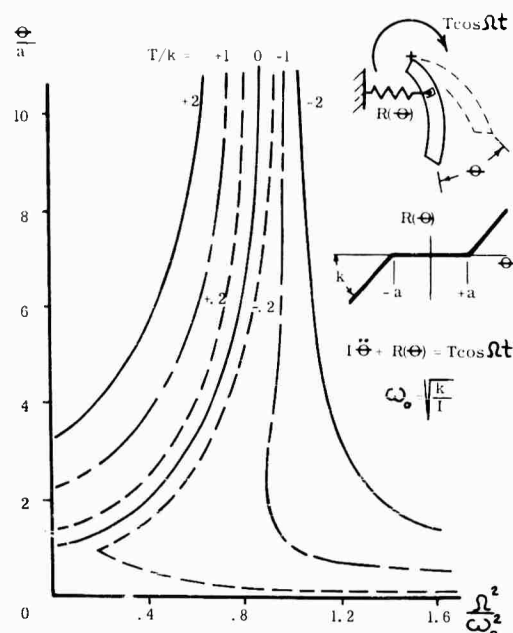
Fig. 4 - Forced door response,
with backlash
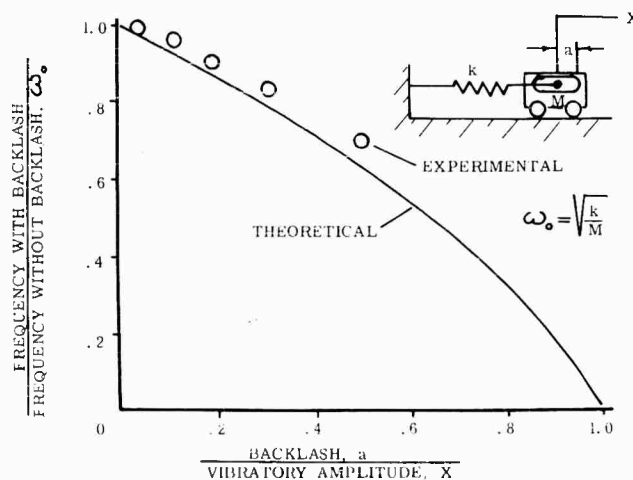
Fig. 5 - Effect of backlash on natural frequency

produce the solid curve, given approximately
by $F = k_2 X^2$, which provided satisfactory vibra-
tion characteristics. The uncoupled pitching
motion of the stabilizer was the most significant
single factor in this study and as such justified
a single-degree-of-freedom analysis. The re-
sponse curves for the original and final bearing,
as computed by the averaging method of Ritz
[1,3], are compared on Fig. 9. The response
amplitudes are considerably reduced at low F/k
and Ω/ω_o ratios of practical importance.

EXAMPLE 4.   CONTROL SURFACE
DAMPER

A large portion of the nonlinear literature
deals with various damping representations:
i.e., Coulomb, viscous, quadratic, cubic, etc.
The forced response of a simple oscillator with
each of these damping forces has been derived,
but it is frequently less clear what damping
characteristic the mechanical system under
study actually possesses. Tests reveal that

148

$$1\ddot{\Theta} + C(\dot{\Theta}) + k\Theta = T\cos\Omega t$$

$$\omega_o = \sqrt{\frac{k}{1}}$$
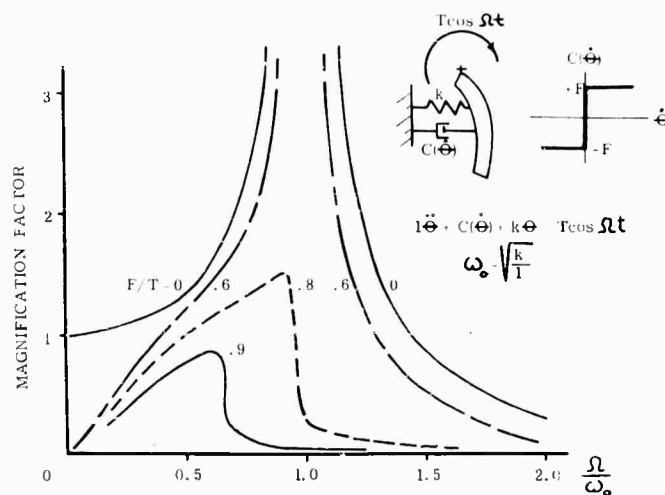
Fig. 6 - Forced door response,
with friction damper

PLASTIC
INSERT
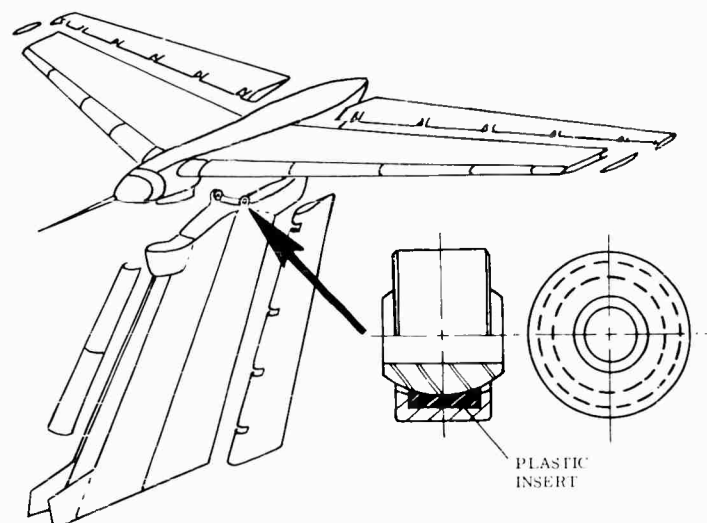
Fig. 7 - Empennage bearing

even simple damping devices evidence combined relationships whose coefficients vary through substantial limits, depending upon the test conditions and the method of measurement. A typical rotary damping device is shown in Fig. 10. This unit consists of a thin disc which rotates within a silicone-filled housing. This device has been analyzed by Schlichting [4], who finds that, for laminar flow and small clearances, the resisting viscous moment is proportional to the rotational velocity to the first power while, for turbulent flow and larger clearances, the moment is proportional to the rotational velocity to the 9/5 power. Damping

output of several of the units was measured by three separate methods. The results are compared on Fig. 11. Points along the solid curve were obtained by rotating the damper shaft at a constant angular velocity and measuring the resisting torque. Points along the dashed curve were obtained by oscillating the damper shaft sinusoidally and measuring the peak resisting torque. The dotted curves were obtained from tests on three separate units by oscillating the damper shaft sinusoidally and plotting the load deflection hysteresis loop. The enclosed area represents energy dissipated per cycle, which may be interpreted in terms of an equivalent

149
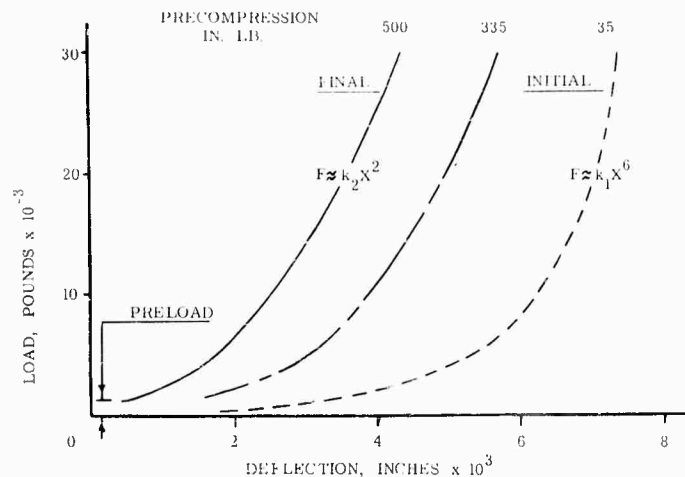
Fig. 8 - Deflection characteristics
of empennage bearing
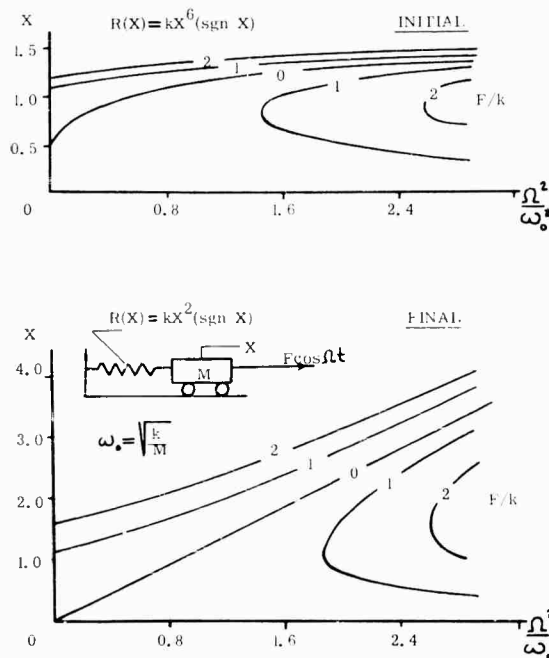
Fig. 9 - Response of fix stabilizer with
2nd and 6th order spring characteristics

Fig. 10 - Control surface damper

viscous damping torque. The shaded area represents data scatter for the three units tested. The results for each individual method of evaluation are seen to be quite consistent, but they differ from each other according to test technique. The variation from the theoretical prediction is at least partially attributive to Coulomb friction in the fluid seals and shaft bearings.
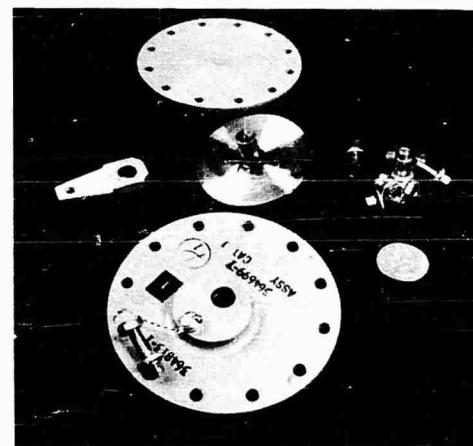
In such a situation involving the determination of damping capacity, the engineer is faced with uncertainty in basic design information. This problem may be solved by (a) specifying a minimum design damping level determined by a test which approximates the actual service condition, (b) detailed consideration of damper attachment flexibility and linkage backlash, and (c) an assumed certainty of unit wear and fluid leakage. The result will be a unit of conservative size with an output of several multiples of the design value. This exact overcapacity will be influenced by critical safety and reliability considerations. These factors are at least as important as knowledge of the mathematical damping relationships, which can only be determined experimentally, and at best fairly approximately, from a practical standpoint.

150
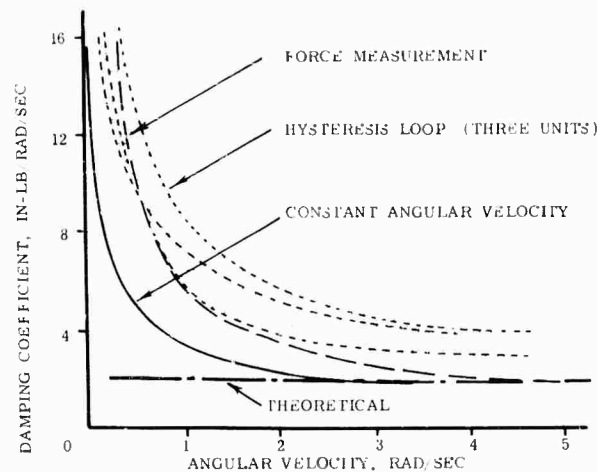
Fig. 11 - Rotary damper characteristics

EXAMPLE 5. BUCKLED SHEAR PANELS

Potentially the most damaging nonlinearity confronting the structural dynamicist is a loss of rigidity arising from skin panel buckling. Flutter of excessive vibratory amplitudes may result when structural deformation reduces the stiffness and corresponding frequencies to certain critical values. A typical aircraft stabilizer, fabricated from thin sheet metal elements, is shown as an insert in Fig. 12. The measured reduction in torsional rigidity for this stabilizer is shown as a function of torsional moment, at a representative spanwise station. Experimental load-deflection points are plotted in the lower portion of the figure. Skin buckling [5] is accompanied by a reduction in torsional rigidity to about 5/8 of the unbuckled value. In general, buckles result from shear stresses in excess of the critical panel buckling values, from compression stresses arising from bending loads, or from a combination of both. It follows that uncoupled bending and torsion frequencies may be reduced by different amounts.

The flutter characteristics of an aircraft empennage cannot in general be estimated by simplified procedures; but once the flutter properties of the linear system are understood, a surprising amount of information may be obtained about the influence of individual nonlinearities on the system. For example, the flutter speeds of the stabilizer, as obtained from a ten-degree-of-freedom digital analysis, are shown on Fig. 13 as a function of uncoupled torsion frequency. By approximating the softening spring characteristic by a cubic polynomial and following the analyses of Woolston [6] and
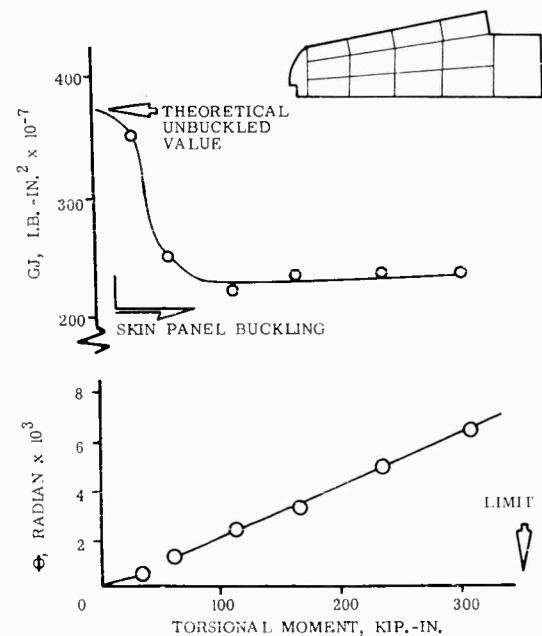
Fig. 12 - Torsional rigidity of aircraft stabilizer

Woodcock [7], the flutter properties of the nonlinear system can be shown as functions of initial deflection in the torsion mode (Fig. 13). Woodcock's solution for the hardening cubic spring illustrates in general that the nonlinearity does not alter the flutter speed but does limit the oscillatory amplitude. Other cases considered by these authors include those of hysteresis damping and backlash. For complex self-excited multi-degree-of-freedom systems the conclusions reached by analyses of this

151
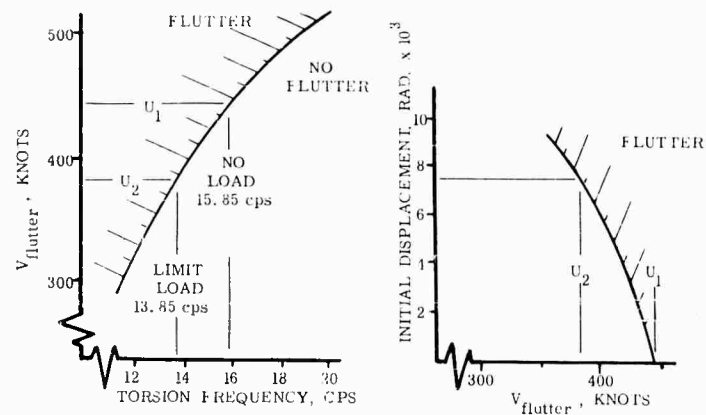
Fig. 13 - Flutter characteristics
of aircraft stabilizer

type should be considered as tentative and used only as a design guide. Little theoretical or experimental experience is currently available in these situations.

CONCLUDING REMARKS

The effects of typical structural nonlinearities encountered in design have been analyzed by simplified procedures. The principal dynamic effects are altered natural frequencies and response characteristics which are functions of the system initial conditions. The existence and significance of subharmonics and ultraharmonics, with related stability questions,

are of lesser importance, at least in the initial structural design stage.

Little published information is available on the form of nonlinearities encountered in structures, and virtually no experimental verification is available to substantiate the analytical solutions of the applicable nonlinear equations. Frequently no exact solution to these equations exists, and solutions from the various approximate methods can only be compared as the best indication of computation accuracy. The experimental investigation of nonlinear effects constitutes an almost untouched field which should provide investigations with ample opportunity for future research.

REFERENCES

1. H. F. Bauer, "The Averaging Method of Ritz," unpublished notes, Department of Engineering Mechanics, Georgia Institute of Technology, 1963.

2. J. P. Den Hartog, Trans. Am. Soc. Mech. Eng., 53:107 (1931); also, S. Timoshenko, Vibration Problems in Engineering, (D. Van Nostrand Co., New York, 1937) page 59.

3. K. Klotter, "Non-Linear Vibration Problems Treated by the Averaging Method of W. Ritz," N6-ONR-251 Task Order 2, Stanford University, 1951-2.

4. H. Schlichting, Boundary Layer Theory (Pergamon Press, New York, 1955) pp. 445-447.

5. P. Kuhn and J. Peterson, "A Summary of Diagonal Tension, Part I, Methods of Analysis," NACA TN 2661, May 1962.

6. D. S. Woolston, H. L. Runyan, and R. E. Andrews, "An Investigation of Effects of Certain Types of Structural Nonlinearities on Wing and Control Surface Flutter," J. Aeronaut. Sci., Vol. 24, No. 1, Jan. 1957.

7. D. L. Woodcock, "Structural Nonlinearities," AGARD Manual on Aeroelasticity, Vol. I, Part I, Ch. 6.

*   *   *

PACKAGING ELECTRONICS FOR 250,000-g APPLICATIONS

D. W. Finger
Harry Diamond Laboratories
Washington, D.C.

Techniques for packaging telemetry components and systems to with-
stand gun launch accelerations up to 250,000 g are discussed, and the
necessary and sufficient conditions for their survival are established.
The principal requirements are that all voids be eliminated from the
package and that any encapsulating resin be adequately contained to
prevent its rupture. The ultra-high-g projectiles used in hypervelocity
research for which these telemeters were designed are briefly de-
scribed. In addition, a brief description is given of high-g telemetry
systems used in the gun-fired rockets and projectiles of project HARP.

In recent years aerodynamic research has
progressed to the point where wind tunnels can-
not provide air flows of sufficiently high veloci-
ties and pressures. Therefore, test vehicles
must be flown through a free flight range, and
the desired data, such as temperature measure-
ments, electron density determination, and in-
frared attenuation, must be telemetered. To
obtain the required velocities, accelerations as
high as 250,000 g may be required. Under
sponsorship of the Ballistic Research Labora-
tories at Aberdeen Proving Ground, the Harry
Diamond Laboratories, a segment of Army Ma-
terial Command, has developed several on-
board telemetry systems to transmit the re-
quired data from such hypersonic projectiles
during flight.

Some of the projectiles involved are small.
Figure 1 shows a model re-entry vehicle, the
GE type-3.1 design, which has a high-drag
shape. This round is launched from a 105-mm
smooth-bore gun with discarding sabot at muz-
zle velocities up to 8000 fps. Peak launch ac-
celeration is 250,000 g. A thin-film, platinum,
resistance thermometer is mounted in the nose
to measure heat transfer into the surface of the
structure from the stagnation region. It is of
incidental interest that these rounds have been
fired through a horizontal test range several
hundred feet long and recovered from a flat
grassy impact field. Because of high drag with
consequent low impact velocity, some of the
projectiles have been recovered and fired again,
with electronics still operable.

Figure 2 shows an RVX shape, which is
also fired horizontally to obtain basic aerody-
namic research data. An accelerometer is
mounted transversely in the aft section of this
model to measure in-flight pitch and yaw. This
cone-cylinder-flare configuration has been
fired successfully from a 240-176-76-mm light
gas gun with propellant powder in the 240-mm
section, a plastic piston for driving helium in
the 176-mm section, and the projectile with
sabot in the 76-mm section. This gun produces
muzzle velocities of 12,000 fps, with setback
acceleration of 250,000 g, for a longer period
than that attained with the ordinary powder gun.
In addition, higher time derivatives of distance,
such as jerk, are present to a greater degree.

The Harry Diamond Laboratories has also
designed telemetry systems for vehicles fired
vertically for the High Altitude Research Probe
Project (HARP). One of these is a dart of low-
drag shape (Fig. 3), which, when fired from a
5-inch gun by chemical propellant, travels to an
altitude of 250,000 feet. Muzzle velocity is
about 5000 fps, with setback acceleration in the
gun of around 60,000 g.

Figure 4 shows a larger vehicle, which is
fired vertically with discarding sabot from a
16-inch smooth-bore gun. In addition, teleme-
try has been installed in several types of gun-
launched rockets. These were single-stage
rockets fired from a 16-inch gun at a muzzle
velocity of about 4000 fps. These rockets and
projectiles reach altitudes up to 400,000 feet.
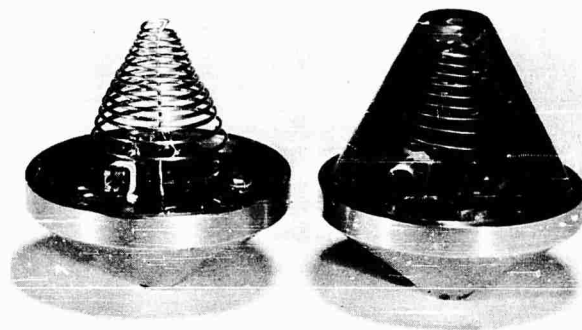
Fig. 1 - Model re-entry vehicle
before and after potting
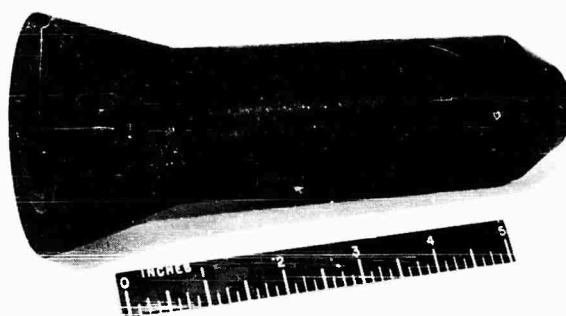
Fig. 2 - RVX vehicle

Figure 5 illustrates an early version of this type vehicle.

Only a small number of these various rounds have been fired to date but operation of the telemeters has been quite satisfactory. The small re-entry shape described previously has been fired 24 times. Data were received from all of the 20 rounds that successfully traversed the range. The round with the accelerometer has been fired only twice with telemeter on board, and some information was received both times. A total of seven of the 5-inch gun rounds has been fired; data were recovered from six. Of eleven 16-inch gun vehicles successfully launched, data were received from eight. It should be emphasized that little or no flight testing of the telemeter was possible prior to final fabrication.

TECHNIQUES

Experience with radio-type proximity fuzes has shown that it is possible to fire electronic assemblies from a gun and have them operate afterward. The techniques employed previously, however, are not suitable for the more severe environmental conditions encountered in these high-velocity aerodynamic research vehicles.

The problem of electronic system survival under these conditions can be divided into two

Fig. 3 - Five-inch gun dart
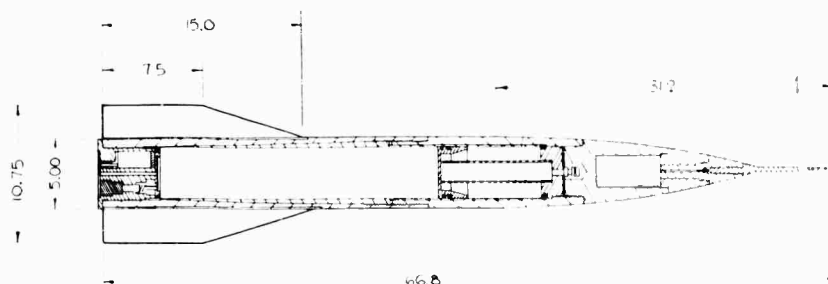
Fig. 4 - TMA payload and telemetry unit

154
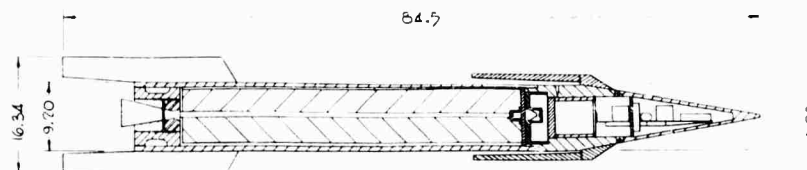
Fig. 5 - Rocket vehicle with magnetometer payload and telemetry

somewhat related parts. First, the individual component must withstand the forces encountered; second, the component must be supported so that its inherent ruggedness is not compromised. Previous experience had shown that vacuum tubes would not survive the expected shocks; therefore transistors, being solid, were the only hope for an oscillator for this environment. Previous tests, however, had indicated that transistors, as a class, are marginal, even for conventional gun setback forces, with survival reliability being questionable at 20,000 g. Therefore, increasing the inherent ruggedness of transistors is required for a 250,000-g environment. At this point let us digress a bit and consider what we know or can postulate about the fundamental aspects in the ruggedization of electronics.

First, let us think of all solids as being springs. Second, since breakage of things requires separation of molecules, we recognize that things cannot break in compression. Compressive forces can cause things to break in tension or shear, but pure isostatic compression cannot rupture a solid object. Although an object cannot be broken by isostatic compression, it can be affected. For example, the phase of a material could change, such as ice to water; a spring can compress and become smaller, which affects its performance; the resistance of an ordinary carbon composition resistor decreases when subjected to an isostatic compressive force; and the capacitance of ceramic and glass dielectric capacitors is increased when they are made smaller by a compressive force uniformly surrounding the component envelope.

Now let us consider what the structure of a ruggedized electronic package should be like. From our discussion above, we can conclude that tensile strength of the various components, such as capacitors and resistors, is much less than their ultimate compressive strength. Therefore, our structure should support the components to minimize tensile forces, both direct and indirect. An example of indirect tensile forces are those developed radially when a right circular cylinder has a force applied to

each end. The tensile strength required may be minimized by providing adequate hoop strength to contain it radially. Similarly, an electronic assembly may be potted with a material that contains each component in all directions. Then, if we form this potting material in a solid cylinder and provide sufficient hoop strength to prevent radial stress in the cylinder from exceeding its elastic limit, the electronic assembly should be satisfactorily contained. Most practical projectiles are more than two calibers in length, so the shape we expect to have for the electronics is a long cylindrical cavity. Furthermore, structural requirements on the shell itself to prevent collapse in the gun tube are likely to provide adequate hoop strength and rigidity to prevent fracture of the potting material. One exception to this configuration is the one first mentioned, the GE 3.1 high-drag reentry shape. The length of this projectile is about the same as its diameter, and there is no steel shell surrounding it. In this case the shell is composed entirely of the potting material, with a steel windscreen to prevent burning in flight. The mechanical hoop strength of this projectile is provided by the gun barrel itself, with forces being transmitted and distributed by a plastic launching sabot.

It is believed that there are three first-order effects due to high-g acceleration of a potted electronic assembly. One of these is the hydrostatic pressure generated during acceleration by elastic flow of the potting material. This pressure probably cannot be avoided. It can be reduced somewhat by the use of low-density casting resin, such as those incorporating glass microballoon fillers, but the density cannot be reduced very far without unacceptable loss of shear strength caused by the hollow filler balls. Another possibility for reducing this load is to shorten the column length by introducing steel bulkheads across the axis to support several short columns instead of one long one. This method has the obvious disadvantages of taking a lot of space.

A second effect is compression waves generated by the fast rise time of the pressure pulse driving the projectile. This effect is

155

particularly large for guns in which rupture of a diaphragm permits a heavy shock wave to impact the projectile. These compression waves are transient and should not affect data transmission unless in-barrel telemetry is required. Moreover, they should cause no permanent damage. Tension waves, however, develop at discontinuities, which reflect a portion of the compression wave energy, and these can cause permanent damage. To minimize damage from these tension waves, the shock waves must be attenuated or discontinuities eliminated.

A third adverse effect develops during acceleration because of density difference between component and potting material. If the component is heavier, as is usually the case, the force tending to make it sink through the potting material is proportional to acceleration times density difference. This force can be reduced by using a potting material of greater density, but this is contradictory to our previous desire for a low-density medium. We feel, however, without direct corroborating data, that heavy potting material is usually better than a low-density material, if adequate container hoop strength is provided.

At this point let us summarize the requirements of the potting materials. In the first place, the potting material, prior to curing, must be a low-viscosity liquid in order to flow into cracks and crevices. Furthermore, this liquid must have high wetting ability and must creep into fissures, pushing air out as it goes in. Molten waxes meet these criteria but are unsuitable because of high shrinkage, which causes the material to pull away from the container walls during hardening instead of merely reducing the level of the potting material. The resultant voids would permit development of high radial tensile forces. Thus we can add high adhesive force to the list of requirements for our potting resin, the idea being that good adhesion helps prevent shrinkage voids. These requirements bring to mind the epoxy and polyester polymers, both of which are usable without high-temperature curing. The polyesters exhibit less shrinkage than does epoxy and, in addition, are lower in cost and release less heat while curing. The epoxies are considered superior, however, because they have better adhesion and wetting ability. One other feature that is required is ease of use. A projectile telemeter of the kind used here may be fabricated in steps that require potting to be done in several stages, from individual component through subassembly to final assembly. A potting material such as NBS casting resin, which

requires a number of chemical steps for completion, is highly undesirable since electronic engineers and technicians must be able to handle the necessary chemical steps without difficulty. Another significant factor for some applications is dielectric constant and loss factor for high-frequency current. NBS casting resin is superior in these respects, but, even so, the difficulties involved in its use makes one willing to accept the higher loss factor of more conveniently used material.

Considering these factors, it appears that epoxy resins are most nearly suited for these applications. Even so, they exhibit several undesirable characteristics, such as considerable heat release during curing, large loss tangent, and brittle fracture at relatively low stresses. By addition of appropriate modifiers and additives, however, this class of resin works quite well for ruggedizing electronic assemblies for a quarter million g. A modifier to increase impact strength was necessary to obtain intact launch of the small high-drag shape mentioned previously. A 60:40 mixture of epoxy and polysulfide rubber resins was found to be satisfactory. This mixture has an impact strength a factor of ten larger than that of the epoxy. The polysulfide rubber modifier copolomerizes with the epoxy to produce a tough, slightly flexible resin, which has other significant advantages. The exothermic reaction is reduced so that larger sections can be potted. More important, the residual internal stresses, as disclosed by polariscopic examination, are essentially eliminated, whereas epoxy resins generate severe internal stresses while curing.

Use of another additive has significantly alleviated other shortcomings inherent in the straight epoxy resins. For casting large sections, a silica filler is added, but not in the usual manner; 20-30 mesh Ottawa silica is used in a quantity of four parts by weight of silica to one part of resin. The desired mixture is a resin completely saturated with the silica or, expressed differently, a potting material composed of sand with the interstices between grains filled with resin. Mixing is accomplished by either of two ways. The first method is to pour resin into the cavity then sprinkle in the sand, which sinks to the bottom. As sand is added, the level is raised by a factor of about three. The second method is to pour the cavity full of sand, then pour resin over the sand. If the bottom is vented so that air can escape, by a small hole or tube extending to the atmosphere, air pressure of 15 psig will force the resin down through about 20 inches of sand before it thickens too much for further wetting.

156

The net result is a concrete with density about 2.1 gm/cc, which has a coefficient of thermal expansion more nearly matching that of the embedded parts, lower loss tangent for high frequencies, and greatly reduced exothermic reaction so that large castings can be cured rapidly at room temperature. In addition, the residual stresses due to curing are substantially reduced. This capability for casting large volumes is quite desirable in cases like the rocket vehicle shown in Fig. 5, which contains over a gallon of potting material.

A third additive has been used for yet another property. The RVX shape shown in Fig. 2 is also composed mostly of potting material. The epoxy, modified with polysulfide rubber, was not strong enough to withstand launch, so the resin body was reinforced with an outer shell made of fiberglass-reinforced resin. These were launched successfully, demonstrating the very high strength of this composite material. Shells reinforced with roving, tape, and mat also were satisfactory.

ELECTRONIC COMPONENTS

Several years ago, the provision of sufficiently rugged transistors was the most pressing problem. High-frequency devices were available only in germanium, and since none of these were potted by the manufacturers, it was necessary to develop techniques to internally pot available transistors. One basic technique of value is to adjust the coefficient of thermal expansion of the potting material to more nearly match that of the wafer material. A mixture of fine-mesh silica and epoxy may be used for this purpose. Another technique, which worked very well on the 2N502, was to precoat the inside surfaces with a thin film of silicone oil. This helped prevent contamination of the germanium by the amine catalyst. This coating does not cause the wafer to break at 250,000 g, and, in fact, it is felt that it improves the ruggedization of potted components. The situation today is much better, since all silicon devices seem to be largely undamaged by the direct application of epoxy resins. Such potted transistors may not survive extensive temperature cycling, but they have proved to be adequate for these applications. In addition, there is at least one commercially available transistor that is potted as supplied. Further, there is a high-frequency high-power transistor that has survived 50,000-g impact tests as supplied. It is not potted but is reported to have aluminum lead wires inside instead of the usual gold, which has a much lower strength-to-weight ratio. Carbon composition resistors of various

ratings have been successfully used, ranging from 0.1 to 1 watt. Limited data have shown a 2-percent shift in value for a 250,000-g launch acceleration. To date only solid resistors have been used, but recent laboratory tests show that the resistor formed on a glass tube with molded case has about one third as much shift in resistance due to hydrostatic load. Film resistors and potentiometers have not been evaluated. Laboratory tests show about 21-percent change in resistance for the solid composition resistor for 10,000 psi isostatic load and about 7-percent change for the glass-tube composition resistor.

A variety of ceramic and glass dielectric capacitors have been used successfully. In fact, no failures due to capacitors or resistors have occurred to date. Failures due to wet-type tantalum capacitors have been reported. We have successfully flown the dry slug-type tantalum, with vacuum-applied conformal case, without gross failure. There seems to be some question remaining about its stability under conditions of heavy g-loading.

One electronic component likely to be ignored is connecting wires. For example, a piece of copper wire 0.5 inch long supported axially by one end would develop breaking stress at 250,000 g without support from the potting resin. For this reason, all spaghetti is avoided, and only magnet wire or bare copper is used for this g level. If a long axial run is necessary, the wire is spiraled or bent back and forth ladder fashion so the resin can provide adequate support without relying too heavily on its adhesive properties. Coaxial cable should not be used for long axial runs since the adhesion between center conductor and insulator is usually poor. Connectors, of course, are not used, but circuit boards with either printed wiring or terminal construction have been employed. It is believed that orientation of components or type of layout is not critical.

Several sizes of mercury cells have been used as power supplies without known failures, except for usual shelf-life or temperature-extreme problems. There is some slight evolution of gas from these, however, which may crack or craze the resin after some months on the shelf. Nicad button cells have been used for 20,000-g applications and have been tested satisfactorily at 50,000 g. We plan to use small cells of this type for 250,000-g applications.

Antennae present a problem that must be solved within the boundary conditions imposed by the individual vehicle configuration, which is predetermined by aerodynamic and mechanical requirements. The antenna for the projectile

in Fig. 1 is a helix which occupies the aft end and radiates through the potting resin. This particular resin is quite lossy, but the transmitting range is only a few feet, so the loss can be easily tolerated. The RVX vehicle also required only a short transmission distance and uses a similar antenna. An early version of the 5-inch gun dart used an insulated nose with loading coil to complete a dipole antenna, but it was very inefficient because of the large capacitance across the antenna. Later versions use a loaded quarter-wave stub imbedded in a plastic nose. The 250-Mc carrier frequency matches this antenna, and good efficiency is achieved, which permits reception over the 50-mile or greater range required. The 16-inch gun projectile also uses a quarter-wave stub antenna, except no loading coil was included, and the length was 14 instead of 8 inches. The rocket shown in Fig. 5 used a so-called quadripole antenna, with feed-point near the ground connection.

CONCLUSION

Our experience has shown that it is practicable to ruggedize certain electronic circuits used for telemetering in-flight information from shells launched with setback accelerations up to a quarter million g. The necessary and sufficient conditions are removal of all voids from transistors and other individual components as well as the complete assembly, with replacement by appropriate potting material, and avoidance of components containing liquids. The potted assembly must in turn be supported by a surrounding container of adequate hoop strength.

*   *   *

COMBINED ANALYTICAL AND EXPERIMENTAL APPROACH FOR DESIGNING AND EVALUATING STRUCTURAL SYSTEMS FOR VIBRATION ENVIRONMENTS*

J. C. McClymonds and J. K. Ganoung
Saturn Engineering, Douglas Aircraft Company, Inc.
Space Systems Center
Huntington Beach, California

This paper presents a combined analytical and experimental approach for the prediction of the fatigue life of a complex structural installation in a cryogenic environment subjected to various vibration spectra. Existing state-of-the-art techniques are employed which include (1) a digital redundant force analysis to obtain influence coefficients, (2) a forced response analysis to obtain dynamic loads, (3) a photoelastic analysis to obtain detailed stress distributions, (4) static and fatigue tests of system elements at cryogenic temperature, and (5) a cumulative fatigue damage prediction.

This approach is applied to the analysis of the cold helium sphere installation (S-IV) on the Saturn I space vehicle, and the results are compared with the results from both sinusoidal and random vibration qualification tests performed at cryogenic temperature.

INTRODUCTION

With the advent of large manned and unmanned space vehicles, such as the S-IV stage of the Saturn I vehicle (Fig. 1), the importance of structural reliability has been reemphasized. Often, however, the large size of the components and complexity of the imposed environments create difficult design and testing problems. The high cost of testing and the inadequacies of testing equipment, originally developed to test small components, preclude complete reliance on experimental verification of structural integrity and necessitate a combined analytical and experimental approach. For example, the high cost of testing large specimens (often a single specimen) in combined environments (e.g., vibration and cryogenic temperature) necessitates the establishment, analytically, of high confidence in the design prior to the test. The complexity of equalizing and controlling the vibration exciters, when the test specimens are large, increases the probability of overtesting which may result in premature failures. Structural integrity in such cases can often be demonstrated by interpreting the available test data on the basis of a thorough structural dynamic analysis. The cost of uprating vehicles also can be minimized if previous test results can be extrapolated on the basis of a valid structural dynamic analysis.

This paper describes a combined analytical and experimental approach used to establish structural integrity in vibration environments, with a specific example being demonstrated[1]: the three cold helium storage spheres located in the liquid hydrogen tank of stage S-IV of Saturn I (Fig. 1). The details of the cold helium sphere installation are shown in Fig. 2. Each titanium sphere is supported by four stainless steel straps and a neck which is welded to the tank wall. The straps, which grip the sphere by a collar at the top boss, are attached to the

NOTE: References appear on page 174.
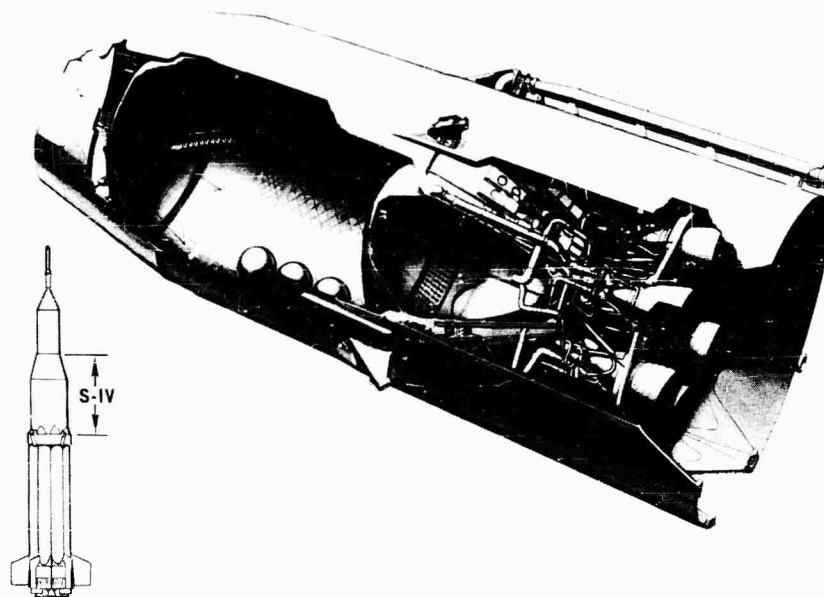
Fig. 1 - S-IV stage of Saturn I space vehicle

tank wall by hooks. Turnbuckles are located between the hooks and strap ends to provide a strap pre-load. The sphere is pressurized to 3000 psig and immersed in liquid hydrogen at a temperature of -423°F. The installation is subjected to random vibration during ground acceptance firing and flight and to sinusoidal vibration during air transportation aboard the "Pregnant Guppy" aircraft. The vibration

design and test criteria established by the Marshall Space Flight Center included sinusoidal sweep and dwell plus random vibrations about three orthogonal axes. The qualification test specimen was a single sphere installed on a section of tank skin, as shown in Fig. 3. The test fixture incorporated a tank so that the sphere could be pressurized and immersed in liquid hydrogen during the tests. It should be
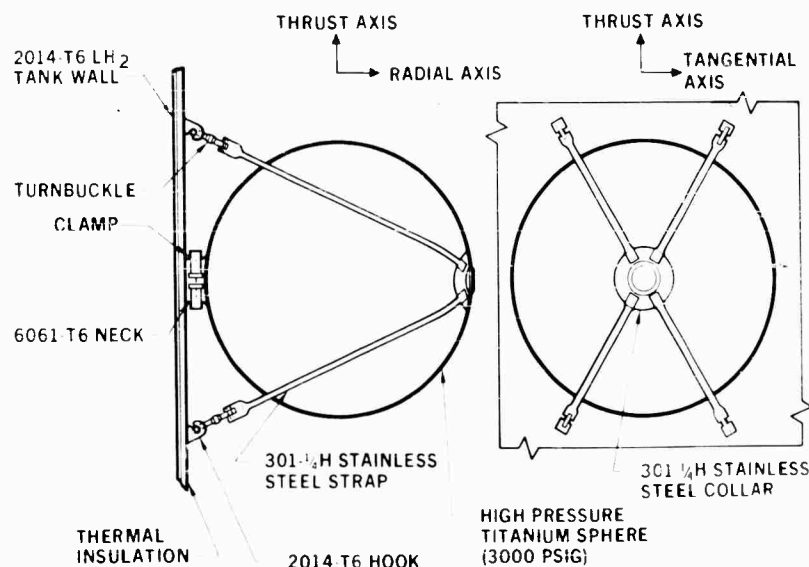
Fig. 2 - Installation of cold helium sphere

160
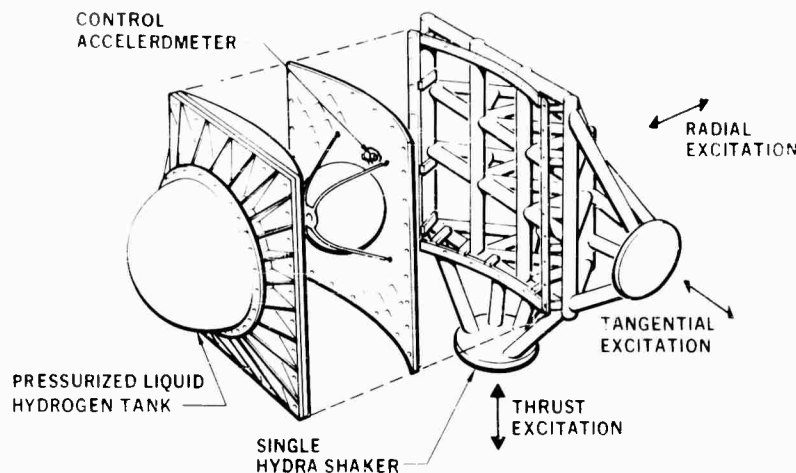
Fig. 3 - Sketch of test specimen mounted
for vibration qualification test

pointed out that the test jig support structures
protruding from the side and bottom of the jig
are not attached simultaneously, as shown, but
are used individually during a test in a given
axis.

Figure 4 shows diagramatically how the
analytical and experimental procedures are
used together to establish structural integrity.
The dashed arrows indicate auxiliary analyses
and tests which may be performed to establish
greater confidence in the results of the struc-
tural evaluation. All of these procedures were
employed in the design and evaluation of the
cold helium sphere installation. Each step is
discussed in detail in the following paragraphs
and, whenever possible, the results of the
structural dynamic analysis are compared with
experimental data. Although the preliminary
design considerations are briefly described,
this paper is primarily concerned with the de-
sign evaluation and qualification phase of devel-
opment.

PRELIMINARY DESIGN

The preliminary design of the cold helium
sphere installation was based on a quasi-static
analysis, with the method of "least work" used
to solve for the internal load distribution in the
redundant structure. The loads at the sphere
center of gravity were estimated on the basis
of an assumed dynamic amplification factor and
the vibration specification in existence at that
time. A fatigue analysis was not attempted
during initial structural sizing; but the effects
of vibration and fatigue were considered in

material selection and in the avoidance of
stress concentrations.

DYNAMIC ANALYSIS

After the structural elements have been
sized according to the preliminary design pro-
cedures, a more complex structural dynamic
analysis can be initiated. The three major
steps in this analysis are the structural ideali-
zation, the calculation of influence coefficients,
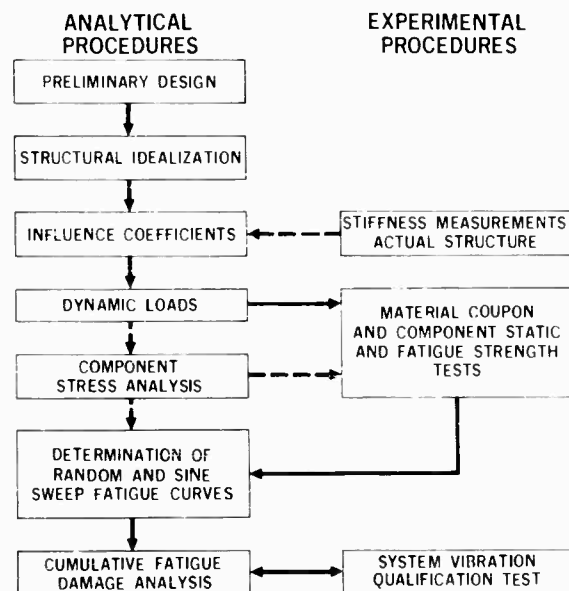
Fig. 4 - Approach to fatigue life prediction

161

and the calculation of the dynamic response. Since it was considered impractical to test more than one cold helium sphere, the response of the three-sphere installation in the vehicle to predicted vehicle environments and the response of the single test environment were both evaluated analytically.

STRUCTURAL IDEALIZATION

The idealized structural models for both the three-sphere and single-sphere configurations are shown in Fig. 5. The models consist of a set of members which carry axial and bending loads and are connected by a set of panels carrying shear loads. The idealization is three dimensional and simulates the tank radius of 110 inches. Unit loads are applied and deflections obtained at each joint. The additional stiffness provided by the pads around the sphere neck and strap attachments is included in the models. The spheres were assumed to be rigid but the neck flexible. It was also assumed that the straps would not slip relative to the sphere. The longitudinal edges of the three-sphere model were assumed pinned to simulate node lines in the vehicle. Fixed ends were assumed to simulate the stiffness at the forward and aft tank domes resulting from the attach rings and the tank curvature. All edges of the single-sphere specimen were assumed fixed to simulate the rigid attachment to the test fixture. The elastic properties of all structural elements were based on the modulus of elasticity at their predicted operating temperature.

Influence Coefficients

Influence coefficients were calculated by means of the Douglas redundant force method described briefly in Appendix A. Table 1 shows the close agreement of the predicted and experimental rotational compliance at the neck of the sphere for both the thrust and tangential axes on both a full-scale production vehicle and on vibration qualification test panel.

TABLE 1
Comparison of Analytical and Experimental Rotational Compliances at Sphere Neck

Axis	Rotational Compliance $(\text{rad/in.-lb} \times 10^6)$	
	Analytical	Experimental
Flight Vehicle		
Thrust	3.3	3.2
Tangential	3.8	3.6
Test Panel		
Thrust	3.6	2.8
Tangential	4.2	4.0

Dynamic Loads

Dynamic loads and transfer functions (ratio of response to vibration input) were computed by the method described in Appendix B. The
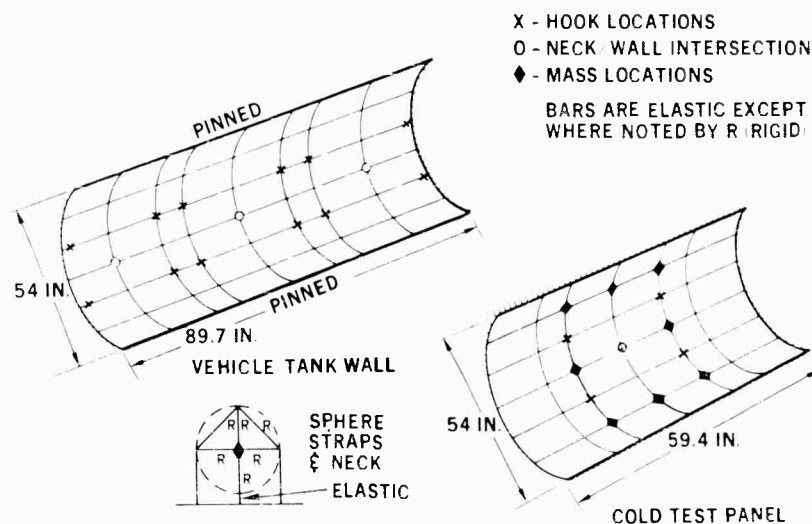
Fig. 5 - Structural idealizations for influence coefficients and model analysis

analytical transfer functions for the strap loads in the single-sphere test specimen are compared with the sinusoidal sweep and random vibration test results in Fig. 6. The agreement is quite good in both magnitude and frequency in the thrust and tangential axes. The frequency discrepancy in the radial axis is probably the result of the greater dependence on plate stiffness in this axis. Greater accuracy might have been obtained by assuming more degrees of freedom in the plate. Similar comparisons of the neck moments also indicated good agreement between theory and test. Both analytical and experimental transfer functions represent the ratio of the strap load to the vibration input at the neck of the sphere. The transfer function for the random vibration test was determined by taking the square root of the ratio of the strap-load power spectrum to the input power spectrum at the sphere neck. Some smoothing of the test data was required for the comparison to eliminate the effects of extraneous crosstalk inputs. The analytical transfer functions were determined prior to the test by assuming a dynamic amplification of three from the sphere neck to the sphere center of gravity. This factor was chosen on the basis of previous tests of a similar installation; although in the analysis of most large complex structural systems on the S-IV which are subjected to high vibration levels, amplification factors of three to five are generally assumed. A possible reason why the random transfer functions are greater than the sinusoidal transfer functions

is that the random loads and responses were generally lower, which would result in less damping and thus produce higher amplification factors. This trend was consistent in all three axes.

Table 2 shows a comparison of predicted and measured strap loads for each axis and each type of test excitation. The measured strap loads were corrected to eliminate the effects of excessive test inputs. The good agreement with the test results indicates that the analytically determined loads were suitable for design. Also shown are the installation preloads induced by applying torque to the turnbuckles and the static preloads resulting from sphere pressurization and thermal contraction of the straps, since these will be referred to later in the discussion of component strength tests.

COMPONENT STRENGTH TESTS AND ANALYSES

To perform an adequate structural analysis, once the loading is known, the static and fatigue strength capability of the individual components must be determined. For this step in the design evaluation procedure the relative effort to be spent between analysis and testing is determined by the complexity of the component and the environments. Generally, however, since fatigue failures occur in areas of stress

TABLE 2
Comparison of Predicted and Measured Strap Loads

Axis	Excitation	Predicted	Measured[a]
Thrust	Sine sweep	±315	±135
	Sine dwell	±158	No data
	Random (rms)	54	69
Tangential	Sine sweep	±355	±248
	Sine dwell	±178	±151
	Random (rms)	28	33
Radial	Sine sweep	+256	±240
	Sine dwell	±128	No data
	Random (rms)	56	24
Installation preload		225	250
Sphere pressurization		170[b]	-
Thermal load		295[b]	-
Total static load		690	680

[a]Actual test loads corrected to eliminate effects of excessive test inputs and crosstalk.
[b]Extrapolated from preliminary tests with 1000-psig pressure and immersion in liquid nitrogen.

163

(a) Thrust axis

RANDOM VIBRATION TEST

$$|TF(f)|^2 = \frac{\text{POWER SPECTRAL DENSITY OF STRAP LOAD}}{\text{POWER SPECTRAL DENSITY OF INPUT ACCELERATION}}$$

ANALYTICAL

SINUSOIDAL SWEEP TEST

$$[TF f] = \frac{\text{STRAP LOAD}}{\text{INPUT ACCELERATION}}$$

FREQUENCY (CPS)

TRANSFER FUNCTION—|TF f|—POUNDS PER $\bar{g}$

(b) Radial axis

RANDOM VIBRATION TEST

$$|TF(f)|^2 = \frac{\text{POWER SPECTRAL DENSITY OF STRAP LOAD}}{\text{POWER SPECTRAL DENSITY OF INPUT ACCELERATION}}$$

SINUSOIDAL SWEEP TEST

$$TF(f) = \frac{\text{STRAP LOAD}}{\text{INPUT ACCELERATION}}$$

ANALYTICAL

FREQUENCY (CPS)

TRANSFER FUNCTION—|TF(f)|—POUNDS PER $\bar{g}$

(c) Tangential axis

RANDOM VIBRATION TEST

$$|TF(f)|^2 = \frac{\text{POWER SPECTRAL DENSITY OF STRAP LOAD}}{\text{POWER SPECTRAL DENSITY OF INPUT ACCELERATION}}$$

ANALYTICAL

SINUSOIDAL SWEEP TEST

$$|TF(f)| = \frac{\text{STRAP LOAD}}{\text{INPUT ACCELERATION}}$$

FREQUENCY (CPS)

TRANSFER FUNCTION—|TF f|—POUNDS PER $\bar{g}$

Fig. 6 - Comparison of analytical and experimental transfer functions for strap load

164

concentration, it is advisable to perform simple static and fatigue tests on the components, supplemented by stress analysis techniques. Because of the relatively small amount of fatigue data available at liquid hydrogen temperature (i.e., -423°F), coupled with the various stress concentration factors peculiar with the components involved in the cold helium sphere installation, it was necessary to make maximum use of material coupon and component testing to generate S-N curves (allowable stress versus cycles to failure) for the strap, hook, and neck components. The results of this testing are reported in Refs. 2, 3, and 4. Various stress analysis techniques also were employed.

Component Tests

Standard fatigue coupons were used to determine the shape and relative position of a family of S-N curves for the various materials involved at both room and cryogenic temperatures. The coupons contained a weld bead or drilled hole to simulate stress concentration factors or material degradation in the vicinity of a weld. Because of the preloaded nature of the helium sphere installation, the S-N curves were determined for various mean values and stress ranges (i.e., for various R values). Fatigue and ultimate test results of the actual strap, hook, and neck components were then used to position the family of curves. The hooks and straps, being immersed in liquid hydrogen, were cryogenically tested at -423°F

with the use of a cryostat. The thermal gradient, to which the neck is normally exposed, was simulated during the tests by immersing the specimen in liquid nitrogen and exposing the part which touched the outer portion of the tank wall to heat lamps. Summaries of both static and fatigue test results, as well as the experimentally determined S-N curves, are presented in Figs. 7, 8, and 9 for the hook, strap, and neck, respectively.

Stress Analyses

A static stress analysis was performed to (1) obtain confidence in the design prior to initiating the tests, (2) gain an understanding of the stress distributions in areas of discontinuities to better interpret component test results, (3) provide a basis for component design improvement if required, and (4) insure that, with the expected random loading, a 3σ peak strap load did not exceed the allowable yield load which would have relaxed the strap pre-tension load.

The complex stress distribution occurring at the intersection of the sphere neck and the hydrogen tank wall, where steep stress gradients exist, was analyzed by use of photoelastic techniques [5]. Two three-dimensional full scale epoxy models of the structure were subjected to moment, shear, and axial load combinations to simulate design conditions. The birefringent plastic model "freezes" the

COMPONENT   MATERIAL 2014-T6

ULTIMATE STRENGTH

TEMP F	LOAD LB
70	2470. 2580
-320	2840. 3060
-423	3100. 3450. 3460

FATIGUE LIFE

TEMP F	LOAD LB	CYCLES N
-423	1200±700	11.200 15,000

MATERIAL COUPONS

CENTRAL HOLE STRESS RISER

S-N CURVES

Pm = STEADY STATE HOOK LOAD
— · — Pm = 1200 LBS
— — — Pm = 925
— — — Pm = 700
——— Pm = 590

11 MATERIAL COUPON TESTS CONDUCTED IN CRYOGENIC ENVIRONMENTS TO DETERMINE SHAPE OF S-N CURVES

Fig. 7 - Results of hook component and coupon test

Figure 8

COMPONENT ULTIMATE STRENGTH   **301-¼H STAINLESS SHEET**

TEMP F	LOAD LB
-423	3215. 2500. 2395

FATIGUE LIFE

TEMP F	LOAD LB	CYCLES N
-423	1200±700	11,300
-423	700±400	NO FAILURE AT 20,000 ~
-423	700±400	NO FAILURES AT 50,000 ~ (3 SPECIMENS

MATERIAL COUPONS

S-N CURVES

• COMPONENT TESTS

LH$_2$

70°F

—·— Pm = 1200 LBS
----- Pm = 925
—— Pm = 700

MAXIMUM STRAP LOAD - LBS

N CYCLES

13 MATERIAL COUPON TESTS CONDUCTED IN CRYOGENIC ENVIRONMENTS TO DETERMINE SHAPE OF S-N CURVES

CENTRAL HOLE STRESS RISER

Fig. 8 - Result of strap component and coupon test

stresses during a controlled heating, loading, and cooling cycle. Radial and hoop boundary stresses are obtained from slices of the stress-frozen models by measuring fringe orders. Figure 10 illustrates the specimen, stress-freezing oven and loading mechanism, isochromatic fringe pattern, and the resulting stress distributions.

It should be noted that, although the neck design was considered adequate for the S-IV stage, a design improvement was desirable for a similar installation in the S-IVB stage of the Saturn IB and Saturn V vehicles. A parametric photoelastic study [6] was made to develop the required design modification. The results of the study, when compared to the photoelastic

Figure 9

COMPONENT   **MATERIAL 6061-T6**

MOMENT
RADIAL LOAD

ULTIMATE TEST (RADIAL LOAD 6300 LB)

TEMP (F)	M (IN LB)
+70 F	37.400
-320 F	38.900

CRYOGENIC FATIGUE TESTS (RADIAL LOAD 2330 LB)

SPECIMEN NO.	MOMENT (IN LB)	CYCLES N
1	12.800	10,000
1	18.000	1,195
2	12.800	19,622

MATERIAL COUPONS

S-N CURVES

LH$_2$

70°F

2,000 LH$_2$
7,200 70°F
LH$_2$

MAXIMUM MOMENT (IN. LB)

N CYCLES
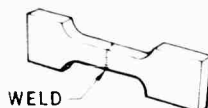
21 MATERIAL COUPON TESTS CONDUCTED IN CRYOGENIC ENVIRONMENTS TO DETERMINE SHAPE OF S-N CURVE

WELD
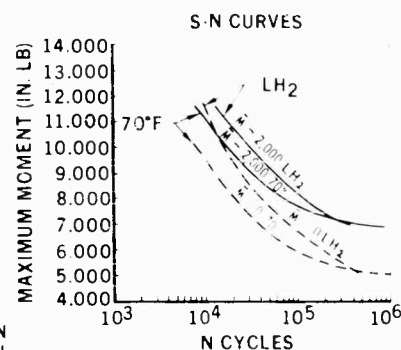
Fig. 9 - Result of neck component and coupon test

TEST SPECIMEN

ISOCHROMATIC FRINGE PATTERN

STRESS FREEZING TECHNIQUE
STRESS DISTRIBUTION DUE TO MOMENT AND SHEAR LOAD
(5.33 IN. LB MOMENT, 1.50 LB SHEAR)
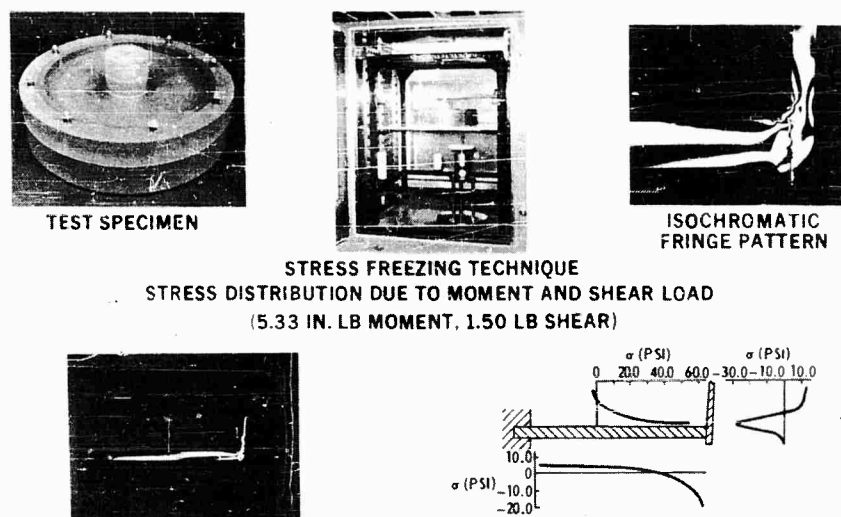
Fig. 10 - Photoelastic stress analysis of neck/wall intersection

analysis of the S-IV installation, verified the improved strength of the new design.

FATIGUE ANALYSIS

Once the allowable S-N curves for the various structural elements have been established and the vibration environment and component loads defined, a fatigue analysis can be undertaken. The analysis consists of calculating random and sinusoidal sweep S-N curves based on the results of the component tests and performing a cumulative fatigue damage analysis to predict the fatigue life of the structural system.

Calculation of Sweep and Random
  S-N Curves

Because of the various types of cyclic loading encountered (i.e., sinusoidal sweep, sinusoidal dwell, and random vibration), additional S-N curves must be developed from the constant amplitude tests as described above. Figure 11 presents an example of the three wave shapes corresponding to the response resulting from the various loadings. The sinusoidal dwell response can be seen to provide a direct correspondence with the S-N curves of the constant amplitude component test, although the responses to the sinusoidal sweep and the random excitation produce different amounts of fatigue damage.

Miner's cumulative damage theory is used to establish the "sweep S-N" curves and "random

S-N" curves, and for the random response a Rayliegh probability distribution of peak loads is assumed [7]. This technique is summarized in Appendix C.

Three significant points should be emphasized here. (1) The sinusoidal sweep loading produces significant fatigue damage for only that period of time during which the exciting frequency is sweeping through the bandwidth bounded by the frequencies at the half-power points of each resonance. (2) The random loading produces fatigue damage at each resonance for the full duration of the test, and the number of cycles likely to occur at any load level is predicted statistically, with the damage at each frequency being determined and accumulated. (3) The S-N curves thus determined are referenced to the peak resonant load for the sweep excitation and to the rms load for the random excitation. It should also be noted that the use of the "Rayliegh-Miner" method for random S-N curve determination has been experimentally verified within a reasonable fatigue scatter band in Refs. 8, 9, and 10 as summarized in Ref. 11.

Prediction of Fatigue Life

The cumulative damage concept (i.e., Miner's theory) is used to predict the fatigue life of each structural component. With the environment defined, the total number of cycles (n) at any referenced load level can be determined and ratioed to the expected life (N) obtained from the S-N curves. The total damage is the sum of the incremental values thus

167
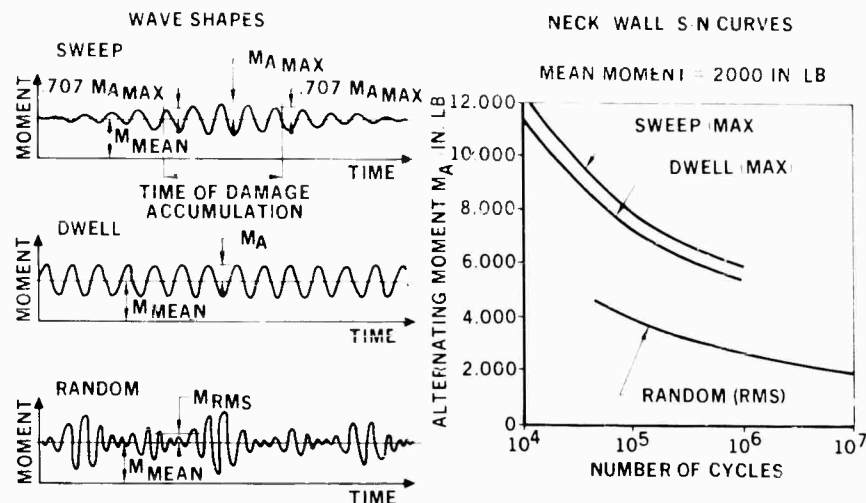
Fig. 11 - Neck/wall S-N curves for analysis
of cumulative fatigue damage

determined (i.e., $D = \Sigma(n/N)$ summed for the various axes and resonances). The details of this procedure are outlined in Appendix D.

A convenient method of presenting allowable fatigue life as well as a comparison of relative strengths of each structural component is to plot relative load vs. number of life blocks, as shown in Fig. 12. One life block is defined as a single, complete cycle of all specified loadings, whereas one relative load is defined as 100

percent of the specified loading over the complete cycle.

A margin of safety relative to load and/or life can be readily obtained from this representation. It can be seen that the strap, with a load capability of approximately 1.8 times the specified loading, is the most critical element; from a "life" standpoint it could withstand the specified loading approximately 8 times the specified load cycle. This plot also illustrates
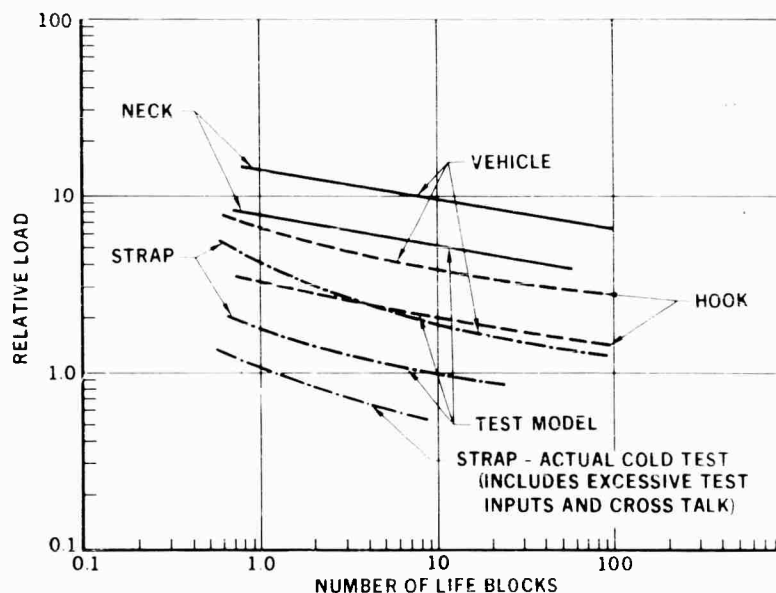
Fig. 12 - Predicted fatigue life

168

that the margin of safety for the specified flight loading is greater than that for the test environment; or, in other words, the qualification test requirements are, as one should expect, more severe than what the structural installation would be required to withstand in the flight environment.

It should be pointed out here that an additional experimental data point comparison was obtained as a result of a premature failure of one of the straps during the cold vibration qualification test. Review of the test data revealed a considerable amount of overtesting. The specification input level was exceeded by a large percentage because of the control problem, as will be explained in the following section. A post-test fatigue failure analysis, following the methods outlined above, disclosed that the strap would have been predicted to come close to failure with the excessive loads applied. The predicted strap "load-life block" curve for the actual test loading is superimposed for comparative purposes. The analytical-experimental comparison in this case is therefore within 10 percent relative to loading level (analytical procedure being on the unconservative side), which is felt to be within a reasonable tolerance for structural designs subjected to the hostile environments described.

VIBRATION QUALIFICATION TEST

The final step in assuring the flight worthiness of a system is the vibration qualification test. As cited earlier, the high cost and complexity of this test necessitates a sound analytical program to insure proper interpretation of test results and the successful completion of the test in a minimum number of runs. A brief summary of the cold helium sphere test [12] is presented to illustrate the complexity of current structural qualification test setups and the problems likely to be encountered.

Test Setup

A photograph of the test setup is shown in Fig. 13. The shaker was mounted on a reaction mass on the opposite side of the specimen. The combined test specimen and fixture weight was approximately 1000 pounds. The excitation was provided by a 50,000-pound-force hydraulic shaker. The fixture was mounted on a slip table in two of the three axes and stabilized by flexures. A 40,000-cubic-foot helium trailer with valving and pneumatic transfer lines was required for pressurizing the sphere and for the various purges. A 9,000-gallon liquid hydrogen

supply tank, together with valving and flexible vacuum-jacketed supply lines, was used to simulate the cryogenic temperatures. Elaborate fire control and hydrogen leak detection systems also were required. Special sealing techniques were employed to contain the liquid hydrogen and the entire specimen was insulated with a thick layer of foam material which had to be reapplied after each specimen inspection.

Instrumentation

Twenty accelerometers were used to measure inputs and responses of the specimen. Endevco type-2242C accelerometers were calibrated by vibrating them in liquid hydrogen prior to attaching them to the boss of the sphere. The straps were strain gaged with Budd type-C-15-624 gages which were sealed by a Douglas developed process. Excellent strain and acceleration data were obtained from the instrumentation even though it was immersed in liquid hydrogen.

Test Procedure and Results

Many preliminary test runs were made at reduced input levels to find control accelerometer locations which provided suitable control and also satisfied the intent of the specification (i.e., input defined on the skin near the neck of the sphere). An 80-channel equalizer also was used. Despite these precautions, considerable difficulty was experienced and excessive inputs and cross talk were measured at the control location. Figure 14 shows the acceleration spectral density of the inputs, cross talk, and response at the sphere boss, as measured during the thrust-axis random test. The specimen successfully withstood the random test environment in all axes and the sweep and dwell environments in the radial and tangential axes. A strap failure occurred during the sweep test in the thrust axis (last axis tested); but, as previously mentioned, the excessive loading was shown analytically to have been the cause of failure.

CONCLUSIONS

A combined analytical and experimental procedure has been presented to determine component loads and fatigue life for a complex structural system subjected to a variety of static and vibration loads.

An example has been described in which experimental comparisons were made at
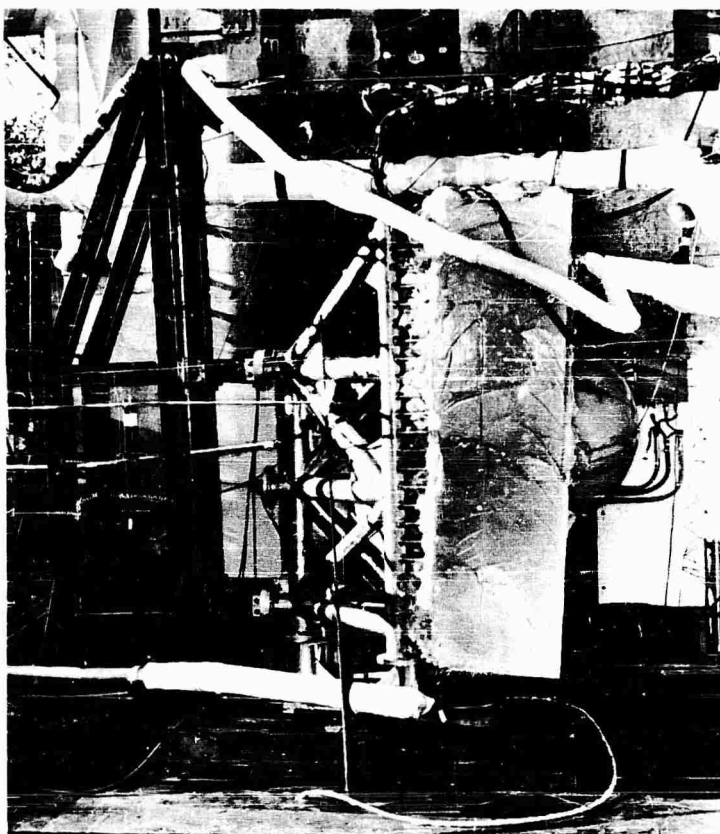
Fig. 13 - Overall view of setup
for vibration qualification test
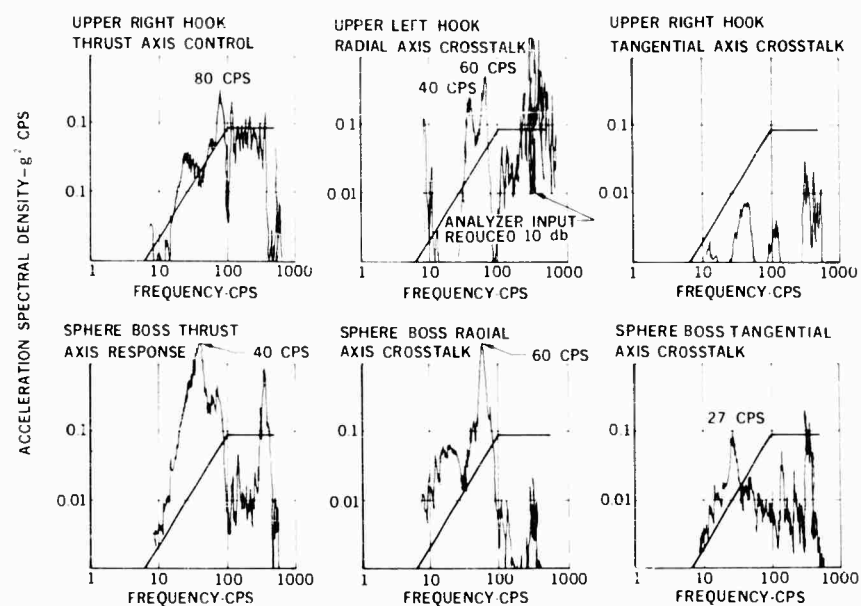
Fig. 14 - Measured inputs and responses
for thrust-axis random vibration tests

170

various stages of the analytical procedure. Reasonable agreement was obtained throughout. The example also illustrated how the analysis was used to interpret test results and to improve the design for a similar installation in another vehicle.

'Realizing that the "ultimate" test for integrity of a structural system occurs during the operational phase of a vehicle, it should be noted that the cold helium sphere installation performed satisfactorily during the recent

successful flights of the Saturn SA-5, SA-6, and SA-7 vehicles

ACKNOWLEDGMENT

Appendix A

DETERMINATION OF INFLUENCE COEFFICIENTS

The influence coefficients required for an accurate modal analysis are best determined with the use of a large digital computer. For the example illustrated in the text, the Douglas-developed "redundant force method" [13] was used. This highly automated analytical tool is used for determining stresses as well as deflections in complex, statically indeterminate structures.

The method is basically a vector and matric formulation of the "force approach," which includes the equilibrium and continuity equations with the required transformations and provides for the automatic selection of redundants by the computer. The structure is idealized and represented to the IBM 7094 computer as an array of bars, joints, and flat or warped panels. The degrees of freedom of the bars, as well as the section and material properties

of the structural elements, are indicated to the computer. The geometric locations of the structural elements are made known to the computer by a table of joint coordinates. The idealized bars along the curved panel have radial components which simulate the effects of panel curvature. For a given set of loads (thermal and/or mechanical) the redundant force program computes the displacements of a load point in the direction of the load at that point, the forces in the bars and along the panels, the external reactions, the stresses in the bars, and, if allowable stresses have been fed into the computer, the margins of safety.

To generate the influence coefficients for the sample problem in the text, it was only necessary to apply unit loads at all interior joint locations, which then resulted in the required stiffness matrices.

Appendix B

CALCULATION OF DYNAMIC LOADS AND TRANSFER FUNCTIONS

The method used to calculate the dynamic loads and transfer functions is described in detail by Fuller and Roudebush [14]. Application of the method begins with the calculation of a mass matrix $[M]$, a stiffness matrix $[K]$, an influence coefficient matrix $[K]^{-1}$, and a structural damping matrix $[B]$. For most practical applications the damping has little effect on the normal modes and frequencies and is omitted in the calculation of the eigenvalues and eigenvectors for convenience in avoiding complex arithmetic. The damping is included in the

response calculations, however, to control the amplitudes at resonance. The matrix equation for the total response of a lumped parameter system to base excitation is

$$H'(w) = -\ddot{X}_b [\gamma] \left(-w^2 [M_g] + i [B_g] \right.$$
$$\left. + [K_g] \right)^{-1} [\hat{\gamma}] [M] \{U\} . \qquad (B.1)$$

For a base input $(\ddot{X}_b)$ of unity, Eq. (B.1) yields the transfer function $H(w)$.

The parameters in the matrix equation are defined as follows:

$H'(w)$ = Total system response as a function of frequency,

$H(w)$ = Transfer function, indicating response per unit input acceleration,

$\ddot{X}_b$ = Scalar, defining basc input acceleration,

$[\gamma]$ = Matrix of desired response parameters (load, moment, etc.) of the mth degree of freedom for the nth normal mode.

w = Input frequency (radians per second),

$[M_g]$ = $[\tilde{\psi}] [M] [\psi]$ = Generalized mass matrix,

$[B_g]$ = $[\tilde{\psi}] [B] [\psi]$ = Generalized damping matrix,

$[K_g]$ = $[\tilde{\psi}] [K] [\psi]$ = Generalized stiffness matrix,

$[\psi]$ = Matrix of normal modes,

$\{U\}$ = Matrix of direction cosines between force vectors and degrees of freedom,

$[\ ]$ = Symbol for rectangular matrix,

$\{\ \}$ = Symbol for column matrix,

$[\sim]$ = Symbol for transposed matrix.

Appendix C

CALCULATION OF RANDOM AND SINE SWEEP S-N CURVES

SINE SWEEP S-N CURVES

The sinusoidal sweep S-N curves are used for evaluating the damage incurred during the logarithmic sweep testing procedure. The damage suffered by sweeping through a resonant frequency is so great, relative to other frequencies, that it needs to be evaluated only for the resonant responses. The damage done at load levels below the half-power points (i.e., $1/2\sqrt{2}$ of the response peak), is negligible. The damage done in sweeping this defined intcrval is evaluated by dividing the interval into tcn discrete response levcls, as shown in Fig. C-1, and then summing the damage associated with each level by using the dwell S-N curves. An equivalent life cxpectancy for this response sweep is thcn determined as a function of the peak response. The damage resulting from a resonance sweep is denoted by

$$D_s = \frac{n_s}{N_s} = \sum_{i=1}^{5} \frac{\frac{n_s}{5}}{N(P_i)} = \frac{n_s}{5} \sum_{i=1}^{5} N^{-1}(P_i) .$$

Since $N_i = N(P_i)$, as defined by the dwell S-N curve,

$$N_s = 5 \left[\sum_{i=1}^{5} N_i^{-1} \right]^{-1} ,$$

which is a function of the peak rcsponse, P_A.

RANDOM S-N CURVES

For the random response problem the probability of occurrence of a given peak load or stress can be predicted by the Rayliegh probability density distribution. This probability is

$$P(x) = x e^{\frac{-x^2}{2}} .$$

where

$$x = \frac{\text{peak load}}{\text{rms load}} .$$

The probability of occurrence for $(x_0 \leq x \leq x_0 + \Delta x)$ is then defined as

$$\frac{n_x}{n_R} = \int_{x_0}^{x_0 + \Delta x} P(x) \, dx ,$$

where n_R is the total number of random occurrences.

For example, the probability of the peak load exceeding the rms load (also called the standard deviation) is about 60.65 percent. The probability of its exceeding 3σ is only about 1.11 percent.

Since the frequencies of occurrence for particular load levels can be predicted

172

PARABOLIC RESPONSE ASSUMED OVER THIS INTERVAL

$1/2\sqrt{2}\,P_A$

(HALF-POWER POINT)

P_A

$P_1 = 0.997\ P_A$
$P_2 = 0.974\ P_A$
$P_3 = 0.927\ P_A$
$P_4 = 0.857\ P_A$
$P_5 = 0.763\ P_A$

n_s CYCLES
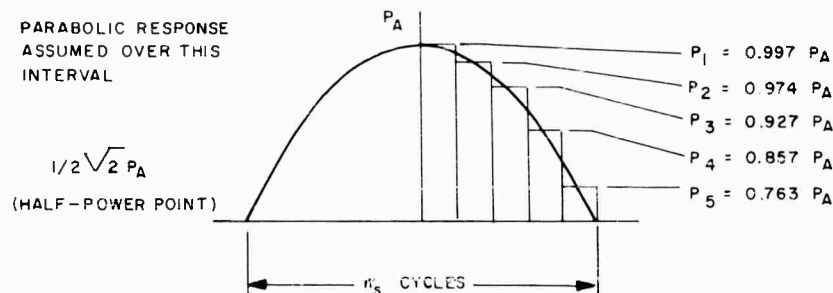
Figure C-1

statistically, then the damage too can be predicted statistically as follows:

$$D_R = \frac{n_R}{N_R} = n_R \int_0^\infty \frac{P(x)}{N(x)}\ dx \ .$$

where $N(x)$ is, for any particular rms load, a function of P_i and therefore defined by the dwell S-N curve.

$$N_R = \left[\int_0^\infty \frac{P(x)}{N(x)}\ dx \right]^{-1} ,$$

which is a function of the rms load.

For the dwell S-N curves used in this analysis, the integral given above is highly convergent. Therefore, its evaluation is carried out by a Fortran 7090 digital computer program. The program evaluates the integral

$$\int_0^P \frac{P(x)}{N(x)}\ dx$$

for larger and larger P, until further damage contributions become negligible.

Appendix D

PREDICTION OF FATIGUE LIFE

THEORETICAL RANDOM RESPONSE

Responses to random vibration inputs are best described in terms of power spectral densities (PSD's). The response PSD's are determined by multiplying the input PSD's by the square of the transfer function. The areas under these curves then, by definition, represent the mean square random responses. The random rms load is then the square root of these areas. For the cases considered in this analysis, the areas were most conveniently determined by the following expression [15]:

$$P_{rms}^2 = \frac{(TF)\,w_n\,S_o}{4} ,$$

where

$(TF) = \dfrac{w_n}{\Delta w_n} = \dfrac{f_n}{\Delta f_n} =$ Transfer function at resonance (strap load per g),

$w_n =$ Resonance frequency $(2\pi f_n)$,

$S_o =$ Mean square acceleration spectral density of the input. Also,

$S_x(max) = (TF)^2 S_o =$ Mean square spectral density of the strap load,

173

which, when substituted into the preceding equation, yields

$$P_{rms} = \sqrt{\frac{\pi}{2} f \wedge S_x(max)} = 1.253 \sqrt{\wedge f \, S_x(max)} .$$

THEORETICAL SWEEP RESPONSE

The theoretically derived response loads developed during the sinusoidal sweep tests were determined by multiplying the environmental sweep input g-levels, as defined by the qualification specifications, by the theoretical transfer functions.

PREDICTED DAMAGE DURING RANDOM TESTING

During random testing a complete spectrum of input frequencies are applied simultaneously, which results in the structure responding at its resonant frequencies. The number of cycles, n, is therefore dependent on the resonant frequencies, f_n (cps), and the test duration, which was five minutes per axis for these tests. Therefore

$$n = 5(60) \, f_n = 300 \, f_n .$$

The rms response loads were then used with the random S-N curves to establish the allowable number of cycles, N. Finally, the damage accumulated during this test phase was predicted by

$$D = \sum_{axes} \frac{n}{N} .$$

PREDICTED DAMAGE DURING SWEEP TESTING

During sinusoidal sweep testing, the frequencies are swept at a logarithmic rate. The number of cycles, n, experienced during a logarithmic sweep (up and back) between half-power points at resonance is given for the 1-minute-per-octave sweep rate [16] employed in this test by

$$n = \frac{2(60)}{\ln 2} \, f_n \, \ln \frac{f_n + .5 \wedge f}{f_n - .5 \wedge f} = 173 \, f_n \, \ln \frac{f_n + .5 \wedge f}{f_n - .5 \wedge f} .$$

The peak response loads were used with the sweep S-N curves to establish the allowable number of cycles, N. Finally the damage accumulated during this test phase was computed by

$$D = \sum_{resonances} \frac{n}{N} .$$

PREDICTED DAMAGE DURING DWELL TESTING

During sinusoidal dwell testing, the cold helium sphere installation was subjected to 8 minutes at each of the major resonances. The number of cycles, n, experienced during the resonance dwell was then computed by

$$n = 8(60) \, f_n = 480 \, f_n .$$

The allowable number of cycles, N, was read from the dwell S-N curves as a function of the peak response loads found above. Finally, the damage accumulated during this test phase was computed as

$$D = \sum_{resonances} \frac{n}{N} .$$

TOTAL PREDICTED DAMAGE

Summing the damage due to the above-described random, sweep, and dwell loadings resulted in the total damage and thus a predicted fatigue life.

REFERENCES

1. "Structural Investigation of S-IV Cold Helium Sphere Installation," Douglas Aircraft Co. Report SM-46565 (March 1964).

2. C. Woo, "Static and Fatigue Tests of Cold Helium Sphere Retainer Hook and Strap,"

Douglas Aircraft Co. Report SM-44325 (March 1964).

3. H. Holguin, "Cold Helium Sphere Mounting Support Test at Cryogenic Temperature," Douglas Aircraft Co. Report SM-44327 (January 1964).

174

4. R. H. Christensen, "Cryogenic Fatigue Characteristics of S-IV Helium Bottle Support Components," Douglas Aircraft Co. Report SM-45862.

5. W. C. Jenkins, "Three-Dimensional Photoelastic Investigation of the Saturn DSV-IV Cold Helium Bottle Support—Liquid Hydrogen Tank Intersection," Douglas Aircraft Co. Report SM-45898 (March 1964).

6. W. C. Jenkins, "Photoelastic Investigation of the Saturn DSV-IVB Cold Helium Bottle Support—Liquid Hydrogen Tank Intersection," Douglas Aircraft Co. Report SM-47633 (May 1964).

7. A. L. Eshleman, J. D. Van Dyke, and P. M. Belcher, "A Procedure for Designing and Testing Aircraft Structure Loaded by Jet Engine Noise," ASME Paper 59-AV-48 (March 1959).

8. A. K. Head and F. H. Hooke, "Random Noise Fatigue Testing," International Conference on Fatigue of Metals—Joint Inst. of Mech. Eng. and ASME, London and New York (1951).

9. S. R. Swanson, "An Investigation of the Fatigue of Aluminum Alloy Due to Random Loading," UTIA Report No. 84 (February 1963).

10. J. R. Fuller, "Research on Techniques of Establishing Random Type Fatigue Curves for Broad Band Sonic Loading," SAE Paper No. 671C, National Aeronautical Meeting, Washington, D. C. (April 1963).

11. A. L. Eshleman and J. D. Van Dyke, "A Rational Method of Analysis by Matrix Methods of Acoustically-Loaded Structure for Prediction of Sonic Fatigue Strength," Douglas Engineering Paper No. 1922 (April 1964).

12. L. G. Smith, "LH_2 Vibration Qualification Test of Cold Helium Sphere," Douglas Aircraft Co., Report SM-46639.

13. P. H. Denke, "A Matrix Method of Structural Analysis," Proceedings of the Second U. S. National Congress of Applied Mechanics (June 1954), p. 445.

14. C. M. Fuller and D. N. Roudebush, "Analysis of Complex Structures Subjected to Random Excitation," Douglas Engineering Paper No. 3090 (October 1964).

15. S. H. Crandall, et al., Random Vibration (John Wiley and Sons, New York, 1958).

16. H. R. Spence and H. N. Luhrs, "Structural Fatigue under Combined Random and Swept Sinusoidal Vibration," JOSA, Vol. 34, No. 8 (August 1962).

DISCUSSION

Mr. Himelblau (North American Aviation): Of the three types of excitation applied, which one did you feel in general was the controlling environment: sinusoidal dwell, sine sweep, or random?

Mr. McClymonds: The sinusoidal dwell produced most of the fatigue damage.

÷　　＊　　＊

THOR 20-CYCLE LONGITUDINAL OSCILLATION STUDY*

W. F. Davis, T. F. Lynch, and T. R. Murray
Douglas Aircraft Company, Inc.
Santa Monica, California

The Thor family of launch vehicles exhibits a longitudinal instability near the end of first-stage burn time. This paper presents the results of a Douglas study initiated to define the nature of, and recommend solutions to, this problem.

The observed phenomenon is described, and the explanation is presented as it is currently known, i.e., that of a closed-loop positive-feedback system coupling the airframe, the propellant feed system, and the engine. The impact on design is discussed, and the results of various statistical studies which were used to evaluate structural margins of safety are noted.

The mathematical model is presented, and the analog simulation, as well as digital techniques which were used to evaluate it, is outlined. The methods and techniques involved in correlating model results with the flight test data are reviewed, and finally conclusions and recommendations are stated.

In addition, for those interested in the mathematics involved, two appendices are included which cover the model derivation and the development of a more complex set of pump-engine transfer functions.

The Thor booster, when coupled with certain upper stages, demonstrates a longitudinal oscillatory instability near the end of first stage burn time. The oscillations are characterized by a build-up, maximization, and subsequent decay just prior to main engine cut-off. The vehicle oscillates in its first compression mode, which is at this time near 20 cps; hence the alternate name, the 20-cycle problem. This longitudinal instability results in higher vibration levels for the vehicle, equipment, and payload, as well as increased structural loads throughout the vehicle. This type of oscillation is evidenced by other liquid boosters, and in the case of the Titan an extensive program was initiated to lower the oscillatory g level so that it could be man-rated for the Gemini program. The Atlas also exhibits a short-duration longitudinal instability at liftoff that is attributed to a closed loop which couples the fuel pressure, thrust chamber, and structure with the ullage pressure control system.

Associated with the longitudinal oscillations are pressure fluctuations at the LOX and fuel pump inlets and the combustion chamber. Figure 1 illustrates a sample trace of the axial acceleration. The basic phenomenon, as it is commonly understood, is that of a closed-loop positive-feedback system. In the closed-loop system (Fig. 2) the oscillatory engine thrust causes a longitudinal acceleration response in the first axial mode; the acceleration in turn acts on the mass of propellants in the tanks and feedlines, causing cyclic pressure perturbations at the inlet to the propellant pumps; the system is then closed by the pressure perturbation at the pump inlets resulting in perturbations of the pump flow rate and thus an oscillatory engine thrust. When sufficient gain is available around the loop, such that the acceleration response to an acceleration input is larger than the input, an unstable condition exists, allowing the amplitudes of all the variables to increase in magnitude.
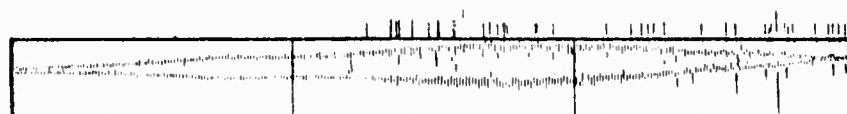
MECO – 15 SECONDS   MECO – 10 SECONDS

Fig. 1 - Sample data recording of vehicle
axial acceleration at the engine section

The characteristic buildup and decay of the oscillations may be explained by the interaction of two lightly damped resonances, one of which sweeps past the other with progressing burn time. For example, consider a system consisting of two second-order subsystems in series, as illustrated in Fig. 3.

Assume gain constant K_1 and resonant frequency ω_1 both increase with time, but let ω_2 and K_2 remain constant. Assume that at t_1, ω_1 is less than ω_2; at t_2, ω_1 is equal to ω_2; and at t_3, ω_1 is greater than ω_2. Plots of amplitude ratio and phase for the two systems are presented in Fig. 4 at these three discrete times. To determine the magnitude of the loop gain, the gains of the two subsystems are simply multiplied. To find the phase angle of the resultant feedback vector, the angles of the two subsystems are added. For the system to be unstable, since it has positive feedback, the magnitude of the feedback vector must be greater than one at a phase angle of zero degrees. At time t_1 there is not enough gain for instability. At t_2, however, where $\omega_1 = \omega_2$, the gain is greater than one, the phase angle is zero degrees, and the system is divergent. At

t_3 there is even more gain, but the phase angle has shifted 90 degrees, and the zero phase gain is reduced. Thus the system is again stable.

In the Thor-Agena vehicle, the dynamic characteristics of the first compression mode provide one of the lightly damped resonances. (Structural damping is on the order of 1 to 3 percent critical.) The structural gain and the resonant frequency increase rapidly with burn time because of decreasing vehicle mass. The second required resonance is contained in the response of the propellant pump inlet pressure to oscillatory accelerations. The concept of an acoustical resonance (organ pipe mode), a mass of fuel coupled with a spring consisting of cavitation bubbles or a coupling of both types, serves equally well to explain a second-order lightly damped system which will describe the perturbation response. The system may then be viewed similarly to the simple system previously discussed. With the pressure response resonance fixed, for example at 20 cps, and the structural resonance following the prescribed increase of frequency with increasing burn time, the interaction of these two resonances may be investigated. Since for any realistic
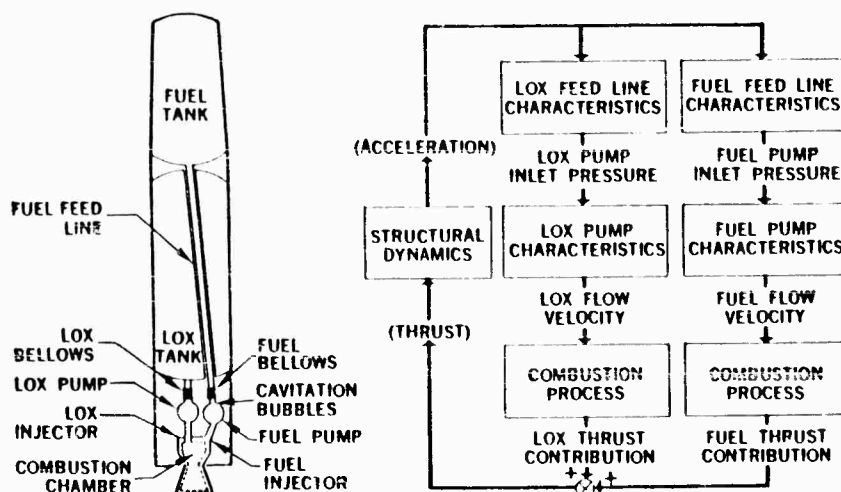
Fig. 2 - Propellant transfer functions

178
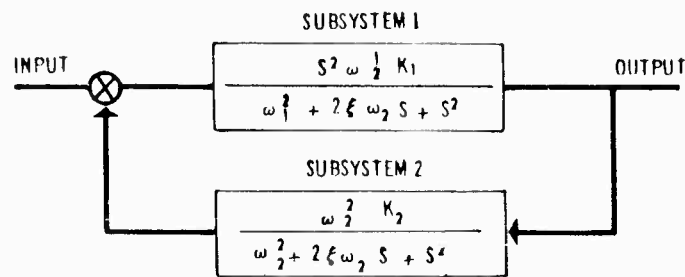
Fig. 3 - Closed-loop positive-feedback system

pump gain (the reasoning behind this will be discussed later) the inlet line resonances have considerably more damping than the structure, the loop frequency tends to stay very close to the structural resonance. Early in time, the structural frequency is well below 20 cps, and the vehicle mass is large, so that the system response, which is a function of the product of these two resonances, is small. In this case, both the response from the 20-cps resonance and the acceleration response of the structure are small. As the burn time progresses toward 140 seconds, the Thor-Agena structural frequency approaches 20 cps, and the system response increases very rapidly. When both resonances are at 20 cps, the product of their respective gains becomes quite large at zero

phase and is sufficient for instability. Toward the end of burn time, the structural resonant frequency is above 20 cps so that the magnitude of the pressure perturbation response has fallen off sharply, and significant lag exists to result in a decreased system response and hence a return to stability.

This concept of the interaction of two lightly damped resonances may be used to explain the low-level oscillation of the Thor-Delta vehicle. The important difference in this regard between the Thor-Agena and the Delta is that the Delta is a lighter vehicle and has a higher structural frequency and a lower structural gain than does the Thor-Agena at a comparable flight time. The result of the higher
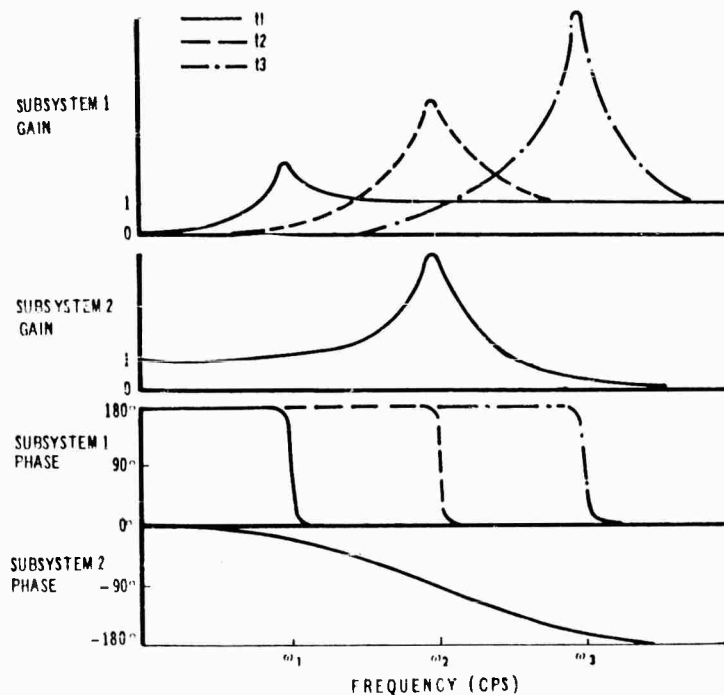
Fig. 4 - Frequency response for sample subsystem

179
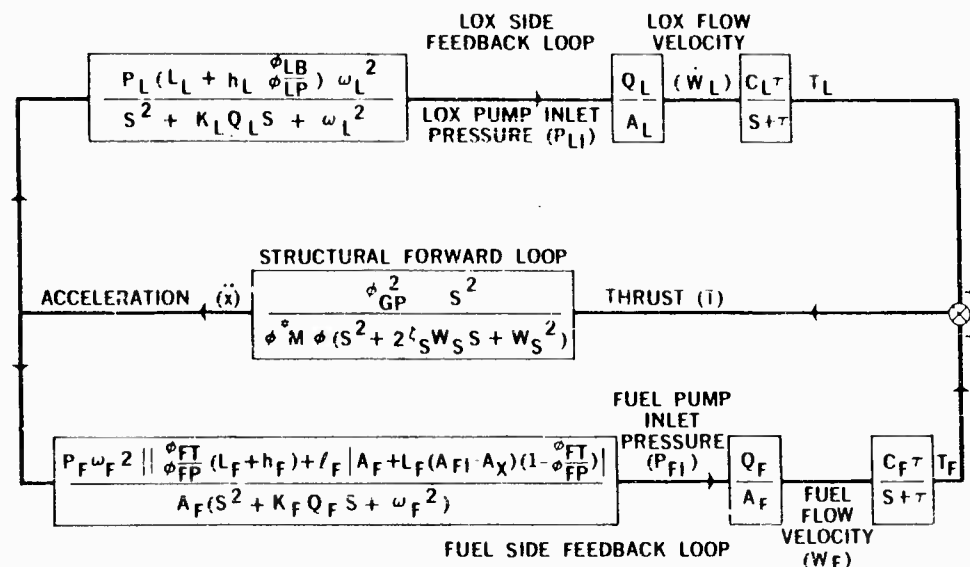
Fig. 5 - Block diagram of mathematical model

structural frequency throughout flight is that the coalescence of the structural resonance with the pressure perturbation resonance (20 cps) occurs considerably earlier in flight when the vehicle structural gain is still too small for an instability condition to exist. Thus the system will display somewhat the same gain buildup and decay as does the Thor-Agena, but earlier in flight and with insufficient gain for instability.

Figure 5 illustrates the simplified block diagram of the mathematical model which is based upon one proposed by E. D. Calkin in March of 1961. (Appendix A presents the derivation of the various transfer functions.) Comparisons of this model and more recently developed models will be made subsequently. The structural equation describes the acceleration response at the engine gimbal block to a thrust input of the gimbal block for the first axial mode. Any other modes considered important may be included by putting their transfer function in parallel with that of the first mode.

The feed lines provide, as mentioned previously, a mass of fuel and either an acoustic resonance or a vapor bubble acting as a spring. The propellant pump gain introduces damping by pumping compressed fluid (or vapor and fluid) out of the line and hence takes energy out of the feed line system.

The pump itself is considered to be a flow device, that is, the flow out (in the 20-cps range) is proportional to the inlet pressure and totally insensitive to the discharge pressure. This type of pump model was needed for two main reasons: (1) little information was available on pump behavior in an environment of heavy cavitation and rapidly changing inlet pressures, and (2) the discharge line pressures had not been monitored on flights so that no comparison between model results and flight data could be made.

In the combustion chamber the slight mixture ratio effect is neglected, and the thrust is considered to be proportional to the oscillatory flow of LOX and fuel independently. There is a first-order lag which at present has a time constant of 0.0027 seconds. This is included because no thrust perturbation will be observed if the period of the oscillations is much less than the time required for a propellant particle to travel through the chamber and out the nozzle. For example, consider that 20 pulses of fuel are injected into the chamber during the time it takes for the first pulse to burn and exit through the nozzle. Because of normal molecular activity and the circulation in the combustion chamber, these pulses will mix with each other, resulting in, if any at all, very-low-amplitude thrust oscillations. System stability is profoundly affected by small changes in structural damping, LOX and fuel feed line resonant tuning, LOX and fuel pump gains, and the combustion lag.

In order to gain a feeling for the ranges of these parameters for which the instability would occur, root locus plots were made. The dc gain could be calculated at any time, and then

the poles and zeros could be moved such that the desired stability (or instability) could be obtained, always, of course, with the reasonable or intuitive bounds of the parametric values in mind.

Once these parametric limits were established, an analog simulation covering the critical flight time was used to evaluate the various combinations. The time-varying analog system proved to be valuable in determining the shape of the oscillatory envelope and in comparing flight test parameter ratios with model parameter ratios, however, it has certain limitations that should be noted. Since the equations are linear, the oscillatory amplitude is proportional to the noise level at the onset of instability, and unless extremely high signal-to-noise equipment is used the amplitude becomes nearly random. The time-varying analog model could be stopped at any time of interest, and the gain margin could be calculated. This "time slice" technique can give meaningful parameter ratios,

however, only at the instant when the time-varying model is at marginal stability. This is because at any other condition the input to any given transfer function is either getting larger or smaller every cycle. Hence, no definite relationship exists between input and output. While the time-varying analog technique is valuable, and probably necessary, for gaining a "ballpark" understanding of the problem and its general trends, it has two significant drawbacks. First, it gives no insight into whether the system is gain stabilized or phase stabilized unless an additional lag and/or lead is added that may be changed without changing gain, and, second, a large number of manhours is required for data reduction.

For these reasons, a digital program was written to predict gain margin and amplitude ratios. Figure 6 presents a plot of gain vs flight time for a particular set of parameters. Again as with the analog, the amplitude ratios are meaningful only at a gain of one.

ω_F = 20 CPS $\quad$ ξ_F = 20% C/C_c

ω_L = 40 CPS $\quad$ ξ_L = 4% C/C_c

$\frac{\omega}{r}$ = 126 (−45° 20 CPS)

ξ = 1.3% C/C_c
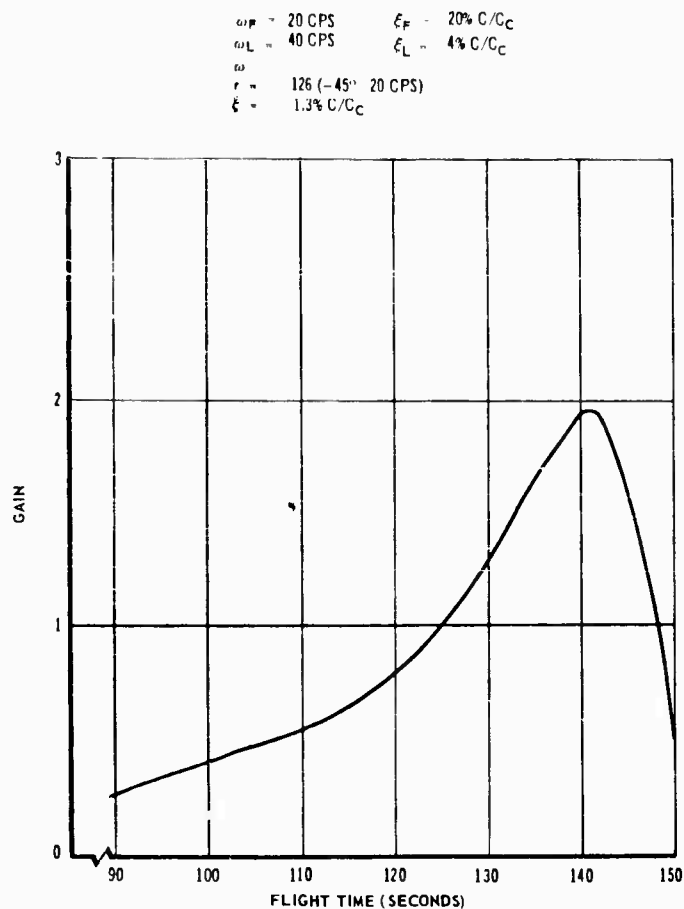
Fig. 6 - Open loop gain at zero phase

181

To understand the system characteristics further, a program was used to apply the Nyquist criterion. Figure 7 presents Nyquist plots (amplitude vs frequency for the open loop) for three system conditions: the gain-stabilized loop, a phase-stabilized loop, and an unstable loop.

a GAIN STABILIZED

b PHASE STABILIZED

c UNSTABLE

Fig. 7 - Nyquist plots

(a) STABLE SYSTEM

(b) UNSTABLE SYSTEM
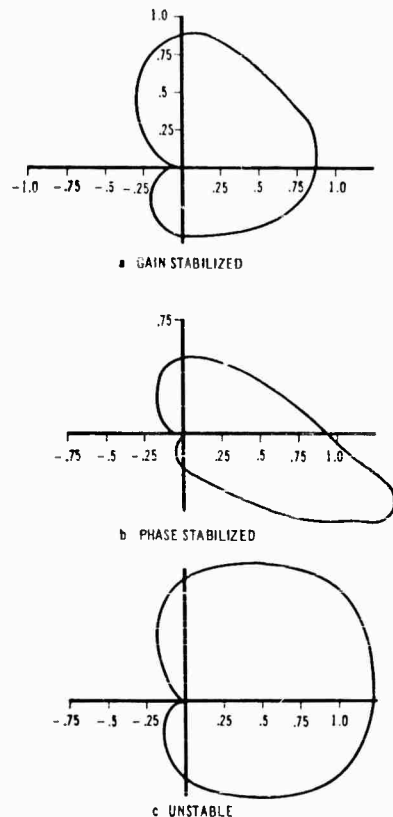
Fig. 8 - Nyquist plots

Because it is most difficult to pin down the phase shifts in the system, it is desirable to achieve gain stabilization. The dangers of phase stabilization are illustrated in Fig. 8. Figure 8(a) is a Nyquist plot of a system that is stable and has a zero phase gain of only 1/2. If this gain were found by the conventional analog techniques, the system would appear quite stable. If just a 10-degree lag is added, however, as illustrated in Fig. 8(b), the system is divergent. This critical phase stabilization has been found on both the Thor and Titan, and any attempt to stop these oscillations must take this into account, for the addition of just a few degrees of lead or lag can, as illustrated above, significantly affect the system stability.

At present other contractors associated with Thor and Titan programs have used a more complex pump model than the one utilized by Douglas for the majority of our investigations. Figure 9 presents a block diagram of this more complex system. (Appendix B presents the derivation of the equations.) Note that the pump is now considered to be a bilateral pressure device. The pump characteristics are taken from steady-state curves of change in head for change in inlet pressure at constant flow and change in head vs change in flow at constant pressure. Utilization of these steady-state characteristics is very suspect, however, as there is little reason to believe a cavitating pump in such a dynamic environment behaves as it would in steady flow. Rocketdyne, in an attempt to better define the system, has done extensive work with nonlinear pump gains and flow characteristics, but at the present time available results are not definitive enough to be included here. These pump equations (excluding nonlinearities) were investigated extensively; it was found that for the particular Thor configuration, in the neighborhood of 20 cps, the transfer function from pump inlet pressure to chamber pressure had similar amplitude ratios to the simpler "flow device" pump; however there was some, possibly significant, additional lag introduced that was due primarily to the inclusion of the mass of fuel in the discharge line. Note also the inclusion of pump inlet pressure times pump inlet area feedback term. This term was found to be of importance in the Titan phenomena.

These pump equations were never included in the complete Douglas stability model, and it

182
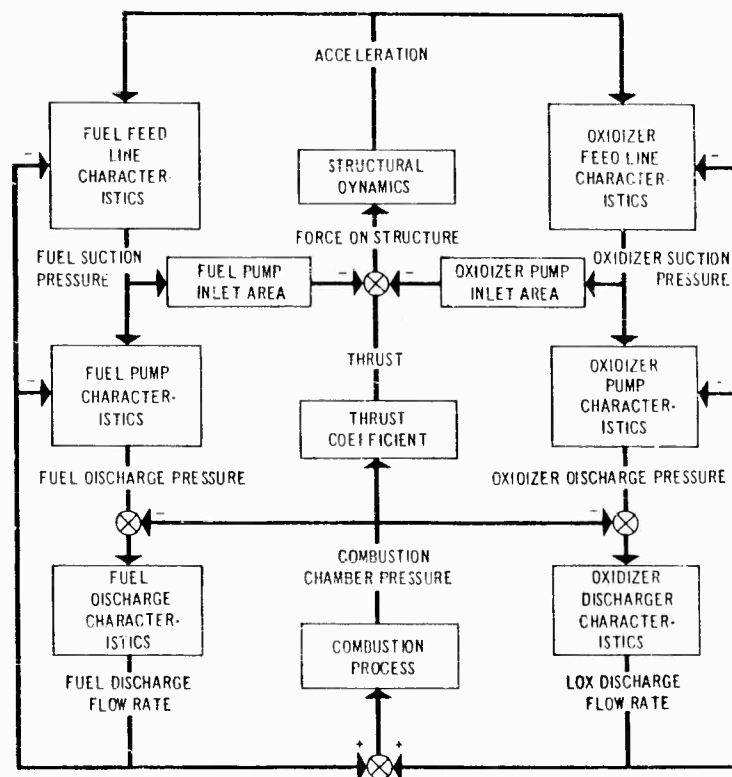
Fig. 9 - Block diagram of a more complex system

would appear that they do not significantly change the Thor model. This equivalence would almost certainly not exist for other configurations. Thus, for future work, the use of the complex equations and, if available, any significant new pump data is recommended. It should be pointed out that these equations, along with an extensive test program, led to a successful fix and virtual elimination of the Titan problem.

On several Thor-Agena flights the oscillation amplitudes have been large enough to endanger the Thor structure. (On one flight 10.5-g p-p were measured in the engine section.) An examination of flight test data from some 60 or 70 flights revealed a correlation between configuration and oscillation amplitude. Figure 10 presents a plot of boosted weight vs acceleration level. A statistical study was initiated in which this data were used in an attempt to predict failure probabilities.

A parameter β,

$$\frac{\text{(Thor boosted weight)}}{\text{(peak-to-peak g's at engine section)}} ,$$

was hypothesized to be normally distributed. This hypothesis was subjected to a chi-square test and found to be acceptable. By utilizing this parameter, the probability of exceeding any given load at any given station could be predicted. Figure 11 presents these probabilities for a boosted weight of 17,200 pounds.

The allowable load at any station is a function of tank pressure, skin temperature, material properties, and flight trajectory, all of which have associated probabilities. If these allowables are treated statistically, the probability of a structural failure is quite low for a boosted weight of 17,200 pounds. For any configuration the phenomenon of structural damping must be considered, since in a riveted structure the damping will almost certainly increase with increased structural deflections and thus, for high amplitude oscillations, the system may limit cycle before failure. Propellant flow oscillations also may limit cycle when pressure perturbations become exceedingly large. Thus, while the inclusion of these non-linearities make problem solution much more difficult, in terms of the structure, they may be saving graces.

183
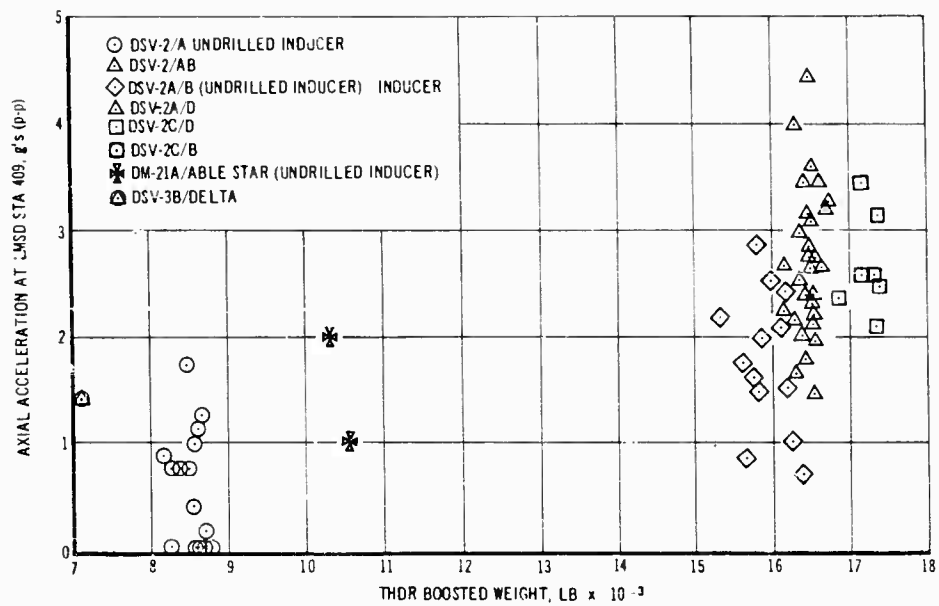
Fig. 10 – Amplitude of longitudinal accelerations
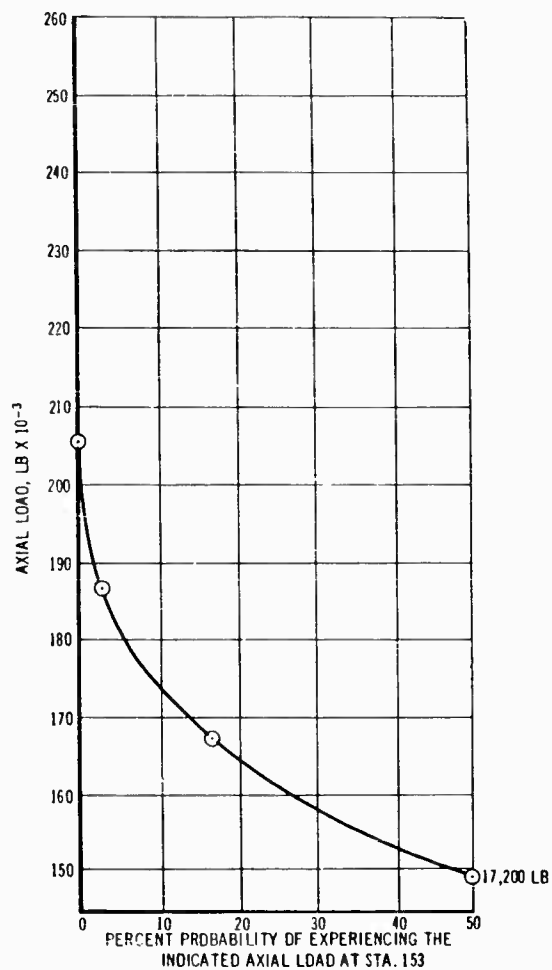
Fig. 11 - Allowable axial loads at station 153 (fuel tank) and percent probability of experiencing a given axial load (Thor boosted weight = 17,200 pounds)

As a result of present investigations, it appears that the fuel feed line has a greater influence on the system stability than the LOX feed line. If the elasticity of the feed line walls, as well as that of the fuel, is considered, it can be shown that the first open-closed organ pipe mode would be 22 cps. For this reason, efforts to alleviate or eliminate the oscillation have been directed primarily toward the fuel side. One device investigated was a constant-volume bellows inserted in the fuel feed line immediately upstream from the pump. This device, illustrated in Fig. 12, maintains a constant feed line volume when there is a relative motion between the tank bottom and the pump. The pressure at the pump inlet would be

$$P_{inlet} = \rho h \ddot{X},$$

where ρ is the density, h is the column height, and $\ddot{X}$ is the acceleration. The inclusion of an ideal constant-volume bellows effectively lowers h from more than 20 feet (the feed-line length) to a few inches, since none of the fluid above the centerline of the bellows would be displaced when the pump moves.

The constant volume bellows, when included in the stability model, significantly lowers the loop gain. There are, of course, certain problems that must be considered, the main one being our uncertainty as to the natural resonant frequencies of the feed lines. Several "worst cases" were studied, but in no case did the bellows worsen the instability. There are, of course, several other proposed and existing fixes. The Titan II utilizes a standpipe on one line and a mechanical accumulator on the other. Small gas-filled bags which may be installed in the lines to lower the first resonant frequency and raise the second frequency are being studied for use on Titan III. Size and initial bag-fill pressure can be regulated such that no dangerous resonance can exist. The use of varied
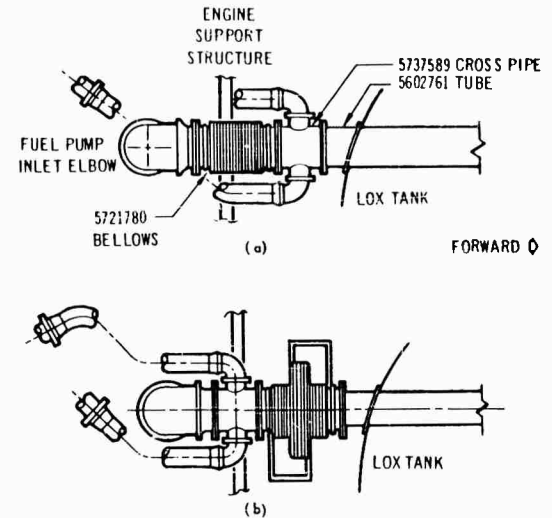
Fig. 12 - Device to maintain constant feedline volume: (a) present configuration, (b) proposed pressure compensating bellows showing constant volume linkages

materials for the induction lines can put organ pipe modes out of dangerous ranges. A hardware fix for the Thor will consider all these possibilities.

In conclusion, it should be noted that there is still much work being done throughout the industry in order to gain a better understanding of this problem. A study contract has been granted to synthesize the various company efforts and techniques with the objective of developing a mathematical model which would be applicable to all present vehicles and serve as a useful design tool for future vehicles. With the increasing size of boosters and the continuing efforts to put men into space, the problem is vital for current use and future design and development of spacecraft boosters.

Appendix A

Presented here is the complete derivation of the mathematical model (Fig. A1) used to study the Thor-Agena instability. A number of assumptions were required in its development; the following are the more important:

1. Vehicle acceleration occurs in its first axial mode; contributions from rigid body and higher mode dynamics are negligible.

2. The propellants are incompressible.

3. The propellant suction lines have negligible flow resistance.
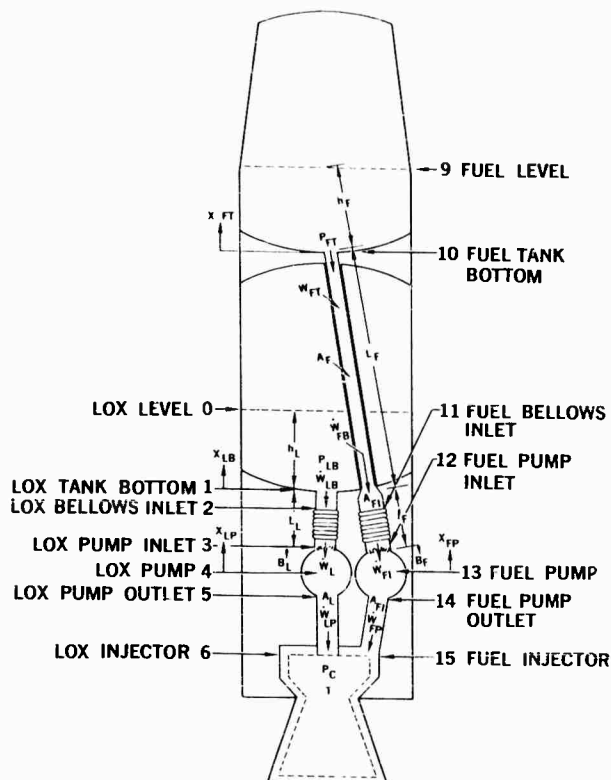
Fig. A1 - Nomenclature diagram

4. Cavitation vapor bubbles form on the pump impeller blades and act as a spring on which the supported column of propellant may oscillate.

5. Because of the cavitation bubbles formed, the pumps act as flow devices rather than pressure devices. Thus the pump discharge velocity is proportional to the inlet pressure and insensitive to the discharge pressure.

6. A first order lag exists between the flow into the combustion chamber and the attendant oscillatory thrust thus developed.

With these assumptions utilized along with Newton's Law for pressure relations, continuity for flow relations, and spring-mass dynamics for the bubble description, and the vehicle response, the following pages present the derivation of the Douglas Longitudinal Oscillation Model culminating in the block diagram of transfer functions shown in Fig. 5.

LOX SYSTEM EQUATIONS

The continuity equation between 1 and 3 can be written as the difference in flow between points 1 and 3 and is equal to the bellows extension between points 2 and 3,

$$\dot{W}_{LT} A_L - \dot{W}_{L1} A_L = \dot{X}_{LB} A_L - \dot{X}_{LP} A_L$$

$$\dot{W}_{LT} - \dot{W}_{L1} = \dot{X}_{LB} - \dot{X}_{LP} .$$

By rearranging terms

$$\dot{W}_{LT} - \dot{X}_{LB} = \dot{W}_{L1} - \dot{X}_{LP} .$$

186

The structural mode relationship between points 1 and 3 is

$$X_{LB} = \frac{\phi_{LB}}{\phi_{LP}} X_{LP} .$$

By substituting for X_{LB} in the continuity equation,

$$\dot{W}_{LT} - \dot{W}_{L1} = \left(\frac{\phi_{LB}}{\phi_{LP}} - 1 \right) \dot{X}_{LP} . \tag{A1}$$

Consider the mass of fluid in the feed line, the acceleration of the mass, and the pressures on the mass.

$$\rho_L (L_{LT} + \ell_L) (\ddot{W}_{L1} - \ddot{X}_{LP}) = P_{LB} - P_{L1} ,$$

where

$$\ell_L = \ell_o + (X_{LB} - X_{LP}) = \ell_o + \left(\frac{\phi_{LB}}{\phi_{LP}} - 1 \right) X_{LP} .$$

In substituting for ℓ_L,

$$\rho_L \left[(L_{LT} + \ell_o)(\ddot{W}_{L1} - \ddot{X}_{LP}) + \left(\frac{\phi_{LB}}{\phi_{LP}} - 1 \right) (\ddot{W}_{L1} + \ddot{X}_{LP}) X_{LP} \right] = P_{LB} - P_{L1} .$$

Neglecting second order terms and letting

$$(L_{LT} + \ell_o) = L_L ,$$

the previous equation becomes

$$\rho_L L_L (\ddot{W}_{L1} - \ddot{X}_{LP}) = P_{LB} - P_{L1} . \tag{A2}$$

Cavitation can be expressed as a bubble having a bulk modulus K_L and a volume $A_L B_L$,

$$P_{L1} = K_L A_L B_L . \tag{A3}$$

Flow from the LOX pump is written as a function of the inlet pressure

$$\dot{W}_{LP} = \frac{\phi_L}{A_L} P_{L1} , \tag{A4}$$

where ϕ_L is the pump gain.

The continuity equation between points 1 and 5 is now written. The difference in flow into the feed system and out of the pump is the sum of volume changes due to bellows extension and cavitation bubble compression,

$$\dot{W}_{LT} - \dot{W}_{LP} = \dot{B}_L + \left(\frac{\phi_{LB}}{\phi_{LP}} - 1 \right) \dot{X}_{LP} . \tag{A5}$$

The LOX tank bottom pressure can be written as

$$P_{LB} = \rho_L h_L \ddot{X}_{LB}$$

187

or, more desirably, as

$$P_{LB} = \rho_L h_L \frac{\phi_{LB}}{\phi_{LP}} \ddot{X}_{LP} .$$

By substituting for P_{LB} in Eq. (A2),

$$\rho_L L_L (\ddot{W}_{L1} - \ddot{X}_{LP}) = \rho_L h_L \frac{\phi_{LB}}{\phi_{LP}} \ddot{X}_{LP} - P_{L1} .$$

By rearranging terms,

$$\rho_L L_L \ddot{W}_{L1} + P_{L1} = \rho_L \left(L_L + h_L \frac{\phi_{LB}}{\phi_{LP}} \right) \ddot{X}_{LP} . \tag{A6}$$

Equations (A1) and (A3-A6) are now combined in matrix form:

$$
\begin{bmatrix}
0 & 1 & 0 & 0 & -1 \\
1 & 0 & 0 & -K_L A_L & 0 \\
-\frac{Q_L}{A_L} & 0 & 1 & 0 & 0 \\
0 & 1 & -1 & -S & 0 \\
1 & 0 & 0 & 0 & \rho_L L_L S
\end{bmatrix}
\begin{vmatrix}
P_{L1} \\
\dot{W}_{LT} \\
\dot{W}_{LP} \\
B_L \\
\dot{W}_{L1}
\end{vmatrix}
=
\begin{bmatrix}
\frac{\phi_{LB}}{\phi_{LP}} - 1 \\
0 \\
0 \\
\frac{\phi_{LB}}{\phi_{LP}} - 1 \\
\rho_L \left(L_L + h_L \frac{\phi_{LB}}{\phi_{LP}} \right) S
\end{bmatrix}
\dot{X}_{LP} .
$$

The transfer function LOX-pump inlet pressure to LOX-pump velocity can be solved from the above matrix equation.

$$
\frac{P_{L1}}{\dot{X}_{LP}} =
\begin{bmatrix}
\frac{\phi_{LB}}{\phi_{LP}} - 1 & 1 & 0 & 0 & -1 \\
0 & 0 & 0 & -K_L A_L & 0 \\
0 & 0 & 1 & 0 & 0 \\
\frac{\phi_{LB}}{\phi_{LP}} - 1 & 1 & -1 & -S & 0 \\
\rho_L \left(L_L + h_L \frac{\phi_{LB}}{\phi_{LP}} \right) S & 0 & 0 & 0 & \rho_L L_L S
\end{bmatrix}
\Bigg/
\begin{bmatrix}
0 & 1 & 0 & 0 & -1 \\
1 & 0 & 0 & -K_L A_L & 0 \\
\frac{-Q_L}{A_L} & 0 & 1 & 0 & 0 \\
0 & 1 & -1 & -S & 0 \\
1 & 0 & 0 & 0 & \rho_L L_L S
\end{bmatrix}
$$

$$
\frac{P_{L1}}{\dot{X}_{LP}} = \frac{\rho_L K_L A_L \left(L_L + h_L \frac{\phi_{LB}}{\phi_{LP}} \right) S}{\rho_L L_L \left(S^2 + K_L Q_L S + \frac{K_L A_L}{\rho_L L_L} \right)} .
$$

Let

$$\frac{K_L A_L}{\rho_L L_L} = \omega_L^2 = \text{LOX feed line cavitation resonance.} \tag{A7}$$

Then

$$\frac{P_{L1}}{\ddot{X}_{LP}} = \frac{\rho_L \left(L_L + h_L \frac{\phi_{LB}}{\phi_{LP}}\right)\omega_L^2}{S^2 + K_L Q_L S + \omega_L^2} . \tag{A8}$$

The transfer function of thrust to LOX pump outlet fluid velocity $\dot{W}_{LP}$ is given as

$$\frac{T}{\ddot{W}_{LP}} = \frac{C_L \tau}{S + \tau} , \tag{A9}$$

where τ is the combustion lag and C_L is the gain. Now Eqs. (A4), (A8), and (A9) can be combined to form the transfer function of thrust to LOX pump acceleration, which is the total transfer function for the LOX side of the engine system.

$$\frac{T}{\ddot{X}_{LP}} = \frac{P_{L1}}{\ddot{X}_{LP}} + \frac{\dot{W}_{LP}}{P_{L1}} + \frac{T}{\dot{W}_{LP}} . \tag{A10}$$

Equation (A10) in block diagram notation looks like this:
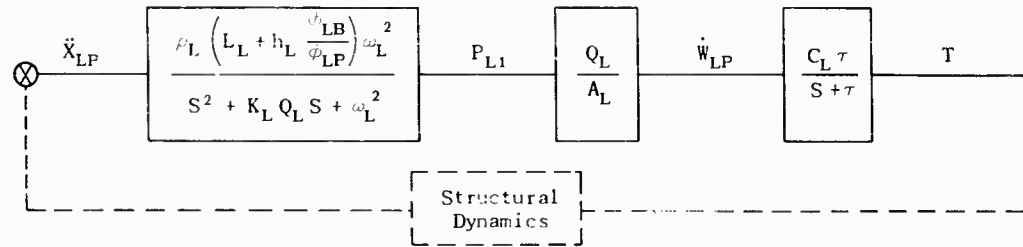
To complete the block diagram, the structural block must be derived.

STRUCTURAL EQUATIONS

For perturbation effects, only longitudinal vibration modes need be considered; rigid body equations are excluded from the analysis. The first mode longitudinal acceleration can be written in model coordinates as

$$\ddot{X}_{LP} = \phi_{LP} \ddot{A}_1 . \tag{A11}$$

The mode dynamic equation is

$$\phi^* M \phi \ddot{A}_1 \pm \phi^* D \phi A_1 + \phi^* K \phi A_1 = \phi_{GP} T . \tag{A12}$$

Equation (A12) can be solved for the transfer function modal acceleration to thrust, yielding

$$\frac{A_1}{T} = \frac{\phi_{GP} S^2}{\phi^* M \phi (S^2 + 2\xi_S \omega_S S + \omega_S^2)} , \tag{A13}$$

189

where

$$W_s = \frac{\phi^* K \phi}{\phi^* M \phi} = \text{First longitudinal mode resonant frequency,}$$

$$2\xi_s W_s = \frac{\phi^* D \phi}{\phi^* M \phi} \; ,$$

$$\xi_s = \text{First longitudinal mode damping ratio.}$$

Equations (A11) and (A13) can be combined in block diagram notation to form the structural dynamics block:
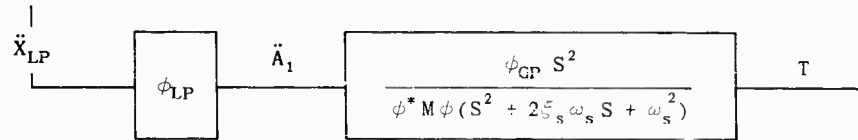
The complete block diagram combining LOX system and structural dynamics is
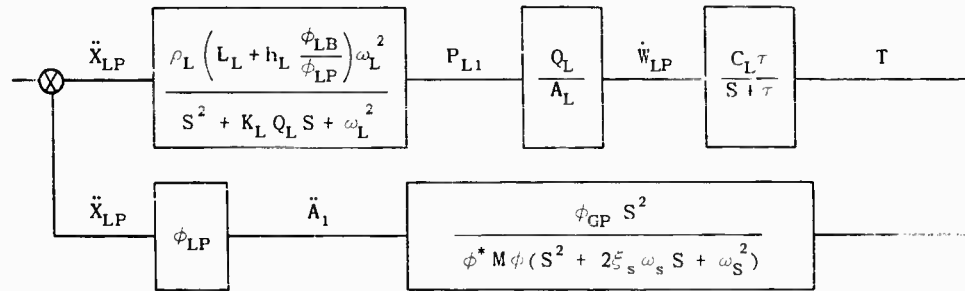
FUEL SYSTEM EQUATIONS

The continuity equation between points 10 and 11 can be written as

$$\dot{W}_{FT} A_F - \dot{W}_{FB} A_{FI} = 0$$

or

$$\dot{W}_{FB} = \frac{A_F}{A_{FI}} \dot{W}_{FT} . \tag{A14}$$

Now consider the mass of fluid in the feed line between points 10 and 11, the acceleration of the mass, and the pressures acting on the mass,

$$\rho_F L_F A_F (\ddot{W}_{FT} - \ddot{X}_{FT}) = P_{FT} A_F - P_{FB} A_F . \tag{A15}$$

The pressure P_{FT} at point 10 can be written as a function of the head of fluid in the tank and the acceleration of the tank bottom,

$$P_{FT} = \rho_F h_F \ddot{X}_{FT} . \tag{A16}$$

190

The structural mode relationship between fuel tank bottom displacement and fuel pump displacement is

$$X_{FT} = \frac{\phi_{FT}}{\phi_{FP}} X_{FP} \quad \text{and} \quad \ddot{X}_{FT} = \frac{\phi_{FT}}{\phi_{FP}} \ddot{X}_{FP} . \tag{A17}$$

By substituting for $\ddot{X}_{FT}$, the pressure P_{FT} becomes

$$P_{FT} = \rho_F h_F \frac{\phi_{FT}}{\phi_{FP}} \ddot{X}_{FP} . \tag{A18}$$

Upon substitution of P_{FT} and $\ddot{X}_{FT}$ in terms of $\ddot{X}_{FP}$, the force equation, Eq. (A15), becomes

$$\rho_F L_F \ddot{W}_{FT} + P_{FB} = \rho_F \frac{\phi_{FT}}{\phi_{FP}} (L_F + h_F) \ddot{X}_{FP} . \tag{A19}$$

The continuity equation between points 11 and 12 is

$$A_{FI} \dot{W}_{FB} - A_{F1} \dot{W}_{F1} = A_{F1} (\dot{X}_{FT} - \dot{X}_{FP}) + A_X (\dot{X}_{FP} - \dot{X}_{FT}) . \tag{A20}$$

Substituting for $\dot{W}_{FB}$ and $\dot{X}_{FT}$ from Eqs. (A14) and (A17), the continuity equation, Eq. (A20), becomes

$$A_F \dot{W}_{FT} - A_{F1} \dot{W}_{F1} = (A_{F1} - A_X) \left(\frac{\phi_{FT}}{\phi_{FP}} - 1 \right) \dot{X}_{FP} . \tag{A21}$$

Now consider the mass of fluid between points 11 and 12.

$$\rho_F \left[\ell_F + (X_{FT} - X_{FP}) \right] \left[\ddot{W}_F - \ddot{X}_{FP} \right] = P_{FB} - P_{FI} . \tag{A22}$$

In substituting for X_{FT} from Eq. (A17) into Eq. (A22),

$$\rho_F \ell_F \ddot{W}_{FI} + P_{F1} - P_{FB} = \rho_F \ell_F \ddot{X}_{FP} - \rho_F \left(\frac{\phi_{FT}}{\phi_{FP}} - 1 \right) X_{FP} (\ddot{W}_{FI} - \ddot{X}_{FP}) .$$

Upon neglecting second order terms,

$$\rho_F \ell_F \ddot{W}_{F1} + P_{FI} - P_{FB} = \rho_F \ell_F \ddot{X}_{FP} . \tag{A23}$$

Cavitation can be expressed as a bubble having a bulk modulus K_F.

$$P_{F1} = K_F A_{FI} B_F$$

or

$$\dot{B}_F = \frac{\dot{P}_{FI}}{K_F A_{F1}} . \tag{A24}$$

Flow from the fuel pump is written as a function of the inlet pressure

$$\dot{W}_{FP} = \frac{Q_F}{A_{FI}} P_{FI} , \tag{A25}$$

where Q_F is the pump gain.

The continuity equation between points 12 and 14 is now written

$$A_{FI} \dot{W}_{F1} - A_{FI} \dot{W}_{FP} = A_{FI} \dot{B}_F .$$

In substituting for $\dot{B}_F$ from Eq. (A24), the continuity equation becomes

$$\dot{W}_{FI} - \dot{W}_{FP} = \frac{SP_{FI}}{K_K A_{FI}} .$$

(A26)

Equations (A19), (A21), (A23), (A25), and (A26) are now written together in matrix form

$$
\begin{bmatrix}
0 & 1 & \rho_F L_F S & 0 & 0 \\
0 & 0 & A_F & -A_{FI} & 0 \\
1 & -1 & 0 & \rho_F \ell_F S & 0 \\
-\dfrac{Q_F}{A_{FI}} & 0 & 0 & 0 & 1 \\
\dfrac{S}{K_F A_{FI}} & 0 & 0 & -1 & 1
\end{bmatrix}
\begin{bmatrix}
P_{FI} \\
P_{FB} \\
\dot{W}_{FT} \\
\dot{W}_{FI} \\
\dot{W}_{FP}
\end{bmatrix}
=
\begin{bmatrix}
\rho_F \dfrac{\phi_{FT}}{\phi_{FP}} (L_F + h_F) S \\
(A_{FI} - A_X)\left(\dfrac{\phi_{FT}}{\phi_{FP}} - 1\right) \\
\rho_F \ell_F S \\
0 \\
0
\end{bmatrix}
X_{FP} .
$$

(A27)

Solving Eq. (A27) for $P_{FI}/\dot{X}_{FP}$,

$$\frac{P_{FI}}{\dot{X}_{FP}} = \frac{\rho_F\left\{\left[\dfrac{\phi_{FT}}{\phi_{FP}}(L_F + h_F) + \ell_F\right] A_F + L_F (A_{FI} - A_X)\left(1 - \dfrac{\phi_{FT}}{\phi_{FP}}\right)\right\} S}{\dfrac{\rho_F}{K_F A_{FI}}(L_F A_{FI} + \ell_F A_F)\left[S^2 + K_F Q_F S + \dfrac{A_F A_{FI} K_F}{\rho_F (L_F A_{FI} + \ell_F A_F)}\right]} .$$

Let

$$\frac{A_F A_{FI} K_F}{\rho_F (L_F A_{FI} + \ell_F A_F)} = \omega_F^2 = \text{fuel feed-line cavitation resonance.}$$

(A28)

Then

$$\frac{P_{F1}}{\ddot{X}_{FP}} = \frac{\rho_F \omega_F^2 \left\{\left[\dfrac{\phi_{FT}}{\phi_{FP}}(L_F + h_F) + \ell_F\right] A_F + L_F (A_{F1} - A_x)\left(1 - \dfrac{\phi_{FT}}{\phi_{FP}}\right)\right\}}{A_F(S^2 + K_F Q_F S + \omega_F^2)} .$$

(A29)

If in the development of the above transfer function, cavitation is neglected, $P_{F1}/\ddot{X}_{FP}$ becomes

$$\frac{P_{F1}}{\ddot{X}_{FP}} = \frac{\rho_F \left\{\left[\dfrac{\phi_{FT}}{\phi_{FP}}(L_F + h_F) + \ell_F\right] A_F + L_F (A_{F1} - A_x)\left(1 - \dfrac{\phi_{FT}}{\phi_{FP}}\right)\right\}}{A_{F1}\left[\left(\dfrac{\rho_F (\ell_F A_F + L_F A_{F1}) Q_F}{A_{F1} A_F}\right) S + 1\right]} .$$

(A30)

The transfer function of thrust to fuel pump outlet fluid velocity $\dot{W}_{FP}$ is given as

$$\frac{T}{\dot{W}_{FP}} = \frac{C_F \tau}{S + \tau} .$$

(A31)

192

The structural mode relationship between fuel tank bottom displacement and fuel pump displacement is

$$X_{FT} = \frac{\phi_{FT}}{\phi_{FP}} X_{FP} \quad \text{and} \quad \ddot{X}_{FT} = \frac{\phi_{FT}}{\phi_{FP}} \ddot{X}_{FP} . \qquad (A17)$$

By substituting for $\ddot{X}_{FT}$, the pressure P_{FT} becomes

$$P_{FT} = \rho_F h_F \frac{\phi_{FT}}{\phi_{FP}} \ddot{X}_{FP} . \qquad (A18)$$

Upon substitution of P_{FT} and $\ddot{X}_{FT}$ in terms of $\ddot{X}_{FP}$, the force equation, Eq. (A15), becomes

$$\rho_F L_F \ddot{W}_{FT} + P_{FB} = \rho_F \frac{\phi_{FT}}{\phi_{FP}} (L_F + h_F) \ddot{X}_{FP} . \qquad (A19)$$

The continuity equation between points 11 and 12 is

$$A_{FI} \dot{W}_{FB} - A_{F1} \dot{W}_{FI} = A_{FI} (\dot{X}_{FT} - \dot{X}_{FP}) + A_X (\dot{X}_{FP} - \dot{X}_{FT}) . \qquad (A20)$$

Substituting for $\dot{W}_{FB}$ and $\dot{X}_{FT}$ from Eqs. (A14) and (A17), the continuity equation, Eq. (A20), becomes

$$A_F \dot{W}_{FT} - A_{F1} \dot{W}_{FI} = (A_{FI} - A_X) \left(\frac{\phi_{FT}}{\phi_{FP}} - 1 \right) \dot{X}_{FP} . \qquad (A21)$$

Now consider the mass of fluid between points 11 and 12.

$$\rho_F \left[\ell_F + (X_{FT} - X_{FP}) \right] \left[\ddot{W}_F - \ddot{X}_{FP} \right] = \Gamma_{FB} - \Gamma_{FI} . \qquad (A22)$$

In substituting for X_{FT} from Eq. (A17) into Eq. (A22),

$$\rho_F \ell_F \ddot{W}_{F1} + P_{F1} - P_{FB} = \rho_F \ell_F \ddot{X}_{FP} - \rho_F \left(\frac{\phi_{FT}}{\phi_{FP}} - 1 \right) X_{FP} (\ddot{W}_{F1} - \ddot{X}_{FP}) . $$

Upon neglecting second order terms,

$$\rho_F \ell_F \ddot{W}_{F1} + P_{F1} - P_{FB} = \rho_F \ell_F \ddot{X}_{FP} . \qquad (A23)$$

Cavitation can be expressed as a bubble having a bulk modulus K_F.

$$P_{F1} = K_F A_{F1} B_F$$

or

$$\dot{B}_F = \frac{S P_{F1}}{K_F A_{F1}} . \qquad (A24)$$

Flow from the fuel pump is written as a function of the inlet pressure

$$\dot{W}_{FP} = \frac{Q_F}{A_{F1}} P_{F1} , \qquad (A25)$$

where Q_F is the pump gain.

The continuity equation between points 12 and 14 is now written

$$A_{FI} \dot{W}_{FI} - A_{F1} \dot{W}_{FP} = A_{F1} \dot{B}_F .$$

191

Equations (A25), (A30), and (A31) can be combined to form the transfer function of thrust to fuel pump acceleration. The structural dynamics block is added to the fuel system to form the complete block diagram for the fuel system:
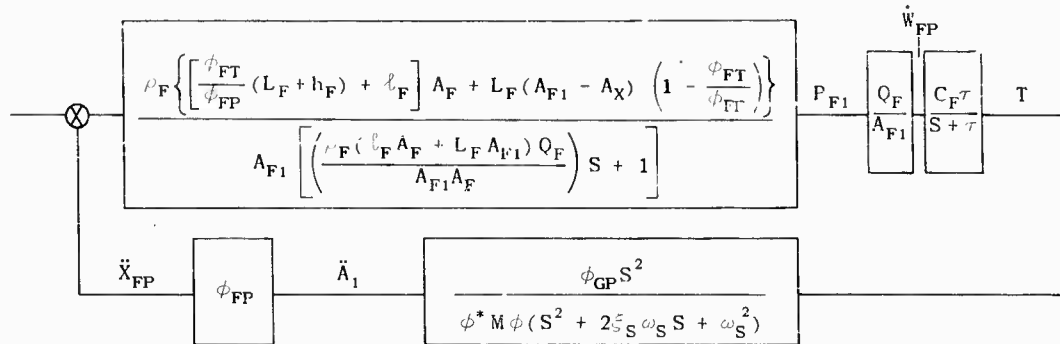
DEFINITION OF SYMBOLS

X_{FT} = Displacement of fuel tank bottom (inches)

h_F = Head above fuel tank bottom (inches)

P_{FT} = Pressure at fuel tank bottom (psi)

$\dot{W}_{FT}$ = Fuel velocity in fuel duct relative to wall (inches/sec)

A_F = Area of fuel duct (square inches)

P_{FB} = Pressure in duct above bellows (psi)

$\dot{W}_{FB}$ = Fuel velocity relative to wall above the bellows (inches/sec)

A_{F1} = Area of fuel pump inlet

$\dot{W}_{F1}$ = Fuel velocity relative to wall at the bubble (inches/sec)

P_{F1} = Fuel pressure at pump inlet (psi)

B_F = Displacement of bubble top (inches)

$\dot{X}_{FP}$ = Displacement of fuel pump

$\dot{W}_{FP}$ = Pump discharge velocity relative to wall (inches/sec)

ρ_F = Mass density of fuel (lb-secs/in.^{4})

ϕ_{FT} = Modal displacement at fuel tank bottom

ϕ_{FP} = Modal displacement of fuel pump

A_x = Area of fix (inches^2)

193

Appendix B

Presented here is the derivation of the pump-engine transfer functions of a bilateral pressure-device pump. Only one feed line will be considered since both have identical form.
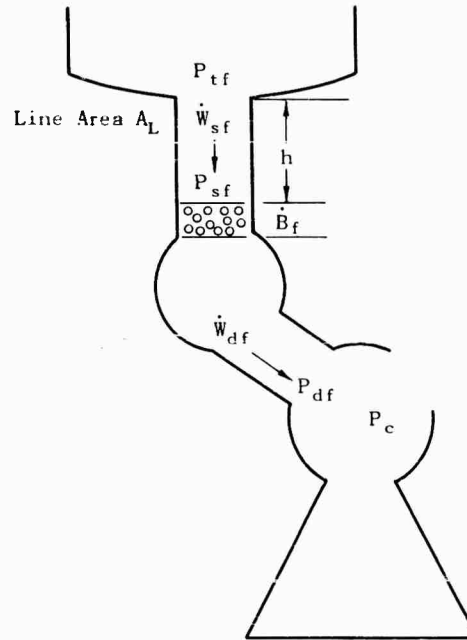
The relation between pressure and flow in the feed line is:

$$P_{tf} - P_{sf} = L_{sf} \ddot{W}_{sf} , \tag{B1}$$

where $\ddot{W}_{sf}$ is the weight acceleration of the fuel, P_{tf} and P_{sf} are the tank top and tank bottom pressures, respectively, and L_{sf} is the induction line inertance, which is: $L_{sf} = (hA_L)/g$. Newton's law for fluid motion gives

$$\text{pressure} = \text{inertance} \times \text{weight acceleration.}$$

Let us define a bubble such that

$$\dot{P}_{sf} = K_{bf} \dot{B}_f \tag{B2}$$

and

$$\dot{B}_f = \dot{W}_{sf} - \dot{W}_{df} .$$

Therefore

$$\dot{P}_{sf} = K_{bf} (\dot{W}_{sf} - \dot{W}_{df}) . \tag{B3}$$

For flow through the pump,

$$P_{df} = P_{sf} (M + 1) - R_{pf} \dot{W}_{df} . \tag{B4}$$

$(M + 1)$ is the pump gain and R_{pf} is the pump resistance.

194

For flow into the combustion chamber we obtain

$$P_{do} - P_c = L_{df} \ddot{W}_f + R_{df} \dot{W}_{df} . \tag{B5}$$

R_{df} is the linearized orifice resistance and is equal to

$$\frac{2\bar{P}_d - \bar{P}_c}{\dot{\bar{W}}_d} .$$

The chamber pressure, mixture ratio effects neglected, is

$$P_c - \left(\frac{C_+^*}{A_{th}g} \dot{W}_{df} + \frac{C_f^*}{A_{th}g} \dot{W}_{do} \right) \frac{1}{t_c S + 1}$$

where C_f^* and C_o^* are the fuel and oxidizer characteristic velocities, A_{th} is the nozzle throat area and $1/t_c S + 1$ is a first order combustion lag.

Finally, the thrust is

$$T = C_f P_c A_{th} ,$$

where C_f is the thrust coefficient.

A second force on the structure is provided by the pump inlet pressure. This term is

$$F = -P_{sf} A_{pump\ inlet} .$$

DISCUSSION

Mr. Christian (MSFC): We have been investigating this problem on the Saturn vehicles. For the flights of Saturn I, we haven't seen this particular problem existing; but for future flights of the Saturn IB and the Saturn V vehicles, we have determined that we will inject gas into the fuel lines at the outlet of the LOX tank bulkheads as a limited-fix device. I was wondering what you would think about this as a fix?

Mr. Murray: Would that give you a spring or a different fuel line frequency?

Mr. Christian: A different fuel line frequency.

Mr. Murray: It is important that you know for sure the frequency of the structure, and we have a pretty good handle on the frequency change versus the burn of the fuel in the structure. You have to make sure that you have the lowest mode so that if you reduce the fuel line pressure or frequency then you are not going to excite a lower structural mode. I would say that that would be the danger. Be careful that you don't excite a lower mode that you are not aware

of. Dr. Rubin of Aerospace has quite a few methods and also the Titan project people have used the standpipe and the pressure accumulator. We are also thinking about a compliant bag which is similar to a muffler on a car in that the pressure from the fuel line goes into a chamber containing little air bags which essentially take up the pressure perturbation. This is similar to the fixes we are considering. As to injecting gas into the fuel line, this is a new idea to me. I would be careful because Titan did have a problem when one vehicle was fixed. Only one side was fixed, not both, and a serious problem developed.

Mr. Stephens (Langley Res. Ctr.): Have any attempts been made to determine the behavior of the fuel or the liquid motion during this longitudinal buildup?

Mr. Murray: We've done a little work on trying to determine the fuel characteristics. There was some original work done in which pictures were taken of the cavitation bubble which lies on top of the LOX pump. It varies with the pressure fluctuation in the line. We

195

have taken pictures and observed this. Presently, I believe, Rocketdyne is contemplating making some tests and I know that T. Calvert of Lockheed Aircraft Company is doing some pump testing. The dynamic pump characteristics is really the important part of the problem that we don't have a physical grasp of. This is the area in which we need more basic information.

Mr. Fowler (STL): How did you handle your time lag (tau) in your digital program. On the analog you had a time lag.

Mr. Lynch: The answer is quite simple. It's merely a phase lag as you know and it has an attendant reduction in gain across the build up from discharge pressure to thrust, for example. Simple first order decay. I hope that answers your question.

*   *   *

LOW FREQUENCY STRUCTURAL DYNAMICS
OF THE SATURN VEHICLES

D. C. Christian
G. C. Marshall Space Flight Center
Huntsville, Alabama

In order to design structures to withstand dynamic conditions it is necessary to distinguish between applied static forces which might vary with time and inertia forces which are caused by the static forces and which also vary with time. On a structure initially at rest, application of dynamic loads causes oscillations of the structure's masses (all materials used are elastic). Because of the accelerated nature of such oscillations, inertia forces arise on the moving masses of the structure oscillating about the dynamic load positions.

In the space vehicle field, dynamic effects sometimes play an important role. Both the test tower and the launch pedestal (before launch command) are connected to the booster and vehicle, respectively, with elastic members. The thrust of the engines represents the dynamic load. During lift-off the shock received from the holddown points of the vehicle represents the dynamic load and during flight cutoff, the decay of the engine thrust represents the dynamic load. Because of the increasing thrust build-up rate, and because of the fact that it is impossible to keep the system stiffness proportional to increasing missile weight, the vibrations introduced by these dynamic loads cannot be kept low.

This investigation includes comparisons of measured data and calculated data for Saturn booster test firings at the George C. Marshall Space Flight Center. Also measured data and calculated data are compared for flights of the SA-5 and SA-6 Saturn vehicles. The measured responses will include compression loads at certain stations on the vehicle for transient conditions such as engine build-up on the launch pad. Also pressures measured on the inlet to turbine pumps on the engines are compared with calculated data. Theoretical calculations are also presented for studies being made on the Saturn V vehicle. These studies include analyses of engine build-up and build-up -- lift-off vibration transients. This paper presents the results of studies which indicate why a release mechanism is needed for the vehicle at lift-off.

This presentation concentrates on comparisons of theoretical calculations with measured results. Therefore, this will be a test of the method indicating the importance of higher modes in the actual response of a system as compared with the effects of the higher modes in the theoretical calculation. The method used to perform the analysis is based on assuming that the response of a multi-degree of freedom system can be obtained by a summation of the modal responses. The modal acceleration method is utilized in this analysis to obtain more accuracy. A small portion of this work using the single-spring mass system was presented in Detroit, Michigan at the Shock, Vibration, and Associated Environments Symposium on October 10-12, 1961. The paper was entitled, "Dynamic Investigation of Thrust Build-up and Cutoff for the Saturn Vehicle," by R. F. Glaser and D. C. Christian.

Data used to substantiate the conclusions was obtained from computer calculations by the IBM 7094 machine. The flight data was obtained from instrumentation on the actual flight vehicles. The loads for the vehicle in the test tower were obtained from strain gauges located on the tower vehicle support points.

INTRODUCTION

Dynamic studies must be performed for every applied load condition that exists throughout the flight history of a space vehicle. This report will consider several specific times during flight that are important in most dynamic analysis of space vehicles.

In order to design structures to withstand dynamic conditions it is necessary to distinguish between applied static forces which might vary with time and inertia forces which are caused by the static forces and which also vary with time. On a structure initially at rest, application of static loads causes oscillations of the structure's masses. Because of the accelerated nature of such oscillations, inertia forces arise on the moving masses of the structure oscillating about the static applied load. Therefore, the effective acting load is a superposition of the static load and the arising inertia forces. The inertia force is sometimes greater and sometimes smaller than the static load. The amplitude of these inertia forces depends not only on the system (mass and stiffness) but also on the shape of the static load as a function of time. With decreasing stiffness, increasing load, and increasing slope of the static load function, the inertia force increases.

Dynamic effects play an important role for the Saturn vehicles. In the longitudinal direction, large inertia loads are seen at a time just before flight cutoff because the vehicle has a large acceleration at this time. These load conditions influence the design of a large percentage of the vehicle structure; however, other considerations of the vehicle which may not be designed by these load conditions are the propellant containers in the first stage boosters, tension in the vehicle skin after flight cutoff, downward loads on the engines in case of emergency cutoff on the pad, and the loads that occur in the holddown arms for emergency cutoff. Because of increasing thrust buildup rates, and because of the fact that it is impossible to keep the system stiffness proportional to increasing vehicle weight the inertia loads at these conditions cannot be kept low. In the case of an engine cluster (like the Saturn I and Saturn V), to keep these inertia loads down, it is necessary to insert properly chosen staggering times between different engine thrust buildups and decays. By this method superposition of the inertia loads can be spaced in a manner that avoids resonance effects. At lift-off a large shock force is created at the base of the vehicle (if the vehicle is released instantaneously) which sometimes causes large inertia loads. The shock force, which is equal to the difference

between engine thrust and vehicle weight, can be lowered with automatic release devices that cause the vehicle to release slowly. The only other approach is to make sure the vehicle is designed to take these loads, with resultant payload decrease.

Finally, it is necessary to indicate several points of difficulty in the treatment of this problem. One is the inability to predict exactly the single engine thrust curve and particularly the starting time of a given engine. This indicates that statistical methods should be used in conjunction with the approach of appendix A, this could lead to the elimination of high loads that have a small probability of occurrence. Second, the difficulty of calculating accurate spring constants for the fuel tank propellants to simulate higher modes of the tank wall and bulkhead combinations. Present methods involve approximations only and it is not known how accurate these are. The Dynamics and Loads Branch at Marshall Space Flight Center is presently working with contractors to obtain improved methods in this area.

SATURN I

Saturn Test Vehicles

For the Saturn I Block I vehicle it was found that a single spring mass system was adequate to describe the loads in the supports of the vehicle in the test tower. By utilizing strain gages, load-vs-time measurements were taken as shown by the plot in Fig. 1 indicated as the actual response (load cells). This measurement indicates that the system is vibrating at mainly a single mode frequency. Based on this idea response equations were written as shown in Ref. [1]. This reference gives the response equations for a single spring and mass due to the applied thrust of engine clusters. An example of the applied thrust can be seen as the top graph in Fig. 1. The solid curve on the bottom graph in Fig. 1, called the resulting thrust, is a point-by-point summation of the applied thrust of each engine in the engine cluster. From this analysis a response curve was calculated which is indicated as the dashed curve in Fig. 1. These curves show the accuracy that was obtained by comparing the two loads as they oscillate about the static thrust of the engines. From this study, adequate staggering times were determined for the engine start sequences to lower vibration loading for the vehicle in the test stand. The same staggering

NOTE: Reference appears on page 207.

198
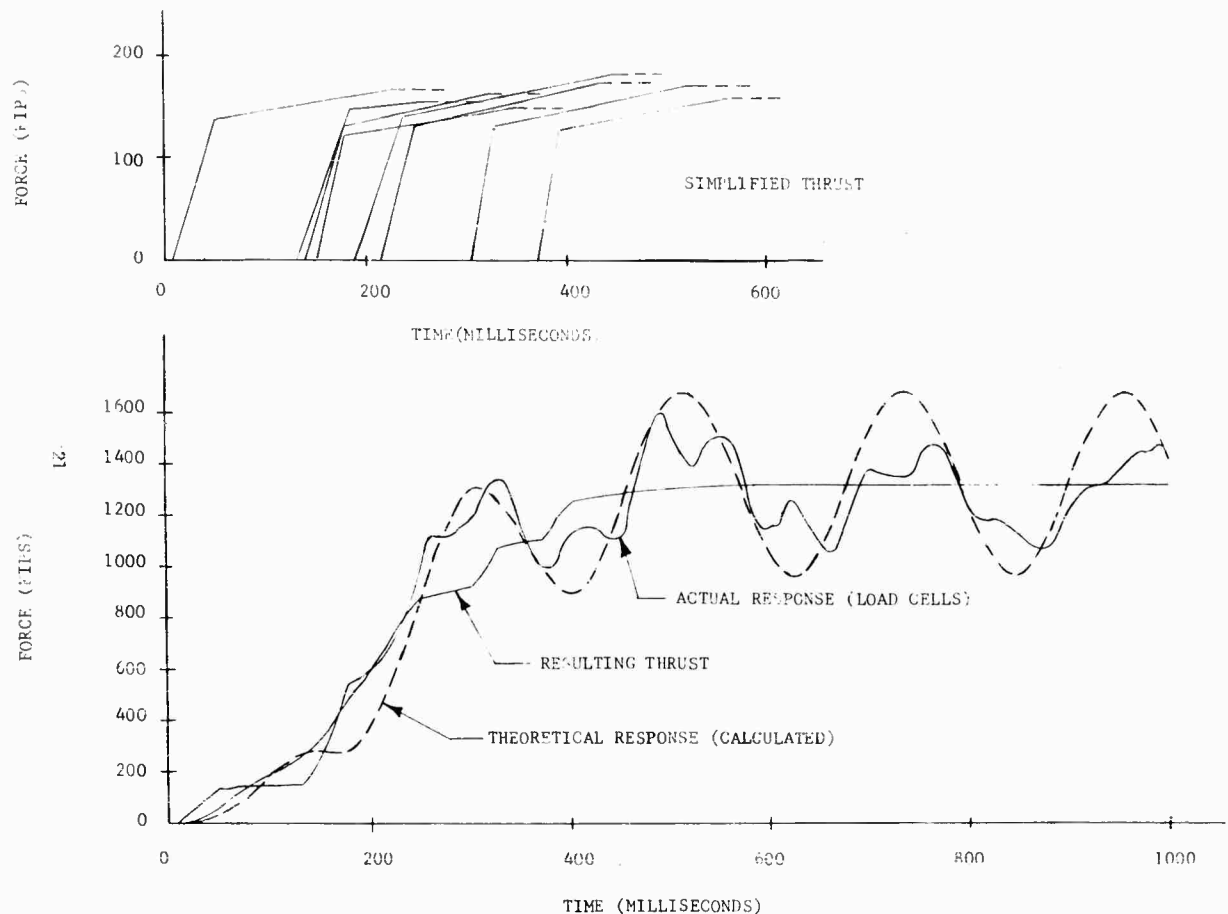
Fig. 1 – SA-T-15 Response in holddown arms

times for the vehicle on the launch pad was utilized since the frequency of both launch pad and the vehicle test stand are similar. For a system that can be simplified to a single spring mass it was found that the time between starting single engines or groups of engines should be π/ω, where ω is the frequency of the structure in radians per second and π is 3.14. An analysis using a multi-spring mass system, as derived in appendix A, was performed for the Saturn I vehicle also. This analysis gives better agreement for small deflections and better detailed vehicle deflection than the analysis indicated in Ref. [1]. The results of this analysis can be seen in the next two sections.

SA-5 Flight Vehicle

A longitudinal response analysis was made for SA-5 flight of the Saturn I vehicle using the methods described in appendix A. The mathematical model used in the theoretical analysis, to simulate the vehicle, is shown in Fig. 2. Dry

structure is represented by the rectangles and propellants are represented by the circles. The springs indicated on the mass model represent the stiffness for the corresponding areas shown by the drawing of the vehicle. The propellant spring constants were derived by the method described in appendix B. Outrigger and holddown arm stiffness is represented by the springs attached to the ground.

For flight evaluation, an investigation was made to determine the calculated response of the system for the observed applied forces, during buildup. The calculated response is compared with the measured response. The instrumentation was not sufficient to obtain measured values for the transients after lift-off.

Buildup is defined as the time interval from ignition of the first engine to lift-off. A staggering time of 100 ms between engine pairs was expected to keep the vibratory force lower or equal to 20 percent of the maximum static thrust. Figure 3 shows the engine staggering

199
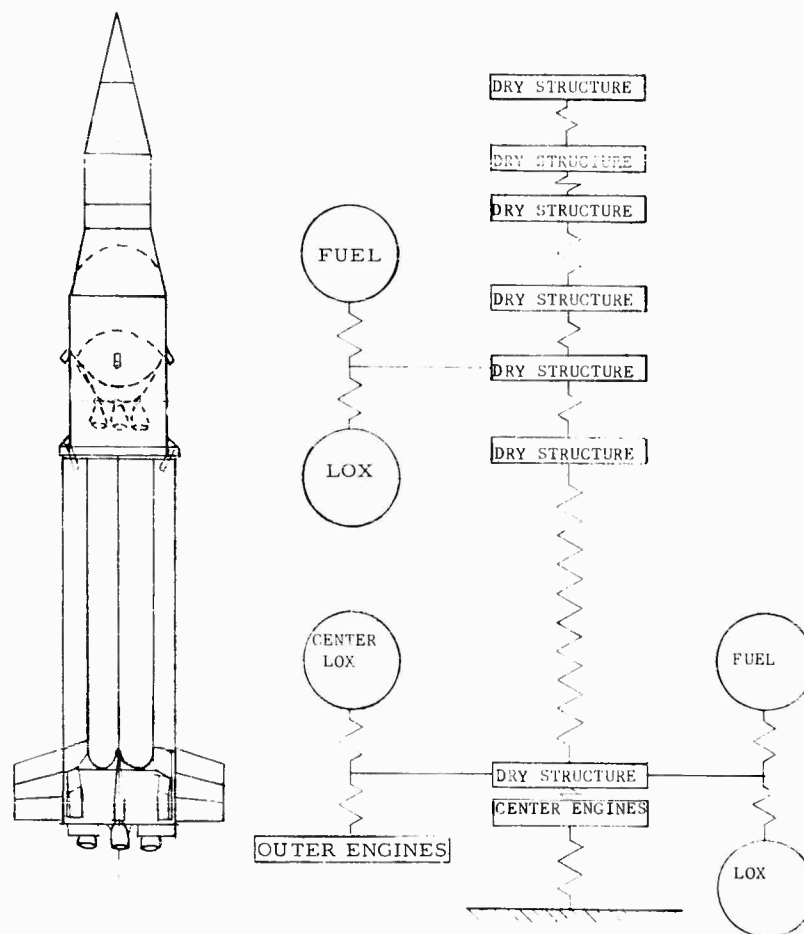
Fig. 2 - SA-5 Mass model

time to be random and the resulting thrust to be almost a constant slope. The maximum response obtained for the flight was 13 percent of the maximum static thrust.

The vibration load in one fuel tank skirt is shown in Fig. 4. The solid curve was measured by strain gages while the dashed curve was calculated. Good agreement exists between the measured and calculated loads, in both amplitude and frequency.

The vibration for fuel pump inlet pressure for engine number 4 is shown in Fig. 5. The pressure gage measures the static head of the liquid, ullage pressure in tank, and vibration of liquid head all superimposed. Good agreement exists between the measured and calculated pressure in both amplitude and frequency.

The curves recorded are for the vibration around the static loads.

SA-6 Flight Vehicle

A longitudinal response analysis was also made for SA-6 flight of the Saturn I vehicle using the method described in appendix A. The mathematical model used in the analysis is similar to that used for SA-5, shown in Fig. 2. This flight had the same instrumentation as SA-5 in addition to accelerometers located on the holddown arms.

Two engines were scheduled to start simultaneously, with a 100-millisecond delay between pairs, in order to limit the vibratory force to 20 percent of the maximum static thrust.

200
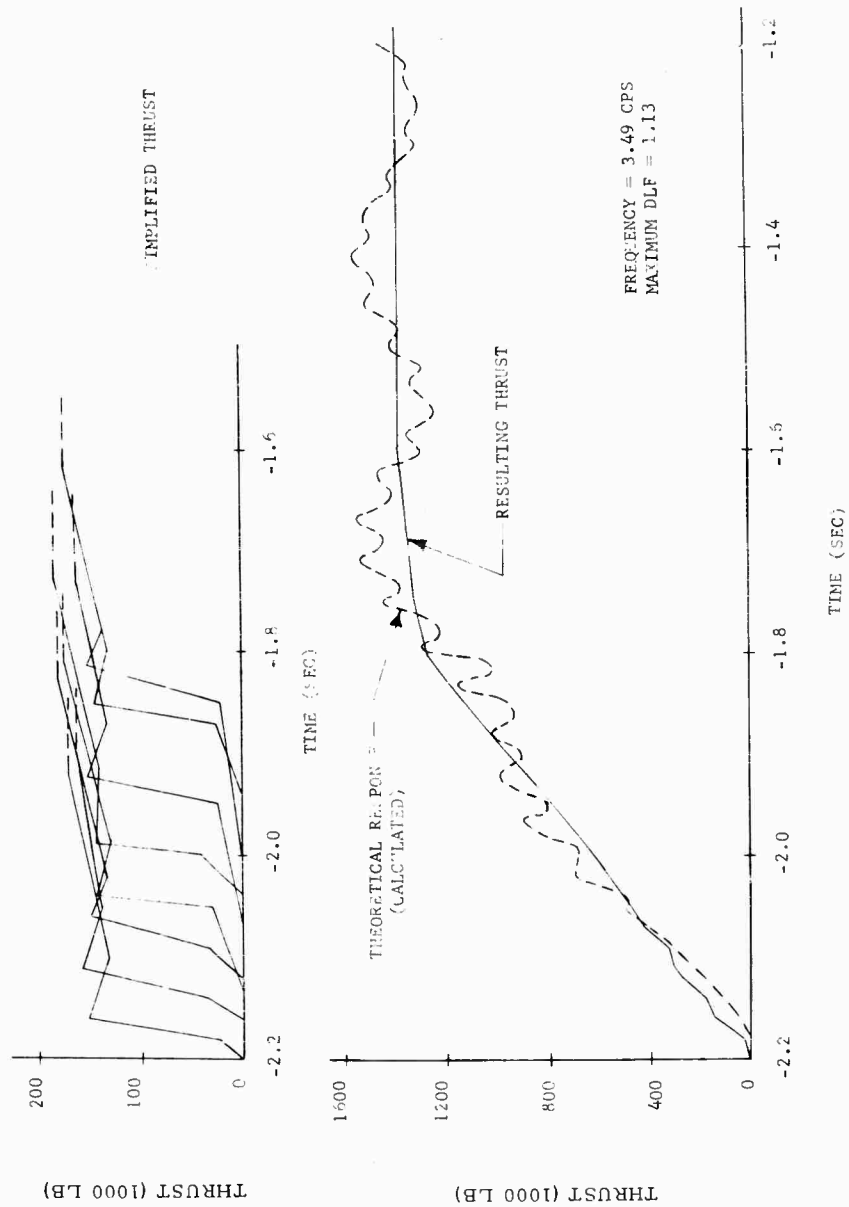
Fig. 3 - SA-5 Response in holddown arms
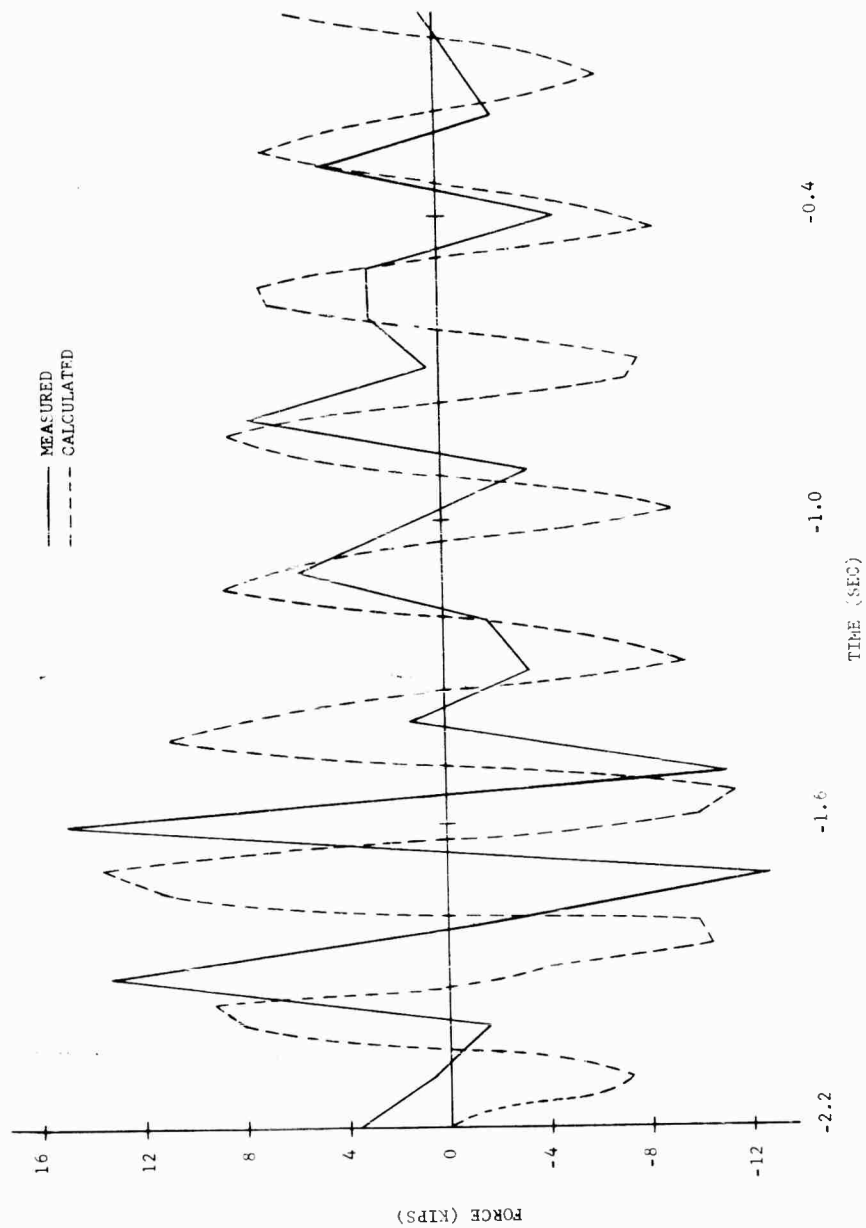
Fig. 4 - SA-5 Vibration load in one fuel tank skirt

202
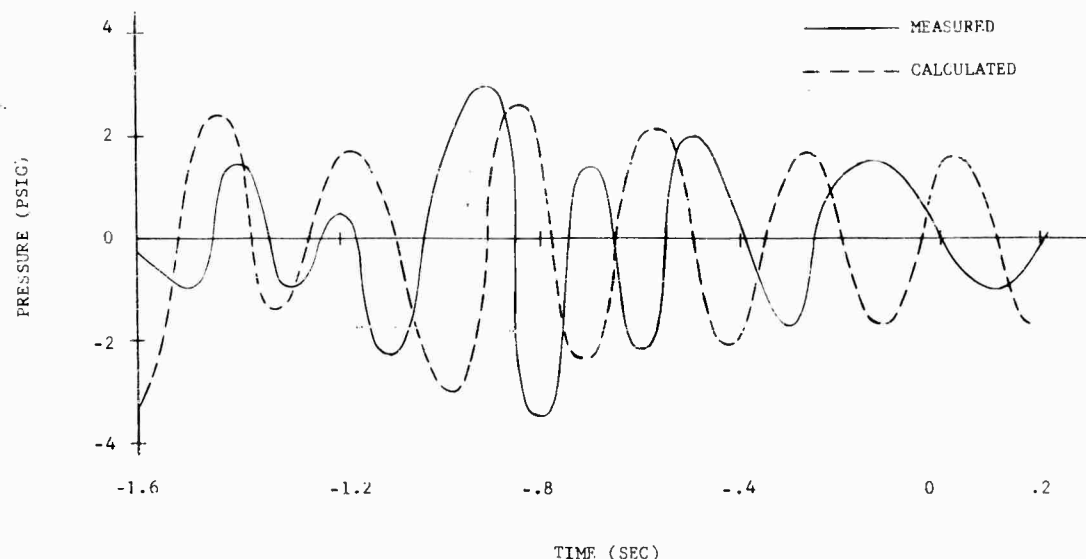
Fig. 5 - SA-5 Fuel pump inlet pressures engine no. 4

Figure 6 shows the engine staggering time to be erratic; however, the maximum response was only approximately 13 percent of the maximum static thrust. Figure 6 also shows two predominant frequencies which correspond to the frequency of the first vehicle mode (4 cps) and to the third main beam frequency (20 cps) of the vehicle.

For this flight no agreement was found between the fuel tank strain gages and the engine pump inlet pressure, as was found for SA-5. This is probably due to the presence of the third main beam mode which is a frequency that these instruments cannot properly record.

The vibration acceleration in one holddown arm is shown in Fig. 7. Good agreement exists between the measured and calculated accelerations, in both amplitude and frequency for this gage. The predominant frequency for the holddown arms corresponds to the third main beam frequency mentioned above.

The curve plotted on the graph in Fig. 7 gives vibration around the static acceleration vs time.

SATURN V VEHICLE

Saturn V studies were made to obtain vibration loads utilizing the mathematical model shown in Fig. 8. The propellant spring constants were derived based on methods of appendix B. The method of appendix A was used to calculate the loads.

Analysis was made for the vehicle for buildup rebound, buildup release, and flight separation. No unusually high loads occurred for buildup rebound or flight separation; however, some unusually high loads did occur on the vehicle for the buildup release case. This was caused by the instantaneous release of the holddown arms. This process causes a shock force to act on the vehicle which is equal to the thrust minus the weight of the vehicle. This shock causes large vibrations to be propagated through the structure of the vehicle. For instance Fig. 9 shows a time history of the pressure on the bottom of the S-IC LOX tank bulkhead. The vehicle was released at a time of approximately 4 seconds and the resulting oscillations introduced at this time can be seen on the figure.

To lower this shock load at lift-off, a release mechanism is being developed for the Saturn V vehicle. Controlled release is simulated by assuming the action of a linearly decreasing downward force (Fig. 10) at Station 100. It is assumed that this force does not act until the holddown arms of the vehicle are released. From Fig. 10 it can be seen that the release mechanism force is a function of the deflection at the base of the vehicle. The method used for the insertion of this into the equations of appendix A can be seen in appendix C.

203
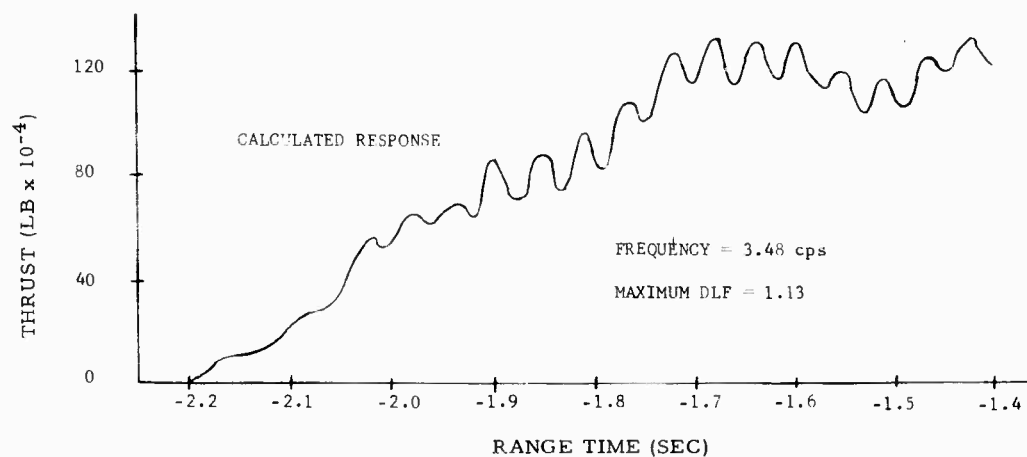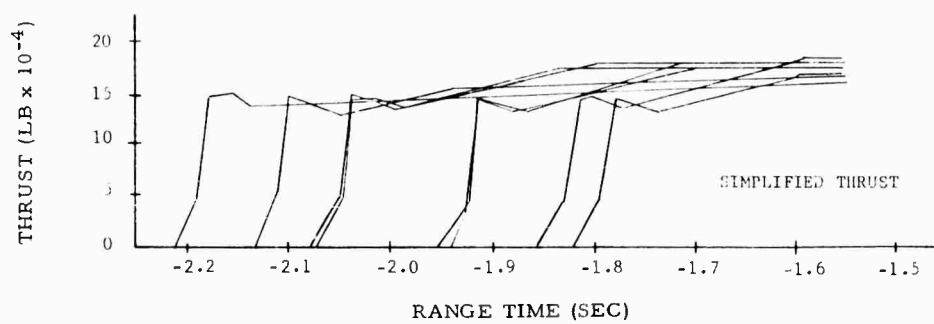
Fig. 6 - SA-6 Response in holddown arms
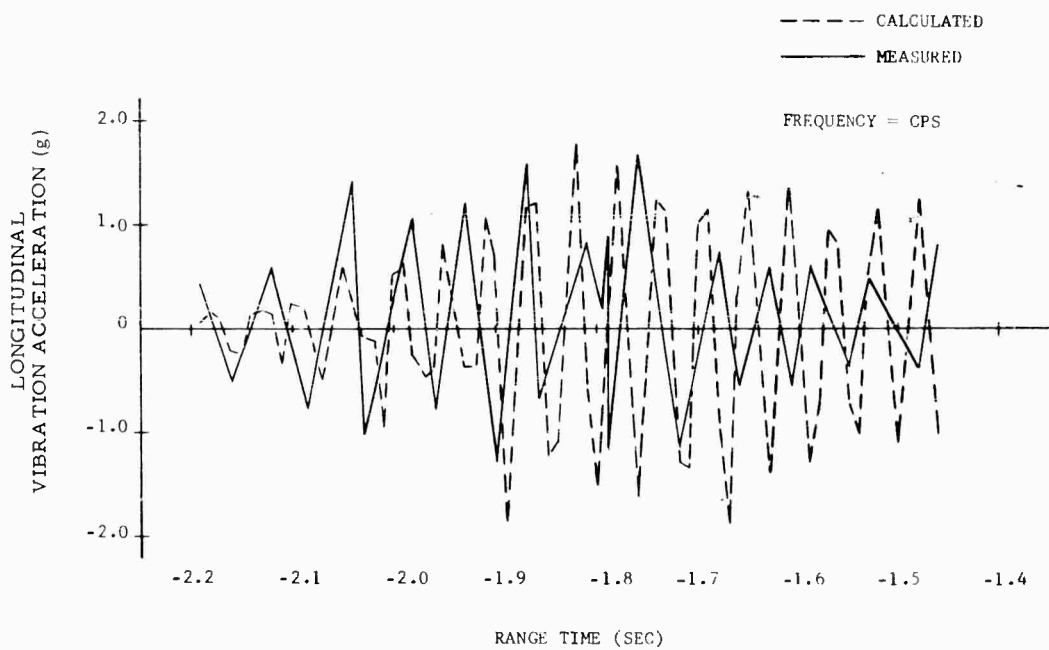
Fig. 7 - SA-6 Measured vibration acceleration of one holddown arm
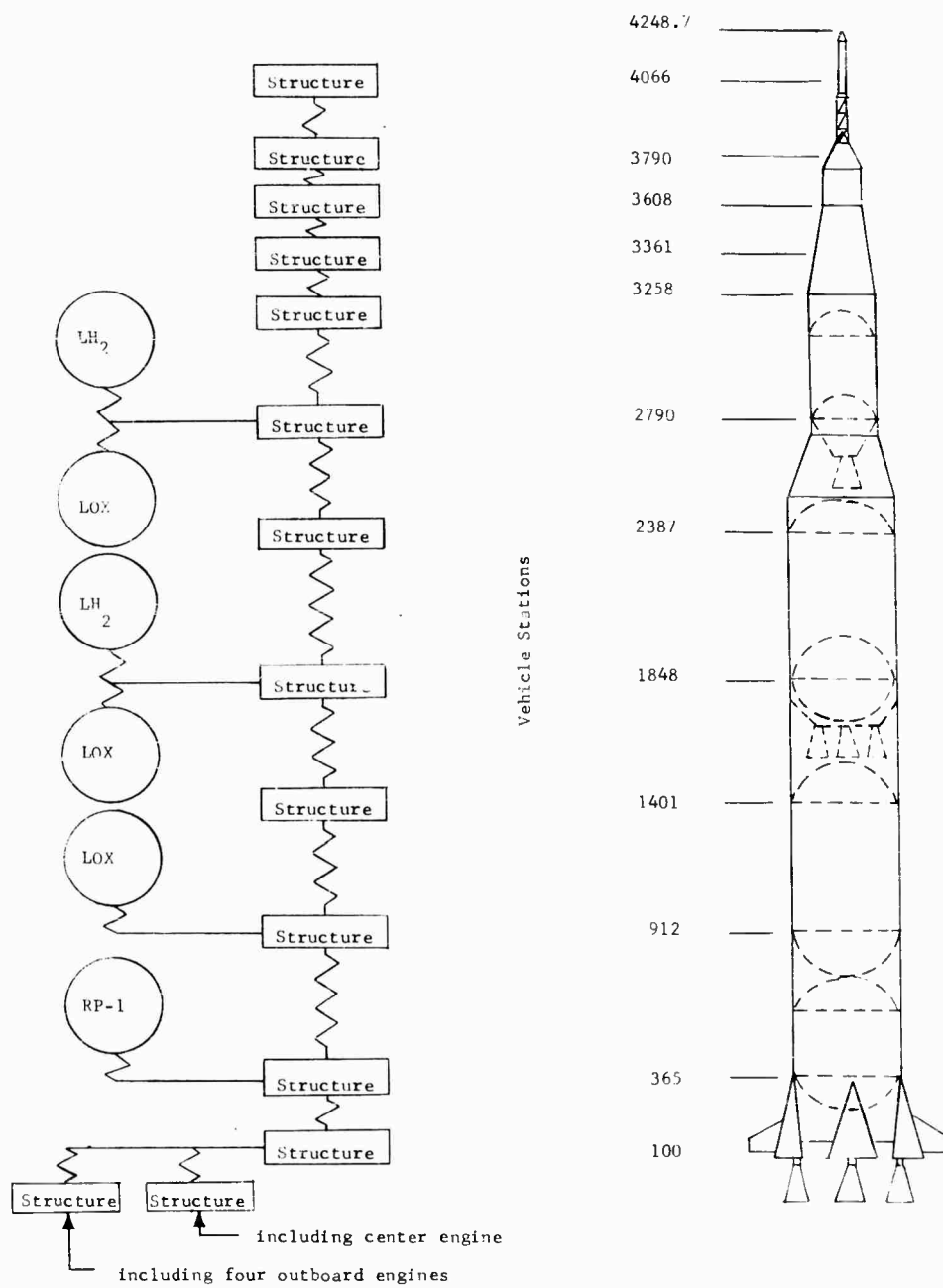
Fig. 8 - Saturn V mass model

205
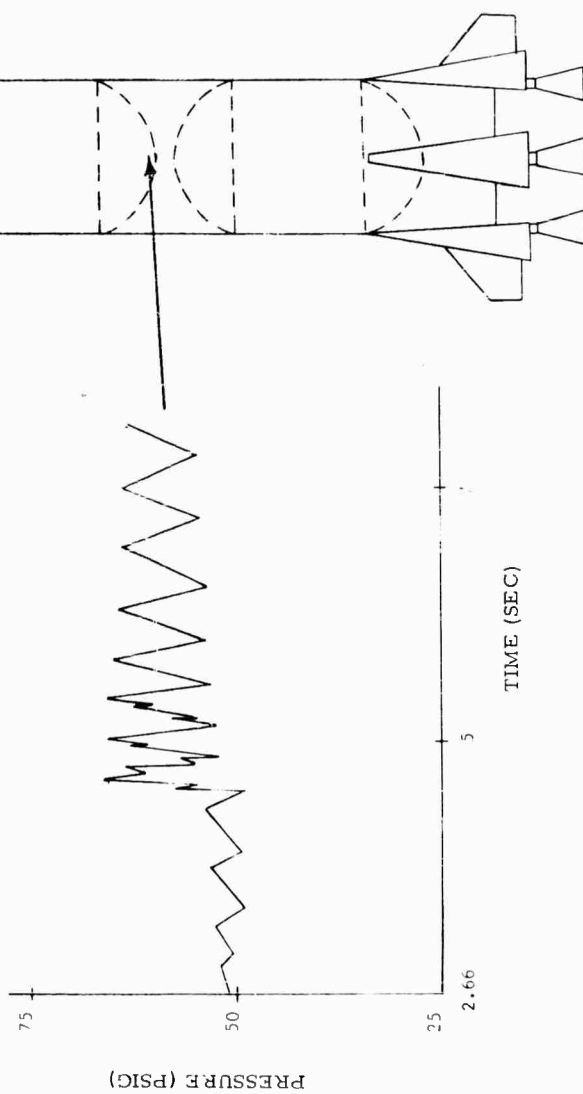
Fig. 9 - Saturn V S-IC LOX bulkhead buildup and lift-off pressure
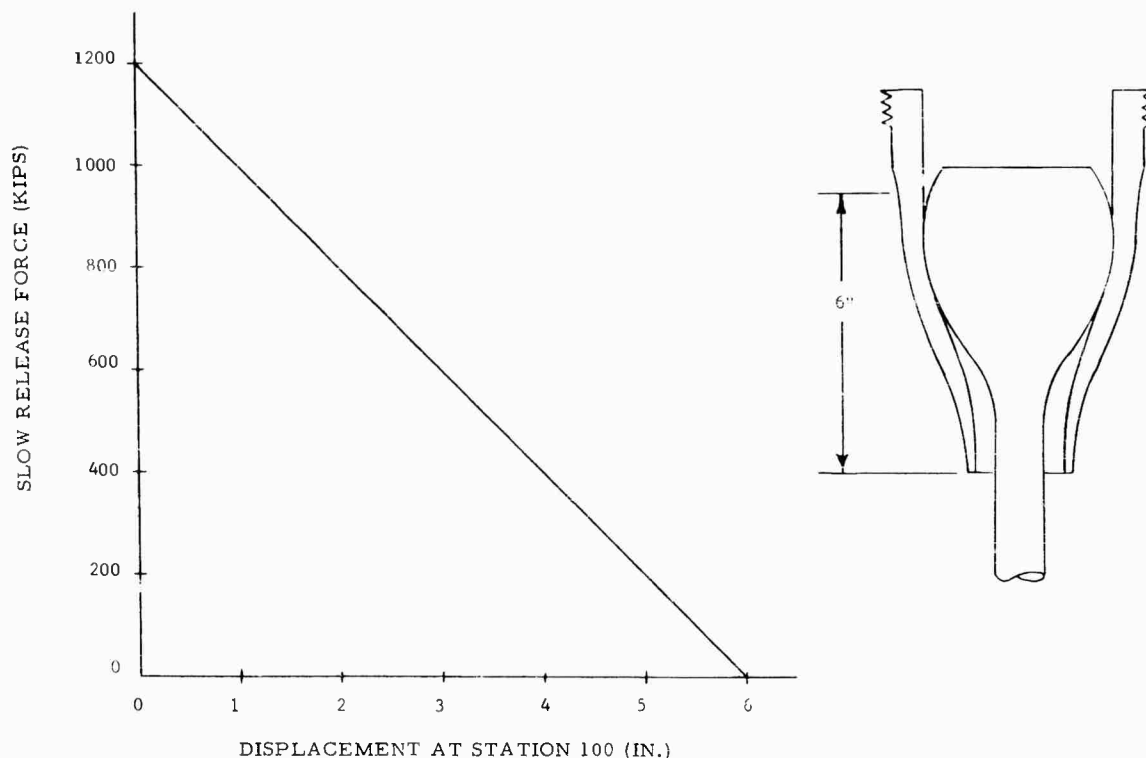
Fig. 10 - Saturn V slow release force vs displacement

It was determined that a force which varies from 1,200,000 to 0 over a displacement of 6 inches would lower the vehicle loads a sufficient amount. Figure 10 also shows a picture of a release mechanism design under consideration at the present time. The sleeve part is attached to the vehicle while the mandrel is attached to the launch pad. Figure 11 shows a typical illustration of the longitudinal dynamic loads in the S-IC stage LOX tank. It represents the envelope of maximum values from different curves like the one in Fig. 9, with engine staggering times as the variable. This figure shows that for instantaneous release the pressure in the S-IC stage LOX tank exceeds the design value regardless of stagger time for the five F-1 engines in a serial 1-2-2 sequence and also shows the converse for a controlled release.

Also studies were made to see if release time of the vehicle had a significant effect on the LOX tank loads. The results of this study is shown in Fig. 12. The solid curve shows instant release loads on the LOX tank vs time, while the dashed curve shows slow release LOX tank bulkhead loads. From this curve it can be seen that the time of release is insignificant as far as LOX tank loads are concerned. The range of times that minimum loads occur

is so short that it would be impracticable to try to release the vehicle at the minimum values shown on the graph.

The release mechanism makes possible a weight savings in the booster of several thousand pounds, thus allowing an increased payload capability.

Studies were also made to determine the best engine staggering times for the vehicle. Based on this study, a 300 millisecond staggering time was chosen for the engines with a starting sequence of 1-2-2. Figure 13 shows the loads at various sections of the vehicle vs time. These are maximum load envelopes that occur with the vehicle on the launch pad. The minimum loads on the graph occurs for a staggering time of 300 milliseconds which is the reason for choosing this time.

REFERENCE

1. R. F. Glaser and D. C. Christian, "Dynamic Investigations of Thrust Build-up and Cutoff for the Saturn Vehicle," NASA Report MTP-M-S&M-S-61-5 (June 12, 1961) (Unclassified).
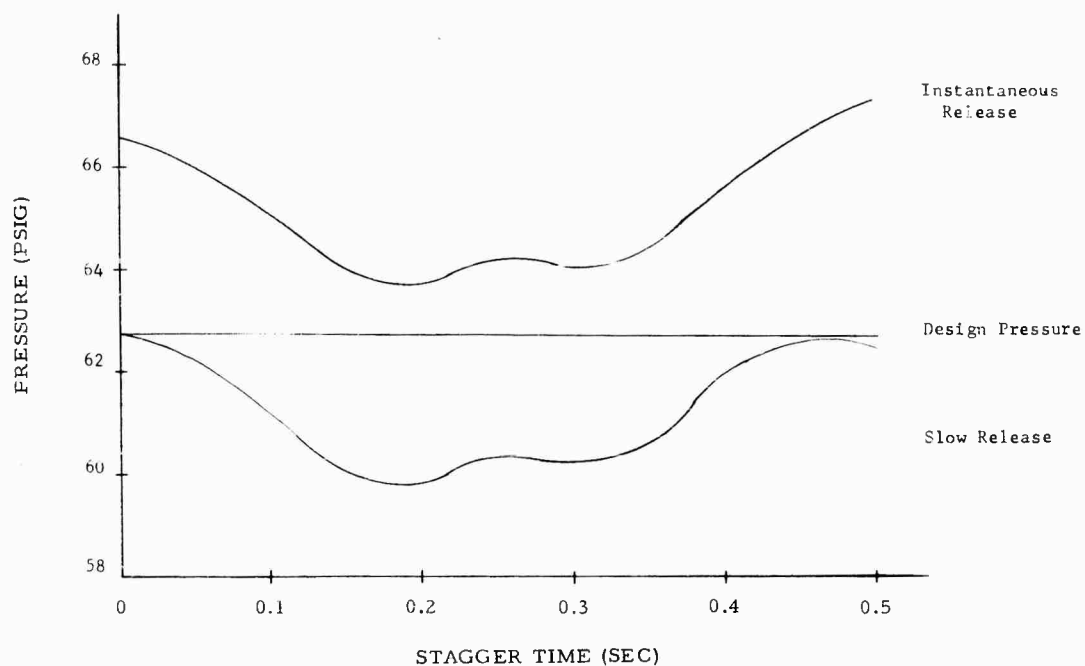
Fig. 11 - Pressure vs stagger time LOX tank
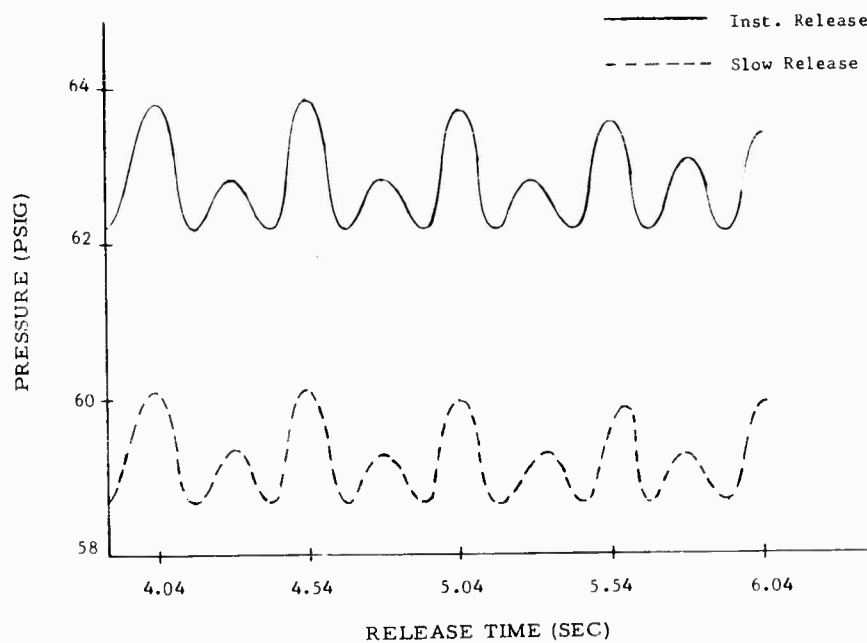
Fig. 12 - Saturn V S-IC LOX maximum bulkhead pressure
vs release time 0.25 staggering time — Jan. 64 thrust

208
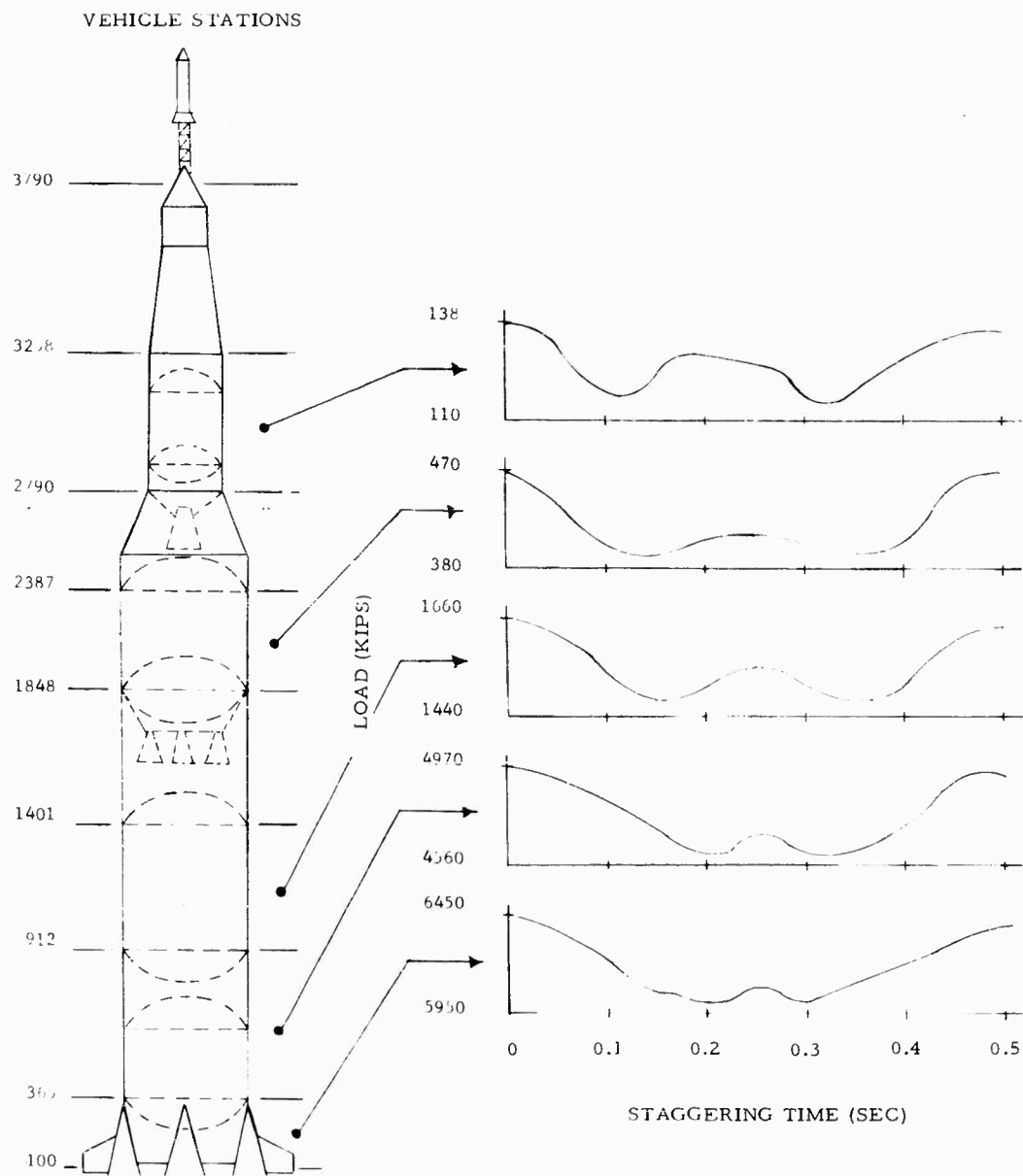
Fig. 13 - Load vs staggering time

209

Appendix A

RESPONSE EQUATIONS FOR A MULTI-SPRING MASS SYSTEM

The following is a very brief summary of the method used in calculating the response of the systems shown in the report. These equations are used to simulate structures which are cantilever or free-free. The equations are normally utilized to calculate the dynamic response for space vehicles with engine thrust, ullage rockets, and retro rockets as forcing functions. Initial conditions for each structure mass in the model are input as displacement and velocity. The input also includes the mode shapes and frequencies of the system. A system that can be analyzed using these equations is shown in Fig. 2.

The mathematics involve the use of generalized mathematical equations. They can be derived by utilizing the LaGrange equation or by writing the equations of motion for the system using Newton's laws of motion. The equations of motion can be written as follows

$$[M]\ddot{X}_i + [C]\dot{X}_i + [K]X_i = f_i. \qquad (A1)$$

where

$[M]$ = Mass matrix,

$[C]$ = Damping matrix,

$[K]$ = Stiffness matrix,

f_i = Forcing function column,

$\ddot{X}_i$ = Acceleration column,

$\dot{X}_i$ = Velocity column,

X_i = Displacement column, and

i = Mass number on mass model.

To solve the problem, Eq. (A1) is put in generalized form by substituting Eqs. (A3) and (A4) below into Eq. (A1) and multiplying both sides of the equation by a row of the mode shape. Thus the generalized equation for the response of each mode is given as follows

$$\ddot{q}_n + 2 \xi \omega_n \dot{q}_n + \omega_n^2 q_n = \frac{\sum f_i \Phi_{in}}{\sum m_i \Phi_{in}^2}, \qquad (A2)$$

where

$\ddot{q}_n$ = The generalized acceleration of each mode (in.),

$\dot{q}_n$ = The generalized velocity of each mode (in.),

q_n = The generalized displacement of each mode (in.),

ξ = Percent of critical damping for each mode,

ω_n = Natural frequency of each mode (rad/sec),

f_i = Forcing function on each mass (lb),

m_i = Mass (lb-sec^2/in.),

Φ_{in} = Normalized mode shape of each mode, and

n = Mode number.

The term $\sum m_i \Phi_{in}^2$ represents the generalized mass of the structure. Equation (A2) is solved utilizing the fourth order Runge-Kutta method. The generalized acceleration and velocity are then multiplied by each mode and summed as shown in the following equations:

$$\ddot{X}_i = \sum_1^n \ddot{q}_n \Phi_{in} \qquad (A3)$$

and

$$\dot{X}_i = \sum_1^n \dot{q}_n \Phi_{in}. \qquad (A4)$$

Equations (A3) and (A4) are then substituted into Eq. (A1) and the results are obtained from a modal acceleration standpoint.

Appendix B

EXPLANATION OF METHODS TO CALCULATE PROPELLANT SPRING CONSTANTS

The spring constants for the breathing of the propellant tank containers were calculated by dividing the weight of the propellant by the deflection of the center of gravity of the liquid in the container; this is based on the assumption that the static weight of the propellant caused this deflection.

Appendix C

APPLICATION OF RESPONSE EQUATIONS TO INCLUDE RELEASE MECHANISM

The equations described in appendix A were altered to include a force at one mass which is a function of the displacement of that mass. Therefore, the f_i term in Eq. (A1) will contain variable X_R which is the deflection at the point on the structure where the release mechanism is attached. Also the equation of motion for the center of gravity of the structure has to be written to obtain the deflection of this point relative to the ground. The sum of the vibration of this point and the vehicle center-of-gravity movement is the deflection of this point relative to the ground. The equations of motion for the response of the structure including the release mechanism are given as follows:

$$[M]\ddot{X}_i + [C]\dot{X}_i + [K]X_i = \begin{bmatrix} \frac{m_1}{m_T} f_R \\ \cdot \\ \cdot \\ \cdot \\ -f_R + \frac{m_R}{m_T} f_R \\ \cdot \\ \cdot \\ \cdot \\ \frac{m_i}{m_T} f \end{bmatrix}$$

$$+ \begin{bmatrix} -\frac{m_1}{m_T} f_o \\ \cdot \\ \cdot \\ f_o - \frac{m}{m_T} f_o \\ \cdot \\ \cdot \\ -\frac{m_i}{m_T} f_o \end{bmatrix} + \begin{bmatrix} -\frac{m_1}{m_T} f_B \\ \cdot \\ \cdot \\ f_B - \frac{m_B}{m_T} f_B \\ \cdot \\ \cdot \\ -\frac{m_i}{m_T} f_B \end{bmatrix} \quad \text{(C1)}$$

The equation for release mechanism force is given as

$$f_R = C \cdot R (X_{c.g.} + X_R - X^o_{c.g.} - X^o_R). \quad \text{(C2)}$$

Equation of motion for structure center of gravity is given as

$$f_o + f_B - f_R - M_T = m_T \ddot{X}_{c.g.}. \quad \text{(C3)}$$

where

f_o = Thrust of outboard engines (lb),

f_B = Thrust of inboard engines (lb),

f_R = Release mechanism force (lb),

M_T = Total weight of structure (lb),

m_R = Mass located at point where release mechanism force acts (lb-sec^2/in.),

m_o = Mass located at point where outboard engine thrust acts (lb-sec^2/in.),

m_B = Mass located at point where inboard engine acts (lb-sec^2/in.),

$X_{c.g.}$ = Motion of structure center of gravity (in.),

X_R = Deflection with time for the vehicle release mechanism attach point (in.),

$X^o_{c.g.}$ = Initial deflection of structure center of gravity at lift-off (in.),

m_T = Total mass of structure (lb-sec^2/in.),

211

X_R^o = Initial deflection of structure at release mechanism attach point at lift-off (in.),

C = Initial force of release mechanism (lb),

R = Slope of release mechanism force (lb/in.), and

i = ith mass of structure.

The following substitutions are made into Eqs. (C1), (C2), and (C3):

$$X_i = \sum_1^n q_n \Phi_{in}, \qquad (C4)$$

$$\dot{X}_i = \sum_1^n \dot{q}_n \Phi_{in}, \qquad (C5)$$

and

$$\ddot{X}_i = \sum_1^n \ddot{q}_n \Phi_{in}, \qquad (C6)$$

where

Φ_{in} = Mode shapes for structure,

q_n = Generalized displacement for structure, and

n = nth mode of structure.

After substitution of Eqs. (C4), (C5), and (C6) into (C1), (C2), and (C3), the results are then multiplied through by the mode shapes transposed or a row of the mode shape. These operations give the following final form of the equations.

The response of each mode is obtained as:

$$\ddot{q}_n + 2 \zeta \omega_n \dot{q}_n + \omega_n^2 q_n = \frac{-f_R \Phi_{Rn} + f_o \Phi_{on} + f_B \Phi_n}{2m_i \Phi_{in}^2}, \qquad (C7)$$

where

Φ_{Rn} = Deflection in nth mode where release mechanism is attached,

Φ_{on} = Deflection in the nth mode where outboard engine acts, and

Φ_{Bn} = Deflection in nth mode where inboard engine acts.

From Eq. (C2) the f_R force term is obtained as:

$$f_R = C - R \left(X_{c.g.} + \sum_1^n q_n \Phi_{Rn} - X_{c.g.}^o - \sum_1^n q_n^o \Phi_{Rn} \right), \qquad (C8)$$

where

q_n^o = initial generalized displacement of each mode.

Equation (C3) remains the same.

At this point the final equations are solved using fourth order Runge-Kutta to obtain all the variables in the equations vs time. These results are then substituted into Eq. (C1) which is solved from a modal acceleration standpoint for displacements and vehicle loads vs time.

DISCUSSION

J. Ved (Ralph M. Parsons Co.): You mentioned that you set up the equations and solved them on IBM 7094 machines. Can you briefly describe the form in which you set up the equations?

Mr. Christian: We used a modal acceleration approach where we generalized coordinates. We assumed that each mode behaves as a separate sinusoidal-type oscillation and solved the differential equation for each mode.

Mr. Ved: Do you believe at this time that the analog computer might be more useful than the digital computer?

Mr. Christian: I don't believe so. We at Marshall have run quite a few different vehicles. On the digital program we can load in any vehicle we want, but we couldn't do this on an analog. It would take too long to set up each vehicle, therefore the analog would be of little value to us for this type of analysis.

*   *   *

DESIGN AND TEST OF AN AIRJET ACOUSTIC
NOISE GENERATOR TO REPRODUCE A
MISSILE FLIGHT ENVIRONMENT

D. Richards
The Johns Hopkins University
Applied Physics Laboratory
Silver Spring, Maryland

A Mach 2 annular airjet was built in an experimental approach to simulate the high level three dimensional vibrations experienced by missiles in flight. The design and installation is described, and results of free jet and ramjet missile tests in random noise environments exceeding 170 db are discussed. Sound pressure spectra and resulting vibration acceleration spectra at air flow rates to 70 lb/sec are presented.

INTRODUCTION

The in-flight vibration of a missile structure and attached components is generally impossible to simulate accurately in ground test, due to the nature of the inducing sources, unless full scale engine or wind tunnel tests are made. Missile component vibrations are generated by the diffuser, engine, and boundary layer pressure fluctuations, and the complexity of the vibration transmission paths and responses are such that calculation is well nigh impossible above the basic body flexing modes. The variations, telemetered from test flights, in vibration levels due to speed, maneuver, altitude, and burning rate variables are such that criteria for vibration specifications are difficult to determine and prediction of vibration levels for component specifications thus is mainly empirical.

A number of acoustic tests on complete missile assemblies have been made at The Johns Hopkins University Applied Physics Laboratory (APL) in past years to correlate vibration levels with acoustic input, mainly with the use of electro-pneumatic drives, with both sinusoidal and random noise. The sound pressure levels and waveforms in these tests have been recognized, however, to provide no more than a general guide. As an experimental approach to the simulation of the TALOS missile flight vibration environment it was proposed to generate wide band oscillatory pressure fluctuations by means of an airjet, which could be applied to a TALOS missile inlet to produce effects similar to those occurring in flight. Airjet noise has been the subject of considerable work by others, particularly in structural panel fatigue investigations, and of interest to the present tests were the studies made at NASA, Langley Research Center [1] where turbulence was generated by sharp pipe bends ahead of the nozzle, resulting in a quite flat spectrum. The intent, of course, was to utilize the radiated sound outside the jet boundary layer.

In utilizing airjet noise for excitation of the TALOS missile it was desired to generate turbulence with as much low frequency content as possible, and play this into the missile inlet. It appeared that if the jet boundary layer were made large by a suitable nozzle configuration it would be possible to generate a more intense noise, for a given mass flow. An annular airjet was selected as a logical approach to obtain both boundary layer area and a large mixing volume, thus possibly attaining the spectrum of a large jet in a short distance and with a relatively small nozzle area. Similar principles of large boundary layer area are used in jet aircraft noise suppressors, but noise suppressor designs generally break a large jet into a number of smaller jets with the intent of reducing the peak noise directivity through inter-reflection.

NOTE: References appear on page 222.

213

DESCRIPTION OF THE TEST EQUIPMENT

The design of the annular nozzle with the TALOS missile inlet in place is shown in Fig. 1. Air is admitted via the supply pipe and flows radially in the plenum formed between the nozzle block and a circular nozzle plate held by through bolts. The clearance between the nozzle block and the edge of the nozzle plate forms the annular nozzle which directs the air toward the missile inlet. Air is supplied from the 2000 psi compressed air storage tanks of the APL Propulsion Research Facility, and control valves operated from the facility control room are set to maintain the stagnation pressure at the nozzle inlet. Cold air flow rates of 50 lb/sec can be maintained for about 2 minutes, and the nozzle was designed for a Mach 2 exit air velocity at 15 psia with this flow rate (300°R jet temperature). Nominal nozzle stagnation pressure is 117.5 psia and throat area 18 square inches, although the design pressure capability was made 600 psia in anticipation of higher flow rates of short duration. The nozzle throat area was designed to be adjustable from 10 to 24 square inches by the position of the nozzle plate (Fig. 1), however, no changes were made from the 18 square inch setting in the tests reported here.
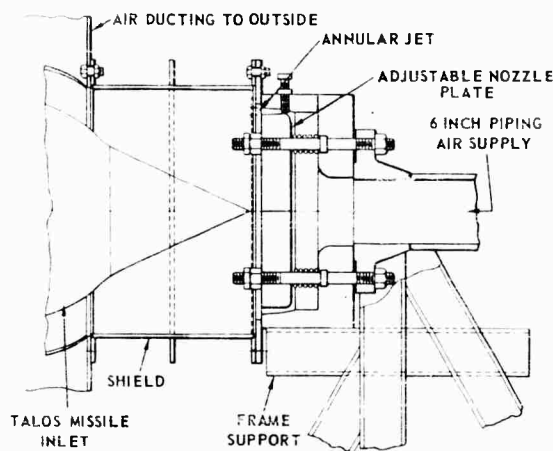
Fig. 1 - Airjet acoustic generator

The Mach 2 nozzle exit velocity was based on the paper by Lighthill [2] where it is shown that the acoustic efficiency for undisintegrated jets increases linearly with Mach number and approaches a maximum at Mach 2. It was assumed that this acoustic efficiency Mach number maximum would also hold for generated turbulence. Lighthill also quotes measurements by Laurence (1956) of the turbulent mixing length

for a Mach 0.3 airjet and these measurements were extrapolated linearly to a Mach 2 jet to determine the shield length shown in Fig. 1. These dimensional parameters are given in Fig. 2 although no studies were made that would confirm the assumption of linearity. The shield length happened to match the TALOS nose while the diameters of the nozzle annulus and shield were made to suit the missile inlet dimensions.
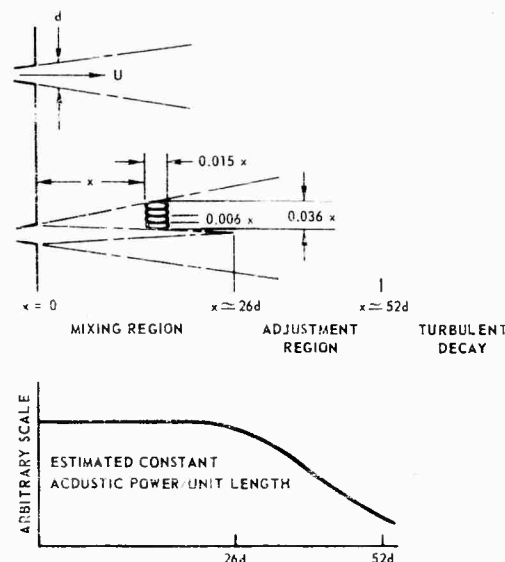
Fig. 2 - Jet dimensional parameters

General schematics of the complete installation with and without the missile installed are shown in Figs. 3 and 4, and give the location of all data points.

A view looking into the nozzle is given in Fig. 5, which also shows one of the microphone supports with a pressure transducer mounted at the center of the nozzle plate. Jet spoilers shown equally spaced around the shield in the jet discharge were added as a possible means of tailoring the spectrum. The spoilers were made from 3-inch diameter steel bars cut across the diameter, so that both angle of attack and cross section could be adjustable. As shown they are positioned at 0, 45, and 90 degrees sequentially around the periphery but, as later discussed, were not used in missile tests.

Exterior views of the nozzle assembly and the tunnel are shown in Figs. 6 and 7. The tunnel was built to duct the air flow out of the light set-up building in which the tests were made, as at the 50-lb/sec airflow rate the
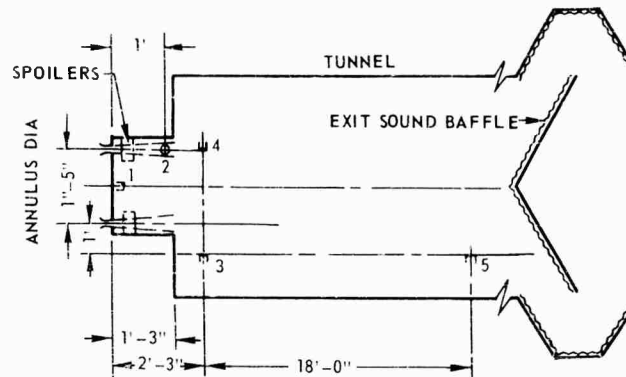
Fig. 3 - Microphone locations in survey tests

energy dissipated by the jet approximates 3000 kw.

INSTRUMENTATION

Acoustic measurements at locations 1 and 2 (Figs. 3 and 4) were made with a Columbia Model 100P pressure transducer, while measurements at locations 3 through 6 were made with Gulton Industries Model MA 299501 microphones. The latter microphones are acceleration compensated and were mounted on a very heavy support with a natural frequency of about 700 cps. Spectral analysis of data from the Gulton microphones does not show peaking near the support frequency.

To check possible mounting acceleration effects on the Columbia pressure transducer, an Endevco Model 2218 crystal vibration

accelerometer was mounted at location 1, and the acceleration levels (and spectra) recorded conformed closely to the effects expected in the acoustic environment, reported in Ref. [3], confirming the acoustic data from the Columbia instrument. Additional vibration pick-ups were located on several parts of the structure to monitor the general rms levels, however, time did not permit analysis as the data were not considered relevant.

All the above instruments were pre-calibrated with their cathode followers, and attenuation frequencies (roll off) in all cases were above the frequencies of interest. Cathode follower outputs were fed directly to FM sub-carriers and recorded by Precision Instrument tape recorders located in an adjacent building. Initial measurements indicated that line noise was infinitesimal, and amplification of the input signal was not required to improve signal-to-noise
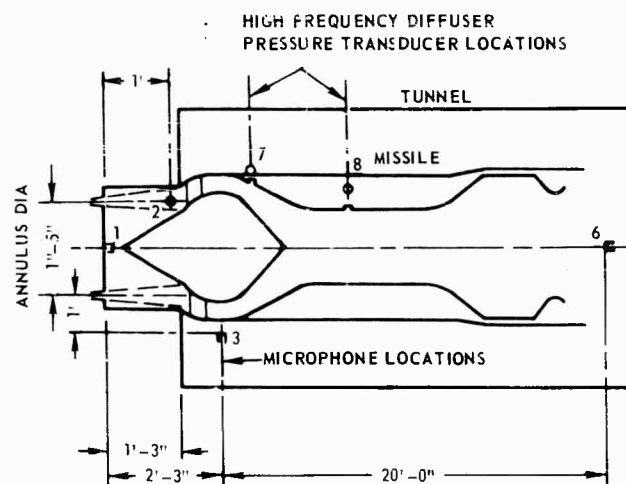
Fig. 4 - Missile acoustic test schematic

215
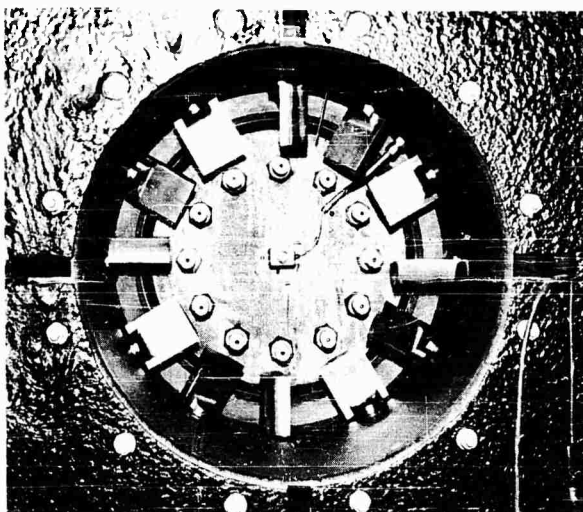
Fig. 5 - Annular nozzle exit
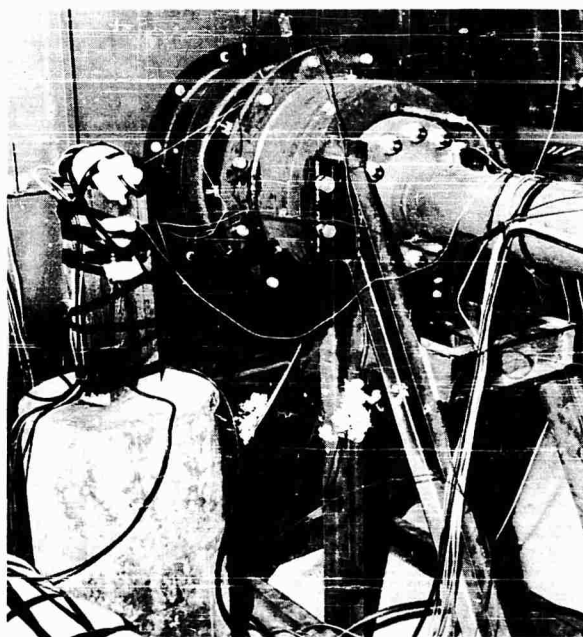
Fig. 6 - Annular nozzle assembly

ratio. During the tests the rms signal levels were monitored selectively with a Ballantine rms VTVM, and subsequent check of the taped data replayed through a similar meter indicated no loss of signal.

Missile data were recorded by flight instrumentation utilizing the missile telemetering
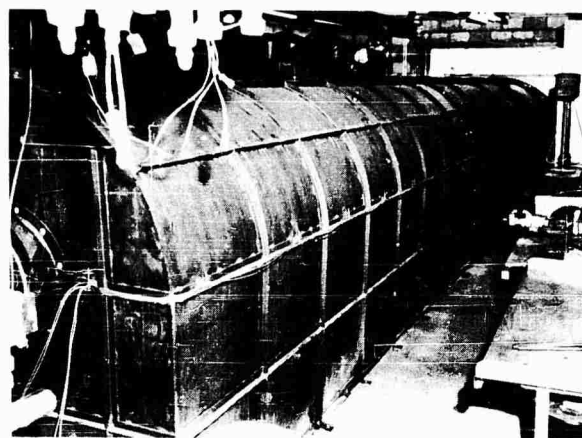
Fig. 7 - Air tunnel

system with a roof mounted antenna transmitting to a ground station in the APL data reduction facility, where the data was recorded by an Ampex FR-600 instrumentation tape recorder. Measurements of the missile diffuser pressure oscillations were made with Kistler Model 701A pressure transducers, and the sound pressure levels recorded by a Gulton Model MA 299501 microphone located in the missile as part of the telemetering instrumentation indicated that acoustic effects on the missile vibration pickups could be neglected.

DATA REDUCTION

Power spectral density analyses were made by a Gulton electronic wave analyzer. This machine uses a swept local oscillator as part of the heterodyne filter system, and the data are read into the machine from a tape loop, made from a sample of the original taped data. Tape loops, made of the data recorded on the Precision Instrument recorders were 4 seconds in length, and therefore, the run time at each nozzle pressure level in the survey tests exceeded this time. Actually, at least a 20-second-run at each level was made in order to assure steady pressure and a sufficient sample from which to make the loop.

Telemetered missile data were commutated in many cases, with one second sampling time and tape loops made of the missile functions were necessarily of 1-second duration. Test run time on the missile was therefore made somewhat longer in order to obtain at least three samples of each commutated function, again to ensure a typical sample.

216

The tape loop signal is detected according to the type of output desired, and for a power spectral density curve the mean square value

$$ms = \frac{1}{T} \int_0^T \left[f(t) \right]^2 dt ,$$

is obtained by passing the square of the data through an RC averaging network operating as a low pass filter. Since the Gulton wave analyzer uses an RC averaging circuit rather than true integration, the averaging time required to find the corresponding values to a true arithmetic mean is important, and in all the analyses presented here an averaging (RC) time constant of 0.5 sec was used with a 20-cycle bandwidth, resulting in an oscillator sweep of 5 cps/sec. With the 1-second loops the averaging time thus extended over four loop circulations. The amplitude error of the power spectral densities obtained, due to instrumentation responses and time lags as given in Ref. [4] is less than 2 percent except for highly peaked spectral response characteristics. In most of the data obtained and presented, the data resonance bandwidth to analyzer bandwidth ratio for the peaks are such that the maximum peak errors are probably less than 10 percent, and the overall accuracy thus within the statistical uncertainty of the assumption of stationary random data for the tape loops.

Sound pressure level vs octave band curves were obtained by planimeter measurements of the power spectral density curves, where

$$db = 20 \log_{10} \left[\frac{P_{rms}(\Delta f)}{P_{ref}} \right] ,$$

and P_{rms} is the square root of the area under the power spectral density curve between f_1 and f_2

$$= \left[\int_{f_1}^{f_2} P^2(f) \, df \right]^{1/2} .$$

and

$$P_{ref} = 0.0002 \ dyne/cm^2 .$$

SURVEY TEST RESULTS

A series of survey tests were made with sound pressure levels recorded at the locations given in Fig. 3. These tests were run with nozzle stagnation pressures of 150, 125, 100,

and 75 psia, each pressure was held constant for approximately 20 seconds in each run in order to obtain sufficient tape loop sampling time. Two test runs were made with the microphones at locations 1, 3, and 5, one without spoilers and one with the spoilers placed as shown in Fig. 5. The microphones were then relocated to positions 2, 4, and 5, and three more test runs made, one without spoilers, one with the spoilers aligned with the flat side parallel to the jet stream, and one with the spoilers again as shown in Fig. 5.

Oscillograph records made from the taped data show increasing amplitudes with increasing nozzle pressure but only data from the test runs at 150 and 100 psia were selected to make power spectral density (PSD) analyses. Figures 8 and 9 show analyses for the 150-psia test runs and are similar to, but of higher level than the 100-psia analyses. The sharp peaks appear to be second and higher harmonics related to the structure dimensions, the particular peak at 1350 cps at location 2 appears to be a function of the shield dimensions. The octave band sound pressures of Fig. 10, obtained from the PSD analyses, are typical of the levels attained and are repeatable.

The general effect of adding spoilers in the jet was to lower the overall db level and to shift the spectra toward the higher frequencies. One analysis from location 3 was extended and showed a flat spectrum out to 5 kc. Spoiler alignment did not appear to be significant, however, different shapes or locations could possibly produce distinct frequency shaping. The data from tests without spoilers show significant low frequency power in the region of the nozzle (locations 1, 2, and 3) which is apparently generated by the large vortices induced in the cavity or interior of the annular jet, and it is possible that the shock waves from the spoilers tend to suppress this vortex generation in addition to producing high frequency turbulence. The missile diffuser pressure fluctuations in flight generally have a large low frequency content and therefore the spoilers were left out for missile tests.

MISSILE RESPONSE DATA

A TALOS missile was installed in the airjet and tunnel, shown schematically in Fig. 4 supported in its handling dolly which provided both leveling capability and pitch restraint. Jet thrust and yaw effects were counteracted by a thrust ring attached to the missile via fittings inserted in the wing sockets while the thrust ring was held by two braces bolted to the test
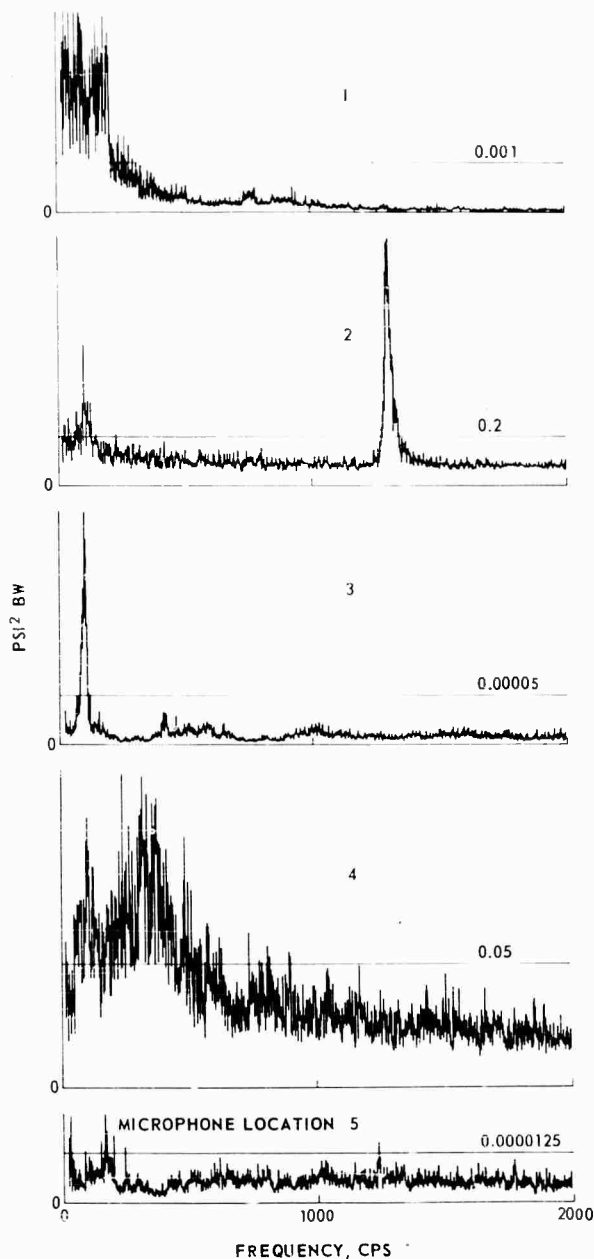
Fig. 8 - Acoustic power spectral densities survey tests at 150 psia (no spoilers)

Fig. 9 - Acoustic power spectral densities survey tests at 150 psia (spoilers in jet)
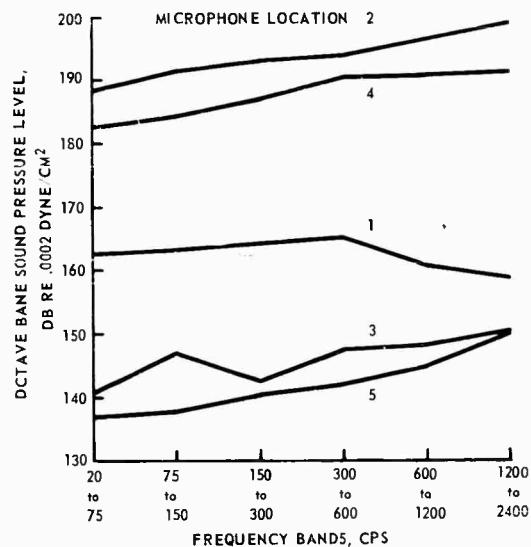
Fig. 10 - Octave band sound pressure level survey tests at 150 psia (no spoilers)

cell floor. This method of support has, of course, a definite effect on the vibration transmission, particularly the natural body modes, and also a probable general damping effect through the hard (support) points. The installed missile is shown in Fig. 11.

Of the missile tests, the main interest was in the telemetered diffuser pressure oscillations
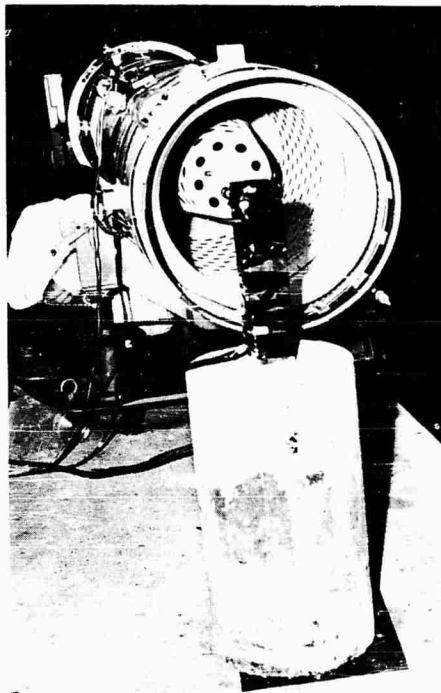
Fig. 11 - Missile test assembly

(pressure transducers at locations 7 and 8) and the resulting vibration acceleration levels. Flight vibration instrumentation and other missile functions were similarly telemetered; while sound pressure levels external to the missile were recorded from microphones at locations 2, 3, and 6, as in the survey runs.

Original plans called for a minimum amount of airjet testing on the missile as it was a flight test vehicle; however, several flight instrumentation malfunctions and mounting problems occurred that earlier mechanical shake tests did not show, and as a result a number of flight instrumentation checkout runs were made with missile access covers off; this presented the opportunity to obtain additional vibration data. The diffuser pressure oscillations and the missile vibrational responses in the airjet tests compared with those obtained from earlier flight tests were considered to be sufficiently similar that a missile systems test for flight operability was made in the airjet environment.

Power spectral density analyses of the oscillatory air pressure data at nozzle pressures of 150, 100, and 50 psig are presented in Figs. 12, 13, and 14 and the corresponding octave band sound pressures for the 150 psig test in Fig. 15. It is interesting to note the spectrum

shift at each location, and particularly the frequency peaks at about 1050 and 2100 cps carried throughout in the 50 psig test. There is an apparent air flow rate below the 50-lb/sec flow at 100-psig nozzle pressure where the lower frequencies are attenuated. This may be due to critical flow rate through the missile combustor can as evidenced by the data from location 6.
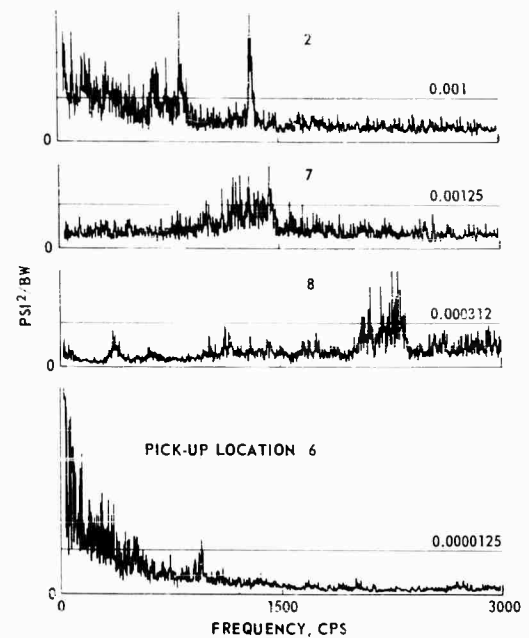
Fig. 12 - Acoustic power spectral densities missile test at 70-lb/sec air flow
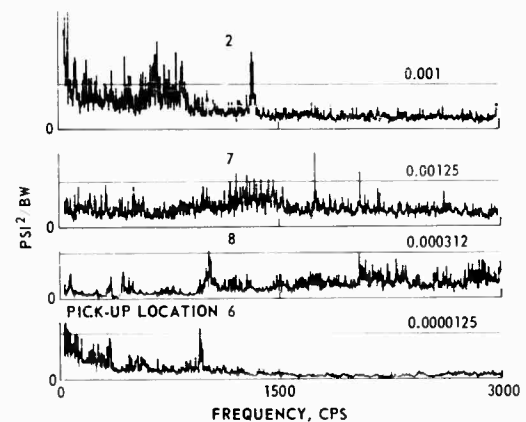
Fig. 13 - Acoustic power spectral densities missile test at 50-lb/sec air flow

219
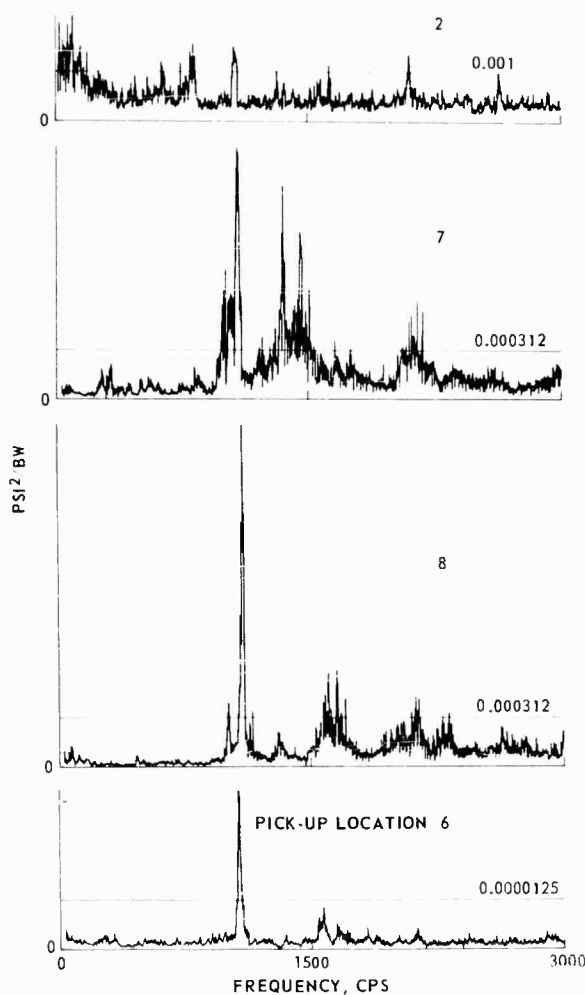
Fig. 14 - Acoustic power spectral densities missile test at 28-lb/sec air flow

Fig. 15 - Octave band sound pressure levels missile test at 70-lb/ sec air flow
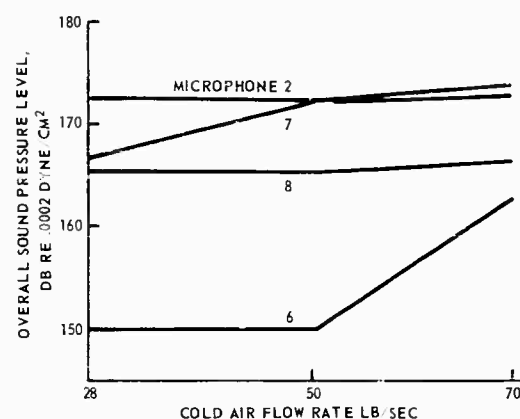
Fig. 16 - Overall sound pressure vs air flow rate

The levels recorded at location 2 in the missile tests are significantly lower than in the surveys, but the 1350-cps spike is still prominent except in the 50-psig test. In missile tests this pick-up is probably behind the compression shock at the missile inlet and hence in a subsonic flow. Also evident is the flatter spectrum, probably due to suppression of the larger vortex generation by the missile nose cone. There is very little reduction in the overall db-level between locations 2 and 7, at least in the 150- and 100-psig tests, whereas there is an attenuation of 5 to 8 db between location 7 and 8 where the annular flow is combined. The overall sound pressure levels versus air flow rate, shown in Fig. 16, appear to confirm the combustor air flow rate is a critical factor in maintaining the diffuser db-level at the lower frequencies.

Vibration measurements were taken mainly on components and component mountings, however, two relevant diffuser vibration PSD analyses are shown in Figs. 17 and 18. Figure 17 is for an accelerometer mounted longitudinally on a flange close to the acoustic pick-up at location 7; and Fig. 18 is for an accelerometer mounted radially on a component attached to the diffuser close to the acoustic pick at location 8.

Typical of the three dimensional vibrations induced in components are the longitudinal and radial acceleration power spectra shown in Fig. 19 for a particular component mounted in the electronics basket, which in turn is attached to the diffuser by isolation mounting.

A microphone in the electronics compartment recorded an overall acoustic pressure
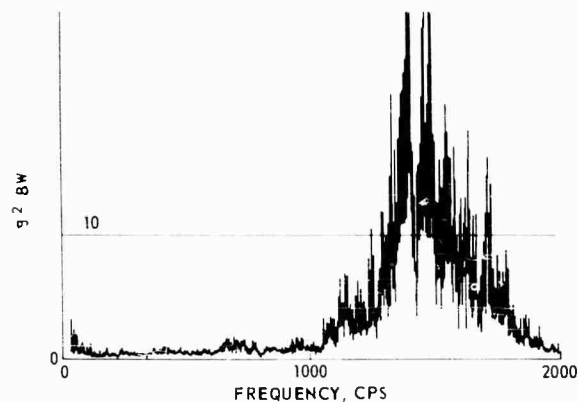
Fig. 17 – Longitudinal acceleration
spectrum on diffuser bell
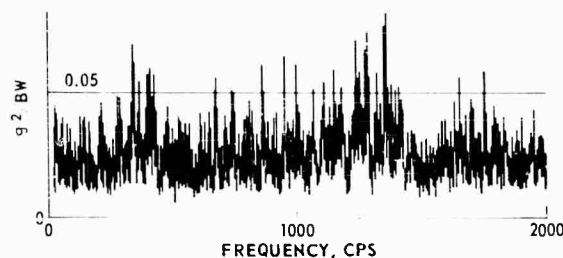
Fig. 18 - Radial acceleration spectrum
on a component attached to the diffuser
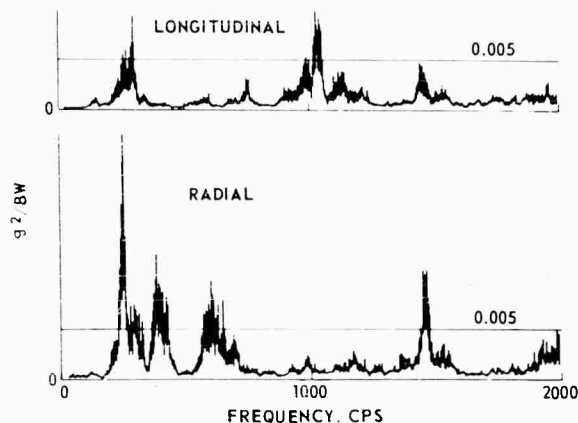
Fig. 19 - Longitudinal and radial accel-
eration spectra of an electronics module

level of 130 db, with a broad frequency content
as shown in the PSD analysis of Fig. 20. As a
result of this measurement the lower dynamic
range of this microphone was set at about 150
db (for flight test) which proved to be too high.
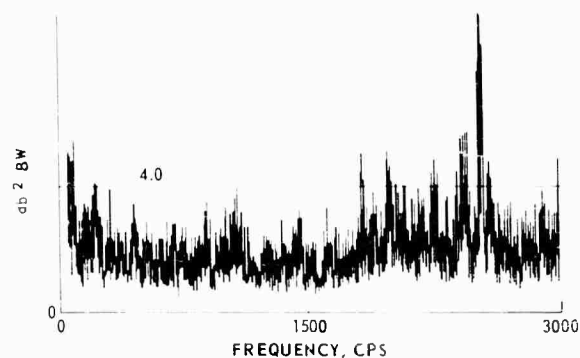
Fig. 20 - Sound pressure spectrum in
electronics compartment. Acoustic
test at 50-lb/sec air flow

Thus, assuming a 140-db sound pressure level,
it would seem that acoustic noise in flight added
no more than about 0.5 g equal acceleration sig-
nal to the flight vibration measurements.

CONCLUDING COMMENTS

From the data of both survey and missile
tests it is evident that the acoustic power spec-
trum can be "tuned" somewhat. It is interest-
ing to speculate that spectral variation might
be obtained by varying the cavity volume or
shape, by modulating the upstream air, or en-
larging the shield length or diameter, although
in relation to the shield length the survey data
from the microphones at locations 1 through 4
appear to confirm that the extrapolated mixing
length of Fig. 2 was not far off. It is hoped that
further testing may define some of the design
parameters from which other possible test uses
and test equipment designs can be derived.

The missile on which the acoustic tests
were made was flight tested in July of this year,
and, at the time of writing full spectral analyses
and correlation of the flight data with the airjet
test data have yet to be completed. Sufficient
information is available, however, to show that
acceleration levels and spectra in the forward
part of the missile are in close agreement. In
the aft part of the missile both pressure oscil-
lations and acceleration levels were consider-
ably lower in the airjet tests, as was expected.

Although the annular airjet noise generator
was designed for a ramjet application, it is ap-
parent that its usefulness is not necessarily
limited to ramjet missiles, but can be utilized
to simulate the flight environment of a rocket
missile. In fact, with all the turbulent air
flowing over the outside of the missile body,

221

the overall simulation of boundary layer excitation might well be closely duplicated.

The airjet acoustic noise generator appears to overcome a number of the limitations of electrodynamic shakers in the testing of complete missiles, the principal advantage being the ability to test a complete missile system at a representative flight vibration level with a distributed forcing function. It is probable that an airjet acoustic noise source cannot provide precise duplication or control of a specified environment as the control parameters are not sufficiently sensitive. In this regard it is questionable whether a high degree of precision in

duplication is necessary, in view of the wide variations of flight test data both in magnitude and frequency content not only from flight to flight but within any one flight profile. With a vibration or acoustic spectrum standardized as representative of a flight environment, the airjet noise generator can be calibrated and geometry fixed to provide a repeatable environment for acceptance tests of complete missile systems.

REFERENCES

1. Phillip M. Edge, "Random Noise Testing of Aircraft and Missile Components with the Aid of a Laboratory Airjet," Shock and Vibration Bulletin No. 27 Part II (June 1959).

2. M. J. Lighthill, "Jet Noise," AIAA Journal (July 1963).

3. Wilson Bradley, Jr., "Effects of High Intensity Acoustic Fields on Crystal Vibration Pick-ups," Shock and Vibration Bulletin No. 26 Part II (Dec. 1958).

4. J. F. Burns, "Description of Data Processing Methods for Wave Analysis on an Analog Computer," APL Internal Memo BID T-0229 (May 26, 1964).

DISCUSSION

Mr. Roberts (Martin, Orlando): It isn't apparent whether you are trying to simulate flow rates or scale of turbulence or separation inside this inlet. Would you describe the test a little bit more and try to validate the procedure relative to the objective of the test?

Mr. Richards: We are trying to simulate the oscillatory pressures, particularly inside the diffuser, in this missile. Later on we may try to simulate on other types of missiles the boundary layers, which are the source of the vibrations so that we can test any particular component to a fairly wide band, random frequency, or whatever the input is into the structure, as part of the environmental program. Now, if we can closely simulate the spectra for the diffuser and the pressure oscillations in the diffuser then we are repeating on the ground the main sources of oscillation on the missile structure that we would see in flight. This is done by blowing air through the missile essentially.

Mr. Roberts: Is the flow rate aerodynamically correct?

Mr. Richards: No, the flow rate in the missile varies all over the map. It depends on the Mach number and the altitude. It can go up to 200 lb/sec.

Mr. Roberts: How did you choose the maximum flow rate?

Mr. Richards: The flow rate here was chosen just based on what the facility could supply. We didn't know what we were going to get. The 50 lb/sec for 2 minutes is what the facility could supply and we designed the nozzle for that.

Mr. Roberts: What is the cause of the excitation within the turbulence?

Mr. Richards: The series of shocks at the diffuser intake, the flow changes generating turbulence in its own right, and the flow through the combuster can are inducing some oscillations. There are shocks racing up and down with sudden fuel flow changes. As we got in the flight test, we get a sudden shock racing up and

down the diffuser. All of these are pressure oscillations which are putting force inputs into the panel structure of the missile.

Mr. Roberts: Is there any reason to believe that the acoustic method here is in any way approaching the excitations which are taking place inside the diffuser? It would appear that what you have here is not a simulation of the event.

Mr. Richards: I can't tell you that we're not simulating the events in the diffuser. The diffuser is the prime source of vibration in this particular missile. We are getting close to it. We don't have as much low frequency power and unfortunately we don't have the flight diffuser pressures reduced yet, but we hope to be able to get a very close simulation of the spectrum. I believe we can do this. At what body station? You are not going to get an identical simulation with body station. You will be able to pick one body station and get something close. We are not going to be able to reproduce everything exactly, but we are going to be able to shake the missile and get the spectra on the components and on the structure to simulate very closely that of flight.

*   *   *

GRAPHICAL METHOD OF CALCULATING RMS VALUES
FOR SHAPED RANDOM VIBRATION SPECTRA

H. Himelblau
Space & Information Systems Division
North American Aviation, Inc.
Downey, California

By using a composite of straight line segments, the rms displacement,
velocity, and acceleration for any random vibration spectrum can be
calculated. Equations and graphs for performing these calculations are
presented.

INTRODUCTION

Most random vibration spectra are presented on log-log graph paper with acceleration spectral density as the ordinate and frequency as the abscissa. Design and test criteria are often given by a composite of straight line segments, such as Fig. 1. For non-white portions of these spectra, the slope of each segment is usually called out in terms of its roll-off (or roll-up) rate, i.e., so many db/octave. Random vibration data from field measurements and analytical predictions may be similarly approximated by a series of straight line segments, with the requirements for accuracy determining the number of segments to be utilized.

It is often desirable to find the rms displacement, velocity, and acceleration associated with these spectra once they have been plotted. The following method, proposed by Sandia personnel [1] and Sandler [2], has been used for this determination.

RMS ACCELERATION

The familiar relationship of the mean square acceleration $\ddot{x}_r^2$ and the acceleration spectral density $F(f)$ is

$$\ddot{x}_r^2 = \int_{f_a}^{f_b} F(f) \, df , \qquad (1)$$

NOTE: References appear on page 237.
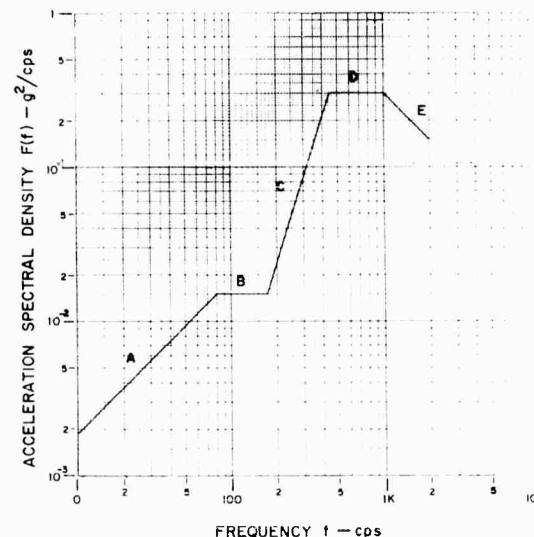
Fig. 1 – Typical random vibration
design and test criteria

where f_a and f_b are the lower and upper frequency limits of the entire spectrum. Let a portion of the spectrum be represented by a straight line segment from f_1 to f_2. The acceleration spectral density at any point of the segment at frequency f is given by

$$F(f) = F(f_r) \left[f / f_r \right]^{R/3} . \qquad (2)$$

where f_r is the arbitrarily-selected reference frequency for the segment ($f_1 \leq f_r \leq f_2$), and R is the roll rate in db/octave (R = 0 for a white spectral segment, i.e., constant acceleration

225

spectral density, $R > 0$ for roll-up or positive slope and $R < 0$ for roll-off or negative slope). By substituting Eq. (2) into Eq. (1), the mean square acceleration for the segment is

$$\Delta \ddot{x}_r^2 = F(f_r) \, f_r^{-R/3} \int_{f_1}^{f_2} f^{R/3} \, df . \qquad (3)$$

Thus, for $R \neq -3$:

$$\Delta \ddot{x}_r^2 = \frac{3F(f_r)}{(R+3)f_r^{R/3}} \left[f_2^{(R+3)/3} - f_1^{(R+3)/3} \right] . \qquad (4)$$

For $R = -3$:

$$\Delta \ddot{x}_r^2 = F(f_r) \, f_r \, \ln (f_2/f_1) . \qquad (5)$$

For a white spectrum ($R = 0$), the obvious result is

$$\Delta \ddot{x}_r^2 = F(f_r) \left[f_2 - f_1 \right] . \qquad (6)$$

By using a composite of straight line segments, the total rms acceleration can be calculated from

$$\ddot{x}_r = \left(\sum_{i=1}^{k} \Delta \ddot{x}_{ri}^2 \right)^{1/2} , \qquad (7)$$

where i is the number of the segment and k is the total number of segments. If $F(f)$ and f are expressed in (g^2/cps) and cps, respectively, then $\ddot{x}_r$ is in g rms.

RMS VELOCITY

The relationship between the mean square velocity $\dot{x}_r^2$ and the velocity spectral density $V(f)$ is

$$\dot{x}_r^2 = \int_{f_a}^{f_b} V(f) \, df . \qquad (8)$$

At frequency f, the velocity and acceleration spectral densities are related by [3]

$$V(f) = 3774 \, f^{-2} F(f) , \qquad (9)$$

where $V(f)$ and $F(f)$ are expressed in (in.^{2}/sec^2 cps) and (g^2/cps), respectively. By substituting Eqs. (2) and (9) into Eq. (8), and using the roll rate R as defined above (as the slope of a segment on log-log graph of $F(f)$ vs

frequency), the mean square velocity for a straight line segment is

$$\Delta \dot{x}_r^2 = 3774 \int_{f_1}^{f_2} f^{-2} F(f) \, df \qquad (10)$$

$$= 3774 \, F(f_r) \, f_r^{-R/3} \int_{f_1}^{f_2} f^{(R-6)/3} \, df . \qquad (11)$$

Thus for $R \neq +3$:

$$\Delta \dot{x}_r^2 = \frac{11.32 \times 10^3 \, F(f_r)}{(R-3) \, f_r^{R/3}} \left[f_2^{(R-3)/3} - f_1^{(R-3)/3} \right] . \qquad (12)$$

For $R = +3$:

$$\Delta \dot{x}_r^2 = 3774 \, F(f_r) \, f_r^{-1} \ln (f_2/f_1) . \qquad (13)$$

By using a composite of the same straight line segments mentioned above, the total rms velocity can be calculated from

$$\dot{x}_r = \left(\sum_{i=1}^{k} \Delta \dot{x}_{ri}^2 \right)^{1/2} , \qquad (14)$$

where $\dot{x}_r$ is expressed in (in./sec) rms.

RMS DISPLACEMENT

The relationship between the mean square displacement x_r^2 and the displacement spectral density $H(f)$ is

$$x_r^2 = \int_{f_a}^{f_b} H(f) \, df . \qquad (15)$$

At frequency f, the displacement and acceleration spectral densities are related by [3]

$$H(f) = 95.60 \, f^{-4} F(f) , \qquad (16)$$

where $H(f)$ and $F(f)$ are expressed in (in.^{2}/cps) and (g^2/cps), respectively. By substituting Eqs. (2) and (16) in Eq. (15), and using the roll rate R as defined above, the mean square displacement for a straight line segment is

$$\Delta x_r^2 = 95.60 \int_{f_1}^{f_2} f^{-4} F(f) \, df \qquad (17)$$

226

$$\Delta x_r^2 = 95.60 \ F(f_r) \ f_1^{-R/3} \int_{f_1}^{f_2} t^{(R-12)/3} \, df . \quad (18)$$

Thus for $R \neq +9$:

$$\Delta x_r^2 = \frac{286.3 \ F(f_r)}{(R-9) \ f_r^{R/3}} \left[f_2^{(R-9)/3} - f_1^{(R-9)/3} \right] . \quad (19)$$

For $R = +9$:

$$\Delta x_r^2 = 95.60 \ F(f_r) \ f_r^{-3} \ \ln \ (f_2/f_1) . \quad (20)$$

By using a composite of the same straight line segments mentioned above, the total rms displacement can be calculated from

$$x_r = \left(\sum_{i=1}^{k} \Delta x_{ri}^2 \right)^{1/2} , \quad (21)$$

where x_r is expressed in in. rms.

LOWER FREQUENCY REFERENCE

It is often convenient to use either the lower frequency f_1 or the upper frequency f_2 of a particular segment for the reference frequency f_r. If the lower frequency is selected (i.e., $f_1 = f_r$):

$$\frac{\Delta \ddot{x}_r^2}{F(f_1)f_1} = \frac{3}{R+3} \left[\left(\frac{f_2}{f_1} \right)^{(R+3)/3} - 1 \right] \quad (R \neq -3) \quad (22)$$

$$= \ln \ (f_2/f_1) \qquad (R = -3), \quad (23)$$

$$\frac{\Delta \dot{x}_r^2 \ f_1}{F(f_1)} = \frac{11.32 \times 10^3}{R-9} \left[\left(\frac{f_2}{f_1} \right)^{(R-3)/3} - 1 \right] \quad (R \neq +3) \quad (24)$$

$$= 3774 \ \ln \ (f_2 \ f_1) \qquad (R = +3), \quad (25)$$

$$\frac{\Delta x_r^2 f_1^3}{F(f_1)} = \frac{286.8}{R-9} \left[\left(\frac{f_2}{f_1} \right)^{(R-9)/3} - 1 \right] \quad (R \neq +9) \quad (26)$$

$$= 95.60 \ \ln \ (f_2/f_1) \qquad (R = +9). \quad (27)$$

The first two, middle two, and last two equations are plotted on Figs. 2-4, 5-7, and 8-10, respectively. In each figure, use (f_2/f_1) as the abscissa and the values of R applicable to (f_2/f_1) which is designated in the upper right-hand corner.

UPPER FREQUENCY REFERENCE

By using the upper frequency as the reference frequency for a particular segment (i.e., $f_2 = f_r$):

$$\frac{\Delta \ddot{x}_r^2}{F(f_2)f_2} = \frac{3}{R+3} \left[1 - \left(\frac{f_1}{f_2} \right)^{(R+3)/3} \right] \quad (R \neq -3) \quad (28)$$

$$= \ln \ (f_2/f_1) \qquad (R = -3), \quad (29)$$

$$\frac{\Delta \dot{x}_r^2 \ f_2}{F(f_2)} = \frac{11.32 \times 10^3}{R-3} \left[1 - \left(\frac{f_1}{f_2} \right)^{(R-3)/3} \right] \quad (R \neq +3) \quad (30)$$

$$= 3774 \ \ln \ (f_2/f_1) \qquad (R = +3), \quad (31)$$

$$\frac{\Delta x_r^2 f_2^3}{F(f_2)} = \frac{286.8}{R-9} \left[1 - \left(\frac{f_1}{f_2} \right)^{(R-9)/3} \right] \quad (R \neq +9) \quad (32)$$

$$= 95.60 \ \ln \ (f_2/f_1) \qquad (R = +9). \quad (33)$$

The first two, middle two, and last two equations are also plotted on Figs. 2-4, 5-7, and 8-10, respectively. In each figure, use (f_1/f_2) as the abscissa and the values of R applicable to (f_1/f_2) which is designated in the upper right-hand corner.

By using these figures (or Eqs. (22) - (33) if greater accuracy is desired) together with Eqs. (7), (14), and (21), the rms acceleration, velocity, and displacement for any random vibration spectrum can be calculated.

EXAMPLE

The rms displacement, velocity, and acceleration are desired for the random vibration spectrum of Fig. 1. Considering each straight line segment of the spectrum separately, the rms values are calculated following the procedure outlined in Table 1.

DEFINITION OF SYMBOLS

f = frequency (cps)

f_r = reference frequency

f_1, f_2 = lower and upper frequency of a straight line segment, respectively

227

R = slope of a straight line segment on a log-log graph of $F(f)$ vs frequency (db/octave)

$x_r, \dot{x}_r, \ddot{x}_r$ = rms displacement (in. rms), rms velocity (in. rms/sec), and rms acceleration (g rms), respectively

Δ = incremental value for a straight line segment

$H(f), V(f), F(f)$ = displacement spectral density (in.^{2}/cps), velocity spectral density (in.^{2}/sec^2 cps), and acceleration spectral density (g^2/cps), respectively, at frequency f.
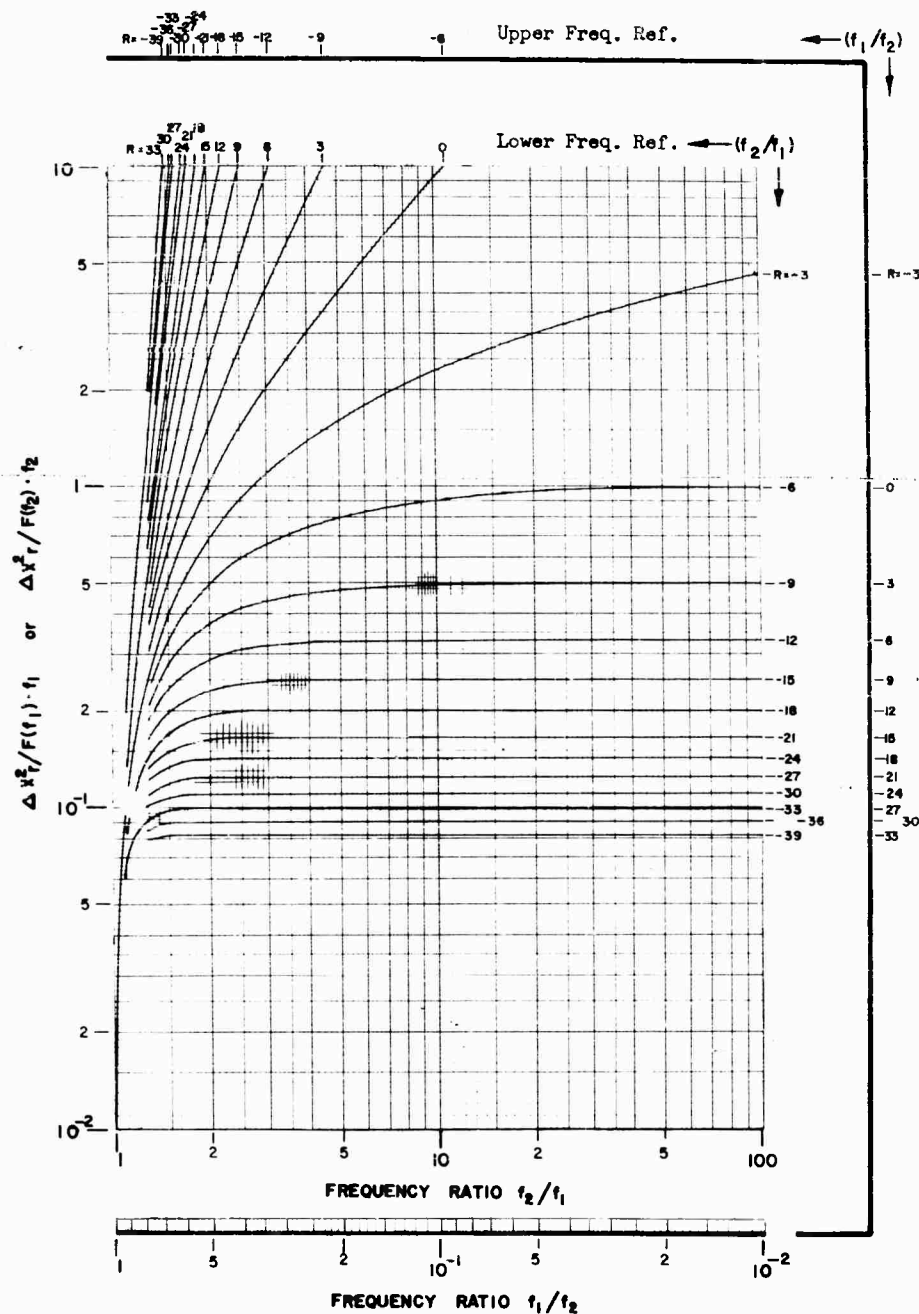
Fig. 2 - Nomograph for calculation rms acceleration for values of $\Delta \ddot{x}_r{}^2/F(f_r) f_r$ between 10^{-2} and 10
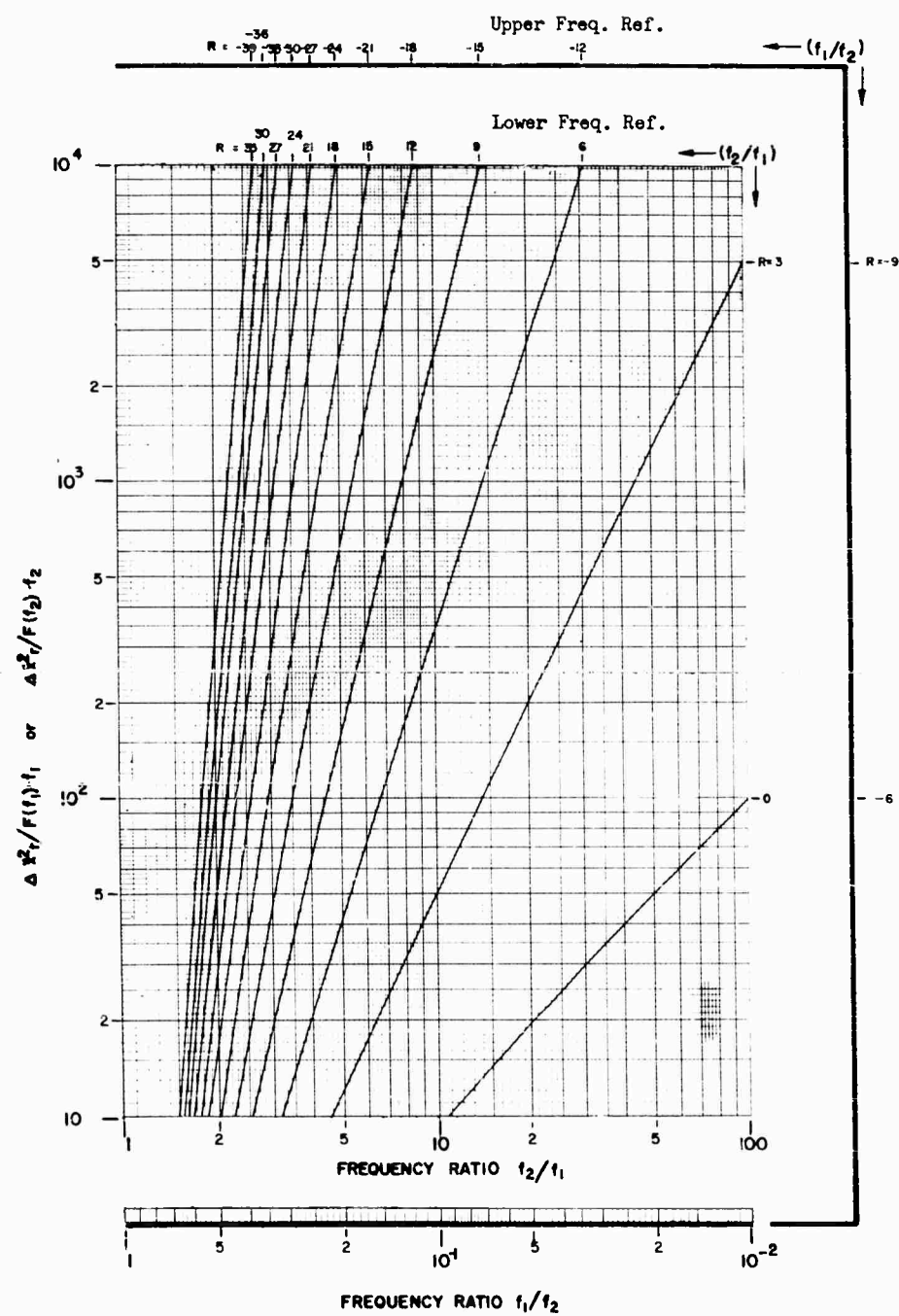
Fig. 3 - Nomograph for calculating rms acceleration for values of $\Delta \ddot{x}_r^2 / F(f_r) \, f_r$ between 10 and 10^4
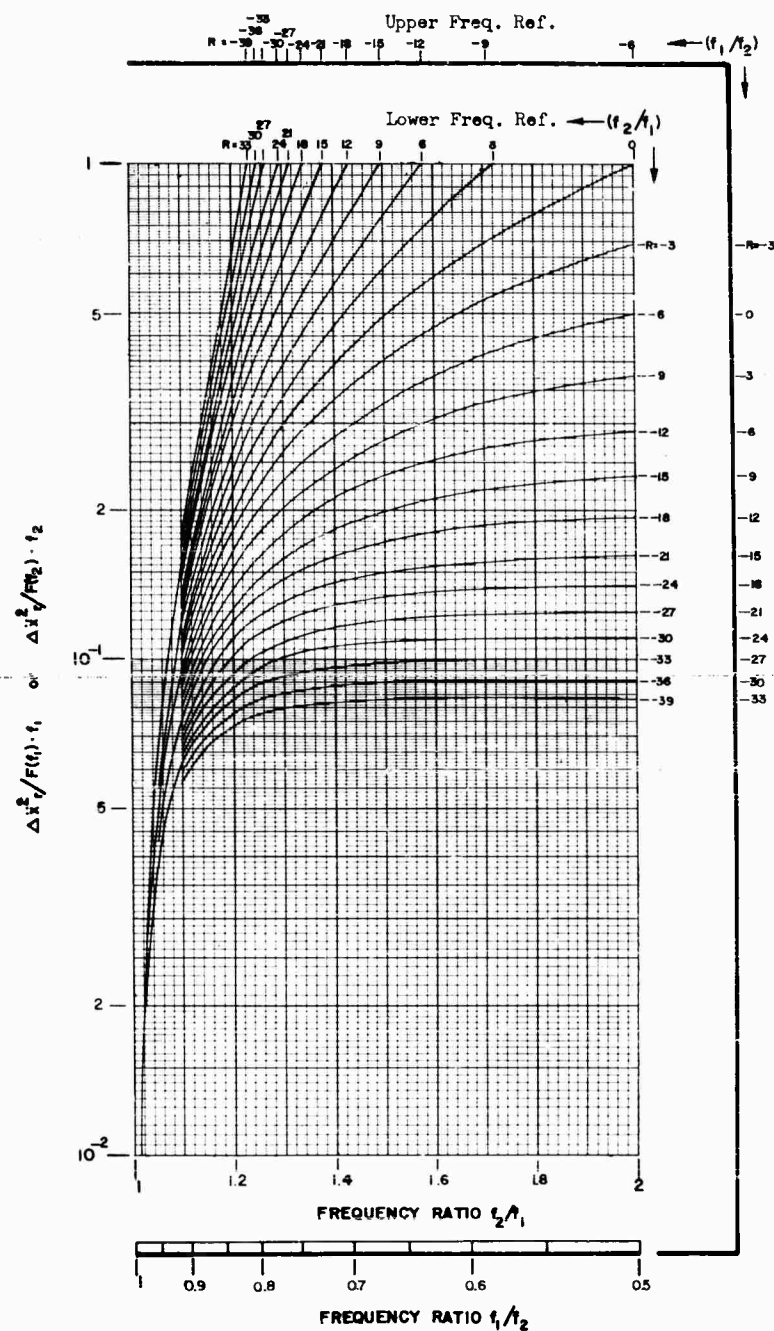
Fig. 4 - Nomograph for calculating rms acceleration for values of $\Delta \ddot{x}_r^2 / F(f_r) f_r$ between 10^{-2} and 1 for $(f_2/f_1) < 2$ or $(f_1/f_2) > 0.5$

Fig. 5 - Nomograph for calculating rms velocity for values of
$\Delta \dot{x}_r{}^2 f_r / F(f_r)$ between 10 and 10^4
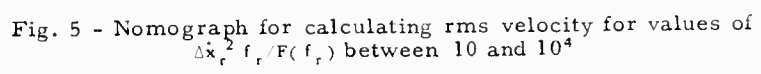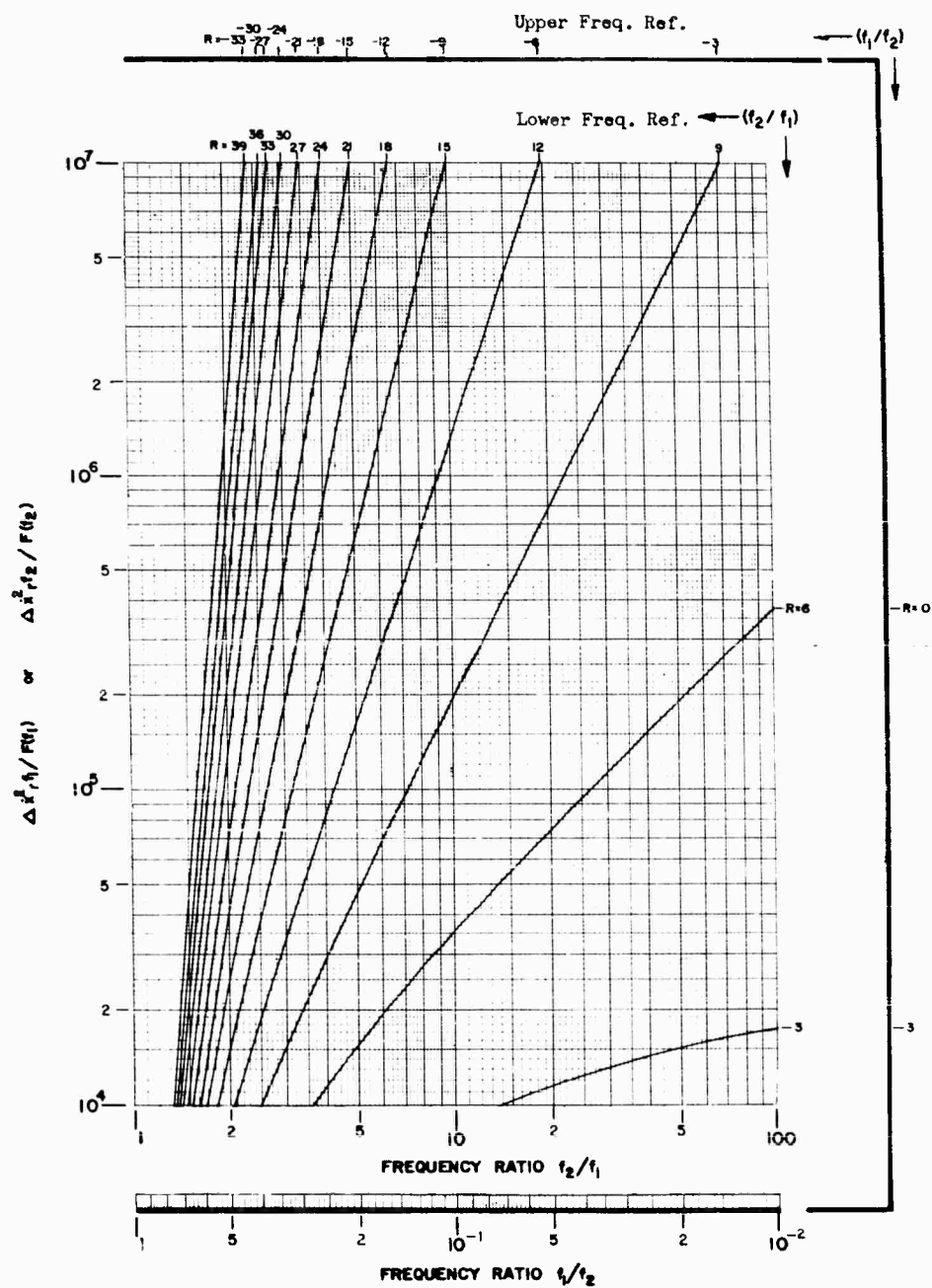
Fig. 6 - Nomograph for calculating rms velocity for values of $\Delta \dot{x}_r^2 f_r / F(f_r)$ between 10^4 and 10^7
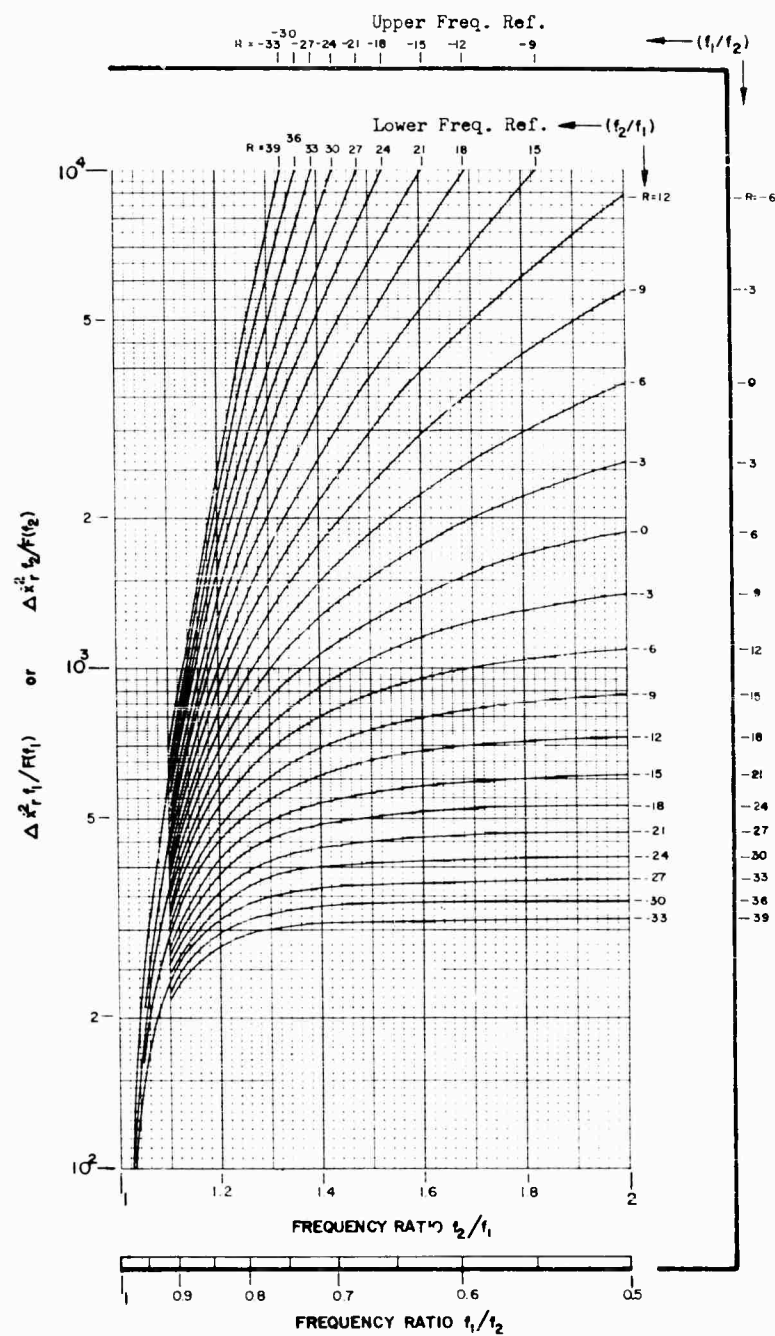
Fig. 7 - Nomograph for calculating rms velocity for values of $\Delta \ddot{x}_r^2 \, f_r / F(f_r)$ between 10^2 and 10^4 for $(f_2/f_1) < 2$ or $(f_1/f_2) > 0.5$
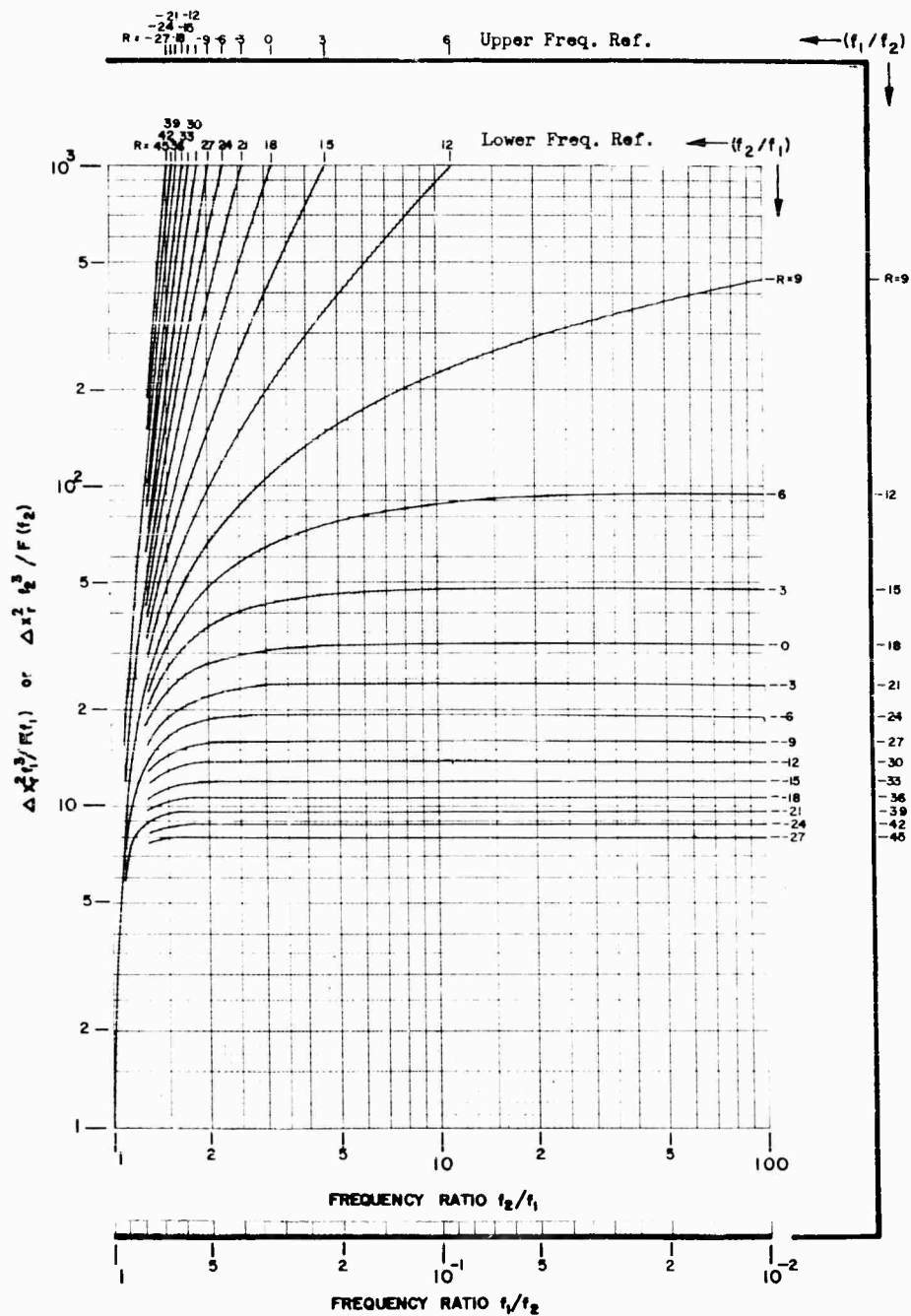
Fig. 8 - Nomograph for calculating rms displacement
for values of $\Delta x_r^2 f_r^3 / F(f_r)$ between 1 and 10^3
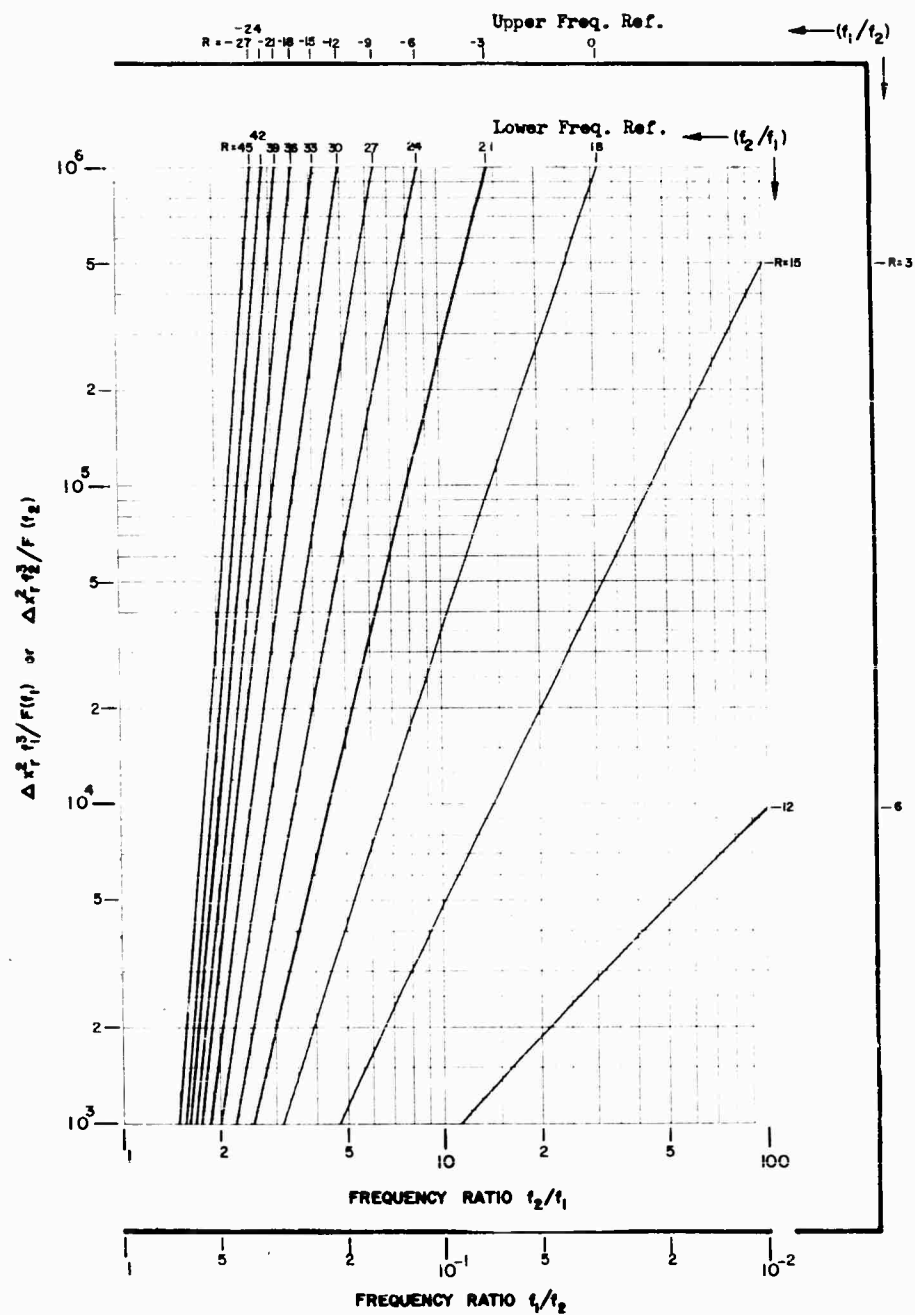
Fig. 9 - Nomograph for calculating rms displacement
for values of $\Delta x_r^2 f_r^3/F(f_r)$ between 10^3 and 10^6
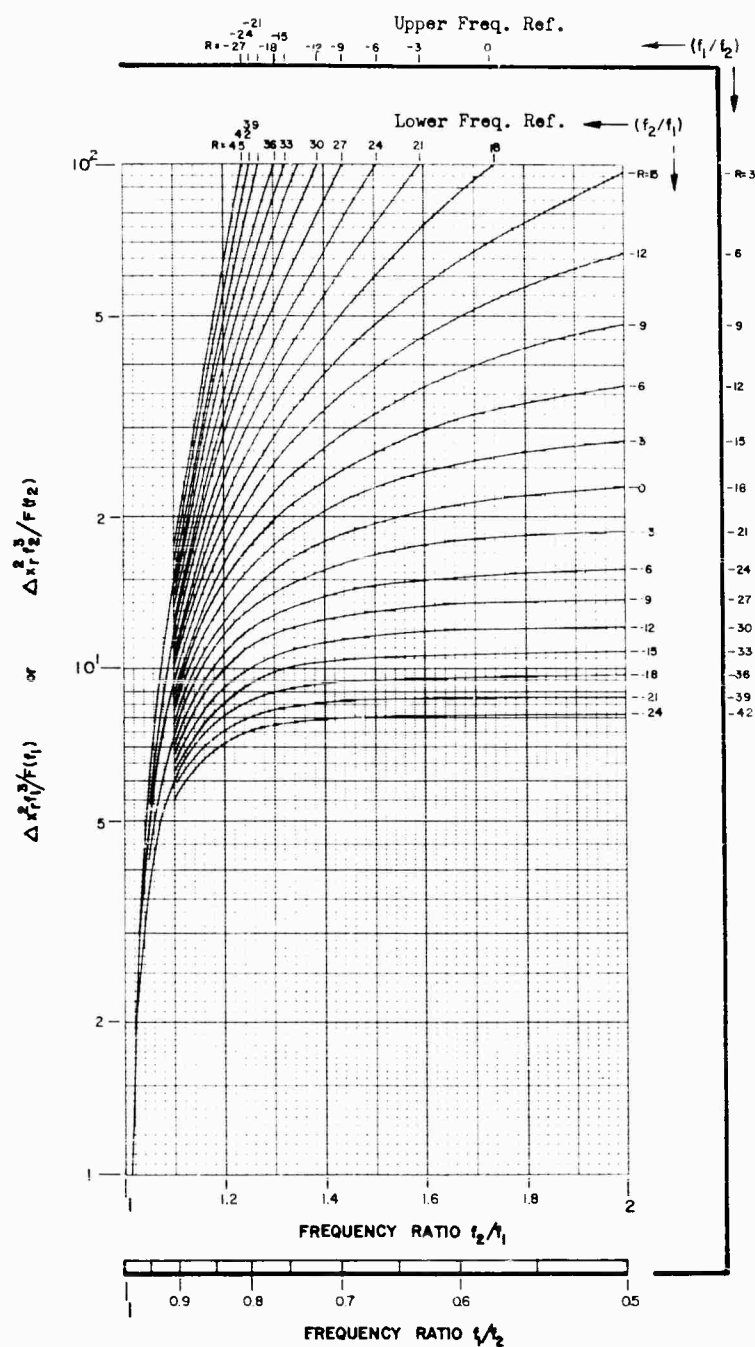
Fig. 10 - Nomograph for calculating rms displacement for values of $\Delta x_r^2 f_r^3 F(f_r)$ between 1 and 10^2 for $(f_2/f_1) < 2$ or $(f_1/f_2) > 0.5$

236

TABLE 1
Typical Calculation of rms Displacement, Velocity, and Acceleration

$$\ddot{x}_r = (408)^{1/2} = 20.2 \text{ g rms} \qquad\qquad x_r = (89.4 \times 10^{-6})^{1/2} = 0.00946 \text{ in. rms}$$

$$\dot{x}_r = (4.72)^{1/2} = 2.17 \text{ (in./sec) rms} \qquad\qquad = 9.46 \text{ mil rms}$$

Seg-ment	Ref. Freq. f_r	Ref. Freq. (cps)	Spectral Density at f_r (g^2/cps)	Roll Rate (db/oct)	$f_1/f_2{}^a$ or f_2/f_1	$\dfrac{\Delta\ddot{x}_r^2}{F(f_r)f_r}$	$\Delta\ddot{x}_r^2$ (g^2)	$\dfrac{\Delta\dot{x}_r^2 f_r}{F(f_r)}$	$\dfrac{\Delta\dot{x}_r^2}{F(f_r)}$ (in./sec)^2	$\dfrac{\Delta x_r^2 f_r^3}{F(f_r)}$	Δx_r^2 (in.^{2})
A	f_2	80	0.015	+3	0.125	0.492	1	7850	1.47	3010	88.2×10^{-6}
B	f_1	80	0.015	0	2.19	1.19	1	2050	0.38	29	0.8×10^{-6}
C	f_2	450	0.3	+9	0.389	0.244	33	1600	1.07	90	0.3×10^{-6}
D	f_1	450	0.3	0	2.22	1.22	165	2080	1.38	29	0.1×10^{-6}
E	f_1	1000	0.3	-3	2.0	0.693	208	1420	0.42	·22	--
SUM:							408		4.72		89.4×10^{-6}

[a] Values of $(f_1/f_2) \cdot 1$ and $(f_2 f_1) > 1$.

REFERENCES

1. "Engineering Development, Sandia Corporation, Standard Test Methods," Rept. SC-4452A(M) (Feb. 1962).

2. I. J. Sandler, "Techniques of Analysis of Random and Combined Random-Sinusoidal Vibration," Shock and Vib. Bull. No. 31, Part III (Apr. 1963), pp. 211-224.

3. H. Himelblau, "Random Vibration Nomograph," Noise Control, Vol. 5, No. 3 (July 1959), pp. 49-50.

DISCUSSION

Mr. Clevenson (Langley Research Center, NASA): It is pretty well known that in getting the rms level you have gotten the area under these various curves. Since you are using log-log paper, how did you manage to get the areas which must be based on linear measurements?

Mr. Himelblau: The alternative technique is to replot the curve. For example, if you happen to have the data read out from a field experiment in terms of linear coordinates, then you can simply take the area under the curve. Most often it is on log-log. The mathematical relationships still apply, and this is simply what I used, so, in effect, it is the area under the curve which you can obtain by the planimeter method or other normal graphical methods if it is on linear. If it is on log, this technique usually is not the one to use, and one can rely on the basic mathematical expressions for determining the values. I don't know if I've answered your question, but I tried.

DESIGN EVALUATION THROUGH VIBRATION TEST PROGRAM*

D. A. Hausrath and J. R. Read
Autonetics
Division of North American Aviation, Inc.
Anaheim, California

INTRODUCTION

The qualification test activities presented in this study are the results of the proposed use of an Autonetics off-the-shelf VERDAN computer in a particular airborne installation where it would be subjected to a severe random vibration environment. A significant factor regarding this use of the computer was that it be hard-mounted (i.e., having no vibration isolators) to its installation supports, since preliminary design of the equipment compartment was based on this type of mounting system.

The vibration spectrum, which was originally submitted to Autonetics as the Qualification Test requirement, is shown in Fig. 1. It represents an overall acceleration value of 7.5 g rms. Qualification of the computer to this environment required that this level of random excitation be maintained for 30 minutes in each of the three orthogonal axes. The VERDAN has successfully passed previous vibration tests, consisting of sinusoidal excitation at levels up to 3.5 g, but it was not known if it could operate successfully in the proposed random vibration environment.

DESCRIPTION OF COMPUTER

The VERDAN is a combined general-purpose computer and digital differential analyzer; it weighs approximately 82 pounds. The size of the package is $15.5 \times 8 \times 19.5$ inches or approximately 1.4 cu ft (see Figs. 2-5).

One important concept to be understood about the VERDAN computer is that the chassis is not a strong container in which components are placed to be free from external stresses. Rather, all components lend physical support to one another — a condition too complex for the usual analytical methods of vibration analysis.

It was the complexity, however, coupled with the intricacies of computer operation, that made this study a challenging one.

TEST I

The vibration axes, as shown in Fig. 6, were defined by a combination of two directions, such as fore-aft, up-down, or left lateral - right lateral. These directions were based upon the proposed orientation of the computer within the service environment.

1. The Environmental Laboratory would prepare a programmed magnetic tape to provide 30 minutes of calibrated input signal for the vibration amplifier system according to the specified random vibration spectrum.

2. The computer would be turned on, and then mounted upon the shaker for vibration in one of the three axes. A rectangular aluminum plate would be used as a mount fixture. The up-down and left-right lateral axes would utilize a granite slip-table or oil-slick on which the fixture would rest. The fixture would tie directly to the shaker for vibration in the up-down axis. Figure 7 shows a typical test setup with the VERDAN mounted in the fore-aft axis.

3. An input accelerometer would be mounted on the shaker plate at the base of the computer, and an output accelerometer would be mounted on the computer with axis sensitivity parallel to the shake direction.

4. Before starting the vibration test in a given axis, the system would be equalized in that specific axis by subjecting the entire system to a low level, sinusoidal "survey sweep" of approximately 2 to 4 g.

5. After equalization, the computer would be subjected to the required vibration spectrum,

---

Fig. 1 - Specified random vibration spectrum

Fig. 2 - VERDAN computer; closed position

starting with a value of 2 g and increasing by successive 0.5-g increments until a computer malfunction occurred. Note: The vibration level was to be varied by the value of overall rms acceleration only, with the spectrum shape being held within tolerance at all times. The spectrum would continue to have the same shape, having a uniform change of the power
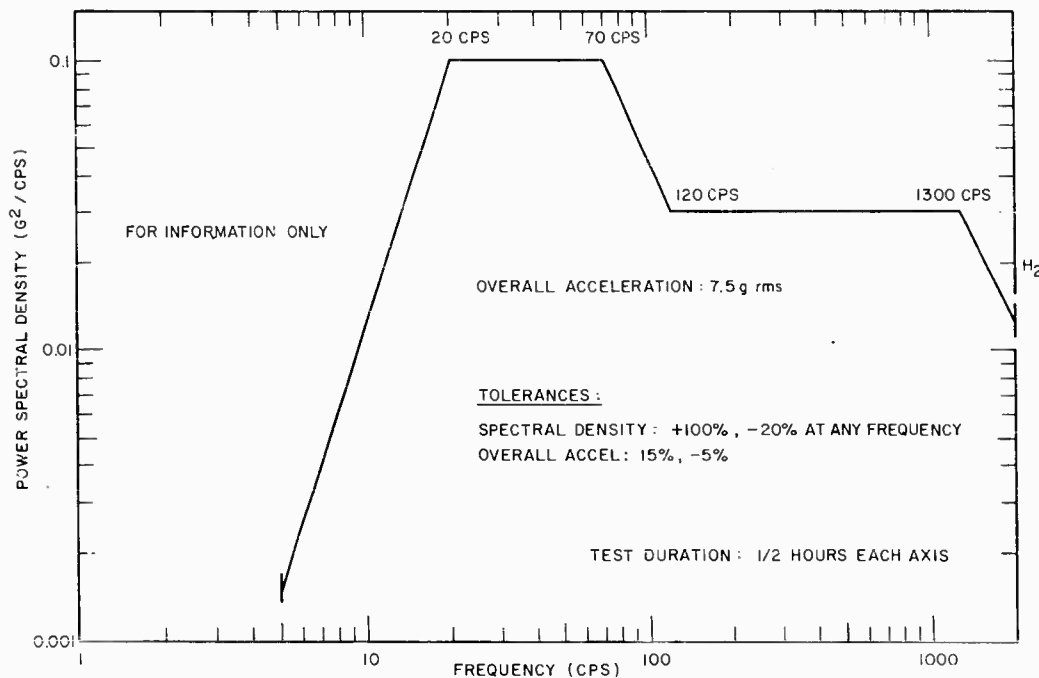
spectral density for each frequency. The vibration level at the time of computer malfunction would then be known, and could be reproduced after computer repair for analysis of the corrective action.

6. If a malfunction occurred, the computer would be removed from the slip-table or shaker and mounted on the VERDAN test stand for analysis and correction. After correction of the malfunction, testing would be resumed at 2 g and increased as stipulated. This type of repetitive shake and fix routine would continue until 7.5 g or the design limitation of the computer was exceeded. If a malfunction was intermittent or was of such a nature that it did not recur when vibration of the computer ceased, the test procedure would be altered to permit vibration of the computer for diagnostic purposes.

One intermittent computer error indication occurred during this test. The malfunction disappeared when vibration ceased. Because of this type of malfunction, it became necessary to define the condition which would constitute proof that VERDAN was incapable of meeting the specified requirements. It was decided that any malfunction of the computer which demonstrated that the design limitations had been exceeded would be designated as a failure. Malfunctions which could be attributed to faulty

240

Fig. 3 - VERDAN computer; open position

components, poorly soldered connections, or manufacturing errors, however, would not be taken to indicate a computer failure per se, but rather that special attention to these areas could increase the vibration capabilities and reliability of the package. In light of this reasoning, Test II was developed.

TEST II

The purpose of Test II was to establish the design limitations of the VERDAN computer when subjected to various levels of random vibration below 7.5 g. The testing procedures were the same as for Test I, except that the equalization process was simplified by the use of an equalizer-analyzer. A low level (approximately 2-g rms) random signal was fed to the shaker system with the computer mounted and operating. The input was then adjusted to the specified spectrum.

In each test, throughout the program, a record of the input spectrum was kept by recording a 10-second "burst" of the input accelerometer at the specified level of 7.5-g rms. In this manner, a plot of the power spectral density vs frequency could be made and analyzed for verification that specifications were met throughout the frequency range. Analyses of spectrum shapes were accomplished with a 10-cycle bandwidth filter. The maximum roll-off rate was 12 db per octave.

Vibration of the computer package was monitored with accelerometers at a few strategic points. Measurements on the cover plate indicated amplification values of as high as four. Both computer covers were flexing. During the vibration, computer malfunctions occurred which were caused by broken wires, intermittent diodes, and "cold" solder connections. Also, the memory solenoid became disconnected from its mounting. The top half of
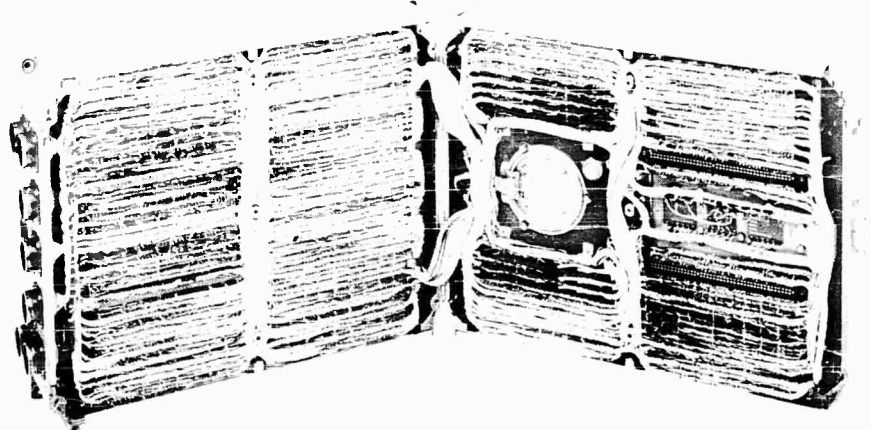
Fig. 4 - VERDAN computer; wiring harness area

241
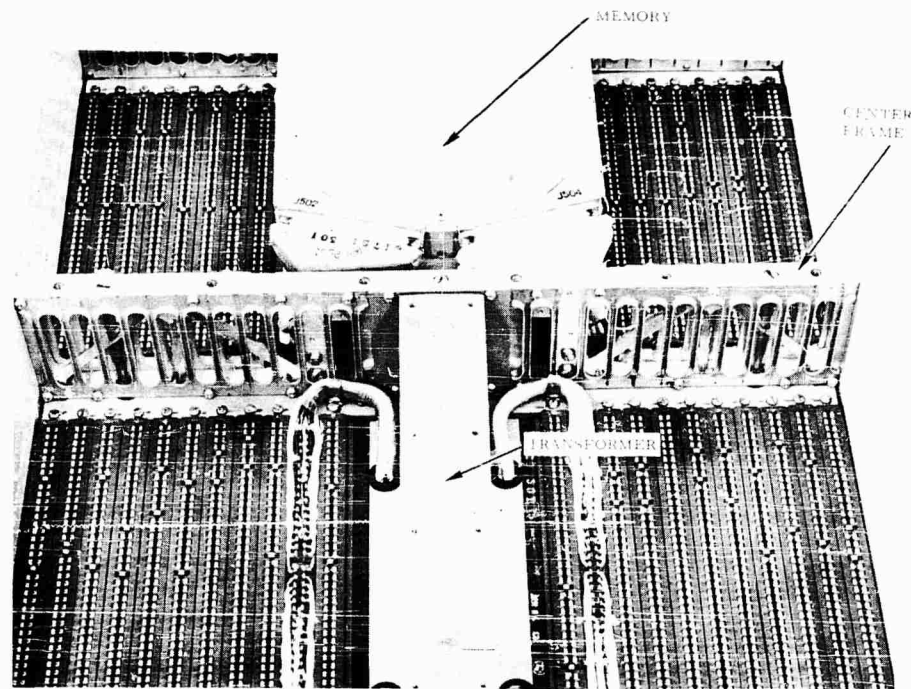
Fig. 5 - VERDAN computer; chassis
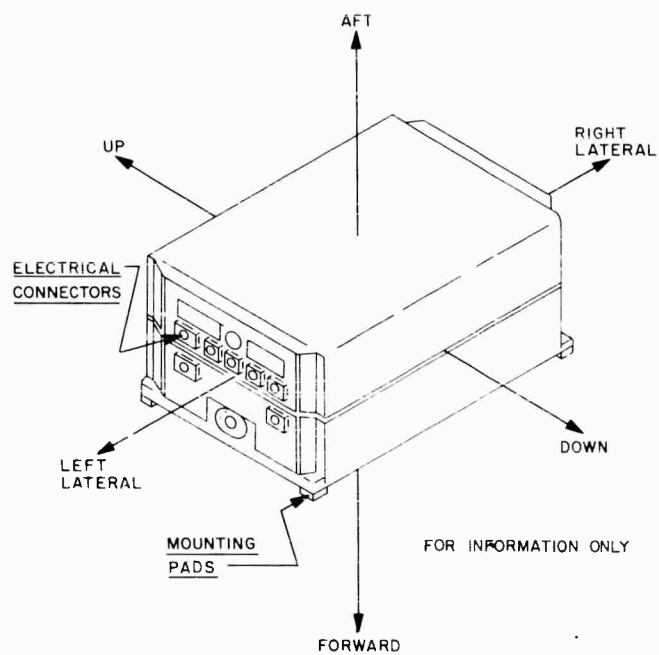
Fig. 6 - Axis designation sketch
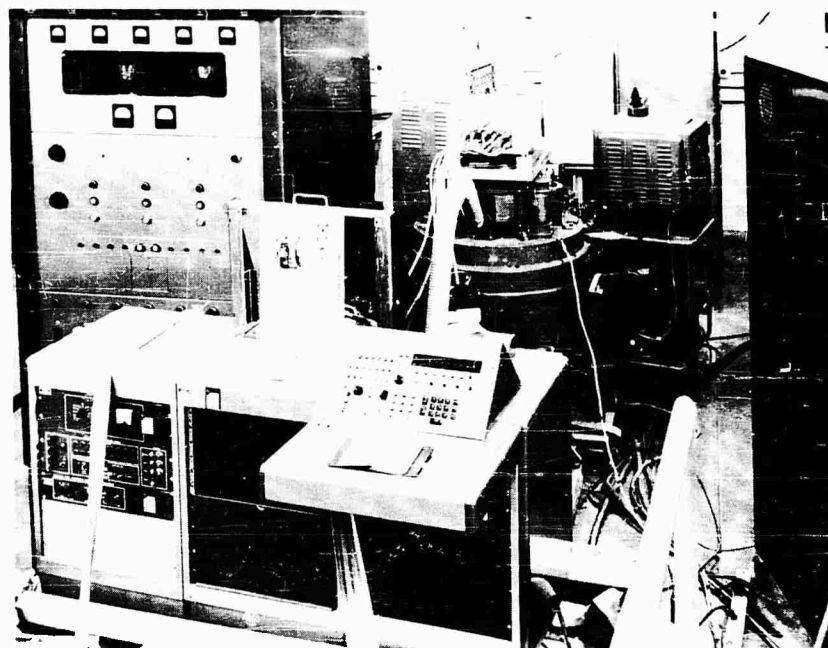
Fig. 7 - Typical test setup for VERDAN in fore-aft axis

the computer was sliding relative to the bottom half. The leads of large tantalum capacitors on one module and the leads of the power rectifiers on another module were broken from fatigue. These malfunctions prevented sustained computer operation at the required vibration level for the designated time.

DIAGNOSIS AND MODIFICATION OF COMPUTER

On the basis of the Test II results, it was decided that the remainder of the test program would be utilized in evaluating modifications designed for strengthening and stiffening the computer housing to raise its resonant frequency, and consequently to lessen the energy transmitted to the components.

The most adverse conditions found within the computer were cold solder joints and broken wires. The broken wires were assumed to have resulted from the excessive board movement and the relative motion of the top and bottom halves of the computer. Non-functioning or broken diodes indicated that prevention of board vibration should be investigated.

A major factor in regard to board vibration was felt to be the "dish-panning" of the covers during vibration. This could easily induce

severe shocks in the boards, and indicated the need for stiffening the covers.

Since several malfunctions during Test II had been attributed to intermittent and open diodes, 20 diodes were extracted from 12 different boards of the computer and dissected. The circuits were not malfunctioning at the time the diodes were removed. Photographs of the diodes revealed imminent diode junction separation, extensive visible markings on the diode crystal, and apparent fracture of the diode envelope.

The following modifications were incorporated into the package as a result of the analysis:

● The cover was stiffened by adding ridges (see Fig. 8).

● The thickness of the rubber strips and Ensolite used on the underside of the cover was increased to provide additional support and damping to the circuit boards.

● The center castings were strengthened by the addition of truss-like braces between the upper and lower members.

● The two-halves of the computer were fastened together in the center region.

243
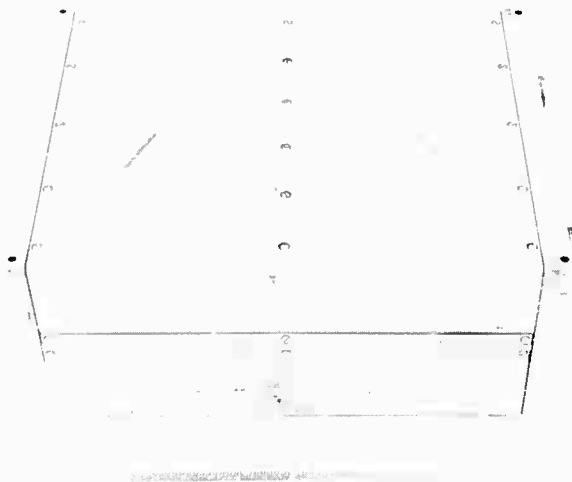
Fig. 8 - VERDAN computer; test model
with strengthened covers

The intent of the above modifications was
to rigidize the package so that less relative
motion would occur between the components.
At this stage of the analysis it appeared that
relative displacement, rather than acceleration
force, was the chief offender.

TEST III

The purpose of Test III was twofold: first
to determine whether or not the modifications
of the computer would improve the vibration
capabilities of the package, and second, to de-
termine at what level of random vibration the
computer would operate for 30 minutes in each
axis. The same test procedure was used as
with Test I, except that at each incremental
level of vibration input, the period of testing
was continued for the full required time of 30
minutes.

Accelerometers had been placed on the
capacitor, diode, and logic boards, on top of
computer cover (center), and on the side of
right-lateral end-bell casting to monitor the
vibration of selected computer locations. The
results of this phase of testing indicated that
the design modifications to the computer re-
duced the acceleration levels measured on the
boards and covers.

During Test III, several malfunctions oc-
curred in the computer which are worthy of
note: One circuit board failure, one broken
wire, one loose etched board connector, and
memory plug wiring breakage (three times in
succession). Testing to this point showed

somewhat improved computer capability under
vibration due to the modifications; however, it
was evident that the computer would not suc-
cessfully pass 7.5-g rms vibration for 30 min-
utes. A meeting was held by all responsible
personnel to discuss the results of the tests
performed to date. The following approach was
agreed upon at that time:

"Modify a standard VERDAN with im-
provements which can be simply in-
corporated and submit it to a retest at
less than 7.5 g rms (probably 5 g rms).
If the test is successfully concluded,
repeat the test at a higher level. The
results of the test could be the basis
for requesting a deviation to the 7.5-g
requirement." Exploratory vibration
tests were also conducted as follows:

CHASSIS EVALUATION

The primary purpose of the chassis evalu-
ation was to determine the areas and causes of
high resonance in the VERDAN chassis. Data
from each run yielded material for analysis,
which in turn produced objectives for subse-
quent runs.

The tests in this series of investigations
were performed with sinusoidal inputs to the
test package. These inputs were mainly of a
0.5-g magnitude with occasional frequency
sweeps at accelerations up to 3 g. Sinusoidal
testing was utilized for these tests for several
reasons:

● Random vibration, although offering a
better simulation of service environment,
yielded a minimum of data from which design
changes could be made.

● Structural changes which would reduce
vibration of the structural and electronic parts
under sinusoidal conditions would be equally,
if not more, effective under random excitation,
since resonance phenomena does not occur
under random vibration to the extent that it
does with sinusoidal vibration.

● Sinusoidal testing requires less com-
plex facility equipment than does random test-
ing. Also, more test runs can be made in less
time with sinusoidal testing since equalization
procedures are not required.

The testing procedure for any given run
was to perform a frequency sweep through res-
onant points at a constant input acceleration.
The computer cover was modified to permit

244

observance of the internal portions of the computer during dynamic excitation. The standard cover was removed and replaced with a cover which had been modified with observation ports. These ports were approximately 1-1/2 inches in diameter and were placed in such a manner that they would not affect the neoprene strips which press against the circuit boards. Reinforcing rings were bonded to the ports to re-establish the original stiffness of the cover. A stroboscopic lamp set could be directed through these cover ports to illuminate the relative movement of the boards, memory, and transformer. The strobe lights were connected through the shaker oscillator and adjusted to 3 cps out of sync with the driver frequency. In this manner, a slow-motion effect was produced on all moving components illuminated by the lights. This technique proved to be a valuable tool in subsequent evaluations by indicating areas of maximum relative disturbance where it would be desirable to place accelerometers.

The first series of tests demonstrated that the memory was making a rolling motion about the memory mount in the fore-aft axis. It was also noted that almost all circuit boards demonstrated significant displacement at resonance between 120 and 190 cps.

Since the memory is the largest single mass within the computer, the effect of its primary modes of resonance were noticeably induced into the cover and chassis. The aforementioned rolling mode occurred at approximately 200 cps.

Perhaps the most important result obtained in this evaluation was the fact that the chassis, memory, and transformer had independent resonances all in the same frequency range of 190 to 230 cps. The obvious effect of this condition was that amplification was compounded within the resonant frequency range to produce excessive displacement and acceleration.

Based on this information, efforts were directed towards the separation of these resonant points. It was felt that in this manner the resonance of the memory, for example, would be damped rather than reinforced by the transformer and chassis. Several possible design modifications were tested to determine their effect. The memory support casting was replaced with a laminated aluminum sheet support. The laminations were riveted together in an attempt to create additional shear-type damping. Several tests were made with a 3-pound weight attached to the memory cover to determine the effect of lowering the natural frequency of the memory mount system. It is interesting to note

that this particular innovation reduced memory amplification by a factor of four. Testing continued with different schemes such as the replacement of the side panels with heavy solid plates which had the effect of "unitizing" the package. Methods of vibrationally isolating the memory with rubber were also tried. In many of the runs, the covers were left removed to allow for instrumentation.

It was decided to review as much of the data as possible and decide what modifications would be most effective in producing an improved package. The VERDAN was then modified in accord with the resulting diagnosis. A new model number was designated, and the list of modifications is as follows:

1. The computer was wired with 300-volt wire, replacing the larger diameter 600-volt wire, and thereby reducing the mass contained in the wire harness and allowing stress relieving loops to be formed at each connection point. This change also allowed the removal of two connector-like switches located between the computer halves. These switches had demonstrated significant abrasive wear and were a possible cause of shorting.

2. Improved center support castings were installed to give additional stability to the computer chassis.

3. A laminated memory mount casting replaced the existing support to provide increased damping.

4. Thicker aluminum side-plates were added to the computer to provide a means of holding both halves of the package together (see Fig. 9). These plates replaced the side-panels,
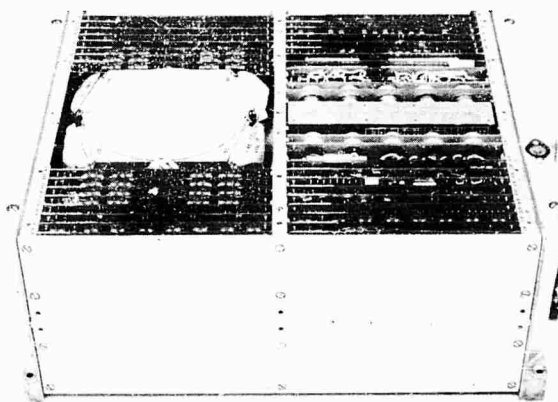
Fig. 9 - VERDAN computer; test model with strengthened side plates
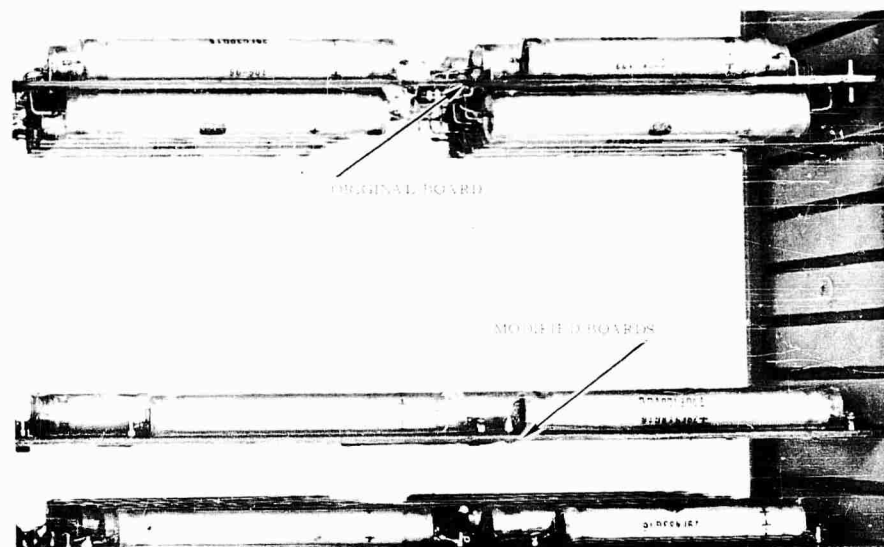
Fig. 10 - Capacitor circuit board modification

but did not increase the overall dimensions of the computer.

5. Additional cover screws were installed to stiffen the cover and to dampen vibration of the component boards by maintaining a more consistent pressure on the rubber strips which hold them down.

6. The capacitor board was fabricated as two boards to reduce the concentration of weight and mass on one board (see Fig. 10).

7. The diode rectifier board was modified to provide additional support to the rectifier terminals which had experienced excessive fatigue.

The customer was concerned as to what type of functional test would be performed on production computers to guarantee that they would function properly under the required environment. Additional sinusoidal vibration tests would be necessary to obtain this information.

SINUSOIDAL TESTS

While planning the sinusoidal test procedure, it appeared desirable to find a pseudo or quasi-correlation between sinusoidal and random vibration which would apply to the VERDAN. Several articles had been read at that time concerning attempts by other researchers to equate the two forms of vibration. It seemed evident that no reliable method of this type could be found for complex structures in

general. It was felt, however, that a specific correlation could be obtained for VERDAN in the following manner:

● Measure the rms response at selected locations on different components at resonance, while subjecting the package to a constant input value of sinusoidal excitation. This would, in effect, establish a series of transmissibilities from the chassis mount to various spots with. the computer.

● Determine what level of random vibration (shaped as per specification) was necessary to produce the same rms output levels as were produced with the sinusoidal input.

The sinusoidal tests were conducted. A total of 39 frequency response curves were obtained, all of which indicated that the chassis, memory, and transformer were exhibiting peak amplifications within the same narrow frequency range.

The final sinusoidal evaluation tests were performed on the old and new configurations to record the frequency response of the top cover, center frame, and connector end-bell in all three axes, in the following configurations. The effect of independent resonances of the chassis, memory, and transformer could be fully defined in this manner:

● Computer chassis without memory or transformer.

● Computer chassis with memory but without transformer.

246

• Computer chassis with transformer but without memory.

As a result of these tests it was known that the relative component displacements of the modified package were less than that of the original, and that the modified computer should exhibit better performance during random vibration than did the original. The program then proceeded to the previously planned random vibration test.

FORMAL RANDOM VIBRATION TEST

According to the original objective and procedures of the random vibration tests, the computer would be mounted in the fore-aft axis, equalized, and then subjected to a slowly increasing level of excitation until 7.5 g rms was reached. This level would then be maintained for the required period of 30 minutes. Though the package was known to have been improved, the possibility still existed, however, that the full required level of 7.5 g rms could not be met. It was anticipated that if failure was encountered, the customer would want to know, as before, what level could be passed successfully. Therefore, the test plan was changed with the intent to qualify first at a lower level of 5 g rms. The essential portions of the modified test plan are as follows:

1. The fore-aft axis (considered to be the worst case) would be run last instead of first.

2. The first run in each axis would be at a level of 3 g rms for a period of 10 minutes.

3. The acceleration level would be increased to 5 g rms and held for the full qualifying time of 30 minutes.

4. After all axes had been qualified to the 5-g rms level, the acceleration would be increased to the required 7.5 g rms and held for 30 minutes.

The computer successfully passed the 5-g rms level for the full 30 minutes in the up-down and left-right lateral axes, but exhibited memory problems in the fore-aft axis.

The memory output signals were monitored and it was found that these signals were fluctuating in amplitude as a result of the vibration input to the computer. This condition, called "amplitude modulation," prompted the first of three auxiliary investigations performed for the purpose of improving component performance within the computer.

All modifications to the package up to this point in the program had been of a structural nature with the intent of diminishing the environment actually "seen" by the components. Since this aspect of modification appeared to be optimized, the only other method of reaching the qualification level appeared to be that of improving the operational characteristics of the critical components. In addition to testing the memory, the previously written plan for diode investigation was adopted, and tests on selected circuit boards were performed. The following three sections describe the auxiliary tests performed on the memory and circuit boards.

Isolated Memory Test

At the conclusion of the previous random vibration tests, an investigation of the computer indicated that the memory modulation was the only factor which could have caused computer failure. To verify this diagnosis, the D9H computer was again mounted on the shaker in the fore-aft axis and the memory was physically removed from the package. It was suspended immediately above the computer by "bungee" cords and connected electrically to the computer by means of extension cables. A dummy memory was installed in the computer chassis to retain the same mass concentration and the computer was subjected to random vibration again. With this unusual implementation in effect, the D9H operated successfully while subjected to 5 g rms for the total time of 30 minutes. The vibration level was then raised to 8 g rms, and the computer continued to operate, without malfunction for a time period of 8 minutes. The obvious conclusion to this test was that the limiting factor in the previous random vibration test had, in fact, been memory susceptibility to vibration.

Memory Modulation Tests

At this time, an informal test of the memory was performed to determine the extent and characteristics of the amplitude modulation which appeared to be the major obstacle preventing qualification of the computer.

The test memory was mounted in a non-operational D9A-2 VERDAN computer. Wiring necessary to operate and monitor the memory was run from the standard memory connectors through a special top cover on the computer. Holes in this cover allowed the wiring to be conveniently routed to the test instrumentation. Testing consisted of filling the memory with test "words" in various channels, then monitoring

247

with an oscilloscope the modulation of signals occurring in these channels while the memory was exposed to vibration. The fore-aft axis was used for these tests. The results showed conclusively that the memory exhibited excessive modulation, even at low level vibration inputs.

Circuit Board Tests

This test was implemented to determine if sinusoidal vibration has a definite and adverse effect on the operating characteristics of diodes. The reliability of the diodes under vibration had been in question since the beginning of the program. It was conjectured that if the thin whisker within a diode had been improperly fused to its wafer connection, a vibratory disturbance could very easily cause a break in this connection, and thus produce an intermittent signal. Since spring tension in the whisker would allow continuity to be maintained when the diode was not vibrating, any investigation of this problem would require a system capable of monitoring the diodes during vibration. A plan was devised to test an entire diode circuit board at one time by mounting the board in a fixture on a shake-table. A connector cable was used to connect the board circuitry, via an extender card, into an active VERDAN computer (see photograph of test setup, Fig. 11). The board and fixture assembly was then subjected to frequency

sweeps from 5 to 2000 cps while the board was performing its normal function. These sweeps were performed on 13 different diode circuit boards at accelerations up to 12 g. An accelerometer was mounted on the surface of each board to measure outputs. The results of these tests were interesting in that all but one circuit board operated perfectly throughout each run. With input accelerations at the 15-g level, outputs of as high as 250 g were measured on some boards.

Since the diagnosis of previous intermittent computer errors indicated that they originated from the circuit board area, attention was given to the next probable cause: electrical shorting of the connector wires. Each printed circuit board has 86 individual contacts with its mating connector. The underside of each connector, therefore, has up to 86 separate pins to which connector wires are soldered. If each pin, while soldered to its mating wire, were not bent from its normally straight position, the chance of shorting would be remote; however, an investigation of soldering techniques disclosed that since wire length tolerances could not be kept as close as those of connector pin spacing, the pins were occasionally bent to accommodate the attachment of a "short" wire. The resulting proximity of this pin to the adjacent pin allowed the possibility of their intermittent contact during vibration.
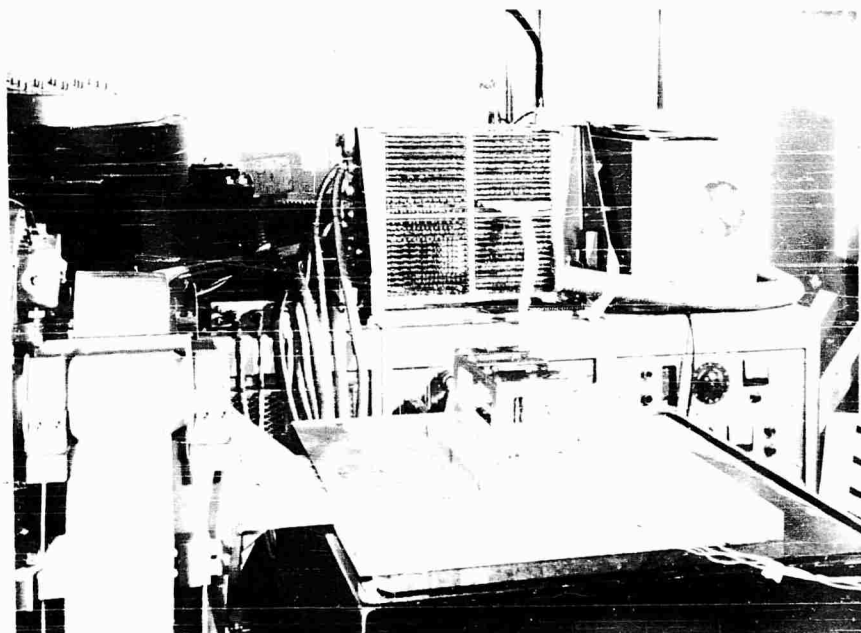
Fig. 11 - Typical test area showing circuit board connections and fixture

Therefore, an examination of wired connectors was planned. This examination was phased-in, however, with a parallel chassis evaluation which had been continuing on a dummy package to investigate a rigid memory mount, a modified transformer bracket, and a variation of the computer cover. These evaluations are presented in order of their occurrence.

Memory and Transformer Mount Evaluations

The reduction of data obtained during the original chassis evaluation had shown conclusively that the "weak-link" of the computer structure was the center frame. The inability of the center frame to support both the memory and transformer was evident by the large relative movement (in the fore-aft axis) of the center section with respect to the ends of the computer. The memory mount and the transformer did not form a rigid, unitized beam from one end-bell to the other, but rather were free to "hinge" at the center. The following methods of rectifying this problem were tried:

1. A center boss was added between the upper and lower center castings to reduce relative motion and the length of effective span from side to side.

2. Additional tie-down bolts were placed through the center frame to increase the rigidity of the package.

3. An aluminum mounting strap was positioned across the top of the transformer from the end-bell to the center frame. This strap was rigidly attached to the transformer and formed an auxiliary bracket for this member.

Several locations on the transformer, center frame, and memory were monitored with accelerometers, and frequency response characteristics of these components were recorded to evaluate the effectiveness of the modifications. Unfortunately, the results of this investigation showed that structural "additives" would not provide significant improvement, and that memory amplification was largely inescapable without a complete redesign of the package.

Variation of Computer Cover

During the previous vibration tests of the printed circuit boards, it was noticed that the neoprene strips on the computer cover were placed so as to apply pressure at one-third

intervals along each board edge. Since these locations were natural nodal points for the third resonance mode of the boards, it was suggested that the location of the neoprene strips be changed to apply board pressure at uneven intervals of length. An experimental cover was modified as shown in Fig. 12, but tests did not show enough reduction in board amplification to warrant a formal design change. One reason for this appears to be that the strips did not produce enough pressure at any one point to cause that point to be completely nodal.
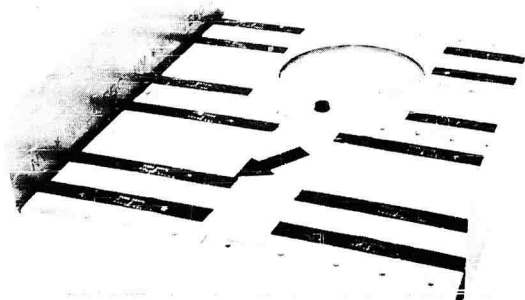
Fig. 12 – VERDAN cover showing modified position of neoprene strips

Connector-Pin Short Prevention

The aforementioned condition of bent connector pins and the possibility of electrical shorting in this area were investigated in the following manner. Six wired connectors were made as test samples. These connectors were wired according to the usual wiring techniques, and the connector pins were then modified, yielding one pair of connectors for each of three suggested methods of shorting prevention. These methods are shown in Fig. 13. The test setup is shown in Fig. 14. Frequency sweeps from 5 to 2000 cps were performed on each sample at increasing "g" levels until either a short, or 30 g was reached. The polysulfide bead method proved most effective in preventing shorts.

FINAL REVIEW OF DATA AND PROGRAM REDIRECTION

By this time almost every component of the VERDAN computer had received some type of investigation. Numerous attempts had been made to structurally improve the package, to

POLYSULFIDE BEADED

INSULATION LACING of CONN. LUGS

SHRINKABLE TUBING ISOLATORS

UNMODIFIED CONNECTOR
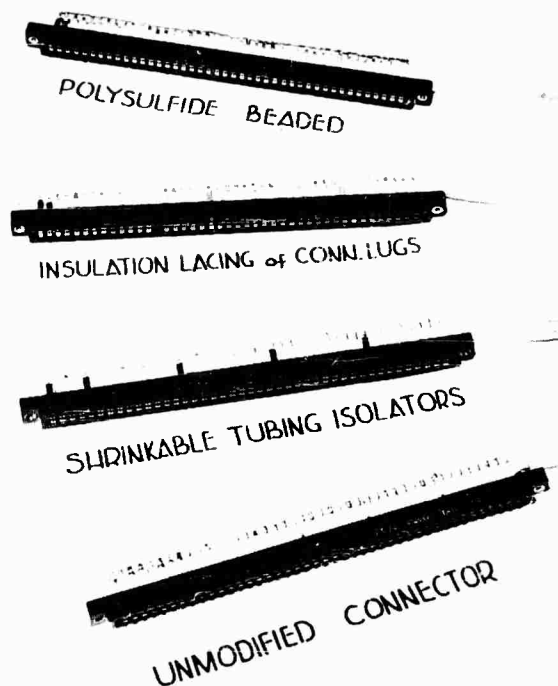
Fig. 13 – Test sample connectors showing
three methods of pin-short prevention

dampen responses, to shift frequency ranges, and to improve computer component operation. A final review of all test data indicated that the VERDAN performance under vibration could be improved significantly by incorporating several

modifications. It was equally clear, however, that these modifications would not provide enough improvement for satisfactory computer operation in the required environment. A major redesign of the computer package appeared necessary to isolate the memory unit from severe vibration.

A detailed study of the space and vibration problems of the installation was made. As a result, permission was obtained to install vibration isolators in the computer mounting feet, provided that the resulting natural frequency of the isolated computer would be above a specified value.

The use of vibration isolators, coupled with the experience gained in testing the "hard mounted" package, formed the basis for redesign and successful qualification of the VERDAN computer.

SUMMARY

Although this paper was written to describe the activities of a specific program, several items can be generalized upon to provide an insight for others engaged in design analysis programs involving the vibration of complex structures:

Planning the Vibration Program

By far the most important lesson learned in this program was that unless data is analyzed
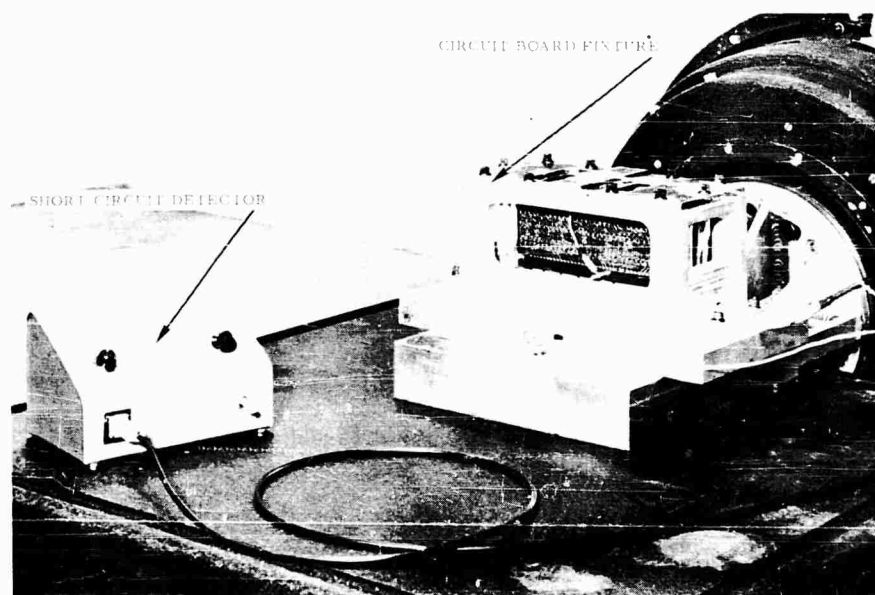
Fig. 14 – Typical circuit board test setup

at, or near, the time it is obtained, it probably never will be analyzed. It is extremely easy to plan tests without planning the data analysis phase. As a result, little or no thought is given to the question of what use the data will be, or why it is being obtained. If more emphasis could be placed upon this phase of the program, it is likely that actual testing time would be reduced.

Failures and What They Represent

Many qualification programs are performed on a strict "pass or fail" basis. Although this type of approach may be warranted by the procuring activity, the conditions of a so-called "failure" should be anticipated, if possible, before the test, and investigated thoroughly if they occur. The reasons for this are at least two-fold. First, the program should have a primary goal of obtaining the true characteristics of the test sample. Such variables as accelerometer placement, fixture resonance, excessive magnetic fields and the like, can all contribute to the "failure" of the test sample, and should be accounted for when determining true characteristics. Secondly, random type failures can occur on complex equipment independently of environmental subjection. It is therefore necessary to show, if possible, that a definite cause and effect relationship has been established by the vibration environment. For example, if a part breaks loose from its mounting during a particular test run and is remounted

with subsequent success, should the first failure cause disqualification? This paper has pointed out that such an incident should not cause disqualification, but should prompt action to improve the method by which the part was originally mounted.

Approaching a Design Improvement Problem

In dealing with random vibration requirements of a broadband nature, the use of rigidization of structural members as a solution to resonance problems is often unsatisfactory. If failures can be attributed to excessive relative displacement, then rigidization will probably help. With the usual problem of reducing acceleration amplifications, however, the increased structural stiffness may react with local mass properties to produce new resonances that cause more damage than those that existed initially. This paper pointed out many attempts to strengthen and rigidize various structural members. The rigidizing caused a shift in the structural natural frequencies but did not alleviate the problem of excessive accelerations or critical components. It is therefore suggested that vibration design improvement be directed towards either total system isolation or increased levels of component tolerance. It should also be mentioned, however, that in instances where a separation of resonant frequencies is needed on close or mated component parts, rigidization of one or more of these parts may produce the desired result.

*   *   *

251

DESIGNING FOR THE DYNAMIC ENVIRONMENT OF THE GEMINI INERTIAL PLATFORM*

G. R. Grabow and J. E. Cottle
Honeywell, Inc., Aeronautical Division
St. Petersburg, Florida

This paper deals with a portion of the design-development program conducted on the Inertial Measurement Unit (IMU) being supplied by Honeywell, Inc., for the Gemini spacecraft guidance system. This portion of the development program was conducted to assure that the production model of the IMU would meet its operating requirements during exposure to a 12.6-g rms random vibration environment while hard mounted.

In the developmental sequence, the design progresses from an initial 6-g capability to a 9-g capability, and then to a 12.6-g capability. The final capability was achieved by the incorporation of a resilient mount internal to the case of the Inertial Platform. The form of this mount is considered a novel solution to the design problem.

The reliability and accuracy of the entire guidance system of the spacecraft depends on the ability of the inertial sensors (gyros and accelerometers) contained in the inertial platform of the IMU to maintain preset references and provide continuously accurate information. One of the major hazards to the reliable maintenance of this reference is the dynamic environment of a blast-off or re-entry phase of a space flight.

The problem was not the ability of the unit to maintain structural integrity during the vibration exposure, since the unit had demonstrated its ability to survive this environment. The problem was to reduce the level of response seen by the gyros and accelerometers and minimize certain oscillatory motions which develop misleading guidance information during vibration.

The solution therefore had to accomplish two things. The transmissibility from the mounting points to the inertial sensors had to be reduced and the response of the structure had to be made as symmetrical as possible to minimize rocking, cross-talk, and other such effects.

Previous Honeywell practice was to provide vibration isolators external to the case for this type of unit. This could not be done with the Gemini platform because of the installation requirements.

A configuration was conceived for the use of a pair of mounts internal to the case. The mounts are of annular-ring construction using molded BTR elastomer to provide radial and axial "springs." The required spring rates, damping constants, and other parameters were established for optimum dynamic response characteristics of the structure.

Environmental testing to 12.6-g rms random vibration for periods up to 15 minutes on a unit incorporating the mounts has shown that the inertial sensors maintain acceptable performance, and that the general platform response matches well with design analysis.

253

INTRODUCTION

This paper deals with a portion of the design-development program conducted on the Inertial Measurement Unit (IMU) being supplied by Honeywell, Inc., for the Gemini spacecraft guidance system. This portion of the development program was conducted to assure that the production model of the IMU would meet its operating requirements during exposure to a 12.6-g rms random vibration environment while hard mounted.

In the developmental sequence, the design progresses from an initial 6-g capability to a 9-g capability, and then to a 12.6-g capability. The final capability was achieved by the incorporation of a resilient mount internal to the case of the Inertial Platform. The form of this mount is considered a novel solution to the design problem.

BACKGROUND

At present, the National Aeronautics and Space Administration has programmed two missions for the Gemini spacecraft, long duration flight and rendezvous. The mission function of the guidance system is threefold: (1) to serve as back-up guidance during the boost phase; (2) to guide Gemini to the Agena target vehicle in rendezvous missions; and (3) to guide spacecraft maneuvering for re-entry.

Navigation is defined as the process of controlling the course of a vehicle through the use of calculations as to position and direction. In inertial navigation, the properties of mass inertia are used in the IMU to provide navigation information for processing by a computer. In the mathematical scheme used, computations of spacecraft position and velocity are done with respect to a three co-ordinate reference frame whose spatial position is arbitrarily selected at the time the system is designed. The desired position, heading, and velocity of the spacecraft at discrete points during a given mission can be related mathematically to this reference and programmed into the computer. During flight, this programmed information is compared to position, heading, and velocity information being generated by the IMU-computer combination.

The choice of frame of reference is generally made with ease of computation in mind. For this reason, two frames of reference are used on Gemini. During ascent and re-entry, a space-stabilized reference is used. During rendezvous, an orbital co-ordinate reference is used.

THE IMU

The function of the IMU is to provide a measurement of spacecraft acceleration in each direction of a three co-ordinate system, and a measurement of the attitude of the spacecraft with respect to this co-ordinate system. This information is integrated to yield velocity and position. For the information to be useful, the relation of this co-ordinate system to the master computational reference must be described and maintained. It is described by establishing a mechanical relation between appropriate components at a given point on the flight profile and specifying their alignment requirements. It is maintained by gyroscopic control of a three-degree-of-freedom gimballed system. Guidance accuracy depends on the ability of the inertial measurement unit to maintain this selected reference, called "inertial reference."

The IMU consists of four units or "black boxes": power supply unit, system electronics unit, inertial platform (hereafter called "platform"), and platform mount. In this paper, the effects of the structural design of the latter two units on the ability of the IMU to maintain inertial reference will be considered.

THE PLATFORM AND PLATFORM MOUNT

The platform (shown in Fig. 1) consists of a stable element containing three single-degree-of-freedom rate integrating gyros and three accelerometers of the force-rebalance type mounted in an orthogonal arrangement to describe a three-axis co-ordinate system. The stable element is isolated from spacecraft motions by a servo-controlled, four-gimbal, three-axis structure, of which one gimbal is redundant to prevent gimbal lock.* Thus the platform is equipped to make the basic attitude and acceleration measurements for the IMU.

The platform mount is bolted to the spacecraft airframe after being aligned to the spacecraft pitch and yaw axes reference. The platform,

___

*Gimbal lock is a loss of one of the three degrees of rotational freedom that occurs in a three gimbal system when the inner axis becomes aligned with the outer axis, as after a 90-degree rotation of the vehicle about the middle axis.

HONEYWELL
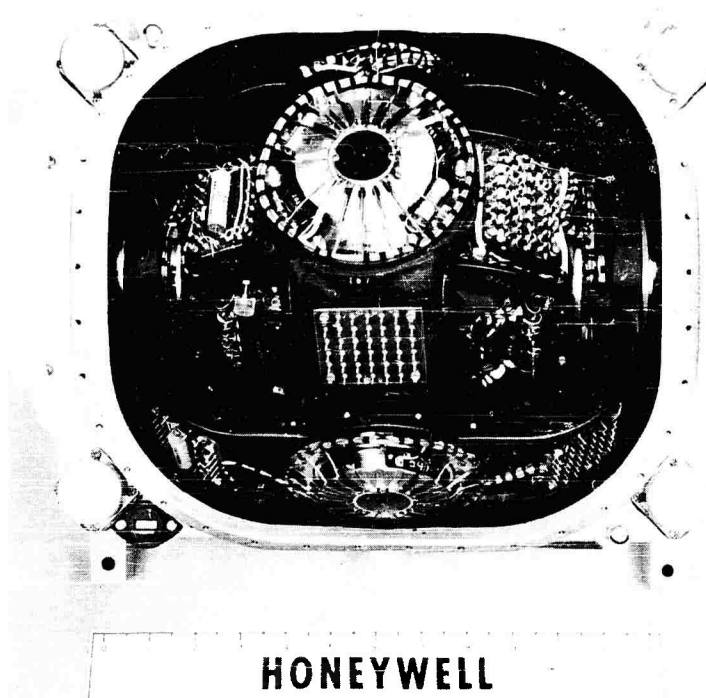
Fig. 1 - Gemini inertial platform with top cover removed

when attached to the platform mount, is automatically aligned to the spacecraft by use of a dowelled interface. Integral with the mount and actually forming the mount-to-platform interface surface is a cold plate. When coolant lines are attached, the cold plate becomes an integral part of the spacecraft and its cooling system.

In order to obtain an accurate measurement of spacecraft acceleration it is necessary to know the alignment of each of the three accelerometers with respect to the reference axes. This is done by assembling the accelerometers into the stable element such that they are prealigned to the platform-platform mount interface within a given tolerance. Compensation for the actual slight misalignment is then programmed into the computer.

Once established, the relation of the accelerometers to the computational frame of reference must be maintained. This is the function of the gyros. The gyros sense angular movement (roll, pitch, yaw) of the vehicle and through the control electronics, drive torque motors on each gimbal axis to adjust angular position so that the stable element maintains the inertial reference. This gimbal movement is detected by resolvers which provide readout signals of vehicle attitude to the computer.

VIBRATION INDUCED GYRO ERRORS

The quality of the acceleration data, and computed velocity and position information, depends upon how well the gyros maintain inertial reference. The imperfections in gyros result in an error called "gyro drift." Units are in degrees per hour. If the gyro drift rate is constant and known, it can be compensated for; however, gyro drifts which are not constants can be induced by vibration. Therefore, the dynamic environment encountered during launch and re-entry constitute a major hazard to guidance accuracy. This environment was specified at 12.6-g rms random over a 20- to 2000-cps bandwidth with a 0.12-g^2/cps power spectral density in the region of fundamental resonance, i.e., 100 cps. Combined with this was a 7-1/4-g linear acceleration along the major axis of the spacecraft.

In further discussion the gyro drift rate will be used as the performance criteria. Percentages of the design-goal maximums will be used since the actual values are classified.

The adverse effect of vibration on gyro performance falls into two general classes. One, errors induced within the gyro due to its response to applied linear accelerations, and

255

two, errors due to angular oscillations of the vehicle on which the gyro is mounted.

Errors of the first type are due to state-of-the-art limitations on gyro materials and construction, and are proportional to the level of g's experienced. Errors of the second type would be present even with perfectly constructed instruments. The most significant of these is called "coning."[*] For any given environment, the method of mounting the gyro can effect coning error considerably. If the gyro is used in a strap-down application, the full angular motions of the vehicle will act on the gyro. In a platform application, the errors would be greatly reduced because of the attenuation of the vehicle angular motion through the platform gimbal system. If, however, the gimbal structure does not respond symmetrically during a dynamic environment, angular motions can again be introduced. The magnitude of the angle and consequently, the magnitude of error, is proportional to the g level felt by the platform.

THE PROBLEM

The first consideration in designing to meet dynamic conditions is the ability of the supporting structure and components of a unit to survive the environment in an operational condition. In many cases this survival is a sufficient criterion for qualification. The effects of vibration on the performance accuracy of an inertial platform can create a problem beyond survival capability. Early vibration testing of a developmental model Gemini platform showed high gyro drift rates and a transmissibility of as much as 17 to the stable element. Observations of the platform under a strobe light showed a significant rocking response of the gimbal structure. Either the high transmissibility or the rocking motion could have been the cause of excessive gyro drift. A preliminary examination lead to the conclusion that the cause of both rocking motion and high response levels were related. The rotary components, which form the trunnion between adjacent gimbals, were of unequal stiffness as well as being "soft" in comparison with the gimbals. The unequal stiffness gave rise to the rocking response mode and developed a coning error. The low stiffness prevented the gimbals (made of high

[*]Vibration induced effects in inertial sensors have been given names descriptive of the nature of their implementation. A detailed discussion of these error sources is beyond the scope of this paper.

damping KIA magnesium) from being stressed sufficiently to contribute damping.

Vibration testing at reduced levels indicated acceptable platform performance to approximately the 6-g rms level. This testing showed that in order to reduce the vibration levels seen by the inertial sensors to a point where acceptable performance in the 12.6-g environment was possible, the resonant transmissibility from the mounting points to the stable element had to be reduced to a value of six or less. To achieve this transmissibility, enough damping had to be added to the structure to give an overall effective damping ratio of 0.08 or greater.

Cross-talk accelerations on the pitch block of as high as 80 percent of in-line response had been noted. Minimizing this type of response by equalization of the spring rates of each side of the gimbal structure was the second consideration; without which, much of the benefit of lowering the response level would be lost.

A modified version of the platform was constructed and tested. The modification consisted of the addition of stiffeners to the rotary component housings in order to increase and equalize their spring rates. New rotary components were not feasible because of schedules. The test results showed gyro drift rates to be lowered, but not to the desired level. Acceptable performance to approximately the 9-g rms level was indicated for this stiffened platform configuration. Test results also showed that transmissibility to the stable element changed very little. System resonant frequency increased from 100 to 120 cps.

At this point isolators began to be considered as a means of obtaining more damping. The design requirements were roughed out and found to be quite rigid. A special test was then run. The modified (stiffened) platform was vibrated with an input that generated the response levels the gyros would experience if isolators were used. The results were very favorable and a redesign effort was initiated to determine hardware configuration for a test model.

THE SOLUTION

The Gemini inertial platform, designed as a hard mounted unit, was a departure from previous Honeywell practice of using external four-point vibration isolators. The use of external isolators was precluded because of the non-flexible spacecraft coolant lines connecting

to the platform mount and the thermal inter-
facing required between the platform mount
and the platform. Therefore, redesign changes
could not alter the external configuration.

If isolators were to be used, they would
have to be located within the platform case.
The major design considerations were sway
space, the effects of increased resistance to
thermal conductivity on platform temperature
control, accelerometer-to-case alignment,
and in developing an isolator that would provide
the proper damping, have the correct resonant
frequency and so on, within the space available.
Lord Manufacturing Company provided excellent
technical assistance and produced the annular-
ring mounts shown in Fig. 2. The outer and
inner rings are aluminum and the interconnect-
ing material is molded BTR elastomer shaped
to provide radial and axial spring action. The
mounts are fitted into a bored-cut platform
case as shown in Fig. 3.

Spring rate of the set is 15,000 lb/in. to
provide a resonant frequency of approximately
70 cps when coupled with the 20 pound stiffened
gimbal structure which had a fundamental res-
onance of approximately 120 cps. The 70 cps
figure was selected to provide a minimum cou-
pling with servo-loop resonances. The damping
ratio of the mounts is approximately 0.15 spec-
ified on the basis of a "rigid-mass" resonant
transmissibility of four or less.

To provide symmetrical response the ra-
dial spring rates of the mounts of a set are
matched so that their individual "rigid-mass"
resonant frequencies are within 0.5 cps. Allow-
able hysteresis is such that alignment of the
outer roll axis with respect to the platform
case mounting surface is not affected by more
than 1 arc-minute over a 10-inch mounting
distance.

Because of limitations of sway space within
the case, provision was made against the pos-
sibility of the gimbal structure striking the
case wall under worst-case build-up of sustained
acceleration, vibration, and shock. Snubbing is
provided by shaping the elastomer to give an
abrupt increase in spring rate when a deflection
of 0.040 inch is reached.

THE RESULTS

Vibration testing of a platform of the rede-
signed configuration indicates reasonable cor-
.relation of actual response with analytical pre-
dictions. The resonant frequency in one axis
was lower than expected but this was found to
be due to variations in response depending on
gimbal orientation. Transmissibility to the
stable element at resonance was approximately
five in all three axes of vibration. Cross-talk
was reduced to approximately one-third of that
on previous units. Sinusoidal response curves
for the vertical axis are compared in Fig. 4.
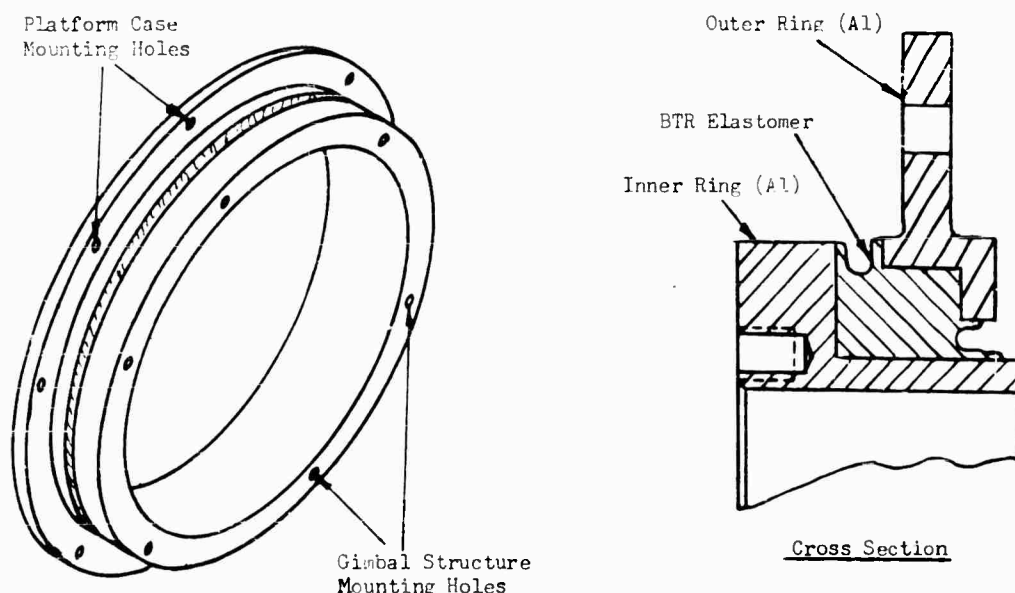
Fig. 2 - Mount used in redesigned platform configuration
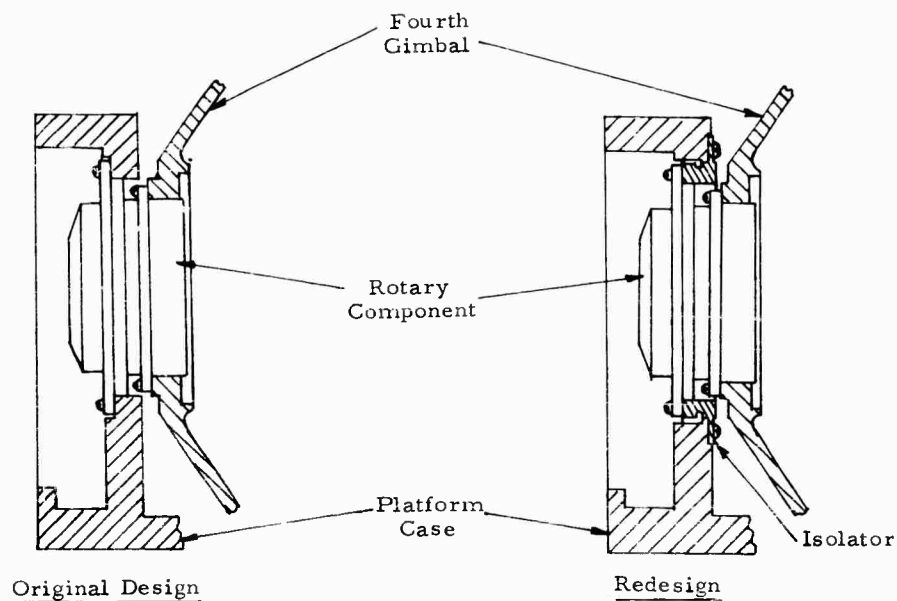
Fig. 3 - Mounting of gimbal structure
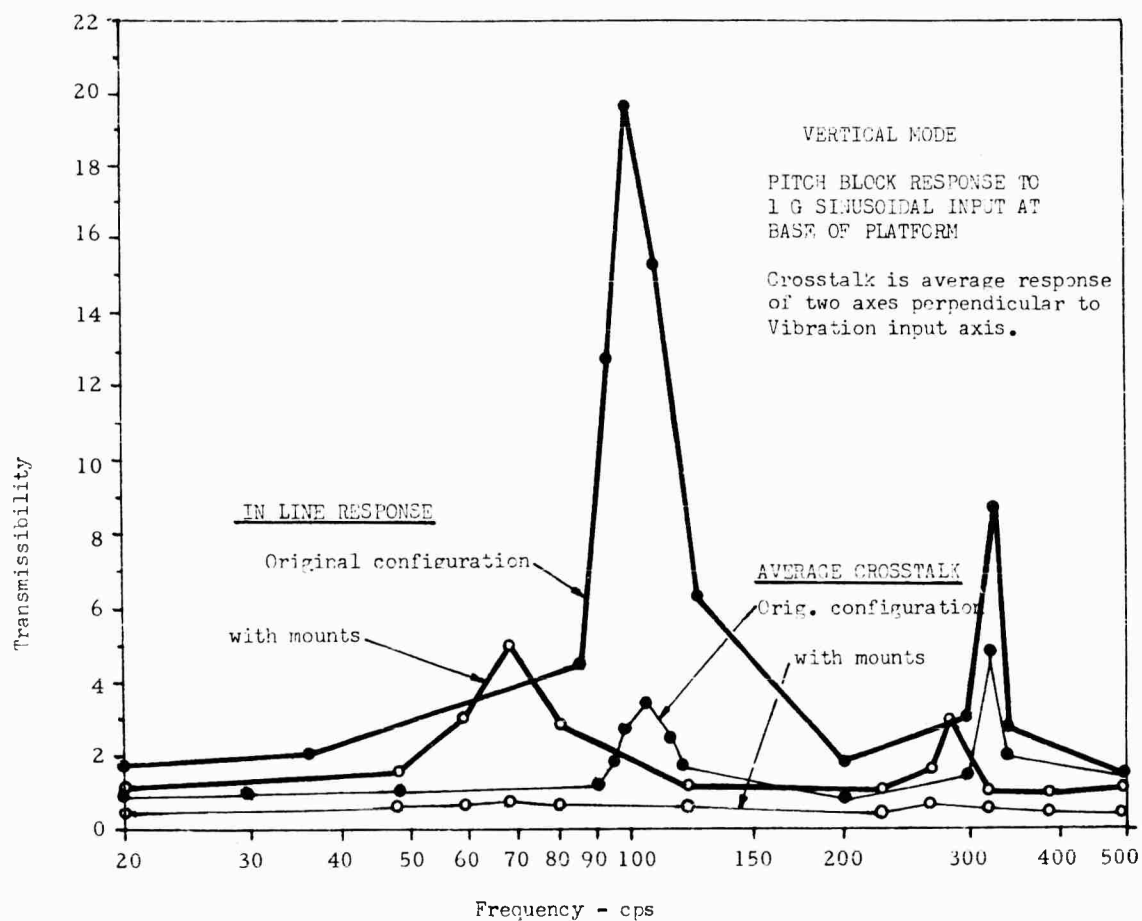
Fig. 4 - Typical sinusoidal response curves for
original and redesigned platform configuration

258

TABLE 1
Gyro Drift Rate Comparison

(Drift rate values are given as percent of design
goal maximum as recorded during vibration testing.)

Vibration Axis	Original Configuration			Redesigned Configuration		
	X Gyro	Y Gyro	Z Gyro	X Gyro	Y Gyro	Z Gyro
Vertical	1060	1600	500	6	60	26
Longitudinal	440	380	800	132	260	40
Lateral	5000	120	840	0	40	160

Gyro performance during vibration was
vastly improved as shown in the comparison
data of Table 1. The gyros were able to main-
tain inertial reference during vibration to the
specified 12.6-g rms random input for exposure
times as long as 15 minutes. Performance
analysis indicates that the isolated platform is
able to meet mission requirements in the spec-
ified environment.

In spite of the very favorable results, the
isolated configuration has not been released for
production. The first Gemini "boilerplate"
spacecraft flight (in early 1964) showed that
vibration levels were lower than originally
specified. Consequently, vibration qualification
testing requirements were reduced to an over-
all 8.8-g rms random, 20 to 2000 cps, with a
0.048-g^2/cps power spectral density at the re-
gion of fundamental resonance. Qualification
testing of the stiffened configuration of the plat-
form to the new requirement is forthcoming.

Based on previous testing it is anticipated that
this requirement will be met without the use of
isolators.

This points up one of the major problems
in design economy for space applications, i.e.,
the difficulty in realistic specification of dy-
namic and other environmental requirements in
the early stages of a program, especially when
a new booster is involved. The specifications
are based on analysis and extrapolation of ex-
isting data, and will necessarily be subject to
modification as flight data becomes available.

In light of the fact that the isolators will
probably not be used on the Gemini platform,
the expense of the development may seem un-
justified. The configuration developed and the
information gained, however, will undoubtedly
find application on future efforts, particularly
where high g capability is required of an iner-
tial platform.

*   *   *

GUN FIRING ENVIRONMENT AND ITS RELATION TO STRUCTURAL AND EQUIPMENT INTEGRITY*

J. E. Gross and R. Pittman
McDonnell Aircraft Corporation
St. Louis, Missouri

A technique is developed for locating instrumentation for fuselage panel stress and pressure measurements during fire of a centerline mounted gun. Judicious location of this instrumentation was used to determine the structural integrity of the configuration and the environment acting on equipment during gun fire. The increased panel fatigue life due to the application of damping tape is discussed. The path of the transmission of the gun firing environment to equipment items located in cavities above the lower fuselage panels is found to change as panel stress increases.

INTRODUCTION

Increased tactical use of the F-4 aircraft has led to the inclusion of a rapid-firing pod mounted 20-mm cannon at the centerline. The pod was to be suspended below a section of the fuselage which has a lower mold line containing a number of structural access doors above which electronic, hydraulic, and pneumatic equipment was installed. Since structural failure of an access door or the malfunction of an equipment item could conceivably result in the loss of an aircraft, it had to be established prior to flight and with such a high degree of certainty that no catastrophic failures would occur. Two areas of severe acoustic and vibration environment produced by gun-firing that could be detrimental to the aircraft have to be considered; these are the structural effects of high intensity noise fields on the lower fuselage skin panels in the proximity of the path of the projectile and vibration transmitted to equipment items through the aircraft structure. This paper describes the experimental and analytical techniques used to assure adequate instrumentation of the aircraft, to measure the desired parameters, to reduce the measured data to define the environment, and to assure the integrity of the structure and equipment items.

GROUND VIBRATION TEST OF FUSELAGE PANELS

The structural access doors located above the gun pod are divided into several flat panels by stiffeners as illustrated in Fig. 1. To determine the gun firing fatigue life of these panels, the stress time history during a firing burst had to be measured near the point of maximum overall panel stress. Because the panels must respond in a combination of their natural modes of vibration and because maximum stress points exist at points with maximum deformation curvature, the panel frequencies and mode shapes had to be determined in order to determine the panel points at which stress time histories were to be measured. Since the skin panels were thin, the mass associated with a panel was small and the mass added by the excitation and measuring systems had to be kept to a minimum. Therefore, the panels were excited by means of a small Goodman electromagnetic shaker (6.5-gram moving mass) and a vibration probe was utilized to determine mode shapes. Also, the panels were acoustically excited by a small speaker to substantiate that the shaker mass had no appreciable effect on the panel frequencies.

---

*This paper was not presented at the Symposium.
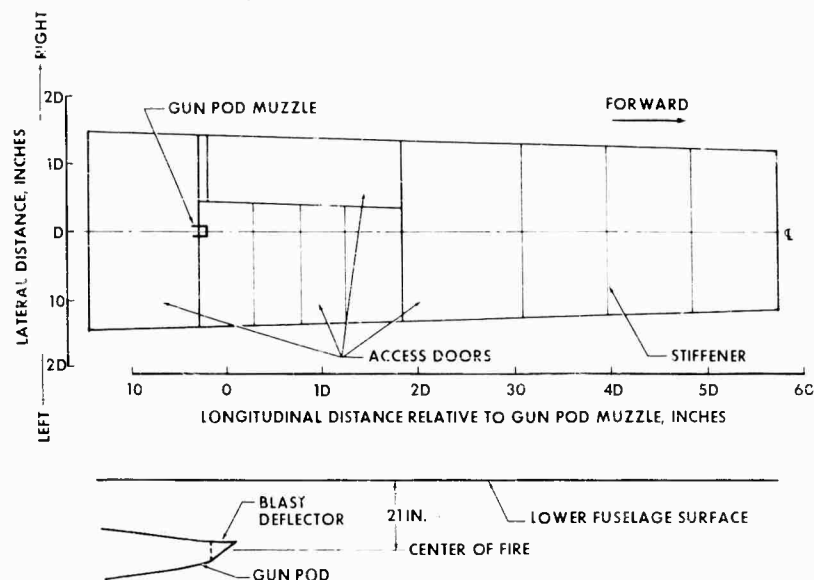
Fig. 1 - Bottom view of the gun-blast-affected portion of the lower fuselage and profile view of gun pod and lower fuselage

With the mode shapes of the panels, the stresses at various panel points were established by comparing the various radii of curvature of the deflection shape. The stresses at the upper surface of a panel, loaded laterally only, are given by

$$\sigma_x = \frac{6D}{h^2}\left(\frac{1}{r_x} + \nu \frac{1}{r_y}\right) = \frac{6D}{h^2}\left(\frac{\partial^2 w}{\partial x^2} + \nu \frac{\partial^2 w}{\partial y^2}\right)$$

and

$$\sigma_y = \frac{6D}{h^2}\left(\frac{1}{r_y} + \nu \frac{1}{r_x}\right) = \frac{6D}{h^2}\left(\frac{\partial^2 w}{\partial y^2} + \nu \frac{\partial^2 w}{\partial x^2}\right) \ .$$

In addition to stress time histories, a significant number of pressure time histories were needed to define the gun-produced environment as inputs for the design of pressure reduction devices, if such devices were proven to be necessary. The pressure transducers, if improperly located, could have added enough mass to the panels to change the natural frequencies and mode shapes and thus change the maximum stress points. To prevent this, the transducers had to be located near minimum response points so that the generalized mass contribution of these transducers would be a minimum. Again the location of these points was dependent upon the deflection shapes of the panel modes of vibration.

Figure 2 presents the first two mode shapes of a typical fuselage panel. For each mode

shape the maximum stress points are indicated by circles. The node lines for each mode are indicated by dashed lines. The contour of the panel shown in Fig. 2 was such that a stiffener was effectively located at the centerline of the airplane, thereby forcing a node line near this location. Since node lines are a locus of points with zero deflection for a particular mode, these points are minimum response points of that mode. If the panel were allowed to respond in only one mode, strain gages located at panel points of maximum curvature indicated by circles and pressure transducers located on node lines would provide realistic stress and pressure time histories. Since generally the panel would be expected to respond in more than one mode, it was necessary to compute an expected response of the panel and locate minimum and maximum deflections for the total response as discussed in the following section.

DESCRIPTION OF ANALYSIS
PERFORMED TO LOCATE
INSTRUMENTATION

An approximate typical blast pressure time history (Fig. 3) was analyzed for frequency content to determine the ability of the blast pressure wave to excite the panel frequencies. The frequency content of the blast pressure time history was determined by expanding the pressure wave in a Fourier sine series of the following form

MODE SHAPE A

f=172 cps

MODE SHAPE B

f=448 cps

UP

FORWARD
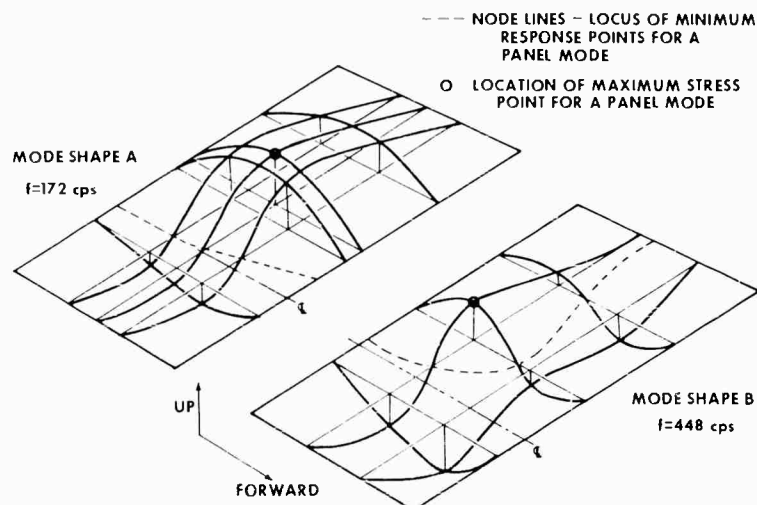
Fig. 2 - Mode shapes of a typical panel
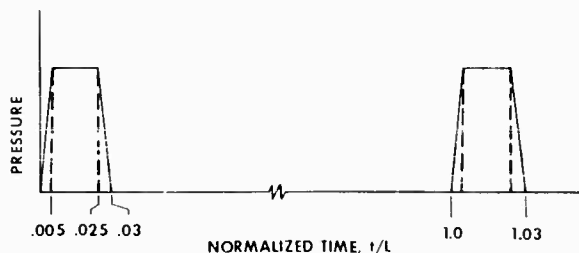
Fig. 3 - Blast-pressure time history
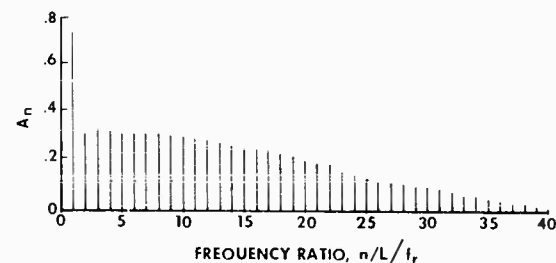
Fig. 4 - Frequency content
of blast pressure wave

$$p(t) = P_o + \sum_{n=1}^{\infty} A_n \sin\left(\frac{2\pi nt}{L} + \delta_n\right) .$$

The results of this expansion are presented in Fig. 4. As can be seen from this figure, the expansion of the pressure wave contains a number of discrete frequencies. The lowest frequency, which is equivalent to the gun-firing rate, has a much greater pressure coefficient than the other frequencies.

Utilizing the frequency content of the blast pressure wave and the panel frequencies and mode shapes, the optimum location of strain gages and pressure transducers can be determined. Since the panels were small relative to the pressure field, they were assumed to have a uniform pressure distribution at a particular time. Each panel mode of vibration was considered to be excited by the important frequencies of the blast wave. The panel mode shapes are designated by ϕ_{mij} where m indicates the mode and i and j indicate grid points of the

panel. The mth mode response was then found by summing the response of this mode to each of the important discrete frequencies of the blast wave. This response is reflected by the generalized coordinate

$$q_m = \sum_{n=1}^{\infty} T_{nm} A_n .$$

T_{nm}, being a function of the parameters ω_m, n/L, D, and so on, is the nth component of the solution of the equation of motion corresponding to the generalized coordinate q_m and was evaluated using the well known convolution integral. The magnitude of the response of the generalized coordinate was then determined for each panel mode of interest.

By summing the response of the generalized coordinates, the panel deflection can then be expressed as a function of time in the following manner

263

$$w_{ij}(t) = \sum_{m=1}^{s} q_m \phi_{m_{ij}} \sin(\omega_m t + \psi_m) .$$

In our specific instance though, lengthy calculations were not required because:

1. As can be seen from Fig. 4, most of the energy of the blast wave is contained at the low frequencies, primarily the frequency corresponding to the gun firing rate.

2. The fuselage panels which were considered critical had fundamental modes at frequencies relatively near to the firing rate with higher mode frequencies considerably above the fundamental frequency.

The response of the panels would occur primarily in the fundamental modes and the shifting in maximum and minimum deflection points caused by the higher modes would be small. Therefore, the maximum stress point for the fundamental mode was selected as a location for the strain gage. The approximation associated with this approach was proven to be minor by the fact that the measured panel response during gun firing was relatively clean with a frequency equal to the lowest natural panel frequency. The selection of location for pressure transducers was simplified considerably by the presence of stiffeners and effective stiffeners such as the "crease" at the airplane centerline; little or no motion was evidenced near these locations in the basic panel modes. A transducer placed near a stiffener would have only a minor effect on panel motion. On this basis, once the panel ground vibration tests had been

conducted and the frequency content of the blast pressure wave determined, instrumentation location could be selected practically by inspection.

GROUND AND IN-FLIGHT FIRING TESTS

In order to provide information concerning the blast environment and the vibration environment transmitted to equipment items, ground firing tests were conducted for the measurement of the pressure field, panel response, and vibration transmitted to various equipment items. In preparation for the firing tests, strain gages and pressure transducers with the required frequency range were located in accordance with the procedures outlined in the last paragraph. Baldwin SR4 paper-back-type strain gages and Statham bi-directional differential pressure transducers were used to measure strains and pressures, respectively. The pressure transducers were vibration compensated. In addition, accelerometers were judiciously placed so as to monitor the environment which was being transmitted to electronic, hydraulic, and pneumatic equipment. The accelerometers used were an Endevco piezo-electric type which has a flat response up to 5 kc. This range was selected so that response to all significant parts of the blast wave frequency content curve would be included. The strains, pressures, and accelerations were recorded on magnetic tape during gun firing.

During ground firing of the gun pod suspended from the centerline of the aircraft a pressure field on the lower fuselage was
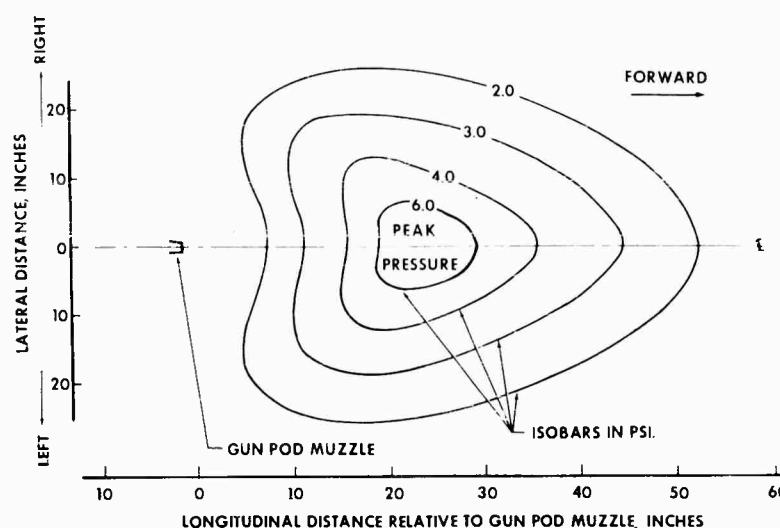
Fig. 5 - Pressure field on the lower fuselage
during ground firing with a blast deflector

264

measured. This field is presented in Fig. 5. The "heart-shaped" pattern taken by the pressure contours is due to the shape of the blast deflector that was placed above and extends forward of the muzzle (see Fig. 1). The shape of the gun pod blast deflector and the distance between the gun pod and the lower fuselage determined the location of the peak pressure on the lower fuselage due to gun blast. To illustrate the effect of the blast deflector, the pressure field for the gun without a blast deflector is presented in Fig. 6. As can be seen, the pressure contours lose their heart shape and the peak pressure shifts aft.

During in-flight firing of the gun pod a blast pressure field is superimposed on the velocity field which normally surrounds the aircraft during flight. The velocity field interacts with the gun firing pressure field and displaces the pressure field obtained during ground firing aft. Figure 7 presents the in-flight firing pressure field for the aircraft subjected to a particular dynamic pressure. The peak pressure has shifted aft with respect to the ground firing results as shown in Fig. 5 and the levels have increased. With this shift of the pressure field, the pressure wave has to travel a shorter distance to impinge on the fuselage panels. Since pressure dissipation is related to distance from the gun muzzle along the pressure wave path, the maximum pressure on the fuselage would be expected to be higher during in-flight firings.

EFFECT OF ENVIRONMENT ON STRUCTURE AND EQUIPMENT

The stress levels occurring on some panels during in-flight firing with the blast deflector resulted in a panel fatigue life which was unacceptable. To create a more favorable condition, several different blast pressure reduction devices were investigated. All pressure reduction devices lowered the blast pressure impinging on the fuselage by directing a portion of blast wave downward. The device which lowered the pressure the largest amount was utilized to help create a compatible aircraft-gun pod configuration. In addition, two layers of aluminum foil damping tape were externally applied to the unsupported portions of the lower fuselage skin panels. As can be seen in Fig. 8, the addition of damping tape has two effects on the panel response: (1) The peak skin stress is reduced by about 12 percent, and (2) the decay rate is increased by a factor of almost 3.

In order to assess the effect of damping tape on the fatigue life of a panel, let us assume that the time histories shown in Fig. 8 apply to a panel with a natural frequency at or near the gun firing rate. This means that, with each shot, the undamped panel would experience a peak stress of 10,900 psi, whereas the damped panel would experience only 9800 psi. Referring to a stress versus number of cycles to fatigue (S-N) curve for the material of the panel,
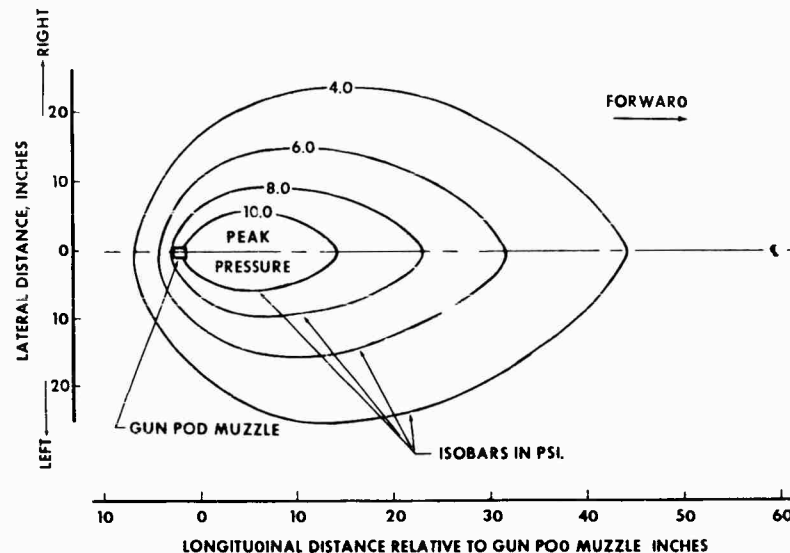
Fig. 6 - Pressure field on lower fuselage during ground firing with no blast deflector
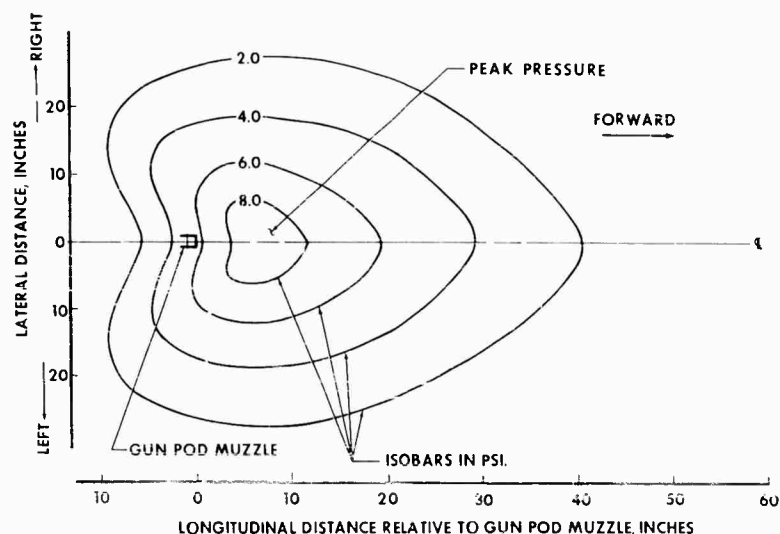
Fig. 7 - Pressure field on the lower fuselage
during in-flight firing with a blast deflector
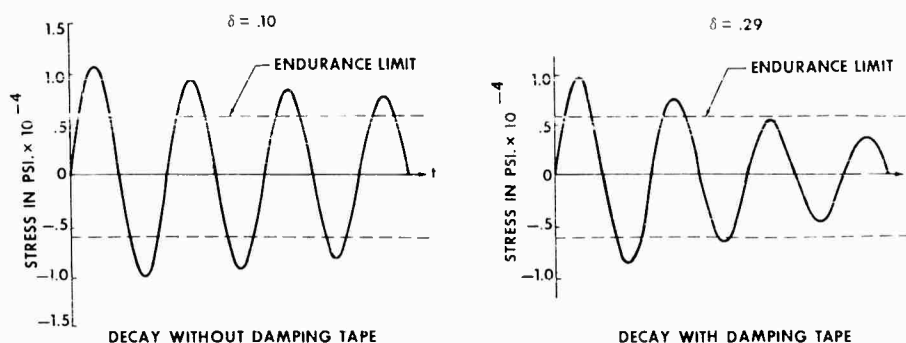
Fig. 8 - Response of panel to one round of fire

such as is shown in Fig. 9, it would be indicated
that the undamped panel will last 800,000 rounds,
whereas the damped panel would be good for
1.3 million rounds — an increase in fatigue life
of over 50 percent.

Due to the panel dimensions, some panels
had fundamental frequencies considerably larger
than the firing rate. To illustrate the effect of
the damping tape on higher frequencies, assume
that a panel had a fundamental frequency near
twice the gun firing rate and that it experienced
the same stress on the first cycle after a round
of fire as the panel in the previous example.
Then it would experience the following stresses
for each round fired: (1) For the undamped
panel — one cycle at 10,900 psi and one cycle
at 9800 psi, and (2) for the damped panel — one
cycle at 9800 psi and one cycle at 6950 psi. By

applying the accumulative damage theory, the
fatigue life of the undamped panel would be
500,000 rounds and for the damped panel, 1.1
million rounds. This means that, for panels
with higher fundamental frequencies, the addi-
tion of damping tape is even more effective in
increasing the panel's fatigue life.

One of the major problems associated with
the addition of a gun to an aircraft is the re-
sponse of aircraft installed equipment to the
environment produced by the firing of this gun.
The environment, as seen by the equipment,
can be broken down into three categories:

(1) Noise transmission through the panels
to the equipment bays, including response of
the air within the bay to skin panel oscillations.

266
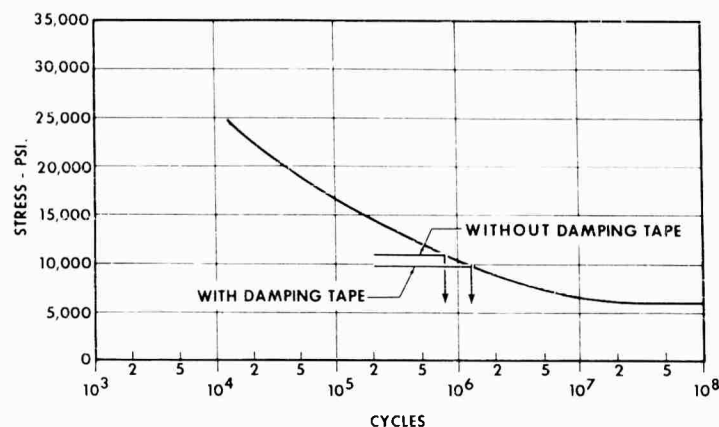
Fig. 9 - S-N diagram 7075-T6

(2) Mechanical transmission of panel response through the support structure.

(3) Transmission of recoil loads from the gun support through the structure.

In order to protect equipment efficiently, it has to be known by which of the above ways the gun-produced environment is transmitted. Table 1 shows the blast pressure on a specific panel, the skin stress on that panel, and the acceleration response of an equipment item mounted in the cavity behind the same panel for various gun configurations. It should be noted here that this was not necessarily the panel experiencing the highest pressures for the configurations being considered. One of the first things that can be noticed in this table is that,

for a given structural configuration (panel with damping tape), maximum skin panel stress, as would be expected, is directly proportional to the maximum pressure on this panel. As mentioned previously, there is an increase in maximum skin panel stress for the same pressure if the damping tape is not installed.

To investigate a possible correlation between skin panel stress and equipment response, these two parameters are plotted against each other in Fig. 10. As can be seen, equipment response is essentially constant for lower skin panel stresses but increases proportional to skin panel stress at higher stress levels. This leads to the conclusion that there is considerable effect on equipment response due to transmission of the recoil load through the structure

TABLE 1
Test Results

Gun Produced Environment	Gun with Pressure Reduction Device "A"	Gun with Pressure Reduction Device "A" (Damping Tape on Skin Panel)	Gun with Pressure Reduction Device "B" (Damping Tape on Skin Panel)	Gun with Pressure Reduction Device "C" (Damping Tape on Skin Panel)
Blast Pressure on Panel (psi)	5.0	5.0	6.7	1.75
Equipment Item "A" Peak Accelerations (g's)	19.0	14.0	33.0	13.5
Skin Panel Peak Stress (psi)	10900	9800	13600	3300

NOTES: 1. All equipment accelerations were at the same frequency.
2. All skin panel stresses were at the same frequency.

267
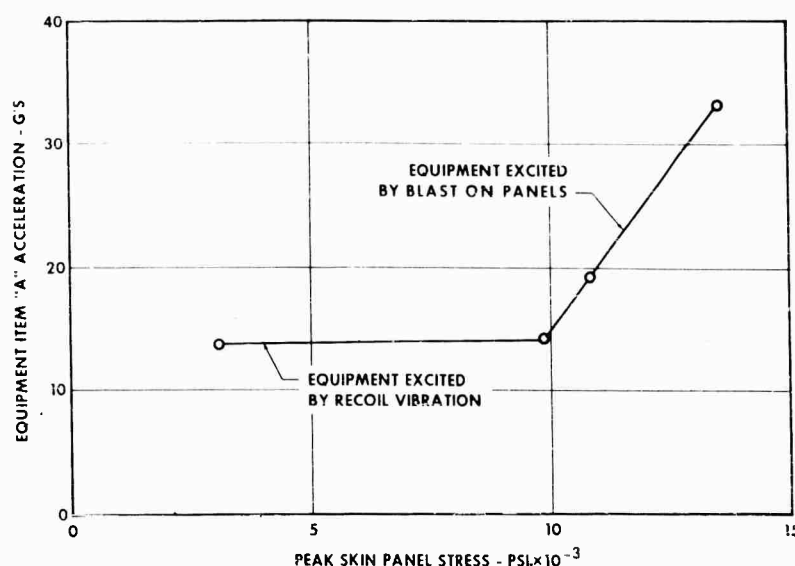
Fig. 10 - Sources of equipment excitation

(this load does not change with changing blast pressure reduction device); in addition, for higher skin panel stress levels and, with its greater panel deflections, there is a direct effect from the skin panel and its supporting structure on equipment response. This effect could be in the form of either mechanical or acoustical transmission to the equipment.

CONCLUSIONS AND RECOM-
MENDATIONS

The following conclusions and recommendations are drawn from the analyses and tests conducted:

1. Considerable care must be exercised in selecting the location and type of instrumentation to be used in a test of this nature so as not to disturb the dynamics of the system and preserve the integrity of the results.

2. The dynamic pressures encountered in flight cause a shift in the location of the pressure field. As a result the entire flight envelope should be considered to assure investigation of the critical flight condition for each panel.

3. Effective gun blast pressure reduction devices are essential to minimize the pressure environment on exposed structure.

4. Damping compounds on thin skin panels exposed to the gun blast are effective in reducing the possibility of fatigue failures.

5. The environment transmitted to equipment items is not entirely the result of blast pressure impinging on the aircraft structure; it also includes vibration transmitted through the structure from the gun-aircraft attach points as well as acoustic resonance in the equipment cavity. The vibration levels can be considerably higher than those normally found in an aircraft structure, requiring special consideration of the gun blast environment in equipment and isolator design.

LIST OF SYMBOLS

A_n Coefficient of the nth term ($lb/in.^2$)

$\mathcal{C}$ Centerline of aircraft

D Flexural rigidity of a panel ($lb/in.$)

f Frequency (cps)

f_r Firing rate (100 rounds per second)

h Panel thickness (in.)

ij Subscripts denoting a point on the panel grid

L Period of blast waves, $1/f_r$ (0.01 sec)

m Subscript denoting mth mode

n Subscript denoting nth term

p_0 — Non-fluctuating pressure due to gun fire (lb/in.^{2})

$p(t)$ — Blast pressure as a function of time (lb/in.^{2})

q_m — Generalized coordinate for the mth mode (in.)

r_x, r_y — Radius of curvature in the x and y directions, respectively (in.)

s — Number of panel modes of interest

t — Time (sec)

T_{nm} — Response amplitude of the mth mode to a unit pressure with a frequency of n/L (in.^{3}/lb)

$w_{ij}(t)$ — Panel deflection at panel point as a function of time (in.)

x — Indicates streamwise direction

y — Indicates direction perpendicular to airstream

δ — Logarithmic decrement

δ_n — Phase angle of the nth term with respect to the first term $n = 1$ (radians)

ν — Poisson's ratio

σ_x, σ_y — Panel stress at the upper surface in the x and y directions, respectively (lb/in.^{2})

$\phi_{m_{ij}}$ — Mode shape at the point on the panel grid identified by ij for the mth mode of vibration

ψ_m — Phase angle of the response of mth coordinate with respect to the first coordinate, $m = 1$ (radians)

ω_m — Angular frequency of the mth panel mode of vibration (radians per second).

*   *   *

REDUCTION OF NOISE AND VIBRATION IN MILITARY VEHICLES

J. W. Cameron
U.S. Army Tank-Automotive Center
Warren, Michigan

This study seeks a better technique for identifying and locating the vibration sources, transmission paths, and radiating panels which are responsible for undesirable noises in military vehicles. A method of determining the relative contribution of each panel to the interior sound level through measurement of vibration velocity for each area is, in conjunction with other data, pointing the way to noise reduction.

INTRODUCTION

Though much effort has been devoted to the reduction of noise and vibration in military vehicles, there is still much to be accomplished. The problem becomes even more serious as the speeds of vehicles are increased. A technique is needed which locates the primary sources of vibrations, the paths through which they are transmitted, and the panels which convert them to airborne noise. In addition the technique should provide data about the significant characteristics of these vibrations in the manner most easily interpreted by the design engineer who must decide which elements to modify and how to modify them to reduce noise and vibration to more satisfactory levels.

APPROACH

A technique for locating the panels which contribute most to the sound level inside the test vehicle (an armored personnel carrier, full tracked) illustrates the approach. The sound pressure in air is proportional to the velocity of the radiating panel and the sound energy is proportional to the square of this velocity. It is possible to get an indication of the relative contribution of each panel to the overall noise by mounting an accelerometer on the panel, integrating the output to convert it to velocity, squaring this velocity, and multiplying it by the area of the panel. This avoids the possibility of erratic results that might be encountered with a microphone because of its position with regard to possible standing waves in the enclosed vehicle.

RESULTS

Because of the complex nature of the vibrations in the panels, five accelerometers were affixed to each as shown on Figs. 1, 3, and 5. Oscillograph recordings were made under many different conditions of operation. Figures 2, 4, and 6 show composite plottings of the velocities and related frequencies. It will be noted that the thinner panels shown in Figs. 2 and 4 show high velocities and several resonances when compared to the thicker panel shown on Fig. 6. Figures 1, 3, and 5 show how the panel was divided into rings or areas with accelerometers at either the center or edges.

For the period of operation showing the highest velocity values the readings of the pertinent accelerometers were averaged to determine the velocity "U" of that ring. This value was then squared and multiplied by the area of the ring to provide "P," the index of sound energy radiation for that ring.

Table 1 shows a summary of these areas and indexes so that the designer may see the relative contribution of each panel to the interior vehicle noise. It is especially interesting to note that the total radiating power index of the first eight panels is 16,789,700 or 93 percent of the total 17,988,435 for all panels. These first eight panels are those which the designer has the greatest freedom to change, as they are not part of the basic structure or armor. The tabulation helps the designer to know how to approach the re-design by showing whether the area of the panel or the velocity of vibration is the most serious contributor to the
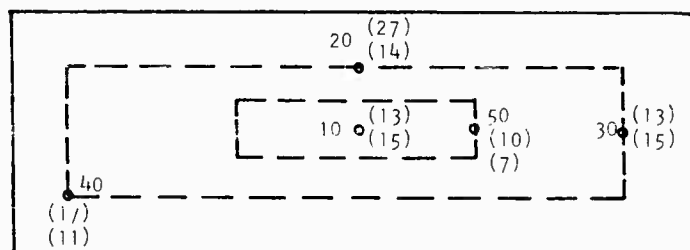
Down Grade Fast			
Ring	A	u	u^2A
1	1024	16.5	279,000
2	4520	16.6	1,268,000
3	6996	9.5	633,000
			2,180,000
In Water			
Ring	A	u	u^2A
1	1024	11.	124,000
2	4520	11.8	624,000
3	6996	6.7	311,000
			1,059,000

Fig. 1 - Arrangement of sampling on right front flooring panel
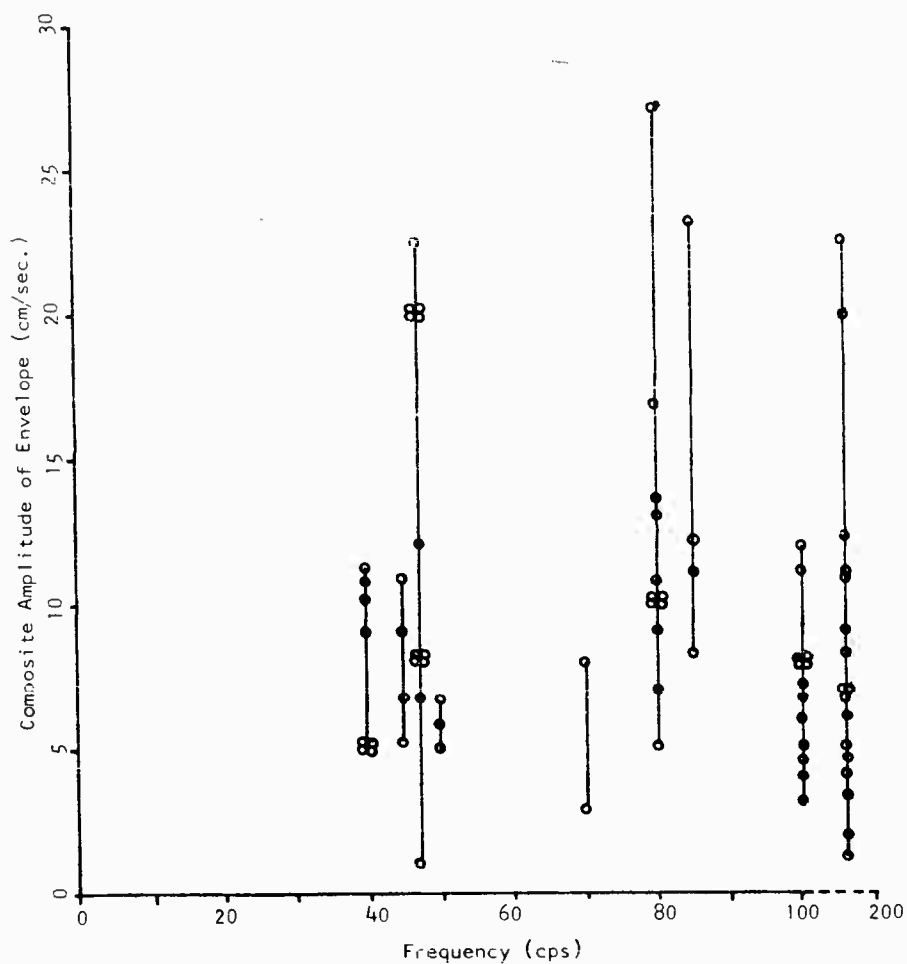
Fig. 2 - Pseudo-spectrum, right front flooring plate, on land

TABLE 1
Summary of Vehicle Interior Vibration Survey

Panel Description	Area (cm^2)	Total Radiating Power u^{2}A (cm^4/sec^2)		
		On Land 25–35 mph	In Water 15 mph	(Track Speed)
Side of Battery Box	1,536	6,140,000	98,300	
Right Bench Back Rest	3,008	3,490,000	3,630,000	
Right Front Floor Plate	12,540	2,180,000	1,060,000	
Fuel Tank Wall (Tank 1/3 Full)	7,676	2,020,000	335,000	
Left Front Flooring Plate	12,540	1,277,000	907,500	
Engine Access Panel, Driver's	6,630	702,000	433,000	
Rear Flooring Plate	8,448	581,000	101,000	
Engine Access Panel, Passenger's	9,880	399,700	233,000	
Total for Sub-floor	35,600	301,000	93,000	
Left Armor Wall	21,584	187,000	41,000	
Right Armor Wall	22,550	99,700	50,000	
Engine Wall Frame, Passenger's	4,880	88,200	48,400	
Outer Plate, Rear Door	7,820	74,300[a]	86,000[a]	
Right Bench Seats	7,471	75,800	18,370	
Top Armor of Left Fender	11,520	64,000	30,500	
Engine Wall Frame, Driver's	5,430	57,100	28,000	
Top Armor of Right Fender	7,144	56,200	25,100	
Rear Top Hatch	8,208	51,200[a]	8,200	
Side Armor of Right Fender	7,336	27,300	36,530	
Driver's Front Armor Wall	7,166	36,000[a]	14,400	
Inner Plate, Rear Door	7,820	17,600	31,400	
Floor of Driver's Area	4,104	19,000	7,150	
Rear (ramp) Wall	8,700	14,800	12,200	
Engine Wall, Passenger's	2,280	13,125	4,185	
Rear Wall (beside ramp)	4,452	10,000	8,420	
Gas Pedal Floor Armor	2,050	4,610	1,153	
Engine Wall, Driver's	1,805	1,800	1,500	

[a]Means too few or badly distributed sampling points.

product. It is considered very probable that changes in material, shape, support, damping qualities, or sound absorbing qualities of these panels can substantially reduce the interior sound level.

Impulse tests have been made to help identify original sources and relative impedances of the transmission paths. Note in Fig. 7 that striking the drive sprocket sets up much larger vibration amplitudes in the various panels than striking the roadwheel. This should lead the designer to consider increasing the impedance in the transmission path. The correction might take the form of vibration isolating material between the sprocket and hub or between the housing and the hull or at both positions. While it is less likely that the degree of impacting can

be substantially reduced at the sprocket by modification, it is possible that the focus of attention on the problem could lead to better track drive concepts at some future date. Figure 7 also shows how slowly damped are the panel vibrations due to impacting the sprocket. Consideration should be given to increasing the damping.

Further tests have been made on the vehicle to locate sources of original vibrations by selectively removing possible sources one at a time. These tests have involved driving, towing, and operating the vehicle on blocks. They, together with other tests, confirm that the primary sources of noise are track interaction with the sprocket and the idler.

273

		(15)	
	3H ○	(5.3)	

(Access Plate)

| 5H ○ (12) (3.5) | 4H ○ (25) (10) | 2H ○ (10) (4.8) |

1H
○
(8.3)
(5.5)
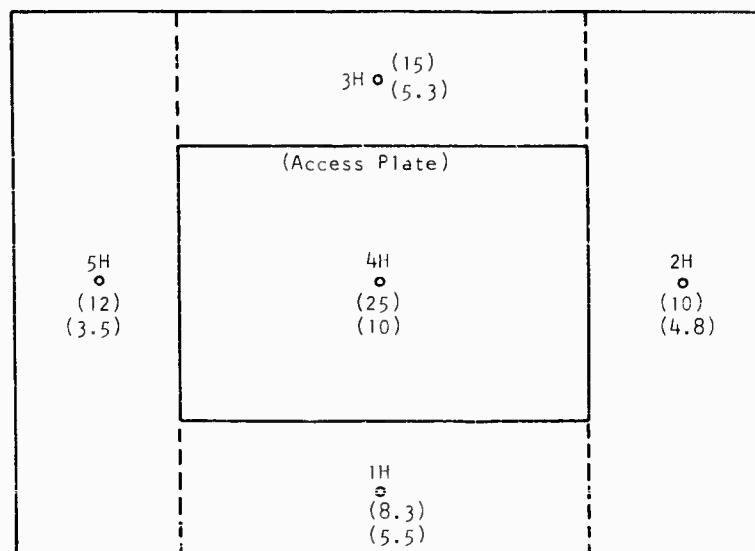
|←— 20 cm —→|

Oown Grade Fast				In Water 0 – 15 mph	(Track Speed)		
Area No.	A	u	u^{2}A	Area No.	A	u	u^{2}A
1	2052	25.	1,282,000	1	2052	10.	205,000
2	1064	8.3	73,000	2	1064	6.	38,300
3	1748	12.	252,000	3	1748	3.5	21,400
4	1064	15.	239,000	4	1064	5.3	29,900
5	1748	10.	175,000	5	1748	4.8	40,200
		Total	2,021,000			Total	335,000

Fig. 3 – Arrangement of sampling on fuel tank wall
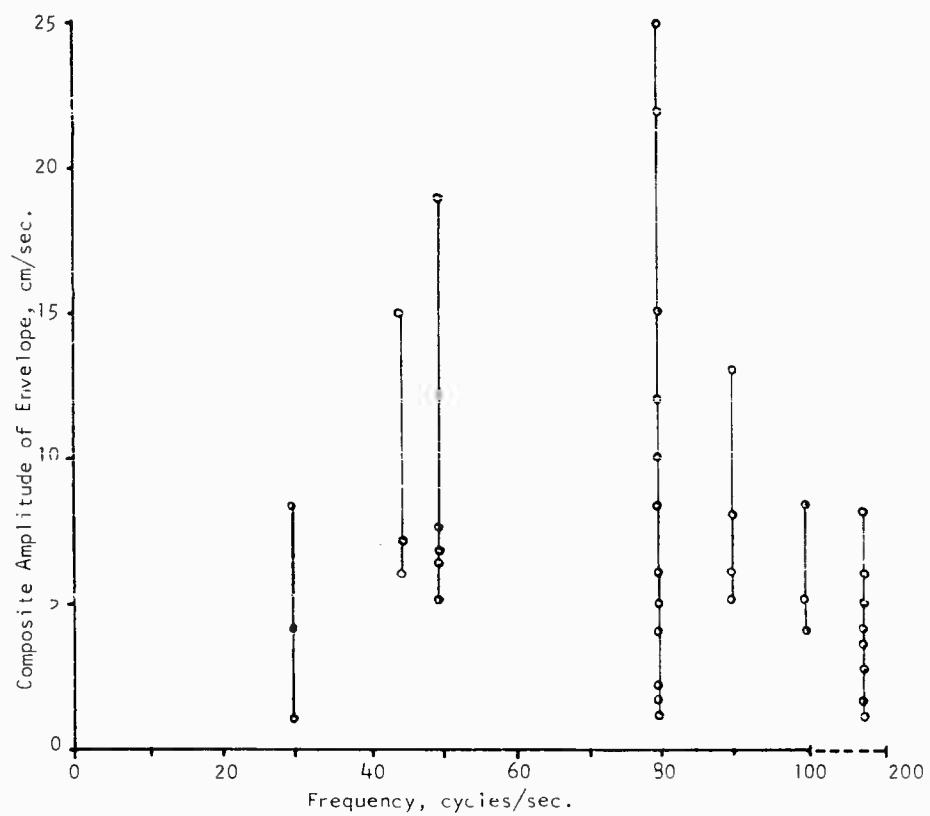
Fig. 4 - Pseudo-spectrum, fuel tank wall (tank 1/3 full), on land

Fig. 5 - Arrangement of sampling for left armor wall
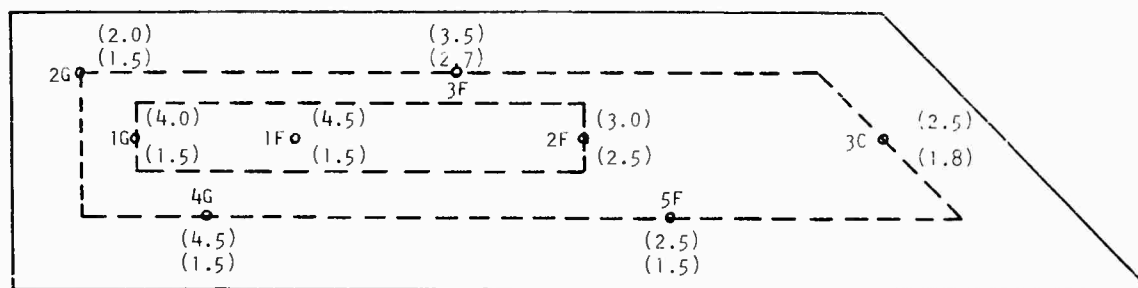
Down Grade Fast			
Ring	A	u	$P=u^2A$
1	2,520	4.00	40,200
2	6,440	3.25	67,600
3	12,624	2.50	78,900
Total			186,700

In Water Accel, 0-15 mph (Track Speed)			
Ring	A	u	$P=u^2A$
1	2,520	1.75	7,750
2	6,440	1.90	23,100
3	12,624	0.90	10,230
Total			41,080
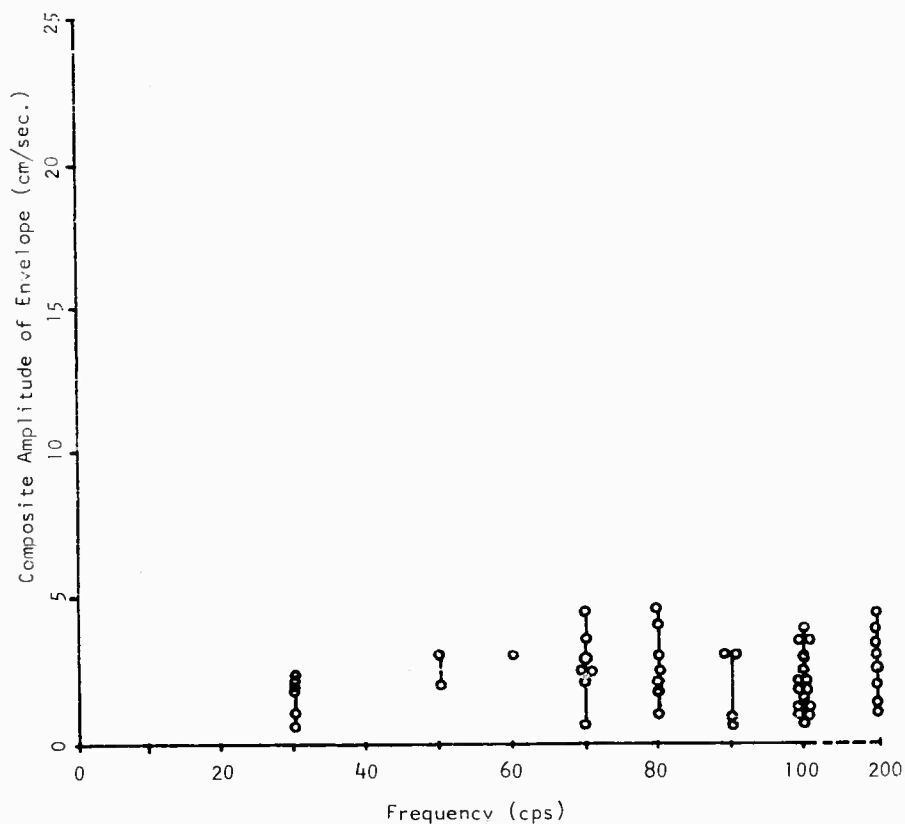
Fig. 6 - Pseudo-spectrum, left armor wall, on land

Eng. Wall
Pass. Comp.

R. Bench
Backrest

L. Wall

R. Floor
Plate

R. Wall

A. STRIKING R. DRIVE SPROCKET   B. STRIKING R. ROAD WHEEL NO. 2
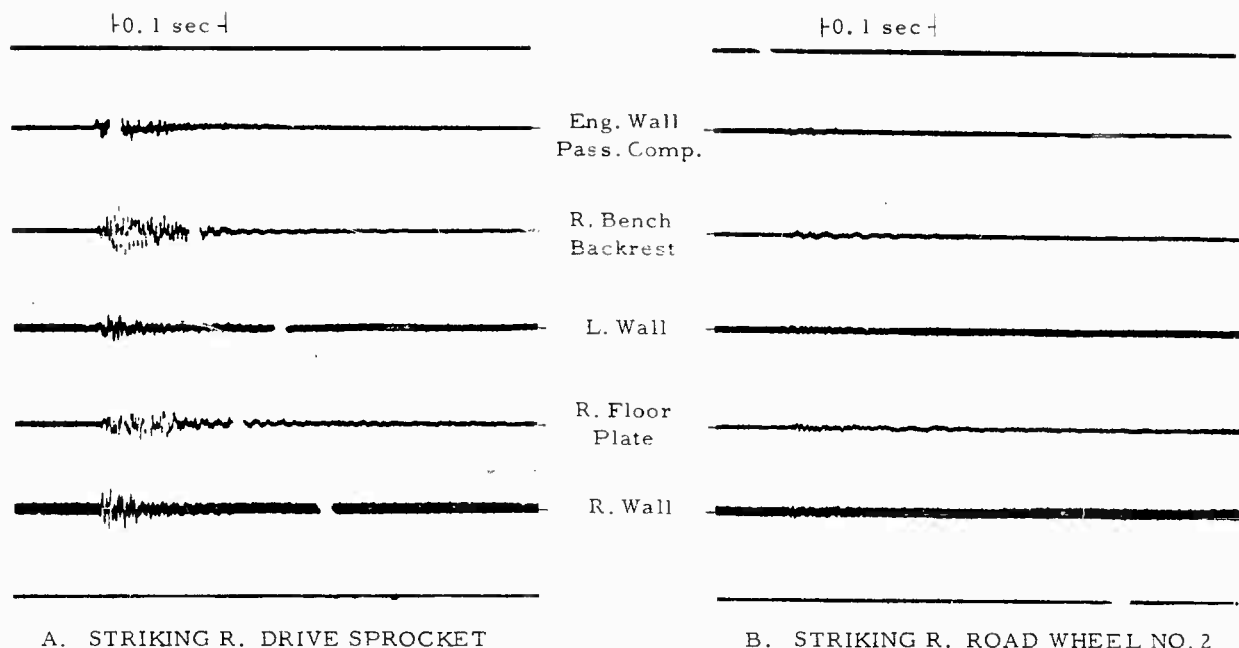
Fig. 7 - Impulse tests, comparing relative impedances

The various conditions of operation have been numbered in Table 2. Shown as Condition 1 is the typical sound pressure level inside the passenger compartment at 10 and 20 mph. This may be used as a reference for all the following tests. In Condition 2 the load from the engine and from the sprocket-track contact was removed but the sound pressure level was unchanged. In Condition 3 the noise of the engine was eliminated. This had no effect at 20 mph. The slight effect at 10 mph would have to be repeated several times to be conclusive. Significant reductions of 12 to 15 decibels in sound pressure level when towing with the tracks removed was shown by tests 4 and 5. Higher accelerations of the roadwheel arm were measured while being towed with tracks off than with tracks on. This would indicate that 9 to 11 of the 12 to 15 decibel reduction is due to track reaction with idler and sprocket, since Condition 6 shows that elimination of the track-road reaction causes a reduction of only 3 to 4 decibels. In tests 7 and 8 the tracks had been removed. The low level of sound pressure verifies the above conclusion. The sound pressure level is even lower than in tests 4 and 5 because the vehicle is not moving - the speeds are as indicated by engine speed.

CONCLUSIONS

The nature of vibrations and associated noises in a full tracked armored personnel carrier are extremely complex. Indeed, the nature of noise and its measurement are complex. This study will not eliminate the problem of noise but it is felt that the technique being developed will make efforts expended on noise reduction significantly more successful. The final technique resulting from this study will stress the importance of the noise and vibration specialist reporting his data to the designer in a form which will minimize the likelihood of worthwhile gains being ignored because they don't appear significant to one unfamiliar with the measurement of noise. It may be necessary to acquaint the designer with the fact that when dealing with sound pressure levels, in decibels, it is necessary to remove 97 decibels in order to reduce a 100 decibel sound pressure level to 97 decibels; this means taking away 50 percent of the sound generating capacity for a 3 decibel improvement.

TABLE 2
Summary of Test Configuration Variations to Show Generation
Sources and Transmission Paths by Selective Elimination

Condition	Purpose	Sound Pressure Level (db)	
		10 mph	20 mph
1. Driving Under Power, Rubber Idler	Determine Total Noise Conditions	114	118
2. Towing, Engine On, Rubber Idler	Eliminate Eng. and Track Loading	114	118
3. Towing, Engine Off, Rubber Idler	Eliminate Eng. Load and Eng. Noise	112	118
4. Towing, Engine On, Tracks Off	Eliminate Eng. Load and Track Reaction	99	106
5. Towing, Engine Off, Tracks Off	Eliminate Eng. Load, Eng. Noise and Track Reaction	99	105
6. On Blocks, Rubber Idler	Eliminate Road-Track Reaction	110	115
7. Eng. Idling, Tracks Off, in Gear, not moving	Eliminate Track Reaction with Road, Sprocket and Idler	94[b]	96[b]
8. Eng. Idling, Tracks Off, in Neutral, not moving	Same as 7 plus Eliminate Transmission Noise	93[b]	94[b]
9. On Blocks, Steel Idler Wheel	Determine Reference Noise Level	118	122[a]
10. On Blocks, Rubber Idler Wheel (2 readings)	Compare Steel and Rubber Idler Wheel	113 112	122[a] 119[a]
11. On Blocks, Rubber Idler With Spacers	Eliminate "Rubbing" Noise of Track on Inside of Idler	111	120[a]
12. On Blocks, Steel Idler, Decagon Rubber Cushion Removed	Compare to 9 to Determine Effect of Rubber Cushion	117	126[a]
13. On Blocks, Rubber Idler, Pads Glued on Sprocket	Reduce Sprocket-Track Reaction	112	122[a]
14. On Blocks, Rubber Idler, Sprocket Wheels Removed Rubber Cushion Wheel Removed, Rubber Belting used as Friction Drive	Eliminate Track-Sprocket Reaction	112	121[a]
15. Removed Idler Wheel and 8 Links of Track, Driving	Eliminate Idler-Wheel Track Reaction	106	116[a]

[a] 25 mph.
[b] Equivalent engine speed.

*   *   *

DESIGNING FOR THE DYNAMIC ENVIRONMENT
PRACTICAL DESIGN TECHNIQUES

Joseph G. Perri
Burns and Roe, Inc.
New York, N.Y.

A chronological synthesis of concepts, theories, methods, and proce-
dures associated with shock and vibration environment and relative
vibration isolation problems is presented in the paper with the dual
objective of partially bridging the wide gap existing between the field
of mathematical and theoretical complexities, and the world of physical
reality featuring an infinite number of engineering applications.

To accomplish effectively, however concisely, the operations required
for getting near the objective stated above, it was necessary to separate
the theoretical exposition from the computational applications.

The separation of the two sections, however, does not interfere with the
continuity and unification of the whole, the contents of which evolve
around the same concept.

Newton's second law for a particle, expressed as an equation of motion,
is briefly discussed at the beginning of the first part to demonstrate how
different interpretations of mathematical terms often lead to new and
fresh ideas which are successively transformed into powerful tools of
analysis; such as that conceived by D'Alembert, who by a simple alge-
braic transposition of a term from the second to the first member
transformed the equation of motion into an equation of static equilib-
rium. The idea of "inertia forces" is by this device wonderfully ap-
plied to vibration problems without destroying the original idea con-
ceived by Newton.

Further confirmation of the preceding remarks is furnished successively
with the inclusion of a discussion about Lagrange's equation; which is
also the result of an idea, that of referring the motion to a system of
coordinates.

The first section of the paper is then concluded with a survey of the
methods and procedures more in line with the types of applications
similar to the one presented in the second section of the paper, with a
discussion about aeroelastic vibration principles, including the phe-
nomenon of self-excitation, and with some remarks about shock en-
vironment.

Four vibration and shock applications are given in the second section
of the paper such as: A 152-foot-high Discrimination Radar Boresight
Tower, a shock mounting assembly for an equipment supporting crib
placed in an underground silo, a 470-foot-high stack for a nuclear
power plant, and a vibration mounting system for a compressor founda-
tion.

The four applications are not just routine computations or mere sub-
stitutions of numbers into the mathematical expressions discussed in
the first section of the paper. They are step by step procedures com-
plemented with observations and remarks which imply deep thinking
and clarity of concept. Worthy of notice are the complementary re-
marks made with respect to the stack self-excitation, also the com-
ments about shock attenuation caused by the interaction between the
cylindrical silo and the soil surrounding it, and the exhausting

discussion about all types of springs for isolation systems, includ-
ing the fluid types.

As a more direct contribution by the author, the application for deter-
mining the natural frequency of the stack is complemented by an orig-
inal direct integration procedure which eliminates tabular summation
and unending numerical work. The derived mathematical formulas are
applicable to all types of tapered stack shells. They yield values for
the fundamental natural frequency which are accurate and satisfactory
for any type of engineering work even when the shell thickness varies
appreciably along the full height of the shell.

SYNOPSIS

A unified and generalized systematic ap-
proach to shock and vibrational reliability de-
sign which takes advantage of simple, basic
theoretical procedures and past experience is
formulated. Application is made to the deter-
mination of the natural frequencies and dynamic
response of actual configurations such as: A
152-foot-high Discrimination Radar Boresight
Tower, a shock mounting assembly for an equip-
ment supporting crib placed in an underground
silo, a 470-foot-high stack for a nuclear power
plant, and a vibration mounting system for a
compressor foundation.

The approach to towers, stacks, and simi-
lar configurations vibration analyses is con-
trasted to the approach to equipment design for
isolation of vibration or shock. The selection
of vibration isolators for low-speed machinery
and equipment subjected to shock motions hav-
ing large displacements is discussed. Because
isolators for military equipment must be suit-
able for absolute performance standards well
beyond the ones usually established for a nor-
mal industrial service, mention is made of
their characteristics. The significance of
shock spectra as criteria of severity of excita-
tion when resonators are coupled together and
of self-excited oscillations is also discussed.

INTRODUCTION

A remarkable revival of interest in recent
years in the subject of dynamics, as applied to
shock and vibration problems, is observed by
reading the large and increasing number of
original papers on both the experimental and
the theoretical aspects of it. The development
of electronic techniques and the very high rates
of loading, associated with the propagation of
stress pulses of large amplitudes and short
duration, which represent matters of consider-
able military importance, are evidently the
reason for the willingness of many to follow in
the steps of Stokes, Poisson, Rayleight, Kelvin,

and so on, and thus obtain solutions for varied
and difficult problems of dynamics.

This paper, which differs from the ones
evolved around one specific subject, because of
its simultaneous presentation of four heteroge-
neous configurations, is likely to originate, at
first sight, some speculation with respect to the
difficulty of preserving unity. It suffices to say
that the author has made a worthy effort to
overcome this difficulty. The criteria for the
analyses of the different problems may be dif-
ferent; the concept on the whole is, however,
unique. The procedures and the computation
techniques followed on the paper are adaptable
for use in electronic computers, the usefulness
of which will be fully realized on the adoptions
of problem-oriented programming languages.

GENERAL REMARKS

An exploration of the writings on the shock
and vibration environment available either in
book form or in any other form, such as that of
a technical paper, a note or an article, reveals
that all theoretical concepts, although expressed
differently and grouped under various headings
by the pertinent authors, are basically develop-
ments of one idea: Newton's Second Law of
Motion [1] as related to Galileo's concepts of
force, energy, inertia, and motion of uniform
acceleration [2].

This well known law, which briefly intro-
duces the concept of proportionality between ac-
celerated masses and relative forces, may be
expressed in several forms, such as

$$X = m\ddot{x}, \quad Y = m\ddot{y}, \quad Z = m\ddot{z}, \qquad (1)$$

$$X - m\ddot{x} = 0, \quad Y - m\ddot{y} = 0, \quad Z - m\ddot{z} = 0, \qquad (2)$$

$$\sum F_x = \frac{d}{dt}(mx), \qquad (3)$$

NOTE: References appear on page 310.

$$\sum F_x \, dt = d(m\dot{x}) = md\dot{x} , \qquad (4)$$

and

$$\sum F(x, \dot{x}, t) = m\ddot{x} . \qquad (5)$$

Equation (1) states that a particle within a dynamic system, and subjected to a set of forces has components of acceleration defined by X, Y, and Z. The same equation is also applicable to a system of particles with a total mass m, which may be constant or changing continually during the motion.

Equation (2) is an alternate way of writing Eq. (1).

Equation (3) states that the resultant force F_x is equal to the time rate of change of the linear momentum (product of mass and velocity).

Equation (4) relates impulse (product of force and time) and change in linear momentum.

Equation (5) which represents Newton's second law in a more general statement may take different forms, depending upon the law of variations of the resultant force F with respect to either displacement, velocity, or time.

Varied and different interpretations of Eqs. (1) to (5) have led many authors to the formation of new concepts which provide several methods of approach in solving problems in shock and vibration environment.

The equations are fundamentally representative of the same idea. They, however, contain terms having special physical characteristics. The term ma_x, as an example, suggested the idea of inertia force to D'Alembert [3]. As a consequence the transformation of problems in dynamics to an equivalent static problem followed as a matter of course.

Equation (2) which is merely an algebraic manipulation when compared with Eq. (1) shows a marked difference of approach to the solution of the physical problem for which Eq. (1) is intended. Equation (2) states that the components of acceleration of the particle are considered to be in equilibrium under the combined action of the applied forces and the inertia forces $(-m\ddot{x})$, $(-m\ddot{y})$, and $(-m\ddot{z})$. The advantages of Eq. (2) to the solution of complex systems of particles are many; for the case of a single particle or body, however, Eq. (1) is also directly applicable.

By the application of D'Alembert's principle, which indicates that all the acceleration components produce inertia forces, the equilibrium equation from statics may be used for the entire system of particles, provided the inertia forces are included in the summation.

In the literature on the subject of dynamics many equations such as:

$$\sum F_x = 0 = m\ddot{y} + k\dot{y} + F_b - W \qquad (6)$$

state that the inertia force $m\ddot{y}$ is in dynamic equilibrium with the gravity force W, the constant force F_b, and the force $K\dot{y}$ which is a function of the velocity, $\dot{y}$, and may be imagined to represent either a drag force or any other type of damping force defined as viscous damping. Ordinarily, according to the conventional notation adopted by the majority in the field of vibrations, the constant c is used for viscous damping, which physically is envisaged as a dashpot filled with oil.

Often the term $C(\dot{y})^n$ is contained in equations similar to Eq. (6). This is to be expected because fluid damping is normally found to be a function of some power of velocity of the vibrating mass. Viscous damping is associated with a laminar flow, i.e., low Reynolds numbers, in which case the value of n is 1, and the force of damping is proportional to the velocity. Any other damping will depend on the degree of turbulence of the medium for which n may approach the value of 2.

It is apparent from the previous paragraphs that a more generalized idea of Newton's mathematical statement was needed to include systems associated with particular frames of reference, such as coordinates consistent with engineering measurements.

Lagrange's equations [4-7] provide this more generalized idea in the form of mathematical expressions in which reference need not constantly be made to particular systems, since the terms are general ones. Any appropriate quantity necessary for developing the configuration of a given system may be used in the procedure. Thus, for a deformed beam which has an infinite number of degrees of freedom, the generalized coordinates q_1, q_2, and so on, are expressed in the form $a_1 = q_1$, $a_2 = q_2, \cdots, a_n = q_n$. When using Lagrange's equations, the generalized forces are obtained by increasing the coordinate q_j by a small amount dq_j. The change in deflection at any point along the length of a beam is given by

$$dy = dq_j \, \bar{X}_j . \qquad (7)$$

The generalized force is defined as

$$Q_j = F(t)\,\overline{X}_j(a) ,\qquad (8)$$

in which the second member expressed the work by the force $F(t)$ on the change in deflection. The Lagrange equation for the jth coordinate becomes

$$\ddot{q}_j + p_j^2 q_j = F(t)\,X_j(a) .\qquad (9)$$

Usually these equations are associated with the general principle of Hamilton [5] which for a non-conservative system is expressed as

$$\int_{t_1}^{t_2} (\delta L - Qi\,\delta qi)\,dt = 0 .$$

The chronological presentation of the three ways of expressing the equilibrium of a dynamic system as necessitated by the vastity of the yield is not to be intended as a digression from the basic and dominant Newton's second law. The special techniques have been described so that they can be used to advantage in formulating the different problems usually encountered in the field of vibration.

METHODS AND PROCEDURES

The fundamental physical and mathematical principles for vibratory systems presented earlier under "General Remarks" are broad statements describing mostly idealized mechanical concepts. Many author's being aware of the difficulty arising from the applications of these concepts to practical mechanical systems, thought it was necessary to transform the broad statement of the second law of motion into more workable engineering tools of analysis. They subsequently established methods and procedures for that purpose.

One of the simplest methods for determining the fundamental frequency of any configuration, such as a power, a stack, which for the purpose of analysis may be considered a vertical cantilever beam placed on an elastic soil, was proposed by Lord Rayleigh. Rayleigh's energy method [8-11], when applied to a typical problem, yields an approximate solution; which most of the time is accurate enough for normal engineering works.

The simplicity of the method results from that it obviates the tedious procedure of solving the differential equation of motion for that particular configuration. The method basically consists of either assuming or determining a reasonable shape for the dynamic deflection curve and then introducing it in the energy expression: which is normally obtained by equating the potential energy of the system to the kinetic energy of the system. With this method, the free-body diagram, as conceived according to D'Alembert's principle, is also eliminated. The fundamental natural frequency as calculated from the assumed shape of a dynamic-deflection curve of a system will be equal to or higher than the true natural frequency of the configurations [12]. How much higher depends on the magnitude of deviation of the assumed shape from the true shape. Small deviations, nevertheless, will not introduce serious errors. A reasonable guess can, in general, be made of the curve because the frequency of an oscillation does not depend on its amplitudes.

The static-deflection method is a special case of Rayleigh's method. Except for a slightly different point of view with respect to the physical aspects of the system as far as its deformation is concerned. If a tower or stack is rotated through 90 degrees so as to be deformed into static gravitational displacements, and then, after having been clamped in this deformed condition, is rotated back into its vertical original position, it will start to oscillate, on being suddenly freed of the clamping. Its velocity will be zero initially and its initial displacement everywhere will be equal to the static gravitational displacement. By this method, the maximum potential energies as well as the maximum kinetic energies can be related to the static displacement curve itself; the total initial elastic potential energy being determined from the summing up at the integration of the work done by the gravitational forces. If conditions require it, or if it is so desired, displacements can be made functions of shear flexure, or any other effect [13-18] consistent with the system to be analyzed including that due to the elastic constraint of the soil surrounding part of the member "planted" in it.

The Rayleigh-Ritz method is a more generalized procedure than the original simple Rayleigh method. It yields more accurate values for the frequencies, and includes steps for estimating several mode frequencies at one time. If the assumed deflection curve is expressed as the sum of several functions in form,

$$X = C_1 f_1(x) + C_2 f_2(x) + C_3 f_3(x) .\qquad (10)$$

The accuracy of the values of the frequencies can be made better by using more functions. The frequencies are estimated as follows:

1. Expression 1 is introduced in the energy equation

$$P_n^2 = \frac{\int_0^L EIX_n^2\,dx}{\int_0^L m X_n^2\,dx} \; ; \qquad (11)$$

2. Equation (8) is equated to zero for each value of ∂c_i thus

$$\frac{\partial}{\partial c_i} \; \frac{\int_0^L EI\ddot{X}_n^2\,dx}{\int_0^L m X_n^2\,dx} \; = \; 0 \; : \qquad (12)$$

and

3. From the n-algebraic equations, the determinant, when set to zero yields the values of the first n-mode of vibration.

Among the many other procedures, two of them are worthy of mentioning, i.e., the force influence coefficients method and the displacement influence coefficients method. The force influence coefficients, which is denoted by the symbol ϕ^* is defined as the force required at mass M_i to move the mass M_j a unit horizontal distance, when the configuration is clamped in such a way that no other mass in it can translate.

From the equilibrium equation applied to a mass M_i given as

$$M_i \ddot{X}_i + \sum_j \phi_{ij} X_i = 0 \qquad (13)$$

and an assumed solution in the form

$$x_i = X_i \cos (pt + a) \, , \qquad (14)$$

a reduced algebraic equation is obtained, thus

$$- M_i X_i p^2 + \sum_j \phi_{ij} X_j = 0 \, . \qquad (15)$$

Finally, an application of the expressions above can be made to a configuration with n-masses by setting up the system of equations given below:

$$\phi_{11} X_1 + \phi_{12} X_2 + \cdots + \phi_{1n} X_n$$
$$\phi_{21} X_1 + \phi_{22} X_2 + \cdots + \phi_{2n} X_n \qquad (16)$$
$$\cdots \cdots \qquad \cdots \cdots \qquad \cdots \qquad \cdots \cdots$$
$$\phi_{n1} X_1 + \phi_{n2} X_2 + \cdots + \phi_{nn} X_n \, .$$

In matrix form Eq. (13) becomes:

$$\phi X = P^2 M X \qquad (17a)$$

$$(\phi - p^2 M) = 0 \, . \qquad (17b)$$

The displacement coefficients, which are denoted by the symbol $\phi^\dagger$ are defined as the displacement of a mass M_i due to a unit force applied at mass M_j, when all other masses are unclamped and free to translate.

As above, for free undamped motion from the equation

$$x_i + \sum_j \theta_{ij} m_j X_j \qquad (18)$$

and an assumed solution in the form

$$X_j = X_j \cos (pt + a) \, , \qquad (19)$$

a reduced algebraic equation is obtained, thus

$$X - \sum_j P^2 \theta_{ij} m_j X_j = 0 \, . \qquad (20)$$

Similarly, as shown for the force influence coefficients, the system of equations is

$$X_1 = p^2(\theta_{11} m_1 X_1 + \theta_{12} m_2 X_2 + \cdots + \theta_{1n} m_n X_n$$
$$X_i = p^2(\theta_{21} m_1 X_1 + \theta_{22} m_2 X_2 + \cdots + \theta_{2n} m_n X_n \qquad (21)$$
$$\cdots \; \cdots\cdots\cdots\cdots\cdots\cdots\cdots\cdots \; \cdots \; \cdots\cdots\cdots$$
$$X_i = p^2(\theta_{ni} m_1 X_1 + \theta_{n2} m_2 X_2 + \cdots + \theta_{nn} m_n X_n \, .$$

In matrix form the set becomes

$$X = p^2 \, dmx \, . \qquad (22)$$

For configurations such as rigid frames with many degrees of freedom, the evaluation of the deflections at mass points for each position of the unit force is a time consuming effort, it is therefore more convenient to set up equations of motion for each of the mass points. The procedure is as follows: From the equilibrium equations of the inertia forces

$$-m_1 \ddot{X}_1 - F_1 = 0$$
$$-m_2 \ddot{X}_2 - F_2 = 0 \qquad (23)$$
$$\cdots\cdots\cdots\cdots\cdots$$
$$-m_n \ddot{X}_n - F_n = 0 ,$$

a set of equations in terms of the frame stiffness coefficients can be set up, thus

$$F_1 = K_{11} X_1 + K_{12} X_2 + \cdots + K_{1n} X_n$$
$$F_2 = K_{21} X_1 + K_{22} X_2 + \cdots + K_{2n} X_n \qquad (24)$$
$$\cdots \quad \cdots\cdots\cdots\cdots\cdots \quad \cdots \quad \cdots\cdots$$
$$F_n = K_{n1} X_1 + K_{n2} X_2 + \cdots + K_{nn} X_n .$$

In these equations K_{ij} is defined as the spring force at mass point i for a unit displacement $(X_i = 1)$ at mass point j, all other displacements being zero. The solutions to Eq. (24) can be obtained by any available method including the one by Stodola [19,20] which is as follows: The iteration is started by assuming a set of deflections x_1, y_2, x_3, $\cdots$ for the right column of matrix and performing the relative operation. The resulting column is then normalized; i.e., reducing one of the amplitudes to unity by dividing each term of the column by the particular amplitude. By successive repetitions with the normalized column, a state of stability toward a definite pattern of the amplitude can be reached.

AEROELASTIC VIBRATION PRINCIPLES

A mathematical statement in the form of a symbolic expression may be considered a great pedagogical accomplishment; its usefulness, however, can depend only on its capability to describe precisely the phenomenon for which it is intended; i.e., it must have scientific value. A mathematical statement with a capability to describe conclusively the phenomenon of self-excitation, which is associated with many configurations exposed to the flow of a fluid, would have both scientific and technical value; unfortunately it is still to be found.

Towers, stacks, and similar configurations often vibrate excessively, even when winds of moderate velocities occur [21-24]. It appears, however, that their frequencies are functions of their rigidities rather than the periodic forces or velocities of winds.

Aeroelastic vibrations of stacks, caused by vortex shedding [25,26] are functions of parameters which depend on supercritical Reynolds numbers. Some studies have been made recently

(as of 1960) on Reynolds numbers with magnitudes well in the range of those which produce resonance in most stacks. They added another step to the stair of knowledge which will gradually lead to a better understanding of related problems.

Theodor von Karman, who described the phenomenon of the vortex trail [27-30], pointed out that when a wind stream passes a cylindrical obstruction alternating vortices are shed periodically. The alternating pressures exerted on the opposite sides of the cylindrical surface act at about 90 degrees from the direction of the wind and their magnitude is given by

$$Pa = C_L \left(\frac{\rho v^2}{2} \right) .$$

in which C_L is a coefficient of lateral forces resulting from vortex shedding still undetermined for large Reynolds numbers.

The frequency of the vortices is obtained from the Strouhal number S which is expressed as

$$S = \frac{fD}{v} = 0.19 .$$

where f is the frequency of the vortex shedding or vibration in cycles per second, D is the diameter of the cylinder, and v denotes the velocity of wind in feet per second. For air, the following relation exists:

$$R = \frac{vD}{\nu} = 6380 \; vD .$$

in which R is the Reynolds number, and ν is the kinematic viscosity.

Reynolds numbers per stacks are in the range of 3,000,000 to 10,000,000; which by far are greater than the values of 120,000 and 250,000 termed critical because of the flow change from "laminar to turbulent." The values of the Strouhal is not constant and is given as having an average of 0.2.

Various types of cross sections have been tested in wind tunnels [31,32] and results show that the rate of vortex shedding is regular or irregular depending on the shape. For the irregular shapes the driving forces have no single frequency.

A close study [33-35] of the wind pattern is not the scope of this paper; besides, as it appears from the preceding references, many discussions on the subject are available. It can be

added that in non ideal potential flows around a cylinder the accumulations of air in the leeward stagnation crowds the streamlines. The release of these accumulations at intervals which depends on the dimensions of the area of the cylinder, gives rise to the periodic discharge of vortices as idealized in many diagrams descriptive of the flow.

SELF-EXCITATION

As mentioned in the Aeroelastic section, the phenomenon of self-excitation belongs to a special and important class of steady-state motion not yet completely solvable mathematically.

A self-excitation system is an independent, self-controlled configuration which derives energy from an external source by virtue of its own periodic motion. Its periodicity is therefore only a function of its natural frequency. A forced system, on the other hand, is a dependent, externally controlled configuration which, in the steady-state of motion, vibrates with the frequency of the external periodic force.

A violin string, as an example, vibrates with its own undamped frequency independently of the bow; it therefore represents a self-excited system which derives energy from the frictional force set up by the moving bow.

The characteristics and magnitude of the excitation element and the dissipation element of a self-excitation system are under intensive studies, especially, with reference to plane wings (flutter studies). The non-linear character of the motion, however, precludes a prior evaluation of these characteristics. It is therefore possible to obtain information about them only by experimental means, which yield empirical expressions for that particular type of configuration only.

From the point of view of mathematics, a criterion of self-excitation for systems surrounded by moving fluids states that if $dFy/d\theta$ is negative, the work is positive and self-excitation occurs. For this particular case, which represents a twofold symmetrical I-beam section suspended in a fluid and fastened by springs, it was found that the moving I-beam will extract work for self-excitation from the fluid stream where the angle of attack, θ, lies within the interval of -0.09 to 0.09 radian. As a conclusion of this paragraph, it can be stated that an unstable motion is the result of negative damping [36,37]; i.e., the disturbance varies as the velocity. Oscillations instead of

being reduced mount progressively. Self-standing towers subject to gusts may be in phase with residual motion from previous gusts, their amplitudes may therefore be augmented by a factor greater than the usual dynamic factor with a value of 2.

SHOCK ENVIRONMENT

Simple Concepts

The complexity of shock phenomena is beyond evaluation, and only recently consistency of efforts has succeeded in tentatively explaining some generalized concepts of the shock environment. Perhaps because the intensive efforts of the military research center personnel of the United States and other countries, together with the extensive application of electronic and electromechanical equipment have stimulated the imaginative potentiality of many investigators toward the proper direction [38-46].

The phenomenon of shock is normally associated with systems which vibrate in a transient manner and in many natural modes simultaneously. Only by discarding the harmonics of the fundamental frequency it is possible to simplify the exceedingly complex analyses of systems subject to shock. This simplification is considered justified [41] because the cushioning afforded by the isolator reduces the suddenness of forces and motion and consequently decreases the response of configurations in their higher modes of vibration. Shock is generally defined as a sudden excitation of the resonators in configurations and equipment by any impulse, or force, or transient motion. In Ref. [45] there is a hint of a wish to make the distinction between "shock" and a steady "acceleration"; the fact that the first effect excites resonances, while the second does not is not, however, a valid reason for such a distinction and the author discards the idea. It is therefore a matter of locating the lowest resonance of the system which is the most important factor for determining the dividing frequency.

Sometimes shocks are produced by sudden velocity changes in mounted equipment, especially in naval vessels subjected to the action of armaments and other combat vehicle; the mounting in this case is analyzed for velocity changes.

Shock isolation mounts are generally investigated for the following conditions:

1. The maximum deflection of isolators is smaller than the shock motion displacement amplitude.

2. The maximum deflection of isolators is smaller than the displacement of the shock force.

3. The maximum deflection of isolators is greater than those produced by the causes mentioned in 1 and 2.

Very lengthy mathematical procedures (related to the ones described previously) are generally required for analyzing the multi-degrees of freedom systems of isolator mounts subjected to shock. It is, however, neither necessary nor desirable to present, describe, and explain all those generalized theoretical approaches and mathematical statements associated with shock because the problem of the crib shock mounting is not the main subject of the paper. Further, all procedures for shock are either similar to the ones already discussed or slightly modified versions of them.

In general, the concept of the behavior of a simple mass system isolator whose support is experiencing either a velocity shock or an acceleration shock is sufficient to explain the shock phenomenon more adequately than a deep philosophical treatment; accordingly, such a system is considered.

For the condition of inelastic impact, the equation of motion of a mass M_z is

$$M_z \ddot{z} = K_z (y - z) ,$$

the relative velocity of the support being

$$y = V_s t .$$

the general solution for the motion of the mass M_z, when $z = \ddot{z} = 0$, and $t = 0$ is

$$z = V_s \left(1 - \frac{1}{p_z} \sin p_z t \right) .$$

The deflection of the spring K_z is given by $d_{yz} = y - z$ or in different form by

$$d_{yz} = \left(\frac{V_s}{p_z} \right) \sin \omega_z t .$$

This expression shows that the maximum displacement

$$(d_{yz})_o = \frac{V_s}{p_z} .$$

If the support is subjected to an acceleration, a, the expressions are as follows:

$$y = \frac{1}{2} a t^2$$

$$\ddot{z} = p_z^2 z = P_z^2 \frac{a t^2}{2}$$

$$z = \frac{a}{p_z^2} (\cos p_z t - 1) + \frac{1}{2} a t^2 .$$

In all expressions above

$$p_z = \left(\frac{K_z}{m_z} \right)^{1/2} .$$

For the case of a support subjected to a velocity V_s, the maximum deflection of the spring K_z and the maximum acceleration $\ddot{z}_o = V_s P_z$ of the mass m_z are a measure of shock severity. For the case of a support subjected to an acceleration a, the compression in the spring $(y - z)$ will vary from zero to a maximum of $2 a / p_z^2$.

Attenuation Capability of a Silo

A vertically oriented silo, especially when its uppermost surface coincides with the ground surface, is not capable of attenuating appreciably the blast induced pressures, when behaving as a unit. It is true that disturbances associated with Rayleigh waves decay exponentially with depth, however, since they spread only in two dimensions, they fall off more slowly with distance than the other types of elastic waves [47-55]. The fact that stress-strain curve for a decreasing stress does not retract its upward path exactly is an important factor in the attenuation of stress waves through solids; however, this effect is more accentuated with a medium such as soil, than with concrete. A total attenuation is therefore beyond any expectation.

A partial attenuation is indisputable under all conditions; nevertheless, no one, even the most experienced analyst in the field of wave propagation, will ever determine its exact magnitude. In order to estimate a satisfactory attenuation value consistent with the silo boundary conditions it will be advisable to first examine, compare, and discuss the physical characteristics of the soil it replaces. Substantial differences, undoubtedly, exist between the dynamic properties of the structure and the properties of the soil. It is not difficult to imagine that the shock structure environment will differ appreciably from the free-field environment. How much it will differ is a question that has not been answered in similar configurations, as it

286

appears from the findings shown in a few papers, some of which are mentioned in the bibliography [56-60].

Untenable assumptions have been made, such as, the state of a rigid body enclosed within a mass of an elastic medium and subjected to a harmonic disturbance. The results seem to demonstrate without proof that a silo, termed an inclusion, tended to follow the motion of the medium for excitations with wave lengths much longer than its diameter and was not responsive to short wave lengths. The explanation is to be found in the idea that the structure will move almost as a unit without discernible distortion if the wave length is very large. As an example, if the ground velocity is 3000 fps and its frequency is 5 cps, the wave length would be $3000/5 = 600$ feet. Since the structure extends about 20 feet in the path of such wave, not more than 20/600, or about 1/30 would be under it at any time; and the greatest displacement between any two points in the diameter of the silo would be 20/300, or 1/15 of the range of the motion.

Even the assumption of considering the soil as an elasto-plastic medium did not yield a satisfactory answer; that was to be expected because of the exclusion of a significant damping factor. On the other hand, an attenuation of significant entity could be predicted for the condition of having the silos enclosed in a rock cavity, free of frangible material and of any other possible fragmentary inclusion.

The concrete silos are neither rigid nor exceedingly elastic, on account of the limited ductility of the concrete. The energy that it can store is merely a fraction of the energy that the more ductile material, steel, can store based on similar conditions; however, it is capable of a certain flexibility which will be sufficient to produce a springy action. As a result, it is possible to envisage that the response spectrum for the mounted crib will be modified to conform to a different reduced input motion. How much reduction is to be expected? The answer, off hand cannot be given if it is intended to be indicative of the true value; however, by thinking about the thickness of the foundation slab, which may be in the neighborhood of 5 feet, and at its frequency, which may be in the interval of 100 or more cps, one might base a judgment on the slab deflection of perhaps 1 inch.

By assuming a stiffness value of perhaps 50,000,000 lb/in. its acceleration may approach the value of about 250 g or more. This attenuation estimate is only a guess, and a future mathematical analyses of the combined shock mount will surely provide a better numerical value.

DISCRIMINATION RADAR BORE-SIGHT TOWER (152 FEET HIGH)

This tactical Discrimination Radar Test Tower for Nike Zeus Weapons Systems, designed by Burns and Roe, Inc., for the Bell Telephone Laboratories, Inc., in 1961, was erected in White Sands, New Mexico.

The four-legged, free-standing, structure-steel tower supporting the test antenna (a reflector 10 feet in diameter and two target flags 2 feet x 2 feet) is a simple configuration made mostly of angles. As shown in Fig. 1, it consists of two units: (1) a 147-foot high tapered unit, 27 feet wide at its lower end and 5 feet 4-1/2 inches wide at its upper end, and (2) a 15-foot straight unit in contact with the upper end of the tapered unit.

The tower is provided with "X" bracing in both the vertical and horizontal planes, to resist the effect of dead, live, and wind loads acting either singly or in combination. The discussion of the statical design procedure of the tower is beyond the scope of this paper; it is sufficient to state that criteria required that the tower be designed for a 90-mph wind operation, that the maximum deflection at center of target must not exceed 4.5 inches including the effect of tilting, that the maximum natural frequency of the tower must not exceed 1 cps, when vibrating as a cantilever beam, and the torsional frequency was not required because of its negligible influence on the testing operation.

Experience and theoretical considerations indicated that in view of the conditions of deformability of the tower framing more appropriate method for determining the tower fundamental frequency would be the Rayleigh-Ritz method. As discussed previously, the method evolves around the concept that a beam can be represented by a series of lumped weights W_1, W_2, ---, and the maximum strain energy can be determined from the work done by these loads. Accordingly, the maximum kinetic and potential energies are given as:

$$T_{max} = \frac{1}{2} \frac{p^2}{g} \left[W_1 y_1^2 + W_2 y_2^2 + \cdots W_n y_n^2 \right],$$

and

$$U = \frac{1}{2} \left[W_1 y_1 + W_2 y_2 + \cdots W_n y_n \right],$$

287
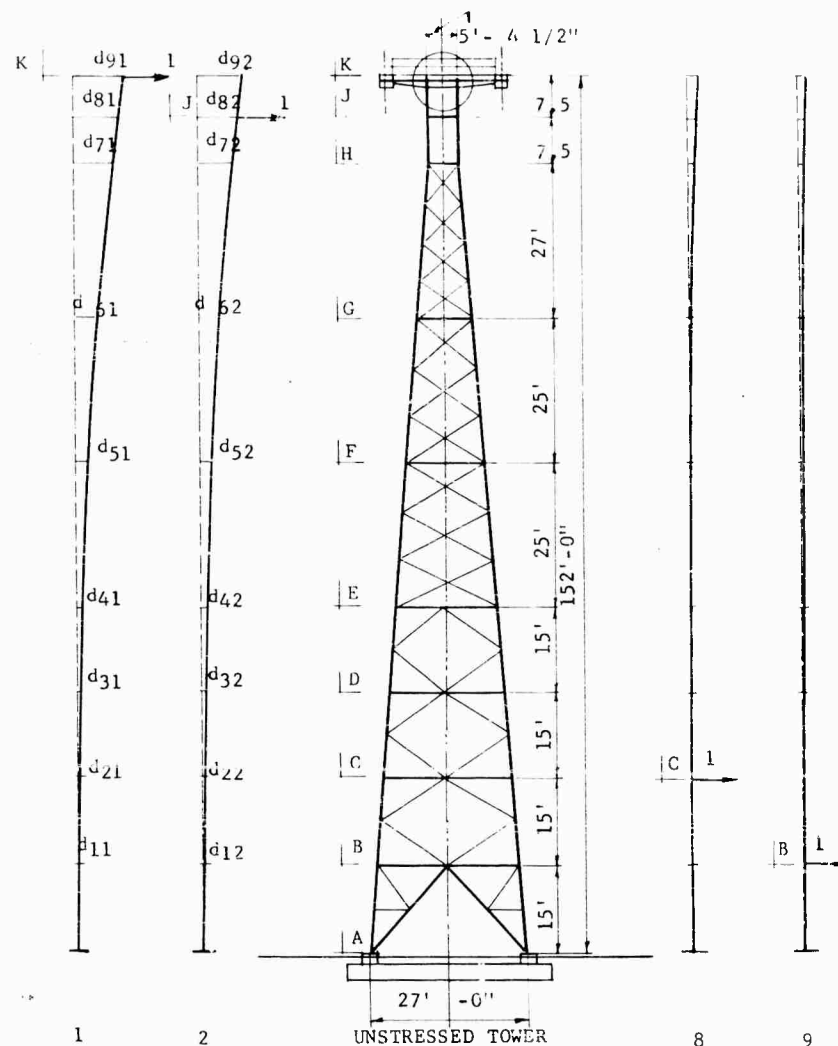
Fig. 1 - Discrimination Radar Boresight Tower--Tower elevations and four out of nine deflection diagrams for a unit load applied at each point A to K

where $y_1, y_2, \cdots, y_n$, represents the static deflections of corresponding points, the frequency equation is derived by equating the two expressions and rearranging terms. The resultant circular frequency is

$$p^2 = \frac{g \Sigma Wy}{\Sigma Wy^2} .$$

Similarly the natural frequency of free motion is

$$f = -\frac{1}{2\pi} \left(\frac{g \Sigma Wy}{\Sigma Wy^2} \right)^{1/2} .$$

The quantity in parentheses is the ratio of two summations with product terms involving W

and y. It was therefore deemed convenient to divide the procedure in two computation schemes: A graphical construction and a computation in tabular form. The graphical construction consisted merely of an application of the Williot-Mohr diagram for determining statical deflections for trusses. Some preparatory computations were actually required to obtain the values relative to lengthening and shortening of the tower members for each loading condition. For this preliminary step, all member stresses were computed for a load of 1000 pounds applied progressively at panel points A to K (nine independent computations were required in all since point A is at the base of the tower). From the use of these stresses in the formula $\delta = NL/AE$, where terms for each bar are as follows: an

288

axial stress N, a uniform area A, a length L, and the modulus of elasticity E, the values of delta were obtained. From this point on the graphical construction was carried out and the magnitudes of the deflections at each panel point were scaled from the completed diagram and recorded in Table 1.

Description of Tabular Procedure

The compilation of Table 1 required computation for the last column only. In column 1 are shown all panel points A to K. In the following nine columns are recorded the 1000-pound load deflections for each point. In the last column are given the total deflections for all nine loadings.

Table 2 contains the point loads such as frame, antenna, platforms, and ladder loads in addition to the deflections due to 1000-pound loads in the second column and the total loads at points in the last column.

Table 3 shows the products of the deflections at points under K to B given in Table 2, and the loads at the same points given in Table 3 (top row). Summation of all row terms yielded the values of the total deflections shown in the last column.

Table 4 contains the products of the loads and deflections; last two columns representing the values to be inserted in the frequency formula. The frequency of the tower vibrating as a cantilever beam was

$$p = \left(\frac{38,112 \times 386}{124,110} \right)^{1/2} = 10.9 \ \text{radians/sec},$$

$$f = \frac{10.9}{2\pi} = 1.73 \ \text{cps} \ .$$

This value of the natural frequency did not satisfy criteria, it was therefore necessary to alter the physical characteristics of the system.

TABLE 1
Summary of Deflections for 1000 Pounds at Panel Points

Point	Loads at Points									Total Defl. (in.)
	K	J	H	G	F	E	D	C	B	
K	0.6880	0.6050	0.5220	0.3070	0.1635	0.0700	0.0348	0.0188	0.0007	2.4098
J	0.6050	0.5482	0.4774	0.2844	0.1540	0.0671	0.0335	0.0128	0.0008	2.1832
H	0.5220	0.4774	0.4295	0.2629	0.1444	0.0531	0.0320	0.0125	0.0011	1.9349
G	0.3070	0.2844	0.2629	0.1848	0.1115	0.0525	0.0273	0.0116	0.0020	1.2440
F	0.1635	0.1540	0.1444	0.1115	0.0801	0.0417	0.0221	0.0104	0.0027	0.7304
E	0.0700	0.0671	0.0531	0.0525	0.0417	0.0331	0.0177	0.0095	0.0036	0.3483
D	0.0348	0.0335	0.0320	0.0273	0.0221	0.0177	0.0146	0.0089	0.0042	0.1951
C	0.0188	0.0128	0.0125	0.0116	0.0104	0.0095	0.0089	0.0083	0.0048	0.0976
B	0.0007	0.0008	0.0011	0.0020	0.0027	0.0036	0.0042	0.0048	0.0053	0.0252
A	0.0000	0.0000	0.0000	0.0000	0.0000	0.0000	0.0000	0.0000	0.0000	0.0000

TABLE 2
Total Deflections at Points for 1000 Pounds at Points and Loads

Panel Point	Deflection Due to 1000-lb at Points (in.)	Frame Loading (Bent) (lb)	Antenna Platform (Steel) (lb)	Other Platform (Steel) (lb)	Ladder (lb)	Total (lb)
K	2.4098	1458	891	—	284	2632
J	2.1832	415	—	—	284	699
H	1.9349	845	—	—	617	1462
G	1.2440	1515	—	425	950	2890
F	0.7304	1857	—	425	950	3232
E	0.3483	1937	—	425	770	3132
D	0.1951	1712	—	—	590	2302
C	0.0976	2494	—	425	590	3509
B	0.0252	2399	—	—	590	2989
A	0.0000	0	—	—	—	0

TABLE 3
Total Deflections at Points Due to Loads

Panel	Loads									Total Defl. at Point (in.)
	2632 K	699 J	1462 H	2890 G	3232 F	3132 E	2302 D	3509 C	2989 B	
K	1.8100	0.4225	0.7640	0.8870	0.5280	0.2190	0.0860	0.0660	0.0021	4.7786
J	1.5900	0.3822	0.6950	0.8200	0.4970	0.2109	0.0770	0.0450	0.0024	4.3195
H	1.3700	0.3340	0.6280	0.7600	0.4660	0.1665	0.0735	0.0438	0.0033	3.8451
G	0.8050	0.1982	0.3845	0.5320	0.3600	0.1645	0.0627	0.0407	0.0060	2.5536
F	0.4300	0.1080	0.2100	0.3220	0.2580	0.1305	0.0507	0.0365	0.0081	1.5538
E	0.1840	0.0469	0.0778	0.1515	0.1330	0.1070	0.0406	0.0333	0.0108	0.7849
D	0.0915	0.0234	0.0468	0.0790	0.0715	0.0553	0.0335	0.0312	0.0126	0.4448
C	0.0495	0.0089	0.0183	0.0335	0.0336	0.0298	0.0204	0.0292	0.0144	0.2376
B	0.0018	0.0006	0.0016	0.0058	0.0088	0.0113	0.0096	0.0168	0.0159	0.0722
A	0.0000	0.0000	0.0000	0.0000	0.0000	0.0000	0.0000	0.0000	0.0000	0.0000

TABLE 4
Products of Loads and Deflections

Panel	Deflection at Point (in.)	Load W at Point (lb)	2	W	W^2
K	4.7786	2632	22.85	12,600	60,200
J	4.3195	699	18.66	3,010	13,000
H	3.8451	1462	14.65	5,600	21,700
G	2.5536	2890	6.55	7,360	18,900
F	1.5538	3232	2.40	5,000	7,750
E	0.7849	3132	0.616	2,460	1,890
D	0.4448	2302	0.198	1,030	455
C	0.2376	3509	0.057	837	200
B	0.0772	2989	0.005	215	15
A	0.0000	0	0.000	0	0
			=	38,112	124,110

In the static equilibrium position, the spring force $K\Delta$ is equal to weight W or

$$\frac{K}{m} = \frac{W}{m\Delta} = \frac{g}{\Delta} .$$

The natural frequency, being a function of the statical deflection, can be changed by properly varying the statical deflection. This change was accomplished by adding a concrete platform on top of the tower. From the application of different platforms at point K, a few frequency values were computed and a curve was plotted. The intersection point of the curve with the abscissa passing through the ordinate having a value of 1.00 indicated that a platform weighing 11,000 pounds was sufficient to lower the frequency to the value of 0.955. Computations for this stage of work are shown in Tables 5 and 6 which are similar to Tables 3 and 4.

With the purpose of comparing the result of a good approximation procedure to the result of a poor approximation procedure, the natural frequency of the tower was determined by assuming that its rigidity could be taken as equal to that obtained from a section at the mass center at about 59 feet from the tower base. The moment of inertia I was computed from $I = 2Ar^2$, in which A is the area of one leg and r is the radius, taken as equal to one half of the tower width at the mass center. Numerically

$$I = 2 \times 3.61(7.73 \times 12)^2 = 62,000 \text{ in.}^4$$

$$K = 12.4 \text{ EI}/L$$

$$K = \frac{12.4 \times 30 \times 10^6 \times 62 \times 10^3}{(152 \times 12)^3} = 3800 .$$

TABLE 5
Total Deflections at Points Due to Loads

| Point | Loads | | | | | | | | | Total Defl. at Points (in.) |
	13632 K	699 J	1462 H	2890 G	3232 F	3132 E	2302 D	3509 C	2989 B	
K	9.3600	0.4225	0.7640	0.8870	0.5280	0.2190	0.0800	0.0660	0.0021	12.3286
J	8.2500	0.3822	0.6950	0.8200	0.4970	0.2109	0.0770	0.0450	0.0024	10.9795
H	7.1100	0.3340	0.6280	0.7600	0.4660	0.1665	0.0735	0.0438	0.0033	9.5851
G	4.1900	0.1982	0.3845	0.5320	0.3600	0.1645	0.0627	0.0407	0.0060	5.9386
F	2.2220	0.1080	0.2100	0.3220	0.2580	0.1305	0.0507	0.0365	0.0081	3.3460
E	0.9540	0.0469	0.0778	0.1515	0.1330	0.1070	0.0406	0.0333	0.0108	1.5549
D	0.4730	0.0234	0.0468	0.0790	0.0715	0.0553	0.0335	0.0312	0.0126	0.8263
C	0.2560	0.0089	0.0183	0.0335	0.0336	0.0298	0.0204	0.0292	0.0144	0.4441
B	0.0095	0.0006	0.0016	0.0058	0.0088	0.0113	0.0096	0.0168	0.0159	0.0799
A	0.0000	0.0000	0.0000	0.0000	0.0000	0.0000	0.0000	0.0000	0.0000	0.0000

TABLE 6
Product of Loads and Deflections

Panel	Defl. at Point (in.)	Load W at Point (lb)	2	W	W^2
K	12.3286	13632	151.300	167,000	2,060,000
J	10.9795	699	121.000	7,680	84,600
H	9.5851	1462	91.870	14,000	134,300
G	5.9386	2890	35.280	17,100	102,000
F	3.3470	3232	11.220	10,900	36,200
E	1.5549	3132	2.400	4,850	7,500
D	0.8263	2302	0.682	1,900	1,570
C	0.4441	3509	0.197	1,560	690
B	0.0799	2989	0.006	240	19
A	0.0000	0	0.000	0	0
			=	225,230	2,426,879

With this value of K the frequency is

$$f_n = \frac{1}{2\pi} \left(\frac{kg}{w}\right)^{1/2} .$$

$$f_n = \frac{1}{2\pi} \left(\frac{3800 \times 380}{33,845}\right)^{1/2} = 1.04 \text{ cps.}$$

This value of 1.04 agrees very well with the value of 0.955 obtained from a procedure which required about 80 hours. The agreement, unfortunately, cannot be used as a basis for being adopted as a standard procedure because one specific case can be thought of as an accidental happening.

SHOCK MOUNTING ASSEMBLY FOR EQUIPMENT CRIB

Criteria and Response Spectrum

The shock mounting assembly and the equipment supporting crib (shown in Fig. 2, which illustrates the underground silo) consists of two sets of helical springs installed between the crib and the silo. The proportioning of these two sets of springs as well as the determination of the maximum "rattlespace" are consistent with the attenuations of ground shocks to the desired survival level of the equipment, as specified in the criteria; which required that the study be carried on for 30-g and 3-g accelerations. As additional requirements,

Fig. 2 - Shock mounting assembly for equipment crib--
section and diagram of vertical ground acceleration

a discussi. about the selection of the types of
spring and the estimating of the magnitude of
the shock attenuation by the concrete silo were
stated in the criteria.

As a preliminary step, a reasonable esti-
mate was made of the maximum values of dis-
placements, velocity, and acceleration due to a
specified air-induced shock. A curve of the
acceleration ordinates was then plotted from
the abscissa, which was drawn parallel to the
wall of the silo. The ordinate showing an

approximate value of 300 g and passing through
the center of gravity of the acceleration curve
was taken as the value to be used for establish-
ing the response spectrum acceleration. The
velocity of 400 ips and the deflection of 16 inches
were similarly evaluated for the same condi-
tions; see Fig. 3.

As explained elsewhere, the values of the
deflections, velocity, and acceleration for a
simple oscillator are functions of the frequency;
it was therefore convenient to plot a combined

Fig. 3 - Combined shock spectrum envelope for earth motion

shock spectrum from a determined set of values consistent with the conditions stated in the criteria. The envelope for the maximum values mentioned previously was subsequently superimposed on the diagram of the combined shock spectrum.

Isolation System

The design criterion for the equipment shock-mounting assembly is merely a reflection of the idea that the plane of the air-induced ground shock front is neither parallel nor perpendicular to the ground surface. The true inclination of the plane with the ground surface is unknown; however, the approximate magnitude of the two vectors for the horizontal and the vertical motion will furnish the necessary and sufficient conditions for the design of the shock-mounting assembly.

The equipment supporting crib is a six-degree-of-freedom isolated mass, and therefore has six modes of vibration, each mode having its own natural frequency. If the center of the isolators is made to coincide with the center of gravity of the isolated mass, the six modes of vibration are the six reference coordinates of the system, namely the three

orthogonal translational modes and the three orthogonal rotational modes. The frequencies corresponding to these modes are obtained by standard one-degree-of-freedom methods. On the other hand, if the center of gravity of the isolators cannot be made to coincide with the center of the crib assembly mass, pure translations and pure rotations will not occur; only combination modes of all six coordinates will result from the eccentricity, and the response of non-linear systems to harmonic input will be that of a different frequency and a non-harmonic correspondence. Since the principle of superposition would not apply to the resulting motion, it would be necessary to solve a system of non-linear differential equation; and it is necessary to state that very few non-linear differential equations have been solved to date.

The exceedingly complex nature of the equipment crib shock motions, resulting from an acceleration applied to the supporting concrete structure, indicates that the effectiveness of the shock isolator to be interposed between the crib and the concrete foundation slab and walls will depend primarily on the perfect functioning of the isolator body.

The ratio of the total horizontal stiffness to the total vertical stiffness, which is the primary

293

and most important variable for the proper control of the shock, is one of the main factors on which the selection of the types of spring hinges.

Numerical Procedure

From the brief theoretical principles outlined previously, the fundamental frequency of the system is

$$f_{yz} = \frac{\ddot{z}_o}{2\pi V_s}.$$

In terms of g, the same formula becomes

$$f_{yz} = \frac{387\,z}{2\pi V_s} = 61.6 \left(\frac{\ddot{z}}{V_s}\right).$$

Also, the deflection is given by

$$d_{yz} = y - z,$$

or for maximum condition

$$(d_{yz})_o = \frac{V_s}{2\pi f_{yz}}.$$

From this point on, formulas are applied for the following conditions:

Condition 1 (Vertical Component of Motion):

$$\left.\begin{array}{ll}
\text{Acceleration} & = 30 \text{ g} \\
\text{Velocity} & = 400 \text{ ips} \\
\text{Deflection} & = 16 \text{ in.} \\
\text{Frequency} & = 46.2 \text{ cps}
\end{array}\right\} \text{Max. Spectrum Envelope}$$

The equipment and crib values are obtained as follows:

$$f_{yz} = \frac{61.6 \times 30}{400} = 4.62 \text{ cps},$$

$$d_{yz} = \frac{400}{2\pi \times 4.62} = 13.8 \text{ in.}$$

The required spring constant, K_z is obtained from

$$f_{yz} = \frac{1}{2\pi}\left(\frac{K_z}{m_z}\right)^{1/2},$$

or

$$K_z = m_z(2\pi f_{yz})^2 = \frac{W}{g}(2\pi f_{yz})^2,$$

in which W is the weight of the equipment and crib. The numerical value is

$$K_z = \frac{45,000}{387}(29)^2 = 97,800 \text{ lb/in.}$$

This condition is satisfied by a set of 52 helical springs 2-1/2 in. x 12 in., each having 16 coils and a stiffness of 1870 lb/in. The total expanded height and the statical deflection due to gravity are 54 in. and 0.464 in., respectively. The maximum shear stress in the wire for this condition is 70,000 psi.

Condition 2 (Horizontal Component of Motion):

$$A = 30 \text{ g}, \quad V_s = 250 \text{ ips},$$

for the crib

$$f_{yz} = 7.4 \text{ cps}$$

$$d_{yz} = 5.36 \text{ in.}$$

This condition is satisfied by a set of 25 helical springs 2-1/2 in. x 12 in. each having 8 coils and a stiffness of 5000 lb/in. The total height and the statical deflection is 24 in. and 0.364 in., respectively.

Condition 3 (Vertical Component of Motion):

$$\left.\begin{array}{ll}
\text{Acceleration} = 3 \text{ g} \\
\text{Deflection} \quad = 16 \text{ in.}
\end{array}\right\} \begin{array}{l} \text{Maximum spec-} \\ \text{trum envelope} \end{array}$$

The equipment and crib values are

$$f_{yz} = 1.36 \text{ cps}$$

$$d_{yz} = 16$$

$$K_z = 8600 \text{ lb/in.}$$

A set of helical springs 2-1/4 x 12 each having 19 coils, a stiffness of 1160 lb/in., and a height of 60 in.

Condition 4 (Horizontal Component of Motion):

$$\begin{array}{ll}
\text{Acceleration} & = 3 \text{ g} \\
\text{Deflection } 16/3 & = 5.33 \text{ in.} \\
K_z & = 25,300 \text{ lb/in.}
\end{array}$$

A set of 10 helical springs 2 in. x 12 in. each having 7 coils, a stiffness of 2420 lb/in., and a height of 19.33 in.

Selection of Springs

Helical Springs. Helical springs are used in tension as well as in compression. Tension

294

springs are most useful when very low natural frequencies must be attenuated, and they are suitable for the special condition of overhead supports. They will usually demand more room than other types of mounts, and require considerable flexibility in the mind of the designer if they are to be successfully applied. In general they are more expensive than compression springs, although they are more stable in applications having large static deflections.

Compression springs are more efficient than tension springs whenever it is necessary to control stiffnesses in various directions, as in the case of the crib, for which all the natural frequencies of the several modes are important. An excessive load can be superimposed on a compressive spring without damaging it because they can be designed in such a manner that the coils close before the safe stress is exceeded.

The supporting equipment crib, as explained previously, will be subjected to vertical as well as to lateral motion; in addition, owing to the arrangement of the equipment throughout its height, the crib will have its center of gravity high above its lowest floor. It appears therefore that a combination of tensile and compression springs will furnish the most satisfactory solution. Even with a combination of tensile and compressive springs, however, instability might result during the instant in which a horizontal deflection is produced. At such time the vertical stiffness of the spring would decrease, owing to the eccentricity of the load, and as a consequence the potential energy of the system would also decrease, since the equipment would be lowered. From the energy relation, the condition that the ratio of the horizontal to the vertical stiffness must be equal or greater than the ratio of the static deflection to the working height of the spring will have to be maintained. With the tensile-compression mount only 50 percent of the horizontal springs will be in tension each time.

The environmental conditions will require springs with large deflections; they will therefore have a tendency to oscillate whenever any equipment within the crib is operated dynamically. To reduce to a minimum such apparent condition of spring instability, it will be appropriate to provide some dampers which will become effective only after the taking place of some small initial horizontal movement of the crib. The selection of the optimum spring set will be quite a problem because the initial conditions can be satisfied by many springs; however, the controlling parameters, such as the

modulus in torsion, the wire diameter, the mean coil diameter at free height, and the number of active coils, will be more than a guide for the task; especially if the wiring index given by the ratio of the mean coil diameter to the wire diameter is properly chosen so as to yield a minimum weight of steel.

The effectiveness of helical springs as shock isolators can be proved by the surge-wave theory which also predicts how fast the spring can expand or contract, and estimates its "velocity barrier"; i.e., the velocity that the spring cannot exceed. Normally, the force applied to the front coil of the spring is not transmitted through the coils instantaneously, but in the form of a shock wave along the axis of the spring wire, almost similarly to the sound wave; and this shock wave requires a specific time to travel from one end of the spring to another. Another advantage of the helical springs results from their being easily used either singly or in sets enclosed partially in steel boxes, i.e., up to their solid length.

Ring Springs. Ring springs are also good shock absorbers with low space requirements in proportion to their capacity, because of high frictional forces, i.e., they absorb shocks with low recoil. Axial loading of the spring causes the inner and the outer rings to act on inclined planes. This forces an expansion of the outer rings and a contraction of the inner rings as the axial length is reduced. Ring springs are used only in compression; they are therefore limited to applications for which heavy load conditions and vertical motion are likely satisfied by a compact system. The springs can continue to function even though several rings are broken, and this would be more than enough for justifying their use in this case; however, with the implication of combining them with helical springs to absorb the horizontal forces. Their total height would be somewhat smaller than the normal height usually required for coiled springs; it is almost five times the allowable deflection.

Liquid Springs. Liquid springs have been used successfully in many fields; however, only recently, perhaps in the last few years, have they been recognized as members of the family of springs. For heavy loads and limited operational space they have no equal. Unfortunately they allow only axial motion which precludes their use where lateral motion is to be attained. Perhaps they might be furnished with special rotational bases capable of permitting motion in the desired simultaneous directions but their cost would probably increase so much to make them impractical.

A few different types of liquid springs have been designed to date; only four types will be described here.

The compression type of any liquid spring operated from compressibility of the contained fluid. The piston rod entering the fluid chamber (not the piston itself) builds up the fluid pressure. The restoring force for the direct compression type equals the fluid pressure times the cross-section area of the piston rod. Orifices or check valves in pistons can speed or restrict motion to any desirable degree in either direction.

The tension type builds fluid pressure when rod moves upward because large-diameter, lower half of rod displaces more fluid than upper half. Restoring force in downward direction, equals fluid pressure times difference in cross-section area of rod.

The long stroke type has hollow shaft to increase rigidity. Restoring force equals fluid pressure times cross-section area of hollow-shaft wall. Strokes up to 5 feet are permissible with this type.

The compound spring has dual spring rate. Zero load finds primary rod in upward position; secondary rod resting on bottom of secondary chamber. As load is applied, primary rod moves downward, compressing fluid in primary chamber, while secondary rod moves small distance into its chamber because of differential pressure against lower end. It will not float in balance until pressures are about equal in both chambers. When load is increased to change-over point, secondary rod will finally be touching bottom of outer cylinder; still more load mechanically forces this rod into its chamber.

The spring action from liquids varies: some liquid will compress to less than 90 percent of the original volume with applications of 20,000-psi pressure. The action is elastic because the energy is absorbed, stored, and fully released when the force is applied. A single liquid spring can provide as much "springiness" as 30 coil springs of the same length and diameter. Some have been designed to reciprocate at 1000 cycles per minute. By restricting fluid flow with orifices in the piston, there is a controlled slow-down effect useful for shock absorption, damping, and timing. Like all other springs, liquid springs also have some drawbacks such as buckling, unseating, clearance, and high costs.

Sealing must be absolutely tight, or fluid will be lost, thus changing the characteristics of the spring. P. W. Bridgeman, of Harvard, in his research on high pressures has developed an unsupported-area seal and thus this problem may be considered solved.

The common fluids used are: Dow-Corning types F-4029 and 200 (silicone based with viscosity of 100 centistokes at 77 F). Other fluids are not very efficient for their low compressibility.

Minimizing Rattlespace. Consistent with the maximum accelerations which can be tolerated by the equipment, and which have been specified prior to the starting of this estimate criteria, the minimizing of the "rattlespace" was accomplished by trial and error selection of specific isolators. Accordingly, the following approximate values may be assumed: for the environment conditions of the concrete lining assume an acceleration of 300 g, a velocity of 400 fps, and a displacement of about 16 inches; and an isolator system consisting of a series of well balanced helical springs and with a frequency of about 4.62 cps will limit the vertical acceleration of the crib and the supported equipment to 30 g, and the vertical "rattlespace" to about 13.8 inches. The total clear height between the upper surface of the bottom concrete slab and the lower surface of the bottom of the crib would be approximately 4 feet 6 inches. This dimension might be reduced by putting the springs in a pocket in the concrete deep enough to accommodate the solid height of the springs.

For the same acceleration, the frequency in the horizontal amounting to 7.4 cps requires a rattlespace of 5.4 inches and a total clearance of 2 feet 0 inch between the face of the concrete wall and the face of the crib.

For an acceleration of 3 g, the crib frequency of about 1.36 cps in the vertical direction requires a rattlespace of 16 inches and a total clearance of 5 feet 0 inch.

For an acceleration of 3 g, the crib frequency of about 2.35 cps in the horizontal direction requires a rattlespace of 5.33 inches and a total clearance of 2 feet 0 inch between the face of the concrete wall and the face of the crib.

NUCLEAR POWER PLANT STACK
(470 FEET HIGH)

General Statements

The hazy notion that tapered stacks are ideal shapes for preventing formation of eddies influenced the customer of the nuclear plant to

the extent of being satisfied with having the stack designed statically; i.e., by an equivalent static loading. The stack was therefore designed for an equivalent wind pressure loading varying from 34.8 lb/ft^2 at the top to 29.4 lb/ft^2 at the bottom (see Fig. 4).

The hazy notions changed subsequently into a more critical point of view; perhaps because many stack failures were being reported either openly in technical publications and other papers or unofficially by word of mouth. The customer then decided to have the stack investigated in accordance with the laws of dynamics.

Dynamic Analysis of Stack

Three different methods were used to compute the fundamental frequency of the stack: The static deflection method by tabular summation, the energy method by direct integration, and the Rayleigh's frequency equation by an iteration procedure suggested by Burgess [62].

1. The static-deflection method was also used in the computation of the frequency for the

lower, however, with a slight variation (i.e., the deflections were obtained from the Williot-Mohr diagram). For the stack it was easier to obtain them analytically by tabular summation.

As shown in Tables 7 to 13 inclusive, 12 slightly unequal spanwise intervals Δx were chosen for performing the integration by tabular summation. The tables are self-explanatory; Tables 7 and 8 show the physical characteristics of the stack, such as dimensions, areas of cross sections, moments of inertia, and weights for each point; Tables 9 to 13 show the computations for the deflections at points; and Table 13 shows the products of the weights by the deflections. Table 14 shows the computations for the shell.

From Table 13 the frequency was computed by using the simple available formula, thus

$$f_n = \frac{1}{2\pi} \left[\frac{g(W_1 Y_1 + W_2 Y_2 + \cdots)}{W_1 Y_1^2 + W_2 Y_2^2 + \cdots} \right]^{1/2},$$

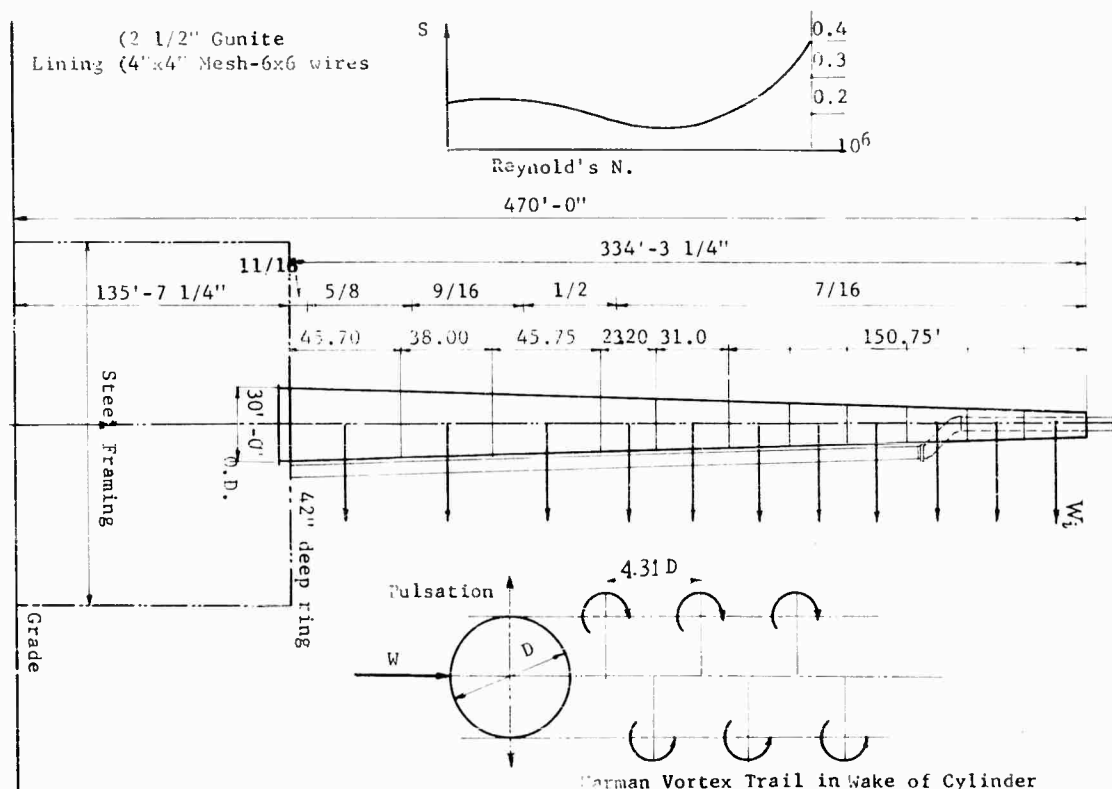$$f = \frac{1}{2\pi} \left(\frac{1064.5}{2022.8} \times \frac{386}{12} \right)^{1/2} = 0.653 \text{ c.s.}$$

Fig. 4 - 470-foot-high nuclear power plant stack--diagram indicating Reynolds-Strouhal number variation, and diagram of Karman Vortex Trail

297

TABLE 7
Stack Weights

Point	x from Free End (ft)	D_{ox} (ft)	Circ. (ft)	Surface (sq ft)	t Actual Thickness (in.)	w_1 Shell (lb/ft²)	$W_s \times 10^{-3}$ Shell (lb)	$W_L \times 10^{-3}$ Lining (lb)	W_1 Ladder (lb)
1	25.75	11.54	36.25	871.3	0.4375	17.9	15.60	32.67	0.77
2	50.75	13.03	40.97	965.3	0.4375	17.9	17.28	36.20	0.75
3	75.75	14.53	45.64	1083.6	0.4375	17.9	19.38	40.60	0.75
4	100.75	16.02	50.34	1199.8	0.4375	17.9	21.48	44.99	0.75
5	125.75	17.52	55.04	1317.2	0.4375	17.9	23.58	49.40	0.75
6	150.75	19.01	59.73	1434.6	0.4375	17.9	25.68	53.80	0.75
7	181.75	20.87	65.56	1942.0	0.5000	20.4	39.62	72.82	0.93
8	204.95	22.25	69.91	1571.4	0.5625	23.0	36.14	58.93	0.69
9	227.83	23.62	74.21	1648.4	0.6250	25.5	42.04	61.82	0.68
10	250.70	24.99	78.51	1746.7	0.6250	25.5	44.54	65.50	0.68
11	288.70	27.26	85.64	3118.8	0.6875	28.1	87.64	116.96	1.14
12	334.40	30.00	94.25	4110.5	0.7500	30.6	125.78	154.14	1.37
							498.76	787.10	10.01
								1296.00	

TABLE 8
Moment of Inertia at Points (Stack)

Point	D_{ox} (ft)	$(D_{ox})^3$ (ft³)	From Point to Point	From Free End to Point	t (in.)	$\frac{\pi}{8} t$ (in.)	$I = \dfrac{(D_{ox})^3 t}{8}$ (ft⁴)
0	10.00	1000.0	0.000	0.000	0.3750	0.1473	12.25
1	10.77	1249.2	12.875	12.875	0.3750	0.1473	15.33
2	12.29	1856.3	25.375	38.250	0.3750	0.1473	22.78
3	13.78	2116.7	25.000	63.250	0.3750	0.1573	32.12
4	15.28	3567.6	25.000	88.250	0.3750	0.1573	43.79
5	16.27	4716.3	25.000	113.25	0.3750	0.1573	57.89
6	18.27	6098.4	25.000	138.25	0.3750	0.1573	74.85
7	19.94	7928.2	28.000	166.25	0.4375	0.1718	113.51
8	21.56	10,021.8	27.100	193.35	0.5000	0.1964	164.02
9	22.94	12,072.0	23.040	216.39	0.5625	0.2209	222.23
10	24.31	14,366.6	22.880	239.27	0.5625	0.2209	264.47
11	26.13	17,840.9	30.440	269.71	0.6250	0.2454	364.85
12	28.63	23,467.4	41.850	311.56	0.6875	0.2700	528.02

The weight of the 2-1/2 inch gunite lining was included in the computations; this frequency is for the lined stack.

Table 15 shows the computations for the unlined stack. The frequency is

$$f_n = \frac{1}{2\pi} \left(\frac{386 \times 1379.6}{9789.5} \right)^{1/2} = 1.08 \text{ cps.}$$

2. The energy method by direct integration is normally applied to beams with uniform cross section, occasionally to beams with cross sections varying with the span, very rarely to hollow-tapered members with constant shell thickness. The stack shell thickness is neither constant nor uniformly variable, it could, however, be expressed as a function of the span length without altering appreciably the magnitude of the frequency because it is a very small entity as compared to the diameter of the stack (which varies from 10 to 30 feet). Since results are not affected more than a negligible entity by

298

TABLE 9
Statical Deflection at Point 12

Point	W_{Total} x 10^{-3} (lb)	Moment x 10^{-3} (ft-lb)	Δx (ft)	$\frac{\Delta x}{I}$	$\frac{M\Delta x}{EI}$ x 10^{-4}	m (ft-lb)	$\frac{Mm\,\Delta x}{EI}$ x 10^{-4}
1	49.04	0	25.75	2.0978	0	12.88	0
2	54.23	1244	25.00	1.6304	4.6965	38.25	179.6
3	60.73	3826	25.00	1.0973	9.719	63.25	614.7
4	67.22	7927	25.00	0.7784	14.283	88.25	1260.5
5	73.73	13,707	25.00	0.5709	18.114	113.25	2051.5
6	80.23	21,331	25.00	0.4318	21.319	138.25	2947.4
7	113.37	32,116	31.00	0.2733	20.318	166.25	3377.9
8	95.76	45,627	23.20	0.1414	14.934	193.25	2889.5
9	104.54	59,320	22.88	0.1029	14.13	216.39	3057.5
10	110.72	75,309	22.88	0.0865	15.079	239.27	3608.0
11	205.74	99,993	38.00	0.1042	24.109	269.71	6502.4
12	281.29	142,444	45.70	0.0866	28.555	311.55	8896.2
					Delta = 3.5385 ft.		35,385.2

TABLE 10
Deflection at Points 1, 2, 3, and 4

Point	m_1 (ft-lb)	$\frac{Mm_1\Delta x}{EI}$ x 10^{-4}	m_2 (ft-lb)	$\frac{Mm_2\Delta x}{EI}$ x 10^{-4}	m_3 (ft-lb)	$\frac{Mm_3\Delta x}{EI}$ x 10^{-4}	m_4 (ft-lb)	$\frac{Mm_4\Delta x}{EI}$ x 10^{-4}
1	0	0	0	0	0	0	0	
2	25.38	119.2	0	0	0	0	0	
3	50.38	439.6	25	243	0	0	0	
4	75.38	1076.6	50	714.2	25	357.1	0	
5	100.38	1818.2	75	1358.6	50	905.7	25	452.9
6	125.38	2672.9	100	2131.9	75	1598.9	50	1066.0
7	153.38	3116.3	128	2600.7	103.0	2092.8	78	1584.8
8	180.48	2695.3	155.10	2316.3	130.0	1941.5	105.1	1569.6
9	203.51	2869.0	178.14	2517.0	153.1	2163.8	128.1	1810.6
10	226.39	3413.8	201.02	3031.3	176.0	2654.3	151.0	2277.3
11	256.83	6191.7	231.46	5580.2	206.5	4977.5	181.5	4374.8
12	298.68	8528.5	273.31	7804.3	248.3	7090.0	223.3	6376.5
		32,991.2		28,297.2		23,781.6		19,512.4
		Defl. 1 = 3.2991		Defl. 2 = 2.8297		Defl. 3 = 2.3781		Defl. 4 = 1.9512

the substitution of the actual thickness with an equivalent thickness, an average value of the thickness, t, was chosen for the derivation of the frequency formula.

Theoretically, all effects associated with the motion of cantilever types of configurations such as: flexural, shearing, shortening or lengthening, gravitational, should be included in the frequency formula [16,17,63]. Practically, except for a few special configurations with high slenderness ratios and supporting heavy concentrating masses, others with very low slenderness ratios for which the shear effect pre-dominates, and others for which more information is needed, it will suffice to include flexural effects .

The frequency formula is given as

$$p^2 = \frac{gE \int_0^l I(x)\,(d^2y/dx^2)\,dx}{\int_0^L A(x)\,y^2 dx}, \qquad (25)$$

TABLE 11
Deflection at Points 5, 6, 7, and 8

Point	m_5 (ft-lb)	$\dfrac{Mm_5 \, \triangle x}{EI} \times 10^{-4}$	m_6 (ft-lb)	$\dfrac{Mm_6 \triangle x}{EI} \times 10^{-4}$	m_7 (ft-lb)	$\dfrac{Mm_7 \triangle x}{EI} \times 10^{-4}$	m_8 (ft-lb)	$\dfrac{Mm_8 \triangle x}{EI} \times 10^{-4}$
1	0	0	0	0	0	0	0	0
2	0	0	0	0	0	0	0	0
3	0	0	0	0	0	0	0	0
4	0	0	0	0	0	0	0	0
5	0	0	0	0	0	0	0	0
6	25	533	0	0	0	0	0	0
7	53	1076.9	28	568.9	0	0	0	0
8	80.1	1196.2	55.1	822.9	27.1	404.7	0	0
9	103.1	1457.3	78.1	1104.1	50.1	708.5	23.0	325.5
10	128.0	1900.31	101.2	1538.4	73.0	1101.1	45.9	692.5
11	156.4	3772.1	131.5	3169.3	103.5	2494.3	76.4	1841.0
12	198.3	5662.7	173.3	4948.8	145.3	4149.3	118.2	3375.4
		15,598.5		12,152.4		8857.8		6234.4
		Defl. 5 = 1.5598		Defl. 6 = 1.2152		Defl. 7 = 0.8858		Defl. 8 = 0.6234

TABLE 12
Deflection at Points 9, 10, 11, and 12

Point	m_9 (ft-lb)	$\dfrac{Mm_9 \triangle x}{EI} \times 10^{-4}$	m_{10} (ft-lb)	$\dfrac{Mm_{10} \triangle x}{EI} \times 10^{-4}$	m_{11} (ft-lb)	$\dfrac{Mm_{11} \triangle x}{EI} \times 10^{-4}$	m_{12} (ft-lb)	$\dfrac{Mm_{12} \triangle x}{EI} \times 10^{-4}$
1	0	0	0	0	0	0	0	0
2	0	0	0	0	0	0	0	0
3	0	0	0	0	0	0	0	0
4	0	0	0	0	0	0	0	0
5	0	0	0	0	0	0	0	0
6	0	0	0	0	0	0	0	0
7	0	0	0	0	0	0	0	0
8	0	0	0	0	0	0	0	0
9	0	0	0	0	0	0	0	0
10	22.9	345.0	0	0	0	0	0	0
11	53.3	1285.5	30.44	733.9	0	0	0	0
12	95.2	2717.5	72.29	2064.2	41.85	1195.0	0	0
		4348.0		2798.1		1195.0		θ
		Defl. 9 = 0.4348		Defl. 10 = 0.2798		Defl. 11 = 0.1195		Defl. 12 = 0

in which

$$I(x) = \frac{\pi t}{8} (a + bx)^3 \qquad (26)$$

is the moment of inertia for a cross section of the stack at x-units from its free end. Equation (26) was obtained from

$$I = \frac{\pi}{64} \left(D_0^4 - D_i^4 \right)$$

which for $D_0 - 2t$ becomes

$$I = \frac{\pi}{64} (8D_0^3 t - 24D_0^2 t^2 + 32D_0 t^3 - 16t^4) ,$$

or by neglecting powers of t higher than the first, it can be reduced to

$$I = \frac{\pi}{8} D_0^3 x t .$$

The outer diameter, D_{ox}, is accordingly

$$D_{ox} \cdot \left(10 + \frac{20x}{L} \right) = (a + bx) . \qquad (27)$$

The cross area

$$A(x) = D_{ox} t , \qquad A(x) = \pi t (a + bx) . \qquad (28)$$

300

TABLE 13
Values of Wy and Wy^2

Point	$W_{Total} \times 10^{-3}$ (lb)	Defl. (ft)	$Wy \times 10^{-3}$ (lb-ft)	$Wy^2 \times 10^{-3}$ (lb-ft)
1	49.04	3.2991	161.79	533.75
2	54.23	2.8297	153.46	434.23
3	60.73	2.3781	144.42	343.45
4	67.22	1.9512	131.16	255.92
5	73.73	1.5598	115.00	179.38
6	80.23	1.2152	97.5	118.48
7	113.37	0.8858	100.42	88.95
8	95.76	0.6234	59.7	37.22
9	104.54	0.4348	45.45	19.76
10	110.72	0.2798	30.98	8.67
11	205.74	0.1195	24.59	2.94
12	281.29	0.0000	0	0
			1064.46	2022.75

TABLE 14
Values of Wy and Wy^2 for Shell

Point	$W \times 10^{-3}$ (lb)	Shear $\times 10^{-3}$ (lb)	Moment $\times 10^{-3}$ (ft-lb)	Ratio $\dfrac{M_{shell}}{M_{total}}$	$\dfrac{Mm \Delta x}{EI} \times 10$	Defl. (ft)	Wy (lb-ft)	Wy^2 (lb-ft)
1	15.60	15.60	0	0	0	1.0687	200.07	2565.9
2	17.28	32.88	396	0.3181	57	0.9183	190.41	2098.1
3	19.38	52.26	1218	0.3183	196	0.7733	179.85	1668.9
4	21.48	73.74	2524	0.3185	401	0.6369	164.00	1255.0
5	23.58	97.32	4368	0.3187	654	0.5102	144.36	883.8
6	25.68	123.0	6801	0.3188	940	0.3285	101.23	399.0
7	39.62	162.62	10,245	0.3190	1078	0.2927	139.15	488.7
8	36.14	198.76	14,652	0.3211	928	0.2074	89.95	223.9
9	42.04	240.08	19,231	0.3242	991	0.1459	73.61	128.9
10	44.54	285.34	24,724	0.3283	1185	0.0949	50.73	57.8
11	87.64	372.98	33,410	0.3343	2173	0.0411	43.21	21.3
12	125.78	498.76	49,019	0.3441	3061	0.0000	0	0
				3.5633	11.664		1379.6	9789.6

With these values of $A(x)$ and $I(x)$, the terms of the frequency will now be derived. The moment at any point C is given by

$$M_c = \int_0^{x_1} \rho A(x)(L - x_1 - x)\, dx , \qquad (29a)$$

$$M_c = \int_0^{L-x} \rho \pi t(a + bx)(L - x_1 - x)\, dx , \qquad (29b)$$

$$M_c = \rho \pi t \left[\frac{a}{2} (L - x)^2 + \frac{b}{6} (L - x_1)^3 \right] , \qquad (29c)$$

or

Also

$$M_x = \rho \pi t \left[\left(\frac{a}{2} x^2 \right) + \frac{b}{6} (L - x_1)^3 \right] . \qquad (29d)$$

$$EI(x) \frac{d^2 y}{dx^2} = -M_x . \qquad (30)$$

From Eqs. (30) and (26)

$$\frac{d^2 y}{dx^2} = - \frac{M_x}{EI(x)} , \qquad (31a)$$

or

$$\frac{d^2 y}{dx^2} = \frac{4\rho}{3E} \left[\frac{3ax^2}{(a + bx)^3} + \frac{bx^3}{(a + bx)^3} \right] . \qquad (31b)$$

The integration of Eq. (31b) yields

$$\frac{dy}{dx} = \frac{4\rho}{3E} \left[(a+bx) + \frac{3a^2}{a+bx} - \frac{a^3}{(a+bx)^2} \right] + C_1 . \quad (32)$$

which, for the boundary condition $x = L$, and $dy/dx = 0$ requires C_1 to be

$$C_1 = -\frac{\rho L^3}{Ea^2} \left(\frac{35}{54} \right) . \quad (33)$$

Again, integration of Eq. (32) yields

$$y = \frac{\rho L^4}{12Ea^4} \left[\frac{(a+bx)^2}{4a^2} + \frac{a}{2(a+bx)} + \frac{3}{2} \ln (a+bx) \right]$$

$$+ C_1 x + C_2 . \quad (34)$$

The value of C_2 for $x = L$, $y = 0$ is

$$C_2 = \frac{\rho L^4}{4a^2 E} \left(\frac{53}{54} - \ln 3a \right) . \quad (35)$$

By use of Eqs. (26) and (31b), the numerator of Eq. (25) can now be integrated

$$gE \int_0^L I(x) \left(\frac{d^2y}{dx^2} \right)^2 dx = \frac{2 \, tg \, \rho^2}{9E} \int_0^L (a+bx)^3$$

$$\times \left[\frac{3ax^2}{(a+bx)^3} + \frac{bx^3}{(a+bx)^3} \right] dx . \quad (36)$$

Equation (36), indicated by N, after integration becomes

$$N = \frac{g\pi\rho^2 \, tL^5}{9 \times 16 \, Ea} \left(-\frac{5}{9} + \frac{9}{4} \ln 3 \right) . \quad (37)$$

Similarly, by means of Eqs. (28) and (34), the denominator becomes

$$D = \rho \int_0^L A(x) \, y^2 \, dx ,$$

and

$$D = \frac{\pi\rho^3 \, tL^3}{9 \times 4E^2 a^4} \int_0^L (a+bx) \left[\frac{(a+bx)^2}{4a^2} + \frac{a}{2(a+bx)} \right.$$

$$\left. - \frac{3}{2} \ln (a+bx) - \frac{55x}{L} + \frac{53}{36} - \frac{3}{2} \ln 3a \right]^2 dx . \quad (38)$$

The integration of Eq. (38) yields

$$D = \frac{\pi\rho^3 tL^3}{9 \times 4a^3 E^2} \left[-\frac{305}{216} + \frac{575 \ln 3}{288} - \frac{9}{16} (\ln 3)^2 \right] . \quad (39)$$

Finally, by Eqs. (36) and (39), the circular frequency is given as

$$p^2 = \frac{N}{D} = \frac{gEa^2 \left(-\frac{20}{9} + 9 \ln 3 \right)}{4\rho L^4 \left(-\frac{305}{216} + \frac{575 \ln 3}{288} - \frac{9(\ln 3)^2}{16} \right)} , \quad (40a)$$

or

$$p^2 = \frac{gEa^2}{4 \rho L^4} \left(\frac{7.6653}{0.113} \right) ,$$

$$p^2 = 16.94 \frac{Ega^2}{\rho L^4} , \quad (40b)$$

from which

$$p = 4.2 \left(\frac{Ega^2}{L^4} \right)^{1/2} .$$

The natural frequency of the stack is

$$f_n = \frac{4.12}{2\pi} \left(\frac{Ega^2}{\rho L^4} \right)^{1/2} ,$$

where

$$E = 30 \times 10^6 \times 144 \; lb/ft^2 ,$$

$$g = 32.2 \; ft/sec^2 ,$$

$$a = 10 \; ft ,$$

and

$$f_n = \frac{4.12}{2\pi} \times \frac{33.35}{(\rho)^{1/2}} = \frac{21.874}{(\rho)^{1/2}} .$$

For an average value of $\rho = 1250$, the frequency of the lined stack is

$$f_n = \frac{21.874}{(1250)^{1/2}} = 0.62 \; cps .$$

For the unlined stack $\rho = 490 \; lb/ft^3$, therefore

$$f_n = \frac{21.874}{(490)^{1/2}} = 0.99 \; cps .$$

These frequency values are much in agreement with the values, 0.653 and 1.08, obtained by tabular summation. The frequency expression (40a) contains natural logarithm terms associated with tapered stacks having a ratio of 3:1, the general expression for any other ratio of the bottom to top diameter is given below

302

$$p^2 = \frac{gEa^2(r-1)^4}{8\rho' L^4}\left[\frac{A + 9\ln r}{B + C\ln r - \frac{9}{2} - (\ln r)^2}\right],$$

where

$$A = \frac{r^4}{4} - 3r^2 + 4r - \frac{45}{4} + \frac{12}{r} - \frac{2}{r^2},$$

$$B = \frac{r^4}{120} - \frac{59r^4}{240} + \frac{8r^3}{15} - \frac{13r^2}{8} + \frac{71r}{30} - \frac{135}{16}$$
$$+ \frac{78}{5r} - \frac{647}{60r^2} + \frac{17}{6r^3} - \frac{1}{4r^4},$$

$$C = \frac{3r^2}{2} - 2r + \frac{49}{4} - \frac{12}{r} + \frac{2}{r^2},$$

and

$$r = \frac{a+b}{a} = \frac{D_A}{D_B}; \qquad \frac{b}{a} = r - 1;$$

D_A and D_B, respectively, represent the large and the small diameter of the stack. For the application $b = 2a$, therefore the ratio of $3a$ to a is 3.

This general formula is simple; the intermediate steps (which were not shown in the preceding derivation, but which consisted of integrating and arranging all terms required) were, however, an exhausting effort.

3. The Rayleigh's frequency equation by an iteration procedure is a tabular summation of Eq. (25). It is similar to the preceding method except for a slight variation which will be evident from the following outline:

A curve is assumed $= y$.

The inertia load is taken proportional to wy.

The shear and the moment are, respectively, $S = \int wy\,dx$ and $M = \int S\,dx$; the summation is performed from the free end of the stack.

The curvature is expressed by $d^2y/dx^2 = M/EI$.

The slope $dy/dx = \int (d^2y/dx^2)\,dx$ is obtained by summing the curvature from the fixed end of the stack where the slope is zero.

The new deflection curve, $y = \int (dy/dx)\,dx$, is obtained by summing the slope from the same end.

The entire procedure is repeated until the results converge to the correct curve; about

two or three repetitions are required for a good approximation.

The terms in the numerator and in the denominator of Eq. (25) are then summed up to evaluate the frequency.

The term ω^2/g is normally omitted in the summation procedure. Equal values of delta x are preferable whenever conditions allow. For this application the small spans were proportioned in accordance with the shell thickness variation. Column 12 in Table 15 contains values of the new deflection curve after one trial. Being very much in agreement with the values of column 3, they were used for the final summation. Column 12 was obtained by normalizing column 11; all terms in column 11 were divided through by the value of 333.24 which is the ratio of the number 1099.4 and the deflection of the same point given in row 1 at column 3. The units used throughout are feet, pounds, and seconds.

The frequency is determined from the values of the summations of columns 15 and 17,

$$f_n = \frac{1}{2\pi}\left(\frac{32.2 \times 3 \times 10^7 \times 144 \times 3335 \times 10^{14}}{23,960 \times 10^{23}}\right),$$

$$f_n = 0.700 \text{ cps}.$$

By repeating the procedure one or more times it is possible to get a value closer to the ones by the other methods.

Forced Frequency; Self-Excitation

As explained in the "Aeroelastic Vibration Principles" section, the frequency of the vortices is given by

$$f = \frac{vS}{D} = 0.20\frac{v}{D}.$$

with the regularity of the impulses depending on the condition of stability of the vortex trail configuration. For high Reynolds numbers (which is the case for stacks) the stack becomes a self-excited system; its natural frequency is therefore the controlling frequency of the eddies. The greatest part of the energy input is contributed by the uppermost 25-percent section of the stack, as it appears from publications; by using the average diameter (10.3 feet) for that section in the formula for the eddy frequency, the wind velocity for the unlined stack is

$$v = f_n D/S = 1.08 \times 10.3/0.20,$$
$$= 55.5 \text{ fps or } 37.9 \text{ mph}.$$

TABLE 15

Rayleigh's Frequency Formula by Iteration Procedure

1	2	3	4	5	6	7	8	9	10	11	12	13	14	15	16	17
Point	$W \times 10^{-3}$	y	$Wy \times 10^{-3}$ (2×3)	$S \times 10^{-3}$ 4	$S/I \times 10^{-3}$ x	$(M)/I$ 10^{-3} 6	$\frac{(Mdx)}{I}$ 10^{-3}	8	$(\frac{dy}{dx})\,dx$ 10^{-8}	$\frac{y}{10^{-8}}$ 10	y_n	$(7)^2 (10)^{-10}$	$(13)I(10)^{-3}$	$(N)10^{-14}$	$(11)^2 (10)^{-20}$	$(D)10^{-23}$
1	49.0	3.2991	161.79	161.8	135.87	135.9	3.49	565.98	145.74	1099.4	3.2992	1.85	0.03	0.1	120.87	5927.4
2	54.2	2.8297	153.46	315.3	351.16	487.0	12.18	553.81	138.45	953.7	2.8617	23.72	0.54	1.4	90.95	4932.1
3	60.7	2.3781	144.42	459.7	357.76	844.8	21.12	532.69	133.17	815.21	2.4463	71.37	2.29	5.7	66.46	4035.9
4	67.2	1.9512	131.16	590.8	337.30	1182.1	29.55	503.13	125.78	682.0	2.0467	139.73	6.12	15.3	46.52	3126.9
5	73.7	1.5598	115.00	705.8	304.81	1486.9	37.17	465.96	116.49	556.3	1.6692	210.87	12.21	30.5	30.94	2281.3
6	80.2	1.2152	97.50	803.3	268.28	1755.2	43.87	422.08	105.52	439.8	1.3196	308.06	23.06	57.7	19.34	1551.6
7	113.4	0.8858	100.42	903.8	222.96	1978.1	61.32	360.76	111.34	334.2	1.0000	391.30	44.41	137.7	11.17	1266.5
8	95.8	0.6234	59.70	963.5	159.16	2137.3	49.59	311.17	72.19	222.4	0.6674	456.81	74.92	173.7	4.95	473.6
9	104.5	0.4348	45.45	1008.9	104.61	2241.9	51.28	259.89	59.45	150.2	0.4566	502.62	111.68	255.5	2.26	235.9
10	110.7	0.2798	30.98	1039.9	89.95	2331.9	53.34	206.55	47.25	90.8	0.2724	543.76	143.82	329.0	0.82	91.2
11	205.7	0.1195	24.59	1064.5	89.80	2421.7	92.03	114.53	43.52	43.5	0.1306	586.44	213.99	813.2	0.19	39.0
12	281.3	0.0000	0.00	1064.5	84.37	2506.0	114.52	0.00	0.00	0.0	0.0000	628.02	331.59	1515.4	0.00	0.0
														3335.2		23,961.4

The lateral pressure for this wind velocity, as it appears from the formula

$$P_L = D_L (0.00116) v^2 .$$

is a function of the constant D_L, which is very uncertain numerically; it can, therefore, be 42.8 lb/ft^2 or 23.6 lb/ft^2, depending on whether D_L is equal to 1.2 or 0.66. How much magnification of this value of P_L was to be expected from the self-excited system—5 times, 10 times, or ---? This was the question brought forward before and after the stack was erected and until it was lined with cement gunite. The fact that the stack did not vibrate noticeably during that period does not justify the thinking that the method of analysis used is incorrect: it cannot, however, be affirmed that a wind velocity of about 38 mph did not occur in the stack site for lack of information.

The wind velocity for the lined stack is similarly

$$v = 0.653 \times 10.3/0.20 = 33.7 \text{ mph} .$$

The determination of the magnification factor for this condition concludes the theoretical investigation of the stack vibration problem.

VIBRATING MOUNTING ASSEMBLY FOR A COMPRESSOR FOUNDATION

A silty-sandy clay substrata with a frequency of about 10 cps was not considered to be a satisfactory support for the unbalanced semi-radial, 200 hp, at 120 psi, 600 rpm compressor; a decision was therefore made to use a concrete base mounted on a spring isolation system capable of reducing transmissibility to an acceptable figure.

Although many compressors with more than 300 rpm have been and still are being installed directly upon beams supported on springs and upon thin reinforced concrete slabs, there always exist the danger that unwanted vibrations may arise through time; especially with reciprocating types like the one being discussed here. It is true that no first harmonics of exciting loads are present in well-balanced compressors with rpm higher than 300; it is also true that no reciprocating compressor can be completely balanced.

On the other hand, massive foundation blocks are a cause of great strains to the machine frame, inasmuch as they absorb most of the engine energy; further, they are not always vibration absorbers, as it was found out by the author [64] in 1944, when he was asked to investigate the design foundation of a heavy reciprocatory compressor which was being kept unoperative because of vibration troubles. In that particular case and others, blocks with mass ratios of 1 to 9 to those of the engines were not sufficient to absorb the transmitted vibrations because of their high center of gravity above their bases.

Prior to the time when the design of the isolation springs was made, the compressor manufacture claimed that the compressor was balanced so that only very small negligible "primary" and "secondary" inertia forces were normally produced during operation. Subsequently, yielding a little to the author's insistence, the manufacturer stated that the only unbalanced forces were a vertical component having a magnitude of 1280 pounds and a 1150-pound horizontal component; both acting at the center line of the crank pin. From the meager information received, which included the statement that the weight of the engine and motor was to be assumed as being equal to 19,000 pounds, it was possible to determine the center of gravity of the system. As shown in the associated illustrative sketch, the center is located 0.68 feet from the top of the concrete block. The same sketch shows the concrete block dimensions to be 9 feet x 7 feet x 2 feet 4 inches from which, and with a small addition for piers, the weight was computed to be equal to 23,200 pounds (see Figs. 5 and 6).

Simplified Procedure for Determining Frequencies

To maintain a consistent relationship between data and mathematical treatment it was decided to simplify the procedure for determining frequencies. This simplified procedure is also justified because the system is symmetrical to the principal plane of inertia and also because results would otherwise differ slightly in this case. Theoretically a system such as this, embodying six degrees of freedom, would require the solution of a sixth order determinant. With better data and heavier, or different types of compressors, it might even be worthy to solve the complexities arising with the use of the more exact theoretical method.

Vertical Motion

Eight sets, each with two 9/16-inch x 2-1/4-inch springs furnish a total k_v stiffness of 43,200 pounds per inch; the natural frequency, therefore, is

CENTER LINE OF COMPRESSOR
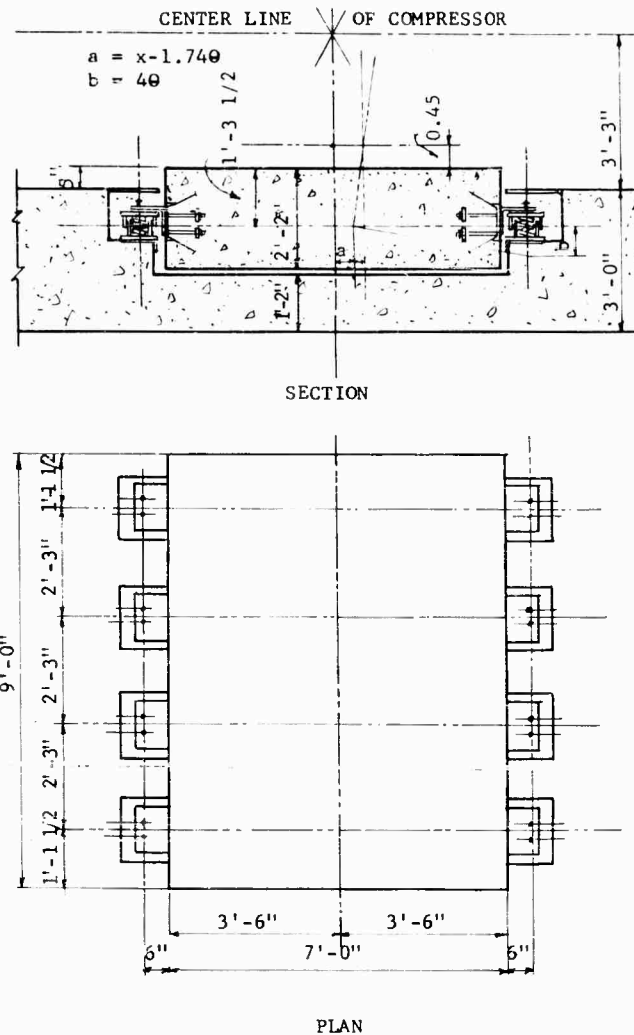
$a = x - 1.74\theta$
$b = 4\theta$

SECTION

PLAN

Fig. 5 - Vibration mounting assembly
for compressor foundation

$$f_n = 3.133 \left(\frac{k}{w}\right)^{1/2} = 3.133 \left(\frac{43,200}{42,300}\right)^2 = 3.16 \text{ cps.}$$

With the forced frequency being $600/60 = 10$ cps, the ration is

$$(f/f_n)^2 = (10/3.16)^2 = 10 .$$

The maximum transmitted force amounts to

$$F_T^2 = \frac{1280}{1 - 10} = -142 \text{ lb .}$$

The maximum amplitude is

$$a_v = \frac{F_T^v}{k_v} = \frac{142}{43,200} = 0.00329 \text{ in.}$$

The system is very satisfactory for the vertical motion. Each of the seven coil springs, with a free height of 4-15/16 inches and a maximum solid height of 3-15/16 inches, will allow a deflection of 1 inch under 2700-pound load.

Rocking Mode

The harmonic horizontal force F_x is not applied at the center of the vibrating system nor is the spring set located at the same center; as a consequence the action of the horizontal force causes the block to translate along the x-axis and to rotate about a center located at a certain distance R below the center of the mass. The translation and rotational motions are therefore coupled.

306

Fig. 6 - Compressor mounting assembly (double spring isolator)

The general expressions for the coupled frequencies are obtained directly from the system characteristics as follows:

$$-m\omega^2 x = k_x(x - 1.74\theta) = F_x,$$

$$-mr^2\omega^2\theta - k_x(x - 1.74\theta)1.74 + k_y 16\theta = 1.38 F_x.$$

By dividing the first equation by k_y and the second one by $k_y r^2$, and noting that $k_y/m = y^2$, one obtains

$$\begin{vmatrix} \left(\dfrac{k_x}{k_y} - \dfrac{\omega^2}{\omega_y{}^2}\right) - 1.74\dfrac{k_x}{k_y} \\[4mm] \left(\dfrac{k_x}{k_y} \times \dfrac{1.74}{r^2}\right) + \left(\dfrac{1.74^2}{r^2} \times \dfrac{k_x}{k_y}\right) + \dfrac{16}{r^2} - \dfrac{\omega^2}{\omega_y{}^2} \end{vmatrix} = 0.$$

The values of the frequencies are determined from the expansion of the determinant or

$$\frac{\omega}{\omega_y} =$$

$$\left\{ \frac{\dfrac{k_x}{k_y}\left(1 + \dfrac{1.74}{r^2}\right)^2 + \dfrac{16}{r^2}}{2} \pm \left\{\left[\dfrac{\dfrac{k_x}{k_y}\left(1 - \dfrac{1.74}{r^2}\right)^2 + \dfrac{16}{r^2}}{2}\right]^2 - \dfrac{k_x}{k_y}\dfrac{16}{r^2}\right\}^{1/2} \right\}^{1/2} .$$

The numerical values of the parameter are

$$k_x = 2220 \times 16 = 35,500 \text{ lb/in.},$$

$$k_y = 2700 \times 16 = 43,200 \text{ lb/in.},$$

$$r^2 = \frac{I_{cg}}{W} = \frac{250,800}{42,300} = 5.92 \text{ ft}^2.$$

With these values the frequencies' ratios are

$$\frac{\omega}{\omega_y} = 1.81 \text{ and } 0.849.$$

$$\omega_1 = 1.81\omega_y; \text{ and } \omega_2 = 0.849\omega_y.$$

Since

$$\omega_y = \left(386 \times \frac{43,200}{42,300}\right)^{1/2} = 19.81 \text{ rad/sec},$$

$$\omega_1 = 35.8 \text{ rad/sec},$$

and

$$\omega_2 = 16.8 \text{ rad/sec};$$

from this

307

$$f_n = \frac{\omega_1}{2\pi} = \frac{35.8}{2\pi} = 5.7 \text{ cps},$$

and

$$f_{n_2} = \frac{168}{2\pi} = 2.67 \text{ cps}.$$

A decoupled horizontal natural frequency for the system would be equal to

$$f = 3.133 \left(\frac{34,900}{43,300}\right)^{1/2} = 2.85 \text{ cps}.$$

MILITARY MOUNTS

Requirements for isolation systems of military mounts have been well established by the Navy, Army, Air Force, and so on, in their specifications; it was therefore not the intent of the author to discuss in detail the particular specialties associated with combat vehicles and other portable field equipment. The detailed discussion about springs was, however, considered of some value. The durability of the isolators and their capability to stand very rough and long operational service and at times exceedingly great destructive forces depends upon three main physical characteristics: The relation between the pitch diameter of coil and its wire diameter; the type of enclosure containing the spring, and how well it protects the spring or springs; and the type of steel used in the spring. Dynamic stress considerations will include prediction of buckling and unseating of coil springs, sidewall deflections, surge wave action in compressive helical springs, initial tension effects, creep by high temperature effects, residual stresses, velocity of expansion, and the like.

For the case of liquid springs, as discussed previously, the type of fluid and the "how" to seal it tightly are problems of extreme importance in shock mounting assembly designs.

There are so many types of spring steels that they cannot be listed here. It suffices to say that some are better for corrosion; some are better for temperature resistance well above 1000°F; and others are better for shock. In general, their elastic limit may well exceed 100,000 psi up to 350,000 psi, and their ultimate may well reach 340,000 psi. Super-alloy springs NS-(L605) are good for several hundred cycles at 1100° and 1400°F.

CONCLUSIVE REMARKS

An effort was made herein to cover the treatment of four different configurations subjected to dynamic loads, including the effects of shocks from nuclear weapons, with the objective in mind of demonstrating that the general theory of vibration can be applied efficiently to actual systems, which often diverge considerably from the idealized ones around which mathematical theories are evolved. On the other hand, no effort was made to conceal the idea that similar procedures and analyses require many years of experience in the field of vibrations.

Two contrasting sections are presented in the paper: The first one is a chronological synthetic presentation of the theoretical concepts associated with vibration and shock environment; the second one is a practical approach to the design and proportioning of isolation mounts. The title of the paper seems to imply that no theoretical development will be found in the contents, no paper on vibration and shock can, however, be completely devoid of some theoretical background. For the selection of the methods used in the applications, it was necessary to discuss how rationalized interpretation of theories often lead to a better understanding of some abstract principles enunciated in the form of mathematical expressions; one worthy of mentioning is D'Alembert's inertia force principle.

From some of the applications it results that, at least for the present, the use of a vibration analysis is sometimes of limited value. In the case of the stack, for instance, knowledge of its natural frequency and the associated wind velocity is not sufficient data for estimating the magnification factor necessary for completing the analysis. The knowledge that a configuration becomes a self-excited system does not represent a conclusive step for solving the inherent problem defining the field of analysis of the configuration.

Similarly, when referring to the design of the isolation mount for the crib, installed within an underground silo subject to nuclear shock, it is necessary to state emphatically that it is very difficult to estimate the magnitude of the attenuation caused by the interaction between soil and the soil around it.

Appendix A

LIST OF SYMBOLS

A = area, sq in. or sq ft (amplitude)

A, B = constants of integration (dimensions)

a, b, c, d = dimensions (ft)

C = constant of integration

c = coefficient of viscous damping (lb/sec/in.)

C_D = drag coefficient

C_L = coefficient of lateral forces resulting from vortex shedding

D_i = inner diameter of stack (ft)

D_o = outer diameter of stack (ft)

d = diameter of cylinder (ft)

E = Young's modulus (psi)

f = forcing frequency (cps)

f_n = natural frequency (cps)

g = acceleration due to gravity (in./$\sec^2$)

h = height (ft)

I = moment of inertia, polar moment of inertia (ft^4, in.^4)

i, j = subscripts in summation from i to j

$\ln$ = natural logarithm

K = linear stiffness, lb/in. (used with subscripts x, y, h, and v indicates stiffness direction)

$L, 1$ = lengths (ft, in.)

M = moment (mass)

m = total mass of rigid body (lb/$\sec^2$/in.)

n = number

p = circular frequency (rad/sec)

q = generalized coordinates

R = Reynolds number

r = radius (ft or in.)

S = shear lb = Strouhal number

T = transmissibility

t = time, sec, thickness of stack shell (in.)

V, v = velocity of a rigid body (ft/sec, mph)

W = total weight of a rigid body (lb)

w = unit weight (lb/cu ft)

y = statical deflection (ft, in.)

X, Y, Z = coordinate axes

x, y, z = in a single-man system, displacement or a rigid body in direction of X, Y, Z axes, respectively, in. Also subscripts indicating displacements of mass M_x, M_y, M_z in the directions X, Y, Z.

Δ = deflection

Δx = small length (ft or in.)

δ_{st} = static deflection (ft, in.)

ρ = mass density (lb/cu ft)

ω = forcing circular frequency (rad/sec)

ω_n = natural frequency (rad/sec)

ν = kinematic viscosity

REFERENCES

1. I. Newton.

2. G. Galileo, Dialogues Concerning Two New Sciences (1638) (Transl. The MacMillan Co., New York, 1914).

3. J. D'Alembert, Traité de Dynamique (1743).

4. J. L. Lagrange, Méchanics Analitique (1788), Tome I, p. 390.

5. G. L. Downey and G. M. Smith, Advanced Dynamics (International Text Book Company, Scranton, Pennsylvania, 1960), pp. 268-270; 298-303.

6. N. O. Myklestad, Fundamentals of Vibration Analysis (McGraw-Hill Book Co., Inc., New York, 1956), pp. 204-207.

7. M. G. Salvadori, Trans. Am. Soc. Civ. Engrs., 119:171-206 (1954).

8. J. W. Strutt (Baron Rayleigh), Theory of Sound (2d. ed., Vols. I and II, 1894), Republished, Dover Publications, New York.

9. L. S. Jacobsen and R. S. Ayre, Engineering Vibrations (McGraw-Hill Book Co., Inc., New York, 1958), pp. 71-121.

10. J. Hannah and R. C. Stephens, Examples in Mechanical Vibration (Edward Arnold Publishers Ltd, London, 1956), pp. 38-40.

11. W. T. Thomson, Mechanical Vibrations (Prentice-Hall, Inc., Englewood Cliffs, New Jersey, 1963), pp. 33-35.

12. A. Stodola, Steam and Gas Turbine, Vol. I (McGraw-Hill Book Co., Inc., New York, 1927), pp. 449-455.

13. G. A. Leonards, Foundation Engineering (McGraw-Hill Book Co., Inc., New York, 1962), pp. 769-809.

14. J. A. Blume, Proceedings, World Conference on Earthquake Engineering, Berkeley, California (Nov. 1-27, 1956).

15. C. S. Whitney, B. G. Andersen, and M. G. Salvadori, J. Am. Concr. Inst., 23:5-28 (1951).

16. L. S. Jacobsen, Trans. Am. Soc. Civ. Engrs. 65:402-439 (1939).

17. L. M. Hoskins and J. D. Galloway, Trans. Am. Soc. Civ. Engrs., Vol. 66, No. 8, part 2, 269-322.

18. D. E. Hudson and G. W. Housner, Trans. Am. Soc. Civ. Engrs., 122:705-721 (1957).

19. S. Timoshenko, Vibration Problems in Engineering, 3d ed. (D. Van Nostrand Company, Inc., Princeton, N. J., 1955).

20. J. P. Den Hartog, Mechanical Vibrations (McGraw-Hill Book Co., Inc., New York, 1956).

21. W. L. Pagon, Eng. News-Record (July 12, 1934).

22. W. L. Dickey and G. B. Woodruff, Trans. Am. Soc. Civ. Engrs., 121:1054-1087 (1956).

23. E. A. Dockstader, W. F. Swiger, and E. Ireland, Trans. Am. Soc. Civ. Engrs., 121:1088-1112 (1956).

24. M. S. Ozker and J. O. Smith, Trans. Am. Soc. Civ. Engrs., 78:1381-1391 (1956).

25. E. Tyler, Phil. Mag. Ser. 7, 11:849-890 (1931).

26. L. Prandtl and O. G. Tietjens, Applied Hydro- and Aeromechanics (McGraw-Hill Book Co., Inc., New York, 1934).

27. E. F. Relf and L. F. G. Simmons, "Frequency of the Eddies Generated by the Motion of Circular Cylinders Through a Fluid," Report and Memoranda, No. 917, Aeronautical Research Committee, London (1924).

28. G. B. Woodruff, The Design of Self-Supporting Steel Stacks, Mode in Designing with Steel (Kaiser Steel Corporation, Fontana, California, May 1960), Vol. 6, No. 1.

29. Y. C. Fung, The Theory of Aeroelasticity (John Wiley & Sons, Inc., New York, 1955) p. 68.

30. A. Thorn, "The Strength and Position of the Eddies Behind a Circular Cylinder," Report and Memoranda, No. 1373, Aeronautical Research Committee, London (1931).

31. A. Roshke, NACH TN 3169, July 1964, Natl. Advisory Comm. for Aeronauticas, Washington, D. C.

32. R. R. Bradshaw, Proc. Am. Soc. Civ. Engrs., Vol. 90, No. ST3, part 1 (June 1964).

33. A. Roshko, J. Aeronaut. Sci., 124-132 (Feb. 1955).

34. J. P. Den Hartog, Proc. Natl. Acad. Sci., U.S., Vol. 40 (1954).

35. Y. C Fung, J. Aerospace Sci., Vol. 27, No. 11, 802 (Nov. 1960).

36. R. H. Scanlan and R. Rosenbaum, Aircraft Vibration and Flutter (The MacMillan Co., New York, 1951).

37. C. Inglis (Sir), Applied Mechanics for Engineers (Dover Publications, Inc., New York, 1963), pp. 373-376.

38. R. D. Mindlin, Dynamic of Package Cushionings, Bell System Tech. J., Vol. 24, Nos. 3 and 4, pp. 353-461 (July-Oct. 1945).

39. I. Vigness, "Some Characteristics of Navy 'High Impact' Type Shock Machines," Proc. SESA, Vol. 5, No. 1, pp. 101-110 (1947).

40. J. P. Walsh and R. E. Black, "The Determination of Shock Isolator Performance," NRL Report 3596 (1950).

41. C. E. Crede, Vibration and Shock Isolation (John Wiley & Sons, Inc., New York, 1962), pp. 88-214; 89.

42. G. F. Kinney, Explosive Shock in Air (The MacMillan Company, New York, 1962).

43. D. D. Barkan, Dynamic of Bases and Foundations (McGraw-Hill Book Co., Inc., New York, 1958).

44. F. R. Erskine Crossley, Dynamics in Machines (The Ronald Press Co., New York, 1954).

45. C. T. Morrow, Shock and Vibration Engineering (John Wiley & Sons, New York, 1963), Vol. 1, pp. 68-88; 105-146.

46. I. Vigness, "Navy High-Impact Shock Machines for Lightweight and Medium weight Equipment," NRL Report 561 (June 1, 1961).

47. E. Strick, "Propagation of Elastic Wave Motion from an Impulsive Source along a Fluid-Solid Interface," Phil. Trans. Roy. Soc., Series A, Vol. 251 (1959).

48. Ewig, Jardetzky, and Press, Elastic Waves in Layered Media (McGraw-Hill Book Co., Inc., New York, 1957).

49. J. L. Sackman, Proc. Am. Soc. Civ. Engrs., Vol. 87, No. EM4 (Aug. 1961).

50. F. M. Sauer, "Ground Motion Produced by Above Ground Nuclear Explosions," AFSWC, TR-59-71(S).

51. S. D. Wilson and E. A. Sibley, Proc. Am. Soc. Civ. Engrs. Vol. 88, No. SM6, pp. 1-3 (1962).

52. W. Heierli, Proc. ASCE. Vol. 88, No. SM6, pp. 33-63 (1962).

53. R. H. Smith and N. M. Newmark, "Numerical Integration for One-Dimensional Stress Wave," SRS, No. 162, Dept. of Civ. Engrg., Univ. of Ill., Urbana (Aug. 1958).

54. M. L. Baron, H. H. Bleich, and P. Weidlinger, "Theoretical Studies on Ground Shock Phenomena," The MITRE Corp. SR-19 (Oct. 1960).

55. "Research Studies of Stress Waves in Earth and Model Earth Media," Final Report, ARF Project, No. K148, Contract No. AF 29(601)-1167 for AFSWC, AFSWC-TR 60-4 (Oct. 1959).

56. M. L. Baron and Matthew, J. Appl. Mech., ASME, Paper No. 61 APM 26 (Sept. 1961) pp. 347-354.

57. R. R. Robinson, "Investigation of Silos and Tunnel Linings," Final Report No. AF 29 (601)-2596, for AFSWC, Armour Research Foundation, Chicago, Illinois (Dec. 1961).

58. M. G. Salvadori, R. Skalack, and P. Weidlinger, Transactions New York Academy of Sciences, Series II, Vol. 21, No. 5 (Mar. 1959), pp. 427-434.

59. A. M. Soldate and J. F. Hook, "A Theoretical Study of Structure-Medium Interaction," Natl. Eng. Science Co., Final Report Contract AF 29(601) for AFSWC (Nov. 1960).

60. T. G. Morrison, "A Simplified Theory of Interaction of Shell Structures with Soil," Shock and Vibration Bulletin No. 29 (July 1961).

61. D. C. Dowell, "Response of Statically and Dynamically Loaded Cylinders Embedded in Granular Materials" (Doctoral Thesis)

(Iowa State Univ. of Science and Tech., Ames, 1964), AD-441 085 Div 25, 13, 18.

62. C. P. Burgess, NACA, TN 746 (Jan. 1940).

63. V. I. Novotorzev, Bulletin No. 70, Academie des Sciences USSR (1935).

64. J. G. Perri, "Discussion," Trans. Am. Soc. Cir. Engrs., $\underline{127}$:902-906 (1962).

*   *   *

DISTRIBUTION

Aberdeen Proving Ground, Md.
    Att: Ballistic Research Lab.   1
    Att: Development & Proof Services   1
    Att: Physical Test Lab.   1

Advisory Group on Electron Tubes, New York
    Att: Secretary   1

Air Defense Command, Ent AFB
    Att: Deputy for Civil Engineering   1
    Att: ADIRP   1

Air Force Packaging Evaluation Agency,
  Brookley AFB
    Att: MOSPR   1
    Att: MONE   1

Air Proving Ground Center, Eglin AFB
    Att: PGTRI, Technical Library   1

Air Force Headquarters, DC
    Att: Operations Analysis Off.,
         Off. Vice Chief of Staff, Library   2
    Att: AFDRD-GW   1

Air Force Logistics Command, W-PAFB
    Att: G. P. Civille, MCTEP   1

Air Force Missile Development Center,
  Holloman AFB
    Att: RRRT/Miss R. Porter   1
    Att: MDS/Dr. M. G. Jaenke   1
    Att: MDSGL-2/Mr. H. J. Dunbar   1
    Att: MDSGS/Mr. J. H. Gengelbach   1
    Att: MDSTE/Mr. P. N. Sonnenburg   1

Air Force Missile Test Center, Patrick AFB
    Att: MT LLL-3 (Classified Material)   2
    Att: MU-135, Technical Library
         (UNCLASSIFIED)   1

Air Force Office of Scientific Research, DC
    Att: Library   1

Air Force Regional Civil Engineer
    Att: North Atlantic Region,
         AFRCE-NA-A   1
    Att: South Atlantic Region,
         AFRCE-SA-E   1

Air Force Rocket Propulsion Lab., Calif.
    Att: Mr. A. J. Davies (RPFDE)   1
    Att: Mr. R. A. Silver   1

Air Force Systems Command, Andrews AFB
    Att: Technical Library   2

Air Force Weapons Laboratory, Kirtland AFB
    Att: Development Test Division   1
    Att: Dr. W. E. Fisher, WLRS   1
    Att: SWOI 631-276   1

Army Air Defense Center, Ft. Bliss
    Att: Technical Library   1

Army Chemical Center, Maryland
    Att: Library   1

Army Electronics Materiel Agency, Phila.   1

Army Electronics Materiel Support Agency,
  Ft. Monmouth   1

Army Electronics R&D Laboratory,
  Ft. Monmouth
    Att: SELRA/SL-ADT   1
    Att: SELRA/SL-PEE   1
    Att: SELRA/SL-PRT   1
    Att: SELRA/SL-G   1
    Att: SELRA/SL-GTF   1
    Att: Mr. J. J. Oliveri   1

Army Engineer District, New York
    Att: NANGD   1

Army Engineer R&D Laboratories, Ft. Belvoir
    Att: Package Development Branch   1
    Att: Mr. A. Carolla   1
    Att: Director of Research   1
    Att: Chief, Spec. Proj. Branch   4

Army Engineer Waterways Experiment
  Station, Vicksburg
    Att: Mr. J. M. Strange   1

Army Erie Ordnance Depot, Pt. Clinton
    Att: Chief, Materiel Testing Div.   1

Army Materials Research Agency, Watertown
    Att: Dr. Reinier Beeuwkes, Jr.   2

Army Materiel Command, DC
    Att: AMCRD-RS-CM   1

Army Materiel Command, Redstone Arsenal
    Att: Technical Library   4

Army Missile Command, Redstone Arsenal
    Att: AMSMI-RB   1
    Att: AMSMI-RG   1
    Att: AMSMI-RL   1
    Att: AMSMI-RS   1
    Att: AMSMI-RT   1
    Att: AMSMI-RTR, Mr. J. M. Taylor   1
    Att: AMSMI-RSM, Mr. E. J. Wheelahan   1

Army Mobility Command, Centerline
    Att: Mr. Otto Renius   1

Army. Office Chief of Engineers, DC
    Att: ENGMC-EM   2

Army, Office of Quartermaster General, DC
    Att: Military Planning Division   1

314